

Western Australian School of Mines

**Design, Construction and Monitoring of
Hard Rock Tunnels at Great Depth**

Christopher William Drover

**This thesis is presented for the degree of
Doctor of Philosophy
of
Curtin University**

October 2018

Declaration by the Author

To the best of my knowledge and belief, this thesis contains no material previously published by any other person, except where due acknowledgement has been made.

This thesis contains no material which has been accepted for the award of any other degree or diploma in any university.

Signed:

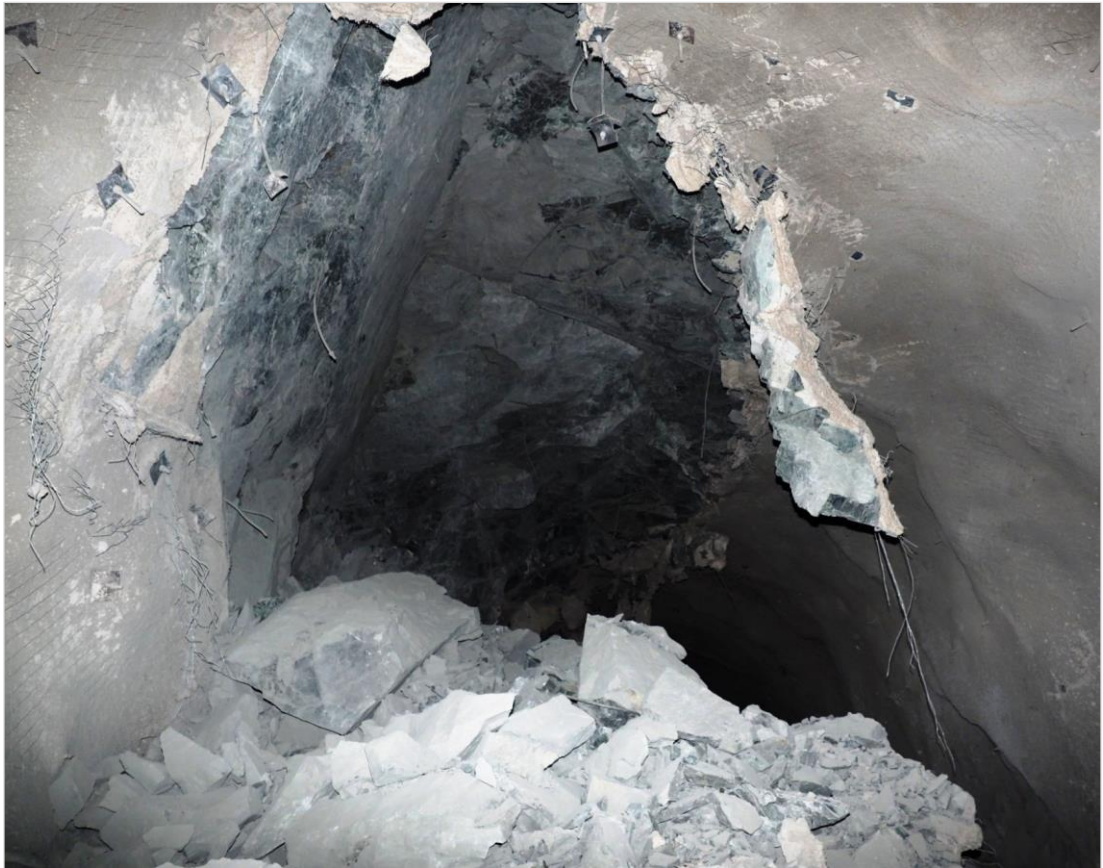


October 31st, 2018

..... Date:

Christopher Drover

Violent stress-driven failure of a hard rock tunnel at great depth.



Abstract

The stability of access tunnels is one of the main engineering challenges in deep underground construction. Many underground hard rock mining operations are now reaching depths where the induced stresses are such that sudden and violent failure of the excavations can occur very soon after construction. The loading conditions on the installed ground support schemes are often underestimated by conventional engineering design methods. Therefore, the actual loading conditions often exceed the ground support capacity. This often results in failure of the excavations and, in extreme cases, potentially closure of mining operations amounting to hundreds of millions of dollars in lost production. More frequently, violent excavation instability at great depth causes operational delays, costly and unplanned rehabilitation, as well as risks to worker safety. In order to address this challenge, this thesis proposes a modern, innovative approach to the design and construction of development at great depth.

The proposed excavation design process follows six main steps. The first step is to characterise the rock mass structure, strain, strength and stress. The second step is a stability assessment, which identifies the predictable modes of excavation failure based on the rock mass characterisation. The third step is the definition of an excavation geometry which is harmonic to the high stress conditions. The fourth step is to prepare a site-specific face destressing drill and blast design. The fifth step is to accurately quantify the expected loading conditions on ground support. The method of doing so is uniquely analytical and probabilistic. It is based on the natural mechanical relationships between rock strength, structure, induced stress and the physical characteristics of the instability, including its mass and ejection velocity. The sixth and final stage of the design process is to specify a ground support scheme arrangement with sufficient strength and displacement capacity to exceed the rock mass demand.

The proposed construction process differs from the common convention in two main aspects. The first difference is the implementation of development face destress blasting, which is designed to reduce the stiffness of the rock mass surrounding the face and in particular the strain gradients in this zone. This has the flow-on effect of reduced violent instability at the face. The second difference is the increased mechanisation of the ground support installation, which significantly reduces the need for human-machine interactions close to unsupported and potentially unstable ground.

The novel design and construction process was tested at a deep mine site. Two full-sized parallel tunnels were developed in close proximity within a high stress environment where failure had previously occurred. The first tunnel was constructed as the control. It had a conventional profile shape, blast design and ground support scheme. A second tunnel was designed and developed according to a novel method. It had a semi-elliptical shape, face distress blasting and a fully-mechanised installation of a ground support scheme. Development face distress blasting was numerically optimised prior to the trials using the HSBM software. The blast concept was designed to create a series of parallel, blast-induced fractures oriented sub-parallel, yet almost oblique to the major principal stress, thus permitting strain energy dissipation from the rock mass via shear, with minimal deformation. The ground support scheme consisted of a unique twin-layer arrangement of reinforcement and surface support, with extremely high energy dissipation capacity in the order of 65kJ/m^2 .

The performance of the excavations during and after construction was consistent with the predictions of the innovative stability assessment methodology, both in terms of the mechanisms of instability and the unstable structurally-controlled block geometries. The ground support scheme was installed safely and successfully using fully mechanised equipment. High resolution seismic monitoring data from the conventional and destressing development was compared. Quantitative spatial analysis of the seismic event counts, radiated energy and co-seismic inelastic rock mass damage indicated that distress blasting had the desired effect of softening the rock mass response surrounding the face. The seismic source mechanisms indicated that distress blasting generated a much wider variety of failure modes, mostly associated with natural joint structures. This behaviour reduced the potential for larger and more violent instabilities. Visual observations of the blast-induced fracture networks indicated that the fracture interactions between destressing charges predicted by the HSBM were achieved. The orientation of the interacting destressing fractures was controlled by the prevailing stress conditions and also the natural joint structures.

Overall, the implementation of this design and construction trial provided a successful standard for future development of hard rock tunnels at great depth. The methodology tested during this research may now be implemented elsewhere, in order to improve the safety and economic viability of deep underground infrastructure in hard rock where the high stress conditions are currently not able to be safely or reliably managed.

Acknowledgements

This thesis exists because of the opportunity offered to me by Professor Ernesto Villaescusa. I would like to extend my sincere thanks to Professor Villaescusa for the enjoyable years I've spent working on this research.

I greatly appreciate the assistance of the Rock Mechanics staff at the Western Australian School of Mines, in particular for their work on rock strength testing and assisting me with student administration.

I am very grateful to Dr. Italo Onederra of the University of Queensland for preparing the HSBM models and offering support and advice regarding development blasting.

My appreciation is extended to the Institute of Mine Seismology for their assistance commissioning seismic hardware and processing raw seismic data.

For generously loaning a 3D laser surveying instrument and providing assistance processing the recorded data, I would like to thank Evan Jones and Beck Engineering.

Thank-you to Riaan Mouton of ASST Pty Ltd for supplying all radar geophysics hardware, assisting with the surveys and providing expert advice regarding the radar geophysics data.

This research was made possible by the sponsors of the *Mine Development at Great Depth* research project, who I gratefully recognise for their commitment to innovation in deep mining.

Finally, a simple and heartfelt thanks to my family for their ever-present support.

Author's Statement of Previous Publications

The following is a list of several publications by the author which are based either in whole or in part on the research carried out during the preparation of this thesis.

Drover, C. & Villaescusa, E., 2015. Performance of shotcrete surface support following dynamic loading of mining excavations. Proceedings of Shotcrete for Underground Support XII, Singapore.

Drover, C. & Villaescusa, E., 2015. Estimation of dynamic load demand on a ground support scheme due to a large structurally controlled violent failure - a case study. Journal of Mining Technology, 125(4).

Drover, C. & Villaescusa, E., 2016. Field performance of fully encapsulated reinforcement during violent failure events. Proceedings of the 7th International Conference & Exhibition on Mass Mining, Sydney, Australia.

Villaescusa, E., Kusui, A., Drover, C., 2016, Ground support design for sudden and violent failures in hard rock tunnels, Proceedings of the 9th Asian Rock Mechanics Symposium, Bali, Indonesia.

Drover, C., Villaescusa, E., Onederra, I., 2018, Face destressing blast design for hard rock tunnelling at great depth, Journal of Tunnelling and Underground Space Technology, Volume 80, pp.257-268.

Table of Contents

Declaration by the Author	III
Abstract	VII
Acknowledgements	XI
Author's Statement of Previous Publications	XIII
List of Abbreviations	XXI
List of Symbols.....	XXIII
List of Units.....	XXV
1 Introduction.....	1
1.1 Background	2
1.2 Research Objectives.....	4
1.2.1 Excavation Design Methodology	4
1.2.2 Experimental Development Construction Process	5
1.2.3 Monitoring of the Rock Mass Response	5
1.3 Thesis Structure	6
2 Current Knowledge & Technology.....	7
2.1 Rock Mass Characterisation.....	8
2.1.1 Stress.....	8
2.1.2 Strain.....	11
2.1.3 Structure	12
2.1.4 Strength.....	14
2.2 Excavation Stability.....	16
2.2.1 Boundary Stress.....	17
2.2.2 Ratio of Strength to Induced Stress	20

2.2.3	Spalling Failure	21
2.2.4	Structurally Controlled Failure	23
2.2.5	Fault Rupture	24
2.2.6	Shear Failure Mode of Pillar Crushing.....	26
2.2.7	Damage and Deformation Prior to Violent Failure	27
2.3	Rock Mass Demand.....	28
2.3.1	Mass of Instability	29
2.3.2	Ejection Velocity and Direction.....	29
2.3.3	Displacement.....	35
2.3.4	Displacement due to Fault Rupture.....	36
2.3.5	Shear Failure Mode of Pillar Crushing.....	39
2.4	Ground Support.....	41
2.4.1	Reinforcement Systems	41
2.4.2	Surface Support Systems	51
2.4.3	Construction Methodology	58
2.5	Face Destress Blasting	61
2.5.1	Applications	62
2.5.2	Mechanisms	62
2.5.3	Blasthole Patterns.....	66
2.5.4	Design Parameters.....	68
2.5.5	Numerical Analysis	71
2.5.6	Quantitative Analysis	73
2.6	Knowledge Gaps	78
2.6.1	Excavation Stability	78
2.6.2	Ground Support Design and Construction.....	78
2.6.3	Development Destressing	79

3	Research Methodology	80
3.1	Excavation Design Methodology	81
3.2	Development Construction.....	82
3.3	Rock Mass Monitoring	83
4	Design	85
4.1	Trial Site Description.....	86
4.2	Development Layout.....	86
4.3	Rock Mass Characterisation.....	89
4.3.1	Geological Setting	89
4.3.2	Structural Geology.....	90
4.3.3	Rock Strength Properties	94
4.3.4	Stress Conditions	106
4.4	Stability Assessment	110
4.4.1	Stress-Driven Instability and Failure Mechanisms.....	110
4.4.2	Mass of Instability	116
4.5	Excavation Design (Control Tunnel).....	138
4.5.1	Profile Geometry	138
4.5.2	Profile Drilling and Blasting	139
4.5.3	Ground Support	143
4.6	Excavation Design (Experimental Tunnel).....	144
4.6.1	Profile Geometry	144
4.6.2	Development Face Destress Blasting	144
4.6.3	Ground Support	174
5	Construction	199
5.1	Development Strategy.....	201

5.2	Development Rate	204
5.3	Development Blasting with Face Destressing	205
5.3.1	Profile Survey Control.....	205
5.3.2	Drilling for Destressing	206
5.3.3	Development Blast Hole Drilling.....	207
5.3.4	Securing the Face	208
5.3.5	Destressing Blast Hole Surveys	208
5.3.6	Charging, Priming and Stemming Destressing Blast Holes	211
5.3.7	Charging and Priming Development Blast Holes	213
5.3.8	Detonator Tie-In and Shot-Firing.....	213
5.3.9	Seismic Exclusions.....	214
5.3.10	Waste Rock Removal	214
5.4	Ground Support Scheme Implementation	214
5.4.1	Clearing Temporary Support	215
5.4.2	Mechanical Scaling	216
5.4.3	Structural Geological Mapping with Photogrammetry	217
5.4.4	Shotcrete Application	218
5.4.5	Primary Reinforcement Mark-Up	219
5.4.6	Installation of Primary Reinforcement and Mesh	221
5.4.7	Secondary Shotcrete Layer Application	229
5.4.8	Installation of Temporary Face Support.....	230
5.4.9	Primary to Secondary Support Installation Sequence	231
5.4.10	Secondary Reinforcement Collar Mark-Up and Drilling	236
5.4.11	Installation of Secondary Reinforcement	236
5.4.12	Installation of Secondary Mesh and External Fixtures	237
5.4.13	Securing of Secondary Mesh Overlaps	241
5.4.14	Final Ground Support Scheme Arrangement.....	243

6	Monitoring & Analysis.....	245
6.1	Local Seismic Monitoring System Design.....	247
6.1.1	Sensor Type.....	247
6.1.2	Array Size and Sensor Locations	248
6.1.3	3D Location Error.....	252
6.1.4	Source Parameter Sensitivity	255
6.1.5	Velocity Model Calibration.....	259
6.1.6	Ray Tracing Location Calculations	266
6.1.7	Location Method and Velocity Model Testing	270
6.2	Seismic Response to Development.....	277
6.2.1	Seismic System Performance Assessment	277
6.2.2	Seismogenic Zone Spatial Characteristics	287
6.2.3	Time History of Seismic Parameters	293
6.2.4	Distribution of Seismicity Across the Excavation Surfaces	300
6.2.5	High Resolution Spatial Analysis.....	303
6.2.6	Source Mechanism Solutions	312
6.2.7	Activity Analysis	334
6.3	Blast-Induced Fracture Network Characteristics.....	338
6.3.1	Modes of Fracturing	339
6.3.2	Cross-Borehole Fracture Interactions	345
6.4	Excavation Profile Performance.....	350
6.5	Ground Penetrating Radar Geophysics.....	358
6.5.1	GPR Instrumentation	359
6.5.2	GPR Survey Methodology	361
6.5.3	Survey Results	364

7	Conclusions and Recommendations.....	369
7.1	Conclusions.....	370
7.2	Recommendations for Future Research.....	375
	References.....	378
	List of Figures.....	393
	List of Tables.....	401
	Appendix A – HSBM Modelling Results.....	403
	Appendix B – Seismic Data.....	423
	Appendix C – GPR Radargrams.....	441

List of Abbreviations

Abbreviation	Description
AHD	Average hypocentral distance
ANFO	Ammonium nitrate fuel oil
BHR	Borehole radar
CLVD	Compensated linear vector dipole
E	East
ENE	East northeast
FRS	Fibre-reinforced shotcrete
GPR	Ground penetrating radar
HED	High energy dissipation
HSBM	Hybrid stress blasting model
HT	High tensile
KE	Kinetic energy
MRS	Mesh-reinforced shotcrete
mH	Height (m)
mW	Width (m)
N	North
NONEL	Non-electronic detonator
OSV	On-site visualisation
PPV	Peak particle velocity (m/s)
S	South
SSW	South southwest
StDev	Standard deviation
UCS	Uniaxial compressive strength
UTS	Ultimate tensile strength
VOD	Velocity of detonation
W	West
WASM	WA School of Mines
WSW	West southwest

List of Symbols

Symbol	Description
ϕ	Friction angle ($^{\circ}$) or Diameter (mm)
γ	Unit weight (T/m ³)
δ	Deformation (mm)
ϵ_x	Normal strain
σ_1	Major principal stress (MPa)
σ_2	Intermediate principal Stress (MPa)
σ_3	Minor principal stress (MPa)
σ_c	Uniaxial compressive strength (MPa)
σ_x	Normal stress (MPa)
σ_{max}	Maximum tangential stress (MPa)
σ_{ave}	Average pillar stress (MPa)
a	Tunnel radius (m)
c	Cohesion (MPa)
d_f	Depth of failure (m)
d	Distance (m)
\vec{E}	Direction vector of violent ejection
E	Modulus of elasticity (GPa)
F	Force/Load (kN)
G	Modulus of rigidity (GPa)
K	Modulus of compressibility (GPa)
M_R	Richter magnitude
M_L	Local magnitude
m_b	Mass of a tetrahedral block (T)
m_u	Mass of instability (T/m ²)
ρ	Density (T/m ³)
U	Strain energy (J)
u	Strain energy density (J/m ³)
V	Volume (m ³)
ν	Poisson's ratio
v_e	Ejection velocity (m/s)

List of Units

Unit	Description
GPa	Gigapascals
g	Grams
g/cc	Grams per cubic centimetre
J	Joule
kPa	Kilopascal
kJ	Kilojoule
kbar	Kilobar
kJ/kg	Kilojoules per kilogram
kJ/m ²	Kilojoules per square metre
kN	Kilonewton
L/kg	Litres per kilogram
MPa	Megapascal
m	Metres
mm	Millimetres
m/s	Metres per second
T/m ²	Tonnes per square metre

Chapter 1

Introduction

1.1 Background

Underground hard rock mining and tunnelling operations are reaching depths where the induced stresses are such that sudden and violent failure of the excavations can occur very soon after construction. Several mines have experienced instability events where the sudden energy demand on the ground support scheme exceeded 80kJ/m^2 (Drover & Villaescusa, 2015b). This level of demand is often not able to be safely managed by the ground support technologies that are available on-site. Failures of this nature occasionally force the closure or suspension of operations. More frequently, violent rock mass failures at great depth cause operational delays, costly and unplanned excavation rehabilitation and risk to worker safety.

Underground mass mining operations are widely viewed as the dominant mineral extraction methods of the future, given that the near surface resources are progressively being depleted. However, rock mass failures of a sudden and violent nature are threatening the ability of the mining industry to continue doing business at great depth. It is often the case that mass mining operations require advanced development access into deep and highly stressed work areas prior to the commencement of production. For example, deep block caving operations are a capital intensive mining method which carry the risk of stress-driven failure of the access infrastructure very early during the project life cycle, both during the development phase and then again during initiation of caving.

The trend to mine much deeper orebodies results in increased loading demands on excavations and installed ground support schemes, due to the increase in rock stress with depth. In many cases, this increase in demand is not met with a commensurate increase in the ground support scheme capacity. Operational methodologies also frequently remain conventional. That is, aligned with historic practices more suited to low or medium rock stress environments. Such conventional practices include empirical ground support design methods, square excavation shapes non-harmonic to the induced stress field and development blasting practices. A step change improvement in design, construction and monitoring methodology is required if deep hard rock tunnels are desired to be safely and economically constructed at great depth.

Chapter 1: Introduction

During the last 20-25 years, a significant body of rock mechanics research has been completed by staff of the Western Australian School of Mines (WASM). This research covers a wide range of topics relevant to the design, construction and monitoring of deep hard rock tunnels. A short list of relevant work includes:

- Characterisation of jointed rock masses (Villaescusa, 1991)
- Deterministic and probabilistic structural block analysis (Windsor, 1999)
- Rock stress measurements from oriented core (Villaescusa, et al., 2002)
- Concepts of reinforcement and surface support mechanics (Thompson & Windsor, 1992) (Windsor, 1997) (Windsor & Thompson, 1998) (Thompson, et al., 2012)
- Dynamic strength testing of rock reinforcement systems, (Player, et al., 2004) (Villaescusa, et al., 2005) (Villaescusa, et al., 2010)
- Dynamic strength testing of surface support systems (Villaescusa, et al., 2010) (Villaescusa, et al., 2012)
- Mechanical behaviour of hard rock tunnels under high stress (Kusui, 2015) (Kusui, et al., 2015).
- Dynamic Strength testing of combined ground support schemes (Villaescusa, et al., 2016a)

The next step in this ongoing research effort, and the focus of this thesis, is to formulate a holistic process for the safe and economical design and construction of hard rock tunnels at great depth, completed with local monitoring. This thesis will focus on deep tunnels at risk of violent stress-driven instability. It will include concise recommendations for data collection, rock mass characterisation, excavation design, quantitative estimation of energy demand on ground support and a ground support scheme arrangement for extremely high energy dissipation. The method will be analytical, rather than empirical, considering parameters of the physical mining environment. The input and output parameters of this method will be quantified according to standard engineering units of measure. The final process will be consistent and generally applicable at all stages of an underground tunnelling project cycle, given availability of the basic set of requisite input data.

1.2 Research Objectives

This thesis has three core objectives, as follows:

1. to propose and implement an innovative methodology for the design of hard rock tunnels at great depth,
2. to demonstrate the constructability of an experimental tunnel design, which includes face distress blasting and a ground support scheme for extremely high energy dissipation, while also constructing a second tunnel nearby as a control,
3. to monitor both tunnels and the adjacent rock mass, visually and with instrumentation, and compare the physical performance of each.

1.2.1 Excavation Design Methodology

Conventional excavation shapes and ground support schemes are failing to ensure the reliability and safety of development tunnels at great depth. This is evident in the many incidences of violent stress-driven excavation failure seen in deep mines around the world. The cause can frequently be attributed to naturally unstable square excavation shapes non-harmonic to the induced stresses, as well as installed ground support schemes having insufficient strength and displacement capacity to meet the rock mass demand. A core objective of this thesis is to propose a holistic design methodology for safe and economical development excavations at great depth. The design method seeks to improve the predictability of violent stress-driven excavation instability and the associated load demand on the ground support scheme.

The design process collates data from a rock mass characterisation program. The potential for violent excavation instability will then be estimated analytically, following an excavation stability hypothesis previously developed at the WA School of Mines. An excavation drill and blast design is then defined, which includes face destressing charges to reduce rock mass stiffness and hazardous strain concentrations adjacent the unsupported face. The design process then seeks to calculate the potential rock mass demand on ground support, based upon the probabilistic determination of structurally-controlled block geometries and their predictable velocity of ejection. From this demand result, a ground support scheme specification will be defined for extremely high energy dissipation. An overall objective is to document a design process which may be applied at any stage of the mine design cycle, provided that the requisite rock mass characterisation data is available.

1.2.2 Experimental Development Construction Process

Conventional tunnel development at great depth using standard jumbos requires the repeated exposure of the human workforce to potentially unstable rock at the face, for example when loading rock bolts and installing weld mesh. This presents a frequent safety risk. This thesis seeks to test and validate the constructability of a unique, fully-mechanised ground support scheme specification, which is suitable for tunnelling conditions of extremely high energy demand approaching 60 kJ/m^2 . The construction process seeks to achieve a more robust ground support scheme installation, with substantially reduced exposure of personnel to rock-related hazards at the unsupported face. This objective was addressed by conducting full-scale tunnelling trials at a deep mine site. A ground support scheme was installed using state-of-the-art mining equipment with a more advanced level of mechanisation than is presently used in Australian mining operations. The mechanised ground support installations were assessed for construction practicality and safety. A related objective of this thesis was also the simultaneous implementation of a novel face destressing blast design concept.

1.2.3 Monitoring of the Rock Mass Response

The third major objective was to use geotechnical instrumentation and visual observations to record and quantify the rock mass response to both the conventional and experimental development constructions. A local seismic monitoring system was designed and installed in order to examine the spatial and temporal micro-seismic response to face destressing. The system was designed to provide very high resolution seismic data at the scale of the tunnel face. Source mechanism analysis of the recorded seismicity was also conducted in an effort to determine what differences existed, if any, between the rock mass failure mechanisms associated with conventional and destressing development. Visual fracture mapping was also utilised to assess the response of natural and blast-induced structure in destressing mechanics, and how the resulting fracture networks were influenced by the stress and structural conditions. 3D laser-scanning was used to capture the final geometry of the tunnel profiles. These scans enabled comparisons between zones of instability and the structurally controlled block geometries that were predicted to occur by the design assessment. Ground penetrating radar (GPR) geophysical surveys were also carried out in an effort to determine the optimal radar frequency range for manufacture of a borehole instrument able to map blast-induced destressing fractures in-situ.

1.3 Thesis Structure

The structure of this thesis is summarised below.

Chapter 2 – Current Knowledge and Technology: a critical review of existing theory relevant to hard rock tunnel construction, including rock mass characterisation, excavation stability, rock mass demand, ground support and face destress blasting.

Chapter 3 – Research Methodology: the general outline of the investigation process for this research project, including excavation design, construction field trials, numerical investigations in rock blasting and geotechnical monitoring.

Chapter 4 – Design: a detailed process for the design of a deep tunnelling construction trial at great depth. This trial tested novel design techniques and was the main source of data for this research.

Chapter 5 – Construction: a description of the step-by-step process of tunnel construction for high stress conditions, including implementation of a semi-elliptical excavation profile, face destress development blasting and mechanised installation of high energy dissipation ground support.

Chapter 6 – Monitoring & Analysis: details of the monitoring techniques as well as analysis of data recorded during the tunnel construction trial. Data analyses examine high resolution local seismicity, visual mapping of blast-induced fracture networks, excavation profile surveys and ground penetrating radar geophysics.

Chapter 7 – Conclusions and Recommendations: concluding remarks drawn from the learnings of this research project, with recommendations for the direction of future investigation efforts.

Chapter 2

Current Knowledge & Technology

2.1 Rock Mass Characterisation

Prior to designing an excavation at great depth, it is necessary to characterise the rock mass conditions where the infrastructure will be constructed. The characterisation produces crucial input data needed to feed into the excavation design process. Accurate input data is important to the design, in order to ensure that the excavation stability is correctly assessed for the environment within which it is constructed. Windsor (2008) recommends that for engineering design purposes, the rock mass characterisation must examine four fundamental factors. These include:

- The *stress* conditions in the rock,
- The *strains* acting on the rock where the excavation is to be constructed,
- The natural rock *structure*, such as foliation, joint sets, shears and faults, and
- The *strength* properties of the rock.

Measurement, analysis and prediction, where necessary, of these four factors throughout the entire project cycle will assist to characterise the mechanical conditions acting on the excavation, as well as the rock mass response, at all stages of the service life.

2.1.1 Stress

The magnitude and orientation of the principal stresses are critical to an understanding of the loading conditions to which deep excavations will be exposed. The complete stress tensor can be measured directly via several methods. Common methods of stress measurement are the CSIRO Hollow Inclusion Cell (Worotnicki & Walton, 1976), the WASM Acoustic Emission method (Villaescusa, et al., 2002), Deformation Rate Analysis (Yamamoto, et al., 1990) and Hydraulic Fracturing (Hubbert & Willis, 1957). Ideally, multiple measurements of the in-situ stress should be taken outside the zone of influence of any pre-existing man-made excavations, in order to define the natural conditions. Measures should also be made at various depths, so as to define the stress gradient as a function of the overburden thickness.

Typical outputs of a stress measurement campaign include a pole plot of the principal stresses, showing magnitude, azimuth and plunge (Figure 1), as well as a stress magnitude gradient plot (Figure 2). It may be useful to present local data within the global dataset (Figure 3). Using the gradient plot, it is possible to estimate the in-situ stress magnitude at any depth within the elevation range of the measurements.

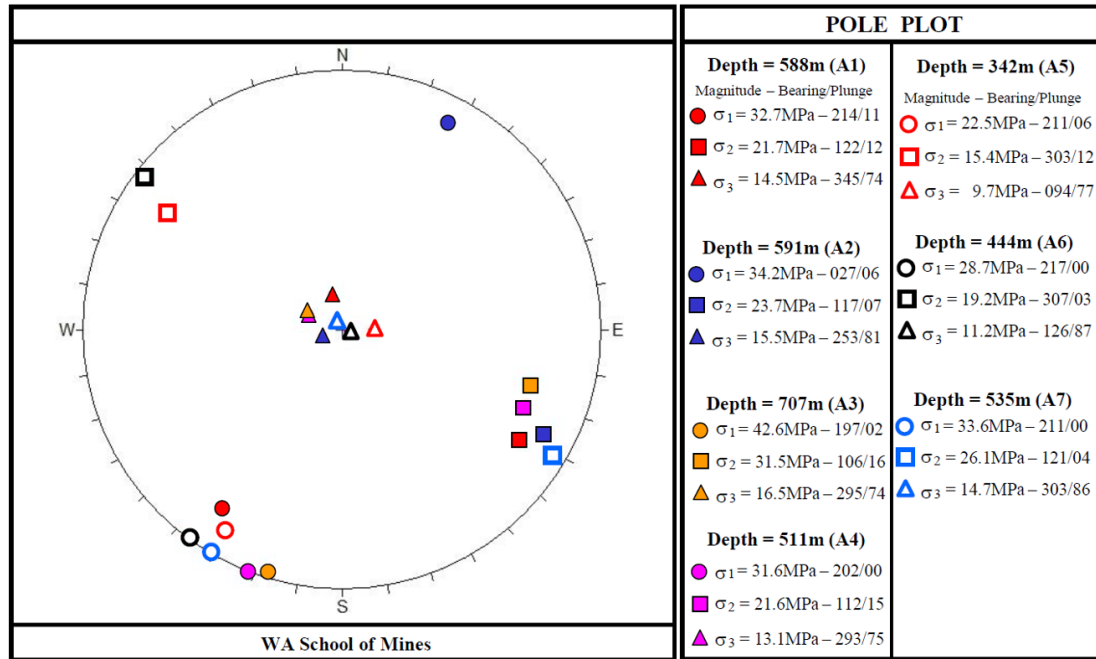


Figure 1 - Pole plot of WASM AE stress measurement data typically used for deep excavation design.

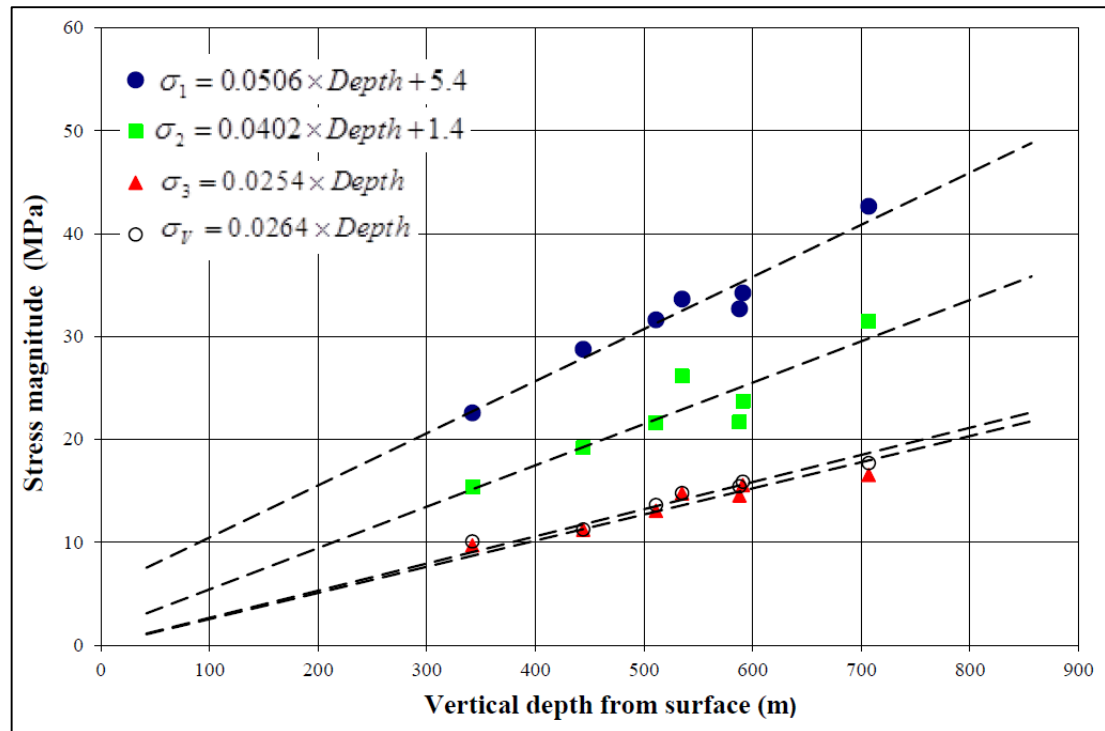


Figure 2 – Stress gradient data showing the increase in stress as a function of vertical depth below surface.

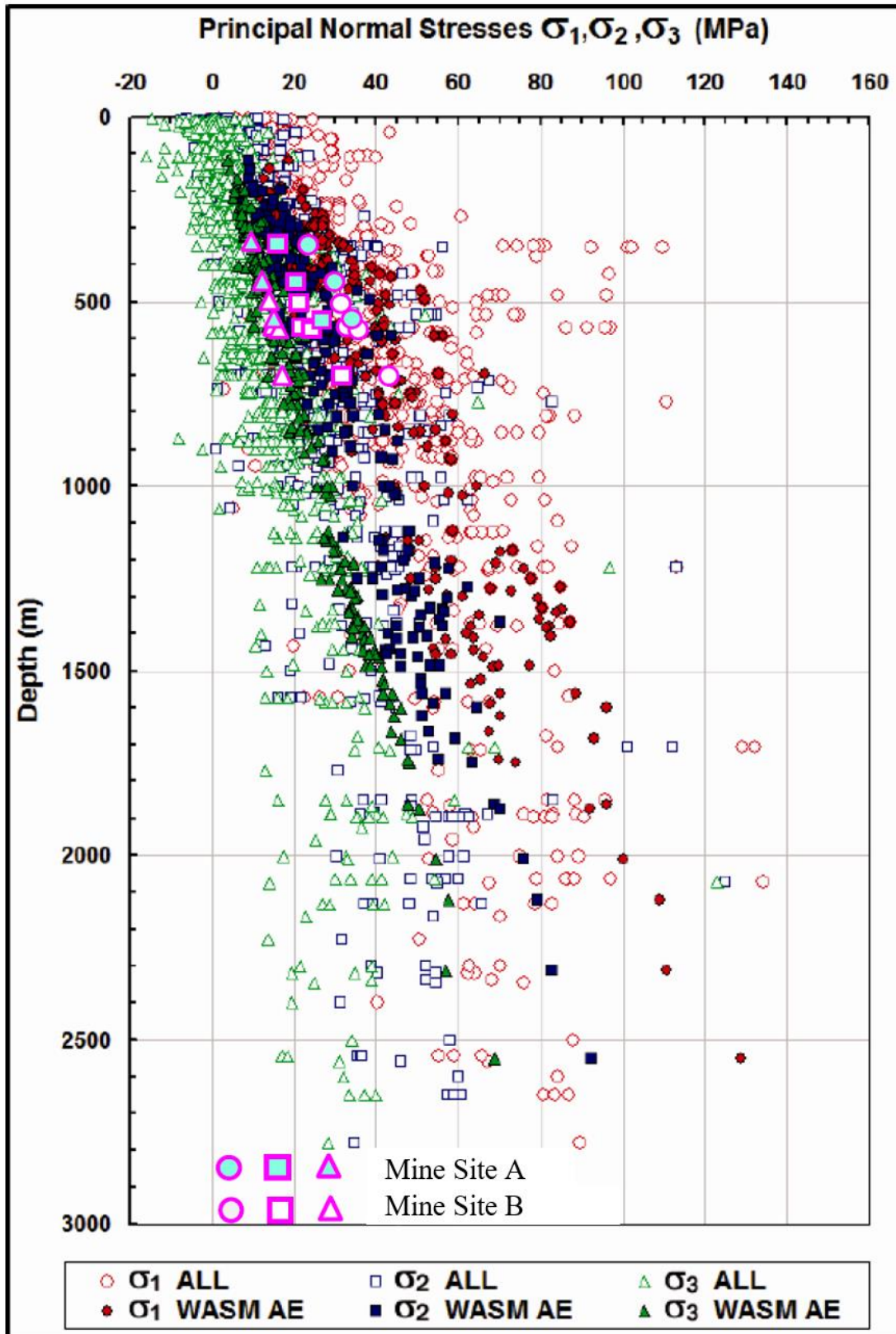


Figure 3 - Comparison of local stress measurement data with the global database.

2.1.2 Strain

Strain in a rock mass may be considered a measure of rock mass damage. The lower the deformation or strain in an otherwise undisturbed rock mass, the less damage that exists. For hard rock, strains in the order of 3-5% indicate significant rock mass deterioration (Figure 4) (Hoek & Marinos, 2000, Beck, 2013). Strains of this magnitude may compromise the serviceability of an excavation. It is necessary to consider rock mass strain before, during and after construction. High strains prior to or during construction may indicate poor ground and difficult excavation conditions. Alternatively, high strains induced post-construction may cause significant damage to the excavation and installed ground support.

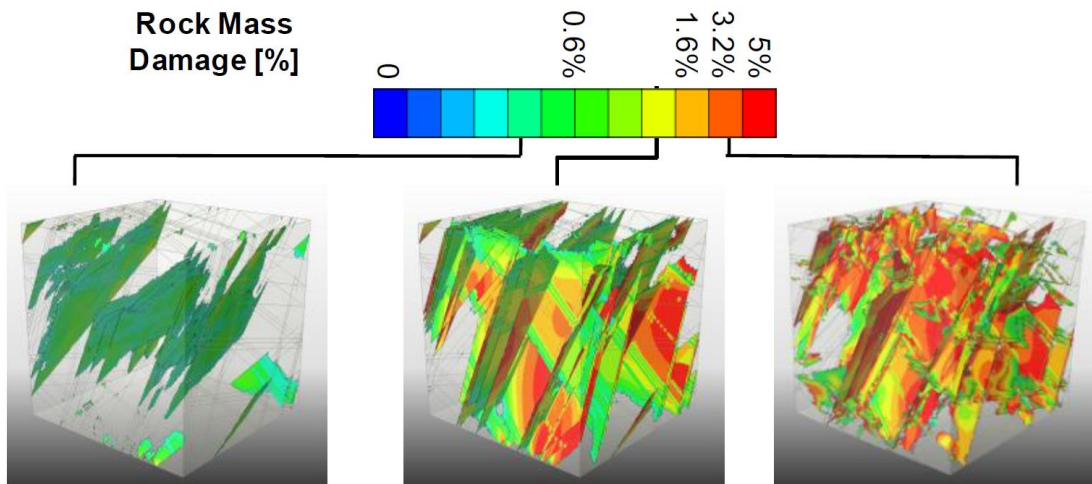


Figure 4 - Simulated damage to a rock specimen at various strain milestones (Beck, 2013).

Strain in the rock mass may be measured on a broad mine scale, and used to infer general excavation conditions at depth or to reconcile with the structural geology. Strains at this scale may be quantified by measuring the relative displacements of surface GPS stations (Windsor, et al., 2006). Strains on a local excavation scale are more useful to detailed tunnel design, but are more difficult to measure with instrumentation. For interpretation purposes, strain conditions at the tunnel scale are arguably best assessed via numerical methods, such as non-linear finite element modelling, some results of which are shown in Figure 5 (Beck, et al., 2010). This level of advanced modelling cannot be performed without first collecting significant model input data on rock stress, strength and structure. Strains quantified at this level of spatial resolution can be compared to the ultimate strain of reinforcement or surface support elements, giving some indication of the likelihood of ground support failure.

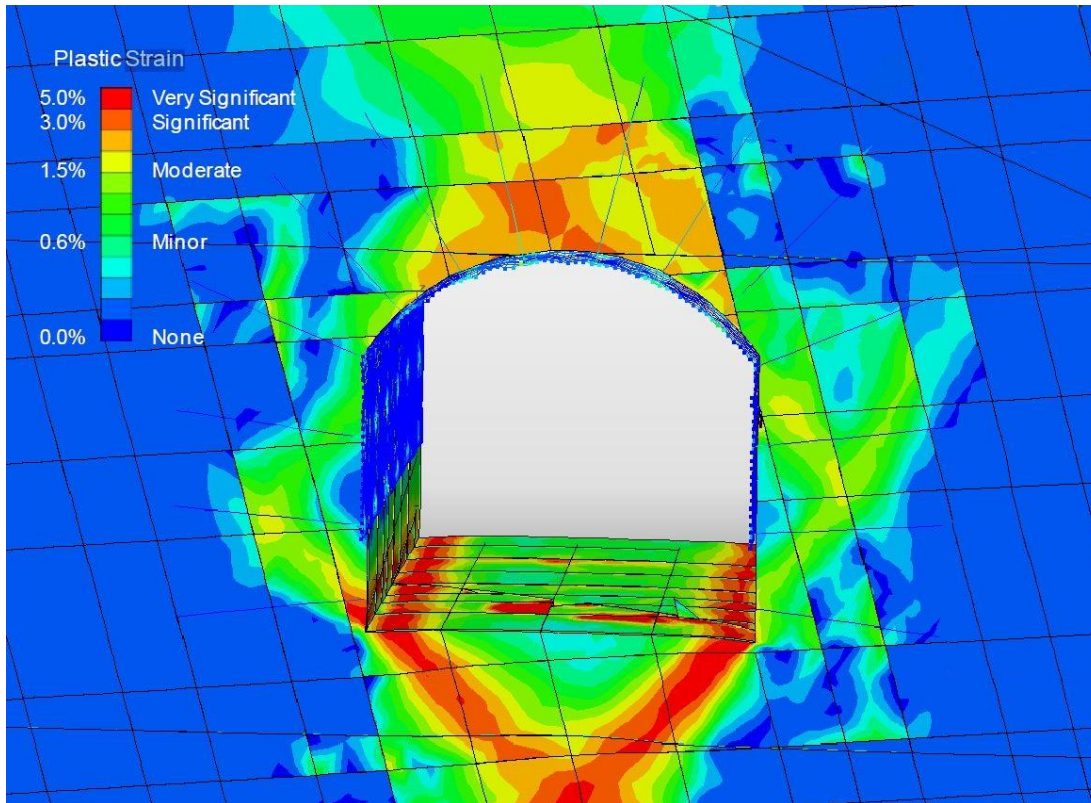


Figure 5 - Rock mass strain as an indicator of damage adjacent a deep mining excavation (Beck, et al., 2010).

2.1.3 Structure

A complete rock mass characterisation of a tunnelling environment must consider the structural assembly of the rock mass at various scales. The structural nature of the rock mass may include primary features at a relatively large scale, such as major faults and shear zones, as well as smaller scale secondary features like local joint sets and persistent foliation (Windsor, 1995). Such structural features are all capable of affecting the constructability and long term stability of deep excavations.

Structural data may be collected in a variety of ways. Core logging and face exposure mapping are two common methods of data collection. Digital photogrammetry has also become popular due to the efficiency and accuracy of data collection (Hagan, 1980), which poses less interruption to the construction cycle time. Sophisticated software tools are now available to simplify and automate much of the data analysis process. In addition, photogrammetry removes the need for personnel to access adjacent unsupported rock faces, which may be unstable. Data should be collected routinely during development of the underground infrastructure, although this can be difficult in cases where shotcrete surface support conceals the rock face.

The main purpose of structural data analysis is to characterise the structural network and, in particular, identify blocks of rock on the excavation boundary which may become unstable. Various software packages are available to analyse structural data for tunnel design. The *Dips* software package (Rocscience, 2018) is commonly used for visualisation and analysis of joint orientation data, and may be used to identify joint set families. The program *Unwedge*, from the same company, is commonly used to assess the geometry, mass and stability of possible wedges formed by the intersection of discontinuities. This program identifies block geometries and gives a safety factor and support requirement output which may consider gravitational loading in isolation or in combination with an applied field stress. One disadvantage of the *Unwedge* software is that it does not define wedge geometries probabilistically. In other words, the wedge geometries may not accurately reflect the actual size and shape characteristics of the real blocks. As such, ground support designs based on an *Unwedge* analysis may be over or under-engineered.

The SAFEX program, developed by WASM, provides both deterministic and probabilistic solutions to wedge geometry. The probabilistic solutions are based on the block theory developed by Windsor, 1999, and are arguably the most realistic representations of the true block geometry. The necessary input data for structural analysis in SAFEX includes the location, dip, dip direction, trace length, spacing, persistence, roughness, planarity, infill material, thickness and weathering condition of the prevailing discontinuities. This data can first be used to identify the joint set families through statistical analysis (Figure 6). Outputs of the deterministic and probabilistic analysis include block apex height, free face perimeter and area, volume, mass, driving force, natural resisting force, out of balance force and the stability index (Figure 7). The various maximum block shapes and sizes may be trace length or span limited. The SAFEX software also performs reinforcement and surface support analyses for stabilisation of the predicted block geometries, based on the theory developed by Thompson (2002).

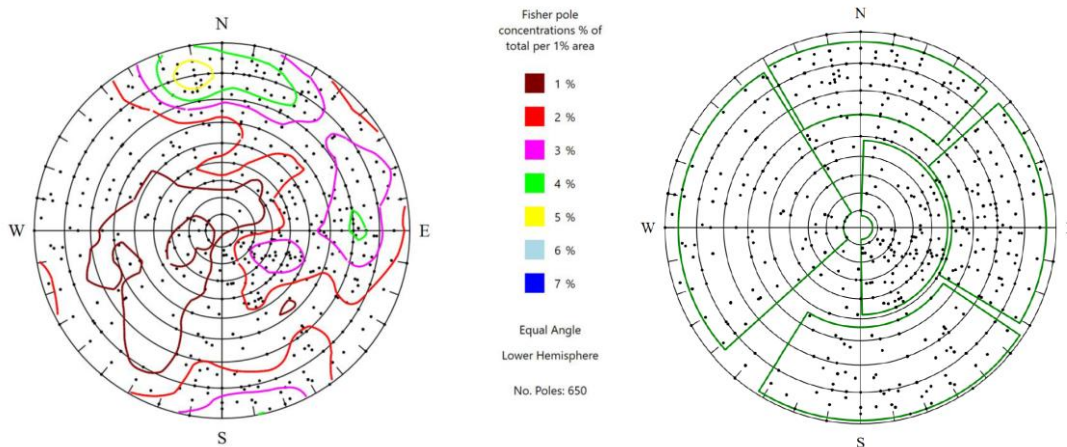


Figure 6 - Fisher pole concentrations for structural data and resulting joint sets defined in SAFEX.

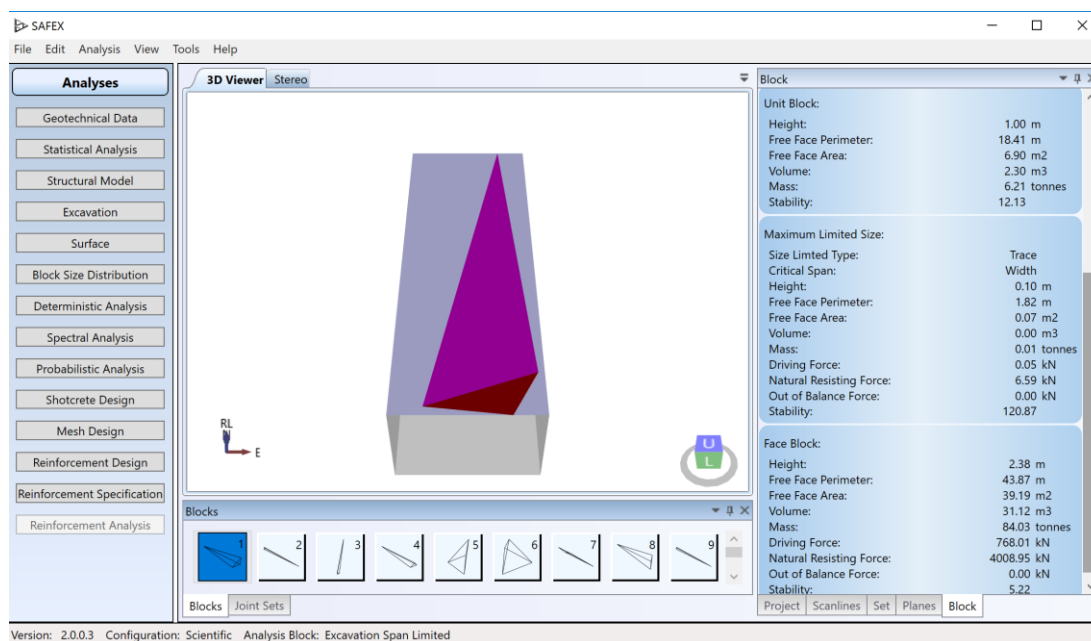


Figure 7 - SAFEX output of deterministic block parameters.

2.1.4 Strength

Prior studies by Kusui (2015) have shown that the material strength properties of the rock play a key role in both the stability of excavations under high stress and in load demand during failure. The material strength parameters also serve as input variables for many analytical or numerical design methods. Laboratory testing of these parameters is therefore another crucial aspect of the rock mass characterisation. The basic set of intact rock material parameters include:

- Unit weight (γ),
- Uniaxial Compressive Strength (UCS),
- Uniaxial Tensile Strength (UTS),

- Moduli of Elasticity (E), Rigidity (G) and Compressibility (K),
- Poisson’s Ratio (ν)
- Friction angle (ϕ)
- Cohesion (c)

This data is typically collected for all distinct rock types within the construction environment. The number of measurements and statistical variation in recorded values should also be noted. Table 1 and Figure 8 present an example of a comprehensive dataset of UCS for a rock mass characterisation at a deep mine.

Table 1 - Example UCS data for rock mass characterisation (Dempers, et al., 2006).

Rock Unit	Rock Sub Unit	UCS Mean (MPa)	UCS Std. Dev. (MPa)	Number of Tests
Felsic	1 All	182	35	34
	1a Stripey	145	68	15
	1b Porphyry	212	46	19
Serpentine	2	123	31	5
Intermediate	3	155	69	5
Olivine	4 All	167	63	25
	4a Soft	109	23	6
	4b Hard	217	40	6
	4c Veined	140	55	6
	4d Undifferentiated	198	62	7
	4b + 4c + 4d	186	60	19

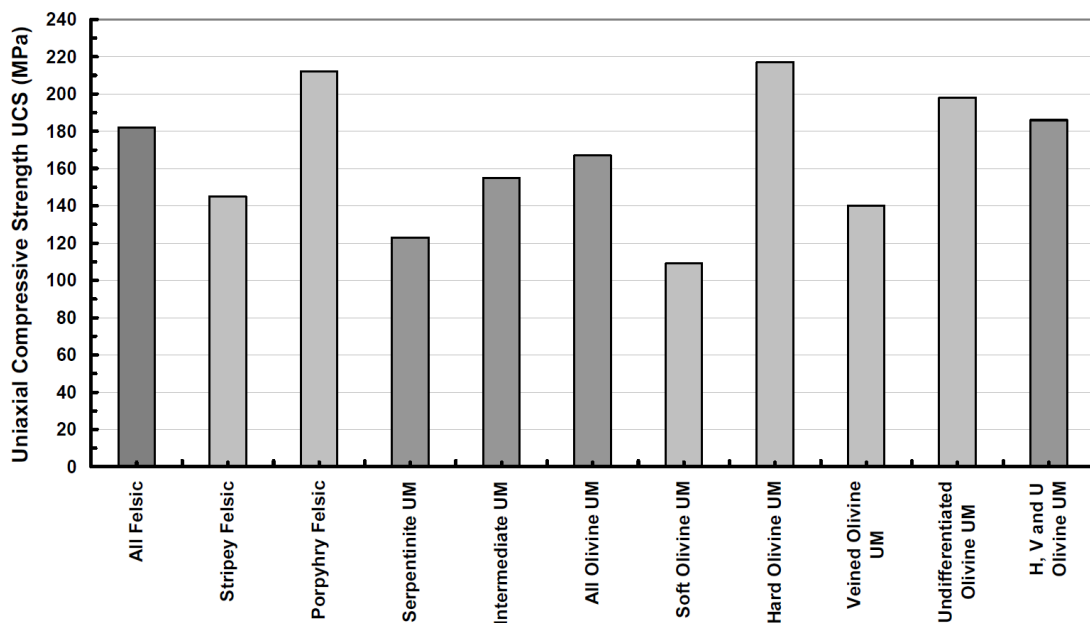


Figure 8 – Chart of UCS data for rock mass characterisation (Windsor, 2008).

2.2 Excavation Stability

Underground excavations are reaching depths where the ratio of intact rock strength to induced stresses is such that violent failure of the rock mass adjacent the excavation can occur very soon after construction (Kusui & Villaescusa, 2016). Observations and geotechnical monitoring indicate that complex high energy failure mechanisms frequently intersect the excavations. In most cases, the depth of failure is less than the length of the rock reinforcement elements. For a typical mining or civil tunnelling excavation, this length is commonly 2.5-4.0 m. If the depth of failure is shallow (<0.5 m), this often involves damage of the surface support, which in some cases does not have the capacity to transfer load to the reinforcement elements (Figure 9).



Figure 9 - Lack of ground support retention following a violent spalling failure of the excavation surface.

In some cases, however, the violent failures mobilise geological structures and the depth of failure can be more significant (>1.0 m), often involving failure through the reinforcement elements. This can occur where geological structures are sub-parallel to the tunnel walls or form wedges that control the shape and depth of failure (Figure 10). Excavation instabilities having a depth of failure ranging from 0.5 to 1.0 m are considered to be transitional and may involve a mixture of both support and reinforcement mobilization (Villaescusa, et al., 2016b).

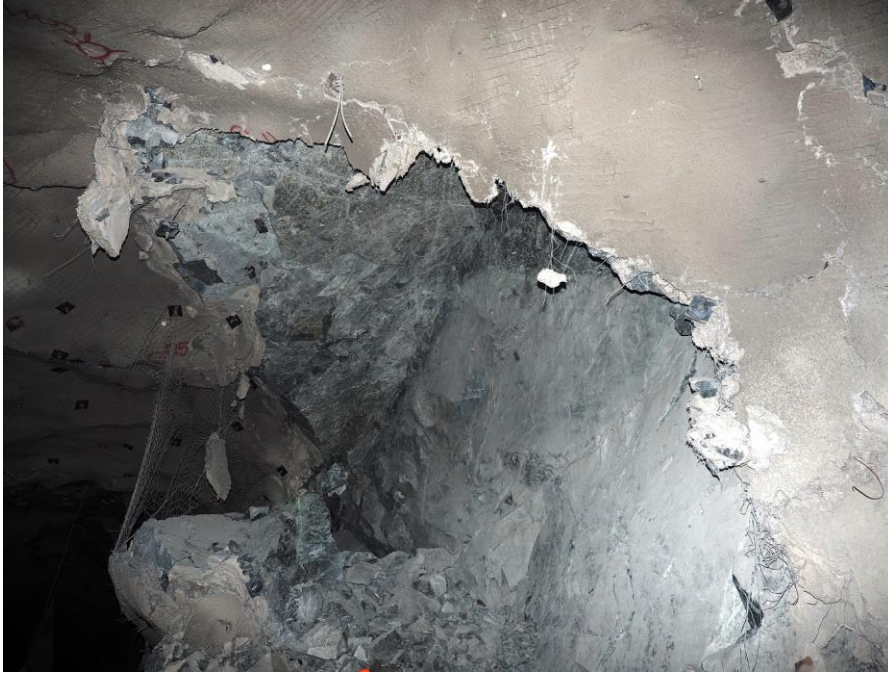


Figure 10 - Failure of reinforcement elements following violent, structurally controlled instability.

The load transfer mechanism for an excavation under high stress is very complex and depends upon the level of pre-existing rock mass damage and potential block size associated with violent ejections. The larger the mobilized blocks, the more reinforcement action that is involved in dissipating energy. Conversely, small block size instability requires membrane support, such as that provided by combinations of shotcrete and mesh (Villaescusa, et al., 2016b). In all cases, the performance of the surface support is critical to achieve load transfer to the reinforcement elements, which in turn stabilize the excavations (Thompson & Windsor, 1992).

2.2.1 Boundary Stress

The creation of an excavation at great depth removes load bearing rock, resulting in a disruption to the local stress field. Stress concentrations and relaxations occur at the excavation boundary as a consequence. As illustrated in Figure 11, excavation surfaces sub-parallel to the major principal stress experience an increase in compressive stress. Conversely, excavation surfaces sub-perpendicular to the major principal stress experience stress relaxation and may enter a tensile loading condition (Brady & Brown, 2004). In general, the greatest risk of violent rock mass damage occurs at the point of maximum induced compressive stress tangential to the excavation (Figure 12). The pre-excavation in-situ stress magnitude and radius of curvature of the excavation are crucial controls on the induced stress concentrations at the excavation boundary. These two factors heavily influence the likelihood of failure.

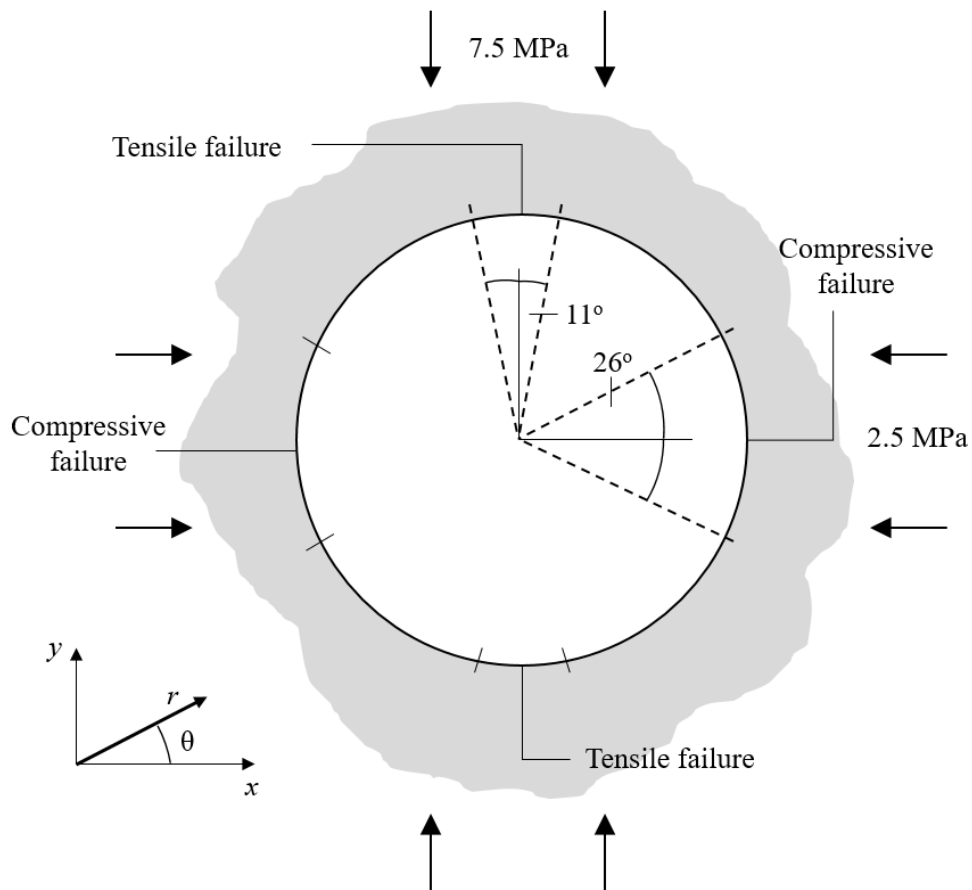


Figure 11 - Prediction of the extent of boundary failure around a circular opening (Brady & Brown, 2004)

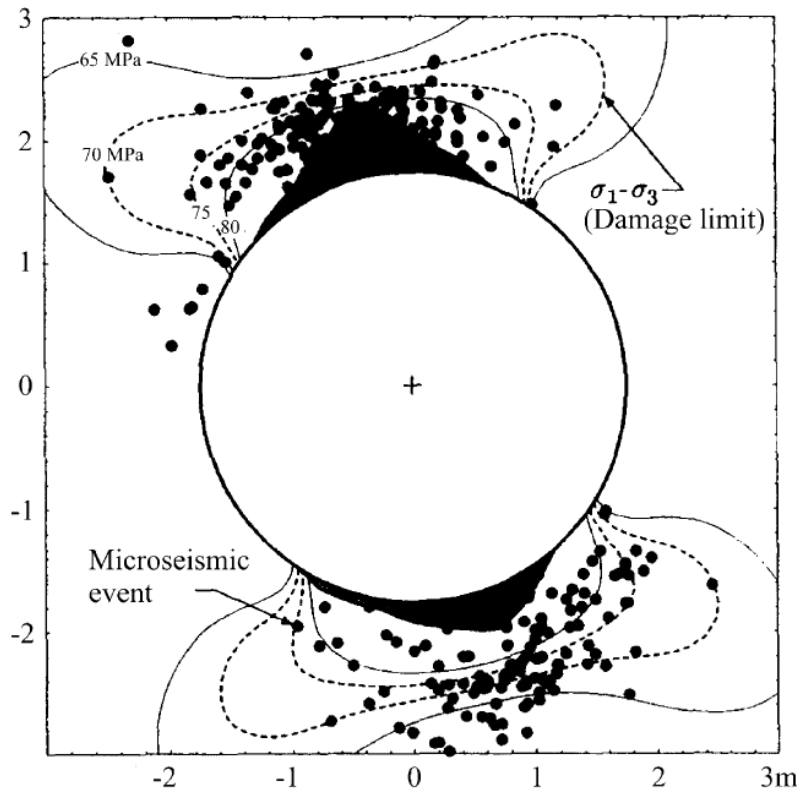


Figure 12 - Rock mass damage in zones of highest stress concentration (Martin, 1997).

The orientation of the excavation relative to that of the major principal stress dictates which of the excavation surfaces experience the highest induced stress. As depicted in Figure 13, the excavation surfaces oriented sub-parallel to the major principal stress carry the greatest stress concentrations and, therefore, the highest risk of violent failure. In particular, apex points on the excavation may experience peak stress concentrations. The span of the excavation also influences the stress concentrations. Larger spans perpendicular to the major principal stress result in higher stress concentrations at the tunnel boundary (Obert & Duvall, 1967).

This concept indicates that for tunnels developed perfectly perpendicularly to a sub-horizontal major principal stress, the most likely zones of violent stress-driven failure are the apex between the face and adjacent walls. In the same conditions, the central face might be expected to generate violent instability only if the stress concentrations of approximately 2.5 times σ_1 exceed the material-specific spalling threshold. The face may be expected to be at the greatest risk of violent instability when the excavation is developed perpendicular to the major principal stress.

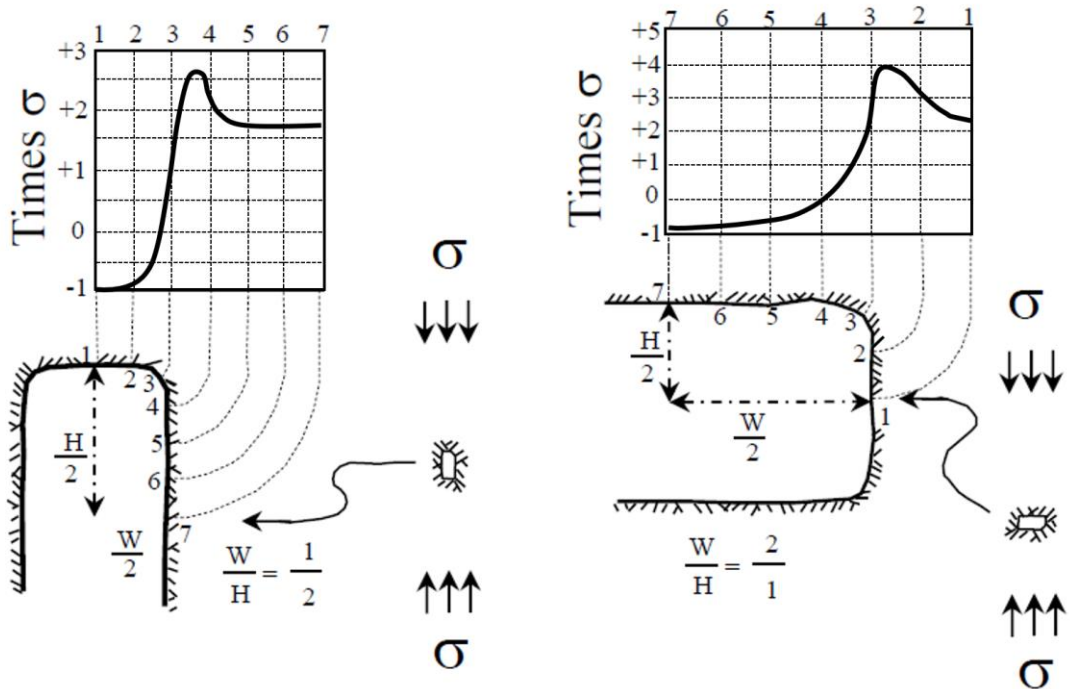


Figure 13 – Cross section views of stress concentrations at the excavation face (Obert & Duvall, 1967).

2.2.2 Ratio of Strength to Induced Stress

The ratio of intact rock Uniaxial Compressive Strength (σ_c) to the maximum induced compressive stress tangential to the wall of an excavation (σ_{max}) has long been recognized as a critical factor controlling excavation stability (Barton, et al., 1974, Matthews, et al., 1980). As the ratio of σ_c/σ_{max} reduces, excavation instability increases, as shown in Figure 14. Data from many years of numerical modelling and observations of open stoping in hard rock at Mount Isa Mines (Villaescusa, 2014) have shown that as the ratio decreases below the value of 3, the instability increases markedly. In general, when excavating in rock with σ_c/σ_{max} ratios below 5, it can be expected that large deformations would be experienced in tunnels driven within a low strength rock, while sudden, violent failure could occur in tunnels excavated in high strength rock (Barla, 2014).

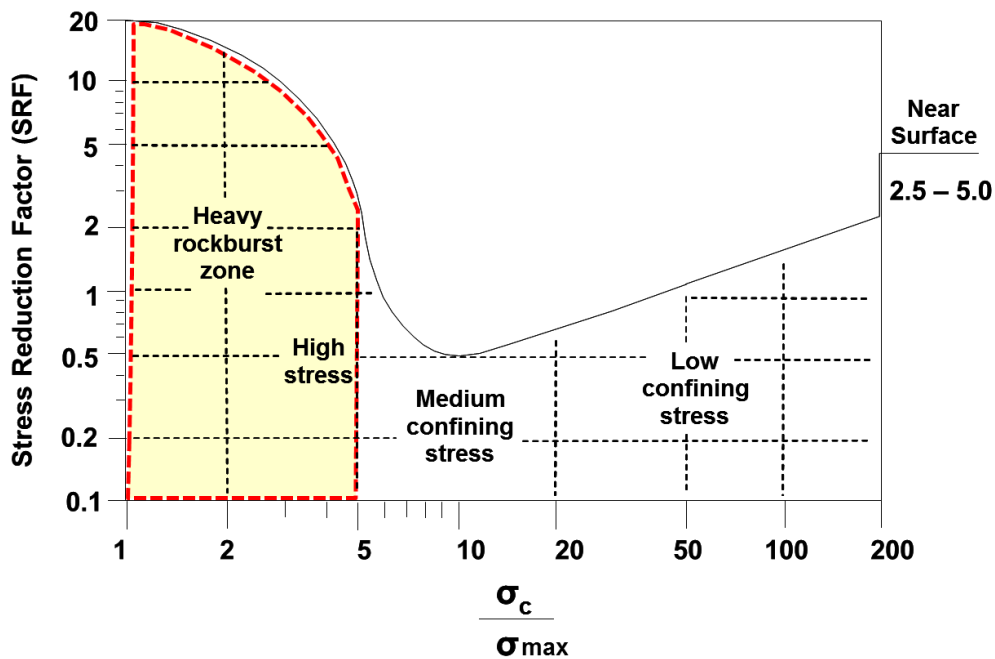


Figure 14 - Excavation behaviour as a function of the strength/stress ratio. (Barton et al., 1974).

The relationship between the rock strength and the induced stress at the onset of failure has been investigated by a number of researchers using stress-strain data from UCS laboratory testing (Diederichs, 2007, Lajtai & Dzik, 1996, Martin, 1997). The research shows that failure initiates when the ratio of the uniaxial compressive strength obtained by laboratory testing (σ_c) to the stress magnitude causing the failure (σ_{max}) ranges between 2 and 3. Martin (1993) also conducted detailed investigations at an underground excavation in granite. The crack propagation process started when the intact strength to induced stress ratio reached approximately 2.

2.2.3 Spalling Failure

Spalling failure of an excavation under high compressive stress is characterised by tensile fracturing of rock in an orientation typically sub-parallel to both the major principal stress component and adjacent excavation surface, often with associated ejection of rock slabs. Spalling fractures may be few, occurring through intact rock, or highly repetitive and closely spaced due to delamination of pre-existing discontinuity surfaces that are suitably oriented (Villaescusa, et al., 2016b). Stress-driven damage in brittle rock often occurs initially as progressive violent spalling of the excavation walls and is localized within areas of maximum induced stress concentrations (Christiansson, et al., 2012). Such failures typically result in an approximately v-shaped notch in the regions of instability (Figure 15).



Figure 15 - Example of notch formation due to stress-driven brittle failure in an underground tunnel.

Recently, Kusui (2015) observed the ratio of compressive strength to maximum induced stress at the sidewalls of scaled-down tunnels which had been progressively loaded to failure. For the first stage of failure, where spalling was experienced, the ratio monitored was the value of compressive strength to maximum tangential stress (i.e. effectively near zero confining stress at the excavation boundary). Laboratory tests on unsupported scaled-down tunnels were performed for a range of intact rock strengths, the results of which are shown in Figure 16.

The ratio of σ_c to σ_{max} was calculated using the Kirsch solution and also checked with finite element modelling using the program Abaqus (Kusui, et al., 2015). The stress value was calculated for both sides of the tunnel during wall spalling. Similar to previous published work by (Martin, 1993), violent ejection from the excavation walls occurred prior to peak intact rock strength. The strength/induced stress ratio at spalling and the uniaxial compressive strength show a strong correlation. The value of σ_c/σ_{max} at spalling ranges from 1.0 to 3.5 for strong to very strong rock. The red dashed line and related equation shown in Figure 16 represents the potential on-set of failure. i.e., what could be interpreted as the practical safe limits prior to spalling failure of an excavation. The samples of moderately strong rock ($\sigma_c < 50\text{MPa}$) did not fail violently.

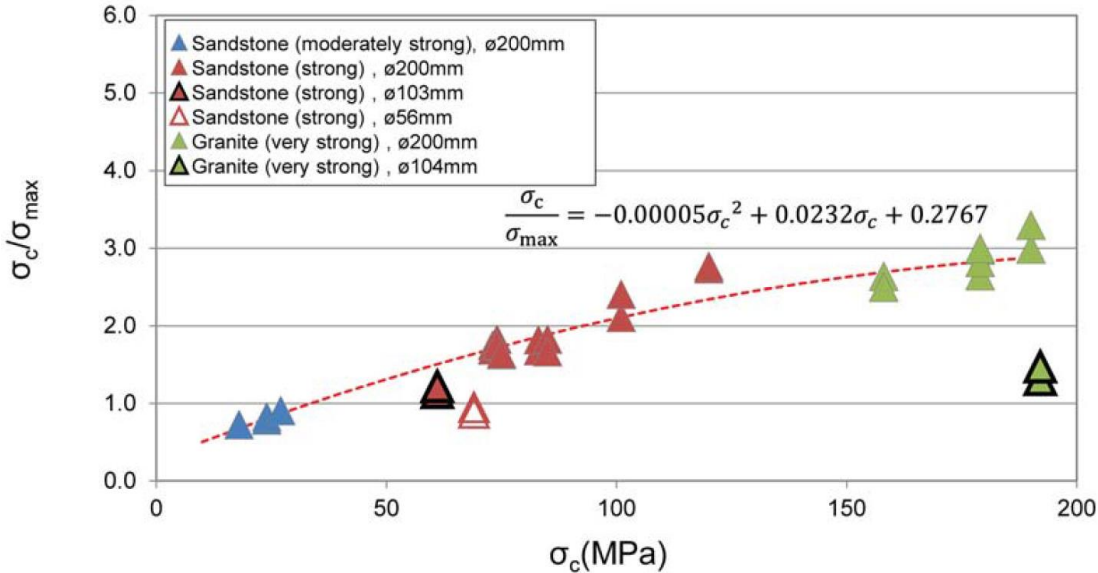


Figure 16 - Unsupported tunnel spalling as a function of σ_c/σ_{max} (Kusui et al, 2016).

The laboratory results from Kusui (2015) correlate well with observations of 4-5m diameter full scale unsupported tunnels excavated within a highly silicified rock mass, as shown in Figure 17. In this example the rock has a Uniaxial Compressive Strength of 250-270 MPa and widely spaced, tightly healed geological discontinuities. The onset of stress driven failure in these full scale unsupported tunnels was experienced where the ratio of intact rock strength to maximum induced tangential stress was approximately 3.5. The mining tunnels were constructed using excellent drilling and blasting techniques. The tunnels were designed with semi-circular walls and a flat floor. Incipient failure of the tunnel back (roof) is evident due to a sub-horizontally oriented major principal stress component.



Figure 17 - Spalling failure of unsupported semi-circular tunnels at the roof (Villaescusa, et al., 2016b).

2.2.4 Structurally Controlled Failure

This mode of failure involves violent stress-driven ejection of large tetrahedral wedges, the shape and size of which are controlled by pre-existing rock mass discontinuities (Figure 18). Similar to spalling mechanisms, structurally controlled ejection of large blocks is generally centralised to excavation surfaces where maximum stress concentration occurs. Wedge size may be limited by the span of the excavation or structure trace length. This mechanism reflects the violent release of plastic strain energy at the excavation surface, with the volume of instability controlled by the block geometry. This mechanism of failure is possible due to excavation scale stress concentration effects and has been observed in advanced development at great depth.



Figure 18 - Structurally controlled failure with a large depth of instability.

The initial direction of the ejected material is typically perpendicular to the orientation of the major principal stress and orientation of least radial confinement. This equates to the radially inward direction at the excavation surface where the greatest stress concentration occurs. Detailed understanding of the prevailing stress field can be utilised to determine which excavation surfaces are most likely to be affected by instability.

2.2.5 Fault Rupture

This mechanism of failure is characterised by the violent shear displacement of a major fault structure, where the mobilised fault surface intersects the excavation. This method is distinct from structurally controlled block ejection as tetrahedral wedges bounded on multiple sides by a joint plane are not necessarily formed. Damage is defined by displacement along a singular major discontinuity. Such mechanisms of failure are typically associated with global stress change effects resulting from large extraction ratio excavations. Evolving stress conditions can significantly alter the shear stresses acting on major fault structures over time. Violent rupture of a structure may be expected if at any time the shear stresses overcome the shear strength of the structure, although this is very difficult to quantify in advance. In the event that the unstable surface of the structure coincides with an excavation, the resulting damage and energy demand can be severe, as shown in Figure 19 (Drover, 2014).



Figure 19 – Fault rupture mechanism of excavation instability causing extreme damage (Drover, 2014).

Unlike stress driven failure such as spalling or structurally controlled block ejection, where excavation damage is primarily confined to the zone of maximum stress concentration, damage related to fault rupture can affect any surface of the excavation with similar severity. The distribution of damage depends on the strike and dip of the structure and where it intersects the excavation. Displacement vectors at the excavation boundary are sub-parallel to the fault plane, and therefore not necessarily radially inwards. This can have the effect of highly complex loading conditions on the installed ground support schemes (Thompson, et al., 2012). Fault rupture mode of failure is suggested to predominantly affect excavations constructed within the zone of influence of large extraction ratio excavations, such as mass-mining cave zones (Figure 20) or large stopes. The zone of stress influence of individual development drifts is generally not sufficient to induce major shear stress change across large structures. As such, there is assumed to be a lesser risk of fault-rupture style failure mechanisms associated with isolated development tunnels in their early stages of development.

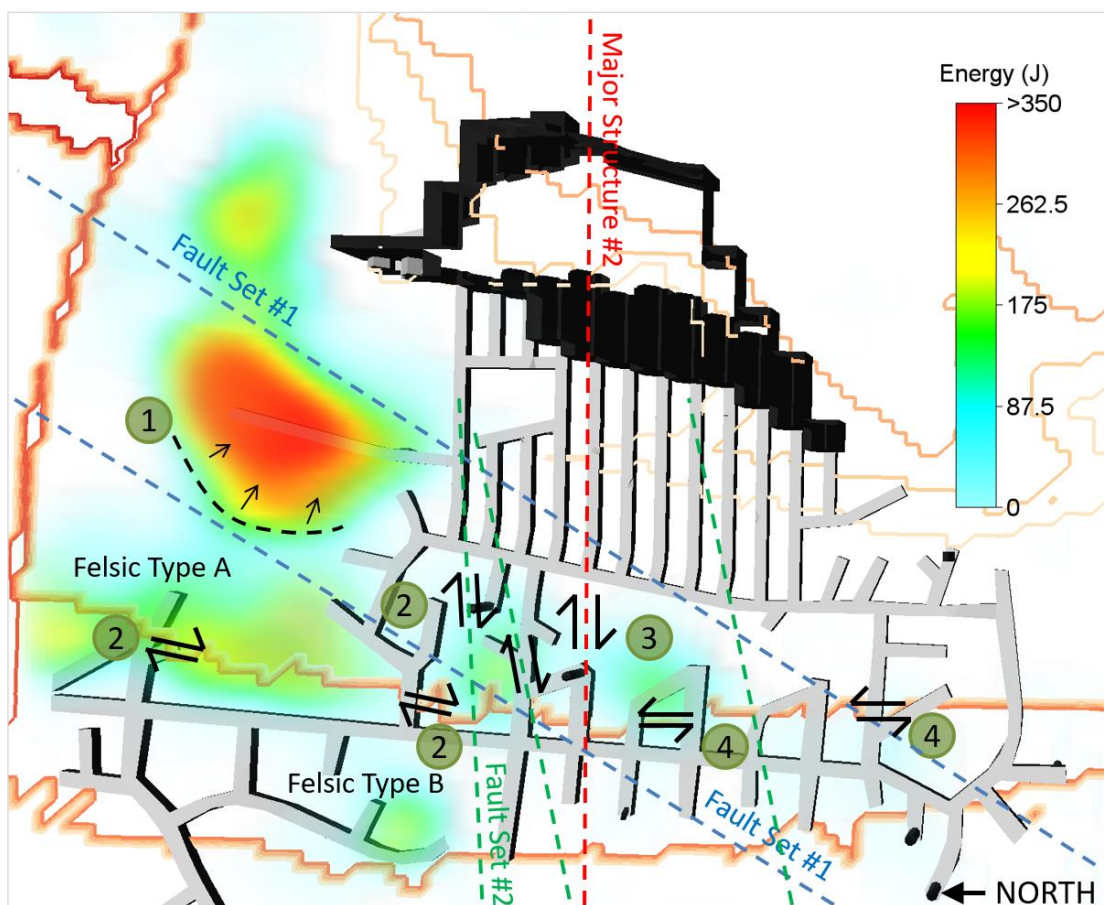


Figure 20 – Global scale instability with numerous large structural reactions (Drover, 2014).

2.2.6 Shear Failure Mode of Pillar Crushing

Testing of scaled-down tunnels by Kusui (2015) has shown that under progressively increased loading conditions, the initial spalling failure is followed by shear failure of the walls adjacent to the excavation. Figure 21 shows the load-displacement profile and acoustic emission count for an example of progressive brittle failure of a tunnel under increased loading. After spalling, large shear cracks can propagate adjacent to the tunnel with shear failure dominating the latest stages of the failure mechanism. The results show the seismic response in which loading was gradually increased from zero until tunnel wall spalling and then pillar crushing were experienced. The seismic activity starts with the creation of a vertical tension crack in the floor and roof of the circular opening, as predicted by theory (Hoek & Brown, 1980). The rate of seismic activity clearly increased prior to the violent ejection in both walls. Significantly, relatively few acoustic emissions were monitored during the period between spalling and the onset of the shear failure mode of pillar crushing. Overall, a significant decrease in load bearing capacity occurs following the final shear mode of failure.

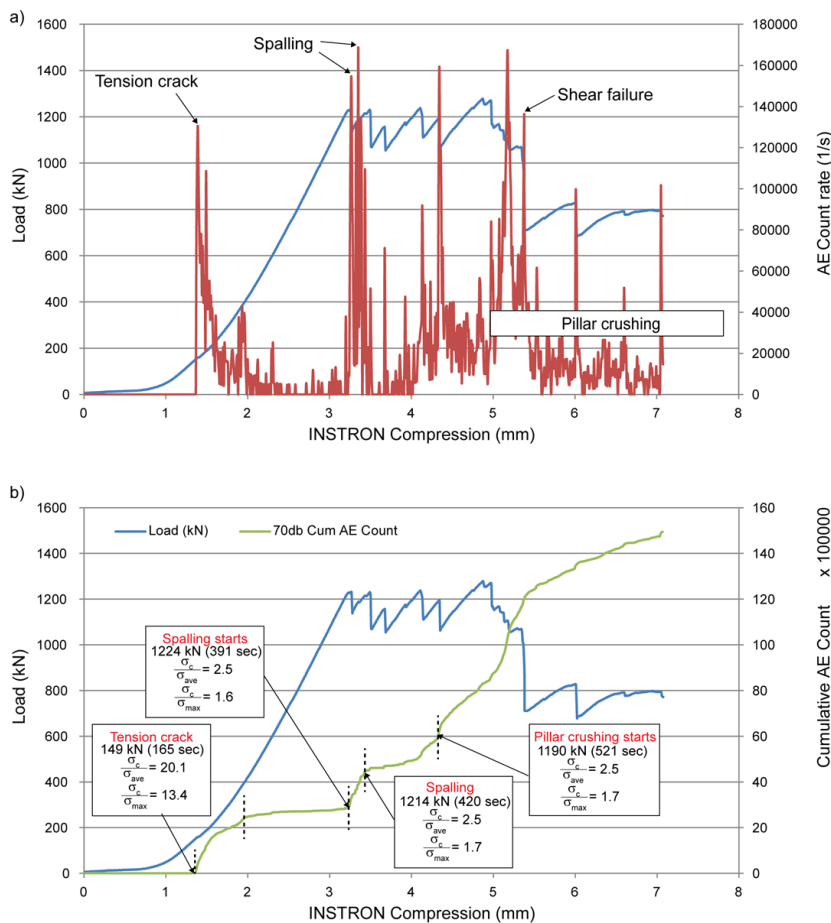


Figure 21 – Load and acoustic emission count vs. displacement during progressive failure (Kusui, 2015).

2.2.7 Damage and Deformation Prior to Violent Failure

The on-set of tunnel damage and progression to violent failure in massive rock has been studied in detail by Kusui (2015). As shown earlier in Figure 21, the complete excavation response has been determined as the induced stress near the excavation boundary is increased with respect to the intact rock strength. The critical levels of strength to induced stress related to the onset of visible instability such as spalling of both walls and the start of pillar crushing were calculated. The results show that the failure threshold values of σ_c/σ_{max} are dependent upon the Uniaxial Compressive Strength. Higher values of σ_c/σ_{max} at failure correlate to lower radial strain at failure (Figure 22). This is in accordance with field data reported by Hoek (1999) and laboratory work on critical strain by Li (2004).

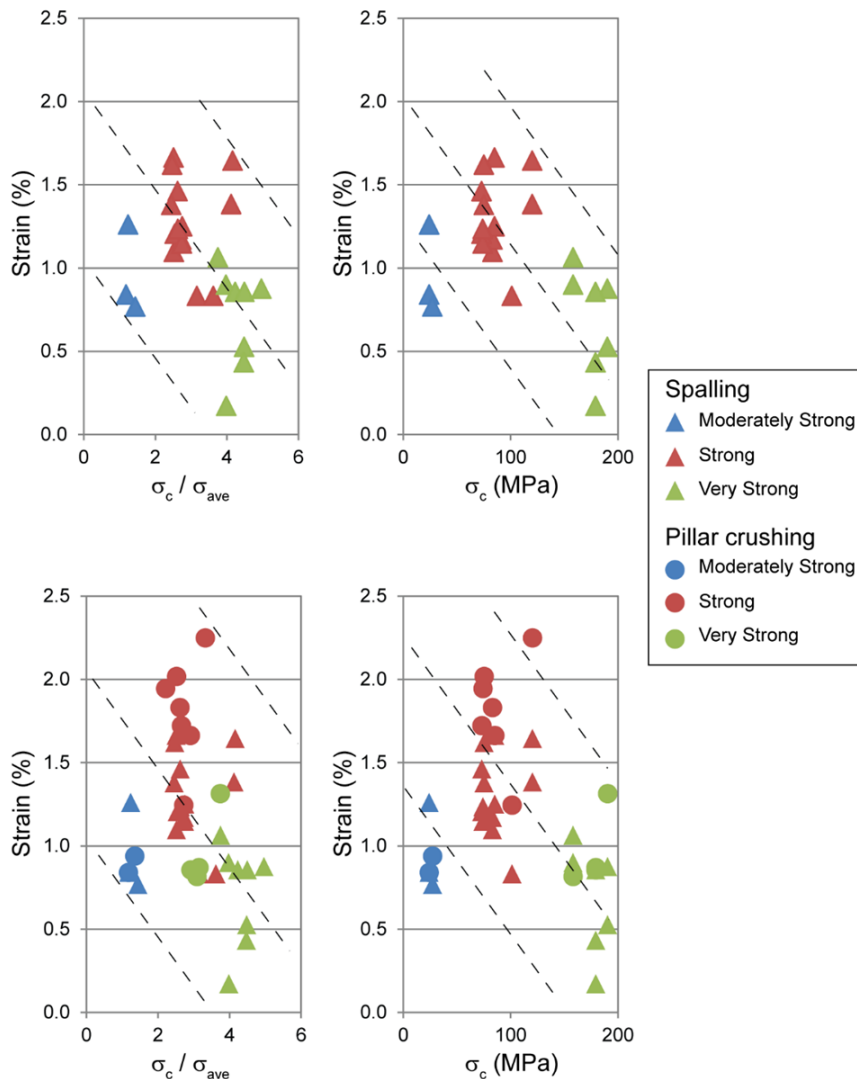


Figure 22 - Higher strength materials exhibit lower radial strain at failure (Kusui, 2015).

2.3 Rock Mass Demand

Ground support design is often based on past experience from similar geotechnical environments and work practices. Challenging this approach is the fact that the rock mass conditions usually change throughout the project timeline and the ground support performance may become unacceptable over time (Villaescusa, et al., 2016b). That is, when the induced stresses increase due to greater depth of mining or global extraction increases, the installed reinforcement and support capacities may not satisfy the rock mass demand. For violent stress-driven rock mass failure, the energy demand on the ground support scheme is controlled by the amount of mass that becomes unstable (m_u) and the initial velocity (v_e) of its ejection. For design purposes, demand may be quantified in terms of the kinetic energy (KE) of ejected rock, according to the formula.

$$KE = \frac{1}{2} m_u v_e^2 \tag{Eq. 2.1}$$

Quantifying the energy demand on the ground support scheme requires accurate input parameters. That is, the mass and ejection velocity of the instability must be defined. The following chart (Figure 23) provides one method of estimating energy demand (E) on ground support for various depths of failure (d) and ejection velocity (v). The major limitation of this chart is that d does not consider the complex instability geometry occurring in reality, and v is not linked in any reliable way to the specific rock mass conditions at the site of the excavation that is being designed.

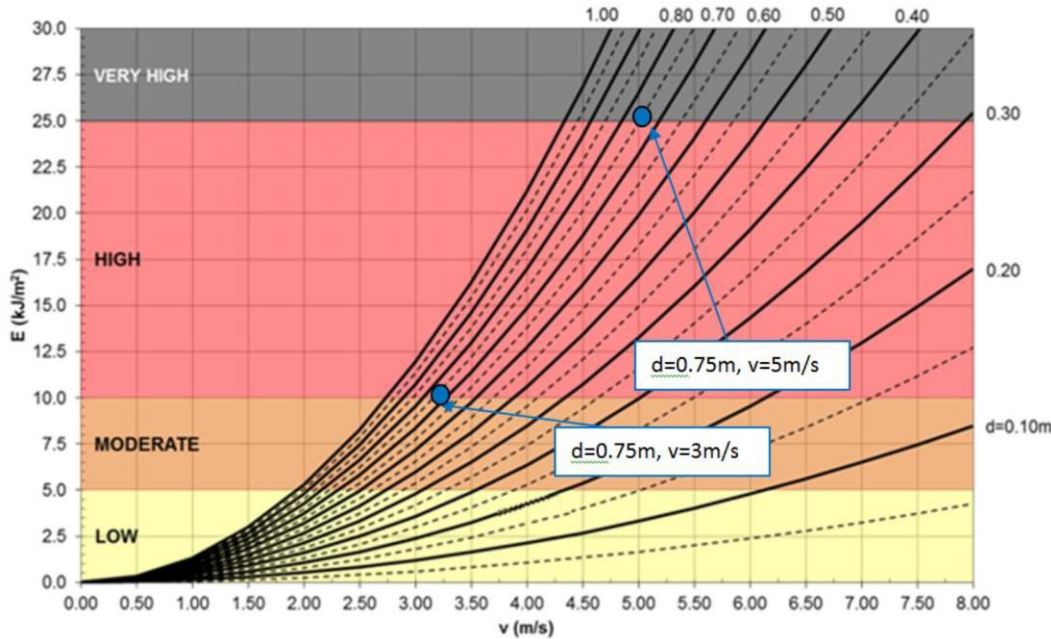


Figure 23 - Chart for assessment of energy demand on ground support (Geodata, 2016).

2.3.1 Mass of Instability

The mass of unstable rock is linked to volume and therefore the depth of failure beyond the excavation boundary. Hence, it is necessary to estimate the depth of failure when quantifying rock mass demand. A common method of estimating the depth of failure is that described by Kaiser, et al., (1996), whereby the depth of failure is measured

‘from a circle or circular arch circumscribing the excavation to unstable or potentially unstable rock’.

These authors describe an empirical relationship for quantifying the depth of failure which considers the tunnel radius (a) and stress magnitude (SL) as the inputs. The equation is:

$$\frac{d_f}{a} = C_1 \frac{\sigma_{max}}{\sigma_c} - C_2 = C_1 SL - C_2 \quad (Eq. 2.2)$$

Where C_1 and C_2 are constants. It is stated that this relationship is applicable only where mining activity causes local stress increases at the tunnel boundary. It is not applicable for failure controlled by stress relaxation and gravitational loading (Kaiser & Cai, 2013). It is suggested here that there are several limitations to this empiricism. For instance, it does not consider structurally controlled failure where the wedge geometry is critical to the overall volume of instability. Furthermore, the formula significantly overestimates the depth of failure when considering shallow spalling mechanisms.

2.3.2 Ejection Velocity and Direction

By common convention, the velocity parameter of the kinetic energy demand equation (Eq.2.1) is almost always derived from the seismic ground motion, otherwise known as the Peak Particle Velocity (PPV). As discussed in Kaiser, et al., (1996), PPV is an oscillating excitation of the rock mass generated by the transient dynamic stress wave radiated by a remote seismic event. The *incoming PPV* is defined as a function of the remote seismic event magnitude (M_R) and the attenuation of the peak particle velocity with distance (d) from the seismic source hypocentre, as follows:

$$PPV(m/s) = \frac{1.4 \cdot 10^{(M_R/2)}}{d} \quad (Eq. 2.3)$$

PPV at the excavation boundary defined by seismicity has been postulated by several authors as an appropriate input parameter for estimation of energy demand on ground support due to sudden violent failure. Ortlepp (1992) stated that:

“the ejection velocity imposed on the rock mass by the seismic wave is probably the single most important determinant of damage intensity in a tunnel.”

Similarly, in the work of Kaiser, et al., (1996), it is stated that

“the ground motion velocity represented by the peak particle velocity ppv is accepted as the most representative parameter to define the dynamic design load”.

PPV is widely used within the mining industry as the velocity input variable for demand estimation in ground support design (Mikula, 2012, Jarufe & Vasquez, 2013). Generally, the incoming PPV from a remote seismic event is multiplied by a factor termed the *site* effect, in order to reach what is assumed to be the ejection velocity of the unstable rock. The site factor assumes that amplification of ground motion defines the ejection velocity, as seismic waves interact with the excavations. The theory of such wave interactions is poorly understood (Webber, 2000). Field measurements by Milev, et al., (2002) suggest that the site effect varied between 1 and 25 across three mine sites. Such large variability suggests that inclusion of the site effect PPV in the design process carries significant uncertainty.

There are several reasons to question whether PPV is a valid measure of ejection velocity. Firstly, the PPV source, or *design event*, is assumed to be remote from the excavation boundary, when in fact the violent instability is often coincident with the tunnel. Such events invalidate values of PPV based on the distance dependency. Secondly, field observations in both mine blasting (Fleetwood, et al., 2009, Fleetwood, 2010) and mine seismicity (Morissette, et al., 2012, Drover, 2014) have shown that PPV frequently bears no relationship to ground support damage. Instead, the damage locations correlate to areas of high stress, relatively weak, but still high strength brittle rock and/or relatively weak geological features.

Ground support designs focusing on PPV as a demand input variable are suggested to be fundamentally flawed. This flaw explains the frequently absent correlation between measured or back-calculated PPV and ground support damage. That flaw, recognised by Thompson, et al. (2012), Morissette, et al. (2012) and Kaiser & Cai (2013), is the assumption that the entire energy of ejection of the unstable rock mass is derived from the incoming seismic wave. In fact, it is the conversion of stored strain energy on the excavation boundary into kinetic energy of ejected rock fragments which is the key source of energy demand.

Strain energy release from rock is becoming more widely recognised as one of the crucial controls of energy demand on a ground support scheme (Thompson, et al., 2012, Cai & Kaiser, 2012). Plastic strain energy is energy stored within a material subjected to plastic deformation. As an applied normal stress increases in a rock mass, and the material undergoes strain, the strain energy density increases. Strain energy density, u (J/m^3), is the strain energy per unit volume. It is given by the formula:

$$u = \frac{U}{V} = \int_0^{\epsilon_1} \sigma_x d\epsilon_x \quad (Eq. 2.4)$$

where, U = strain energy, V = volume, σ_x = normal stress (e.g. σ_1) and ϵ_x = normal strain. Strain energy density prior to failure is equal to the area under the stress-strain curve (Figure 24). Rock that is able to sustain higher strain energy density will experience more violent and energetic failure than other rock types.

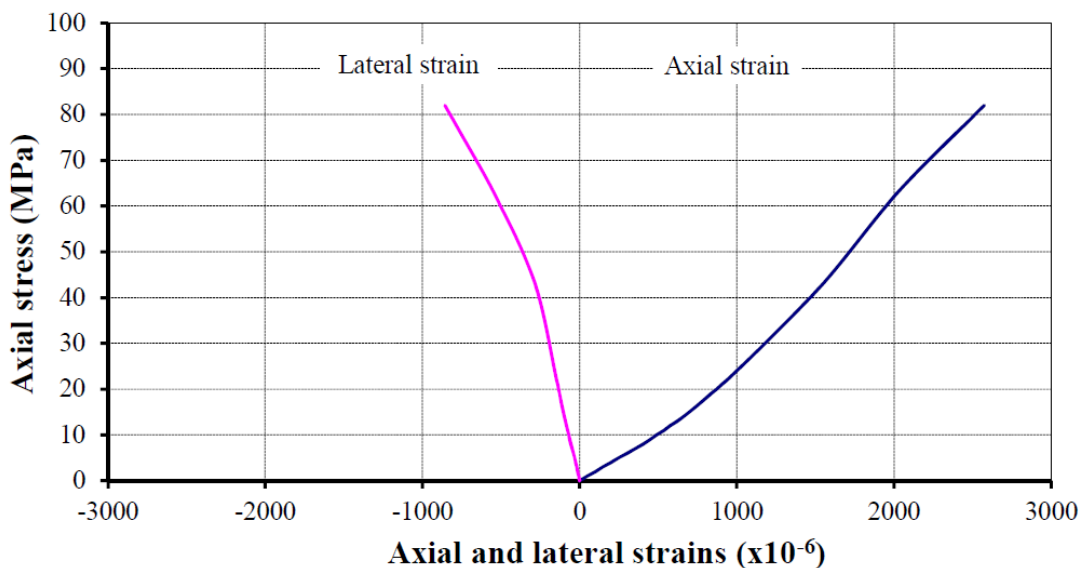


Figure 24 - Stress-Strain curve for a Dacite hard rock.

Strain energy will accumulate in strong, brittle rock under increasing stress until violent failure occurs. At this point, strain energy will be violently released. The quantity released depends on the post-peak stress-strain behaviour of the rock mass. The mechanisms of energy release may include fracture through intact rock (possibly with ejection), radiated seismic waves (Levkovitch, et al., 2013) and heat. The observed ejection of rock during the scale tunnel experiments of Kusui (2015) are classic examples of plastic strain energy release in the form of kinetic energy, with failure coincident with the tunnel boundary and negligible influence by seismic PPV.

During a violent rock mass failure, the partitioning of strain energy release to each of the aforementioned mechanisms (heat, ejection etc) is extremely complex and probably not possible to accurately quantify in a practical mining context. Of most importance to energy demand on ground support is the portion of stored strain energy which is released as kinetic energy of ejected rock blocks. It is not yet possible to partition this ejection energy analytically, due to the geological complexity of each rock mass. However, as a proxy, it is possible to reliably estimate the ejection velocity of different rock types based on experimental observations of laboratory test samples.

Kusui (2015) measured the ejection velocities of 200 mm diameter unsupported tunnels under high stress as a function of the UCS (Figure 25). Ejection velocities ranging from 3-10 m/sec were recorded. This validates back analyses of actual failures in underground mining (Ortlepp, 1993, Ortlepp & Stacey, 1994, Drover & Villaescusa, 2015b). For tunnels constructed in very strong rock, the violent ejection occurred simultaneously with crack propagation along the tunnel axis. Crack propagation was perpendicular to the orientation of the major principal stress. The resulting ejection of rock was consistent with spalling failure.

A typical result for a wall failure is shown in Figure 26, where an ejection velocity of 5.2 m/sec was determined using the background grid (Kusui, 2015). Similar velocities have been used at the WA School of Mines during dynamic testing of rock reinforcement systems (Villaescusa, et al., 2010). Ejection velocities of this magnitude are capable of damaging most commercially available ground support schemes. Generally, the higher the UCS, the higher the measured ejection velocity. Such positive correlation between the intact rock strength and the velocity of ejection is consistent with the tunnel observations of Broch & Sørheim (1984).

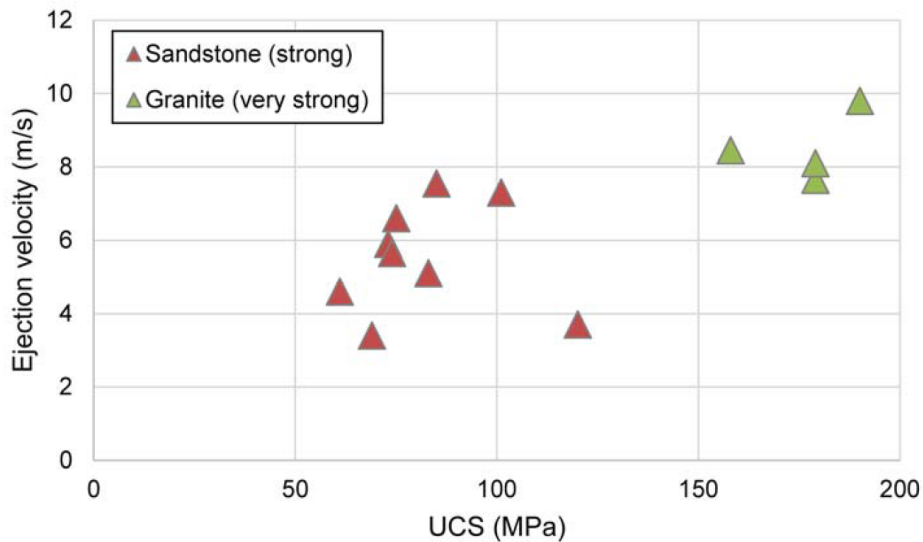


Figure 25 - Ejection velocities at spalling for unsupported tunnels in hard rock (Kusui, 2015)

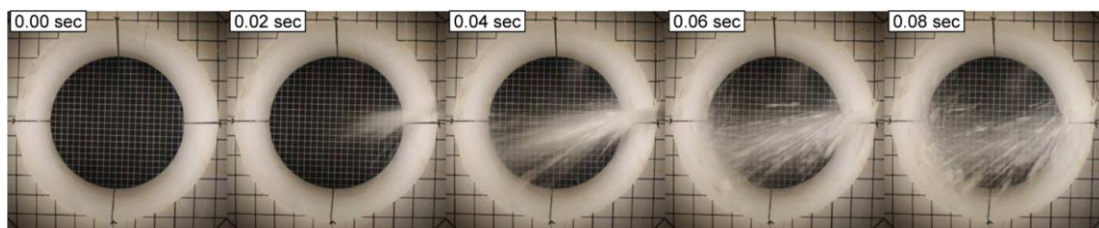


Figure 26 - Determination of ejection velocity using a high speed video camera (Kusui, 2015).

In the experiments of Kusui (2015), the scale tunnels were loaded vertically until failure, with violent ejection of rock observed from the zones of maximum stress concentrations in the tunnel sidewalls. The direction of rock ejection was perpendicular to the major principal stress and tunnel wall at the point where the maximum induced stress was tangential. This is consistent with frequent underground observations of spalling and structurally controlled failure where violent ejection of rock is observed to occur perpendicular to the excavation surfaces which are sub-parallel to the major principal stress. An example is shown in Figure 27 & Figure 28.

Potentially unstable excavation surfaces are those which are sub parallel to a principal stress of sufficient magnitude to induce instability. Roof, shoulder, face and floor damage coincides with a high sub-horizontal stress. Wall damage may occur where high stress acts sub-vertically (Drover, 2014, Villaescusa, 2015a, Villaescusa, 2015b). One possible exception is when major fault ruptures intersect the excavations. Such mechanisms may induce failure of excavation surfaces where relatively low stress concentrations existed prior to failure (Drover, 2014). The ground support loading vector would be parallel to the discontinuity surface, and therefore not necessarily perpendicular to the tunnel wall.

Several important learnings can be drawn from the observations of past researchers, and used to improve future ground support design methods. First, ejection velocity of unstable rock under high stress is proportional to the intact rock UCS. Second, for overstressing failures such as spalling and structurally controlled wedge ejection, the maximum load demand on the ground support scheme occurs where the maximum induced stress is tangential to the excavation boundary. Thirdly, the direction of ejection and thus maximum ground support loading is generally radially inward at the point of maximum tangential stress. Finally, seismic ground motion parameters such as PPV and the site effect vary so greatly from site to site that they have proven to be highly unreliable input variables for ground support demand calculations.

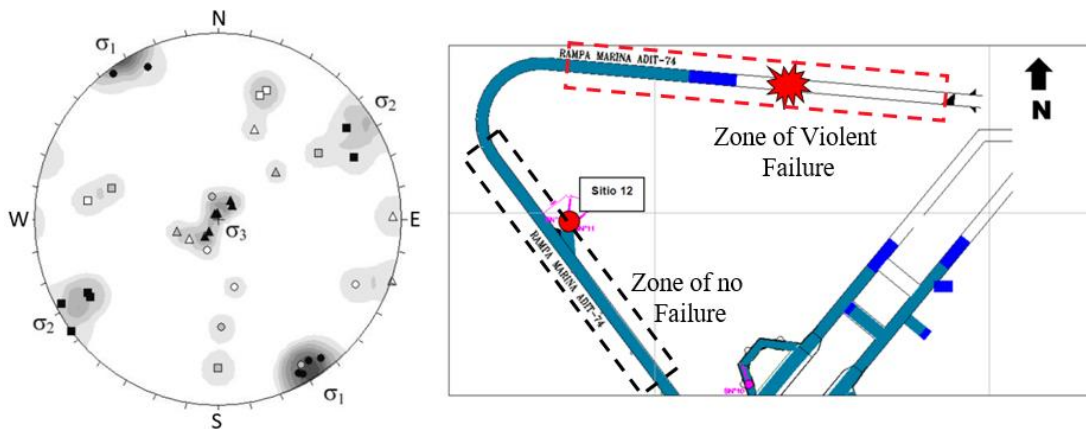


Figure 27 – Stress data (Windsor, et al., 2006) and excavation orientation (Guajardo & Moraga, 2014).

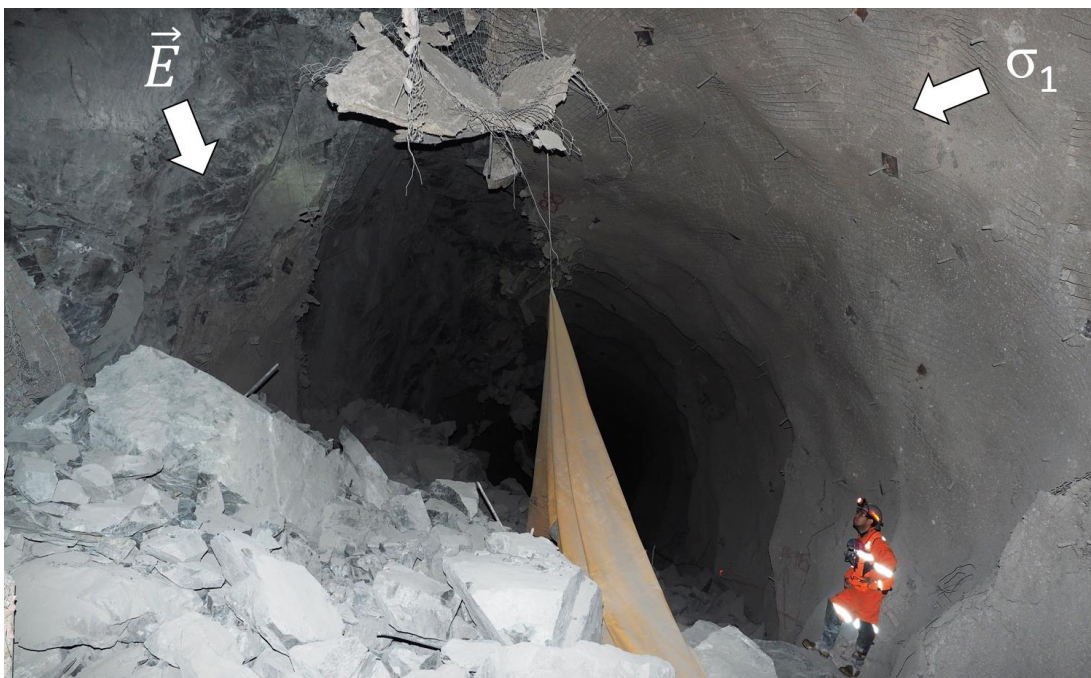


Figure 28 – West-facing view of a violent failure, with ejection vector (\vec{E}) being orthogonal to the σ_1 stress.

2.3.3 Displacement

The demand on the ground support scheme is determined by the force-displacement response of the rock mass. It is generally accepted that some degree of rock mass displacement is inevitable when creating an excavation at great depth. Displacements occur where the creation of a free surface removes confinement on the adjacent rock mass, and stress acting on the excavation subsequently causes failure of intact rock or deformation along discontinuities (Thompson, et al., 2012). The resulting volumetric bulking of the rock mass causes radial closure of the excavation, possibly leading to ejection. This process is highly complex and variable, depending on the rock mass characteristics and failure mechanisms. Displacements in strong, brittle rocks typically occur suddenly and violently, in singular or multiple episodes.

Empirical relationships have been proposed in the past in order to simplify displacement predictions. For example, the depth of failure defined in Eq. 2.2 has been multiplied by an assumed bulking factor to derive an estimate of surface displacement (Kaiser, et al., 1996, Kaiser & Cai, 2013). This method is commonly used in Canada and also Australia (Scott, et al., 2008). One issue with this empirical approach is the implicit assumption that all energy released by the failing rock mass is consumed by fracturing. However, energy release may also cause kinetic ejection. This places additional displacement demand on the ground support which cannot be approximated by a bulking factor. In short, the rock mass may transition from intact, to loosely consolidated (bulked) to completely unconsolidated (ejected) during a failure.

Due to the difficulty in accurately forecasting rock mass displacements empirically, a qualitative approach was suggested by Thompson, et al. (2012) and later modified by Villaescusa, et al. (2014). As presented later during discussion of ground support design, this qualitative approach defines several demand categories ranging from Low to Extremely High. Each category has a corresponding range of displacement, support reaction pressure and energy. These demand categories have been experientially applied to excavations for the purposes of quantifying the demand on ground support (Villaescusa, et al., 2014).

2.3.4 Displacement due to Fault Rupture

Fault rupture mechanisms of excavation failure involve sudden and violent shear-displacements along the planar surfaces of discontinuities that intersect an excavation (Ortlepp, 1997). Such mechanisms of instability are generally driven by large-scale stress adjustments in the global loading system. They may involve complex, extremely high energy load transfer throughout the rock mass. Often the instability is precipitated by a reduction in the confining stress on a structure due to the stress change effects of large void geometries. Increasing shear stresses may also be generated by similar processes. It is possible for fault-related instability to be continuous or semi-continuous over tens of metres of a discontinuity surface, with associated ground support damage over this distance. In extreme cases, structural instability in a mine may extend for more than one hundred metres along such features (Drover, 2014).

Unlike spalling or structurally controlled block instability, which occur very close to the excavation boundary (Villaescusa, et al., 2016b), fault rupture mechanisms may involve energy release throughout a much large volume of the rock mass. This is a result of the generally much broader mechanisms of stress adjustment that precipitate fault rupture (Hudyma, 2007). Evidence of this fact can be derived from observations and analysis of fault-related seismic source parameters, associated excavation damage (Drover, 2014) and advanced numerical modelling of the global stress and energy release characteristics which correlate to the onset of significant fault related instability (Beck, 2013).

As a consequence of their scale, fault rupture mechanisms can potentially generate displacements at the excavation surface which may be impossible to arrest using conventional ground support technologies. The displacement demand on the ground support scheme is the shear displacement of the structure at the excavation surface and within the reinforcement zone. In this context, fault rupture displacements are the result of the brief but continuous driving shear forces. The most extreme displacements may be highly localised to only a few square metres of the excavation (Figure 29 & Figure 30). Fault rupture mechanisms may not result in the formation of wedges, since only one structure may be mobilised. However, if otherwise stable wedge geometries are present in the vicinity, they may be ejected as a consequence of the primary fault instability, leading to large depths of failure (Figure 31).



Figure 29 - Fault rupture failure mechanisms result in highly concentrated loads on ground support.

Displacement demand on ground support due to spalling or structural block ejection is a function of the initial kinetic energy of the ejected blocks and the overall loading response of the ground support scheme. Rock mass displacements associated with fault rupture may not behave in the same way. Fault rupture displacements are controlled by the destabilising and stabilising forces acting on the structure. Displacement during failure may not decay until the shear strength, shear stresses and confining stresses return to equilibrium. None of these forces are able to be substantially controlled with installed ground support.

For this reason, it is suggested here that the typical kinetic energy assessment may not be appropriate to quantify the energy demand on ground support due to fault rupture events. It is therefore necessary to accept that displacement may not be possible to arrest. Instead, the ground support scheme should be designed such that it is capable of transferring the load of failed rock to adjacent stable ground. However, fault displacement is subject to considerable uncertainty and it is not yet possible to predict the demand with an acceptable level of reliability. Empiricism and advanced numerical modelling tools may facilitate a design approach in the context of failure mechanisms which involve extreme fault-related displacements (Beck, et al., 2010).



Figure 30 - Fault rupture causing severe excavation damage, with very high ejection velocity of instability.



Figure 31 - Violent fault rupture causing severe ground support damage.

2.3.5 Shear Failure Mode of Pillar Crushing

Shear failure mode of pillar crushing (Ortlepp, 1997) is typified by growth of large fractures beyond the immediate boundary of the excavation. In laboratory scale experiments, Kusui (2015) confirmed that shear fractures propagate sub-parallel and oblique to the major principal stress and intersect the excavation at the point of maximum tangential stress concentration (Figure 32). Considerable seismic activity may accompany this mode of failure. However, there is typically a period of minimal seismic activity following spalling failure and immediately preceding the onset of shear instability (Kusui & Villaescusa, 2016).

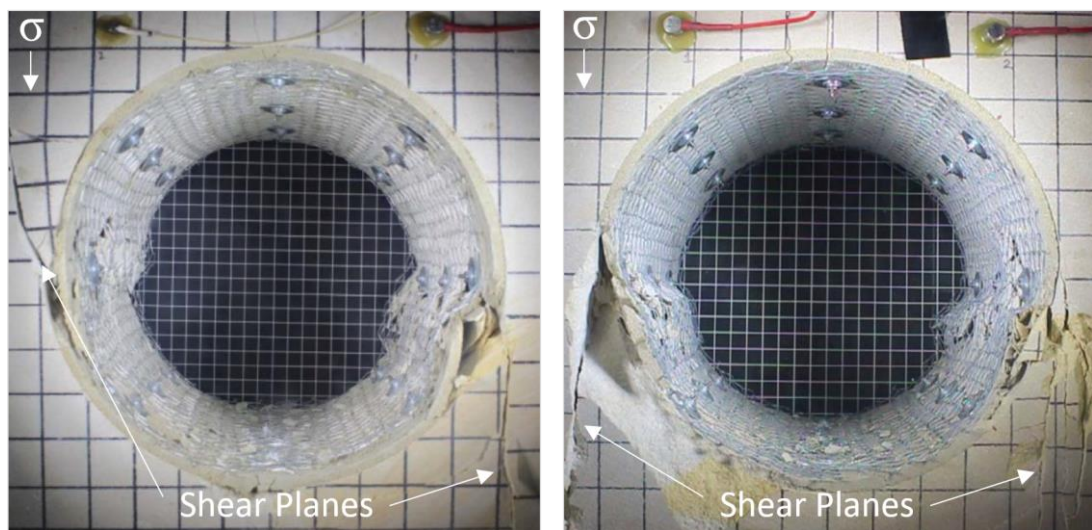


Figure 32 - Shear failure mode of pillar crushing in vertically loaded test samples (Kusui, 2015).

The shear failure mode of pillar crushing may involve ejection of blocks not already mobilised by spalling or structural controls, together with volumetric bulking of the rock mass. Translations and rotations of large blocks may occur, and they may remain somewhat self-supporting post-failure if interlocked with adjacent blocks. The deformations are most significant in the zone of maximum stress concentration. Rock mass bulking is generally driven by the mobilisation of large blocks bounded by the major plane of shear rupture. The rupture process may occur violently. As such, this mode of failure places large displacement demand on the ground support scheme. Energy release during shear failure of pillars is primarily via new fracture creation, reactivation of pre-existing discontinuities and sliding. The principal plane of shear rupture may be mobilised over a distance of one or more excavation diameters. Frequently this results in large shear displacements on reinforcement elements installed in the stress concentration zone (Kusui, 2015).

Major shear failure of excavations is typically restricted to areas where high void extraction ratios exist in the plane perpendicular to the orientation of the principal stress. This results in elevated stress concentrations in the remaining pillars. Examples of vulnerable geometries include the undercut and extraction level development of a block cave mine or sub level cave production level cross-cuts. These mining methods require closely spaced excavations with thin horizontal pillars. The pillars are frequently susceptible to high concentrations of the minor principal stress (σ_3), which may be concentrated with time due to global extraction increases. High extraction ratio geometries such as these have limited load transference to adjacent buttressing zones. As such, displacement demand on the ground support scheme may continue for as long as additional loading is experienced (Figure 33).

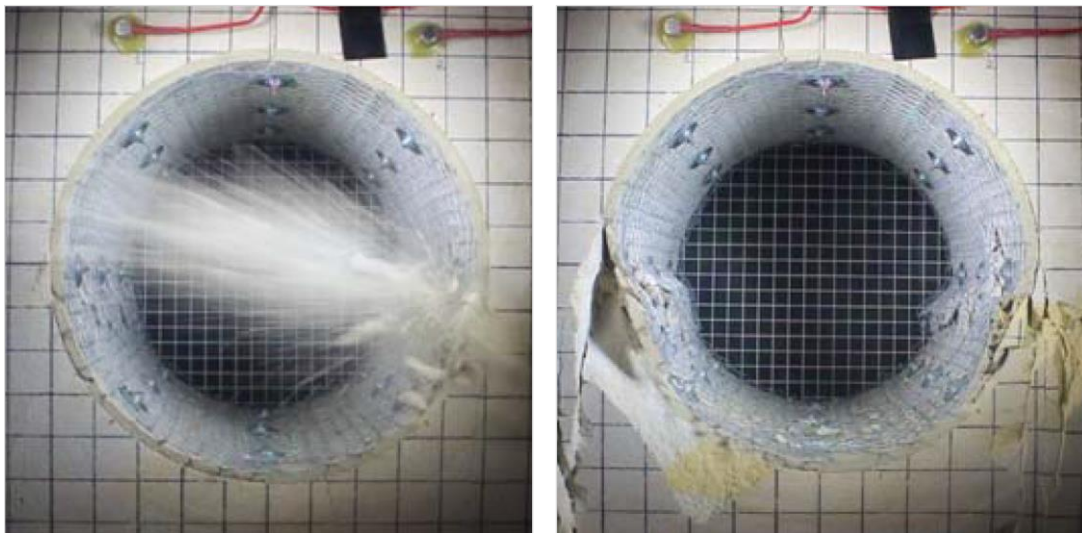


Figure 33 - Displacement demand during spalling (left) and pillar shear failure (right) (Kusui, 2015).

It is necessary to consider the loading context in which an excavation exists, in order to assess the likely duration of loading demand on the ground support scheme following the onset of shear failure. In the case of an isolated development drift, such as a decline access, shear failure may be unlikely due to load redistribution to areas of naturally high rock mass confinement nearby. Conversely, in high extraction ratio geometries, continuous loading may see the excavation pass through spalling, shear failure to complete pillar crushing with time-dependent continuous creep. This may persist for the entire service life of the excavation if load transfer from areas of adjacent activities do not cease to increase or otherwise reach a stable equilibrium with the rock mass. As such, shear failure mode of pillar crushing may eventually mature into continuous, unstoppable displacements.

2.4 Ground Support

Ground support is any artificial material which provides a strength improvement or containment effect on the rock mass surrounding an excavation. In a high stress, hard rock excavation, ground support is intended to prevent unstable rock from ejecting uncontrollably into the work area where it may cause injury or damage. In broad terms, ground support consists of two fundamental systems. These include the reinforcement system, which acts internal to the rock mass, and the surface support system, which acts on the rock externally at the exposed free face (Windsor & Thompson, 1993). Typically, ground support is installed by some combination of mechanised and manual processes. A ground support scheme describes the complete arrangement of reinforcement and surface support components (Thompson, et al., 2012).

2.4.1 Reinforcement Systems

2.4.1.1 Definition and Functional Requirements

Reinforcement systems are artificial materials embedded within the rock mass surrounding an excavation in order to provide a stabilising action surplus to the natural load bearing capacity of the rock (Thompson, et al., 2012). In the hard rock tunnelling and mining context, reinforcement is any linear element that is installed within a borehole. Examples of reinforcement elements include steel rebar or cable bolts. The two main roles of reinforcement are to stabilise large blocks that may be mobilised by deep structural instability and also to provide a load transfer interaction with the surface support system. A generic reinforcement system consists of four components, as depicted in Figure 34. These include the rock mass, the reinforcement element, the internal fixture and the external fixture (Thompson, et al., 2012). Some variations of this arrangement exist, depending on the design and load transfer mechanics of the specific type of reinforcement.

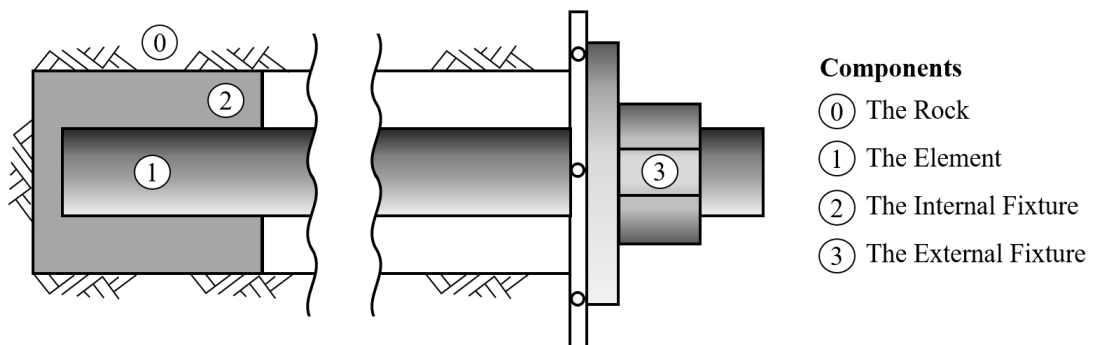


Figure 34 - Generic reinforcement system (Thompson, et al., 2012).

2.4.1.2 Performance Measures

The capacity of individual elements in a ground support scheme may be characterised according to the response to loading, as shown in Figure 35. In this figure, the response to loading of reinforcement may be tensile, compressive or shear and for surface support it may be lateral shear and bending or in-plane combinations of shear with tension or compression (Thompson, et al., 2012). The specific mechanism of reinforcement and/or support loading depends on the mechanism of rock mass failure and the corresponding displacements which act on the installed ground support components. The performance metrics for ground support capacity may be grouped as follows:

Loading Capacities

- F_{max} Maximum Load
- F_{res} Residual Load

Deformation Capacities

- δ_p Deformation at F_{max}
- δ_{max} Maximum Deformation

Stiffness

- K_{ti} Initial Tangent Stiffness
- K_{sp} Secant Stiffness at F_{max}
- K_{sr} Secant Stiffness at δ_{max}

Energy Dissipation Capacity

- E_p Energy Dissipation at F_{max}
- E_r Energy Dissipation at δ_{max}

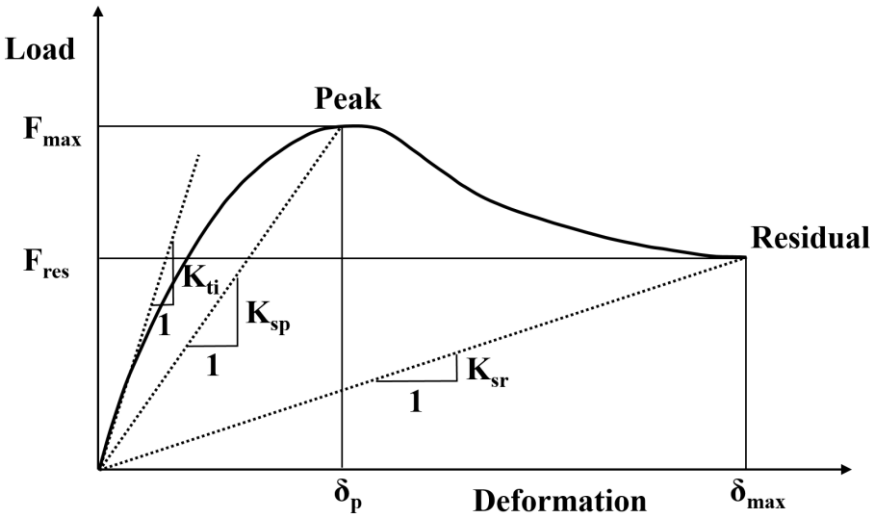


Figure 35 - Ground support capacity performance indicators (Thompson, et al., 2012).

Energy dissipation capacity is an important performance measure for ground support. It is equivalent to the area between the load-deformation response curve and the deformation axis for both static and dynamic loading. The energy dissipation capacity of ground support elements must exceed the rock mass demand partitioned to that element by a sufficient margin, in order to reliably avoid failure.

2.4.1.3 Loading Mechanisms

Reinforcement systems are loaded due to displacement of the rock mass surrounding a borehole (Thompson, et al., 2012). The causes of such displacements may include stress-driven fracturing of intact rock with volumetric bulking or movement across joint structures, potentially followed by ejection of blocks. In the simplest case, material displacements may cause relative axial deformations between the borehole wall and reinforcement element (Figure 36). This leads to strain progressively increasing in the reinforcement element towards the point of maximum displacement. In more complex loading situations, translations of large blocks along discontinuities may lead to combinations of tensile, shear and compressive loading mechanisms (Figure 37). Torsional and bending loads may arise where large blocks are also free to rotate, as shown in Figure 38 (Thompson, et al., 2012).

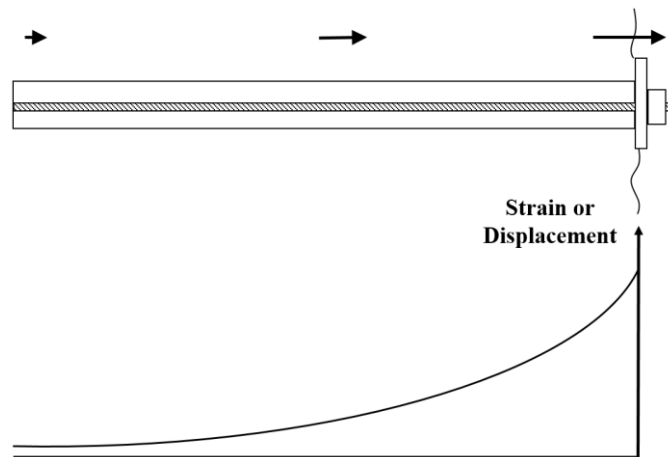


Figure 36 - Reinforcement loading due to axial rock mass deformations (Thompson, et al., 2012).

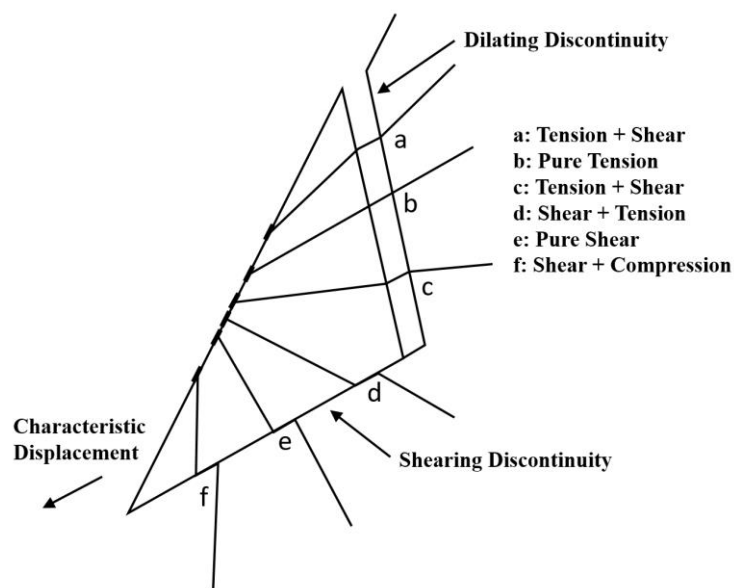


Figure 37 - Reinforcement loading due to block translations (Thompson, et al., 2012)

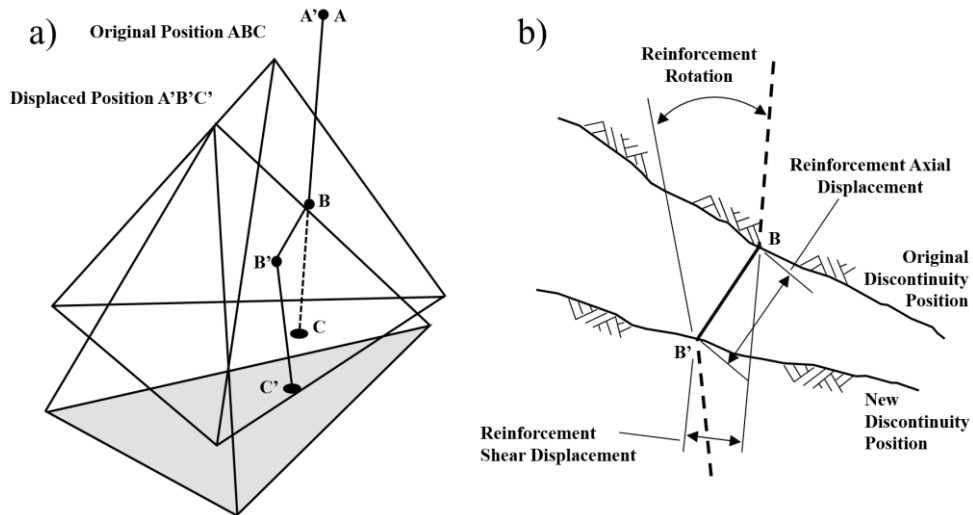


Figure 38 – Reinforcement loading due to block translations and rotations (Thompson, et al., 2012).

2.4.1.4 Load Transfer

Critical to the performance capacity of a reinforcement system is the inherent material strength of the element and the mechanism of load transfer between the rock mass and the element. In this context there are three generic classes of reinforcement based on the internal load transfer mechanism. These include Continuously Mechanically Coupled, (CMC), Continuously Frictionally Coupled (CFC) and Discretely Mechanically or Frictionally Coupled (DMFC) (Windsor & Thompson, 1993, Thompson, et al., 2012). Schematic representations of these three classes of reinforcement are shown below in Figure 39.

TYPE	X - SECTION	LONGITUDINAL VIEW OF ANCHOR
Continuous Mechanically Coupled		
Continuous Frictionally Coupled		
Discrete Mechanically or Frictionally Coupled	 A - A B - B	

Figure 39 - Reinforcement classes defined by internal load transfer mechanism (Thompson, et al., 2012).

Continuously Mechanically Coupled reinforcement systems rely on a medium of internal fixture to provide a combination of mechanical interlock and friction between the rock mass and entire enclosed length of the reinforcement element. Mediums of internal fixture typically include chemical resins or pumped cementitious grouts. Continuously Frictionally Coupled elements rely solely on friction between the reinforcement element and adjacent borehole wall in order to generate load bearing capacity. Discretely Mechanically and/or Frictionally Coupled reinforcement elements utilise one or more of the above load transfer mechanisms, applied at discrete locations along the axis of the reinforcement element. Irrespective of the reinforcement mechanism, the overall intent of the reinforcement element is to transfer load from the unstable to stable region of the rock mass (Figure 40).

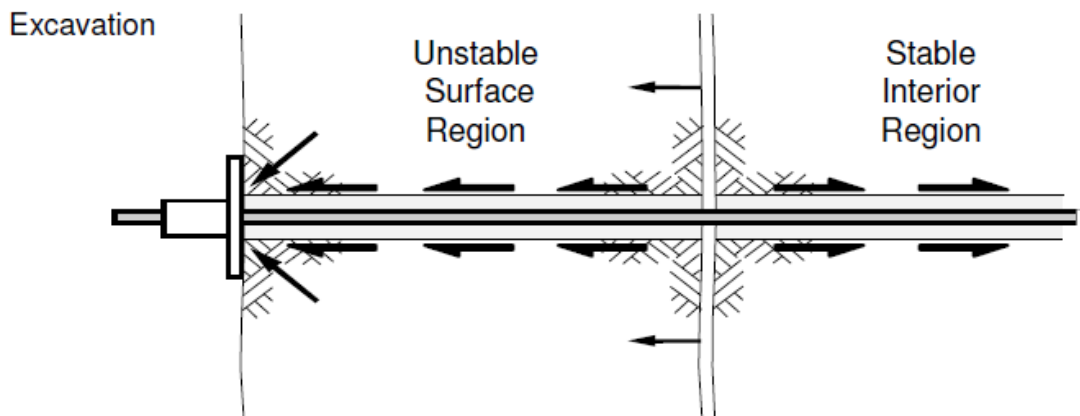


Figure 40 – Reinforcement load transfer from unstable to stable rock (Thompson, et al., 2012).

Reinforcement elements within each of the three aforementioned classes display distinctly different force distributions within the element during an applied dynamic loading. Figure 41 shows the simplified force distributions within each of the element classes for a conceptual scenario involving instability across a discontinuity in the rock mass (Thompson, et al., 2012). Villaescusa, et al. (2010) note that testing and theoretical analysis indicate that CMC class elements exhibit a relatively stiff response when compared to the other reinforcement types. By contrast, CFC class elements have low strength and may exhibit significant displacement under moderate to low loads. Those within the DMFC class are less stiff than those in the CMC class because the element is able to deform more within the decoupled length. Most new technologies for high energy dissipation fall within the DMFC class (Villaescusa, et al., 2010). All these systems rely on deformation in the element relative to the internal fixture within the toe embedment length.

Each of the aforementioned reinforcement classes have various strengths and weaknesses which must be recognised when considering their implementation in a ground support scheme at great depth. For example, CMC elements have the vulnerability of relatively high strain concentrations at the point of rock mass dislocation. However, these elements have the advantage of a more reliable mechanical interaction with the rock mass, due to the greater coupling length between the element, rock mass and internal fixture. DMFC elements have the reverse characteristics. Strain concentrations within the element are generally lower than those of CMC, due to the greater potential for elongation of the element along the decoupled length. This can assist energy dissipation where displacements are concentrated at discontinuities. However, DMFC elements are more susceptible to failure and loss of load bearing capacity at the internal fixture due to the shorter length of the coupling.

The load transfer mechanics of the three reinforcement classes are important to consider in the context of the specific excavation failure mechanisms that may be expected. For example, CFC elements generate load transfer capacity as a function of the length of the frictional coupling between the element and borehole wall. This method of load transfer is poorly suited to deep structurally controlled failure mechanisms where the depth of CFC embedment beyond the zone of instability may be short, resulting in a low capacity. As such, CFC elements are not recommended for reinforcement in deep excavations with complex rock mass structural assemblages. In this context, the length of the CFC element anchored in stable ground may provide substantially less energy dissipation capacity than the demand generated by the instability. In contrast, DMFC elements may be considered unsuitable where bulk rock mass movement is expected. This mechanism of rock mass failure benefits from continuous reinforcement engagement and resistance to displacement along the entire axis of the element.

2.4.1.5 Current Technologies

There exists a wide range of technologies currently available for reinforcement in deep hard rock mining and tunnelling. Many technologies have been used for decades and remain in frequent use today. An exhaustive description of currently available reinforcement technologies is beyond the scope of this thesis. However, several examples from each of the aforementioned classifications which are commonly used in deep and high stress underground construction are referenced below.

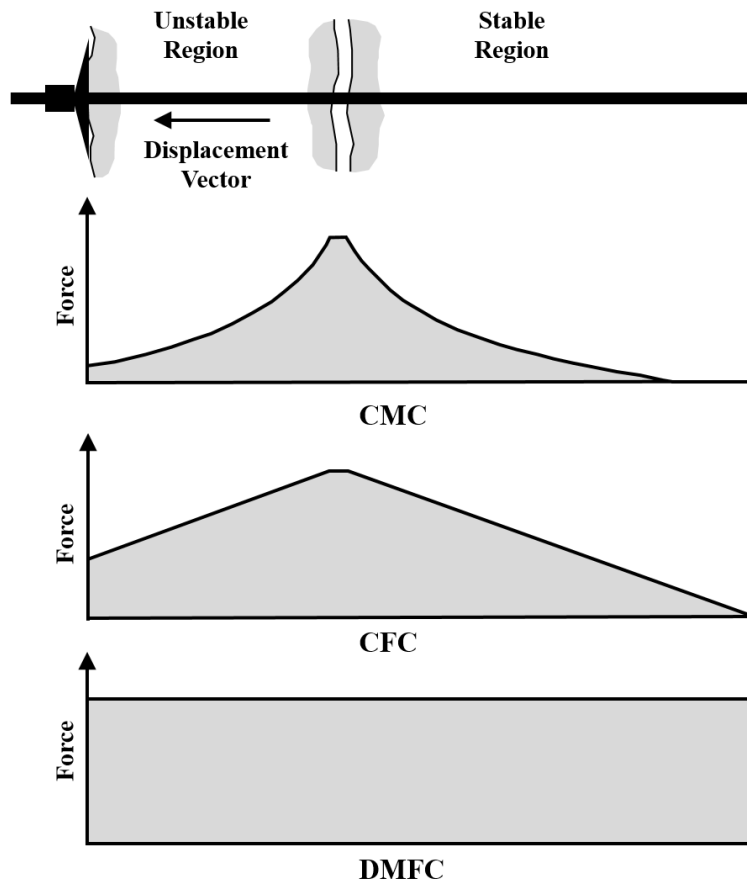


Figure 41 – Element force distributions for the three reinforcement classes (Thompson, et al., 2012).

Continuously Mechanically Coupled

- Cement/Resin Grouted CT Bolt (Dywidag, 2018)
- Threaded bar (Hoek & Brown, 1980)
- Cable bolts (Hutchinson & Diederichs, 1996)

Continuously Frictionally Coupled

- Split Set Friction Stabilisers (Scott, 1976, 1983)
- Omega Swellex (Stillborg, 1994)
- Mechanical Dynamic Bolt (Carlton, et al., 2013)

Discretely Mechanically or Frictionally Coupled

- Garford Dynamic Bolt (Varden & Player, 2008)
- Debonded PosiMix (Dywidag, 2018)
- D-Bolt (Li, 2010)

The dynamic strength performance of these and many more reinforcement elements has been thoroughly investigated by Player (2012).

2.4.1.6 Force-Displacement-Energy Capacity and Design

Reinforcement elements with differing mechanisms of load transfer exhibit considerably different force-displacement and energy dissipation performance when sudden loading is applied. The required force-displacement response and energy dissipation capacity of a ground support scheme should exceed the demand imposed by the rock mass. Depending upon the depth of failure, the reinforcement demand may be applied directly from the rock mass or through the surface support connected to the reinforcement elements. Villaescusa, et al. (2014) previously defined rock mass demand in terms of ranges of allowable displacement and energy dissipation, as shown in Table 2. This was combined with the WA School of Mines dynamic reinforcement capacity database (Player, 2012) to form a reinforcement design chart (Figure 42).

Table 2 - Typical rock mass demand for ground support design (Modified after (Villaescusa, et al., 2014)).

Demand Category	Reaction Pressure (kPa)	Surface Displacement (mm)	Energy (kJ/m²)
Low	< 100	< 50	< 5
Medium	100 - 150	50 – 100	5 – 15
High	150 - 200	100 – 200	15 – 25
Very High	200 – 400	200 – 300	25 – 35
Extremely High	> 400	300	> 35

The WASM reinforcement design chart developed by Villaescusa, et al. (2014) illustrates the energy dissipation capacity of reinforcement elements on the vertical axis. A wide variety of reinforcement arrangements are considered, including numerous examples from the CMC, CFC and DMFC elements. The displacement corresponding to the quoted energy dissipation of each element is shown on the horizontal axis. This design chart requires that an assessment of the likely rock mass demand be made prior to selection of the reinforcement elements. Appropriate elements are chosen such that they plot within the green design region of the chart. That is, such that their energy dissipation and displacement capacity meets the necessary demand, as defined by the demand categories shown in Table 2.

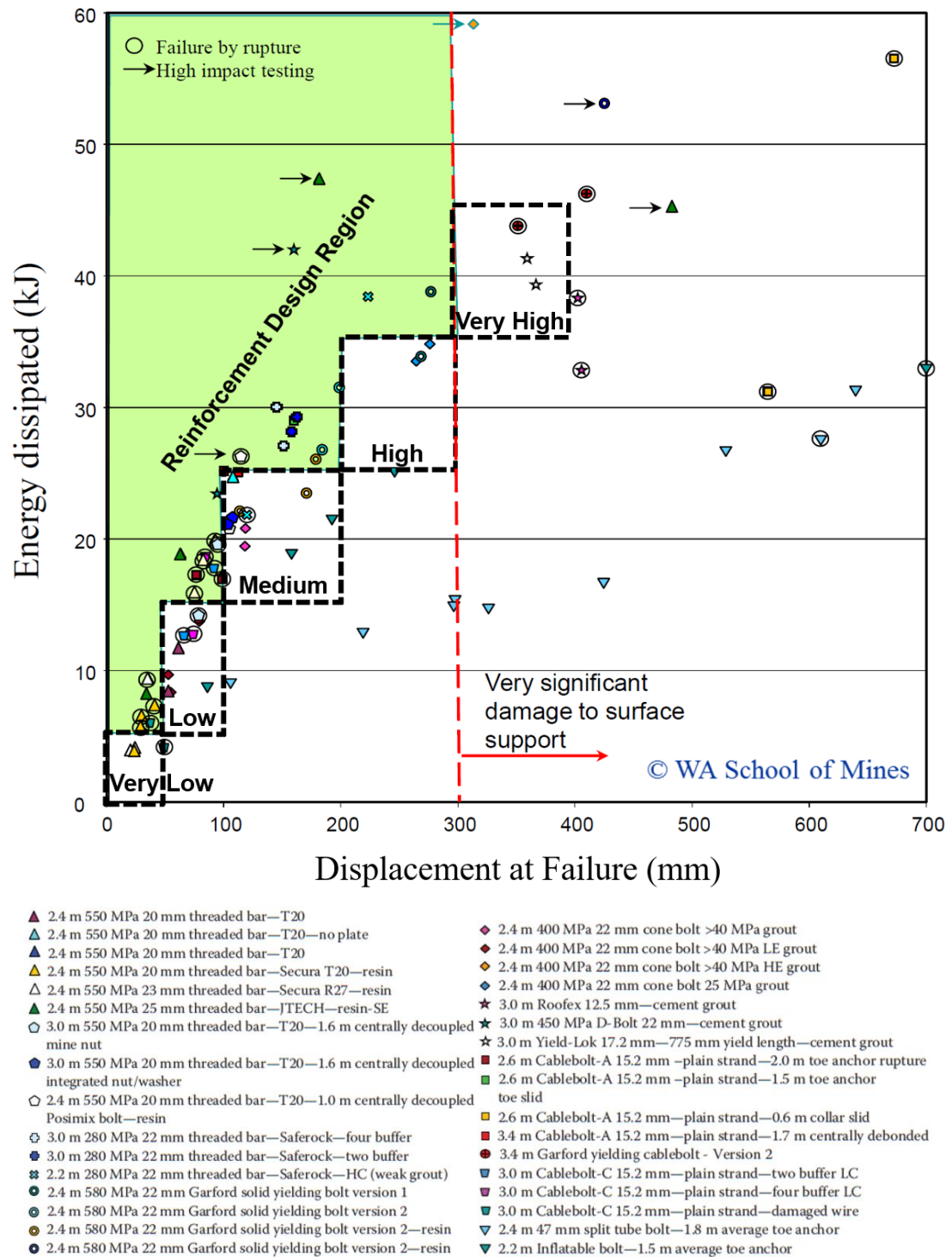


Figure 42 - WASM reinforcement design chart (Villaescusa, et al., 2014).

The energy dissipation and displacement capacities of reinforcement elements are largely a function of the material properties and geometry of the element as well as the load transfer mechanics. Also important for overall system performance is the length of the element with respect to the depth of instability. Reinforcement length should be designed such that the element penetrates the stable rock mass beyond the maximum depth of instability (Windsor, 1997). Sufficient reinforcement embedment within stable ground is necessary in order to ensure that the complete energy dissipation capacity of the element is utilised. Laboratory tests indicate that a minimum anchor embedment length of 1.0m is required to maximise load transfer to the element (Villaescusa, et al., 2010). In field conditions, an embedment of 1.5m may be needed.

The mechanism of load transfer between the rock mass and reinforcement element has a significant influence on the energy dissipation capacity of the element. DMFC elements for example may be adversely affected by rock mass deterioration at the anchor point. Such elements rely on a small number or perhaps only one point of load transfer to the rock mass, rather than load transfer along the entire element axis. Damage to this critical portion of the element can result in complete loss of energy dissipation capacity, even when the rest of the element remains intact. CFC elements by contrast have a continuous load transfer along the entirety of the bar axis. However, laboratory tests and field evidence indicate that once the initial frictional resistance is overcome, CFC elements tend to slip repeatedly under low load (Villaescusa, et al., 2010). In some cases, this may result in potentially very high energy dissipation, but with unacceptably high displacements that are incompatible with the surface support.

Based on laboratory data from the WASM dynamic testing facility (Player, 2012, Villaescusa, et al., 2014), continuously mechanically coupled (CMC) reinforcement elements display the greatest energy dissipation capacity and performance reliability during high impact dynamic testing. Due to their energy dissipation capacity under extremely high dynamic energy demand, CMC elements are considered superior for inclusion in ground support schemes where deep structural instability may be expected. Preferred elements include 25mm diameter, cement encapsulated (fully grouted) 550MPa threaded bars for moderate depth reinforcement (2.5 to 4.0m) and 15.2mm high tensile plain strand cable bolts for deep reinforcement (4.5 to 7.0m). DMFC arrangements of similar reinforcement may be better suited where larger displacements and higher energy demands are anticipated.

2.4.2 Surface Support Systems

2.4.2.1 Functional Requirements

Surface support describes the components of the ground support scheme which are installed external to the rock mass. These components provide a reaction force at the face of the excavation in order to contain deformation of the rock (Windsor, 1997). Typically, excavations constructed at great depth in areas of violent failure potential include some form of surface support system. The primary function of surface support in this context is to contain shallow spalling failures as well as to provide load transfer from unstable to stable regions of the excavation when large block instability occurs. Surface support systems frequently rely on connectivity to reinforcement in order to effectively perform this function (Thompson, et al., 2012). In the absence of integration with a reinforcement pattern, some surface support products may rely on direct adhesion to the rock mass or formation of a self-supporting compression arch.

Surface support systems can be classified as either point, strip or areal (Figure 43). Point surface support systems include small components such as plates which act at the collar of reinforcement systems. Point support components typically facilitate load transfer between the reinforcement and broader surface support system. Strip support systems are characterised by linear components which connect two or more reinforcement elements. Examples of strip support systems include mesh straps, cable laces, steel sets or reinforced shotcrete arches. Areal support systems are arguably the most common form of surface support. These systems extend across the two or three dimensional excavation surface. Types of areal support include welded or woven steel wire mesh and sprayed liners such as shotcrete (Thompson, et al., 2012).

It is beneficial to ensure that the design of the ground support scheme includes some redundancy in the connections between the surface support and reinforcement. This ensures that the system capacity for load transference between the various components does not immediately break down in the event of isolated components failure. For example, overlaps between mesh sheets should be secured by a reinforcement element with a minimum of three wire strands in each sheet. In this arrangement the increased likelihood of mesh failure at the overlapping strand is addressed with redundancy where the mesh interaction with the reinforcement element can cause very high load concentrations. Such redundancies are important, as they allow the system to tolerate isolated material failures while reducing the risk of overall system failure.

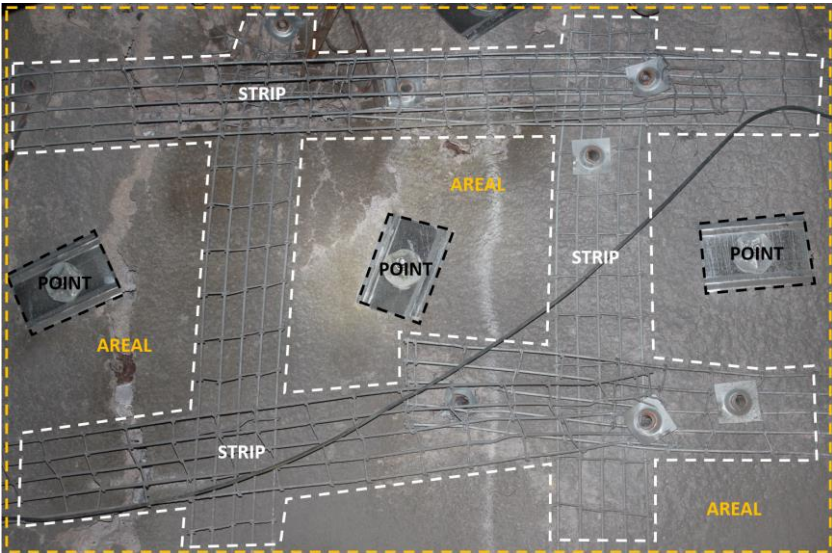


Figure 43 - Examples of point, strip and areal surface support components.

2.4.2.2 Loading Mechanisms and Load Transfer

The loading mechanisms acting on surface support may vary depending on the specific failure mechanics of the rock mass. Where stress concentrations on the excavation boundary are high, convergence may occur due to stress-driven fracturing and associated volumetric bulking of the rock mass. This process may occur in a violent or non-violent manner. Alternatively, in complex jointed rock, loading of the surface support may occur due to instability of structurally controlled tetrahedral wedges. Load transfer through the surface support system from the unstable to stable regions of the excavation can occur in several ways. These include indirectly, via adjacent reinforcement elements (Figure 44), directly, via adhesion to the rock mass (Figure 45), or a combination of both methods (Thompson, et al., 2012).

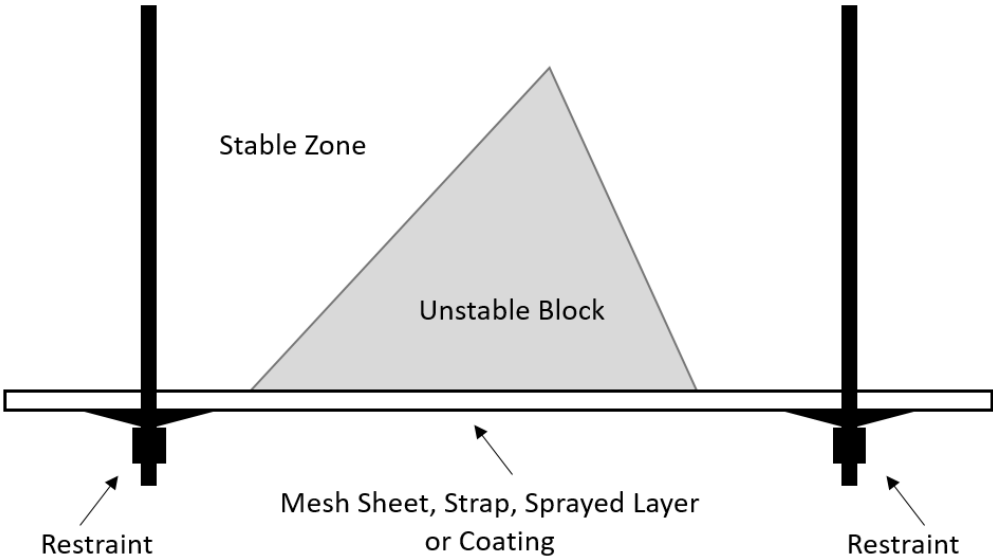


Figure 44 - Load transfer from surface support to adjacent reinforcement systems (Thompson, et al., 2012)

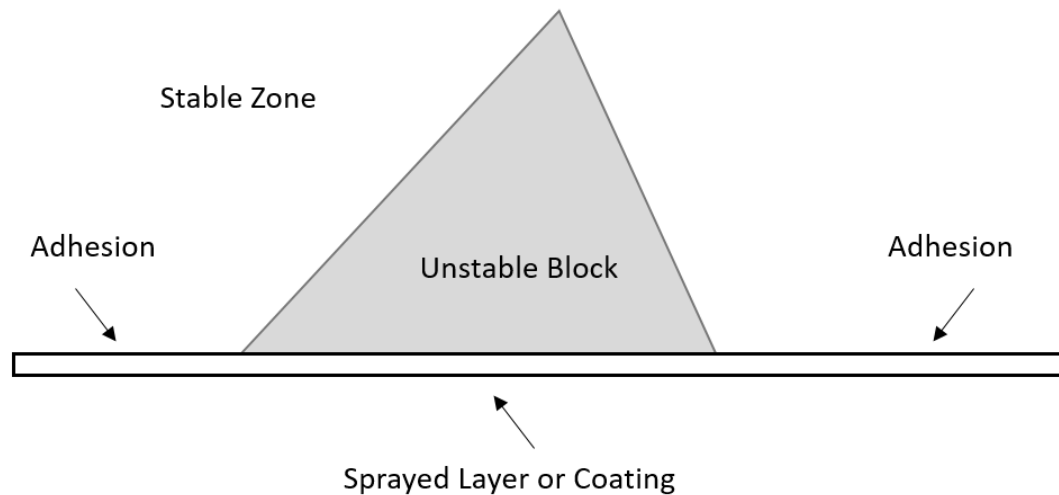


Figure 45 - Load transfer from surface support to surrounding rock via adhesion (Thompson, et al., 2012).

2.4.2.3 Current Technologies

Arguably there are fewer surface support technologies than reinforcement available to the global mining industry. However, the most common technologies in use for the surface support of deep underground excavations, particularly in mining, include the following:

- sprayed shotcrete (both plain and fibre-reinforced),
- mild steel weld mesh,
- high tensile woven chain link mesh.,

A list of these and numerous other surface support technologies and their associated technical specifications has been documented by Louchnikov, et al., (2015).

2.4.2.4 Force-Displacement-Energy Capacity and Design

In deep, highly stressed mining conditions, surface support is often the first step in the installation of the ground support scheme. Shotcrete is typically installed to cover the exposed rock mass and provide a more uniform surface profile. In Australia, a common industry standard in shotcrete design is to apply a 30-35MPa (28 day) uniaxial compressive strength mix. Steel mesh is frequently installed following shotcrete application. Mesh may be installed manually or using a mechanised jumbo.

The manner in which the surface support components are installed and integrated has a significant effect on the load transfer characteristics, and thus the ultimate energy dissipation capacity of the final surface support system. Laboratory strength testing data shown in Figure 46 indicate that surface support energy dissipation capacity is superior where a shotcrete layer is internally reinforced with steel mesh (Morton, et al., 2009). In this arrangement both surface support components are rigidly integrated and thus have a consistent force-displacement response to any applied loading (Figure 47, Figure 48). Shotcrete installed with external mesh frequently fails prior to the mesh dissipating any significant amount of energy (Figure 49).

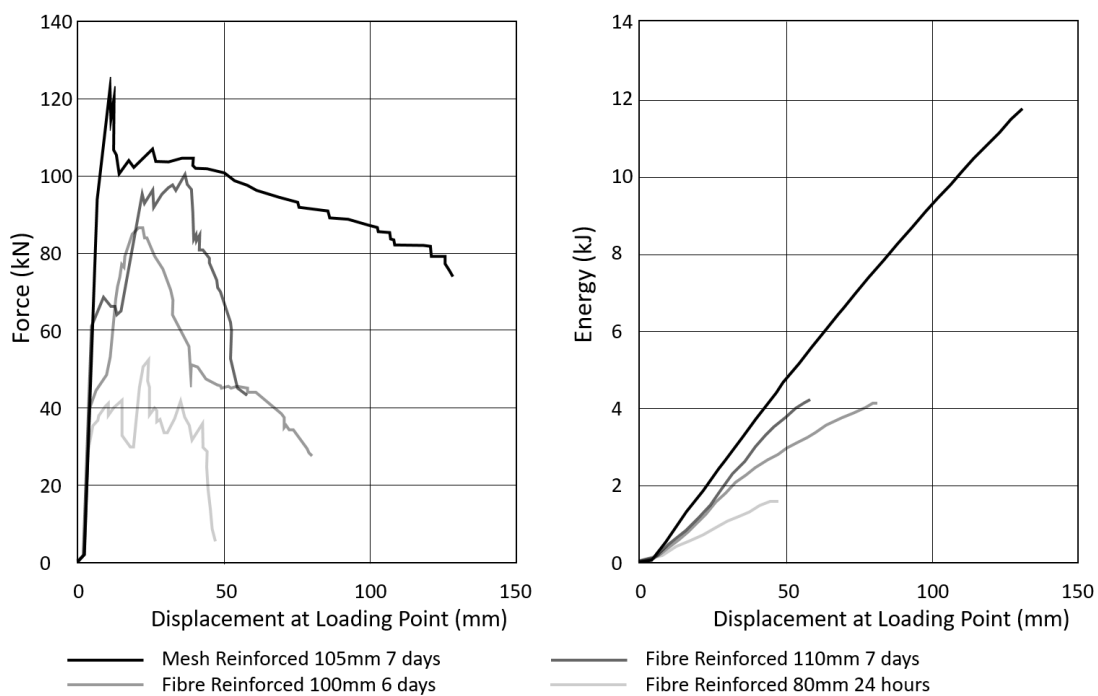


Figure 46 – Shotcrete static load-displacement and energy dissipation results (Morton, et al., 2009).

A 105mm thick shotcrete layer, internally reinforced with mild steel weld mesh may dissipate up to 7 kJ/m². This value could be expected to increase by a factor of 3 in the case that the shotcrete is internally reinforced with high tensile articulating mesh, which would tolerate much larger energy and displacement demand, prior to becoming ineffective.



Figure 47 – Regular damage patterns in mesh-reinforced shotcrete after violent loading (Drover, 2014).



Figure 48 - Mesh-reinforced shotcrete failure in large blocks due to high energy demand (Drover, 2014).



Figure 49 – Shotcrete failure prior to significant mesh loading (Drover & Villaescusa, 2015a).

Laboratory strength testing data (Villaescusa, et al., 2012) and field observations indicate that high tensile woven mesh is superior to mild steel weld mesh for tunnelling applications where sudden violent failure may occur with extremely high energy demand. Woven steel mesh is preferred due to the fact that its force and energy dissipation capacity significantly exceeds that of common variety mild steel weld mesh (Villaescusa, et al., 2012) (Figure 50), while also maintaining tolerable displacements of less than 400mm in most cases.

The ability of high tensile woven mesh to articulate post-fracture of the shotcrete, as well as its superior stiffness and displacement performance under load, also support its selection for extreme demand conditions. Fibres are not required to be included in shotcrete that is internally reinforced with woven mesh in this context, due to the relatively negligible strength performance benefit that fibres provide under extreme loading, both pre and post-fracture (Drover & Villaescusa, 2015a). A 75mm thick, internally mesh reinforced shotcrete layer of this construction can be expected to dissipate approximately 15-20 kJ/m² of energy demand if using, for example, a 4mm wire diameter, 80mm aperture, high tensile woven mesh product with 30-35 MPa (28 day) strength shotcrete.

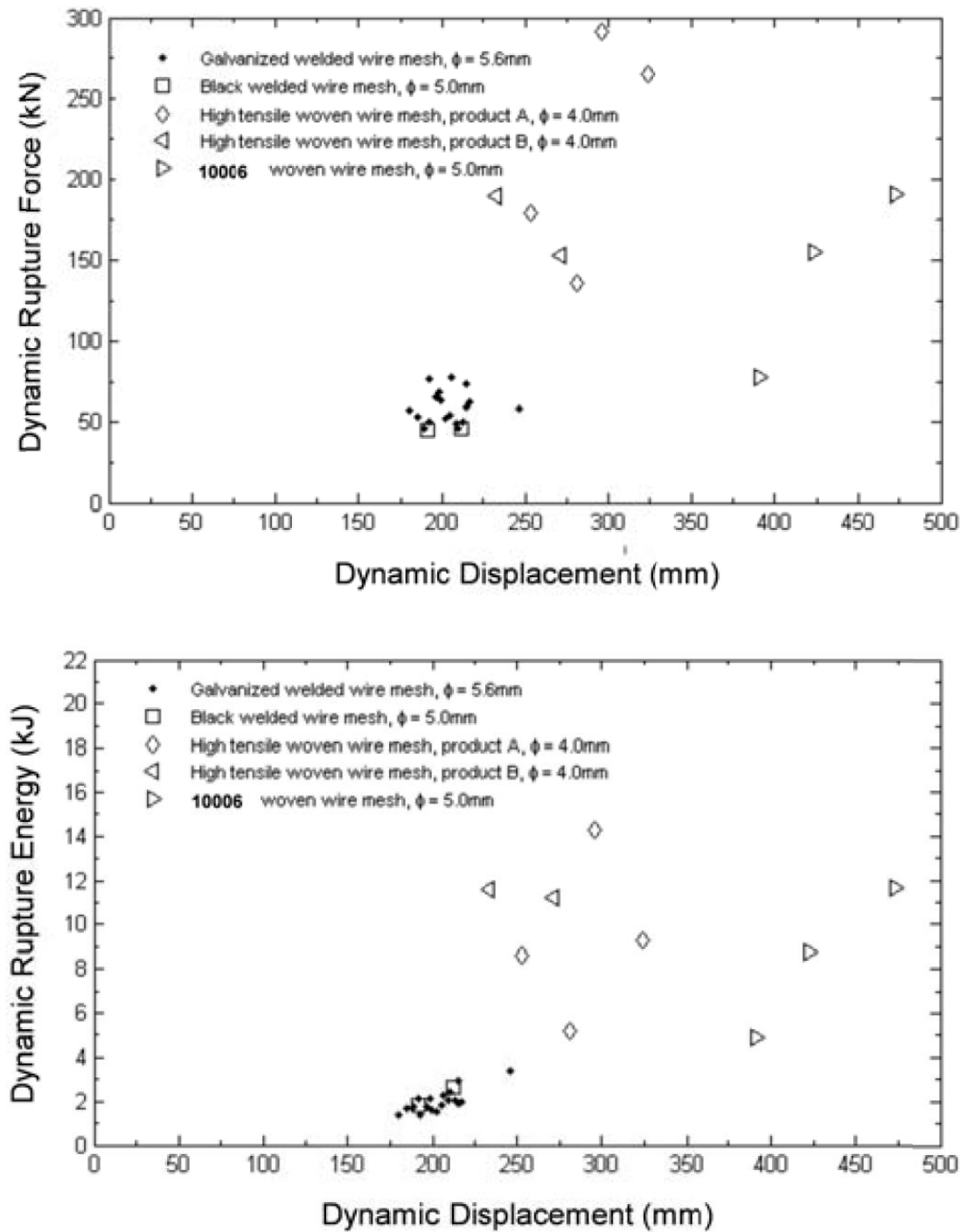


Figure 50 - WASM dynamic database of mesh strength and deformability (Villaescusa, et al., 2012).

2.4.3 Construction Methodology

In Australia, the conventional drill and blast method of deep and high stress development construction exposes the workforce to the risk of rock mass instability at the face. Despite already being significantly mechanised in many, if not most mines, the construction process nonetheless requires personnel to frequently perform manual tasks adjacent unsupported rock (Figure 51). At great depth, stress-driven instability may cause the unsupported face to be violently ejected into the work area. Projectile rock fragments can cause serious or even fatal injuries to anyone nearby. Jumbo operators, ground support off-siders, maintenance personnel and many other workers may be frequently exposed to this hazard when performing their routine tasks.

The following is a list of tasks during which personnel may be required to work adjacent to unsupported or temporarily supported rock, with only a stand-off distance or some minimal physical barrier, like signage, between themselves and the hazard:

- Survey mark-up of tunnel profile and blast pattern,
- Geological mapping,
- Shotcrete application,
- Unplanned equipment maintenance.

The following is a list of tasks where the operators have some physical barrier between themselves and the rock face most of the time, such as a jumbo cab or enclosed elevated work cage. However, they are repeatedly required to bypass this barrier in order to perform manual tasks or inspections with full exposure to the face:

- Development drilling and charging,
- Load and haul of blasted rock,
- Mechanical scaling of the face,
- Installing reinforcement and mesh.

Arguably, the tasks with the greatest risk are those associated with the installation of ground support. This includes shotcrete application and bolting and meshing with a jumbo. Loading the jumbo with the first reinforcement elements adjacent unsupported ground is especially hazardous. All other tasks are either very short in their duration of exposure to the face, or they occur with at least some temporary ground support installed on the face, which may nonetheless be occasionally ineffective (Figure 52).



Figure 51 - Mechanised construction with frequent human-machine interaction at the unsupported face.

Shotcrete application, and in particular rock bolting and meshing, are tasks which occur over relatively long durations. For example, ground support installation may take several shifts to complete for each development round. These tasks require a constant human presence at the face and necessarily occur prior to the installation of temporary face support. A typical Australian ground support process might include the following list of tasks, following shotcrete application:

1. Transport ground support materials (bolts and mesh) to the heading,
2. Jumbo set up,
3. Mechanically drill boreholes for reinforcement,
4. Manually load resin cartridge onto jumbo boom,
5. Mechanically install resin cartridge into the bore hole,
6. Manually move a mesh sheet to the face (next to jumbo boom),
7. Manually load a rock bolt onto the jumbo boom,
8. Mechanically install the bolt and mesh sheet,
9. Repeat as needed for the ground support design,
10. Demobilise the jumbo from the heading.



Figure 52 – Failure of temporary face support due to violent stress-driven instability.

The jumbos commonly used in Australia have the capability to install one reinforcement element at a time, and therefore require a human-machine interaction at the face each time a new bolt is to be installed. Likewise, the convention of using weld mesh sheets at great depth does not allow the full floor-to-floor perimeter of the excavation to be covered with surface support in one single pass. As a result of these conventional methods, steps 4, 6 and 7 above are repetitive and require an operator to regularly approach the unsupported face at the head of the jumbo. This location may easily fall within the arc of projectile rock fragments ejected from a highly stressed face. This conventional construction method is becoming untenable at many operations where flyrock violently ejected from the face is a common occurrence.

Ground support jumbos with an increased level of mechanisation are commercially available. These *Rock-bolters* can install a continuous floor-to-floor bolt and mesh arrangement in one pass, without the need for a human-machine interaction at the face. However, the adoption of such equipment by the Australian mining industry has been negligible to date. This may be partly due to a perceived cost burden, or, more likely, the fact that the practical implementation of the process has not yet been adequately demonstrated. Nonetheless, these machines provide a solution for the safe installation of high energy dissipation reinforcement and support. They are an immediately available technology and are required to be demonstrated to the industry at large.

2.5 Face Destress Blasting

Face destress blasting involves the controlled detonation of explosives ahead of an advancing tunnel with the intent of reducing the frequency and severity of violent rock mass failure at the face. Such failures can pose a serious safety hazard to the underground workforce due to their unpredictable and often violent nature. The intent of destress blasting is to reduce strain energy density around the unsupported face (Tooper, et al., 1999) and create a general softening of the rock mass response, thus reducing the risk of violent instability. This is achieved by fracturing rock ahead of the face using explosives. Conceptually, this fracture zone is created via blast-induced displacement on existing or potentially new rock fractures, resulting in the release of strain energy in the fracture zone (Tooper, et al., 1997). This technique has been suggested to push the highly stressed seismogenic zone further away from the face of the excavation (Roux, et al., 1957, Tooper, et al., 1999) (Figure 53).

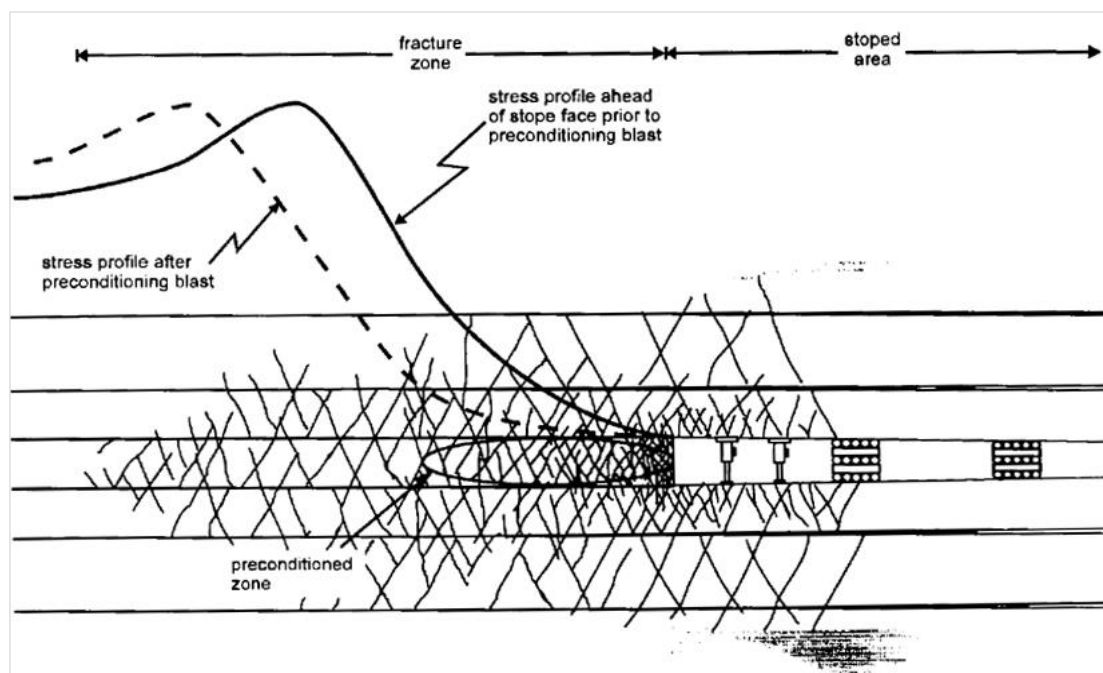


Figure 53 - The theoretical effect of destress blasting on stress concentrations (Tooper, et al., 1999).

The destressing technique has been utilised for several decades in order to reduce the hazards associated with working adjacent highly stressed unsupported rock at great depth. The earliest use of explosives to reduce stress concentrations in the rock mass is thought to have occurred in the deep coal mines of Nova Scotia, Canada during the 1920s (Saharan & Mitri, 2011). However, the technique was not systematically applied in mining until its use in South Africa by the East Rand Proprietary Mines (ERPM) in the early 1950s, in collaboration with the CSIR (Roux, et al., 1957).

2.5.1 Applications

In South Africa, destress blasting has historically been used to reduce stress concentrations at the face of deep gold reef production horizons (Adams & Gay, 1993, Lightfoot, et al., 1996). Elsewhere in the world, such as in Canada, destress blasting is often applied in the pillars or hangingwalls of large stoping mines (Itasca & Associates, 1998). These early concepts of destress blasting have been adapted and modified for use in development tunnelling operations worldwide. Face destress blasting is becoming more widely adopted in civil tunnelling and mining projects as deeper and more highly stressed geotechnical environments are explored. The role of face destress blasting in tunnelling applications is to provide a short time period whereby the risk of violent failure at the face is reduced. This time period provides an opportunity to safely complete construction activities at the unsupported face.

2.5.2 Mechanisms

Prior to tunnel construction, it is likely that the rock mass is in a state of force equilibrium. As an excavation approaches, the void geometry disrupts the in-situ stress field. This causes the loading conditions on intact rock and natural discontinuities in the vicinity of the excavation perimeter to change. Shear and compressive stresses acting on discontinuities may increase or decrease, depending on their location and the stress concentration/relaxation effects of the excavation. Strain energy can accumulate within the rock mass wherever stress increases and displacement along discontinuities is inhibited, for example due to the presence of rigid asperities within the joint plane (Tooper, et al., 1999). Conditions of increasing stress, high strain gradients and energy density may precipitate sudden violent failure at the unsupported tunnel face at any time.

The mechanism of destress blasting is mobilisation of rock mass fractures, such that potentially hazardous levels of strain are either reduced or prevented from accumulating at the face. The discontinuities are intended to be dilated primarily during the blast, when personnel are removed from the area. Destressing explosives are theorised to achieve this by shearing through the asperities and dilating natural fractures due to the action of dynamic stress waves and penetration of explosive gases into the fractures (Tooper, et al., 1999). Conceptually, the displacement along discontinuities releases pre-existing strain in the rock mass. This process may also be achieved via the creation of new fractures in the rock as a direct result of blasting.

The rock fracturing process and thus effectiveness of destressing blasting is believed to depend on the characteristics of the rock mass fracture network (O'Donnell, 1999), the magnitude and orientation of the induced stresses (Kutter & Fairhurst, 1971) and the blasting design (Adams & Gay, 1993). Strain energy accumulation in the rock mass is suggested to be inhibited following destress blasting, due to preferential deformation along the weakened fracture network (Tooper, 2007). The ideal outcome of destress blasting is a change in the failure behaviour of the unsupported face from violent to nonviolent instability. Specifically, the discontinuities are forcibly transitioned from elastic to post-peak plastic or pseudo-plastic behaviour (Cullen, 1998).

The rock mass properties which influence the effectiveness of the destressing process include the strength, stiffness and fracture toughness of the rock, as well as the strength characteristics of the discontinuities (Fleetwood, 2011). The spacing and orientation of natural fractures relative to the major principal stress is assumed to be critical. Existing anecdotal evidence in the literature suggests that destress blasting reduces the incidences and severity of violent rock failure at the face post-blasting by altering the material properties of the rock mass. Specifically, the elastic modulus of the bulk rock mass is reduced (Fleetwood, 2011), as is the peak and residual strength (Cullen, 1998).

The natural rock mass fracture network is disturbed and/or an artificial fracture network created by two principal forces. These forces are the dynamic stress wave and gas action during detonation of explosives (Kutter & Fairhurst, 1971). The stress wave is emitted into the rock mass surrounding the charge due to the expanding high-pressure gases impacting the rock boundary. This causes an impulse loading of the rock with associated strains. The stress wave is most energetic when the explosive charge is fully confined and coupled to the borehole wall, thus ensuring maximum peak pressure during detonation (Tooper, et al., 1999).

The stress wave is generally acknowledged to contain only a small portion of the total energy released by the explosion. However, this energy is highly concentrated adjacent to the blast hole and induced stresses here typically exceed the UCS of the rock. Thus a zone of rock crushing is produced in this region, as illustrated in Figure 54a. This crush zone alters the mechanical properties of the rock in the immediate boundary of the borehole prior to bulk diffusion of the expanding blast gasses (Kutter & Fairhurst, 1971). Radial fracturing may also occur due to tensile stresses (Figure 54b)

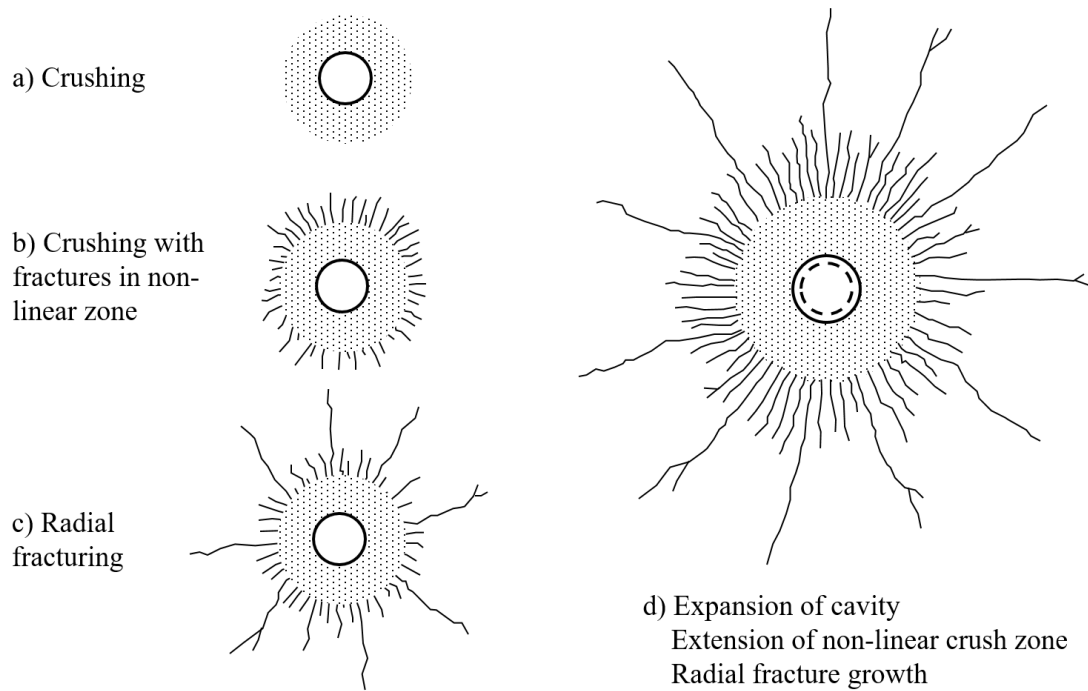


Figure 54 - Consecutive stages in the fracture process of a confined charge (Kutter & Fairhurst, 1971).

Expansion of the blast gases occurs at a much slower velocity than the radiated dynamic stress/strain wave, and hence the gases are the latter of the two blast forces to act on the rock mass beyond the borehole. By the time the gases begin to penetrate past the borehole boundary, the strain wave impulse loading has already created a thin circumferential zone of non-linear deformation around the borehole. Radial fractures created by the stress wave are thought to be produced only within several borehole diameters of the charge column. This mechanism of fracturing ceases once the tangential stress attenuates below the material-dependent critical value, as in Figure 54c (Kutter & Fairhurst, 1971).

As the explosive gases expand, pre-existing natural fractures may be dilated and extended, with new fracturing occurring. Penetration of high pressure gas into the existing fractures can rupture intact rock bridges (i.e. asperities) which connect the opposing discontinuity surfaces. This process reduces the shear strength of the discontinuity. The high gas pressure within the fracture also has the effect of reducing the ratio of normal to shear stress. Under suitable conditions, the discontinuity may then experience immediate shear displacement (Toper, et al., 1999). The surrounding bulk rock mass is then suggested to experience a stress drop and associated reduction in strain. Stored strain energy is released during this process (Toper, 2007), leading to a lower post-blast strain energy density in the rock mass.

The fracture patterns generated by blasting are dependent upon the mining induced stress conditions. Several experimental studies (Kutter & Fairhurst, 1971, Jung, et al., 2001) have shown that the orientation of radial fracturing is highly dependent on the orientation of the major principal stress. For homogeneous massive rock types under isotropic stress conditions, the radial fractures generated by blasting can be expected to propagate equally in all directions (Figure 55a). However, in the presence of a major principal stress, the radial fractures will not easily propagate perpendicular to this stress, due to the increased confinement. Rock fracturing in this situation is preferentially oriented parallel to the direction of the major principal stress and thus perpendicular to the orientation of least confinement, as illustrated in Figure 55b.

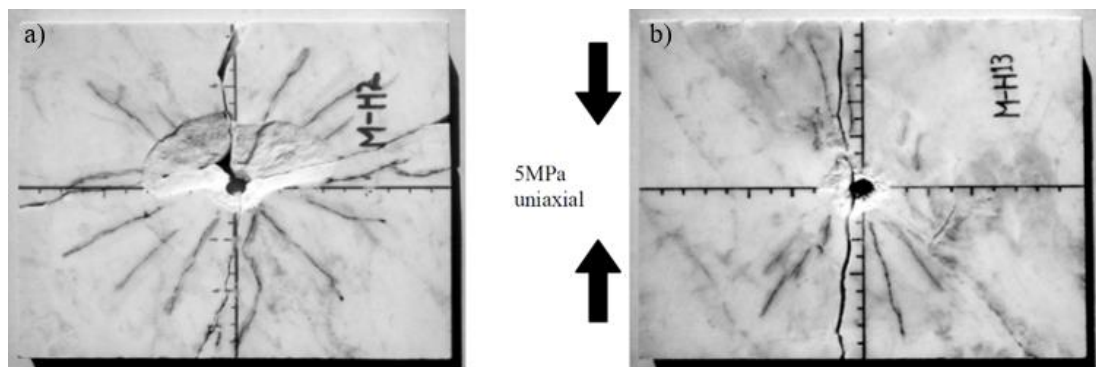


Figure 55 - Effect of stress on the direction of fracturing in rock during blasting (Jung, et al., 2001).

Figure 55 illustrates how an applied stress of 5MPa can have a significant impact on the orientation of blast induced fracturing. In deep underground environments where destress blasting would be applied, the induced major principal stress would commonly be more than an order of magnitude greater than 5MPa. As such, the preferential creation of fractures parallel to the principal stress would be even more pronounced, due to the greater confinement at the fracture tips. This agrees with suggestions that the dominant mechanism of destressing is dilation and displacement along existing discontinuities that are suitably oriented (Itasca & Associates, 1998, Fleetwood, 2011), rather than energy dissipation along newly formed fractures. This mechanism is also supported by anecdotal evidence that destressing is more effective in highly jointed rock than massive rock types (O'Donnell, 1999). Saharan & Mitri, 2011 also advocate the notion that destressing can only be achieved through fractures that have potential for shear movement. At this time there is still considerable doubt regarding the specific mechanisms of destress blasting, with evidence limited to anecdotes, qualitative assessment or inconclusive quantitative field data.

2.5.3 Blasthole Patterns

Development face distress blasting patterns are often conceptually and geometrically similar when applied in excavations of similar size and shape. A largely standardised concept has been developed and implemented at a large number of mines. It is particularly common in Canada and has also been adopted at the few Australian mines known to have applied face distressing (Carr, et al., 1999). The conventional distress blast design includes 2 to 4 horizontal holes in a square pattern drilled perpendicular to and centrally within the face, together with 4 to 8 perimeter holes drilled at oblique angles beyond the planned excavation perimeter. Examples of several designs which follow this standard convention are shown below in Figure 56 to Figure 58.

The number of blast holes in each pattern depends on the excavation size and shape. Examples of distressing blast design in literature primarily relate to excavations with vertical walls and a slight arch in the roof. The dominant concept of square, symmetrical, horizontally aligned drill patterns indicates that the arrangements of explosive charges are dictated primarily by excavation geometry and convention. There is little variation of the design patterns within literature which would indicate that the distressing patterns are optimised from mine to mine in order to consider site-specific stresses. The variability between mines in terms of stress orientations, rock structure and excavation shape would result in variable fracture characteristics and blast performance for these standardised distressing practices.

The work documented by Borg (1988) at the Malmberget mine in Sweden is one example where targeted use of distress blasting in an asymmetric pattern was applied in order to minimise highly localised stress concentrations in the excavation shoulder. In this case, a series of charges were placed in the shoulder in order to limit stress induced overbreak and associated seismicity (Figure 59). It was concluded that seismicity and overbreak of the profile reduced following implementation of this pattern of distressing. Although such targeted distressing has some apparent validity, the use of explosives beyond the excavation perimeter carries significant potential for unfavourable rock mass damage. The distressing charges can result in gas penetration into existing fractures and subsequent instability of large structurally controlled wedges. This may have a negative effect on excavation stability overall. Therefore, distress blasting patterns beyond the excavation perimeter must be conducted with a very high degree of care and conservatism.

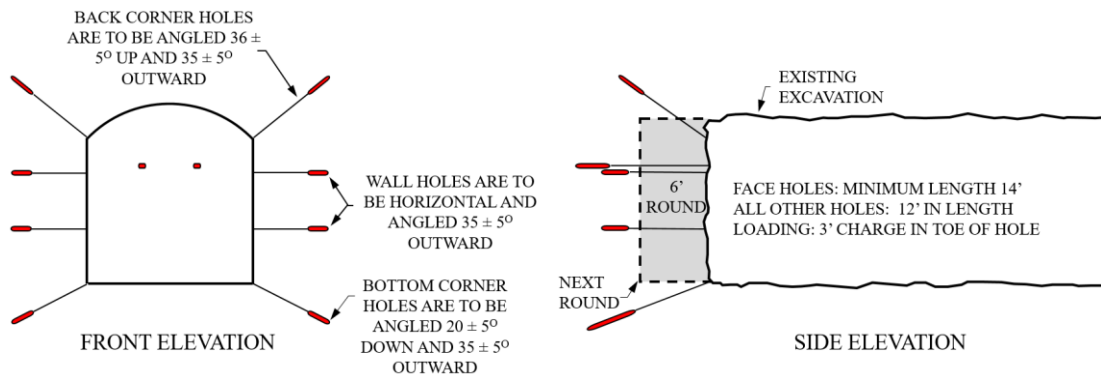


Figure 56 – Standard destress blasting pattern of the Garson mine, Canada (Blake, 2011).

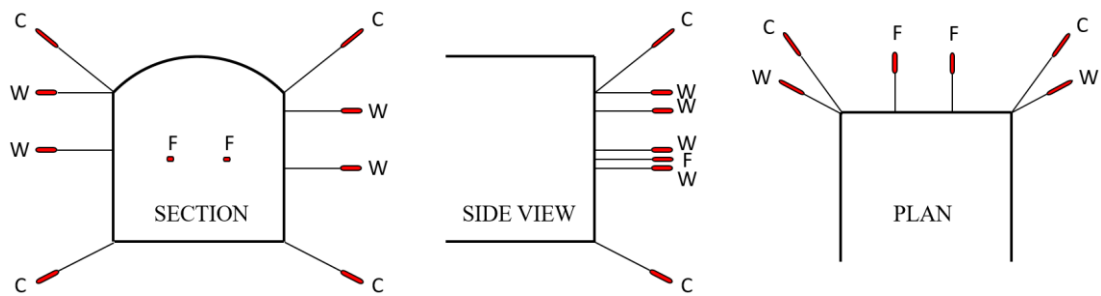


Figure 57 – Standard destress blasting pattern of the Inco mines, Canada (O'Donnell, 1999).

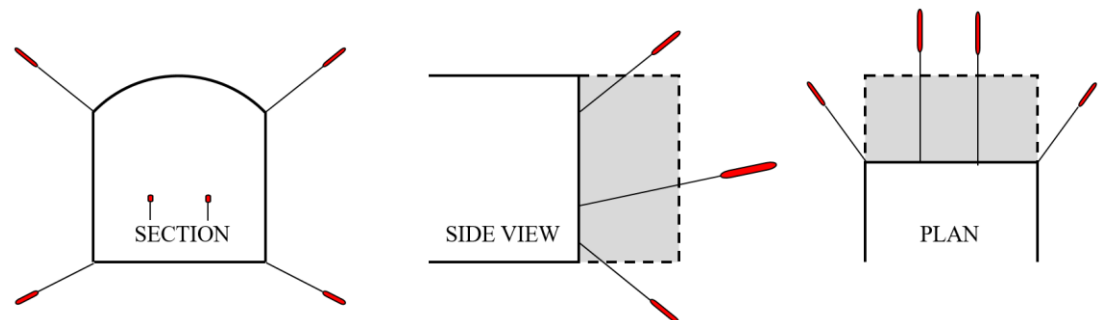


Figure 58 – Standard destress blasting pattern of the Cosmic Boy mine, Australia (Carr, et al., 1999).

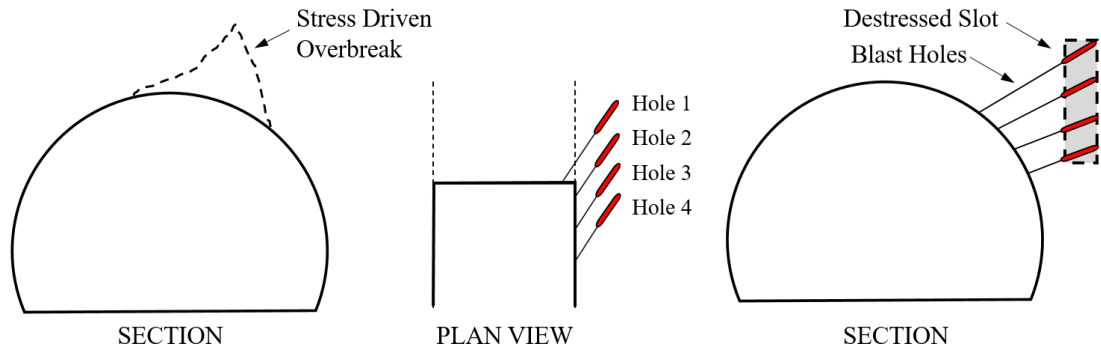


Figure 59 – Perimeter destress blasting for highly localised asymmetric instability (Borg, 1988).

2.5.4 Design Parameters

A variety of explosive configurations have been trialled and assessed in destress blasting applications. Reportedly, the most important design factors to be considered for a destress blasting project include the following:

- Explosive type,
- Blast hole burden, spacing, length and diameter,
- Charge length, diameter and confinement,
- Initiation sequence,
- Booster position.

A range of explosive types have been trialled in destressing experiments. These include high gas volume, low shock energy products such as ANFO (Tooper, 2007) and high velocity of detonation (VOD), high shock energy emulsions (Carr, et al., 1999). It is considered that high gas volume products such as ANFO are the explosive of choice for destressing applications (Tooper, 2007). This conclusion is rationalised by the notion that the greater gas volumes generated by ANFO will penetrate and dilate a larger number of fractures than would be the case for low-gas, high shock energy products (Tooper, et al., 1997). Strain impulse loads generated by high shock energy explosives are deemed to be less effective in rupturing asperities and dilating rock discontinuities that are under high compression. Therefore, such explosives are less capable of generating the fracture instability necessary to effect rock mass destressing.

The burden and spacing of the pattern of destressing blast holes is also reported to have a significant effect on the fracturing generated ahead of the drift face. The tighter the burden and spacing, the more fracturing and thus destressing effect that can be expected. However, the pattern must not be designed with an excessive powder factor which might cause excessive blast damage to the rock mass. Destressing pattern burdens and spacings typically follow convention, which implies 2-4 holes spaced evenly within the face. Such patterns would be unlikely to generate continuous fracture zones across the face. It is therefore postulated that discrete zones of blasted rock destabilise the rock mass sufficiently to cause local stress concentrations and then immediate stress-driven yield of the entire face (Fleetwood, 2011).

Empirical methods may also be used to define blasthole spacing. For instance, Peng, et al. (2015) assumed that the radius of the fracture zone generated by a destressing charge extends for 30 times the charge radius, whereas Saharan & Mitri (2011) assume fractures extend to 50 times the diameter. Designing a destress pattern with this spacing suggests that some degree of fracture interaction between boreholes is necessary to promote destressing. Such designs are more amenable to the creation of continuous fractures which may promote destressing via a shear mechanism (Saharan & Mitri, 2011). However, caution must be used when applying such empiricism, as these rules of thumb are liable to become inappropriate when the rock mass material properties and induced stresses vary significantly between applications.

The drill and charge length of destressing holes also frequently follows convention. Records of prior practices (Carr, et al., 1999, Blake, 2011 and Peng, et al., 2015) indicate that the length of face-perpendicular destressing boreholes is commonly drilled 1½ to 2 times the length of the development round. Often a 1.5 to 2.5m charge is installed. For perimeter destressing outside the final tunnel boundary, the blastholes typically terminate at the same chainage as that of the toe of the associated development round, with less than 25% of the blasthole charged with explosive (Fleetwood, 2011). However, there has been no definitive correlation between the position of destressing charges and the highly stressed seismogenic zone with respect to the face, which would substantiate the effectiveness of this convention.

The diameter of the borehole and explosive charge influence the energy available for fracturing (Fleetwood, 2011) and thus play a crucial role in the spatial extents of damage. Blasthole diameters similar to the normal development round are typically employed for destressing charges. These typically fall within the range of 45-63mm. The destressing boreholes may be slightly larger than those of the development round, so as to accommodate drill-rod couplers which are needed for the longer boreholes. Although such charge diameters are not optimal for the explosive efficiency of ANFO, it has been stated that they have previously been used with success (Itasca & Associates, 1998, Blake, 2011). Charge diameters larger than 63mm are rarely used for development face destressing, and in particular they are avoided for perimeter destressing, due to the likelihood of excessive rock mass damage to the final excavation walls.

Penetration of explosive gases into the fractures adjoining the destressing boreholes is heavily affected by the gas pressure generated during detonation (Daehnke, 1997). In order to ensure maximum gas pressure is obtained and also maximum fracture dilation, it is recommended that destressing charges be fully coupled to the rock mass during detonation (Fleetwood, 2011). Confinement of the charge within the borehole is also critical. Stemming products should be utilised in order to avoid excessive rifling of the gases from the borehole collar and consequent inefficient use of energy (Saharan & Mitri, 2011). It should also be noted that delivery of certain stemming products into horizontal boreholes can be difficult. In particular, whilst coarse aggregate may be optimal, delivery systems for destressing applications are not yet fully developed (Fleetwood, 2011). Alternative stemming products include pre-formed clay packs or blown sand.

Many studies have examined and confirmed the dependence between the orientation and magnitude of the major principal stress and the orientation of blasting induced fractures (Kutter & Fairhurst, 1971, Donzé, et al., 1997 and Saharan, 2004). As discussed by Saharan & Mitri, 2011, the dominant mechanism of destressing likely involves one or more zones of shear failure throughout the face. Consistent with observations of shear failure of rock in other contexts, the shear zone ahead of the face would be expected to occur along a plane sub-parallel to the major principal stress. Such a mechanism necessitates a continuous fracture zone be generated by interaction of destressing blast holes. It is noted that the literature makes no mention of maximising the potential for interaction of blast fractures by arranging destressing charges in rows sub-parallel to the major principal stress.

Final considerations of importance to destress blasting design include the specifics of the initiation timing and position of the booster. Intuitively, for maximum gas pressure during detonation, it is logical to detonate holes on a singular delay, for simultaneous initiation. The position of the booster may be placed at the charge collar, toe or centrally within the charge column. The various effects of these combinations have not been adequately discussed in the literature. However, since the direction of propagation of the explosive affects the directionality of released energy, it is assumed that the booster position influences the effectiveness of a destressing blast.

2.5.5 Numerical Analysis

There is limited quantitative field research data relating specifically to tunnel face destressing mechanics. As such, numerical modelling has been utilised in the past in order to speculate as to the likely mechanical response of excavations and the adjacent rock mass following a destress blasting program. Tang (2000) developed a 3-dimensional finite element model of the stress distributions surrounding a tunnel following destress blasting. This approach simulated the rock mass response to destressing using two assumptions. Firstly, the detonation of explosives reduced the elastic modulus of the rock mass within the blasted zone. A rock fragmentation factor (α) was applied to the model input value of the bulk elastic modulus for this purpose. Secondly, it was assumed that a post-blast stress decrease occurred within the blasted volume. A stress dissipation factor (β) representing the post-blast instantaneous stress drop was imposed on the model geometry. Both α and β were simple multiplication factors of between 0 and 1 which were applied to the model input variables. Three destress blast geometries were modelled, as shown in Figure 60.

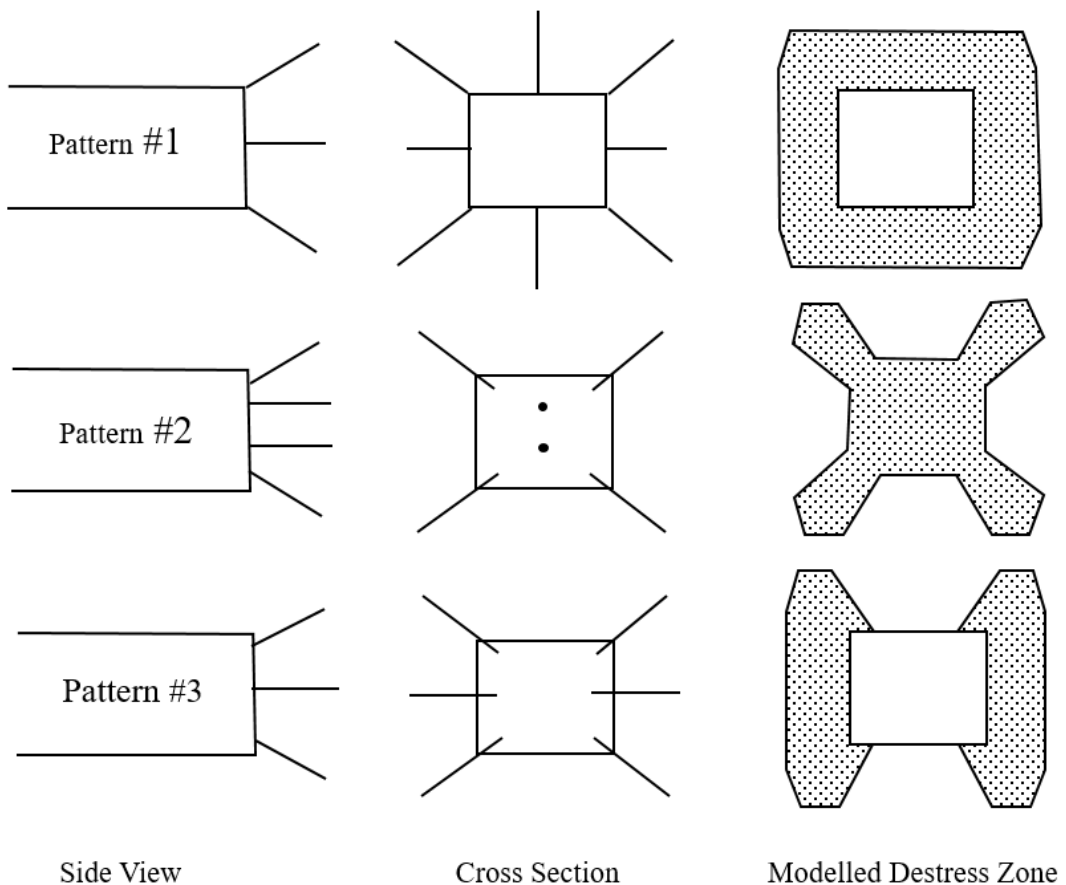


Figure 60 - Modelled destress blast designs, reproduced after (Tang, 2000).

The modelled stress conditions on the excavation boundary were subsequently investigated. The modelling indicated that stress reductions ahead of the face were achieved for all of the destressing scenarios, with reductions of between 27% and 38% in the maximum stress concentration ahead of the face. It should be noted that the assumptions of these simple models may not accurately reflect the characteristics of the rock mass. For instance, the illustrated destressing patterns may not generate the spatial extent and uniformity of rock mass damage as was assumed. Stress decreases may not occur in the rock mass to the extent that was estimated and the effect of blasting on the rock mass elastic modulus is extremely difficult to quantify reliably. These factors must be considered when interpreting any numerical modelling conclusions.

Saharan (2004) also performed a series of exercises in the numerical modelling of distress blasting using the program Abaqus. In this case, the focus of the modelling was on the characteristic fracturing associated with destressing explosives and the interaction of multiple charges, rather than the effect of destressing on excavation loading conditions. Consistent with the experimental results of Kutter & Fairhurst (1971) and Jung, et al. (2001), the modelling indicated that radial fractures preferentially grew in orientations sub-parallel to the major principal stress. The length of radial fracturing decreased with increasing confining stress, as did the radius of the crushing zone immediately surrounding the borehole.

This analysis also made several conclusions which were specifically relating to the massive hard rock conditions typical of the Canadian shield. It was asserted that for such massive rock types, with few if any joints, the superior explosive type for destressing is a high shock energy emulsion in preference to a high gas product. It was also concluded that there was minimal interaction between 45mm blastholes spaced at 0.75m. This spacing is approximately half that typically practiced in South African mines. As such, destressing was considered to be difficult to achieve in such massive types using conventional design parameters. Due to the specific focus of this modelling exercise, these conclusions should not be deemed directly relevant to the complex jointed rock types typically found in many Australian mines.

2.5.6 Quantitative Analysis

The vast majority of destressing analyses within the literature relate to longwall production face destressing. As a result, very little is known regarding the seismogenic, stress concentration and fracture zone characteristics specific to development face destressing. In general, quantitative analyses of destressing comprise three principal investigation techniques. These include local seismic monitoring, ground penetrating radar geophysics and fracture mapping. These investigation techniques are equally suited to the three main destressing applications, which include longwall face, pillar and tunnel face destressing. However, due to the significant differences in design and application of these various destressing applications, the results from one analysis are not likely to be directly relevant or pertinent to the others. Nonetheless, some general conclusions can be drawn from the longwall destressing literature which have relevance to the destressing method in general.

2.5.6.1 Seismic Monitoring

Adams & Gay (1993) recorded seismicity following destress blasting of reef faces and noted the number of events, total radiated energy and cumulative time plot of the rate of events as an indication of the post-blast seismic decay. No attempt was made to separate and compare the seismic response of standard blasts versus those with destressing. Nor was any attempt made to spatially correlate the recorded seismicity to the excavation or location of destressing charges. The only conclusion drawn from this study was that destress blasting triggered seismicity.

In a summation of the seismic monitoring of the Blyvooruitzicht Gold Mine, Lightfoot, et al. (1996) concluded that reef destressing blasts induced stress transfer away from the preconditioned area, released stored strain energy from the rock mass and reduced the stress concentrations. It was asserted that the seismogenic zone migrated away from the vicinity of the destressing blasts, indicating a transfer of stress further away from the face and towards unconditioned rock. It must be noted that the results of this analysis were interpreted at a very broad spatial resolution (~50m scale) with a relatively small number of events observed and without source mechanism analysis. Hence, the conclusions regarding the stress concentrations and position of the seismogenic zone are considered to be speculative. Nonetheless, this analysis provides an early example of spatial analysis of seismicity following destress blasting.

Tooper, et al. (1997) and Tooper (2007) supported the conclusion that seismicity advances ahead of preconditioned excavation faces. However, the local seismic system used in these analyses were stated as being inaccurate in the vertical axis, with seismicity only demonstrating clustering adjacent the preconditioned excavation when viewed in plan (Figure 61). Use of such mine site seismic systems for destressing analysis is common, however the accuracy of their results is limited. Such systems generally cover wide areas of the mine with a sparse sensor array and thus have 3D location error in the order of 10-20m. Systems of this kind are not capable of the very high spatial resolution required for definitive analysis of seismogenic zones and destressing mechanics. However, Tooper, et al. (1997) noted increase in the seismic b-value following destressing, indicating a decrease in the proportion of larger and potentially more damaging seismic events in the overall population. This conclusion was reaffirmed by Tooper, et al. (1999) and Tooper (2007).

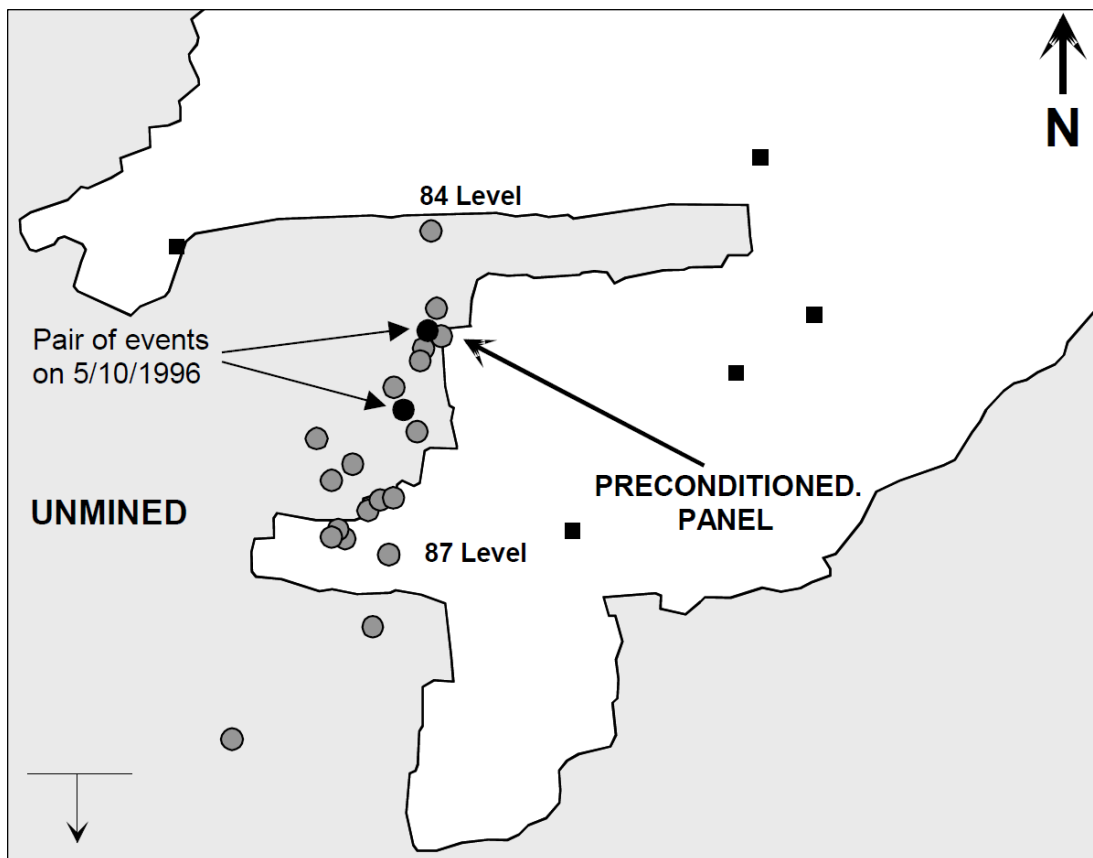


Figure 61 - Spatial analysis of the destressing seismogenic zone at a wide (Tooper, 2007).

2.5.6.2 Ground Penetrating Radar

GPR is an electromagnetic geophysical technique which utilises an antenna to project radar waves into the rock mass, the reflections of which are recorded. The radar reflections of the rock mass provide location information regarding high conductivity features, which may include rock fractures. GPR has been used extensively in South African longwall gold mines in order to attempt to measure the extent and intensity of rock mass fractures before and after destress blasting. The technique is particularly effective in the South African context, since the majority of mines are gold mines where the rock types have favourable conductivity properties, resulting in good quality radar signatures from concealed rock fractures.

Adams & Gay (1993) utilised a GPR to measure the rock fracturing before and after a destressing blast in a longwall face. The results identified pre-existing rock fractures up to a depth of 10m from the face prior to blasting. These same fractures were visible after the destress blasting and appeared to have been dilated and elongated, as evident by the significantly increased strength and density of reflected radar features. Some new fractures were interpreted in close proximity to the destressing charges. Radar results obtained by Topper (2007) also agree with those of Adams & Gay (1993). In Topper's results, a clear increase in reflection features (fractures) is evident when comparing the pre-blast radar results (Figure 62) to those obtained after blasting (Figure 63). Destressing fractures are identified to a depth of 3.5m beyond the current longwall face. Neither of these studies provided any detail regarding the operating frequency of the radar instruments used during data collection.

These radar results support hypotheses by Itasca & Associates (1998) and Topper, et al. (1999), which suggest that destressing charges act primarily to dilate and extend pre-existing rock mass structure. Some localised new fracturing may be created within close proximity to the explosive charges. It should be noted that GPR is not always suitable for use in mapping blast related fracturing. The technique relies on the rock mass having appropriate properties of electrical conductivity. Generally, GPR is most effective when the features desired to be monitored have a higher conductivity than the adjacent rock mass. This fact presents some challenges for mapping destressing fractures in typical tunnelling environments which develop through un-mineralised hard rock of consistently low electrical conductivity.

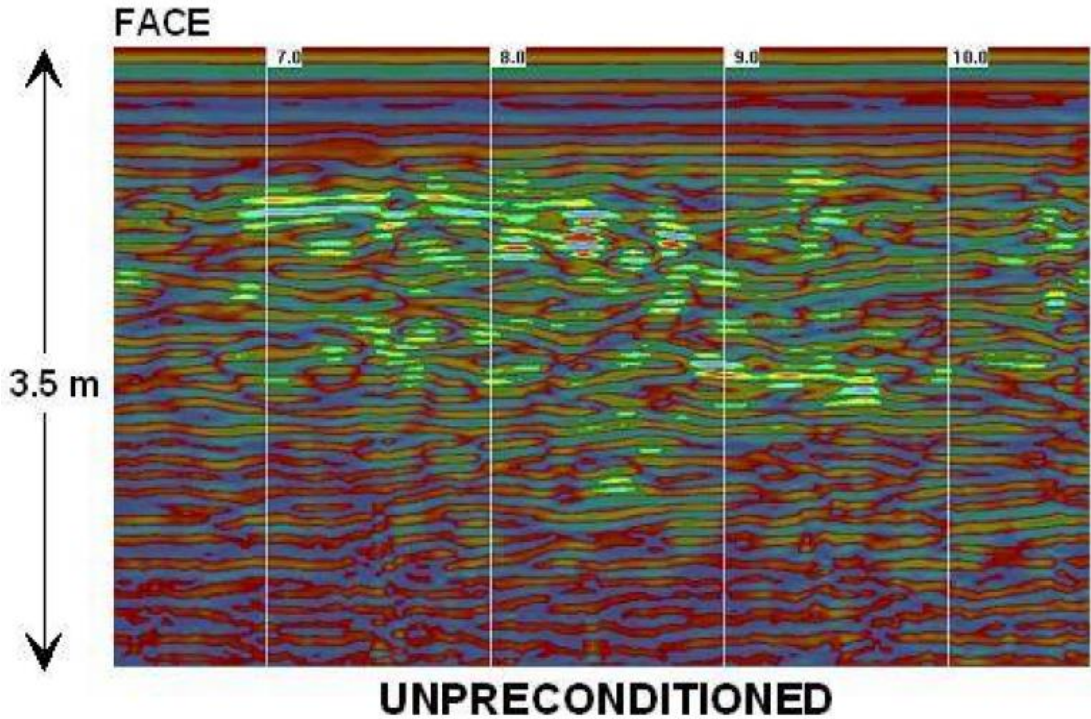


Figure 62 - Ground penetrating radar scan of a rock mass before destress blasting (Tooper, 2007)

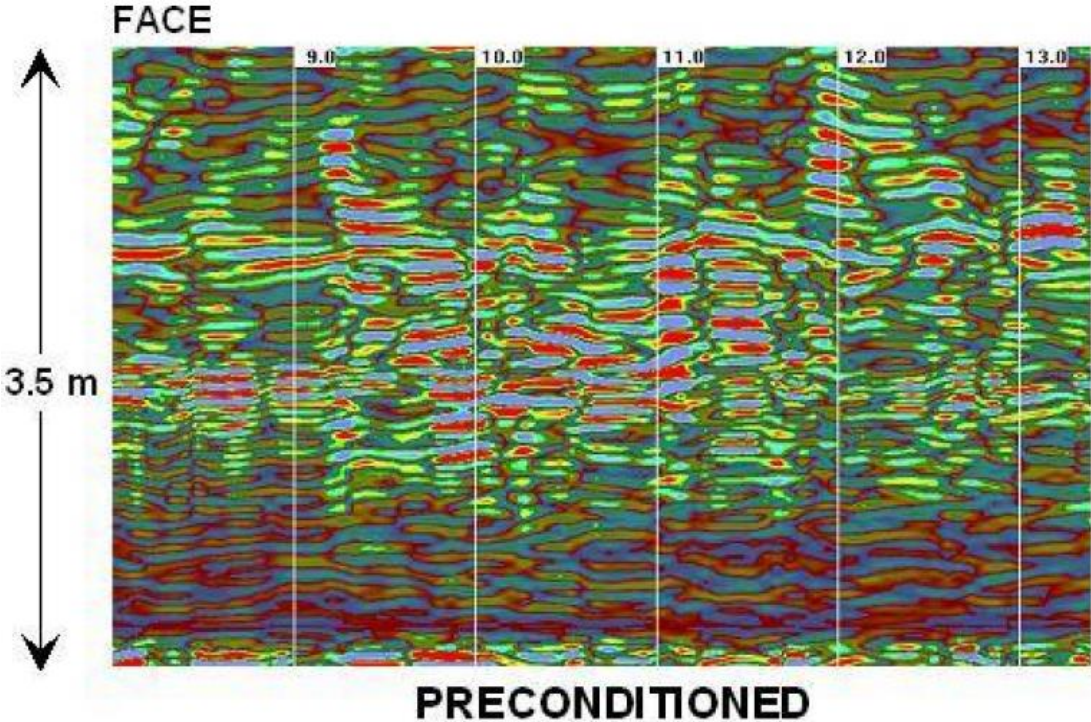


Figure 63 - Ground penetrating radar scan of a rock mass following destress blasting (Tooper, 2007)

2.5.6.3 Fracture Analysis

Quantitative analysis of destressing fractures has been made directly from the exposed rock face using stereo photography (Adams & Gay, 1993) and via manual face mapping techniques (Itasca & Associates, 1998). Borehole cameras have also been used to provide relevant fracture data. Topper (2007) documented a process of fracture mapping of a longwall face both before and after destress blasting. Five joint sets were identified both before and after destress blasting. No significant new fracture orientations were identified after blasting. However, an increase of approximately 25% in the visible number of steeply dipping fractures was noted. It was not clarified whether these newly visible fractures were blast-induced or simply dilation of those that were pre-existing. Irrespective, this observation is consistent with preferential fracture dilation in the orientation sub-parallel to the major principal stress, which in the South African context can generally be assumed to be vertical, due to the high lithostatic load and relatively low horizontal stress regime.

In their report to the CAMIRO Mining Division, Itasca & Associates (1998) noted fracture mapping work by the South African Chamber of Mines Research Organisation (COMRO) at the Western Deeps mine. This investigation of fracturing confirmed that no new discontinuity sets were generated by the destressing charges. Instead, the characteristics of pre-existing natural discontinuities was altered. After destressing, extensive gouge was observed on fractures which were previously extensional only. In particular, sub-vertical fractures were found to have been extended significantly. Again, this is consistent with fracture extension sub-parallel to the vertical major principal stress typical of deep South African gold mines.

2.6 Knowledge Gaps

2.6.1 Excavation Stability

Current methods of excavation design provide no definitive, quantifiable link between the rock mass characterisation and the mechanical conditions indicative of the onset of excavation instability. Existing stability assessment methods carry significant engineering judgement and interpretation into their conclusions. Quantitative relationships between loading, rock mass strength and instability were demonstrated by Kusui (2015). However, it remains to test these relationships at the mine scale and to incorporate those findings into a formal excavation stability assessment method which uses the rock mass characterisation to reliably predict instability.

2.6.2 Ground Support Design and Construction

The two variables defining the rock mass demand on ground support are the mass of instability and its ejection velocity. Current methods for estimating the demand on ground support assess the unstable mass either empirically or via deterministic wedge analyses. Meanwhile, the ejection velocity is quantified using factors derived from the properties of seismic events, such as the PPV and site factor. Site factor is a highly subjective assumption that significantly alters the final result. The conventional methods for defining the input variables to the demand equation often yield results which do not reflect real conditions. This is evidenced by the continuing and frequent incidences of tunnel failures in many mines and civil engineering operations around the world which implement these methods of assessment.

Presently, there is no method to estimate ground support demand strictly analytically, from the point of data collection to the final result. Empiricism and significant assumptions are often applied, for example when estimating the depth of excavation failure and quantifying the dynamic loading characteristics. There is no unique method of quantifying the rock mass demand on ground support which is fully analytical and based only on the readily quantifiable physical characteristics of the rock mass. However, existing theoretical frameworks in relevant disciplines are available, such as structural block theory (Windsor, 1999) and excavation stability (Kusui, 2015), but they are not yet incorporated into a holistic excavation design process. A novel ground support scheme arrangement designed to meet extremely high demand is also yet to be tested for practicality of installation using fully mechanised mining equipment.

2.6.3 Development Destressing

Often, development face destressing is implemented at a new operation according to a standard design convention. Important factors governing destressing performance such as rock mass strength, structure and stress are frequently not considered in the design. There is a need to clearly define the mechanical objective of the destressing blast design and to quantify the important variables required to be considered in the design's preparation. A basic destressing design concept that can be modified to suit different conditions is also needed.

Current literature and quantitative analysis of face destressing is heavily focused on applications related to production mining in deep gold reefs. There are relatively few investigations of destressing in development tunnelling applications. Furthermore, destressing investigations of all applications have some limitations in their analysis technique. For example, investigations into the spatial variability of the seismogenic zones associated with destressing have previously been made over scales of several tens of metres using regular mine site seismic systems, not dedicated high-resolution local monitoring. There are no known seismogenic analyses of destressing made with sub-metre event location error which accurately assessed how the seismogenic zone changed, if at all, at the scale of the tunnel face.

There is also a need to examine the mechanisms of stress-driven failure associated with destress blasting seismicity. It is assumed, but not clearly known, that destress blasting causes a change in the structural response of the rock mass. Detailed investigation of the structural response to destressing also requires very high resolution seismic data be collected in the specific application of development tunnelling. Related to the source mechanisms of the post-destressing failure modes are the characteristics of the fracture networks generated by destress blasting. Existing experimental work by Jung, et al. (2001) identified the fact that the orientation of radial fracturing is heavily dependent upon the magnitude and orientation of the applied loads. This laboratory conclusion requires validation in the field, as it is potentially fundamental to the how the blasting mechanics influences the destressing response.

Chapter 3

Research Methodology

The three principle objectives of this research were:

1. to propose and implement an innovative methodology for the design of hard rock tunnels at great depth,
2. to demonstrate the constructability of an experimental tunnel design, which included face distress blasting and a ground support scheme for extremely high energy dissipation, while also constructing a second tunnel nearby as a control,
3. to monitor both tunnels and the adjacent rock mass, visually and with instrumentation, and compare the physical performance of each.

The methodology implemented in order to address these objectives is summarised as follows.

3.1 Excavation Design Methodology

An excavation design process was developed for hard rock, high stress conditions where violent stress-driven failure can occur. It follows six basic steps:

1. characterisation of rock mass strength, structure, stress and strain,
2. stability assessment and failure mechanism analysis,
3. specification of a naturally stable excavation shape,
4. development blast design including face distressing,
5. quantification of the rock mass demand,
6. specification of the ground support scheme and its installation sequence.

The rock mass characterisation was conducted following the WA School of Mines convention (Windsor, 1995), with output data including rock strength testing results, structural mapping and stress tensor measurements. The results of non-linear numerical modelling were also used to assess induced stress conditions. The rock mass characterisation data was fed directly into a stability assessment for violent excavation spalling and pillar crushing based on the recent experimental findings of Kusui (2015). Stability charts have been created for design use, which allow excavations to be assessed for stress-driven instability using rock UCS and induced stress as the input variables. A naturally stable excavation shape was specified considering the induced stress conditions at a field trial site which were defined by the rock mass characterisation. A matching development blast pattern was designed which includes face distressing charges.

The Hybrid Stress Blasting Model (HSBM) (Furtney, et al., 2009) was used to optimise the destressing blast design. Twenty-two models were prepared and analysed in the HSBM, many of which were standard conventions assessed for basic performance comparison. Final models were prepared using input parameters which replicated the expected rock mass conditions of planned field trials of the designs. The models were prepared specifically to test and optimise the design variables such as charge diameter, spacing, burden, row orientation with respect to the stress field, collar confinement, primer position and initiation timing. The intent of the final destressing designs was to create shear failure in the face and strain energy dissipation, with minimal deformation.

Following the blast design process, design charts were developed to correlate the energy demand on ground support directly to the rock mass conditions. Unlike existing design charts, the charts developed here linked the host rock UCS, ejection velocity and mass of the instability in order to generate a quantified estimate of the energy demand on the ground support scheme. The design charts differentiated between stress-driven spalling and structurally controlled failure mechanisms. A unique ground support scheme arrangement for extremely high energy dissipation was also designed. This scheme consisted of multiple integrated layers of reinforcement and surface support elements capable of dissipating approximately 65 kJ/m² of dynamic rock mass energy demand. The design approach described in this thesis is unique for deep underground construction and built upon the existing body of rock mechanics research from WASM.

3.2 Development Construction

Two excavations were constructed in order to test and compare conventional and experimental development techniques. The first excavation was developed as the control. It was constructed with a conventional excavation shape, blast design and ground support scheme typical from the host mine site. The second excavation was experimental. It had a naturally stable, semi-elliptical profile shape, development blast design with face destressing charges, and fully mechanised installation of the high energy dissipation ground support scheme. The destressing design that was implemented followed the optimised charge pattern and loading characteristics defined by the numerical assessment in HSBM. The practicalities associated with implementation of this process were observed and documented.

The ground support scheme was installed using fully mechanised equipment, so as to remove the operators from potentially unstable rock at the tunnel face. The scheme consisted of two integrated layers of high energy dissipation capacity reinforcement and surface support components. The scheme followed a specific reinforcement pattern and mesh layer overlap arrangement, in order to ensure maximum load transfer between all reinforcement and surface support layers in the event of a dynamic loading. All steps in the mechanised installation process were observed and assessed for their practicality. This included drilling, installing, grouting and tensioning of two staggered patterns of reinforcement – one for shallow and another for deep instability. It also included observations of the installation of several layers of surface support.

The possible mechanisms of tunnel instability may occur at different times in the development cycle. In conditions of sufficiently high stress, shallow spalling failure may occur very soon after the stress redistribution is complete. On the other hand, deep structurally controlled instability generally takes some time to develop. Therefore, an efficient installation sequence and in-cycle timing of the two layers of ground support was also applied during the construction, considering the likely timing of the instability. This installation sequence was tested to ascertain the optimum rate of face advance and in-cycle ground support installation for safe and efficient development.

3.3 Rock Mass Monitoring

In order to quantify the rock mass response to both conventional and face destress blasting, a high resolution seismic monitoring system was installed. The seismic array consisted of tri-axial accelerometers positioned in a 3-Dimensional array completely surrounding both tunnels. The system was calibrated using a velocity model and shown to achieve highly accurate source locations of seismic events. The spatial characteristics of the seismogenic zones surrounding both tunnels were accurately defined and compared, in order to assess what affect destress blasting played on the distribution of instability and likely strain concentrations in the rock. Analysis of the seismic source parameters was also performed, which shed light on rock mass damage and energy release within the seismogenic zones. The nature of the structural response to both conventional and face destress blasting development was also examined using source mechanism seismology.

Chapter 3: Research Methodology

Visual mapping was also utilised to assess the characteristics of the fractures induced by distress blasting. The mapped fractures were compared to known pre-existing natural discontinuities and the orientation of the measured stress field in order to ascertain the influence that these two factors had on the fracture process. Laser-scans of the final excavations were performed in order to measure the profile compliance to design as well as compare zones of instability to the structurally controlled block geometries that were predicted by the design assessment. Ground penetrating radar (GPR) geophysical surveys were also carried out with the intention of determining the optimal radar frequency range for a future borehole instrument which may be able to map blast-induced distressing fractures in-situ.

Chapter 4

Design

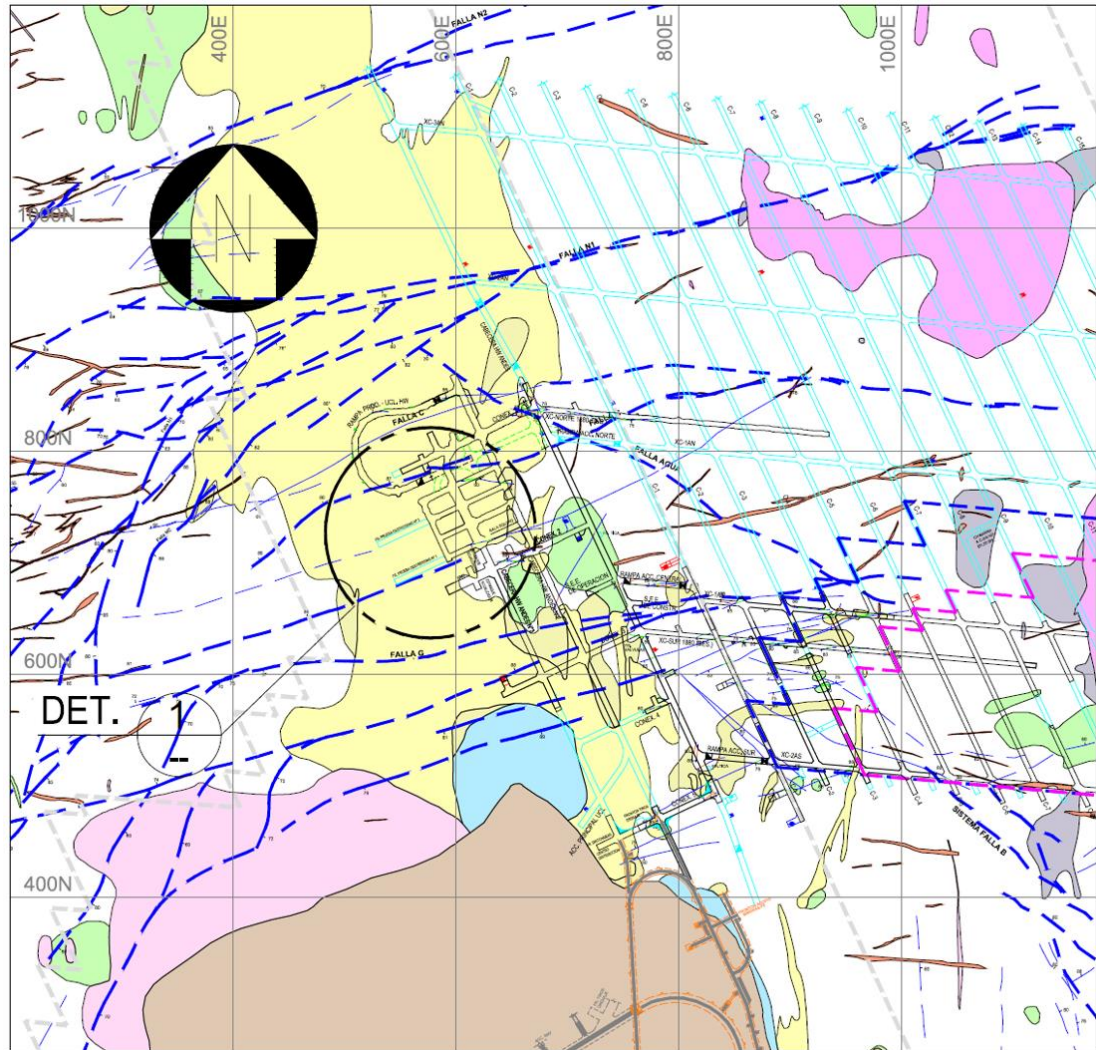
4.1 Trial Site Description

Experimental development trials of full scale tunnel construction were conducted in a deep underground hard rock mine. The tunnels were developed at a depth of approximately 635 metres below surface in a high stress regime. The method of mining at the site was large scale caving. Experimental tunnels were constructed in a development precinct several hundred metres below the existing cave production. The mine site has a long history of stress-related damage to the infrastructure. Previous damaging incidents at the mine include sudden and violent excavation failures with very high energy demand on ground support, and large depths of rock mass failure. The rock stress has increased as the mine infrastructure has advanced to greater depths. This is typical of many mining operations worldwide, in terms of the exposure to high stress and the increasing complexity of the associated engineering challenges.

4.2 Development Layout

Two horizontal tunnels were constructed for this research. The southern tunnel was developed as a control, using the conventional profile shape, development blast pattern and ground support design that is commonly used throughout the mine. The northern tunnel was an experimental excavation for testing, monitoring and quantifying the effect of optimised development techniques. The two tunnels were both constructed on a deep development horizon and at the same elevation. The tunnels were excavated within a high strength, brittle rock mass in a high stress regime. Previous development in the area had experienced violent stress-driven instability. In places, significant profile overbreak had occurred due to overstressing on the tunnel boundary.

The excavations were positioned on the periphery of the existing mine development, where the pre-mining stress conditions were the least disturbed. This position was chosen to avoid the stress shadowing or concentrating effects due to large scale voids, such as the cave. This was important to ensure that the loading conditions on both excavations were essentially identical. Both excavations were developed parallel to one another, such that the sub-horizontal major principal stress was orthogonal to the longitudinal axis of each tunnel. A plan view of the mine infrastructure surrounding the location of the experimental tunnels is shown in Figure 64. The exact location of the tunnels is indicated within the circle denoted as *Det. 1*.



LITHOLOGY

	MAFIC
	BRECHIA
	ANHIDRITE BRECHIA
	IGNEOUS BRECHIA OF DACITE PORPHYRY
	IGNEOUS BRECHIA OF DIORITE PORPHYRY
	DIORITE PORPHYRY
	DACITE PORPHYRY
	LATITE
	CHLORITE BRECHIA

STRUCTURES



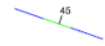
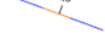

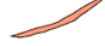


	FAULT
	FAULT PROJECTED FROM UPPER LEVEL
	VEIN (HYDROTHERMAL) OR FAULT
	VEIN OR FAULT
	VEIN
	QUARTZ DYKE
	DYKE
	LOCATION OF EXPERIMENT

Figure 64 – Location of experimental tunnels relative to adjacent mine infrastructure and host geology.

Chapter 4: Design

A detailed view of the arrangement of the two tunnels is presented in Figure 65. The two tunnels were developed in parallel from an existing access. The tunnels were separated by a horizontal pillar of approximately 31 metres width. This pillar was desired to maintain a sufficient offset between the excavations, such that stress interactions between the two excavations, particularly at the face position, were minimal. Both excavations were initially planned to be developed to a length of 50 metres. However, due to time and resource constraints, a total of 34.4 metres and 32.4 metres of development were completed in the south and north tunnel, respectively. Both tunnels were developed at the same rate of advance, such that the face in both tunnels was approximately equidistant from the access, with a difference of no more than one development cut length (i.e. 3.8 metres) at any one time. Drill and blast rounds were alternated from one tunnel to the other in a repeating sequence, in order to maintain the same advance rate.

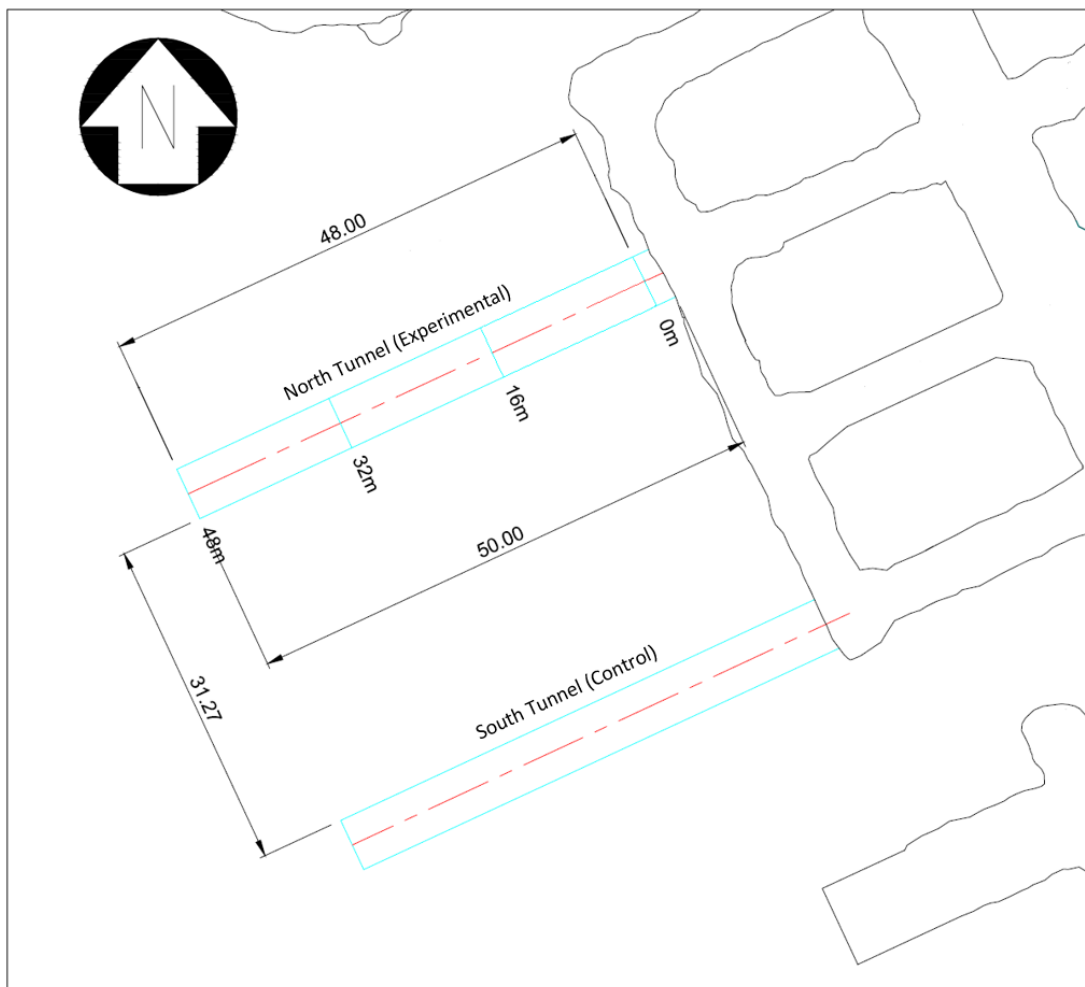


Figure 65 - Detailed plan view of two parallel tunnels constructed for the experiment.

4.3 Rock Mass Characterisation

A characterisation of the rock mass was completed for the zone surrounding the experimental tunnels. The preliminary characterisation utilised existing geotechnical data from the mine site, including in-situ stress measurements, structural data and numerical modelling. For the purposes of this thesis, a pilot geotechnical borehole was also drilled along the longitudinal axis of each of the two tunnels. Rock strength testing of the core from these two pilot holes was completed at WASM. Testing was completed for intact sections of core, as well as core that had experienced stress-related diskings. The testing data was analysed in an attempt to identify potential indicators of excavation instability during the subsequent tunnelling. Additionally, structural mapping data was collected and analysed both before and during the development of the two tunnels, with the rock mass characterisation updated continually.

4.3.1 Geological Setting

The detailed arrangement of geological units surrounding the site of the experimental tunnels was shown above in Figure 64. This figure presents a horizontal section view of the geological boundaries at the same elevation as the research tunnels. This level of the mine is predominantly composed of a Mafic complex and a number of other units, including Diorite, Dacite and Latite. The Mafic units are the most extensive rock types in this precinct of the mine. The production extraction infrastructure is located in Mafic to the east of the research tunnels. Another large Mafic unit lies to the west of the mine development. The smaller Diorite and Latite units are interspersed among the Mafics, within and around the ore zone. Primarily it is the Mafic units which host the mineralisation.

Positioned between the large Mafic units is the Dacite rock type. This unit is bounded to the south by a Brechia, which hosts much of the permanent mine infrastructure. Both research tunnels were constructed exclusively within the Dacite rock type. Neither of the tunnels approached any adjacent lithological boundaries. Development across such boundaries was avoided during the construction process, so as to eliminate potentially significant variations in rock mass strength properties, which might influence the consistency of the rock mass response.

4.3.2 Structural Geology

The structural characteristics of a rock mass often play a critical role in the occurrence of stress-driven excavation damage. Significant structural features are often present wherever a catastrophic excavation failure occurs (Drover, 2014). The severe damage usually associated with structural rupture is likely due to the greater displacement potential that can occur during such failure mechanisms, as well as the potential for large wedges to form at the tunnel boundary. A detailed structural model may be used to define the likely location of instability, its failure mechanism and energy demand. A structural model of the rock mass is therefore a useful source of information for the excavation design process.

A plan view of the interpretation of significant geological structures surrounding the two research tunnels is shown in Figure 66. Structures are depicted by blue dashed lines. Due to the early stage of development of the infrastructure on this level, this structural interpretation is extrapolated from mapping in upper levels of the mine. The interpretation indicates that a geological structure potentially exists to the south of the southern tunnel. No significant structures were known to exist adjacent the northern tunnel.

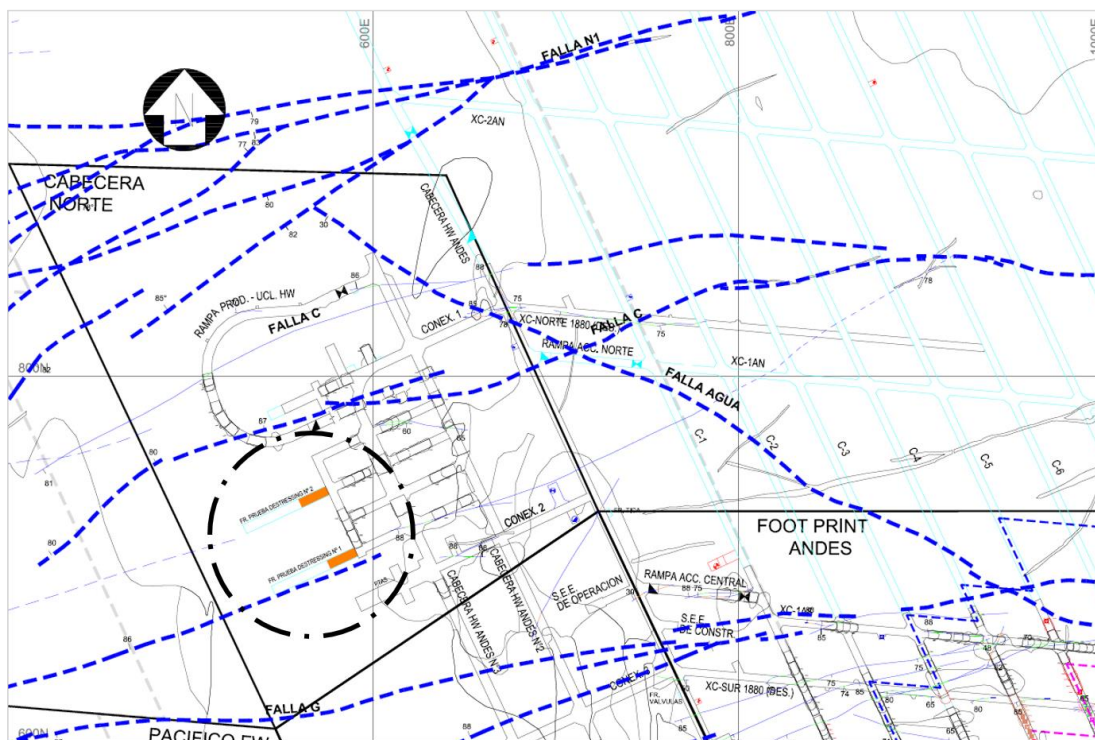


Figure 66 - Plan view of structural interpretations surrounding the location of experimental tunnels.

Chapter 4: Design

During development of adjacent access infrastructure, a database of joint orientations was gathered by the mine site using digital photogrammetry. This data, including 590 individual joint observations, was plotted using the program SAFEX. The stereonet of joint data, including the Fisher Pole Concentration contours, is presented in Figure 67. It should be noted that this data has been collected using photogrammetry of unsupported tunnels developed in only two orthogonal orientations. As such, the data potentially suffers from a sampling bias and not all joint sets were believed to have been observed. For unbiased structural mapping, it is recommended to collect data from rock faces in three orthogonal orientations (Windsor, 1995). Nonetheless, this data was all that was available for the Dacite domain prior to commencing development.

Despite suffering from a sampling bias, the Figure 67 data does indicate at least one clear joint set, and potentially two others. This includes a steeply dipping, E-W striking joint set, where the Fisher pole concentration contours show a tight grouping of observations around the dip/dip direction of 78/160. Potentially there was also a steeply dipping N-S striking set and a shallow dipping E-W striking set, although these were unclear in the data.

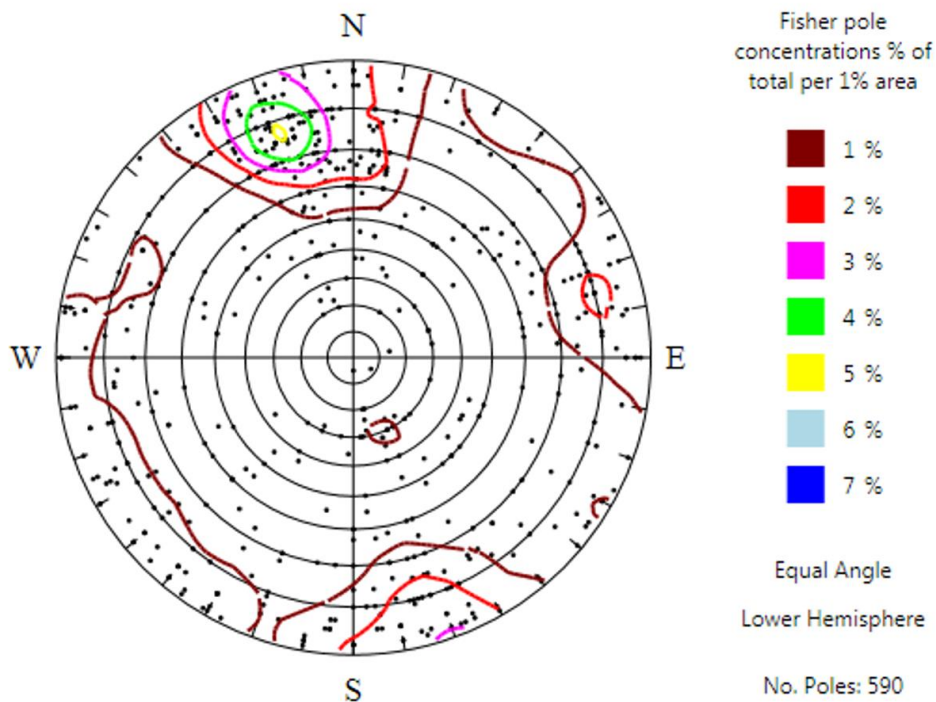


Figure 67 – Photogrammetry data of joint structures in the Dacite rock type.

Face window mapping was conducted during development of the research tunnels in order to expand on the initial photogrammetry data. Due to limited access adjacent unsupported ground and considering the shotcrete application, only the face was mapped. Nonetheless, this data provided more detail on the structural sets in the vicinity of the tunnels. This data was used as a design verification for the depth of reinforcement embedment. The stereonet of 280 individual joint observations, including Fisher pole concentration contours, is shown in Figure 68. Four joint sets were defined in the data. The average dip and dip direction of the structural sets are:

1. 55/161 (Strike: ENE-WSW, Dip: SSW),
2. 82/083 (Strike: N-S, Dip: E, steeply),
3. 83/348 (Strike: E-W, Dip: N, steeply)
4. 36/036 (Strike: NW-SE, Dip: NE).

The frequency distribution of dip and dip direction for this same window mapping data are shown in Figure 69 and Figure 70, respectively.

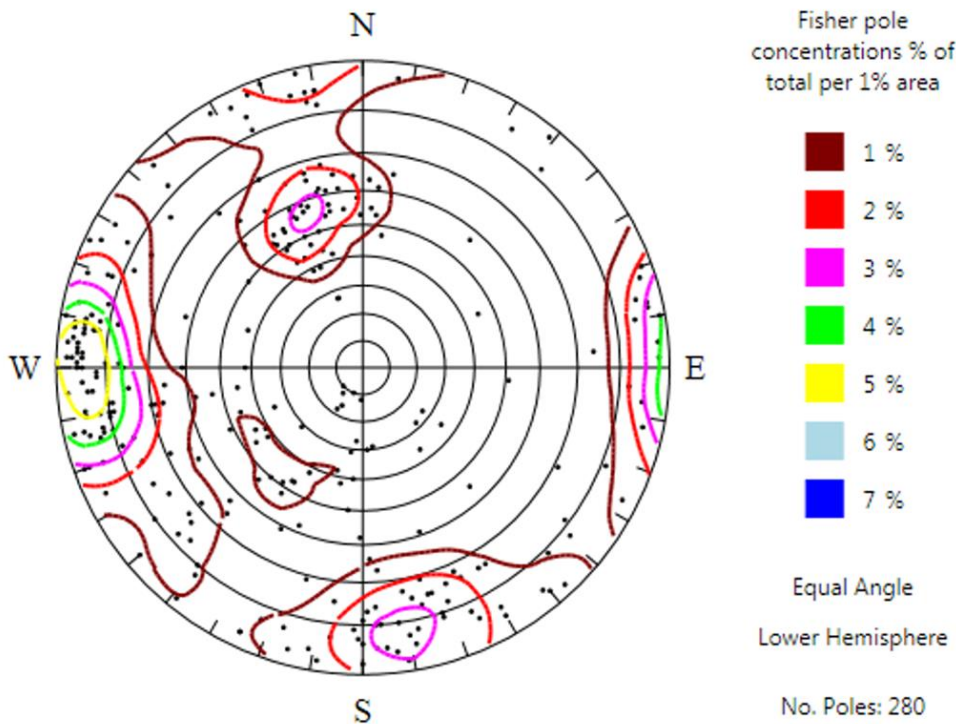


Figure 68 - Window mapping data of joint structures in the Dacite rock type.

Chapter 4: Design

The data indicate that the majority of joints in the development zone are steeply dipping, with the remainder only moderately dipping. There were relatively very few joints identified as having a shallow dip of less than 40 degrees.

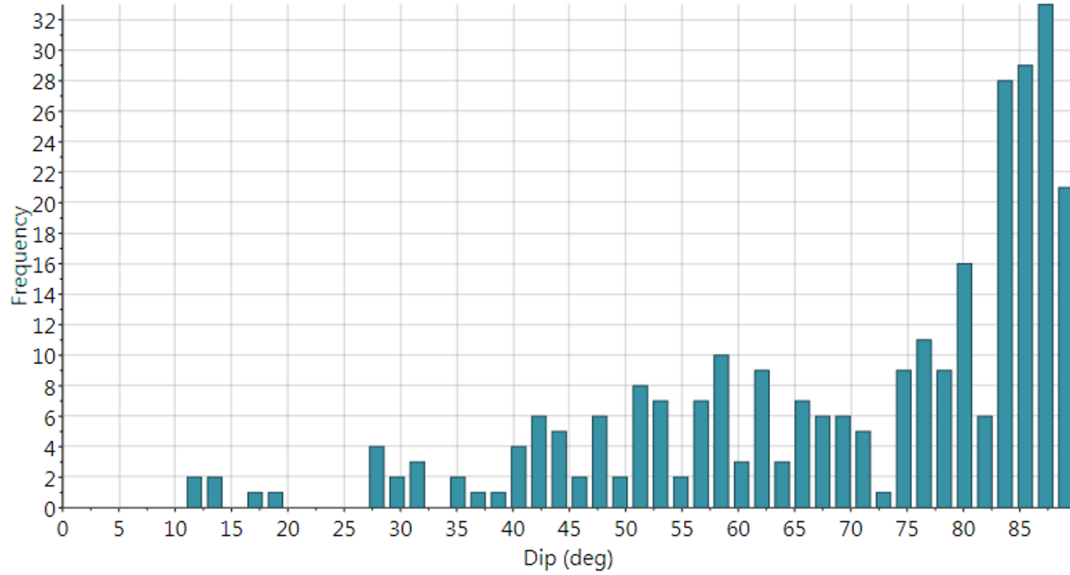


Figure 69 - Frequency distribution for all joint set dip data.

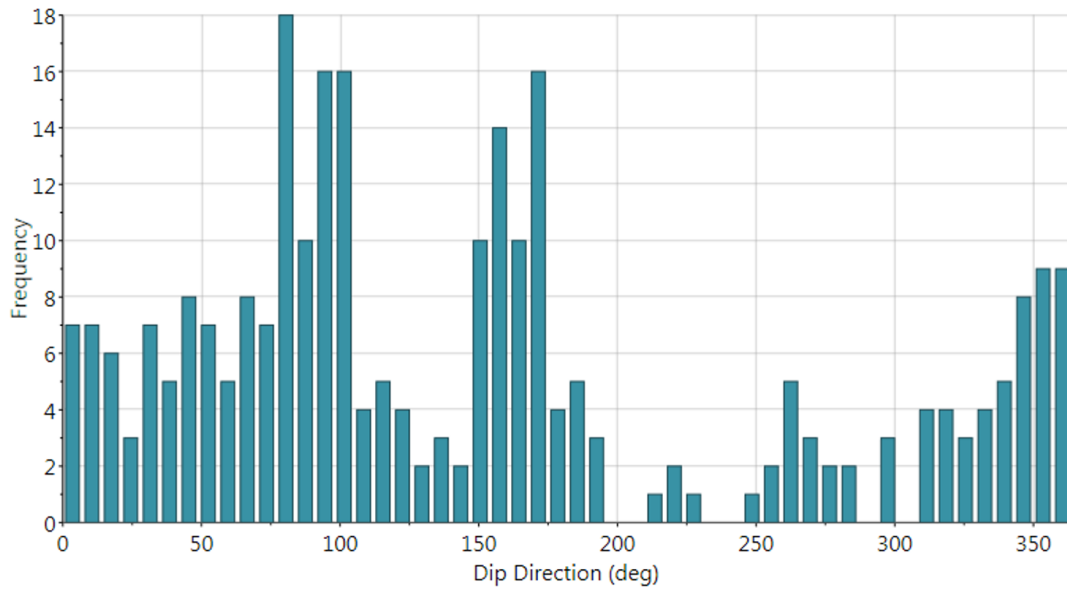


Figure 70 - Frequency distribution for all joint set dip direction data.

4.3.3 Rock Strength Properties

A comprehensive testing program was conducted by the WASM Geomechanics Laboratory, in order to characterise the mechanical properties of the Dacite rock type which hosted the research tunnels. Rock property testing was performed at the exact location of the two research tunnels. For this purpose, a pilot borehole was drilled and core sampled along each tunnel axis (Figure 71). One borehole was made along the centreline of each tunnel at approximately gradeline height, i.e. 1.5m above floor level. The pilot holes were both 50 metres long, allowing the rock mass to be sampled throughout the entire tunnel length. All strength testing results reported in this section are taken from Hogan & Sullivan (2017).

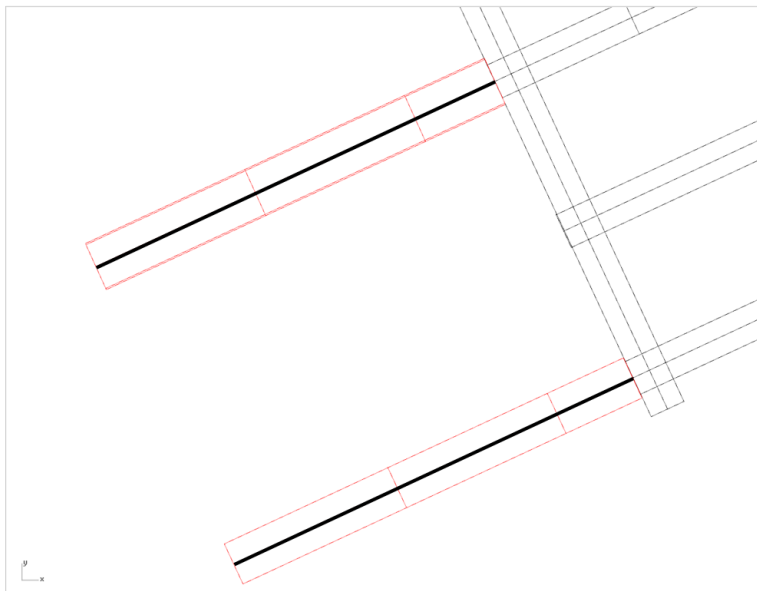


Figure 71 - Plan view of research tunnels showing position of pilot boreholes for strength characterisation.

Rock core was recovered from both boreholes intact, as well as suffering stress-related diking (Figure 72). Core diking sometimes occurs where the drilling process and sudden removal of the rock from its loading environment cause a tensile failure of the core. Where possible, strength testing was performed on both intact and diked core, in order to examine what material differences coincided with the occurrence of such damage, if any. The observations of diking as a function of distance along both the northern and southern tunnel pilot boreholes is shown in Figure 73. In the northern pilot hole, diking was prevalent primarily between the downhole distance of 13 and 22 metres, with almost no diking occurring beyond 25 metres. In the south, diking occurred non-continuously along the entire length of the borehole, although generally only in short lengths of between 1 and 3 metres.



Figure 72 - Examples of intact and stress-damaged disking core taken from the pilot boreholes.

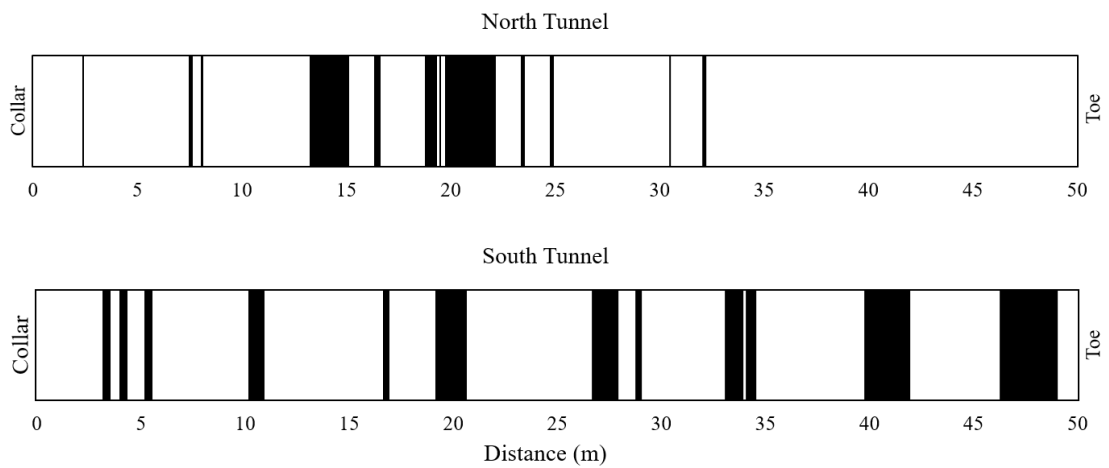


Figure 73 - Stress-related core disking along the north and south tunnel pilot boreholes.

In addition to the stress-related damage, the core was also tested considering the observable differences in the texture of the rock, with the Dacite rock type exhibiting both dark and light mineralogy.

The rock strength testing campaign examined the following properties:

- Uniaxial Compressive Strength (UCS),
- Elastic properties - Young's Modulus (E) & Poisson's Ratio (ν),
- Mohr-Coulomb criterion – Cohesion (c) & Friction angle (ϕ),
- Uniaxial Tensile Strength (UTS – Brazilian), and
- Fracture Toughness (K_{Ic}).

A total of 108 samples were prepared from the total length of core recovered across both pilot boreholes. All tests were conducted at the WASM Kalgoorlie Geomechanics laboratory. Table 1 presents a summary of the mean values of all parameters. Note that both peak and residual values of the Mohr-Coulomb Criterion parameters are stated. The mean values, plus or minus the standard deviation, were used for specifying the range of values for design and stability assessments of the two research tunnels.

Table 3 - Summary of the average mechanical properties of Dacite rock at the trial site.

γ (T/m ³)	UCS (MPa)	E (GPa)	ν	c (MPa)	ϕ (°)	UTS (MPa)	K_{Ic} (MPa m ^{0.5})
2.62	139	46.8	0.334	21.5, 6	58, 46	8	0.924

4.3.3.1 Uniaxial Compressive Strength

Twenty-two individual UCS tests were made on core taken from the pilot boreholes. Twelve samples were tested from the northern borehole and ten from the south. All values reflect the Dacite rock type. The UCS testing returned the following data, presented in Table 4.

Table 4 - Summary of UCS testing data for Dacite rock.

UCS	All Tests	North Pilot	South Pilot
Average (MPa)	139	162	120
Minimum (MPa)	42	120	42
Maximum (MPa)	209	209	184
Standard Deviation (MPa)	40	28	40

Chapter 4: Design

The spatial variability of intact rock UCS as a function of distance along the pilot boreholes (i.e. chainage along the tunnels) is shown below in Figure 74. As indicated by the tabulated data and this figure, the UCS was more consistent within the northern borehole and also slightly higher strength. In the southern borehole the measured UCS values were more variable, with a small number of very low outlying strength values. The frequency of all UCS results is shown in Figure 75. The majority of the test samples failed in a violent manner (Figure 76), indicating that sudden and violent rock mass instability was a valid failure mode in the full scale tunnels.

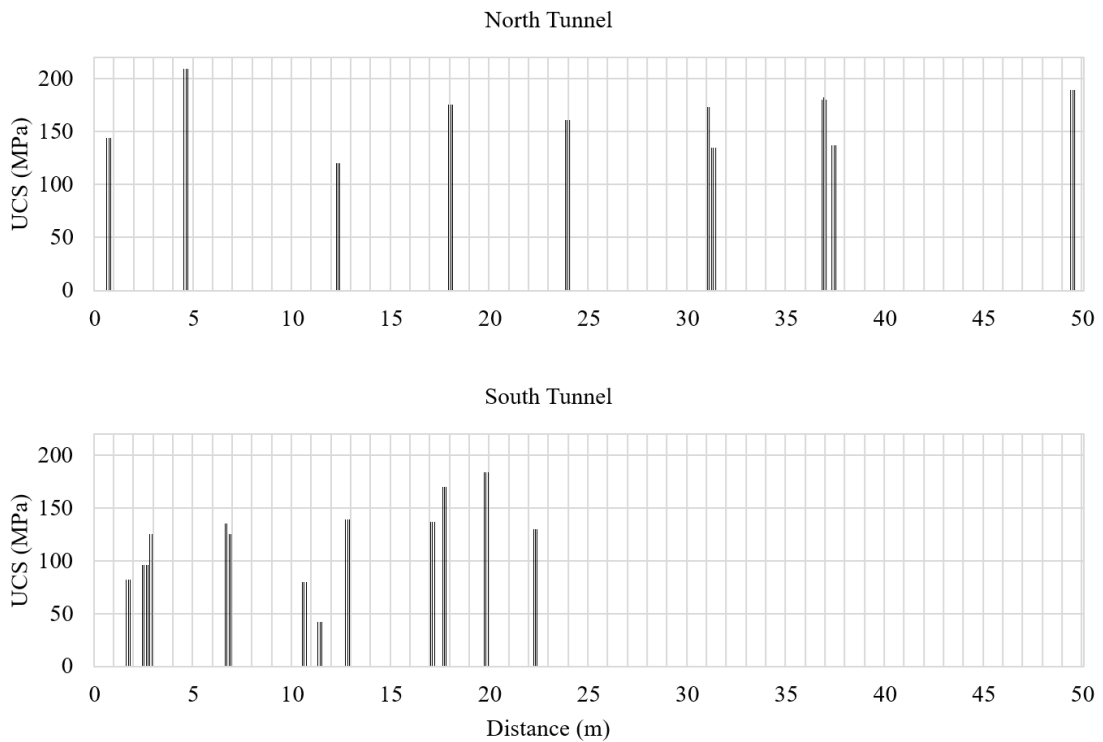


Figure 74 - Variability in Dacite UCS as a function of distance along the research tunnels.

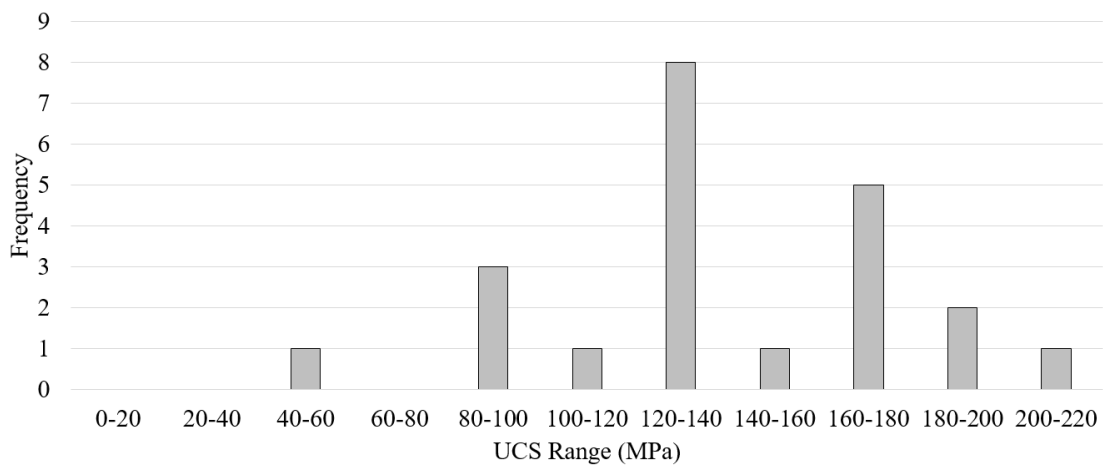


Figure 75 - Frequency distribution of all UCS values for Dacite rock.

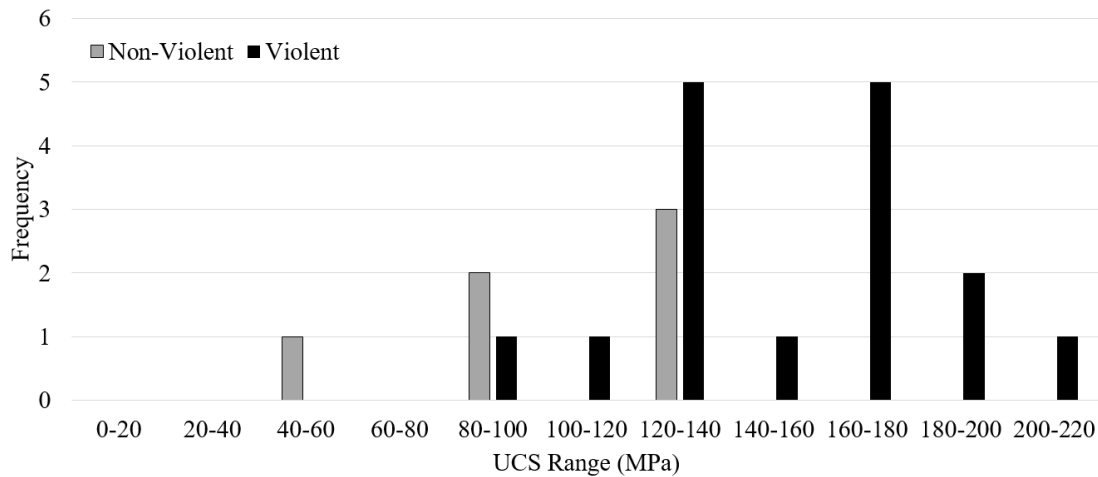


Figure 76 – Frequency distribution of failure mechanism of Dacite rock as a function of UCS.

4.3.3.2 Elastic Properties

Twelve tests were conducted to define the elastic properties of the Dacite rock type. Six samples were taken from each of the pilot boreholes. Table 5 presents the results of all tests, and also those subdivided by borehole. Figure 77 indicates that Dacite rock, both light and dark textures, generally exhibited a lower Young’s Modulus in comparison to Mafic hard rock at the mine. Furthermore, based on the data in Figure 78, the Dacite rock has a similar range of Poisson’s ratio to Mafic.

Figure 79 compares the elastic properties of Dacite and Mafic directly. Considering the similar strength range of both rocks and the fact that Dacite is notably less stiff than Mafic, Dacite could be expected to accumulate lower strain energy density prior to failure. This could manifest as slightly lower ejection energy of rock during violent failure of excavations constructed in Dacite, relative to excavations constructed in the Mafic units, assuming the same loading conditions.

Table 5 - Summary of elastic properties testing data for Dacite rock.

Young’s Modulus (E)	All Tests	North Pilot	South Pilot
Average (GPa)	46.8	49.2	44.4
Minimum (GPa)	37.5	44.9	37.5
Maximum (GPa)	53.3	53.3	51.0
Standard Deviation (GPa)	5.0	4.4	4.6
Poisson’s Ratio (ν)			
Average	0.334	0.348	0.321
Minimum	0.245	0.245	0.257
Maximum	0.400	0.400	0.376
Standard Deviation	0.051	0.056	0.048

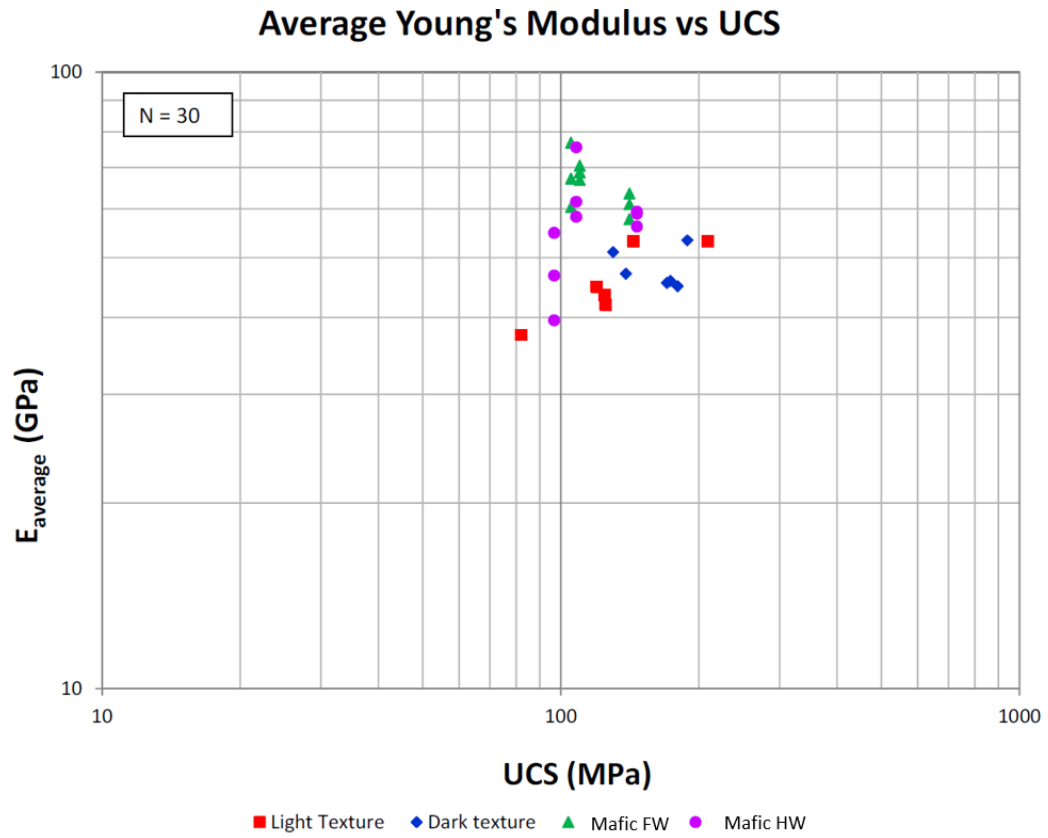


Figure 77 - Analysis of Dacite Young's Modulus with other historic mine data.

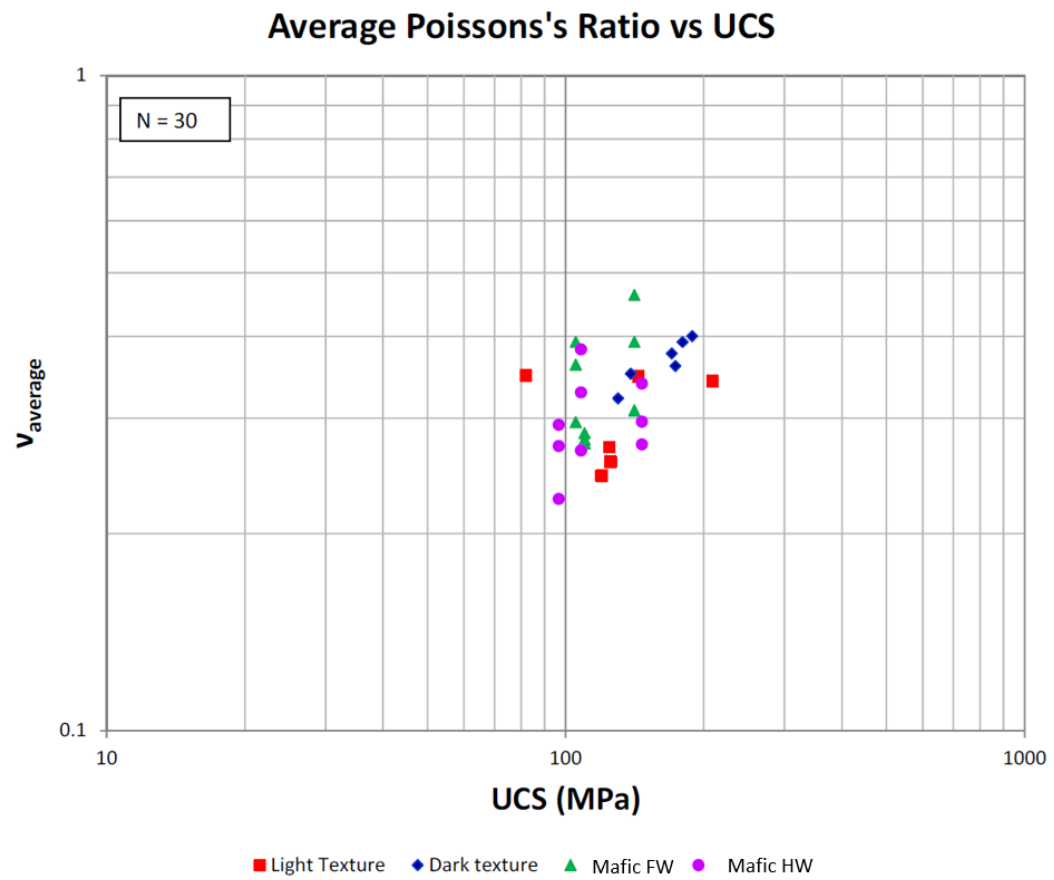


Figure 78 - Analysis of Dacite Poisson's Ratio with other historic mine data.

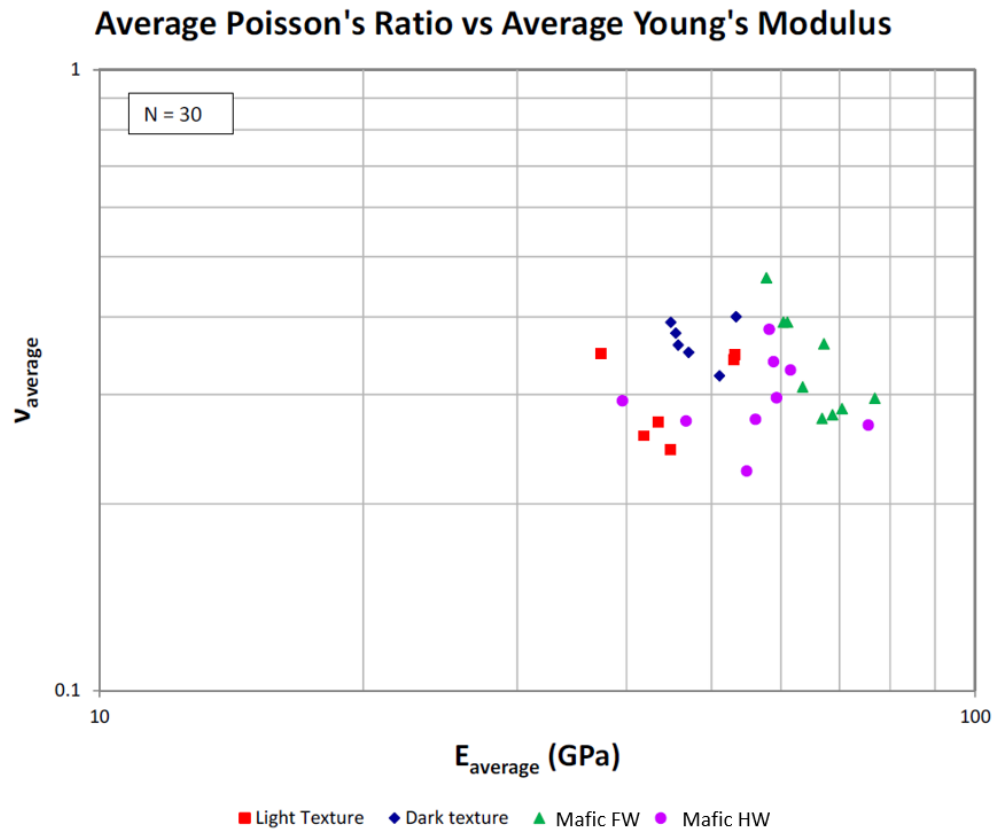


Figure 79 – Comparison analysis of the elastic properties of Dacite and mafic rock types.

4.3.3.3 Mohr-Coulomb Criterion

A total of 38 tests were carried out to define the Mohr-Coulomb failure criterion for the Dacite rock type, including 21 samples from the north pilot hole and 17 samples from the south pilot hole. Nineteen samples were taken from both light and dark textured Dacite. The average results across both textures, subdivided by borehole, are presented in Table 6. The peak values of the triaxial test data are plotted in Figure 80. Figure 81 shows the residual values. A direct comparison of both peak and residual results appears in Figure 82. The results indicate that peak and residual cohesion were both slightly higher in the vicinity of the northern tunnel. The peak and residual friction angle were consistent across both tunnels.

Table 6 - Summary Mohr-Coulomb failure criterion data for Dacite rock.

Peak	All Tests	North Pilot	South Pilot
Cohesion, c (MPa)	21.5	25	19.5
Friction Angle, ϕ ($^{\circ}$)	58	58	56.5
Residual			
Cohesion, c (MPa)	6	6.5	5.7
Friction Angle, ϕ ($^{\circ}$)	46	45	47

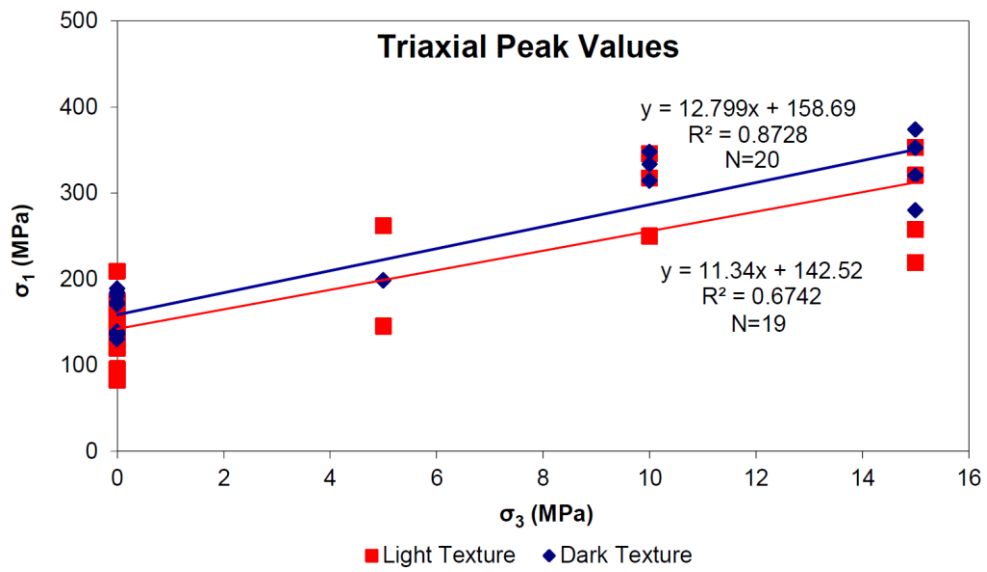


Figure 80 - Triaxial strength testing peak values for Dacite rock.

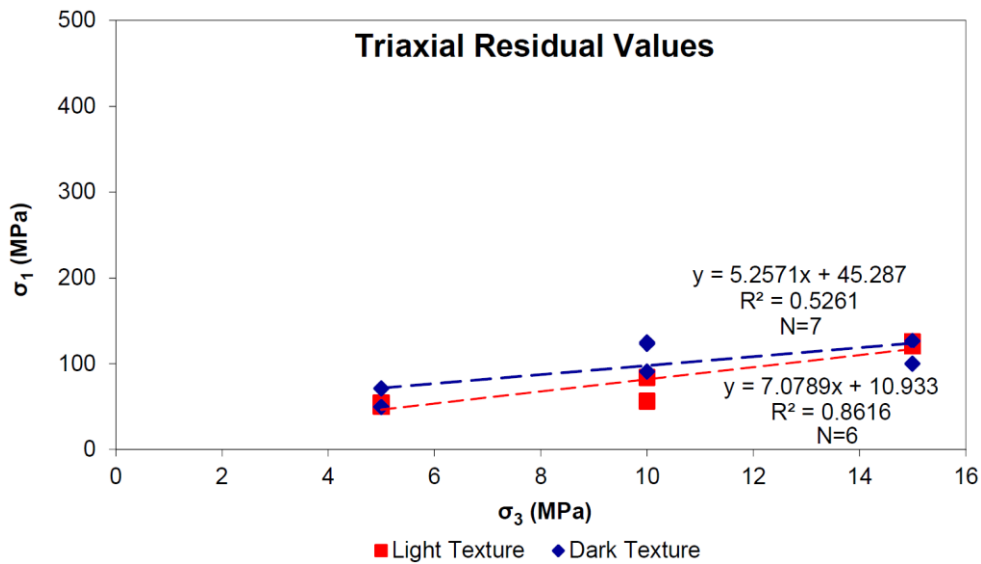


Figure 81 - Triaxial strength testing residual values for Dacite rock.

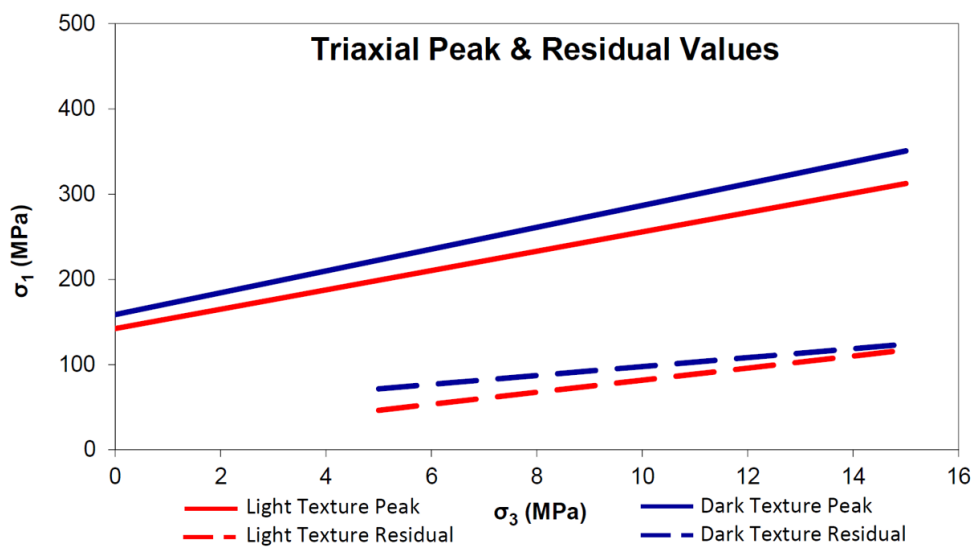


Figure 82 - Triaxial strength testing peak and residual comparison for Dacite rock.

4.3.3.4 Uniaxial Tensile Strength

In total, 30 UTS (Brazilian) tests were conducted on Dacite rock samples sourced from the pilot boreholes. From the southern pilot hole there were 12 samples tested and 18 from the north pilot. The complete data summary, including subdivision by borehole, is presented in Table 7. Figure 83 is a plot of the frequency of all UTS results for the Dacite rock type. The results indicate that the tensile strength of the rock mass was relatively uniform across both tunnels. The frequency of UTS values sampled from core suffering stress-related diskings is charted in Figure 84.

Table 7 - Summary of UTS testing data for Dacite rock.

UTS	All Tests	North Pilot	South Pilot
Average (MPa)	8	8	8
Minimum (MPa)	3	3	4
Maximum (MPa)	11	10	11
Standard Deviation (MPa)	2	2	2

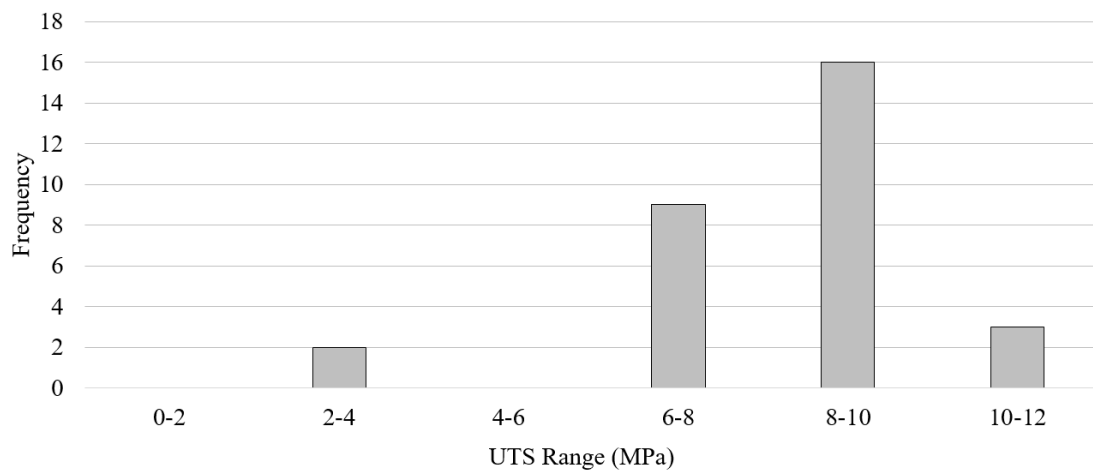


Figure 83 - Frequency distribution of all UTS values for Dacite rock.

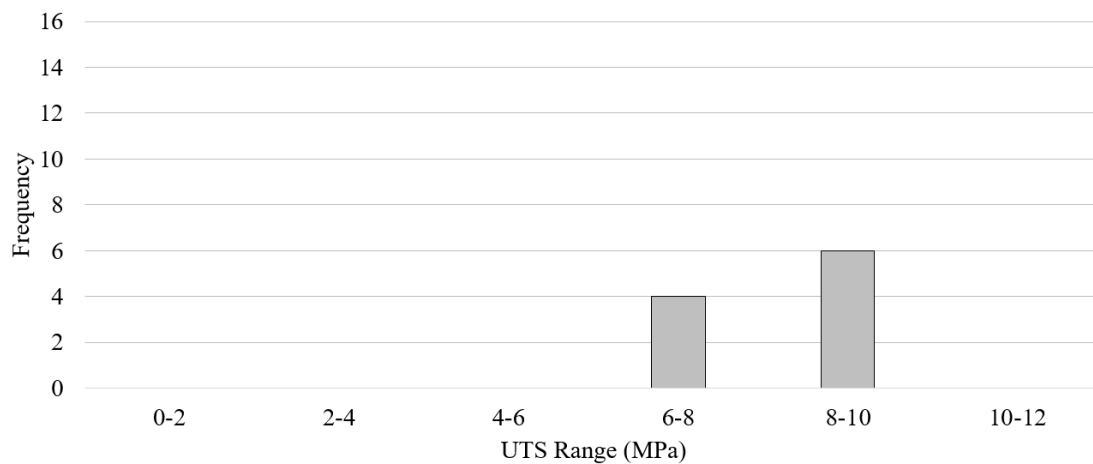


Figure 84 - Frequency distribution of UTS values for Dacite core suffering stress-related damage.

When comparing Figure 83 and Figure 84, it was evident that the UTS frequency distribution for stress damaged core closely resembles that of undamaged core, in terms of the histogram shape. In other words, core dinking occurred where the tensile strength of the rock fell within the normal range for the Dacite rock type. Dinking, in this case, did not appear to occur as a consequence of atypical tensile strength. Since core dinking of the pilot holes might be thought of as a potential indicator of future stress-driven tunnel instability, UTS on its own is perhaps an unreliable parameter with which to assess the potential of this phenomenon occurring, at least in this case.

4.3.3.5 Fracture Toughness

Fracture Toughness is a measure of the resistance of a material to the propagation of a crack (Ashby, 1992). Fracture Toughness tests were carried out on 63 samples of Dacite core. From the southern pilot hole, 25 samples were tested, and 38 from the north pilot. A tabulated summary of test results, subdivided by borehole, is presented in Table 8. A histogram of the frequency distribution of all Fracture Toughness results is shown in Figure 85. The tabulated data and histogram indicate that the majority of test results fell within the range of 0.8 to 1.1 MPa m^{0.5}. This places the Fracture Toughness of Dacite in the upper range for common rocks (Figure 86).

Table 8 - Summary of Fracture Toughness testing data for Dacite rock.

Fracture Toughness (K_{Ic})	All Tests	North Pilot	South Pilot
Average (MPa m ^{0.5})	0.924	0.890	0.977
Minimum (MPa m ^{0.5})	0.507	0.591	0.507
Maximum (MPa m ^{0.5})	1.255	1.114	1.255
Std. Deviation (MPa m ^{0.5})	0.147	0.131	0.158

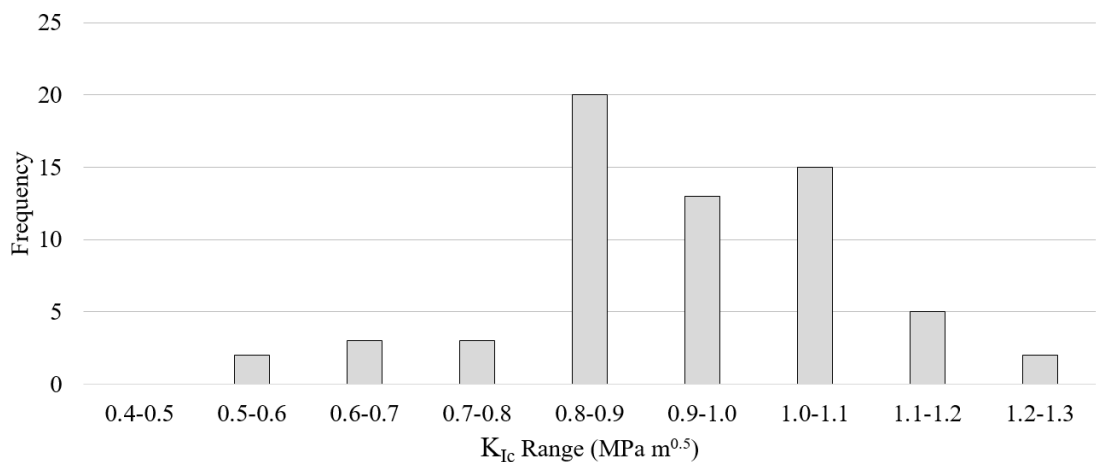


Figure 85 - Frequency distribution of all Fracture Toughness results for Dacite rock.

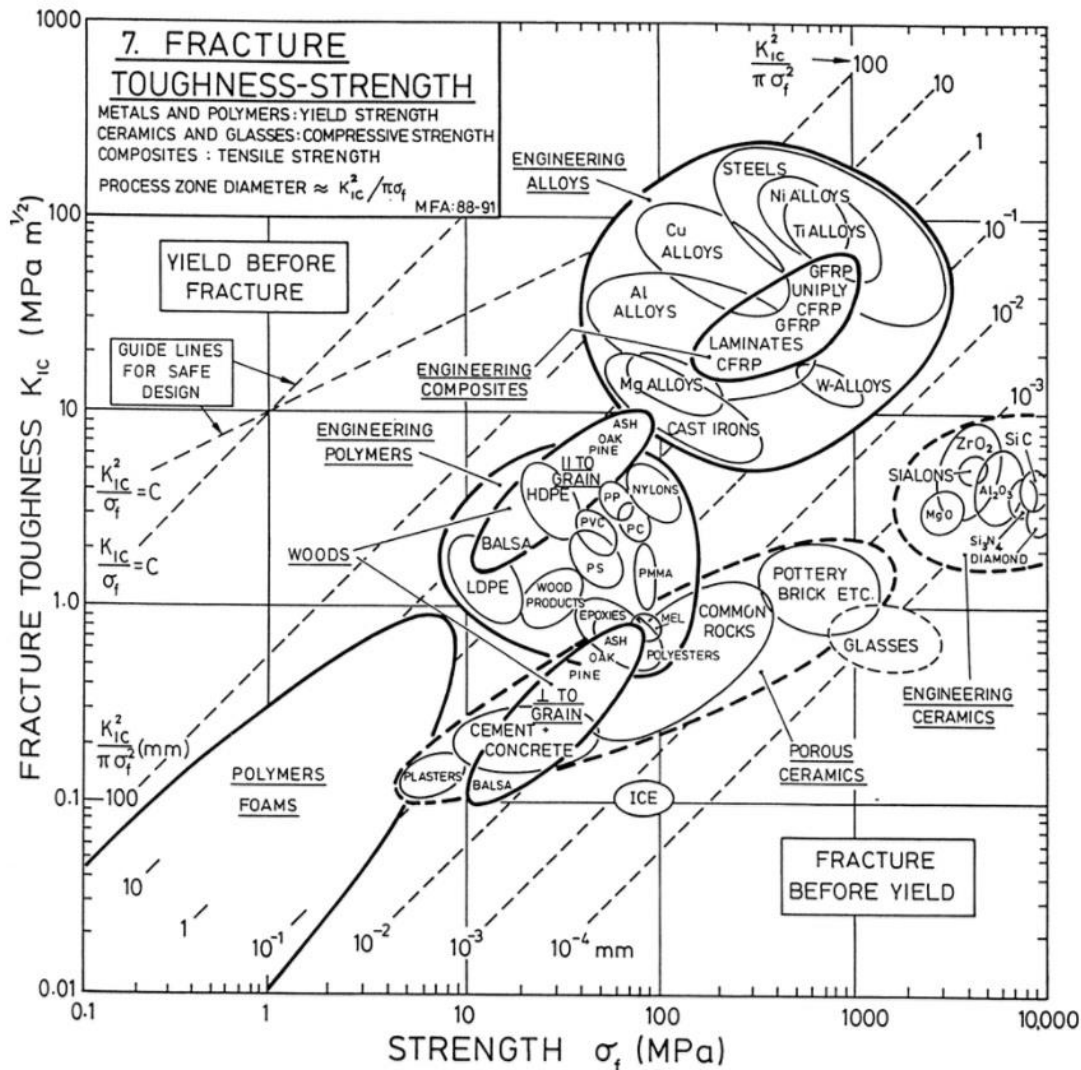


Figure 86 - Fracture Toughness of engineering materials plotted against Strength (Ashby, 1992).

A scatter chart of the Fracture Toughness data plotted against closely co-located UTS results is shown in Figure 87. The data indicate higher Fracture Toughness results for the southern pilot hole core. More viable test samples were able to be taken from stress-damaged core in the northern pilot hole. Eighteen testable samples were extracted from disked core sections of the northern pilot hole, compared to only six from the southern pilot. The sample selections for these tests is illustrated in Figure 88. Sample locations are shown by the blue or orange coloured bars and disked core as black bars. The sampling strategy aimed to examine any variation in Fracture Toughness between intact and stress-damaged core. The results do not tend to indicate that stress-damaged core had a notably lower Fracture Toughness. As illustrated in Figure 89, there was no clear differentiation of the groupings of test results for intact core and stress-damaged, disked core. Instead, the grouping of results were interspersed.

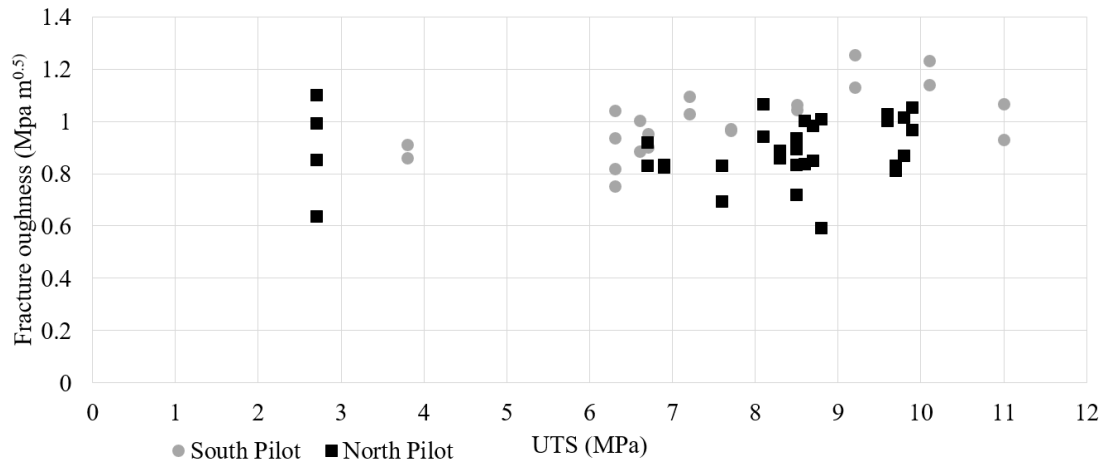


Figure 87 - Fracture Toughness versus UTS for Dacite rock.

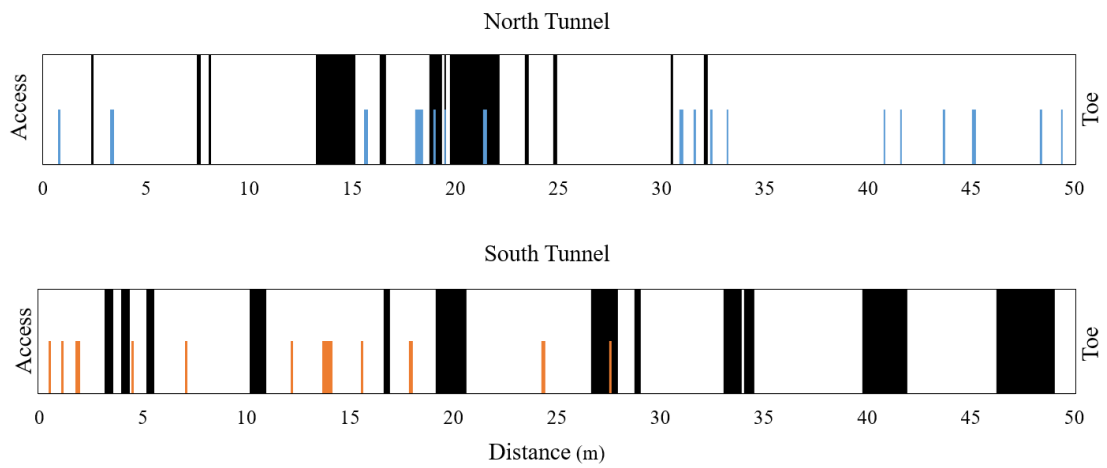


Figure 88 - Fracture Toughness sampling locations (blue/orange) relative to core diskings (black).

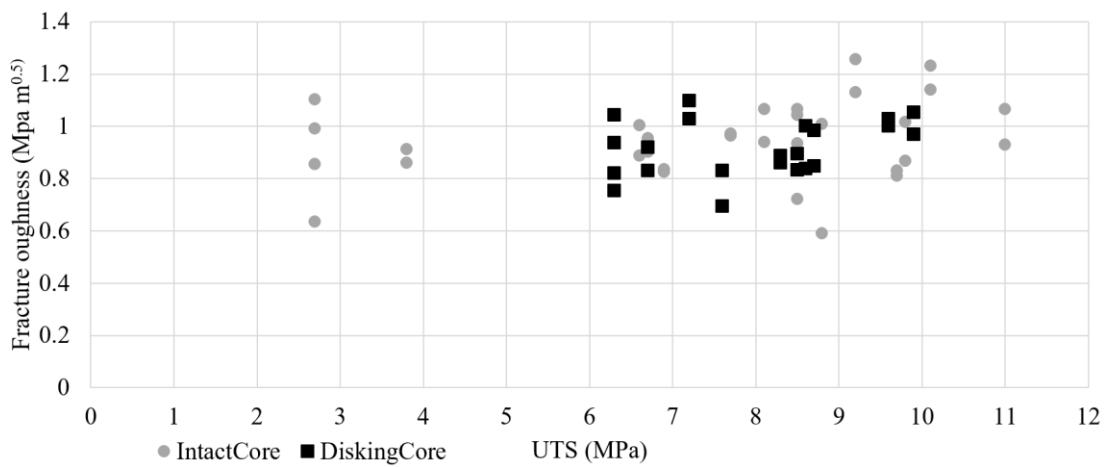


Figure 89 – Fracture Toughness versus UTS data subdivided by the presence of stress-related core diskings.

4.3.4 Stress Conditions

The stress conditions were evaluated at the site of the experimental tunnels using data provided by the mine site, including in-situ stress measurements and numerical modelling results. A large database of stress measurements had been collected at the mine over many years. Windsor, et al., 2006 completed a characterisation of the stress conditions by compiling CSIRO HI Cell and WASM AE data. From that analysis, the chart of the distribution of the principal stress magnitudes as a function of depth is presented in Figure 90. The orientations of the principal stresses are shown in Figure 91. Note that the legend of symbols is common to both figures.

Most of these data represent measurements focused on adjacent future production areas, such as the Brechia and Mafic units, as well as the deepest sector of the current production precinct. The results indicate that the pre-mining major principal stress (σ_1) in the active development zone is predominantly in the NNW-SSE orientation. This stress is typically sub-horizontal, with less than 10° of inclination. The minor principal stress (σ_3) acts almost vertically. WASM AE data indicate that σ_3 is highly consistent with the lithostatic load. These results indicate the pre-mining magnitude of σ_1 and σ_3 to be approximately 40MPa and 17MPa at the 635m depth of the experimental tunnels.

In order to better define the stress conditions local to the site of the experimental tunnels, a series of stress measurements were performed by the mine site engineers using the CSIRO HI Cell (Moraga, 2015). Four measurements were attempted, of which three were successful. Table 9 presents the recorded stresses. Figure 92 illustrates the location of these stress measurements relative to the existing development in that precinct. The elastic properties used for the stress analysis are also presented, where available. Successful measurements at sites 1 and 3 were performed in Dacite rock. The test at Site 4 was made in the nearby Mafic complex. Measurement at site 2 failed due to broken drill rods which prevented overcoring of the HI Cell. A comparison of these HI Cell results with WASM AE suggest that most measurements agree. The HI Cell data show slightly higher stress magnitudes and some orientation variation. This likely reflects induced stress changes close to the excavations. The very high stress values recorded at HI Cell site 3 do not agree with any other HI Cell or WASM AE measurements for this depth or mining area and are considered to be erroneous. As such, this result was ignored.

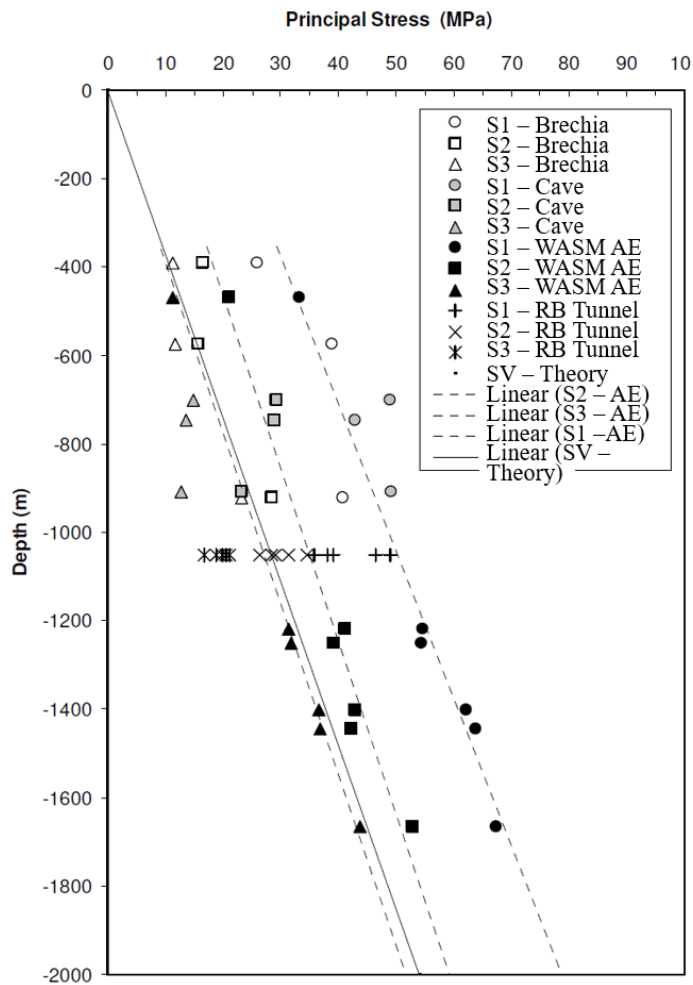


Figure 90 – Principal stress magnitude distribution with depth (Windsor, et al., 2006).

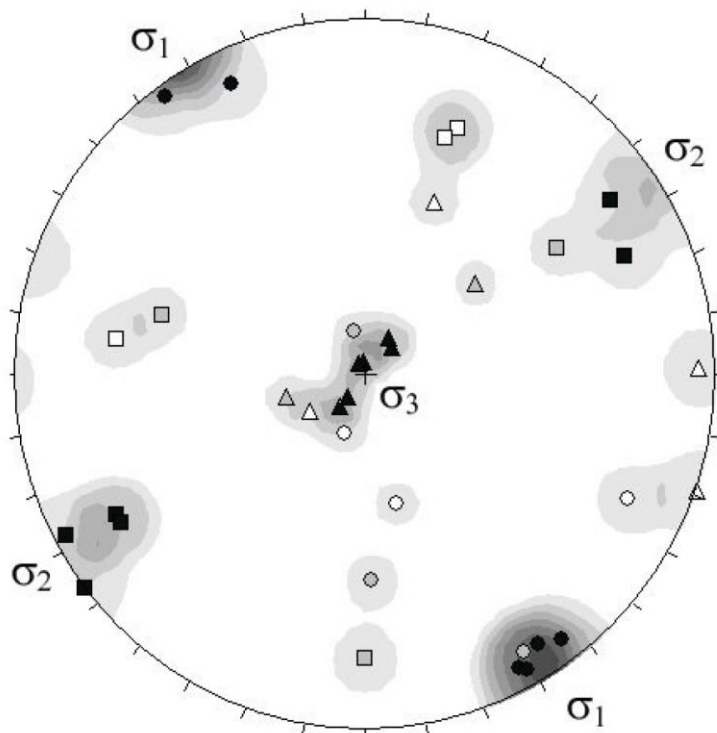


Figure 91 – Principal stress orientations at the mine site (Windsor, et al., 2006).

Table 9 – CSIRO HI Cell stress measurement data localised to the site of experimental tunnelling.

	Site 1			Site 2	Site 3*			Site 4		
	MPa	Azi	Dip		MPa	Azi	Dip	MPa	Azi	Dip
σ_1	48	135	-9	Measurement failure due to broken drill barrel.	63	189	-4	45	126	-29
σ_2	32	225	0		28	280	-3	27	25	-21
σ_3	21	318	-81		22	44	-85	23	263	-54
E	21.44 GPa				29.46 GPa			Not reported		
ν	0.32			0.24			Not reported			

* Results disregarded due to incorrect elastic parameters use in stress analysis.

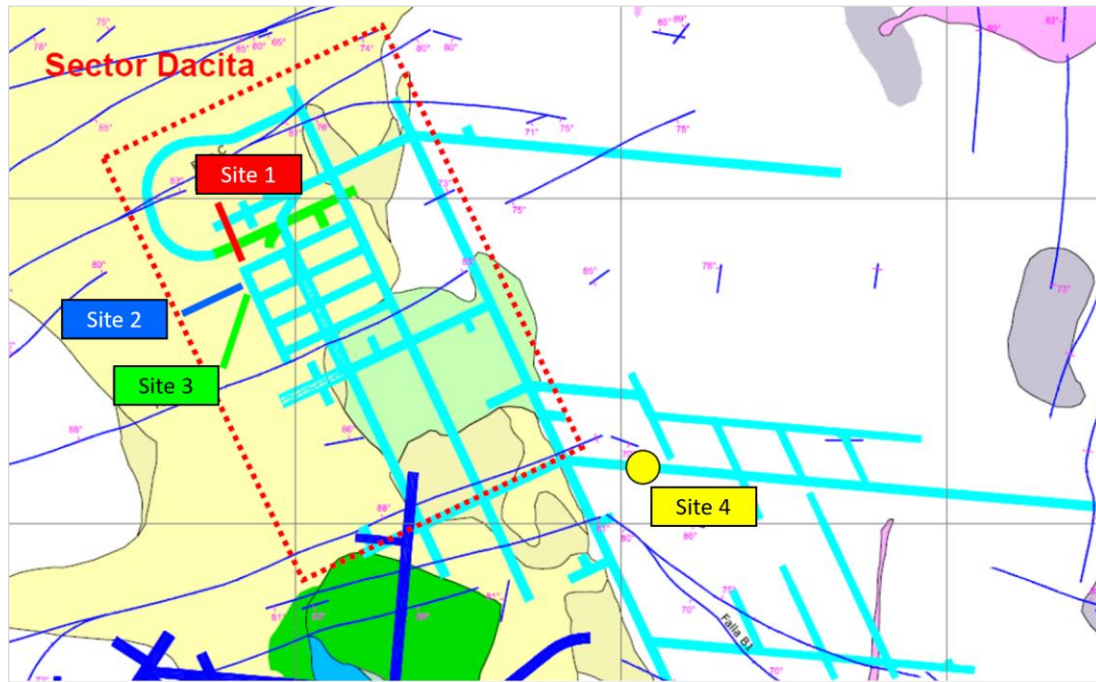


Figure 92 - Location of CSIRO HI Cell stress measurements taken prior to tunnelling (Moraga, 2015).

In addition to the aforementioned stress measurements, the results of numerical stress modelling in the Abaqus program were provided by the mine operator. Horizontal sections of the σ_1 results, taken at the elevation of the experimental tunnels, are shown below in Figure 93. The σ_3 results are shown in Figure 94. The model represents the rock mass conditions prior to commencing development. That is, without the experimental tunnels included in the modelled void geometry. Purely for reference, the approximate position of the tunnels is indicated by dashed lines superimposed on the figures. The modelling agrees with the orientations of the principal stresses indicated by Windsor, et al., 2006 for the new mine level. However, the magnitudes of the modelled mining-induced principal stresses were notably higher than the values measured in-situ. Since the model input boundary stresses were unknown, only the modelled orientations were accepted. Therefore, the WASM AE and CSIRO HI Cell results from sites 1 & 4 were considered to reflect the legitimate stress magnitudes.

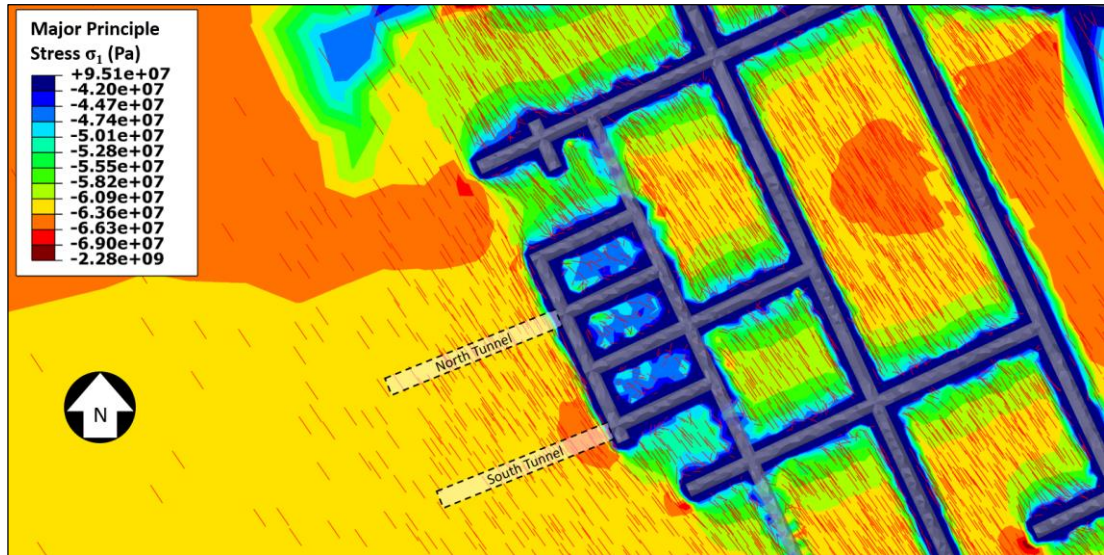


Figure 93 - Abaqus numerical model results of major principal stress (σ_1) magnitude and orientation.

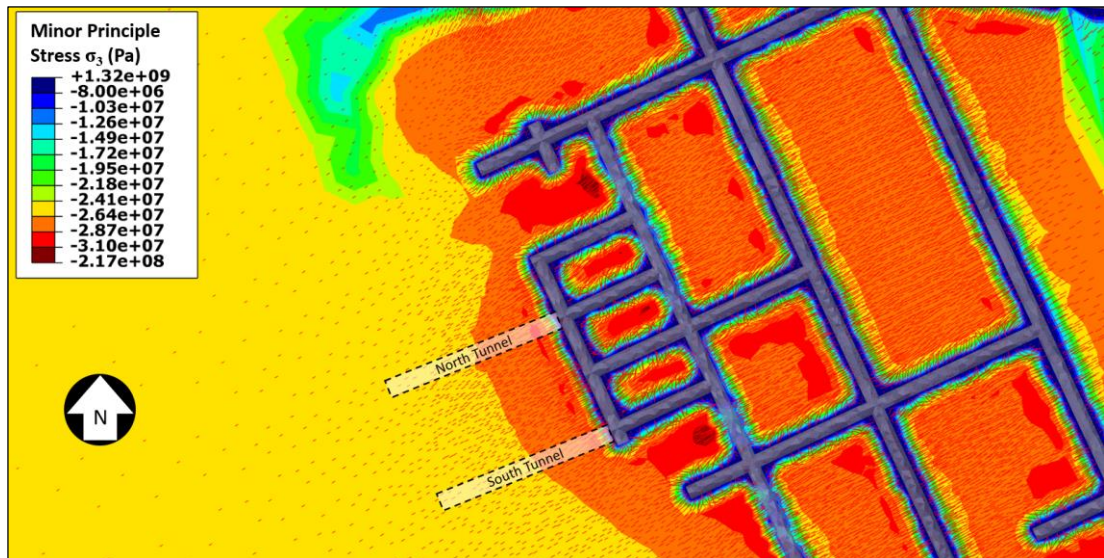


Figure 94- Abaqus numerical model results of minor principal stress (σ_3) magnitude and orientation.

4.4 Stability Assessment

4.4.1 Stress-Driven Instability and Failure Mechanisms

In order to forecast the stability of the experimental excavations, it was necessary to define the plausible modes of failure. A total of five generic mechanisms of failure were considered for the design of the experimental tunnels in hard rock. The first four mechanisms all require violent strain energy release at the tunnel perimeter. They include spalling, structurally controlled block ejection, fault rupture and shear failure mode of pillar crushing. These modes of failure are illustrated in Figure 95 in typically increasing order of violence and volume of damage. A fifth mechanism, seismically induced rockfall (Figure 96) triggered by the dynamic stress wave of a remote seismic event (Kaiser, et al., 1996), was also considered. This mechanism is regarded as instability of rock blocks previously close to the static limit equilibrium, with no associated strain energy release. For this reason, seismic fall is fundamentally different to the first four mechanisms and it generates less demand on ground support.

In order to assess the potential for violent stress-driven spalling, structurally controlled block ejection and shear failure mode of pillar crushing, two novel stability charts are introduced in Figure 97 and Figure 98. These charts plot the excavation host rock UCS (σ_c) on the horizontal axis and the ratio of UCS to induced stress (σ_c/σ_{max} or σ_c/σ_{ave}) on the vertical axis. Stability thresholds for both spalling and pillar crushing are denoted by the black and blue lines on the chart, respectively. Spalling initiates before pillar crushing and hence this threshold is the upper of the two lines in Figure 98. These stability thresholds (or limits) are based on the experimental data from small scale tunnel tests conducted by Kusui (2015).

Figure 97 applies to spatially isolated excavations not formed by thin pillars. The spalling stability threshold is defined by the following equation from Kusui (2015):

$$\text{Spalling: } \frac{\sigma_c}{\sigma_{max}} = -0.00005\sigma_c^2 + 0.0232\sigma_c + 0.2767 \quad (\text{Eq. 4.1})$$

The spalling threshold line in Figure 98 applies where excavation surfaces are formed by thin pillars to adjacent voids. It is defined by the following equation from Kusui (2015):

$$\text{Spalling: } \frac{\sigma_c}{\sigma_{ave}} = -0.00007\sigma_c^2 + 0.0344\sigma_c + 0.4355 \quad (\text{Eq. 4.2})$$

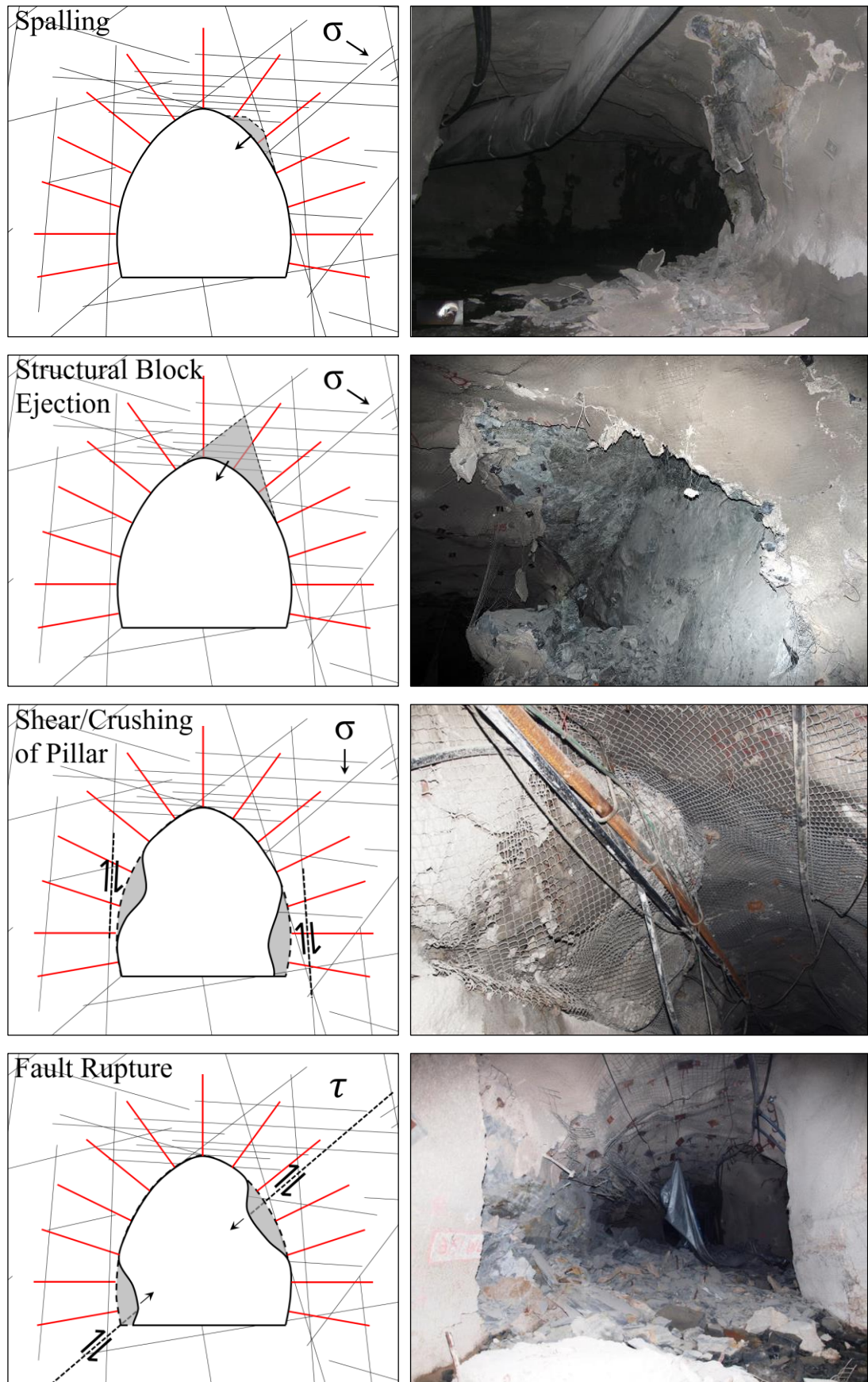


Figure 95 - Generic mechanisms of tunnel instability controlled by the quasi-static stress.

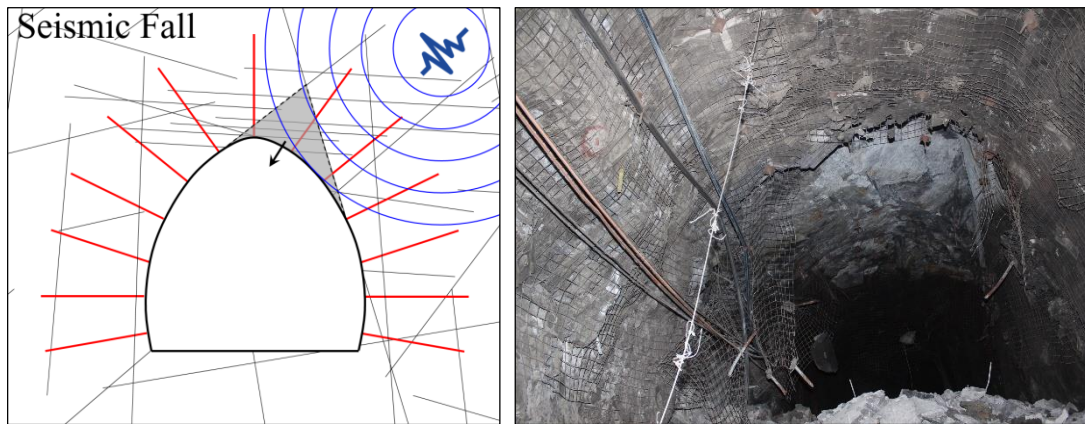


Figure 96 - The generic mechanism of tunnel instability triggered by remote seismicity.

The shear failure mode of pillar crushing threshold line in Figure 98 primarily applies where excavations have thin pillars to nearby voids. However, as an approximation it was also applied to the larger research tunnel pillars. It is defined by the equation from Kusui (2015):

$$\text{Pillar Shear/Crushing: } \frac{\sigma_c}{\sigma_{ave}} = -0.0001\sigma_c^2 + 0.0345\sigma_c + 0.4869 \quad (\text{Eq. 4.3})$$

Spalling and shear failure mode of pillar crushing are indicated to occur wherever the σ_c/σ_{max} or σ_c/σ_{ave} ratio for the excavation plots below the relevant stability threshold line on the chart. Structurally controlled block ejection is also considered to be possible anywhere that removable blocks exist and the strength/stress ratio plots significantly below the spalling threshold of the chart. Above the spalling limit the excavation instability may be regarded as non-violent (i.e. static loading). Should the rock mass conditions plot below both the spalling limit and a UCS of 50 MPa, the mode of failure may be anticipated to be non-violent crushing (i.e. time dependent convergence).

The WASM AE and CSIRO HI Cell stress measurement data relevant to the research tunnels indicated σ_1 to be in the range of 40-48 MPa. This range was defined for σ_{ave} . The plausible range of σ_{max} was estimated by multiplying σ_1 by 1.5. Intact rock strength testing indicated the UCS in the northern tunnel to be 162 MPa, on average, with a standard deviation of 28 MPa (see Table 4). Therefore, σ_c was assumed to vary along the tunnel within the range of 134-190 MPa. Considering the measured variability in the rock mass conditions, the possible values of the stability criteria σ_c/σ_{max} and σ_c/σ_{ave} were calculated for the northern tunnel, as shown in Table 10. The range of values were plotted on the stability charts in order to estimate the excavation response.

Table 10 - Plausible range of the σ_c / σ_{max} and σ_c / σ_{ave} stability criteria for the northern research tunnel.

UCS (MPa)		σ_{max}	σ_{max}	σ_{ave}	σ_{ave}
		60 MPa	72 MPa	40 MPa	48 MPa
σ_c (-1 StDev)	134	σ_c / σ_{max}	σ_c / σ_{max}	σ_c / σ_{ave}	σ_c / σ_{ave}
σ_c (Average)	162	2.2	1.9	3.4	2.8
σ_c (+1 StDev)	190	2.7	2.3	4.1	3.4
		3.2	2.6	4.8	4.0

The excavation stability performance envelope for the northern research tunnel is indicated on each stability chart by the red shaded section with dashed outline.

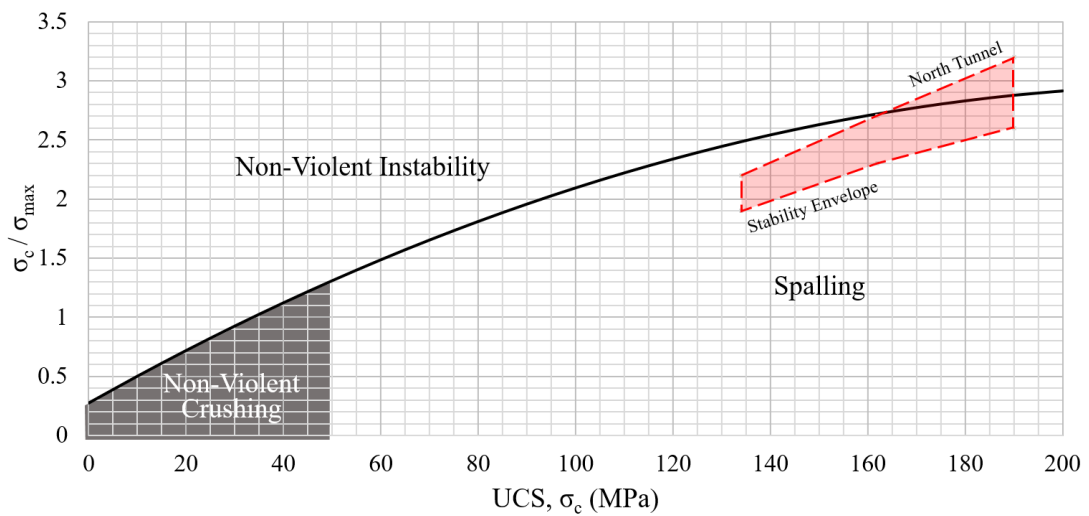


Figure 97 - Stability chart for spatially isolated excavations.

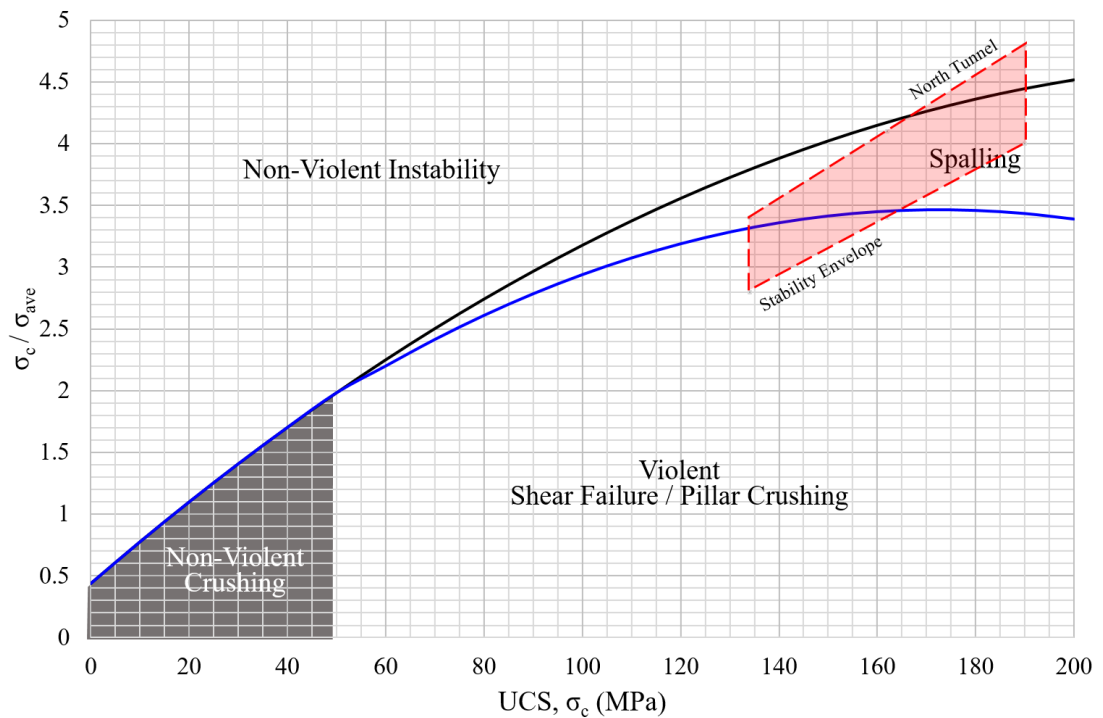


Figure 98 – Stability chart for excavations with thin pillars.

This analysis was specific to the tunnel development stage. It indicated that the northern tunnel stability fell primarily within the spalling zone on the stability chart. Slight overlaps into the pillar crushing/shearing and stable zones of the stability charts reflect outlying rock strength measurements which were unlikely to represent the dominant excavation behaviour. The most likely excavation response was anticipated within the central region of the red shaded zone, reflecting the average rock mass characterisation values. As such, the northern excavation was expected to experience violent stress-driven spalling failure mechanisms during development, with a minimal risk of pillar crushing during the construction phase. The stability analysis indicated that the tunnel could possibly transition to pillar crushing in the event that the stresses significantly increased at a later stage of the excavation's service life.

Structurally controlled block failure and shear failure of the excavation were regarded as possible modes of failure following the onset of spalling. These late stage mechanisms may result from future mining-induced stress increase around the cave. Prior to construction, it was assumed that shear failure could potentially occur in the walls due to σ_3 increase, or in the roof and floor due to σ_1 increase. However, following in-cycle structural mapping during the early development, the shear mechanisms were re-evaluated and the design assumptions refined. It was then anticipated that three shear failure mechanisms were possible. These included:

1. Shear failure of the back and floor through intact rock due to σ_1 increase,
2. Shear failure of the walls along Set#3 joints due to σ_3 increase, and
3. Shear failure of the walls along Set #1 joints due to σ_1 and/or σ_3 increase.

These three mechanisms of shear failure are sketched in Figure 99 to Figure 101. The potential for each mechanism to occur was assumed to be dependent upon the future changes in magnitude and orientation of the principal stresses. Due to a lack of mapped structures with sub-horizontal dip, it was anticipated that a large increase in the major principal stress could cause shear failure through intact rock in the roof and floor of the tunnel, rather than through pre-existing natural structure. Conversely, the large number of steeply north and south dipping joints provided multiple pathways for shear failure to develop within the walls of the excavation in the event that the stresses markedly increased at some time in the future. The associated shear plane was assumed to be the average dip of the relevant joint set.

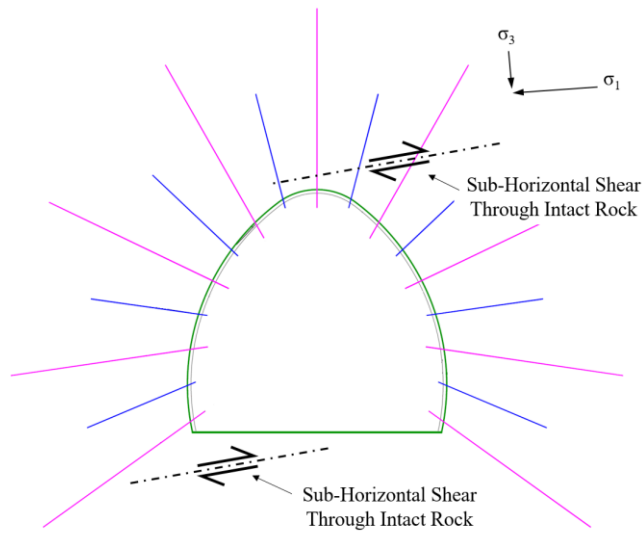


Figure 99 – Mechanism 1: shear failure of the back and floor through intact rock due to σ_1 increase.

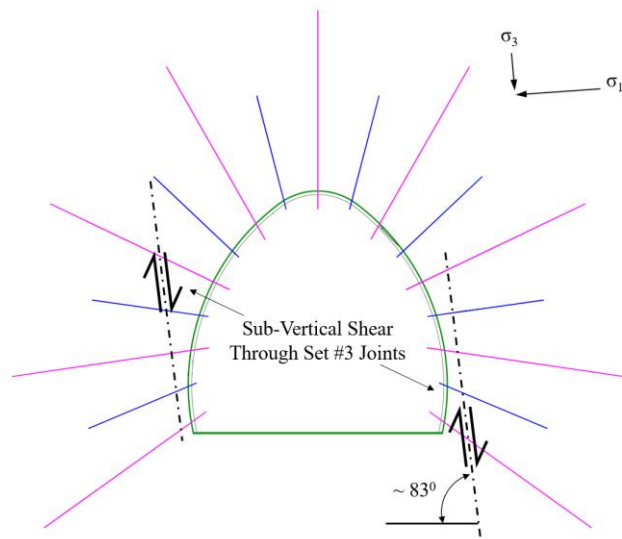


Figure 100 – Mechanism 2: shear failure of the walls along set #3 joints due to σ_3 increase.

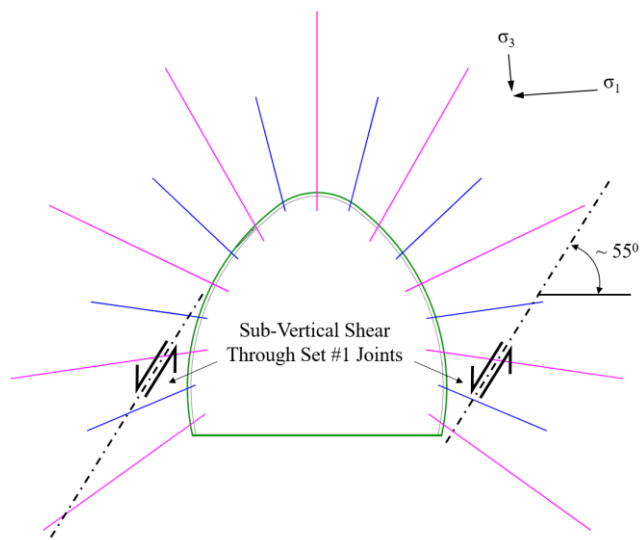


Figure 101 – Mechanism 3: shear failure of the walls along set #1 joints due to σ_1 and/or σ_3 increase.

4.4.2 Mass of Instability

The mass of instability refers to the mass of unstable rock that dynamically loads the ground support scheme during a violent stress-driven failure. It is a critical input parameter in the energy demand analysis for ground support capacity design. The mass of instability is a function of the rock unit weight and depth of failure. For simple mechanisms of spalling, the depth of failure may be determined via observational evidence. Probabilistic block analysis (Windsor, 1999) is recommended to be used wherever failure mechanisms are more complex and structurally controlled.

4.4.2.1 Spalling Failure

Spalling failure preferentially loads the surface support, including shotcrete, mesh and reinforcement surface fixtures in between the reinforcement spacing. For the majority of spalling events, the depth of rock mass failure beyond the tunnel boundary is shallow. The shallow nature of spalling instability can be attributed to the loading and failure mechanisms. Spalling occurs as a result of compressive overstressing characterised by tensile failure perpendicular to the load orientation through intact rock and/or favourably oriented discontinuities on the tunnel boundary. With increasing distance beyond the tunnel perimeter, the confinement on the rock mass increases and the stress orientation on the tunnel boundary may rotate slightly, due to the effect of the void geometry. At a certain distance, the stabilising forces are sufficient to prevent the characteristic compressive overstressing and tensile rupture along planes of weakness. Observational evidence indicates that spalling instability of this nature is typically limited to a depth of failure of 0.5m or less (Figure 102).

The mass of spalling instability may be defined in tonnes per unit area of the excavation surface where failure occurs (T/m^2). It can be estimated using the following equation, where M is the mass of instability, ρ is the intact rock density and d_f is the depth of failure, measured as the perpendicular distance between the tunnel boundary and the apex of the failure geometry:

$$M = \rho d_f \quad (Eq. 4.4)$$

For the majority of hard rocks, which have a unit weight in the order of $2.7 T/m^3$, the mass of instability due to spalling failure is suggested to be generally no greater than $1.5 T/m^2$. Failure mechanisms which exhibit larger depths of failure and associated energy demand are suggested to be structurally controlled.



Figure 102 - Example of spalling failure with a shallow depth of instability.

4.4.2.2 Structurally Controlled Failure (Block Ejection)

Structurally controlled failure can occur where intersecting joints form unstable blocks of rock at the tunnel free face. The depth of failure can be significant, sometimes exceeding two metres where the geological structures approach the span width of the excavation. Because of the potentially large depth of failure associated with complex, structurally controlled mechanisms (see Figure 18), it is likely that the instability will damage a number of reinforcement elements. Failure can potentially develop beyond the depth of reinforcement embedment, causing ejection of the entire element (Figure 103). Such failures can have a mass of instability greatly exceeding 1.5 T/m^2 , and consequently impart energy demand in excess of 25 kJ/m^2 on the ground support. In some conditions the demand may exceed $60\text{-}80 \text{ kJ/m}^2$ (Drover & Villaescusa, 2015b).

A critical aspect of the overall ground support design process is the estimation of the potential block geometry associated with structural failure. Previously, this has been performed via deterministic analysis. Deterministic methods use set values for each joint parameter and typically indicate the worst case, low probability block scenario. However, it is suggested that probabilistic analysis methods provide a more realistic solution for the likelihood of potential block geometries.



Figure 103 – Reinforcement and surface support failure, with ejection of large blocks.

Deterministic analysis first was used in this analysis to gain an initial appreciation of the block shapes and maximum possible geometry. However, for the purposes of ground support design, the structural blocks were estimated according to the probabilistic block theory developed by Windsor (1999). The block geometry was implemented using the SAFEX software package, which has recently been updated by WASM. Structural data such as joint dip and dip direction, trace length and spacing were collected via window mapping in the excavations. The methodology of structural analysis described below serves as an example of that which could be routinely undertaken at operating mines or tunnelling projects, in order to initially quantify the design parameters and then validate them over a broad development precinct on an ongoing basis.

This approach to structural analysis focused on three crucial parameters. These include the *block apex height*, which was used to confirm an adequate length of reinforcement embedment, the *block face area* as exposed on the excavation surface, and the *block mass*. These last two variables were used to calculate the mass of structural instability per unit surface area of the excavation where the failure could occur (i.e. T/m²). The sequence of steps in this analysis were as follows:

Chapter 4: Design

1. Collection of structural data,
2. Definition of a structural model for the Dacite geology,
3. Deterministic analysis of worst-case block geometries,
4. Probabilistic analysis of block apex height, face area and mass,
5. Areal calculation of the mass of structurally controlled instability,
6. Probabilistic analysis of kinematic modes of failure,
7. Spectral analysis of block formation for the development.

Steps 3-7 were initially performed for an analysis of the excavation roof. These steps were then repeated considering the excavation walls, such that the mass of instability for both roof and wall failure was quantified. It must also be noted that the expression of the mass of instability per unit area was necessary in order to apply this value in the kinetic energy equations for calculating the demand on ground support, as described later.

4.4.2.2.1 Collection of Structural Data

In-cycle geological window mapping was performed during the development of both research excavations. Mapping was performed manually after the excavation had been fully supported. Face mesh was installed to floor level (Figure 104), in order to reduce the possibility of rock ejection hazards while mapping. The presence of face mesh was not ideal from a practical perspective. However, other than the increase in time needed for data collection, it did not hinder the data collection process. The structural data was collected primarily from the face. It was also possible to collect some structural data from the sidewalls, although opportunities were limited due to the shotcrete support.

In the best case scenario, structural mapping should be collected for the face, sidewalls and roof of the excavation using digital photogrammetry prior to installation of the first shotcrete layer. Photogrammetry is commonly used for collection of structural data in mine sites (Rees, 2012). It has the advantage of removing the operator from the face, while also collecting data from three orthogonal rock surfaces, reducing mapping bias. A review of the AdamTech photogrammetry technique was conducted during the development construction. It was determined that sufficient information could not be drawn from photogrammetry for a complete analysis in SAFEX. As such, manual window mapping of basic parameters was performed. Implementing SAFEX-compatible photogrammetry data collection is one area for future research.



Figure 104 - Typical face conditions for structural mapping.

4.4.2.2.2 Definition of a Structural Model

A basic structural model requires that joint orientation, trace lengths, spacings, surface cohesion and friction angle be specified. The raw joint orientation data were uploaded to the SAFEX software and plotted on an equal angle lower hemisphere stereonet with the fisher pole concentration contours (Figure 105a). The fisher contours were used to assist in the selection of the joints sets, which were manually defined in SAFEX using the selection windows to enclose all the relevant poles (Figure 105b).

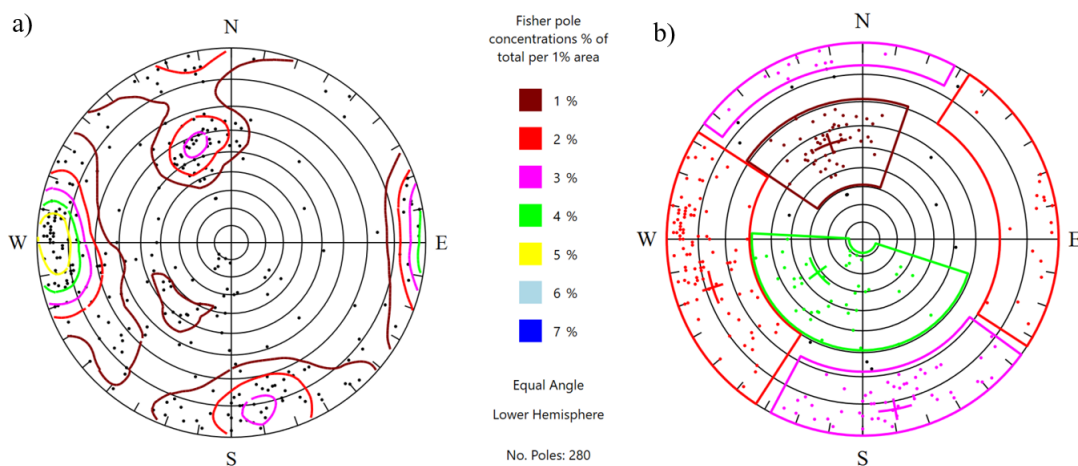


Figure 105 – a) raw joint set data with fisher contours and b) associated joint set selection windows.

Chapter 4: Design

Based on this stereographic analysis, a total of four joint sets were identified in the data. The basic properties of these joint sets are defined below in Table 11. The great circle of the weighted set orientation and pole groupings for each joint set are presented as a series of equal angle lower hemisphere stereonet in Figure 106. The unweighted joint set data were used for the block analysis, and weighted data for plotting.

Table 11 - Basic joint set parameters.

Joint Set		Unweighted (Weighted)		
Number	Total Joints	Plane Orientation	Normal Orientation	Fisher Constant
1	50	55/161 (54/161)	35/341 (36/341)	33.3 (32.4)
2	110	82/083 (78/072)	08/263 (12/252)	14.4 (22.1)
3	63	83/348 (83/349)	07/168 (07/169)	17.5 (16.3)
4	42	33/029 (33/053)	57/209 (58/233)	9.9 (17.7)

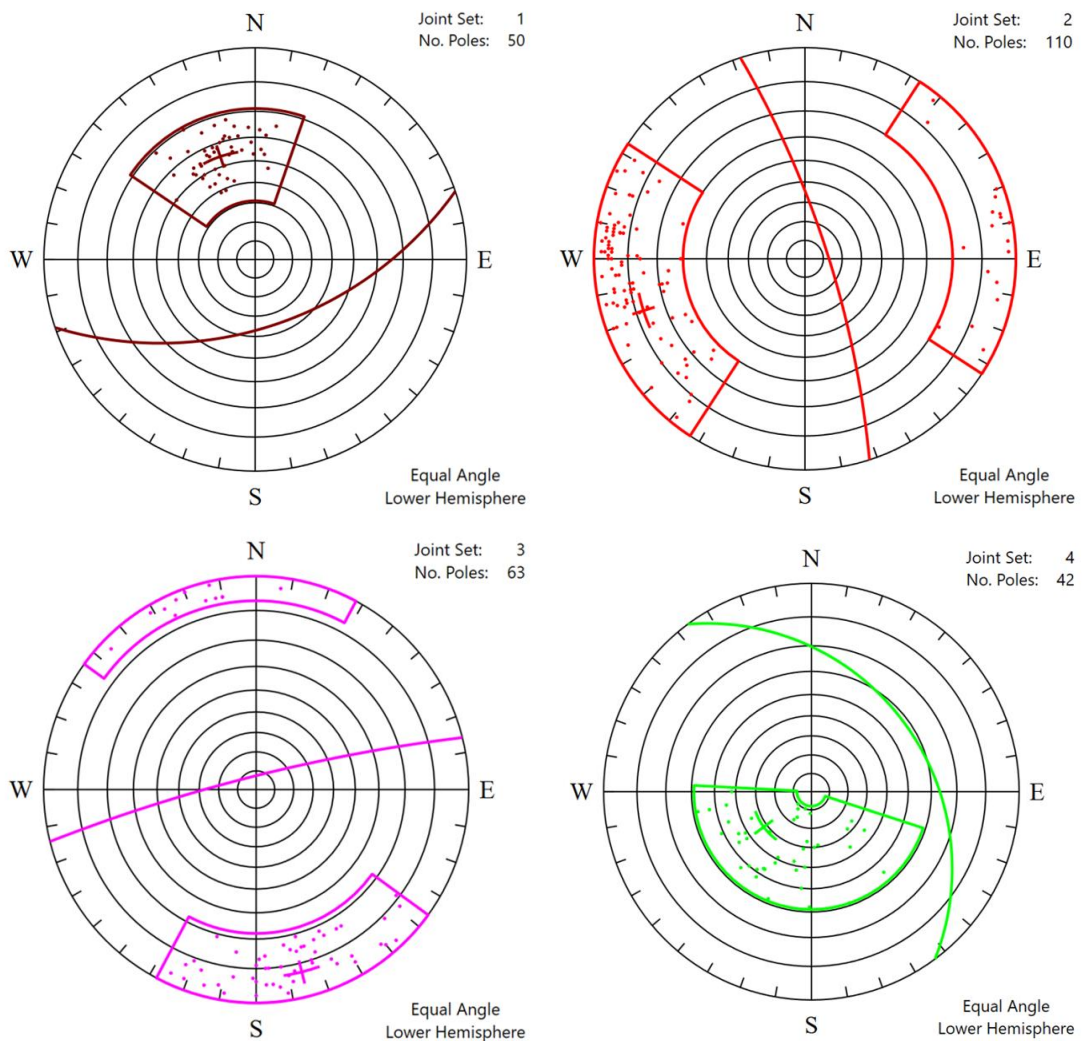


Figure 106 - Joint set great circles (weighted) and pole groupings.

Chapter 4: Design

Joint Set #1 was identified with an ENE-WSW strike and moderate dip of 55° to the southeast. Joint Set #2 was recorded striking N-S with an almost vertical dip to both the east and west. This joint set was regarded as the ‘face forming set’, as these joints frequently formed significant planar surfaces in the face, orthogonal to both the development azimuth and plunge. Joint Set #3 had an ENE-WSW strike nearly identical to that of Set #1. However, this set had a much steeper dip and most observations were dipping primarily towards the north. This set exhibited dispersion of the dip around the vertical. Therefore, some joints in Set #3 also dipped steeply towards the south. These south-dipping joint observations in Set #3 were readily distinguishable from those in Set #1. Joint set #4 was relatively shallow, dipping at an average 36° towards the northeast. Figure 107 presents a photograph of the face of the northern research tunnel highlighting a joint from each of the four sets.

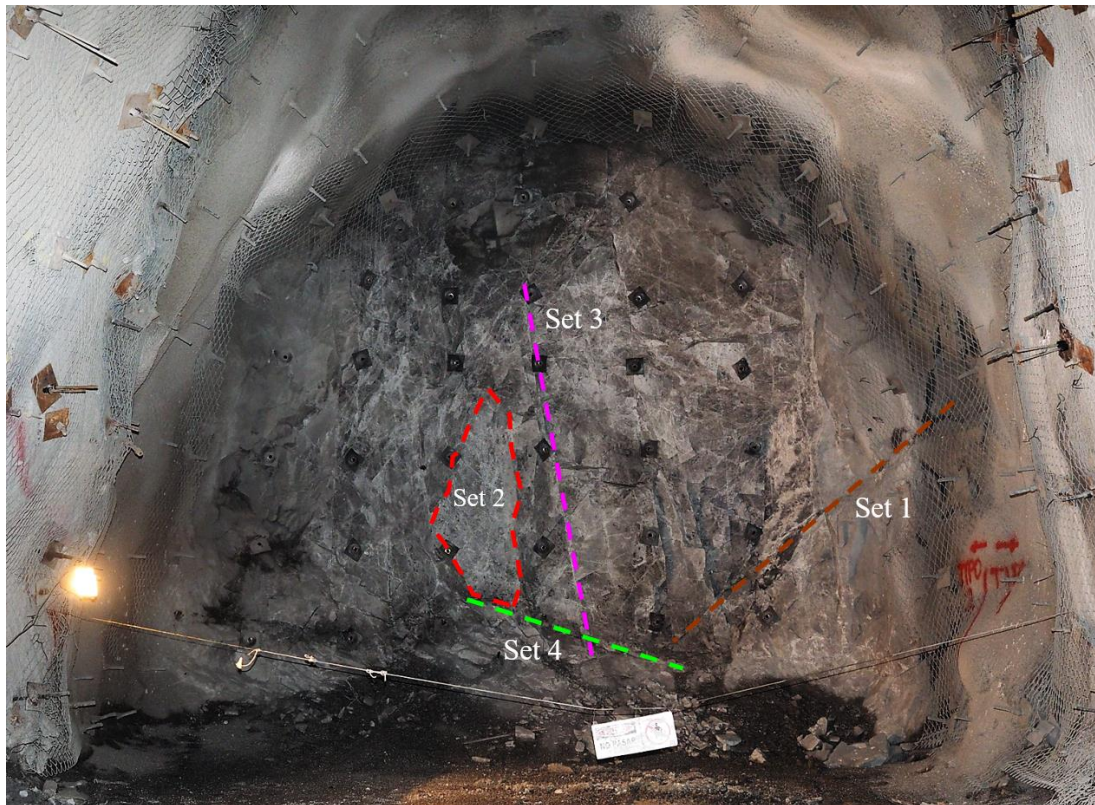


Figure 107 - Typical joint conditions in the face of the northern tunnel.

In order to define the basic structural model, SAFEX probabilistic analysis required the trace length and spacing characteristics of the joint sets to be quantified. These parameters were measured, as shown in Table 12. Frequently, the joint observations were obscured at one or both ends. Therefore, the maximum trace length statistics for the sets were conservatively assumed.

Table 12 - Trace length and spacing data for all joint sets.

Joint Set	Minimum Trace Length (m)	Average Trace Length (m)	Maximum Trace Length (m)	Minimum Spacing (m)	Average Spacing (m)	Maximum Spacing (m)
1	0.8	3.0	10.0	0.20	0.70	2.50
2	1.0	5.0	10.0	0.10	0.20	1.00
3	1.5	3.0	5.0	0.20	0.40	1.00
4	0.5	2.0	4.0	0.25	0.60	1.00

Cohesion was assumed for all joints, considering a characteristic value for tight and rough joint conditions. Friction angle was conservatively defined as being 5% lower than the minimum residual friction angle measured at WASM during the aforementioned laboratory strength testing of Dacite rock (see Section 4.3.3.3).

Table 13 - Cohesion and friction angle data for all joint sets.

Joint Set	Cohesion (kPa)	Cohesion Std. Deviation (kPa)	Friction Angle (deg)	Friction Angle Std. Deviation (deg)
1	200	20	40	4
2	200	20	40	4
3	200	20	40	4
4	200	20	40	4

This data constitutes the basic structural model of the Dacite development domain, in which the two research tunnels were constructed. With the structural model defined, a Deterministic block analysis was then performed.

4.4.2.2.3 Deterministic Block Analysis

The SAFEX deterministic analysis used the mean joint orientation values and a user-defined excavation shape to calculate the list of removable blocks and their worst-case (i.e. excavation span-limited) geometry. SAFEX analyses assumed the three-dimensional excavation had linear horizontal and vertical surfaces. The input parameters necessary to specify the excavation geometry include the tunnel's azimuth, plunge, length, width and height. Due to the difference between the SAFEX excavation geometry and that of the real tunnels, the block calculations were conservative for the roof, but slightly underestimated for the blocks in the walls, due to profile curvature.

Chapter 4: Design

The same excavation geometry was specified in SAFEX for both the deterministic and probabilistic analyses. The geometry is recorded in Table 14.

Table 14 - Excavation geometry for SAFEX deterministic and probabilistic block analyses.

Azimuth	Plunge	Length	Width	Height
245 ⁰	0 ⁰	50 m	7.0 m	6.5 m

The SAFEX deterministic block analysis was run automatically to define four basic block geometries from the structural model. These block geometries and natural stability results are summarised as follows in Table 15. Images of all four blocks are presented in Figure 108. Based on the deterministic analysis, the block initially of most concern from a stability perspective was Block 1. This block had a theoretical stability index of less than 1, which was indicative of failure. The three other blocks had stability factors of between approximately 4 and 19, which indicated that these were stable. However, these deterministic results did not consider natural dispersion of the joint set orientation, which could create new and unstable block geometries.

Table 15 - Summary of SAFEX deterministic analysis statistics for roof blocks.

PARAMETER	BLOCK			
	1	2	3	4
Forming Sets	1, 2, 3	2, 3, 4	1, 3, 4	2, 3, 4
Failure Mode	Sliding	Sliding	Sliding	Sliding
Sliding Plane	2	2	3, 4	2, 3
MAXIMUM TRACE LENGTH LIMITED BLOCK				
Height	0.44 m	0.69 m	0.40 m	0.92 m
Face Perimeter	6.22 m	5.17 m	4.11 m	4.96 m
Free Face Area	0.52 m ²	1.22 m ²	0.22 m ²	1.09 m ²
Volume	0.08 m ³	0.28 m ³	0.03 m ³	0.34 m ³
Mass	0.21 T	0.76 T	0.08 T	0.91 T
Stability	8.11	15.91	262.10	31.82
EXCAVATION SPAN LIMITED BLOCK				
Height	4.72 m	2.75 m	6.22 m	3.70 m
Face Perimeter	66.69 m	20.69 m	63.98 m	19.85 m
Face Area	60.09 m ²	19.62 m ²	53.53 m ²	17.47 m ²
Volume	94.53 m ³	17.98m ³	110.96 m ³	21.53 m ³
Mass	255.24 T	48.56 T	299.59 T	58.13 T
Driving Force	2479.52 kN	471.72 kN	1460.74 kN	559.64 kN
Resisting Force	2140.08 kN	1917.24 kN	27710.17 kN	4550.53 kN
Out of Balance	339.44 kN	-	-	-
Stability	0.86	4.06	18.97	8.13
Unstable Mass	4.25 T/m ²	2.48 T/m ²	5.60 T/m ²	3.33 T/m ²

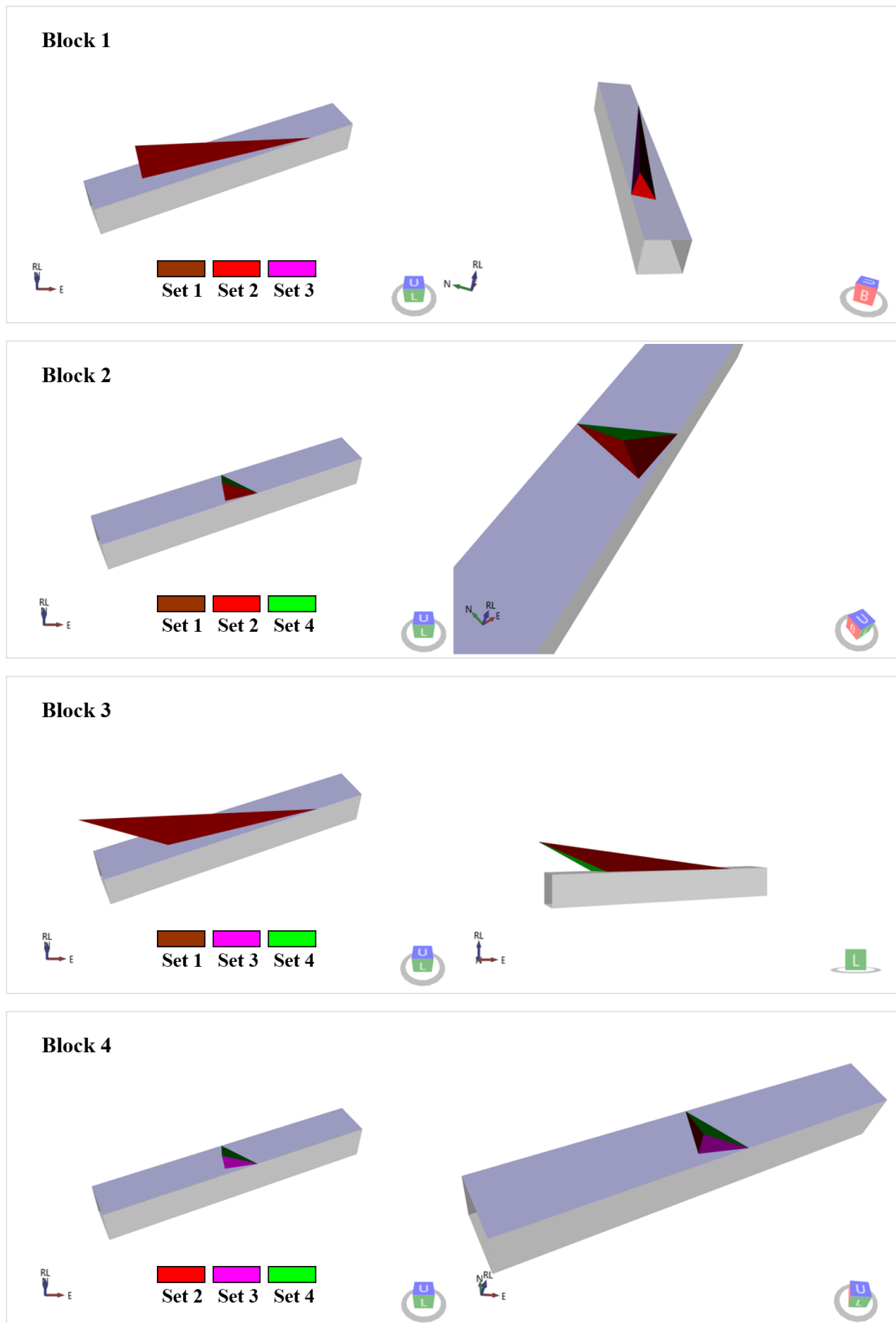


Figure 108 – Deterministically calculated block geometries for the excavation roof.

These deterministic results provided an initial appreciation of the formed geometries and likely candidate block(s) for further stability assessment. It was noted that the deterministic analysis did not identify any free-falling block geometries.

Chapter 4: Design

The basic Block 1 shape was formed by Joint Set #1, #2 & #3. This block was deemed to be unstable and had potential to form a long and slender block sub-parallel to the longitudinal axis of the tunnel, with maximum apex height of 4.72 metres. The maximum potential block length in this direction was approximately 30 metres. Although not deterministically identified as free-falling, the very steep dip of 82° of the sliding plane (Set #2) suggested that with known natural dispersion, this block could become free-falling. Furthermore, SAFEX analysis indicated that the apex height of this block gradually increased as the free face was progressively exposed towards the southwest. Therefore, the load on the ground support scheme was expected to increase towards the southwest. This geometry indicated that deep reinforcement (i.e. cable bolts) was required to be installed prior to a significant length of this block becoming exposed at a free face. A first pass of moderate depth reinforcement was not considered to be adequate to stabilise this block, if exposed in its entirety.

Block 2 was formed by Set #1, #2 & #4. This block formed a wedge which was longer in the excavation transverse axis than the longitudinal axis. It was also assessed to be sliding on Set #2. Again, considering joint orientation dispersion and its relatively low stability value of < 5 , this block may have become unstable and free falling. Although the worst-case apex height of this block was assessed to be 2.75m, this outcome was unlikely. Therefore, a 3.5-metre-long reinforcement element and surface support system would likely be sufficient to prevent instability of this block. This assumption and the realistic apex height were assessed in further detail probabilistically.

Block 3 was formed by Set #1, #3 & #4. This block had a span-limited apex height of 6.22 metres. The distance between this block's extremities was approximately 40 metres, when measured sub parallel to the tunnel's longitudinal axis. This block was thin and narrow, with a kinematic mode of failure determined to be sliding on Set #3 & #4 joints. Despite its size, this block had the highest stability value of all possible block shapes in the deterministic analysis, due to the significant frictional stabilising forces acting on the block-forming joint surfaces.

Block 4 was very similar in shape to Block 2. The main difference was the involvement of Joint Set #3 rather than Set #1. This block had the lowest mass of all deterministic blocks and the second highest stability. Statically, this block was regarded as highly stable. However, this was subject to change following probabilistic analysis.

Chapter 4: Design

The deterministic analysis was repeated for the excavation northern sidewall in order to assess the potential mass of instability for this vertical surface. This analysis also identified four basic block geometries. The maximum trace length limited geometry of these blocks is summarised in Table 16. The block of most concern from a stability standpoint was Block 2, given it had the largest apex height and total mass. This block was formed by Sets #1, #2 and #4 (Figure 109). Block 2 was examined in more detail deterministically, specifically the excavation span limited and spacing limited blocks. The full summary of statistics for this block are presented in Table 17. The mass of instability was greatest for the excavation span limited block, reaching 2.12 T/m². This worst-case scenario was also re-examined probabilistically, in order to decide whether it was valid as a realistic design input.

Table 16 – Summary of SAFEX deterministic analysis statistics for sidewall blocks.

PARAMETER	BLOCK			
	1	2	3	4
	MAXIMUM TRACE LENGTH LIMITED BLOCK			
Apex Height	0.21 m	0.63 m	0.27 m	0.11 m
Face Area	1.46 m ²	0.99 m ²	0.29 m ²	0.44 m ²
Volume	0.10 m ³	0.21 m ³	0.03 m ³	0.02 m ³
Mass	0.28 T	0.56 T	0.07 T	0.05 T
Unstable Mass	0.19 T/m ²	0.56 T/m ²	0.07 T/m ²	0.05 T/m ²

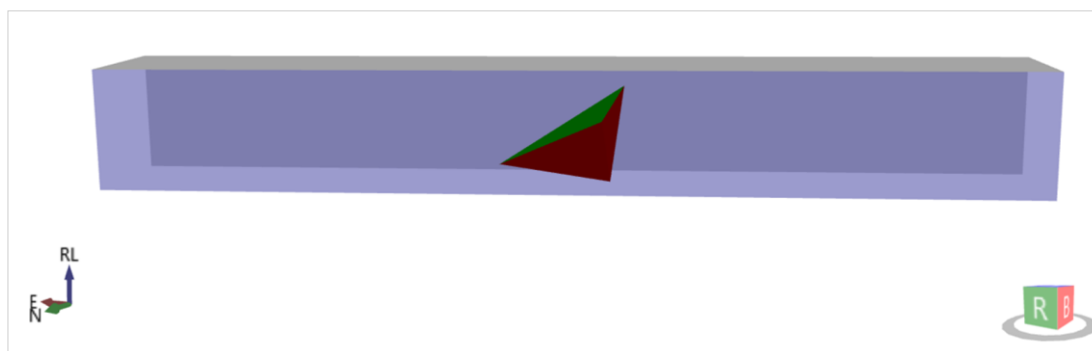


Figure 109 - Deterministically calculated maximum block geometry for the excavation sidewall.

Table 17 – Deterministic maximum span, trace and spacing-limited parameters of sidewall Block 2.

PARAMETER	BLOCK 2		
	Span Limited	Trace Limited	Spacing Limited
Apex Height	2.43 m	0.63 m	0.09 m
Face Area	14.68 m ²	0.99 m ²	0.02 m ²
Volume	11.90 m ³	0.21 m ³	0.001 m ³
Mass	31.18 T	0.55 T	0.003 T
Unstable Mass	2.12 T/m ²	0.55 T/m ²	0.003 T/m ²

4.4.2.2.4 Probabilistic Analysis of Block Geometry

Each of the four basic block geometries from the aforementioned deterministic analysis were re-assessed probabilistically. The SAFEX probabilistic analysis simulated natural dispersion in the structural characteristics of the block-forming joints and calculated the possible range of size of each of the four basic blocks, the stability of these blocks and the probability of occurrence. The potential range of Dip and Dip Direction were simulated by a normal distribution about the mean and considering the trace and spacing characteristics defined in the structural model. Charts of the range of the joint orientation inputs for the probabilistic analysis of each basic block shape are shown in Figure 110. The poles of each possible block-defining plane are presented in Figure 111.

In this case, the probabilistic block analysis performed 5000 simulations, each representing a possible block geometry, given assumed dispersion about the measured structural model values. The first results included a scatter plot of the trace length limited apex height for each simulation (Figure 112). From these results, the maximum apex height of each basic block shape was quantified, as indicated by the red arrows in Figure 112 and summary data in Table 18. It should be noted that a percentage of the blocks may have had geometry larger than the excavation span. Such blocks are not regarded as valid removable blocks which might detach from the excavation surface and load the ground support scheme. Only removable blocks which form at the excavation surface were considered to be valid for design.

Table 18 - Maximum possible apex height of each basic block shape when assessed probabilistically.

	Block 1	Block 2	Block 3	Block 4
Maximum Apex Height	3.70 m	1.25 m	0.92	1.65

In order to assess the removable block geometry and mass characteristics for ground support design, the frequency histogram and cumulative frequency line plot of apex height, free face area and mass were also examined in SAFEX. These charts are filtered probabilistic results specifically identifying the removable blocks and they are shown in Figure 113 through to Figure 116. These block parameters were fundamental in defining the mass that could be expected to become unstable on the excavation boundary.

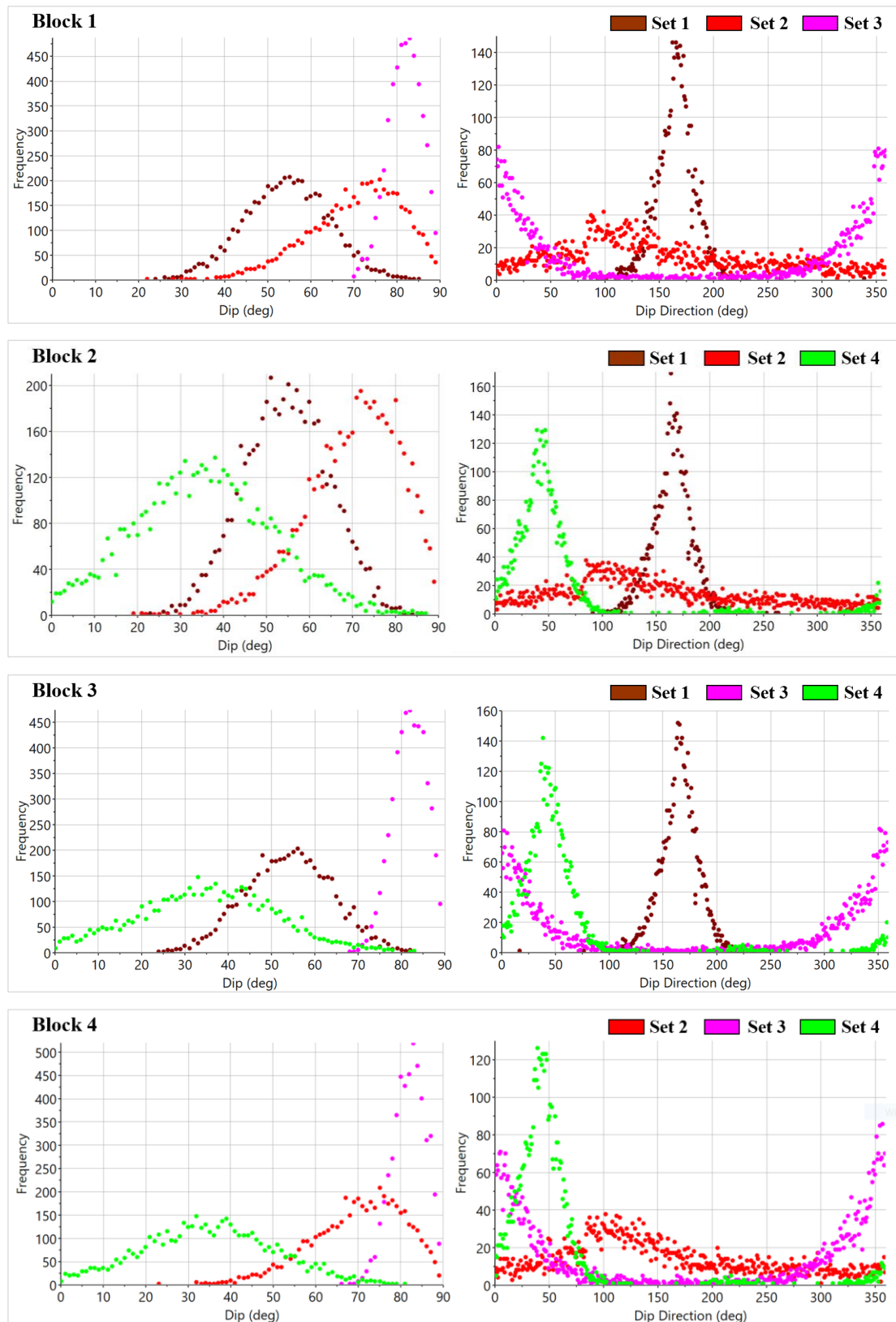


Figure 110 - Range of joint set orientations for all probabilistically simulated blocks.

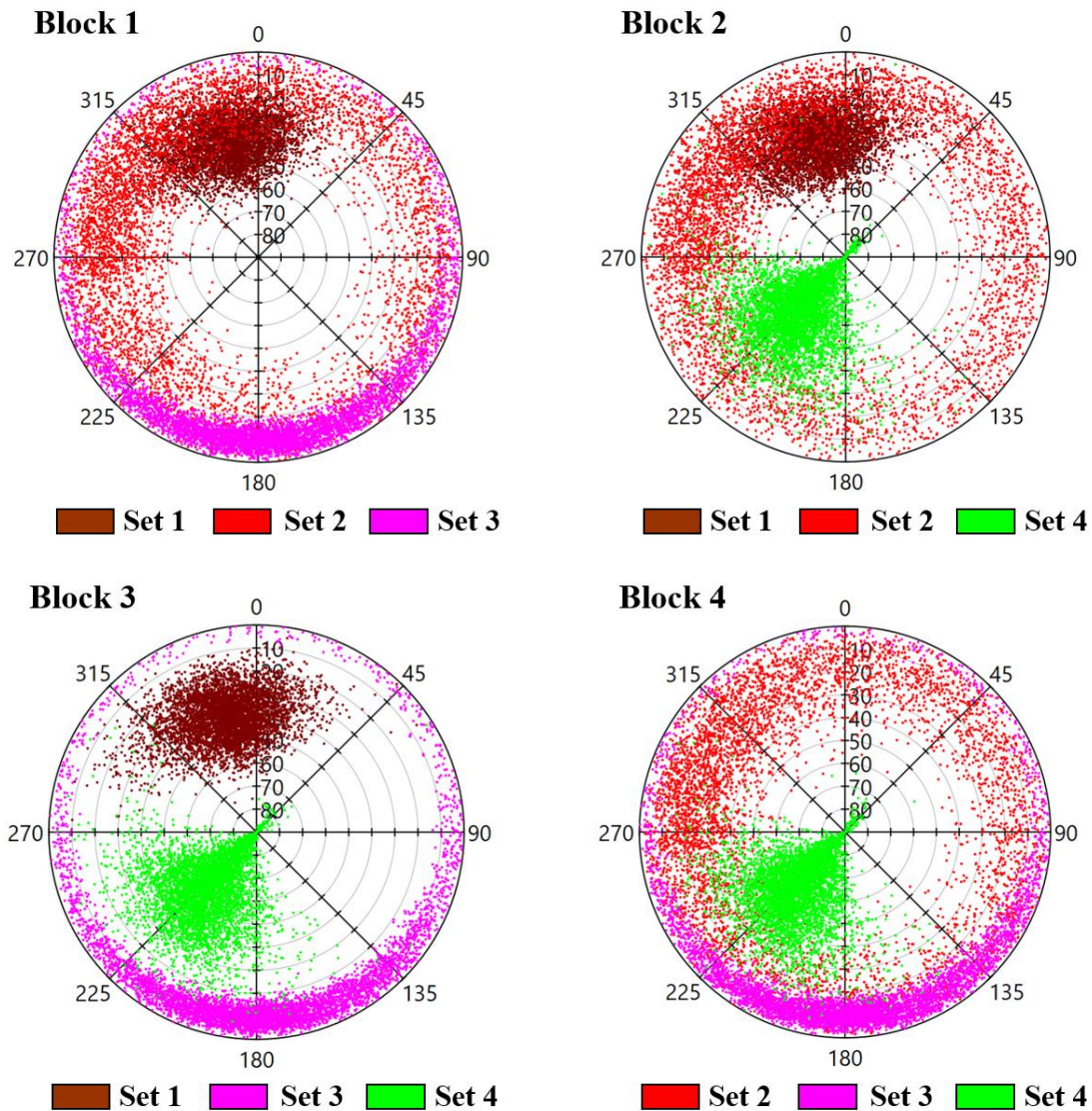


Figure 111 - Equal angle lower hemisphere stereonets of joint poles for all probabilistic block analyses.

The maximum values of block apex height, free face area and mass within the 80th, 90th and 100th percentile groups were investigated for each of the four basic block shapes. These values are presented in Table 19. The 100th percentile values represent the worst case scenario block characteristics that were assessed probabilistically. These values are the outlying extrema and thus have a relatively low probability of occurrence. For example, a Block 1 apex height of 3.70m had a probability of 1 in 5000. Meanwhile, an apex height of greater than 1.5m had a probability of 1 in 1000 (Figure 112). To design the ground support scheme for the 100th percentile of possible blocks may be uneconomic and in some cases practically infeasible. Therefore, engineering judgement was applied to the SAFEX results in order to assess their feasibility and impact on the ground support scheme design. This was done considering underground observations of the block forming conditions.

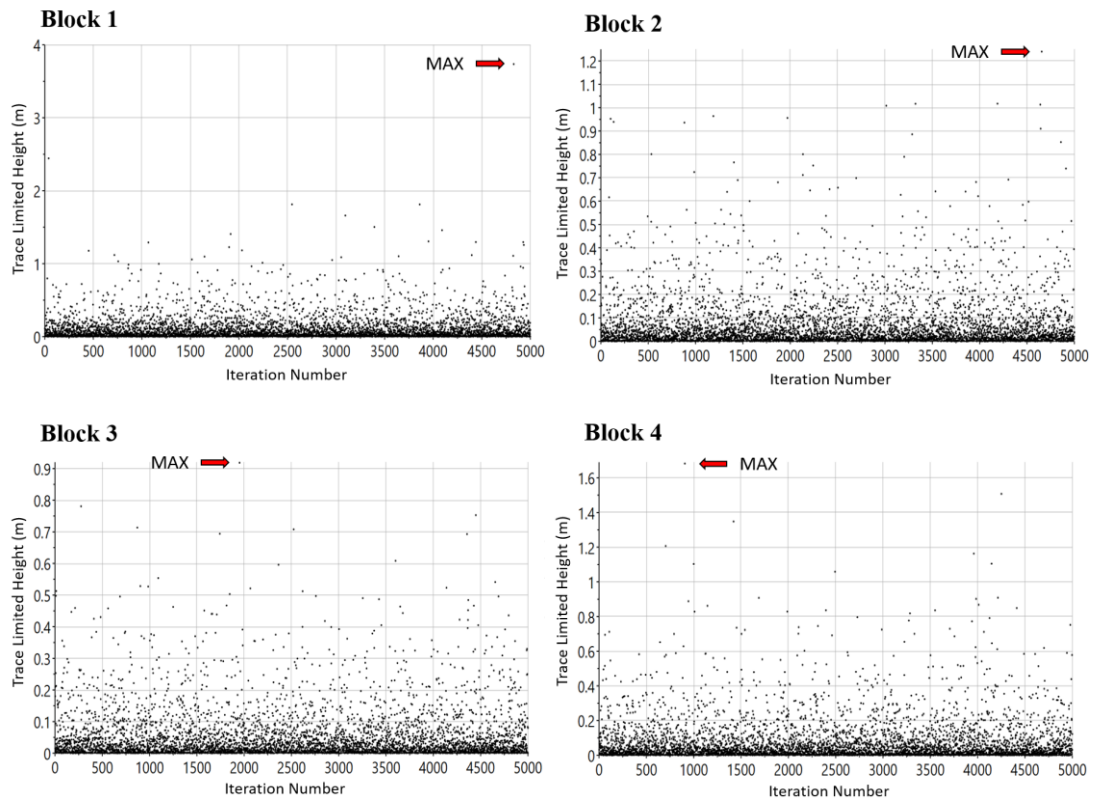


Figure 112 – Probabilistic results of trace length limited apex height for each block shape.

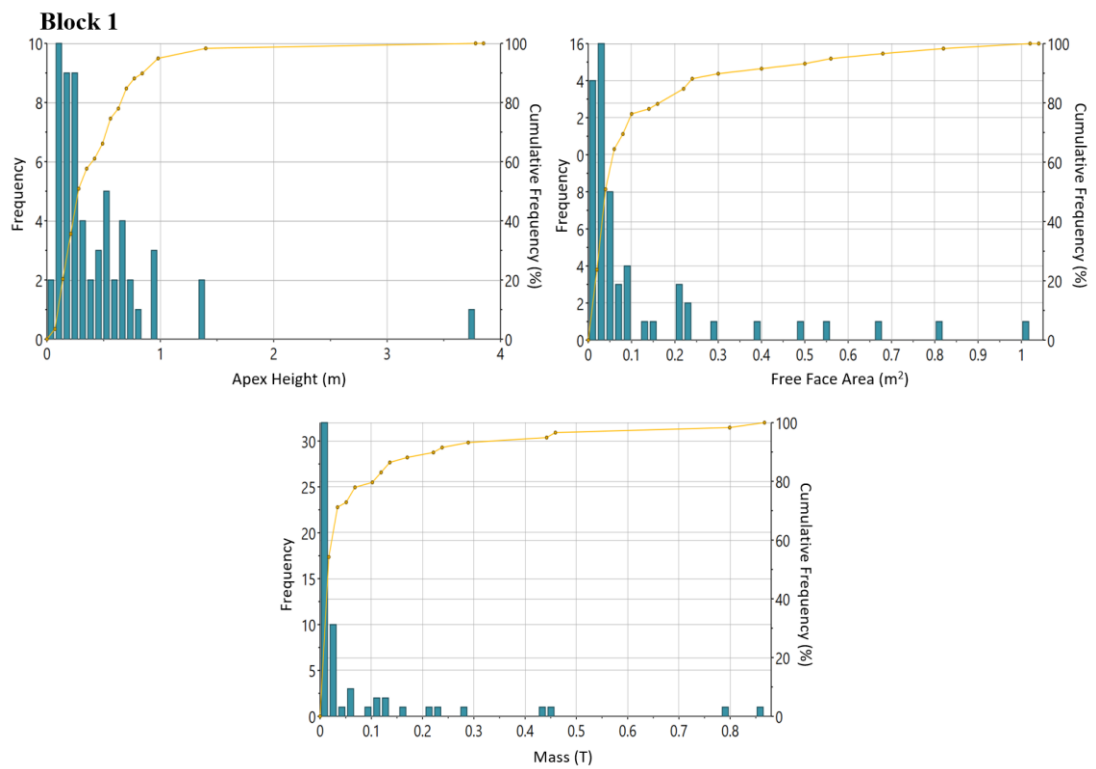


Figure 113 - Probabilistic results for the apex height, free face area and mass of Block 1.

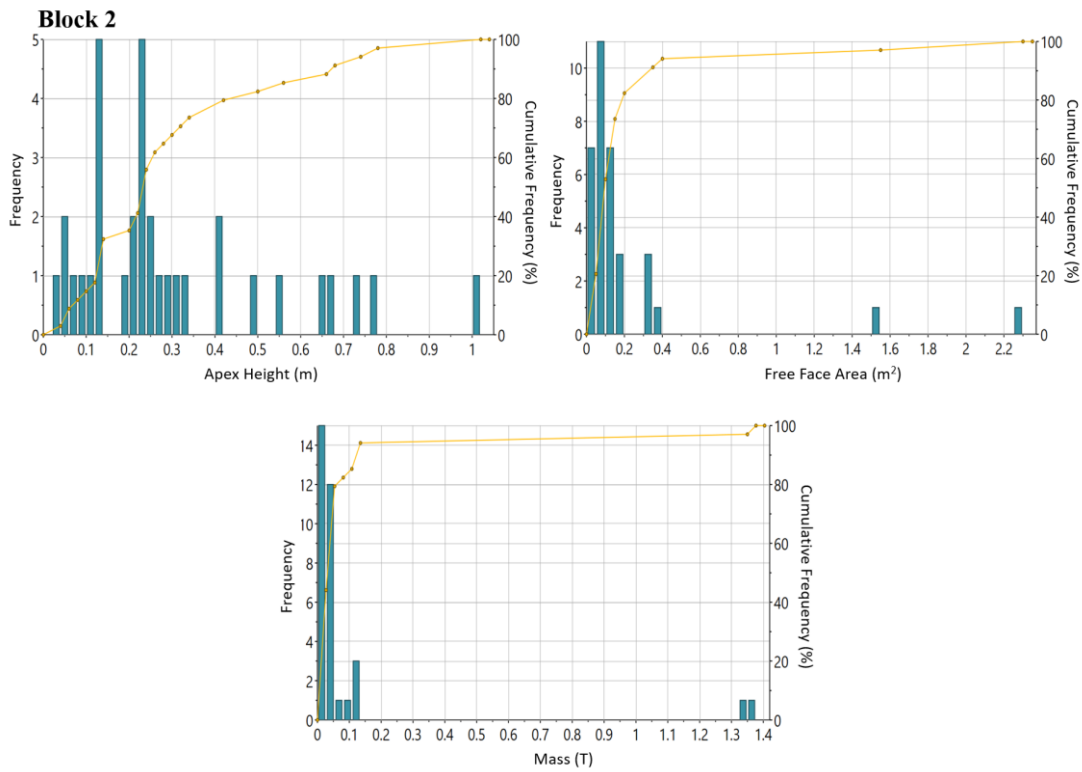


Figure 114 - Probabilistic results for the apex height, free face area and mass of Block 2.

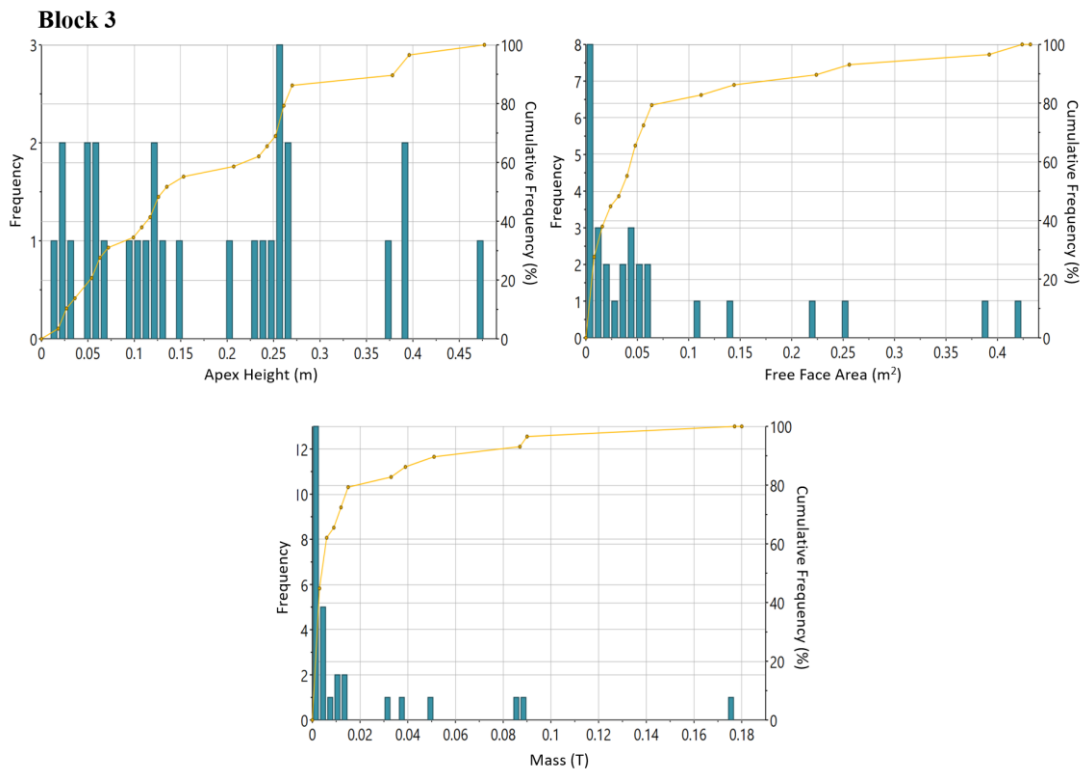


Figure 115- Probabilistic results for the apex height, free face area and mass of Block 3.

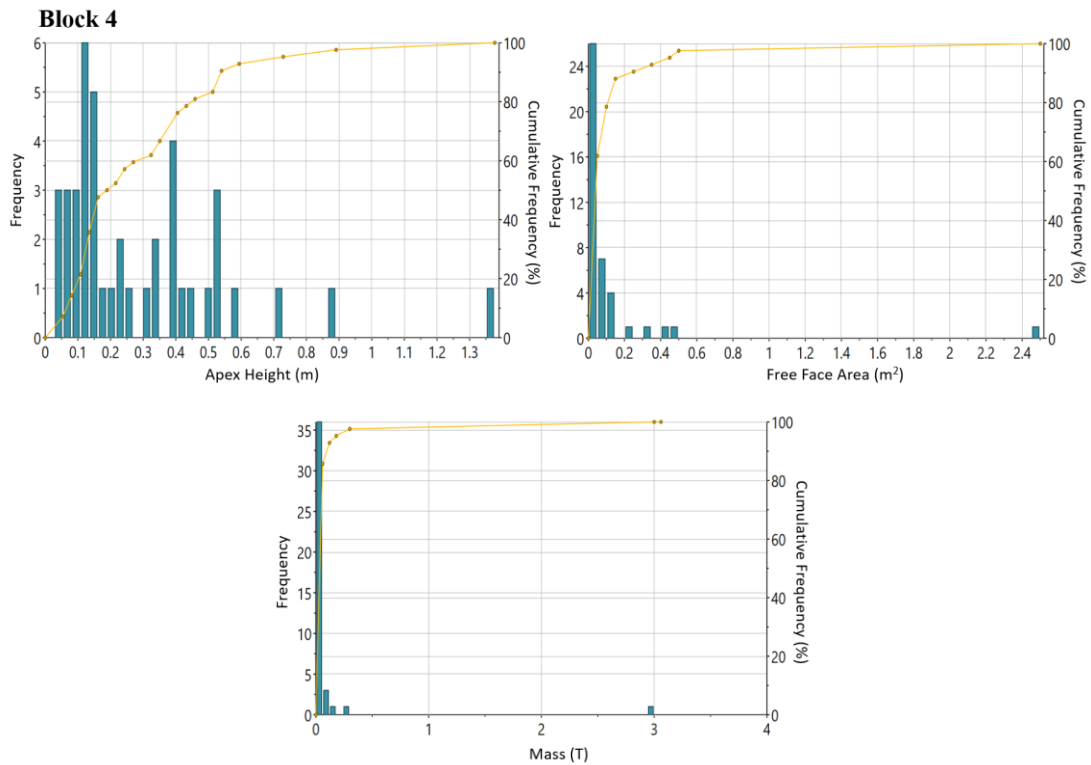


Figure 116 - Probabilistic results for the apex height, free face area and mass of Block 4.

The removable block with the greatest apex height was identified as Block 1 at 3.70m. This was a narrow block with a relatively low free face area when compared to the others. As such, it was not expected to generate the maximum demand. The block of largest mass was Block 4 at 3.0 tonnes. This block also exhibited the equal largest free face area. All potential blocks in this group, formed by Sets #2, #3 and #4, were calculated to have an apex height of 1.38m or less. Based on the probabilistic analysis, Block 4 was regarded as the *priority block* likely to generate the largest instability.

Table 19 - Maximum trace limited apex height, free face area and mass for the 80, 90 and 100th percentiles.

Percentile Group	Block 1	Block 2	Block 3	Block 4
	Max. Apex Height (m)			
80%	0.65	0.43	0.26	0.45
90%	0.85	0.67	0.38	0.54
100%	<u>3.70</u>	<u>1.01</u>	<u>0.50</u>	<u>1.38</u>
Max. Free Face Area (m²)				
80%	0.15	0.19	0.08	0.11
90%	0.30	0.33	0.23	0.23
100%	<u>1.00</u>	<u>2.30</u>	<u>0.45</u>	<u>2.30</u>
Max. Mass (T)				
80%	0.10	0.05	0.02	0.07
90%	0.22	0.12	0.06	0.10
100%	<u>0.86</u>	<u>1.38</u>	<u>0.18</u>	<u>3.00</u>

* *Italicised and underlined text represents the 100th percentile values chosen for design inputs.*

The cumulative frequency chart of trace length limited apex height is presented in Figure 117. These probabilistic results indicate that in the vast majority of possible formations of block shapes 2, 3 and 4, the apex height was 1.0m or less. In the case of Block 1, the trace length limited apex height of the possible formations was 1.5m or less. These values formed the justification for the later selection of the reinforcement length of embedment, such that capacity was extended beyond the zone of structurally controlled instability.

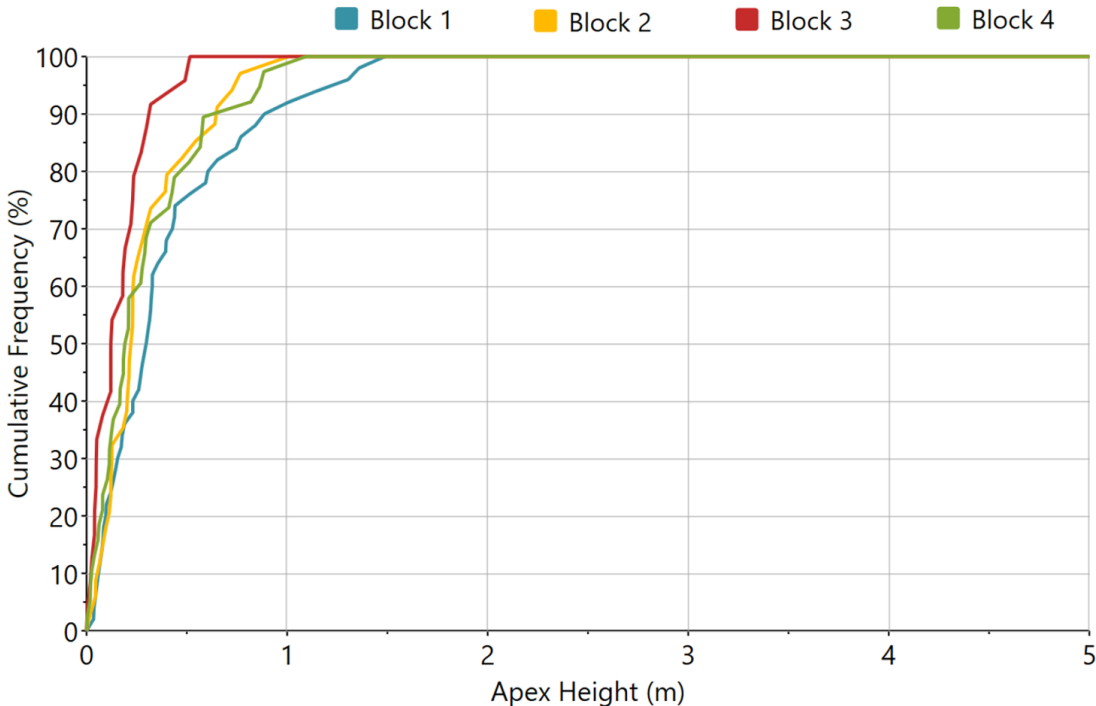


Figure 117 - Cumulative frequency of probabilistically defined apex heights for all block geometries.

The potential mass of instability in the wall of the excavation was also examined probabilistically. As Block 2 was identified by the deterministic analysis as having potential to form the largest geometry, the probabilistic analysis of wall instability focused on this block, which was formed by sets #1, #2 and #4. The frequency histogram and cumulative frequency line plot of the trace length limited apex height, free face area and mass of this block are presented in Figure 118. This analysis concluded that 100% of the potential trace length limited blocks had an apex height less than 0.75m, free face area less than 1.5m² and mass less than 0.9 tonnes. A summary of the maximum values within the 80th, 90th and 100th percentile groups are shown in Table 20. The 100th percentile values were chosen for design purposes in the wall stability assessment.

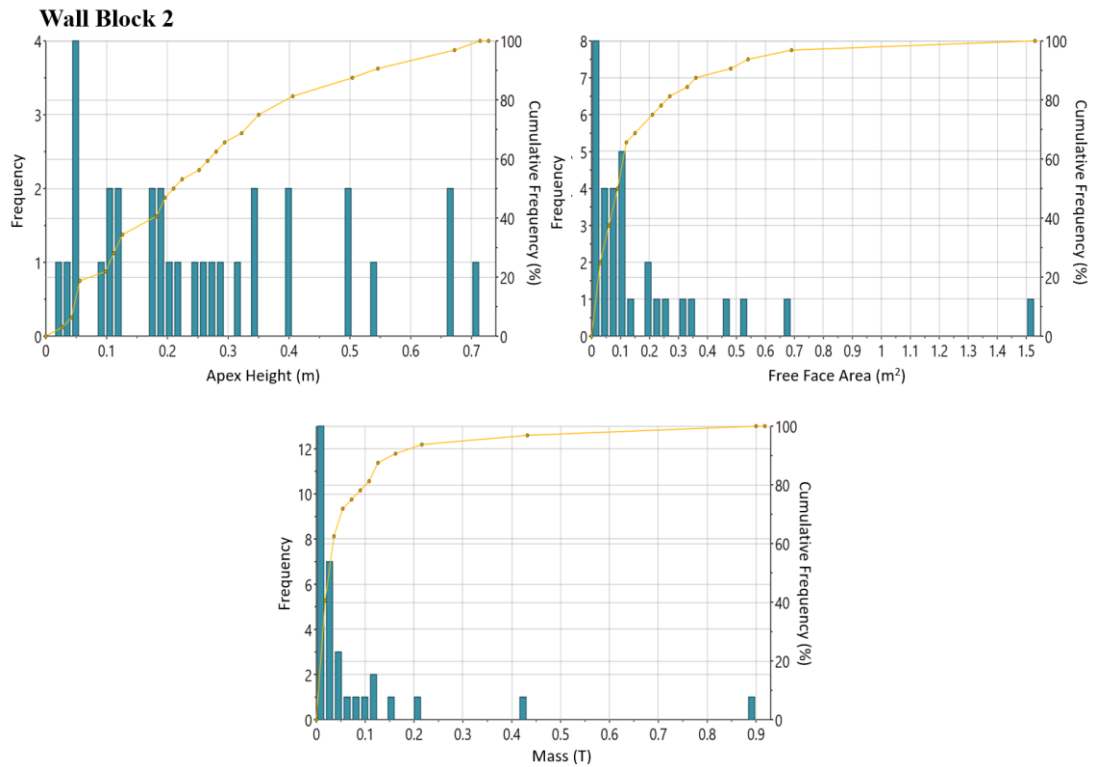


Figure 118 - Probabilistic results for the apex height, free face area and mass of wall Block 2

Table 20 – Max. trace limited apex height, free face area and mass for the 80, 90 and 100th percentiles.

Wall Block 2	Apex Height	Free Face Area	Mass
80%	0.4 m	0.25 m ²	0.1 T
90%	0.55 m	0.45 m ²	0.15 T
100%	0.7 m	1.50 m ²	0.90 T

4.4.2.2.5 Mass of Structurally Controlled Instability for Design

The mass of instability was quantified for each of the four roof blocks and the largest of the sidewall blocks. This important design input variable was expressed in T/m² and was calculated by dividing the probabilistic SAFEX result for block mass by the free face area. The maximum values of the mass of instability for the 80th, 90th and 100th percentile range were calculated for all blocks and the results are presented in Table 21. Engineering judgement was used to decide which of the values were realistic. This decision was made considering observed block forming conditions underground. It was concluded that the 100th percentile groups of removable blocks identified by SAFEX were plausible, given field observations. Therefore, these values were used as the inputs to the final calculations of the mass of structurally controlled instability for the ground support design.

Table 21 - Mass of instability for the variety of structural blocks.

Percentile Group	Roof				Wall
	Block #1	Block #2	Block #3	Block #4	Block #2
80%	0.67 T/m ²	0.26 T/m ²	0.25 T/m ²	0.64 T/m ²	0.40 T/m ²
90%	0.73 T/m ²	0.36 T/m ²	0.26 T/m ²	0.43 T/m ²	0.33 T/m ²
100%	0.86 T/m ²	0.60 T/m ²	0.40 T/m ²	1.30 T/m ²	0.60 T/m ²

4.4.2.2.6 Probabilistic Analysis of Block Kinematics

The aforementioned deterministic analysis in Section 4.4.2.2.3 considered block geometries whereby the forming joints were all of a set orientation. That preliminary analysis indicated that there were no free falling blocks among those four basic geometries that were identified. The probabilistic analysis is a more advanced simulation which considers the orientation dispersion of the block-forming joints. This analysis provides a more realistic determination of the likely range of kinematic modes of block failure. The analysis indicated that all the removable block geometries were unstable, with modes of failure including free-falling and sliding on one or two planes. Figure 119 presents the distribution of kinematic modes of failure for the range of removable blocks within each of the four basic shapes.

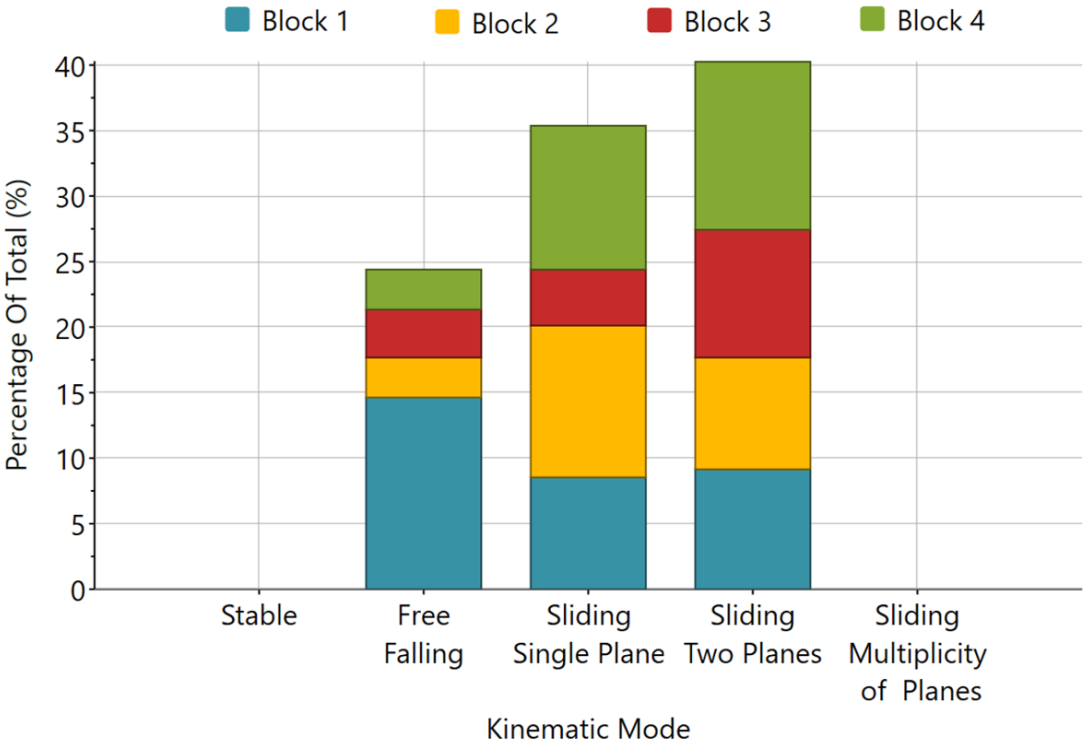


Figure 119 - Kinematic failure modes for all probabilistically identified block geometries.

4.4.2.2.7 Spectral Analysis

The spectral analysis identified the number of blocks able to be formed on a specific surface of the excavation (Figure 120). The larger the number of formed blocks, the potentially less stable that free surface may be. The analysis was performed on all critical surfaces of the excavation, including the development face (90/065), north wall (90/155), south wall (90/335) and roof (0/000). Consistent with the previous deterministic analyses, a minimum of four basic block geometries were able to be formed on each of the excavation surfaces that were examined. Note that the SAFEX convention for face orientation is dipping into the excavation.

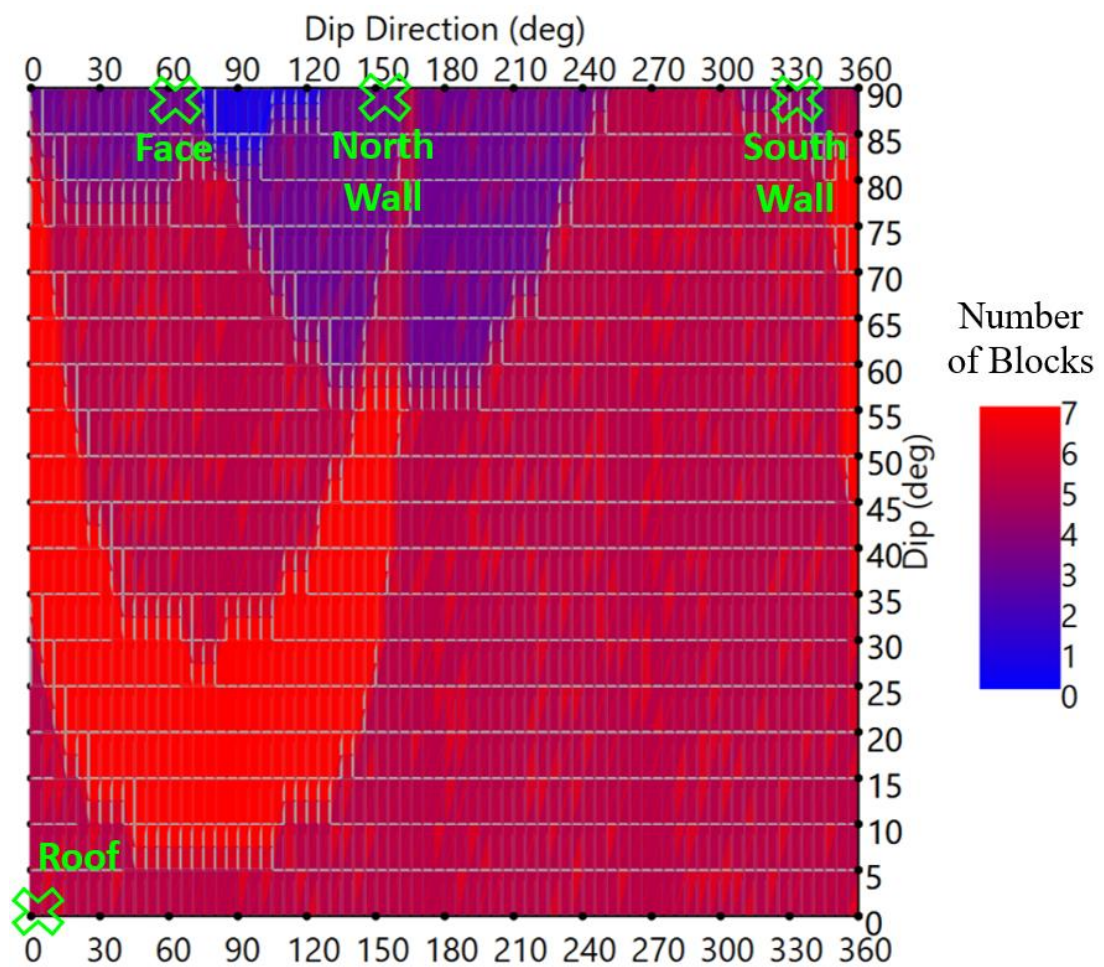


Figure 120 - Spectral analysis results for the Dacite structural model.

4.5 Excavation Design (Control Tunnel)

This section outlines the design specification of the southern research tunnel, which was designed and constructed as a control test following the standard mine site process.

4.5.1 Profile Geometry

The southern research tunnel was developed to a mine standard design shape, which included an arched roof with vertical walls. This tunnel served as a control test which was compared to a semi-elliptical design implemented in the north tunnel. In the past, the squared tunnels in the mine have suffered serious damage during violent stress-driven instability. The southern research excavation was constructed with profile dimensions of 6.2mW by 6.1mH (Figure 121). The diagram of this precise geometry is presented in Figure 122. Development excavations with similar shapes in deep mines frequently experience overstressing of the tunnel boundary, violent instability and overbreak of the profile. This typically occurs at the vertices, where stress concentrations are greatest. Furthermore, where excavation surfaces are linear or convex, the tunnel boundary and surface support system may enter tensile loading almost immediately.



Figure 121 – Conventional excavation shape of the southern research tunnel.

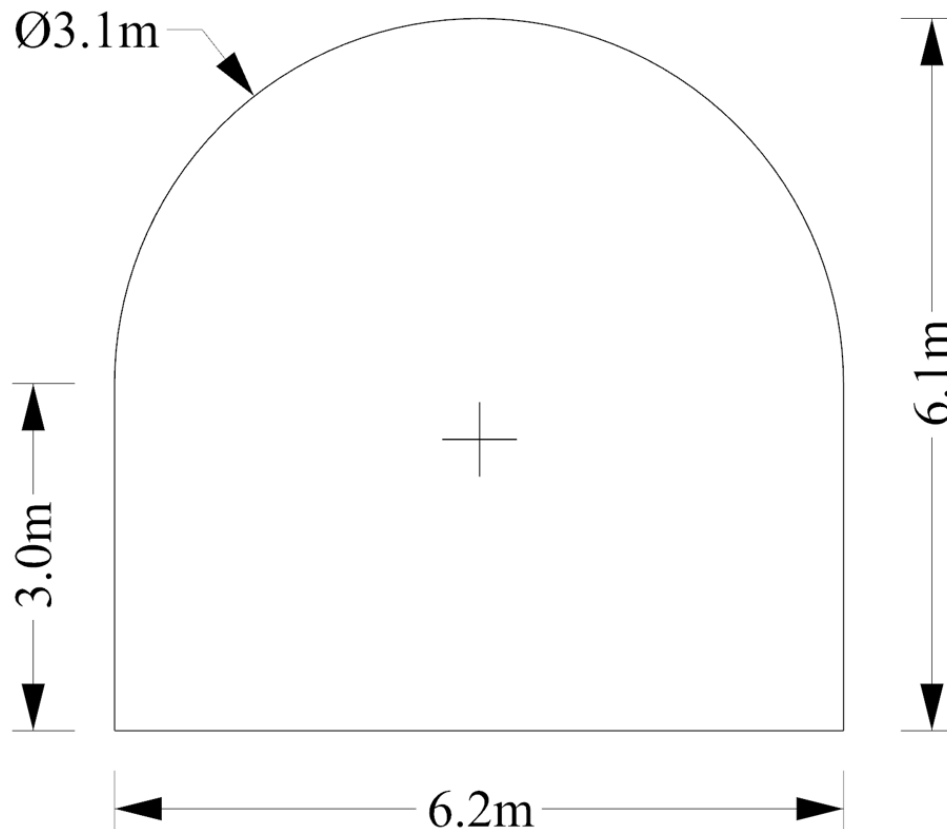


Figure 122 - Profile geometry of the southern research tunnel with conventional square-walled design.

4.5.2 Profile Drilling and Blasting

The two research excavations were developed according to separate drill and blast designs. The southern excavation, being the control, was constructed according to a conventional profile shape and blast design supplied by the mine operator. This design was implemented without alteration throughout the entire tunnel length and is presented in Figure 123. This design is typical of those routinely used in many deep mines in Australia, South America and elsewhere, in terms of both the excavation shape and the drill and blast methodology.

4.5.2.1 Drilling Specifications

The basic drilling parameters of the development blast design for the southern research tunnel, including the number of drill holes, diameter and their length, are presented in Table 22.

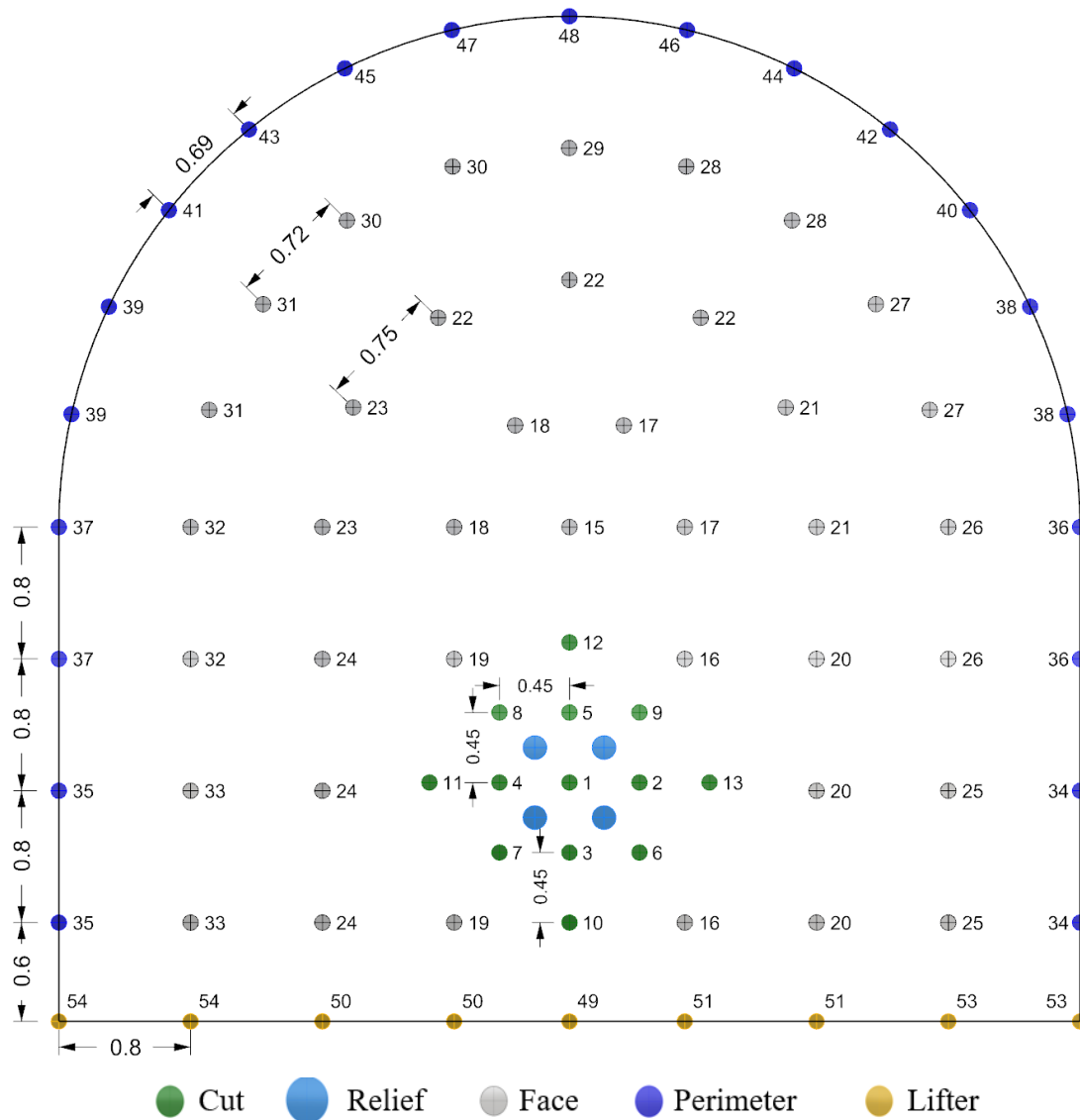


Figure 123 – Conventional development drill and blast pattern design implemented in the southern tunnel.

Table 22 – Basic drilling parameters for the southern tunnel.

		# Holes	Diameter (mm)	Length (m)
Burn Cut	●	13	45	3.8
Relief	●	4	127	3.8
Face Holes	●	39	45	3.8
Perimeter	●	21	45	3.8
Lifters	●	9	45	3.8
TOTAL:		86		

4.5.2.2 Explosive Specifications

Three types of explosive were used for development blasting in the southern tunnel. These included regular blown ANFO for the burn cut and face charges, Softron in the perimeter holes and Tronex for the lifters and as the primer for all other holes. Softron

Chapter 4: Design

is a low-density, low-VOD cartridge product. It is specifically designed for perimeter control blasting in hardrock. Tronex is a packaged dynamite from the same supplier. Tronex was used for the lifters, due to its water resistance, and also as the booster in all holes containing ANFO or Softron. The explosive properties of all three products are presented in Table 23.

Table 23 – Explosive properties of ANFO, Softron and Tronex products.

	ANFO	Softron	Tronex
Unit Size	-	11/16” x 20”	1 1/8” x 8”
Unit Weight (g)	-	141	153
Density (g/cc)	0.85	1.19	1.18
Velocity of Detonation (m/s)	3,600 - 4,100	3,324	5,200
Detonation Pressure (kbar)	28	33	77
Energy (kJ/kg)	3,818	4,480	4,908
Gas Volume (l/kg)	1,050	968	942
Relative Weight Strength	1.00	1.13	1.22
Relative Bulk Strength	0.96	1.72	1.85

4.5.2.3 Charging Specifications and Initiation

All loads in the southern tunnel were toe-primed without stemming, as per the mine’s standard practice. The details of the individual loads of explosive for each blasthole type are presented in Table 24. The total quantity of each explosive type used for the southern tunnel is shown in Table 25. The number of individual charges and distribution of explosive charge weight, per delay, are shown in Figure 124 and Figure 125, respectively. Summary statistics for the entire blast are tabulated in Table 26.

Table 24 - Explosive charge specifications for individual loads.





		Hole Length (m)	Charge Length (m)	Tronex 1 1/8” x 8”		ANFO (kg)	Softron 11/16” x 20”	
				Qty	kg		Qty	kg
Burn Cut		3.8	3.2	1	0.2	4.2	0	0
Face Holes		3.8	3.2	1	0.2	4.2	0	0
Perimeter		3.8	3.2	1	0.2	0	6	0.8
Lifters		3.8	3.2	16	2.4	0	0	0

Table 25 - Summary of total explosives used for the southern tunnel.

Explosive	Qty	Total (kg)	ANFO Eqv. (kg)
Tronex 1 1/8" x 8"	217	33.2	40.5
Softron 11/16" x 20"	126	17.8	20.1
ANFO	-	219.6	-

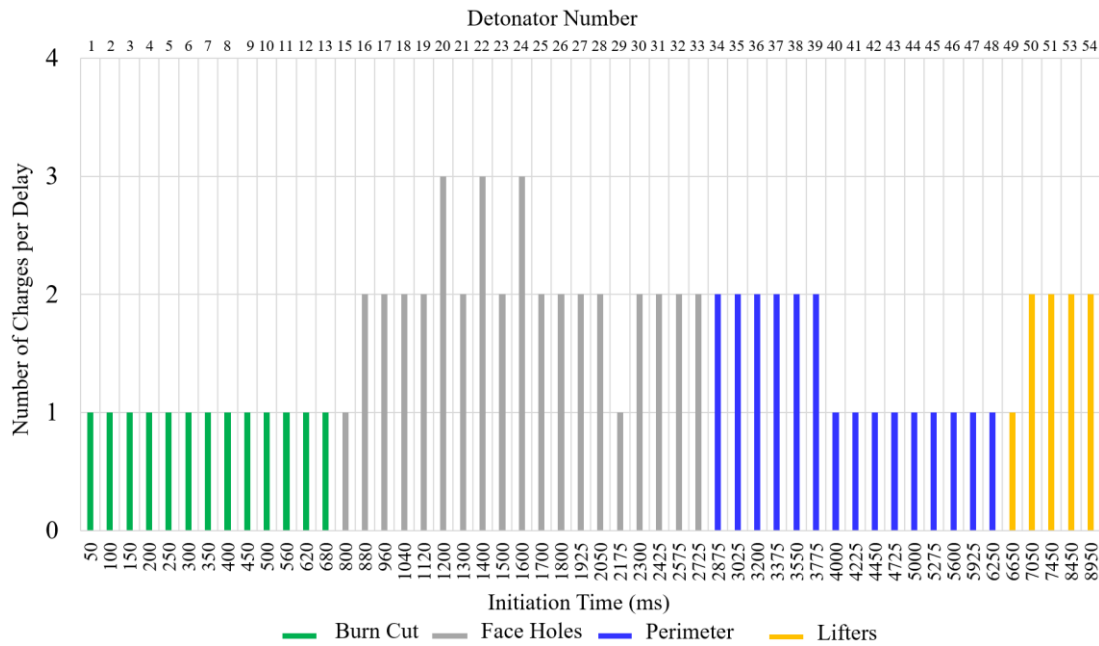


Figure 124 - Number of explosive charges for each detonator delay.

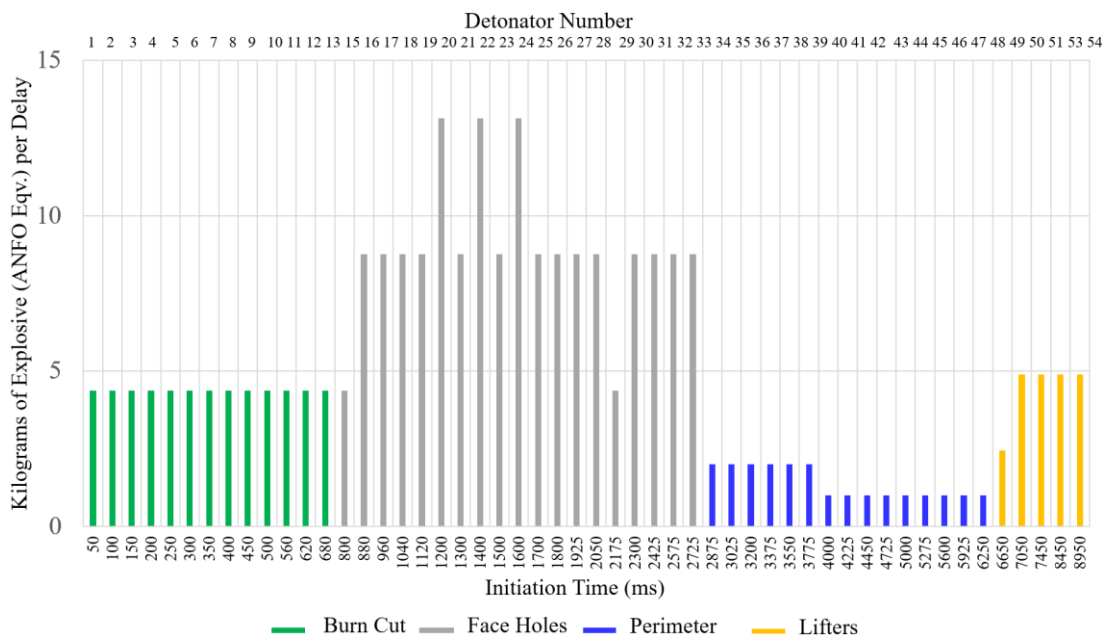


Figure 125 - Distribution of explosive weight to each delay.

Table 26 - Blast summary statistics for the 6.1mW x 6.1mH southern tunnel.

Face Area (m ²)	33.7	Total Explosives – ANFO Eqv. (kg)	280
Volume Blasted (m ³)	128.1	Charge Factor (kg/m ³)	2.2

4.5.3 Ground Support

The ground support scheme in the southern tunnel was consistent with the standard design for this area of the mine. This was installed without modification, as recommended by the mine site geotechnical engineers. This scheme was installed mechanically and consisted of the following arrangement of components:

Surface Support

- 50mm thick primary shotcrete layer (floor-to-floor),
- G80/4 high tensile woven mesh (floor-to-floor),
- Secondary shotcrete overspray of 25mm thickness (floor-to-floor).

Reinforcement

- Continuously mechanically coupled, fully cement grouted, 550MPa mild steel threaded bar, 3.5m length with a 3.25m depth of embedment installed in a 1m x 1m square spacing with 200x200x8mm dome plate and spherical seat nut.

A diagram of this ground support scheme arrangement is presented in Figure 126.

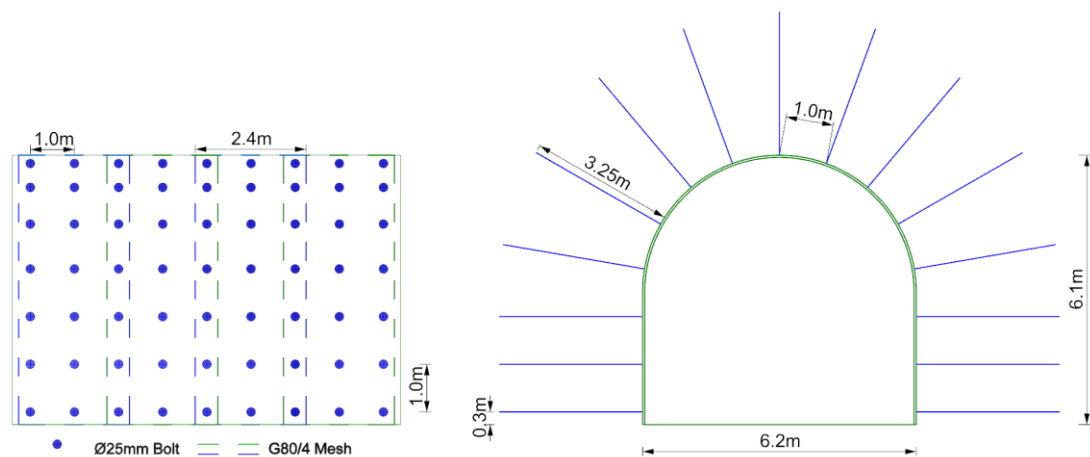


Figure 126 - Installed ground support scheme in the southern research tunnel.

Based on dynamic testing data of similar elements at WASM, the reinforcement system was expected to provide at most 45kJ/m² energy dissipation capacity (see Figure 42), and 20kJ/m² from the mesh-reinforced shotcrete layer (see Figure 46 and Figure 50). Actual energy dissipation of the scheme in-situ was assumed to be 80% of the test values, i.e. in the order of 50kJ/m². This was more than sufficient to manage spalling instability of the rock mass. However, the absence of a second external layer of mesh carried the potential for spalling ejection of the second shotcrete layer.

4.6 Excavation Design (Experimental Tunnel)

This section presents the novel design process for the profile, development blasting with destressing and ground support of the experimental northern research tunnel.

4.6.1 Profile Geometry

The northern excavation was constructed to a semi-elliptical profile of 6.9mW by 6.7mH (Figure 127). This shape was rounded to reduce stress concentrations on the tunnel boundary and to retain compressive loading in both the rock mass and surface support system. The shape was semi-elliptical to suit the dimensions of the mechanised ground support jumbo, while also minimising development waste volumes.

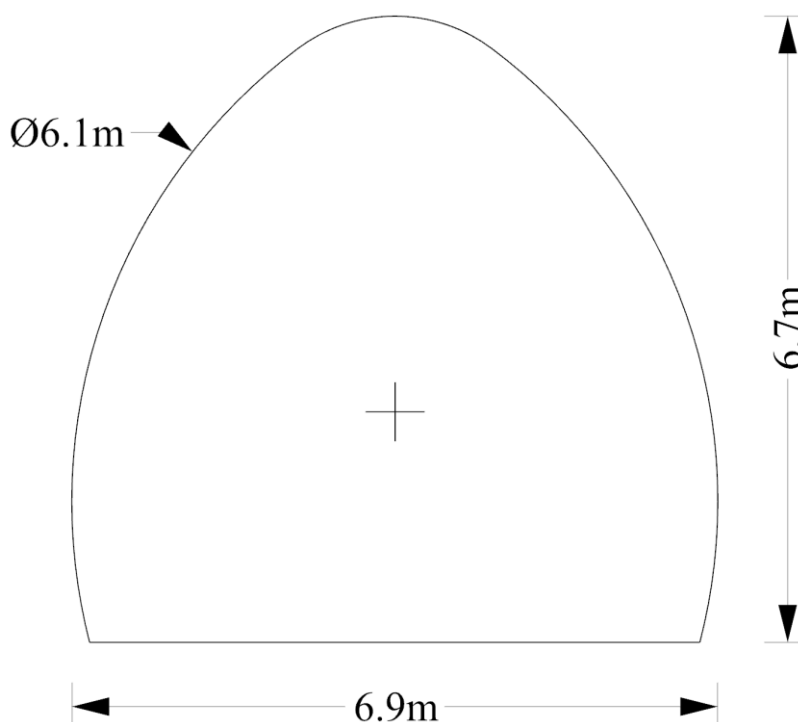


Figure 127 - Profile geometry of the northern tunnel with semi-elliptical shape for improved stability.

4.6.2 Development Face Destress Blasting

The design process for face destress blasting trials followed a sequence of several stages. The first stage involved developing a large number of relatively simple numerical models in the Hybrid Stress Blasting Model (HSBM) software (Furtney, et al., 2009) and examining the blast damage patterns of various charge arrangements. These simple designs were largely based on conventional destressing patterns or slight variations thereof. Basic explosive arrangements were assessed in terms of the likely fracture interactions. A first conceptual destressing design was then produced which sought to create an even distribution of explosive energy throughout the face.

This design was modelled with greater detail in the HSBM package. Design variables such as burden and spacing were adjusted incrementally and the modelled damage assessed. An interim blast design was chosen for trial based on model indications of sufficient fracture interaction between the individual destressing charges. This design was implemented several times during the tunnelling field trial.

Initial observations of this design during development identified several areas for improvement, such as aligning the borehole rows at an inclination with respect to the stress field, as well as modifying the initiation timing of the destressing charges. A second destress blast design was then produced which incorporated several significant changes to the destressing charge pattern and initiation sequence. This design was also optimised using the HSBM package in order to evaluate the desired fracture interaction characteristics, prior to practical trial of the design.

The numerical modelling validated the design parameters and this final design was considered to be optimal for the given rock mass conditions of the trial. This new design was also implemented during the field trials. Following these numerical modelling analyses and field observations, a conceptual face destress blasting design methodology was proposed, and is discussed later. This specific section describes the various stages of design conceptualisation, numerical modelling and optimisation that took place prior to and during the field trials, as well as the final specifications of the blast designs that were field tested.

4.6.2.1 Numerical Analysis

4.6.2.1.1 The Hybrid Stress Blasting Model

A number of numerical models were performed in order to quantify optimal design parameters for a destress blasting concept in the Dacite rock type. The Hybrid Stress Blasting Model was utilised for this purpose. The model takes into account the mechanical properties of the intact rock, rock mass structures and, in a simplified manner, the in-situ principal stresses (Furtney, et al., 2009, Furtney, et al., 2011). In addition, the HSBM uses an in-built non-ideal detonation code to calculate the combined forces (i.e. stresses and gases) from explosive products (Braithwaite, et al., 2009). The model has the capability to determine explosive detonation characteristics and outputs from both fully coupled and decoupled charge arrangements.

The rock breakage engine in the HSBM is designated as *Blo-Up*. It uses a combination of continuous and discontinuous numerical techniques to model detonation, dynamic wave propagation and rock fragmentation. A fundamental aspect of the *Blo-Up* code is the numerical representation of the borehole, explosive charge and rock mass. The borehole, explosive and near-field rock mass are represented as an axis-symmetric continuum using the FLAC code. The explosive is represented as a special constitutive behaviour in the central zones of the FLAC region. The Vixen detonation models, described separately by Cunningham, et al. (2006) and Braithwaite, et al. (2009), give as input to the FLAC model the velocity of detonation (VOD), the parameters of the Williamsburg equation of state, the final reaction extent, the initial density and a reference state. Energy release in the FLAC zones representing the explosive is controlled by a programmed burn (PB) algorithm.

The rock in the near-field is represented as a Mohr-Coulomb material. It is coupled to the explosive reaction products represented by the Williamsburg model. Energy released by the reaction increases the isotropic stress in the zones representing the explosive. The confining material expands in response to the increasing gas pressure, and the new confining volume is transmitted to the Williamsburg equation of state, returning a new isotropic stress. In this way, rock and explosive are fully coupled at all times. The mechanical calculation is fully coupled to a simplified gas flow logic representing the high-pressure reaction product gas. This logic uses an equilibrium pressure parameter to simulate energy losses due to crushing of the borehole wall.

The rock mass is represented with a lattice-type discrete element method, which is a simplification of the full DEM calculation cycle previously performed by the PFC3D code. The main features of the lattice approach have been described by Cundall (2011). In general terms, the lattice applies forces to point masses, which have only translational degrees of freedom, and the connecting springs have a tensile breaking strength. The model geometry is built up of point masses distributed in a non-repeating pattern with a user-specified average separation between nodes (i.e. model resolution). On the lattice, four boundary conditions are permitted: free, quiet, semi-quiet and flex. Free nodes represent a free surface, which may reflect stress waves. Quiet boundaries ensure that wave energy is absorbed at the interior (artificial) model boundaries. This boundary condition is used in the fully confined blasting models discussed here.

4.6.2.1.2 Damage Zone Criteria

For the purposes of the analyses, disturbed or damaged zones were described as regions where the rock mass was likely to experience irreversible deformation or micro fracturing caused by a stress transient. The stress transient was assumed to be directly related to the radial peak particle velocity component. As has previously been applied in other types of preconditioning modelling, particle velocity was used as an index to define the potential areas of the rock mass which were likely to be disturbed by the propagation and interaction of stress waves from detonating charges. These waves were represented in the model by field velocity contours. The application of peak particle velocity as an index to estimate blast damage has previously been demonstrated by researchers and practitioners, including Holmberg & Persson (1980), Onederra & Esen (2003) and Lu & Hustrulid (2003).

Figure 128 illustrates the criteria adopted which is also used to interpret the output generated by the HSBM models described in this thesis. Currently, physical fracturing in the HSBM is displayed by the final state of a point in the rock mass represented by lattice node contacts (i.e. either failed or intact). This is not necessarily valid when identifying regions that may have experienced transient stress loads that could cause micro fracturing or irreversible damage to intact rock.

Because of the ability of HSBM to dynamically display velocity fields in three dimensions, this particular output was used to identify the potential extent of disturbed zones at given distances, at different stages of the simulated stress propagation and attenuation process. It was also used to define whether positive interaction of stresses was achieved between blastholes.

An index of incipient damage of 1,000 mm/s was adopted and used to display the extent of potential disturbed zones as well as interaction caused by the simultaneous initiation of destressing charges. The concept of defining interacting disturbed zones was proposed and demonstrated in blast preconditioning applications by Onederra, et al. (2013). This envelope is expected to have different degrees of damage, ranging from near field fracturing, consisting of mainly macro fracturing, to disturbed zones further away from the blasthole, consisting mainly of micro fracturing of intact rock. After further propagation and interaction of stresses, an interaction zone can be identified between blastholes.

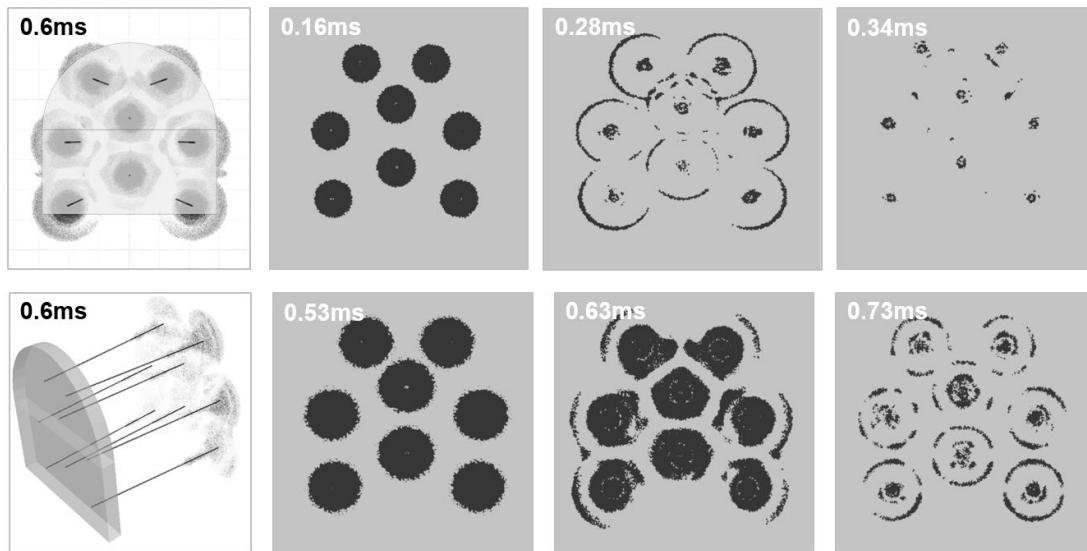


Figure 128 - Example modelling output of 1000mm/s contours defining damaged and interaction zones.

4.6.2.1.3 Input Parameter Calibration

It is important to note that the first stage of modelling work was conducted without a field based calibration process. The aim was to evaluate the capability of HSBM and verify its ability to provide realistic design parameters for subsequent distressing field trials. A number of assumptions were made based on input parameters used in previous preconditioning applications in hard rock. A P-wave velocity estimation for a test rock was conducted and results are shown in Figure 129.

In this analysis, the peak arrival of the radial velocity at a distance of 5.8m was measured and the P-wave velocity estimated to be 6,824 m/s. This value of P-wave velocity on intact rock was deemed to be appropriate for preliminary modelling purposes and corresponded to a rock mass with a density of 2,500kg/m³ and numerical damping coefficient of 0.1. The numerical (spring) tensile strength value of this rock was assumed to be 5 MPa. The adopted damping coefficient and numerical tensile strength values were justified by previous research that focussed on the evaluation of this coefficient (Onederra, et al., 2009). These parameters were chosen as the basis for the theoretical *test rock* used in subsequent modelling.

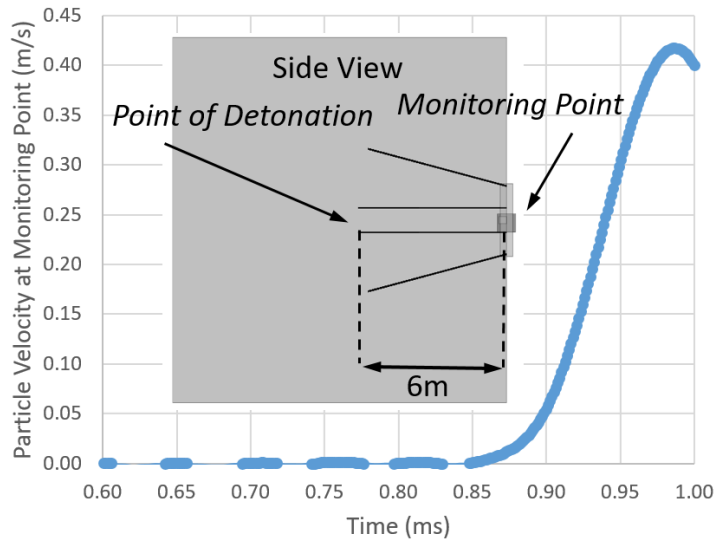


Figure 129 - P-wave velocity estimation.

The damping coefficient took into account the attenuation characteristics of the intact rock, such as rock fabric, mineralisation, porosity, texture and other characteristics which define its heterogeneity. Furtney, et al. (2009) indicated that a damping coefficient may be set from zero to unity. A value of zero corresponds to no-damping and a value of unity corresponds to critical damping. In addition to the above parameters, the in-situ stress field, which was used as input into the HSBM models included a horizontal stress of 50 MPa and a vertical stress of 27 MPa. These values resembled stress measurement data at the mine site where destress blasting was trialled and investigated.

4.6.2.1.4 Preliminary Numerical Models

For the purposes of testing basic model parameters, the HSBM was initially trialled using a simple model geometry typical of a conventional destressing design. The model included two central face holes and four corner holes angled into the walls at the perimeter. All destressing boreholes were 6m in length, 52mm diameter with a 2.4m charge length of regular ANFO at the toe. The model geometry of the simulated excavation and destressing charges is shown in Figure 130. Three scenarios were modelled, each with a different stress field, with results shown in Figure 131. The results illustrate the spatial extent of various states of rock mass damage and the interaction of the damage zones generated between destressing charges. Red contours indicate zones where a simulated mechanical bond between two adjacent nodes in the model has been broken. Black contours indicate zones where consecutive bonds have been broken between adjacent node pairs, thus forming a theoretical fracture.

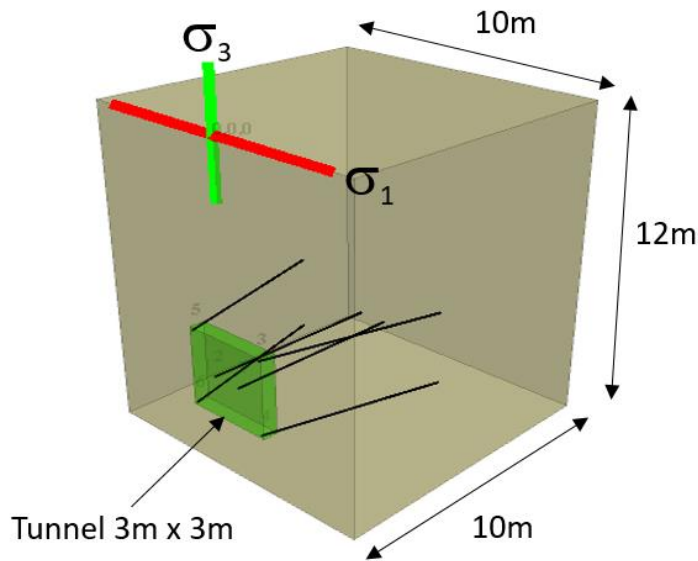


Figure 130 - Preliminary test model destressing geometry.

The results indicate that the extent of fracturing is dependent upon the stress state. As the applied stresses increase, the radial extent of fracturing decreases. A stress state of $\sigma_1=54\text{MPa}$ and $\sigma_3=27\text{MPa}$ is shown in Figure 131c. For typical hardrock tunnelling conditions, this may be considered an approximate lower bound stress state for the onset of violent excavation instability which might require face destressing techniques. The modelling indicated that fracturing of intact rock would be minimal for these stress conditions and zones of micro-fracturing damage would not interact between the widely spaced destressing charges. As such, conventional destress blasting designs of comparable geometry are suggested to have limited effectiveness for conditions of similar or higher stress.

A further fourteen simple destressing designs were also modelled in HSBM and the damage interaction patterns were compared. The number of destressing charges in these models ranged from 6 to 10, with various configurations, such as square and diamond patterns. Models were also assessed using three different in-situ stress fields, including: 100%, which involved the application of nominal in-situ stress (50MPa horizontal, 27MPa vertical); 50%, which involved the application of half the nominal in-situ stress; and 0%, which involved no in-situ stress. A summary description of each model case is given in Table 27. The results for all fourteen preliminary models are presented in Appendix A.

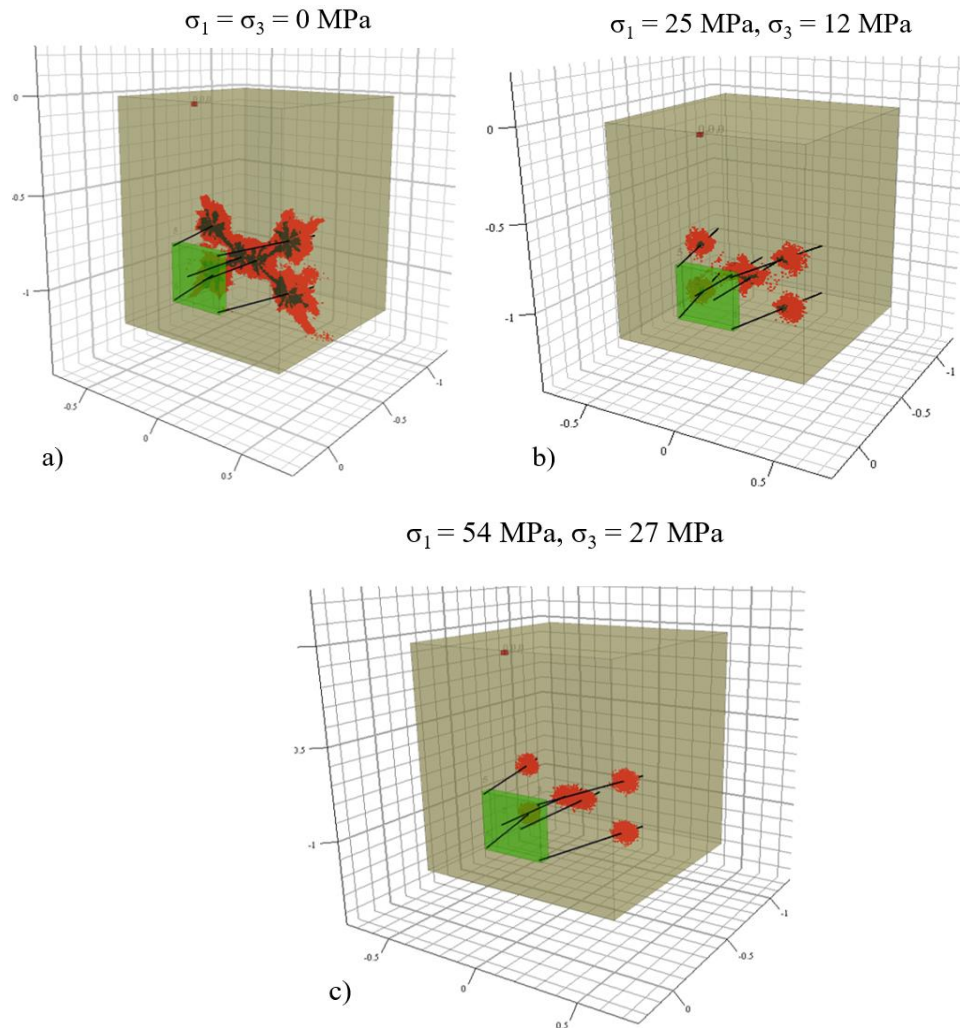


Figure 131 - Modelled damage interaction for a conventional distress blast design under increasing stress.

Table 27- Preliminary HSBM simulations of simple distressing configurations.

Model ID	Rock Type	Stress	Number of Holes	Hole Length (m)	Charge Length (m)	Primer Location
1	Test rock	100%	6	6	2.4	Toe
2	Quartz/Gneiss	100%	6	6	2.4	Toe
3	Quartz/Gneiss	50%	6	6	2.4	Toe
4	Quartz/Gneiss	0%	6	6	2.4	Toe
5	Quartz/Gneiss	100%	10	6	2.4	Toe
6	Test rock	50%	6	6	2.4	Toe
7	Test rock	0%	6	6	2.4	Toe
8	Test rock	100%	10	6	2.4	Toe
9	Test rock	100%	6	6	2.4	Collar
10	Test rock	100%	10	6	2.4	Collar
11	Test rock	100%	8	6	2.4	Toe
12	Test rock	100%	8	6	2.4	Collar
13	Test rock	100%	10	6	2.4	Toe
14	Test rock	100%	10	6	2.4	Collar

The models were constructed with several common input parameters, as follows in Table 28.

Table 28 - Common HSBM model parameters for preliminary analyses.

Blasthole Diameter	52mm
Blasthole Dip	15
Explosive	5,000m/s VOD - 1.15 g/cc
Development Size	3m x 3m x 0.5m
Model Limits	15m x 15m x 15m

For consistency, the three dimensional modelling outputs from each scenario were displayed in long and plan sections to easily identify disturbed zones and the likelihood of stress interaction. The analysis focused on transient stress waves occurring within a few milliseconds after the explosive detonation process. In the analysis, two image viewpoints were taken for each model, being a front and top view. The model viewpoints are depicted in Figure 132. The front view is a cross section at the blasthole toe, looking parallel to the longitudinal axis of the tunnel from the blasthole toe towards the collar. The top view is a horizontal section of the results output looking vertically down on the model. Only the upper row of charges are visible in top view.

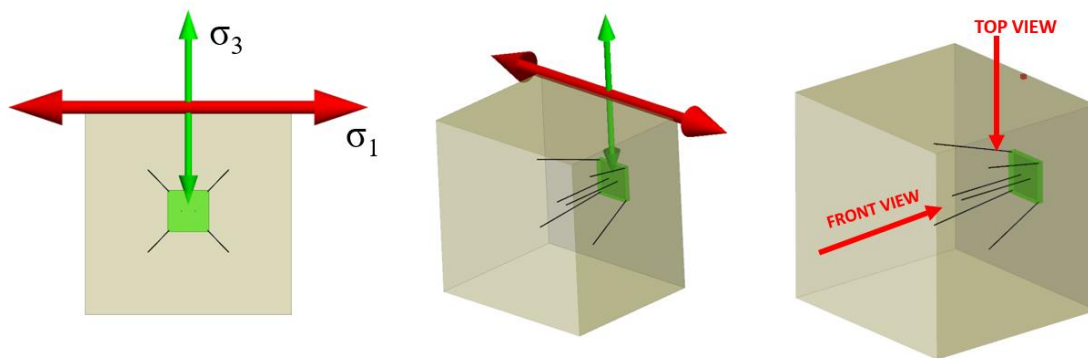


Figure 132 – Example model geometry for preliminary destressing analyses.

Figure 133 and Figure 134 give examples of the typical collar primed and toe primed output from the modelling, describing damage and interaction zones at specific stages. Note that red zones indicate peak particle velocities exceeding 1,000 mm/s at a specific simulation time. The results indicate that the charge initiation point has a strong influence on the shape of the blast-induced damaged zone. Toe priming of the destressing holes resulted in relatively high vibrations at the development free face, which would indicate potential for higher damage there.

Chapter 4: Design

Collar priming the destressing charges reduces the vibrations and associated damage at the face, instead directing explosive energy away from the excavation. This appeared to have the effect of increasing damage in the desired destressing zone and limiting interference with the charged development round.

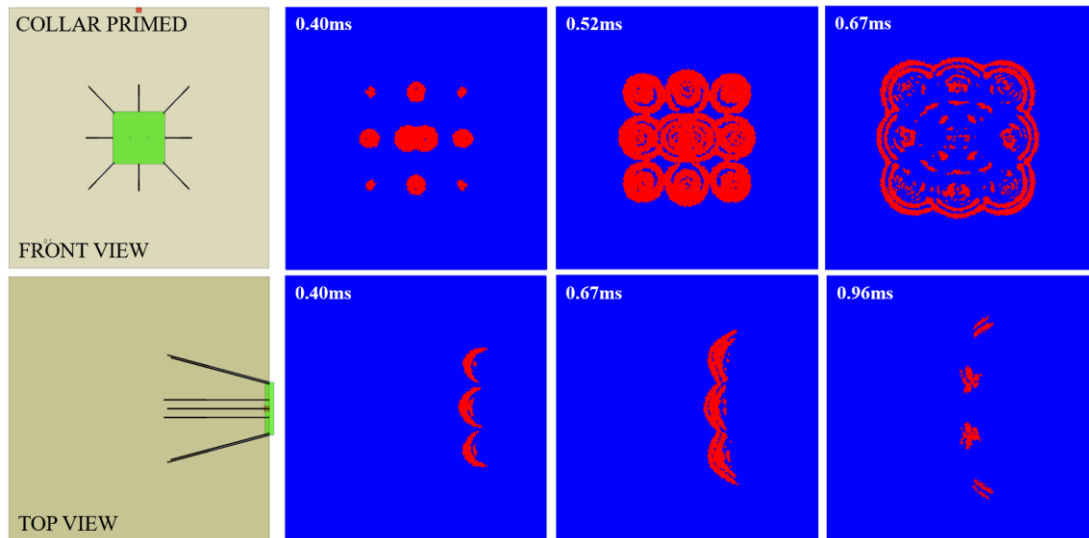


Figure 133 – Example HSBM output for collar primed destressing configuration.

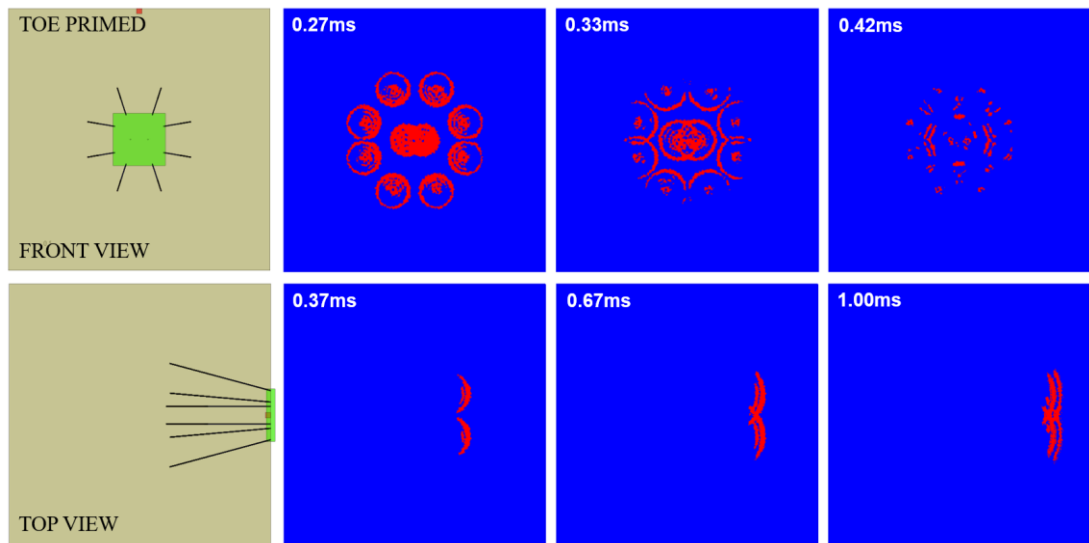


Figure 134 – Example HSBM output for toe primed destressing configuration.

4.6.2.1.5 Detailed Numerical Models

Eight additional simulations were performed on detailed destressing designs using the aforementioned modelling methodology in HSBM. These eight simulations were performed on three separate destress blast design concepts, two of which closely reflected the final designs which were implemented in the field trials. For operational reasons, some design parameters of the modelling were changed slightly at the field implementation stage. Nonetheless, the models provided a theoretical representation of the likely damage envelopes associated with the destressing designs that were field tested. Table 29 summarises the range of input parameters for these eight detailed models.

Table 29 – HSBM input parameters for eight detailed destressing models.

Model ID	Rock Type	Stress	Number of Holes	Hole Length (m)	Charge Length (m)	Primer Location
15	Test rock	100%	10	6	2.4	Toe
16	Test rock	100%	10	6	2.4	Collar
17	Test rock	100%	10	6	2.4	Toe
18	Test rock	100%	10	6	2.4	Collar
19	Test rock	100%	8	6	2	Toe
20	Test rock	100%	8	6	2	Collar
21	Test rock	100%	8	6	2	Collar
22	Test rock	100%	10	7	3	Collar

The purpose of these models was to evaluate the damage zones associated with each unique destressing pattern with a view to selecting a design for practical trial. The pattern configurations included ten and eight-hole layouts. One rock type was used to evaluate model behaviour and quantify potential differences. Model configurations also included the application of an in-situ stress field. For model runs 15-21, the applied in-situ stress was 50MPa horizontally and 27MPa vertically. For model run 22, the stress orientations were adjusted by 10 degrees of inclination to more closely reflect the measured stresses at the trial tunnelling site. It should be noted that models 15 to 20 reflected 52mm diameter charges and an emulsion explosive with 5000m/s VOD. Model 21 simulated a fully coupled 45 mm diameter ANFO charge configuration with a VOD of 4000m/s. Model 22 included the largest of all modelled charges, with a 3.0m length, 63mm diameter and fully coupled ANFO charge. This final model most closely reflected the actual charge design that was field trialled.

Chapter 4: Design

The value range of detailed input parameters for models 15-21 are presented in Table 30. The geometry of the destressing charges and example HSBM results for a ten-hole destressing pattern are shown in Figure 135 and Figure 136, respectively. For comparison, the design geometry and model results for an eight-hole pattern are presented in Figure 137 and Figure 138. The results of these additional HSBM models are also attached in Appendix A.

Table 30 - Input parameters for detailed destressing design, model runs 15-21.

Model Parameter	Value / Range
Blasthole Length	6.0m
Charge Length	2.0 - 2.4m
Blasthole Diameter	45 - 52mm
Blasthole Dip	2 degrees
Blasthole Lookout Angle	5 degrees
Booster	Modelled at both collar and toe
Explosive VOD	ANFO (4000m/s) – Emulsion (5000m/s)
Explosive Density	1.15 g/cc
Sigma 1	50 MPa (0-10 degrees dip)
Sigma 3	27 MPa (80-90 degrees dip)
Development Size	5.8mW x 5.6mH
Model boundary	15m x 15m x 20m

The interpretation of the results of these models reaffirms that the assumed *test rock* input parameters used to simulate stress wave propagation and interaction through velocity fields was adequate for the definition of first pass design parameters. Analysis showed that a blast pattern configuration consisting of 8 holes may produce a disturbed damage zone sufficient for destress blasting trial purposes. However, the effectiveness of this pattern would be dependent on actual velocity attenuation, and in practical terms the accuracy of drilling and detonator timing and the ability of the explosive charge to be fully coupled and confined within the borehole. It was also confirmed that the charge initiation point has a clear influence on the shape of the damage zone. Collar priming of destress blast holes appeared to be an effective way of increasing the destressed zone ahead of the development face. However, in order to avoid potential damage to primers in the development round, or sympathetic detonation, a sufficient buffer distance of unblasted rock was required to be applied between the toe of the development round and collar of the destressing loads. The eight-hole destressing pattern design was the first to be implemented during practical field trials.

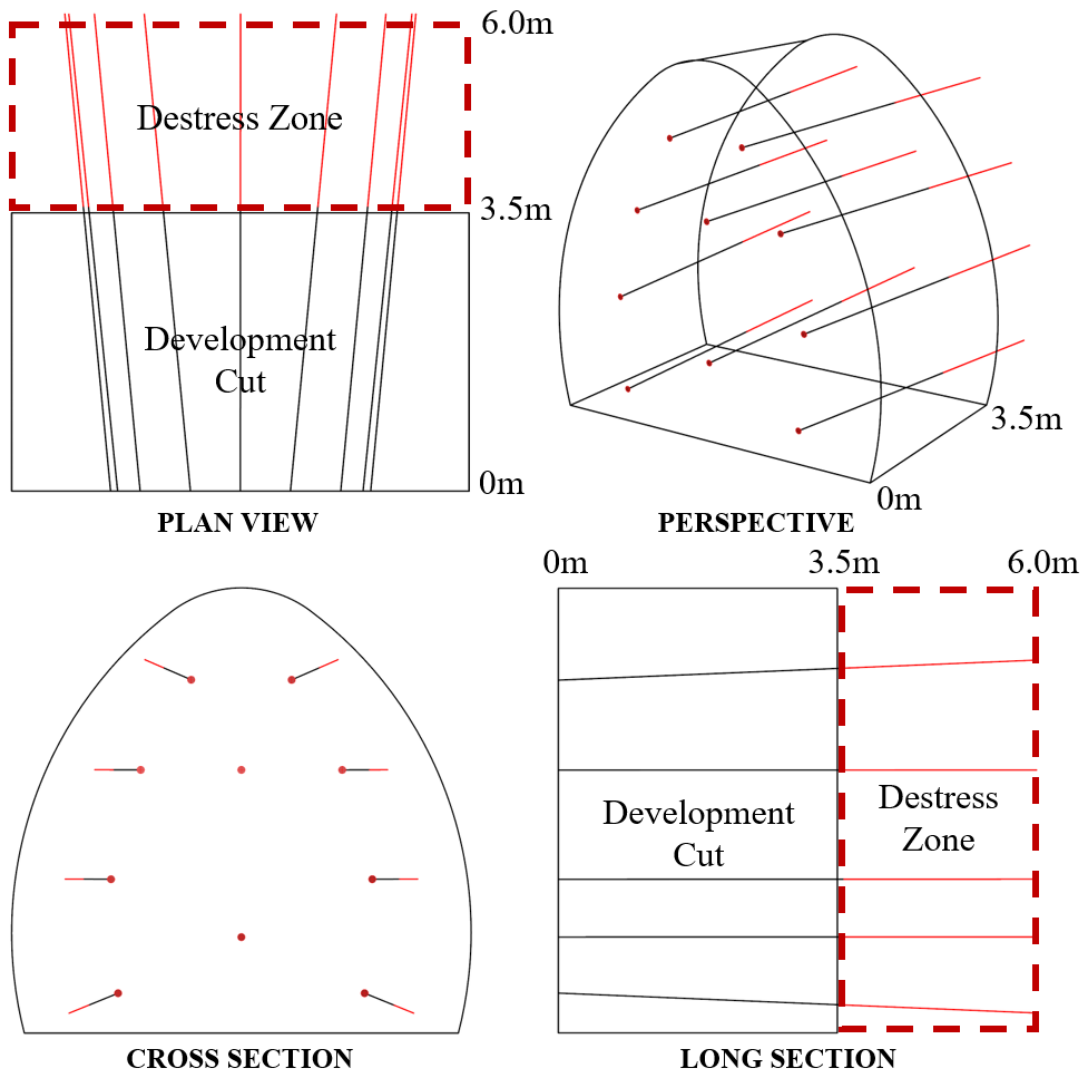


Figure 135 – HSBM geometry for destress blasting simulations 15-18.

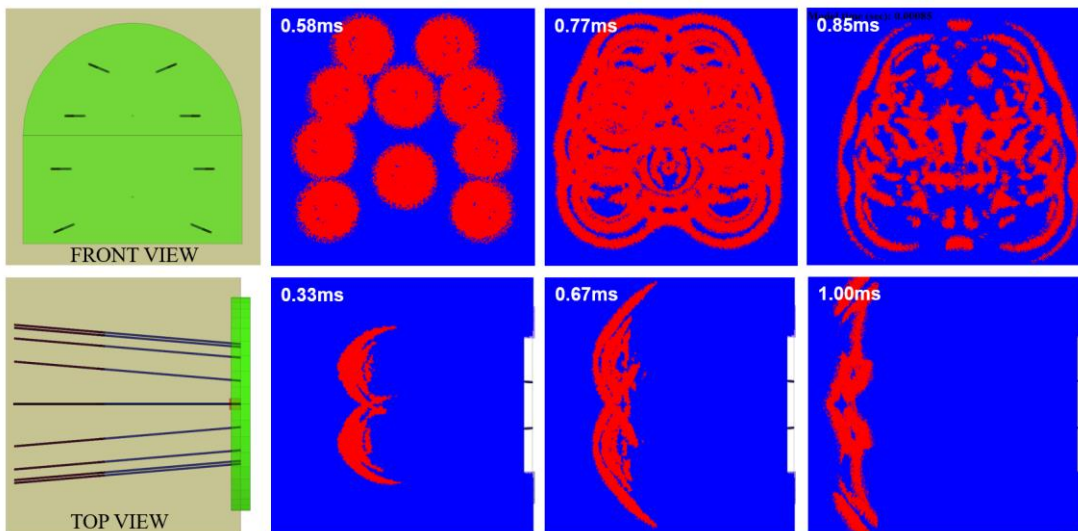


Figure 136 - Example HSBM output of stress wave transient for model run 16.

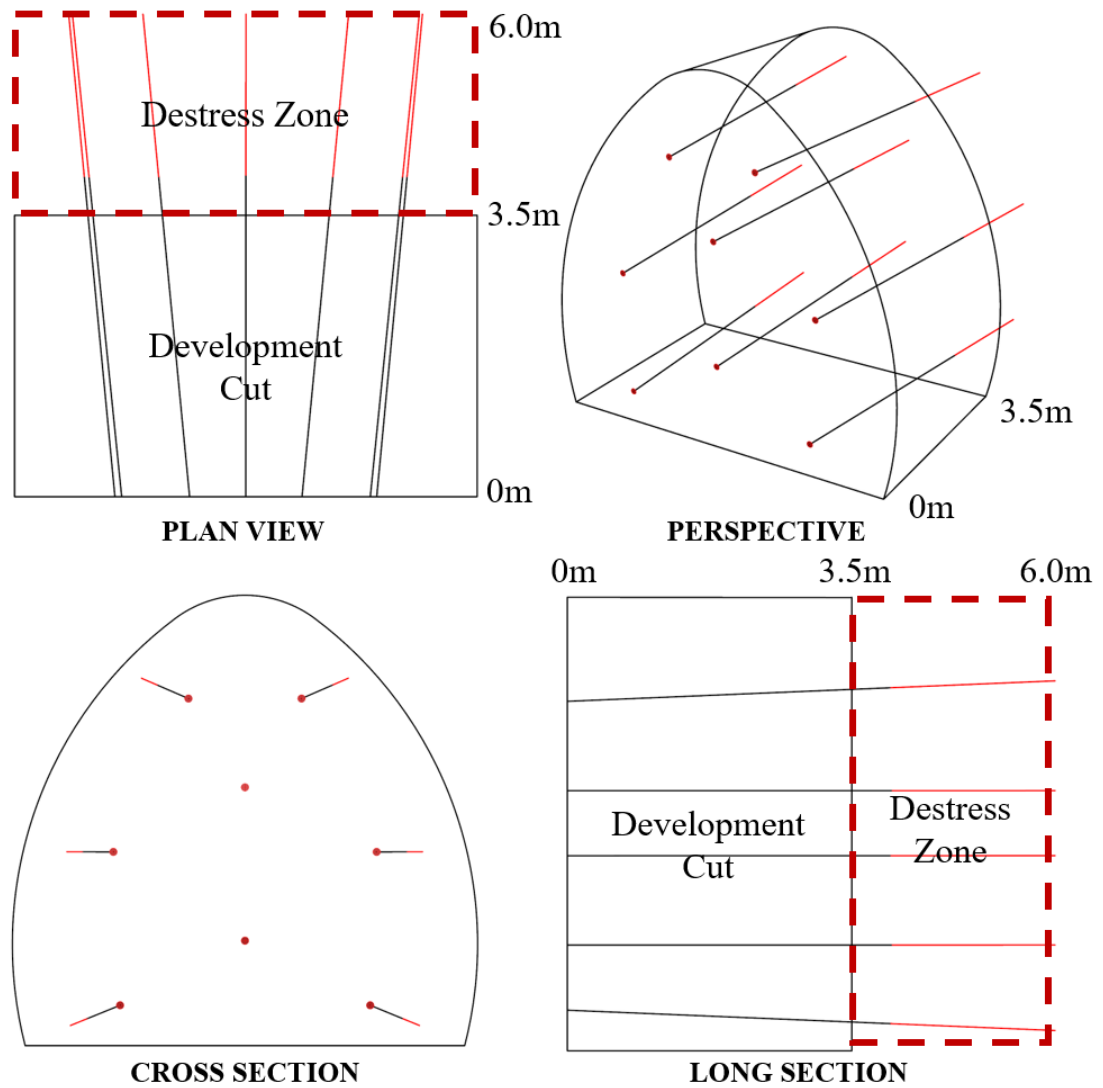


Figure 137 - HSBM geometry for destress blasting simulations 19-21.

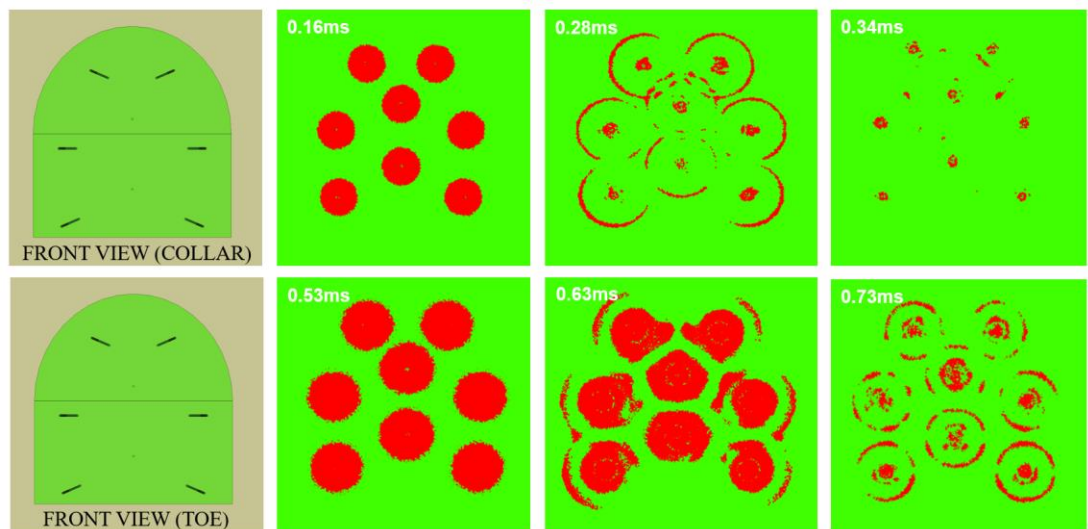


Figure 138 - Example HSBM output of stress wave transient for model run 20.

Chapter 4: Design

The final HSBM model was run 22. This model was developed during the destressing trials following initial field observations. It was the most detailed model in terms of the output results, as well as being the closest representation of the second and optimised destressing design that was implemented during the field trials. This model provided theoretical validation of final design parameters such as borehole and charge diameter, burden, spacing and explosive type. The final input parameters to this model are presented in Table 31. The design consisted of a ten-hole pattern of 7m long holes, with a 3m toe charge. The properties of regular ANFO were chosen as the input parameters for this final model. All destressing charges were modelled as fully coupled and confined with a 1.1 column of stemming.

The geometry of the destressing pattern and explosive charge arrangement for model 22 are shown in Figure 139. The booster position was placed at the collar of the destressing charge, such that the direction of explosive propagation was away from the tunnel face and main development round. All destressing charges were modelled to initiate simultaneously.

Table 31 - Input parameters for detailed destressing design, model run 22.

Model Parameter	Value		
<i>Blasthole Length</i>	7m		
<i>Row Burden /</i>	2.0m x 1.5m / 1.65m		
	From:	To:	Length:
<i>Air Gap</i>	0m	2.9m	2.9m
<i>Stemming</i>	2.9m	4.0m	1.1m
<i>ANFO Explosive</i>	4.0m	7.0m	3.0m
<i>Blasthole Diameter</i>	63mm		
<i>Blasthole Dip</i>	0° (Parallel to drive)		
<i>Booster</i>	3.0m from end of hole		
<i>Explosive</i>	4,000m/s VOD		
<i>Sigma 1</i>	50 MPa, -10°		
<i>Sigma 3</i>	27MPa, -80°		
<i>Development Size</i>	6.6mW x 6.7mH		
<i>Model Dimensions</i>	14m x 15m x 15m		

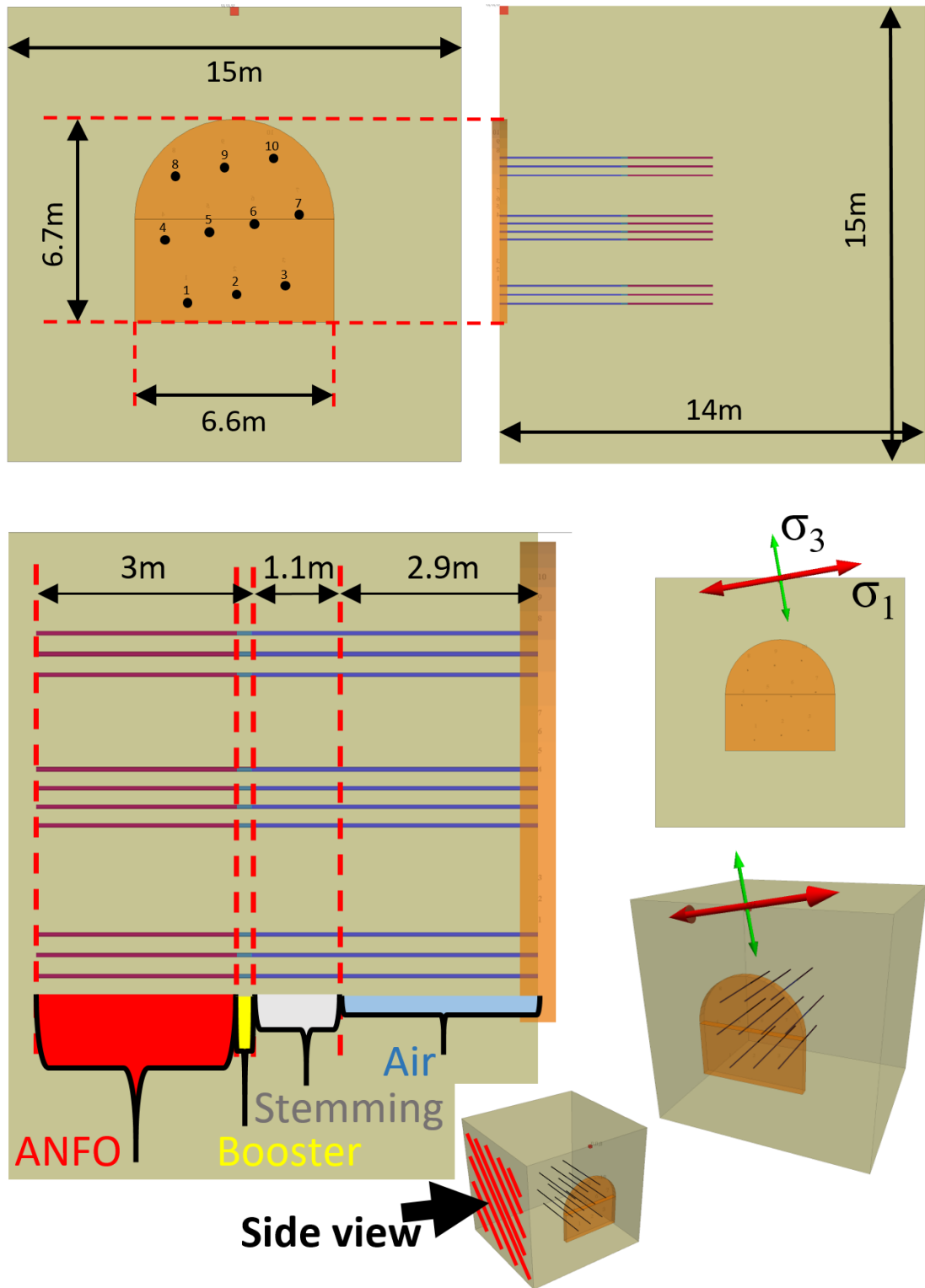


Figure 139 - HSBM Model 22 geometry, explosive charge configuration and rock stress.

Figure 140 presents a series of cross sectional views of the HSBM model results of velocity attenuation for six detonation time steps at 10^{-4} second intervals. The view is a cross section at the mid-point of the charge column, looking parallel to the longitudinal axis of the tunnel. The velocity attenuations are indicated by the colour scale. Black dot markers denote the locations of dislocated nodes (i.e. fractures) in the model, similar to that previously illustrated in Figure 131. The results indicate that fracture interaction between individual destressing charges occurs in-row only. No continuous radial fracture interaction is observed across the burden in the model. This is consistent with previous laboratory findings of radial fracturing patterns under anisotropic stress (Jung, et al., 2001).

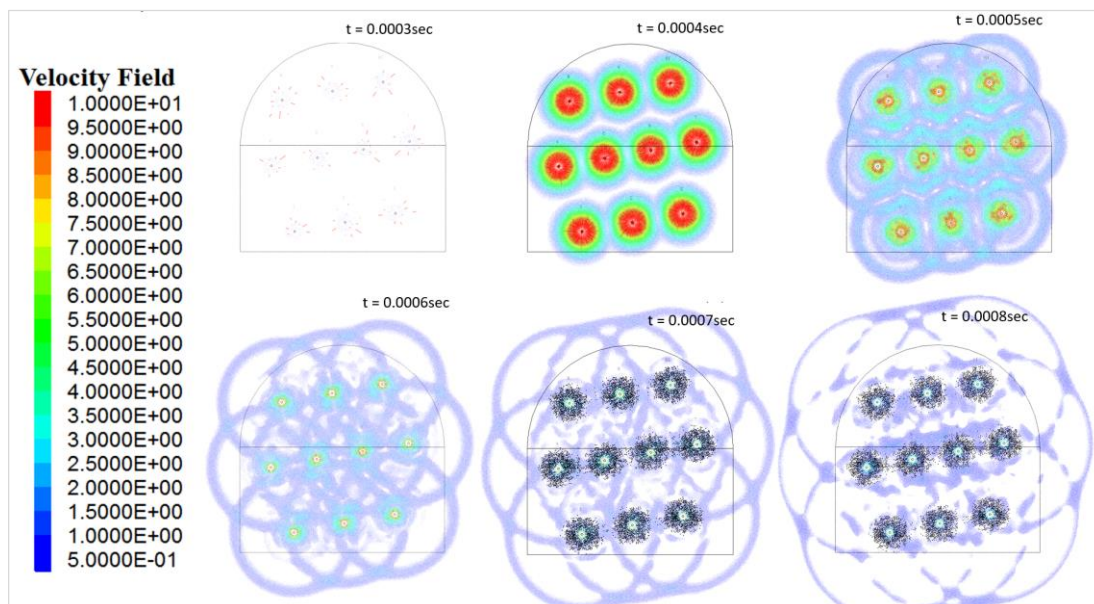


Figure 140 - Cross sectional view of modelled particle velocity attenuation and fracture interaction.

Figure 141 presents two plan view sections of the model results, showing variability in fracture interaction along the longitudinal axis of adjacent destressing blastholes within the same row. It is evident that the closer spacing of 1.5m in the central destressing row of four holes (Figure 141a) produces a longer and more intense zone of interacting fractures when compared to the 3-hole row with 1.65m borehole spacing (Figure 141b). In both cases, the zone of greatest fracture interaction is located at the toe of the charge. The significantly increased fracture interaction between holes in row 2, when compared to the holes in rows 1 and 3, is also illustrated in cross section view in Figure 142. Based on these results, an optimised charge spacing of 1.5m was implemented during the second and final destressing field trial design.

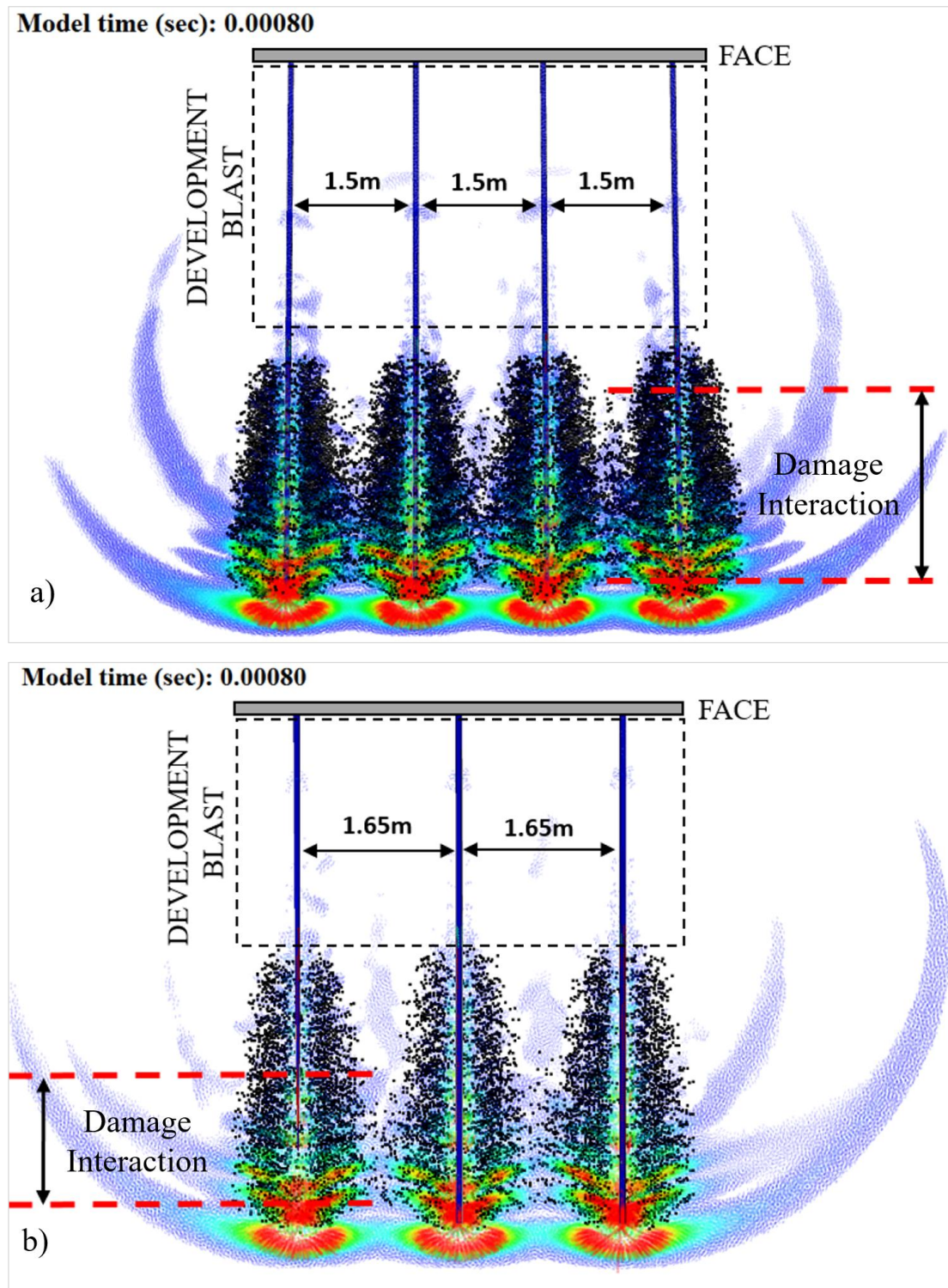


Figure 141 - Plan views of modelled particle velocity attenuation and fracture interactions.

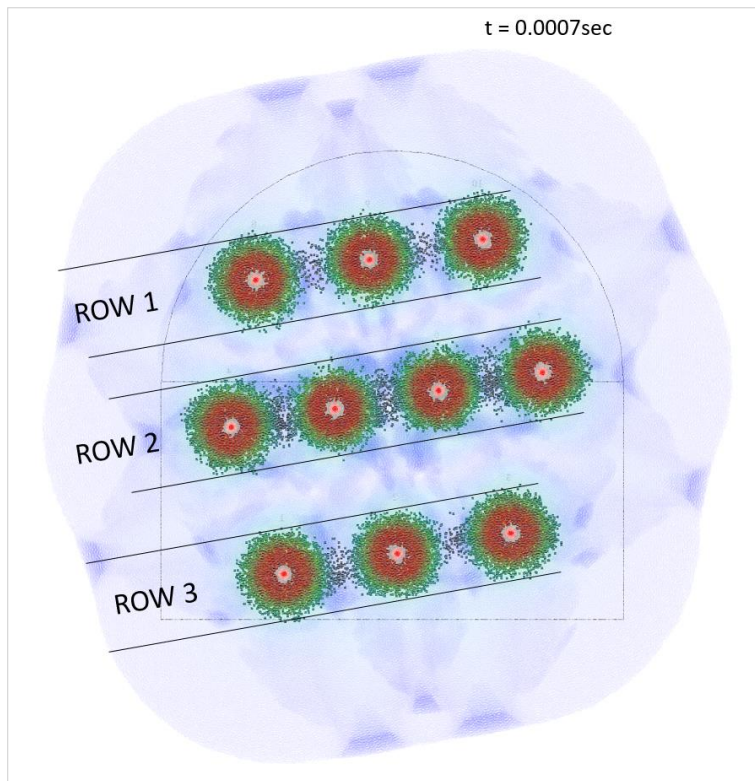


Figure 142 – Modelled fracture interaction in-row only, with no fracture formation across the burden.

4.6.2.2 Field Trial Destressing Design 1

As previously mentioned, two destressing blast designs were implemented during the field trials. The charge pattern and parameters of the first design were chosen primarily on the basis of numerical analyses in HSBM. The second destressing design was optimised following preliminary field observations and further modelled refinements using HSBM. The complete geometry of the first destressing blast design, including the standard development pattern, is presented in Figure 143. This design is referred to as *Destressing Design 1*.

All destressing designs were developed to satisfy the following main criteria:

1. Destressing zone of 3m distance ahead of the face,
2. ANFO charge for high gas content,
3. Fully coupled and confined explosives to maximise gas pressure,
4. Uniform explosive distribution,
5. Face destressing only (no destressing outside final tunnel perimeter),
6. Fracture interaction across the charge spacing.

Destressing Design 1 was implemented for four consecutive blasts in the northern research tunnel before being superseded by an optimised destressing design.

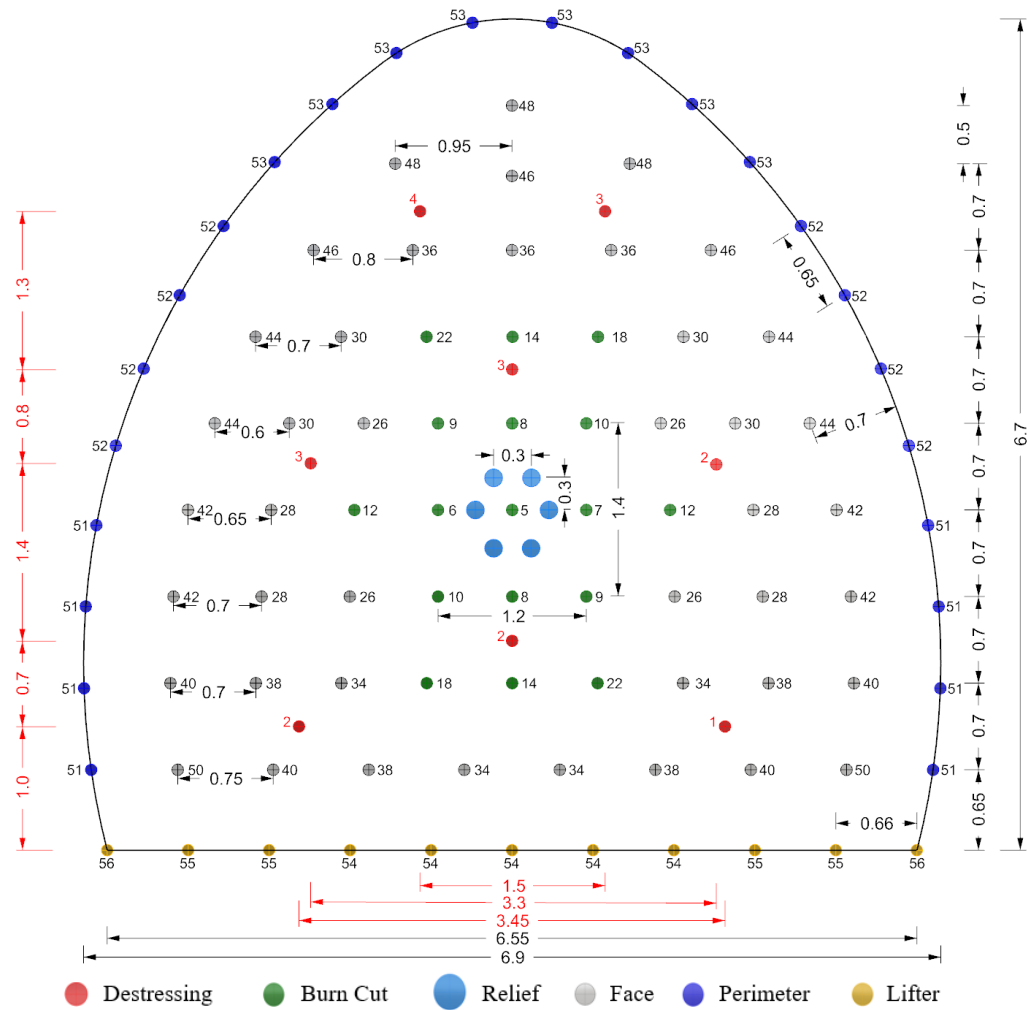


Figure 143- Development Destressing Design 1.

4.6.2.2.1 Drilling Specifications

In this first destressing design, the standard development advance was 3.8m. Destressing boreholes were 7.0m long with a 2.9m long toe charge. The basic drilling parameters for this blast design, including the number of drill holes, diameter and their length, are presented in Table 32. Generally, the spacing of destressing charges in this design ranged from 1.85 to 2.2 metres, although was slightly less in the two top holes.

Table 32 - Basic drilling parameters for Destressing Design 1 in the northern tunnel.

		# Holes	Diameter (mm)	Length (m)
Destressing	●	8	63	7.0
Burn Cut	●	17	45	3.8
Burn Relief	●	6	127	3.8
Face Holes	●	43	45	3.8
Perimeter	●	24	45	3.8
Lifters	●	11	45	3.8
TOTAL:		109		

4.6.2.2.2 Explosives, Charging Specifications and Initiation

The same explosives used in the conventional development, including ANFO, Softron and Tronex, were also used in the development with face destressing. All regular development charges were toe-primed without stemming. The destressing charges were all collar primed, stemmed with a 1.5m column of wet clay pack and initiated simultaneously or on multiple delays prior to the main development round. Details of the explosive loads for each blasthole type are presented in Table 33. The total quantity of each explosive needed for this blast design is shown in Table 34. The number of individual charges per delay and the distribution of explosive charge weight per delay are shown in Figure 144 and Figure 145, respectively. Summary statistics for this destressing blast with semi-elliptical tunnel profile are tabulated in Table 35.

Initially, all eight destressing charges were initiated simultaneously, prior to the main development blast, so as to closely replicate the HSBM analyses. However, this was altered after the first destress firing for two reasons. Firstly, fracture interaction across the destressing burden was not likely to occur. Therefore, simultaneous detonation of destressing blastholes in adjacent rows was deemed unnecessary. Secondly, initiation of all destressing charges simultaneously created a significant concussion effect which posed a hazard to nearby monitoring instruments. As such, for the second and all subsequent blasts in the northern tunnel, the destressing charges were initiated on multiple delays, as per the annotated timing noted in the figures and charts.

Table 33 - Explosive charge specifications for individual loads in Destressing Design 1.

		Hole Length (m)	Charge Length (m)	Tronex 1 1/8" x 8"		ANFO (kg)	Softron 11/16" x 20"	
				Qty	kg		Qty	kg
Destressing	●	7.0	2.9	1	0.2	7.7	0	0
Burn Cut	●	3.8	3.2	1	0.2	4.2	0	0
Face Holes	●	3.8	3.2	1	0.2	4.2	0	0
Perimeter	●	3.8	3.2	1	0.2	0	6	0.8
Lifters	●	3.8	3.2	16	2.4	0	0	0

Table 34 - Summary of total explosives used in each blast for Destressing Design 1 in the north tunnel.

Explosive	Qty	Total (kg)	ANFO Eqv. (kg)
Tronex 1 1/8" x 8"	268	41.0	50.0
Softron 11/16" x 20"	144	20.3	22.9
ANFO	-	329.1	-

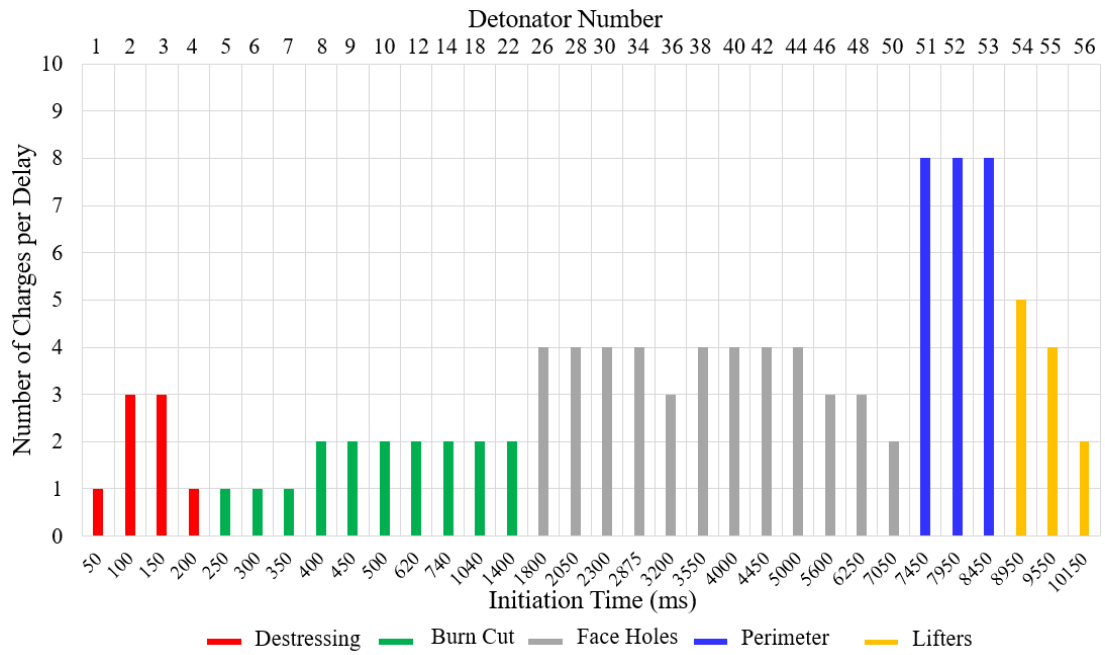


Figure 144 - Number of explosive charges per delay.

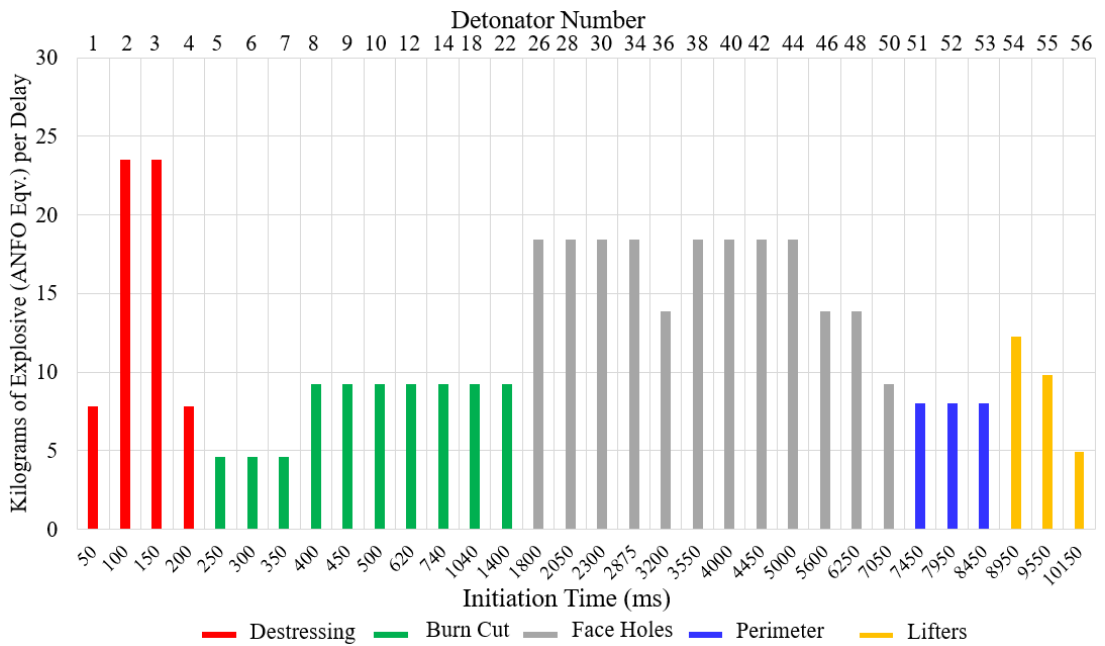


Figure 145 - Distribution of explosive weight per delay.

Table 35 - Blast summary statistics for the 6.9mW x 6.7mH semi-elliptical Destressing Design 1.

Development (6.9mW x 6.7mH)		Destressing (+3.2m)	
Volume Blasted (m ³)	142.1	Volume Blasted (m ³)	119.7
Total Development Explosives ANFO Eqv. (kg)	339	Total Destressing Explosives ANFO Eqv. (kg)	63
Development Charge Factor (kg/m ³)	2.4	Destressing Charge Factor (kg/m ³)	0.5

4.6.2.3 Field Trial Destressing Design 2







Following initial field observations of *Destressing Design 1*, several modifications were made to the destressing design. These changes were made in order to improve the likelihood of fracture interaction between charges and to adhere to a destressing design concept idea that evolved throughout the field work. *Destressing Design 2* closely resembled the HSBM model run 22 specifications.

4.6.2.3.1 Drilling Specifications

Destressing Design 2 implemented in the northern research tunnel is illustrated in Figure 146. Tabulated drilling specifications are shown in Table 36. This design was the second evolution of the trial destressing methodology and it incorporated several changes. Primarily, the destressing charges were realigned into parallel rows which were all sub-parallel to the major principal stress. The number of destressing charges was also increased. This change was made in order to implement the optimal inter-row spacing of 1.5m suggested by HSBM model 22. Minor alterations were made to the regular development round, including a modified burn cut and increased burden and spacing of the perimeter row.

One important characteristic of both of the field trialled blast designs was the absence of destressing charges close to or beyond the final excavation boundary. In this case all destress loads were positioned inside or aligned to the outer row of shot holes. By design they were intended to be no closer than 0.8m to the final tunnel wall. Due to the complex structural conditions of the Dacite rock mass and the potentially negative effect on stability, this design deliberately avoided destressing the tunnel perimeter.

Table 36 - Basic drilling parameters for Destressing Design 2 in the northern tunnel.

		# Holes	Diameter (mm)	Length (m)
Destressing		12	63	7.0
Burn Cut		9	45	3.8
Burn Relief		4	127	3.8
Face Holes		46	45	3.8
Perimeter		21	45	3.8
Lifters		11	45	3.8
TOTAL:		103		

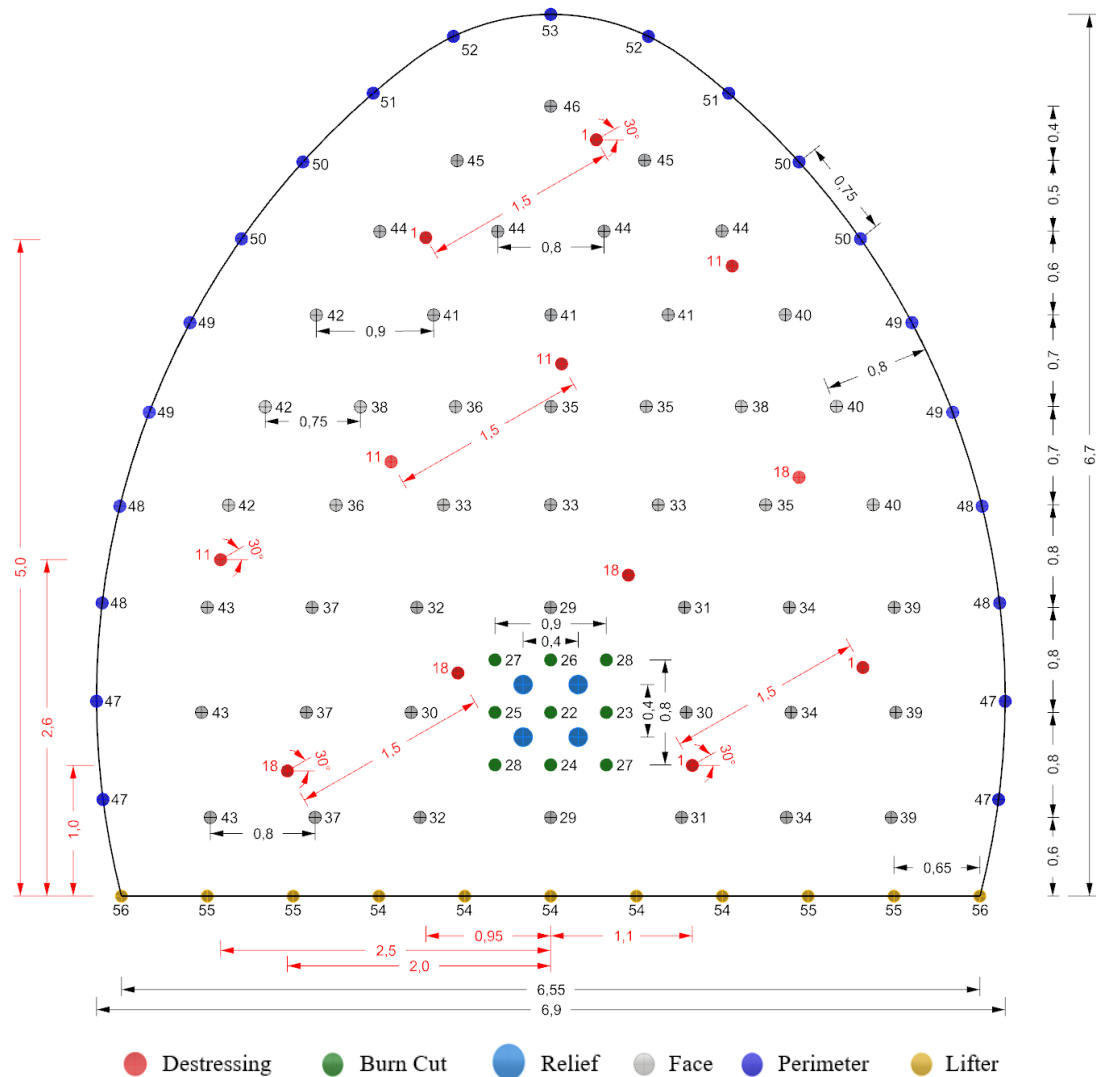


Figure 146 – Development Destressing Design 2

4.6.2.3.2 Explosives, Charging Specifications and Initiation

The basic design of the individual destressing charges remained unchanged in terms of their diameter, length, quantity and type of explosive used, as summarised in Table 37. However, due to the increase in the number of destressing charges from eight to twelve, the charge factor in the destressing zone increased from 0.5 to 0.8 kg/m³.

Table 37 - Explosive charge specifications for individual loads in Destressing Design 2.

		Hole Length (m)	Charge Length (m)	Tronex 1 1/8" x 8"		ANFO (kg)	Softtron 11/16" x 20"	
				Qty	kg		Qty	kg
Destressing	●	7.0	2.9	1	0.2	7.7	0	0
Burn Cut	●	3.8	3.2	1	0.2	4.2	0	0
Face Holes	●	3.8	3.2	1	0.2	4.2	0	0
Perimeter	●	3.8	3.2	1	0.2	0	6	0.8
Lifters	●	3.8	3.2	16	2.4	0	0	0

Chapter 4: Design

The destressing loads were initiated in groups of four on three separate delays, with at most 30.8kg of ANFO detonated on any one delay. The initiation sequence in this design was such that in-row destressing charges were detonated simultaneously. Therefore, the borehole pressures of adjacent charges were maximised at the same time, increasing the likelihood of radial fracturing sub-parallel to the major principal stress. Delays of approximately 500ms were applied between each group of destressing charges, so as to minimise potentially hazardous concussion.

Non-electronic (Nonel) detonators were used for all destressing and development charges. These detonators are not as accurate as electronic detonators, and therefore it is likely that some timing scatter was introduced into the destressing pattern. As such, it is unlikely that the destressing charges were initiated perfectly simultaneously. Electronic detonators were not available for use during the trial.

The number of individual charges per delay and the distribution of explosive charge weight per delay for *Destressing Design 2* are shown in Figure 147 and Figure 148, respectively. The total explosives used in this design are presented in Table 38, and summary blast statistics in Table 39. *Destressing Design 2* was implemented for the final four blasts in the northern tunnel.

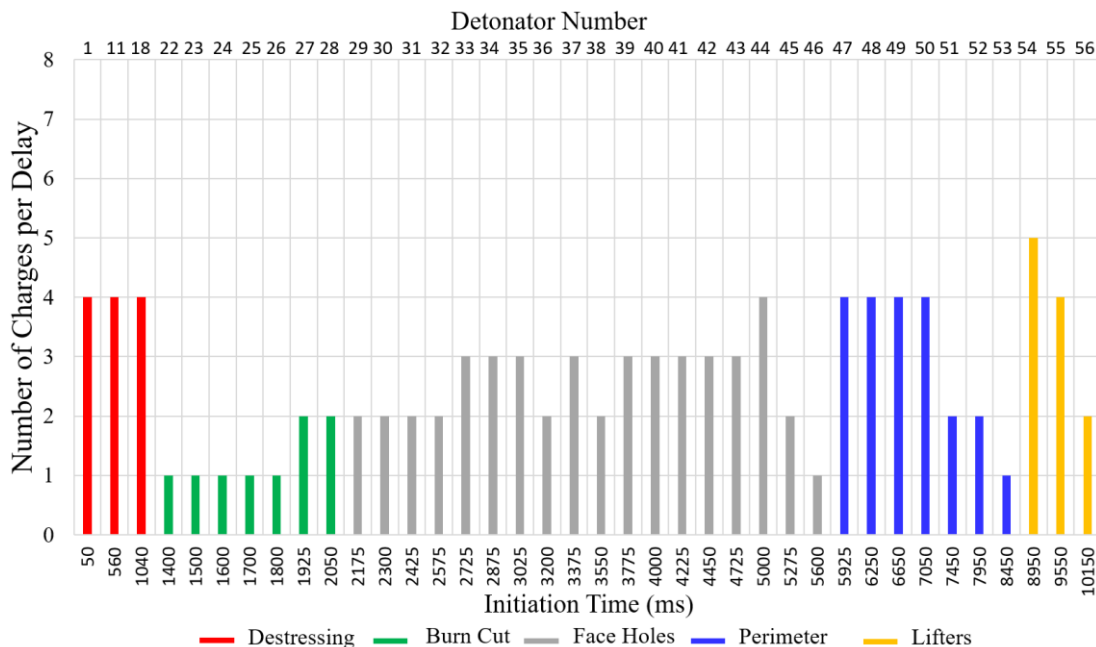


Figure 147 - Number of explosive charges for each detonator delay.

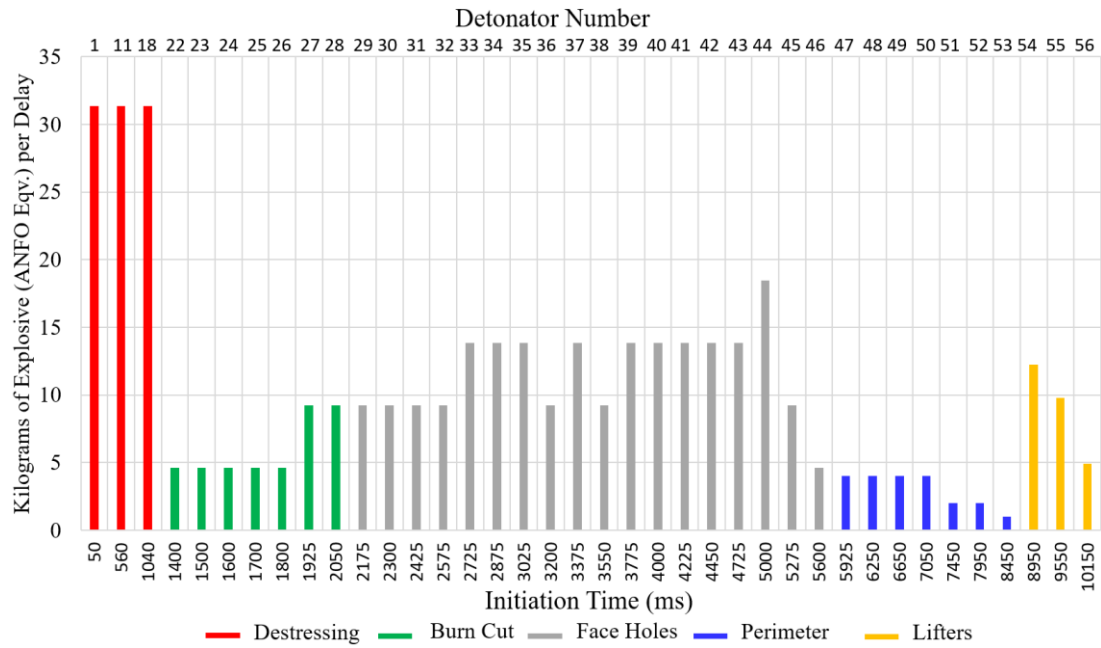


Figure 148 - Distribution of explosive weight to each delay.

Table 38 - Summary of total explosives used for Destressing Design 2 in the north tunnel.

Explosive	Qty	Total (kg)	ANFO Eqv. (kg)
Tronex 1 1/8" x 8"	264	40.4	49.3
Softtron 11/16" x 20"	126	17.8	20.1
ANFO	-	337.6	-

Table 39 - Blast summary statistics for the 6.9mW x 6.7mH semi-elliptical Destressing Design 2.

Development (6.9mW x 6.7mH)		Destressing (+3.2m)	
Volume Blasted (m ³)	142.1	Volume Blasted (m ³)	119.7
Total Development Explosives ANFO Eqv. (kg)	313	Total Destressing Explosives ANFO Eqv. (kg)	94
Development Charge Factor (kg/m ³)	2.2	Destressing Charge Factor (kg/m ³)	0.8

4.6.2.4 Suggested Destress Blasting Design Principles

An optimal face destress blasting concept evolved throughout the design and construction research trials. The suggested design principles are described as follows. The destressing concept requires shear failure of the face with minimal deformation. Shear is desirable on all natural joint orientations, as well as along radial blast-induced fractures. In order to effectively create radial blast cracks, destressing charges should be positioned such that fractures generated by adjacent charges connect. Rows of charges may be aligned to create the desired number of continuous fracture planes ahead of the face or below the excavation floor. Each fracture plane should be oriented at a sufficient angle of incidence with respect to the main component of principal stress that is perpendicular to the tunnel axis. Consequently, the shear force acting across the fracture overcomes the stabilising forces, inducing deformation along the discontinuity. This implies that destressing charges should form rows which are sub-parallel, yet almost oblique, to this stress.

In structured rock, it is also advantageous to align the rows of destressing charges along the same orientation as any persistent joint sets which are also sub-parallel to the aforementioned principal stress component. Co-locating rows of destressing charges along visible pre-existing discontinuities of suitable orientation is ideal. This increases the likelihood of blast gases penetrating these joints during detonation and therefore also the fracture interaction between adjacent destressing charges necessary to form continuous planes of weakness. The cross-sectional symmetry of the blasthole pattern should be reflected around the tunnel centreline, in order to create the same destressing mechanism if developing towards the 180⁰ opposite azimuth.

A conceptual destressing blast pattern design reflecting these principles is presented in Figure 149. This figure indicates the radial fracture networks likely to be created by the destressing charges in a highly anisotropic stress field. Blast-induced rock fractures critical to the shear failure mode of energy dissipation are shown in red. Important parameters to consider in the destressing blast design include:

- b the destressing charge row burden (m),
- s the destressing charge inter-row spacing (m),
- ϕ the destressing charge diameter (mm),
- l_d the destressing charge length (m),

- l_{rf} the maximum length of radial fracturing or joint dilation (m)
- σ_1 the major principal stress (MPa),
- σ_3 the minor principal stress (MPa),
- $\theta\sigma_1$ plunge of the major principal stress (degrees),
- $\theta\sigma_3$ plunge of the minor principal stress (degrees),
- θ_r the angle formed between the horizontal plane and rows of destressing charges and/or the continuous fracture plane,
- θ_f the angle formed between the horizontal plane and the imaginary line joining the opposite ends of the radial fracture tips of adjacent rows of destressing charges,
- θ_{rf} maximum angle of incidence between the plunge of the major principal stress and the angular limit of blasting induced fracturing.

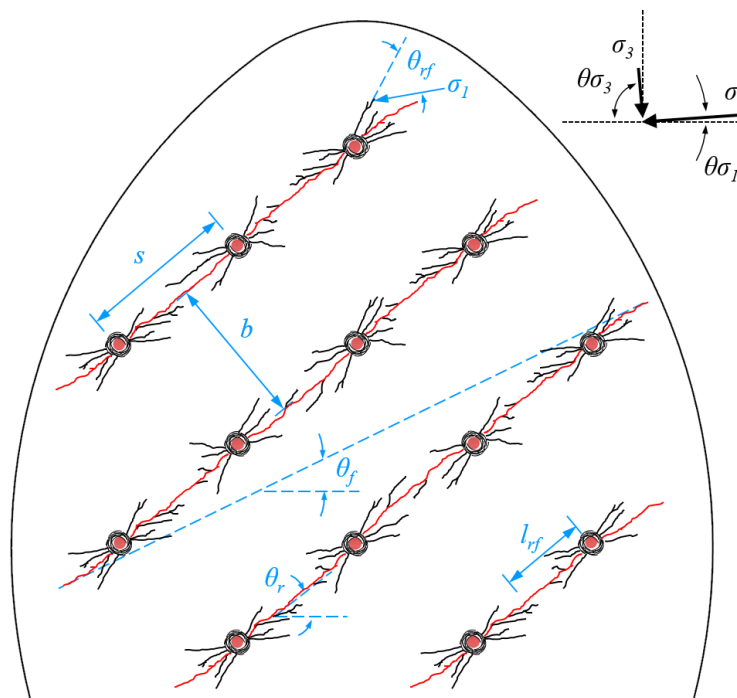


Figure 149 - Development face destress blasting concept and design parameters for the blasthole pattern.

The failure mechanism of this face destressing concept is analogous to that of a UCS test sample (Figure 150), whereby a plane of shear failure exists almost oblique to the major principal stress. The destressing explosives are responsible for artificially creating this critical shear fracture or weakening suitably oriented natural discontinuities in the rock. It is hypothesised that high-gas explosives such as ANFO assist to mobilise and dilate both natural and blast-induced radial fractures, thus reducing rock mass stiffness and the potential for violent stress-driven instability.

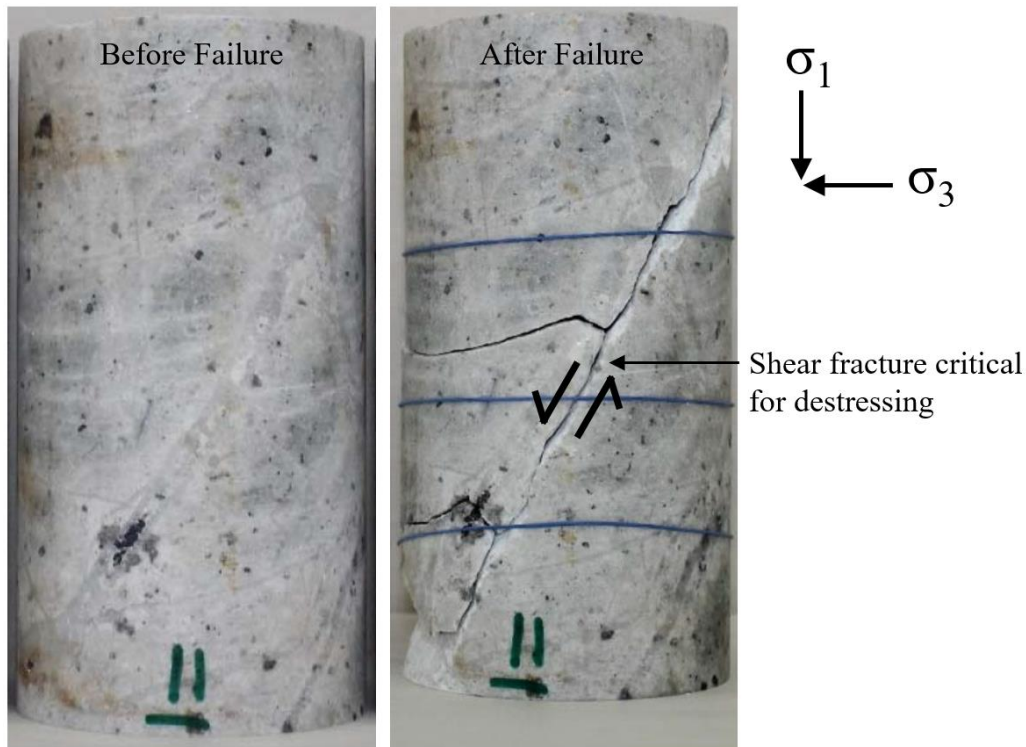


Figure 150 – UCS test sample failure mechanics analogous to face destressing.

Considering the observations of Jung, et al. (2001), the interaction of fractures from adjacent destressing charges is unlikely to occur sub-perpendicular to the major principal stress, i.e. across the burden. Therefore, the spacing between charges is the design parameter of greater importance when assessing crack interaction. The spacing dictates the amount of explosive work required for in-row fracture interaction between the destressing charges, with fracture interaction more likely for tighter spacing.

For fracture interaction to occur reliably, $l_{rf} > s/2$, where l_{rf} may be estimated empirically or, preferably, via numerical blast modelling and field validation. The principal stresses are also critical. The magnitude of the main principal stress component perpendicular to the tunnel axis (usually σ_1) controls fracture confinement, whereas its plunge guides the optimal angle (θ_r) of the rows of destressing charges.

In terms of the geometric design of the destressing rows, ideally θ_f should be greater than θ_{σ_1} by a sufficient angle in order to facilitate shear. Similarly, θ_r would ideally differ from θ_{σ_1} by 30-40 degrees, in order to promote shear deformation of the face. The parameter θ_{rf} may vary, depending upon rock mass strength properties, the explosive energy of the destress charge, the prevailing stress conditions and orientations of any pre-existing discontinuities. Fracture interaction between explosive charges would be expected to occur only where $\theta_r \leq \theta_{\sigma_1} + \theta_{rf}$.

It must be noted that this distress blasting design concept deliberately avoids the placement of charges beyond the planned perimeter of the excavation where permanent ground support will be installed. Attempts at distressing the shoulders, roof and walls of the excavations requires that charges be placed outside the final excavation perimeter. This creates several problems. Firstly, the explosives are expected to cause damage to the rock mass. This is likely to adversely affect the future stability of the excavation and may even facilitate violent failure of the permanent excavation boundary, which might not otherwise have occurred. In order to minimise the risk of such damage, distressing charges should be offset from the final excavation perimeter by a minimum distance equal to that of the burden between the perimeter charges and outer row of face holes.

Secondly, the potential for intersecting misfired distressing charges during subsequent ground support drilling is a safety hazard which requires onerous and time-consuming risk management measures. There are more effective controls available to manage violent instability around the permanent excavation perimeter. These include circular, semi-elliptical or even asymmetric excavation shapes which are harmonic to the stress field, together with immediate targeted installation of layers of high energy dissipation ground support (Villaescusa, et al., 2016b).

4.6.2.4.1 Site Specific Considerations

It is not recommended to implement generic distressing design patterns across multiple structural domains and stress regimes. Each distressing design should be optimised for the specific rock mass conditions within which it is implemented. This requires that all design parameters be assessed and revised if needed, when implementing distressing in a new development precinct. For example, when implementing distressing in a new structural domain and stress field, the distressing design parameters b , s , r and θ_r should all be re-evaluated, in order to ensure that the objective of continuous shear fracture creation is achieved in the new conditions. Whenever distressing is implemented in a substantially different geotechnical environment, the evaluation of these parameters would typically require a numerical modelling simulation to be performed. Each re-evaluation ensures that the site-specific rock mass conditions and related variability in blasting performance are always considered and revised, when necessary, to achieve consistent blast performance.

4.6.3 Ground Support

The ground support design for the northern tunnel followed six principle steps, the first two of which were completed prior to the excavation profile and blast design phase. The two aforementioned design steps include:

1. Excavation stability and failure mechanism assessment,
2. Estimation of the depth and mass of instability,

The subsequent four steps in the ground support design process, described in this section, are as follows:

3. Forecast the rock mass demand on ground support,
4. Select reinforcement and surface support elements with sufficient capacity,
5. Specify a ground support scheme arrangement,
6. Propose an installation sequence.

4.6.3.1 Rock Mass Demand

Ground support design methods of recent years have focused on the energy balance approach. That is, assessing the energy demand of the rock mass and factoring this against the energy dissipation capacity of the chosen ground support scheme. This approach requires that a surplus energy dissipation capacity be available from the ground support scheme, in order to contain any potential failure. An example of this design approach was given earlier in Figure 23.

The main problem with the existing methodology is the lack of any reliable correlation between the rock mass characterisation variables (such as rock strength, stress and potential mass of instability) and the failure variables needed to complete the demand assessment (i.e. ejection velocity and energy demand). Arguably the most widely used approach to calculating energy demand is to attempt to relate the seismic PPV to the ejection velocity and use this in the kinetic energy equation (Kaiser, et al., 1996). However, the mechanics of seismic loading are unproven and design methods exclusively focusing on this factor neglect the primary source of rock mass energy at the excavation boundary, which is stored strain energy. Furthermore, experience shows that the PPV method rarely predicts the actual location and severity of excavation damage (Potvin & Wesseloo, 2013, Drover, 2014).

As discussed earlier, the energy balance demand calculation requires two principal inputs. These are the mass of ejected rock per unit area and its ejection velocity. As an alternative to empiricism, Windsor (1999) provided an analytical solution to defining the unstable mass, using probabilistic block theory. This analytical approach is now formalised in the SAFEX design software. More recently, Kusui (2015) demonstrated the relationship between intact rock UCS and the ejection velocity of a violent, stress-driven failure in the corresponding rock type. An aim of this thesis was to incorporate this knowledge into a holistic ground support design methodology, which takes the rock mass characterisation variables and links them directly to the demand variables. The intent was to produce energy demand charts for ground support design.

The ejection velocity data recorded by Kusui (2015) shows a variability of around 2-3 m/s about the central trend line (Figure 151). This can be interpreted as an upper, mid and lower case ejection velocity for any given rock type. The reason(s) for this variability in the experimental data require further examination. However, it is hypothesised that intact rock rupture occurs with higher velocity and failure through pre-existing natural discontinuities happens at lower velocity. Intuitively, the accumulation of strain energy in structured rock may be limited by deformation along the discontinuities. Depending on the joint surface characteristics and orientation with respect to the stress, this could foreseeably result in structured rock exhibiting lower strain energy density at failure, when compared to massive rock of identical lithology. The ejection velocity may decrease with increasing joint frequency and decreasing joint strength. This theory requires further investigation. However, at this time, the variable range of ejection velocity in the Kusui (2015) data was assumed to be influenced by the pre-existing rock mass structure in the samples.

From the Kusui (2015) data, a first-order polynomial equation was derived for the upper, mid and lower case ejection velocities (Figure 151). These were hypothesised to each represent the maximum ejection velocity for a specific case of tunnel failure. The upper case equation represents the maximum expected ejection velocity due to failure of massive intact rock. The mid and lower case equations approximate ejection velocity in rock with very strong and moderately strong joints, respectively. These equations were used to generate three energy demand design charts, where UCS and the mass of instability were the two input variables. The three equations are as follows, where v_e is the ejection velocity and σ_c is the UCS:

Maximum ejection velocity in massive rock (upper case):

$$v_e = 0.0287\sigma_c + 5 \quad (Eq. 4.5)$$

Maximum ejection velocity in rock with frequent very strong joints (mid case):

$$v_e = 0.0287\sigma_c + 2.5 \quad (Eq. 4.6)$$

Maximum ejection velocity in rock with frequent moderately strong joints (lower case):

$$v_e = 0.0287\sigma_c \quad (Eq. 4.7)$$

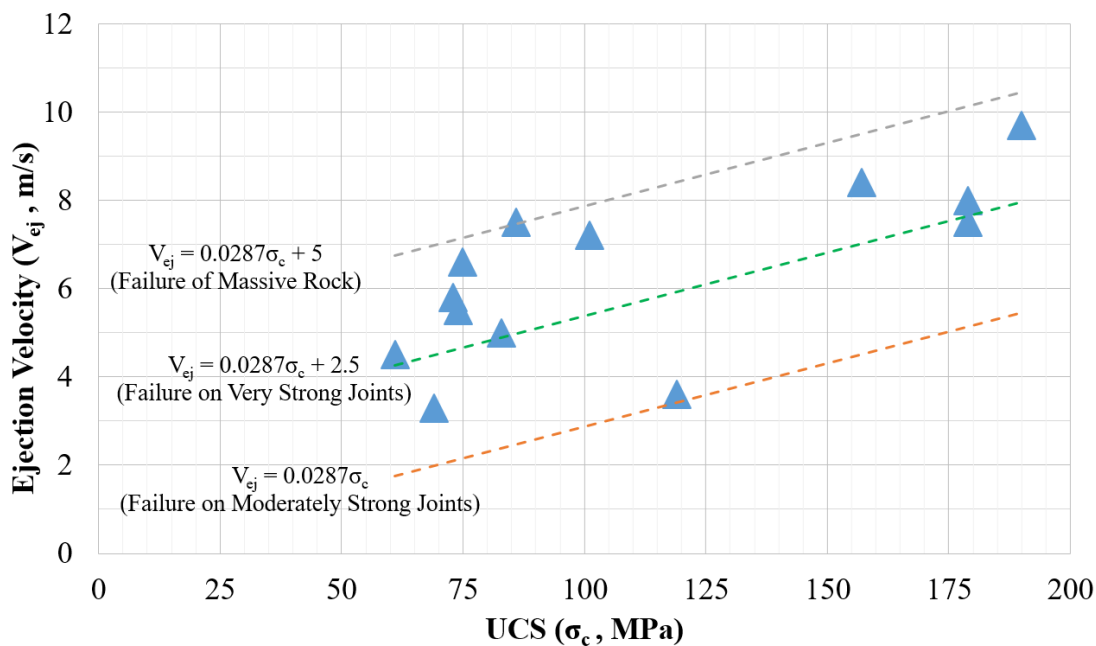


Figure 151 – Hypothesised ejection velocity limits considering rock joint strength (data from Kusui, 2015).

The ground support design chart shown in Figure 152 is proposed to be used for tunnels which are typically constructed in massive rock types with little to no jointing, where stress-driven failure can be expected to occur through intact rock. The design chart in Figure 153 is proposed for tunnel constructions in rock with very strong joints, where tunnel wall failure may be influenced by the joint strength. Finally, Figure 154 is proposed for tunnels constructed in hard rock containing frequent moderately strong joint surfaces. Each charts reflects updated demand categories after Villaescusa, et al., (2014), as shown in Table 40. The typical range of energy demand for spalling and structurally controlled failure mechanisms are indicated on the right hand side of the demand charts. Note that this concept of joint strength influence on ejection velocity does not imply that the event is a *structurally controlled failure*, as defined earlier.

Table 40 - Updated rock mass force-displacement-energy demand categories.

Demand Category	Reaction Pressure (kPa)	Surface Displacement (mm)	Energy (kJ/m²)
Very Low	< 100	< 50	< 5
Low	100 - 150	50 – 100	5 – 15
Medium	150 - 200	100 – 200	15 – 25
High	200 – 400	200 – 300	25 – 35
Very High	400 – 500	300 – 400	35 – 45
Extremely High	> 500	> 400	> 45

The energy demand on ground support in the research tunnels was determined by first selecting the appropriate demand chart to suit the structural characteristics of the rock mass. The demand line corresponding to the maximum unstable mass was then referenced on the chart. For structurally controlled failure, the unstable mass was defined by dividing the maximum expected block mass by the block free face area. The result was expressed in tonnes per unit surface area of the excavation where the failure may occur (i.e. T/m²). The expected ejection velocity was then cross-referenced from the measured UCS of the excavation host rock. The estimated energy demand on the ground support scheme could then be read from the chart's vertical axis, where the ejection velocity intercepts the corresponding demand line.

The energy demand on the north and south research tunnels was estimated separately, considering the structural characteristics, Dacite strength properties, ejection velocity and maximum anticipated mass of instability. The tunnels were constructed in hard rock with moderately strong joints. There was infrequent evidence of low strength infill materials. Therefore, the relevant energy demand design chart was Figure 153. The UCS of Dacite in the northern tunnel typically ranged from 134 to 190 MPa, with an average of 162 MPa. This suggested a plausible range of ejection velocity of 6.3 to 7.9 m/s, most likely around 7.1 m/s. Given the assumed apex height (i.e. depth of failure) of 1.38m for Block 4, as well as free face area of 2.3m² and total block mass of 3.0T (see Table 19), the maximum instantaneous unstable mass in each tunnel was predicted to be 1.3 T/m². From the 1.5T/m² demand line in Figure 153, the energy demand acting on the ground support in the north tunnel was predicted to be in the range of 30-50 kJ/m². The value of 50kJ/m² was chosen for design purposes. This demand range reflects the variable mechanical properties of the rock mass along the tunnel length and hence the potential variability in the mechanical response to loading.

The southern tunnel exhibited a different range of measured strength properties, with a standard deviation of 40 MPa around the lower average value of 120 MPa. Therefore, the ejection velocity in the south tunnel was anticipated to be within the range of 4.6 to 7.0 m/s, and most likely around 5.8 m/s. Assuming the same mass of instability as the northern tunnel, the expected energy demand on the ground support scheme fell within the range of 15 to 40 kJ/m². This energy demand estimation takes account of the specific mechanical conditions relevant to the southern tunnel.

The energy demand defined in this way was assumed to be the maximum that may occur during the life of the excavations. It is likely to occur only if the maximum unstable structural block exists and the σ_c/σ_{max} ratio reduces below the threshold for violent structural instability. As per the stability analysis described in Section 4.4, it was presumed that a spalling demand of approximately 20 kJ/m² could occur at any time during development. Structurally controlled failure would not occur unless the stress conditions increased beyond those measured immediately prior to development. This could occur later during the mine life, for example during future production.

Ideally, numerical modelling should also be used to examine the maximum σ_c/σ_{max} ratio experienced during the excavation's service life. The stability of the excavations would then be re-assessed for that specific condition, as per the method in Section 4.4. This examination would reveal whether or not the future stress conditions are sufficient to induce not only spalling, but also later-stage damage mechanisms, such as violent structural failure and pillar crushing. In the affirmative case, the maximum energy demand indicated by the design chart above is likely to be realised. If the future stress conditions are not sufficient to induce later-stage failure of the excavation, then the spalling demand, limited at approximately 20kJ/m², may be the valid maximum energy demand for ground support design, although this could occur repetitively.

Long term numerical stress modelling results were not available from the mine site in this case. As such, the future maximum σ_c/σ_{max} ratio at the research tunnels remained unknown. However, since the available stability analysis (Figure 98) indicated a small potential for structural failure / pillar crushing, it was assumed that the onset of these mechanisms would increase in probability as the orebody is extracted and abutment stresses inevitably increase in the Dacite unit. Therefore, it was assumed that the maximum energy demand in each tunnel would be likely to occur in the future.

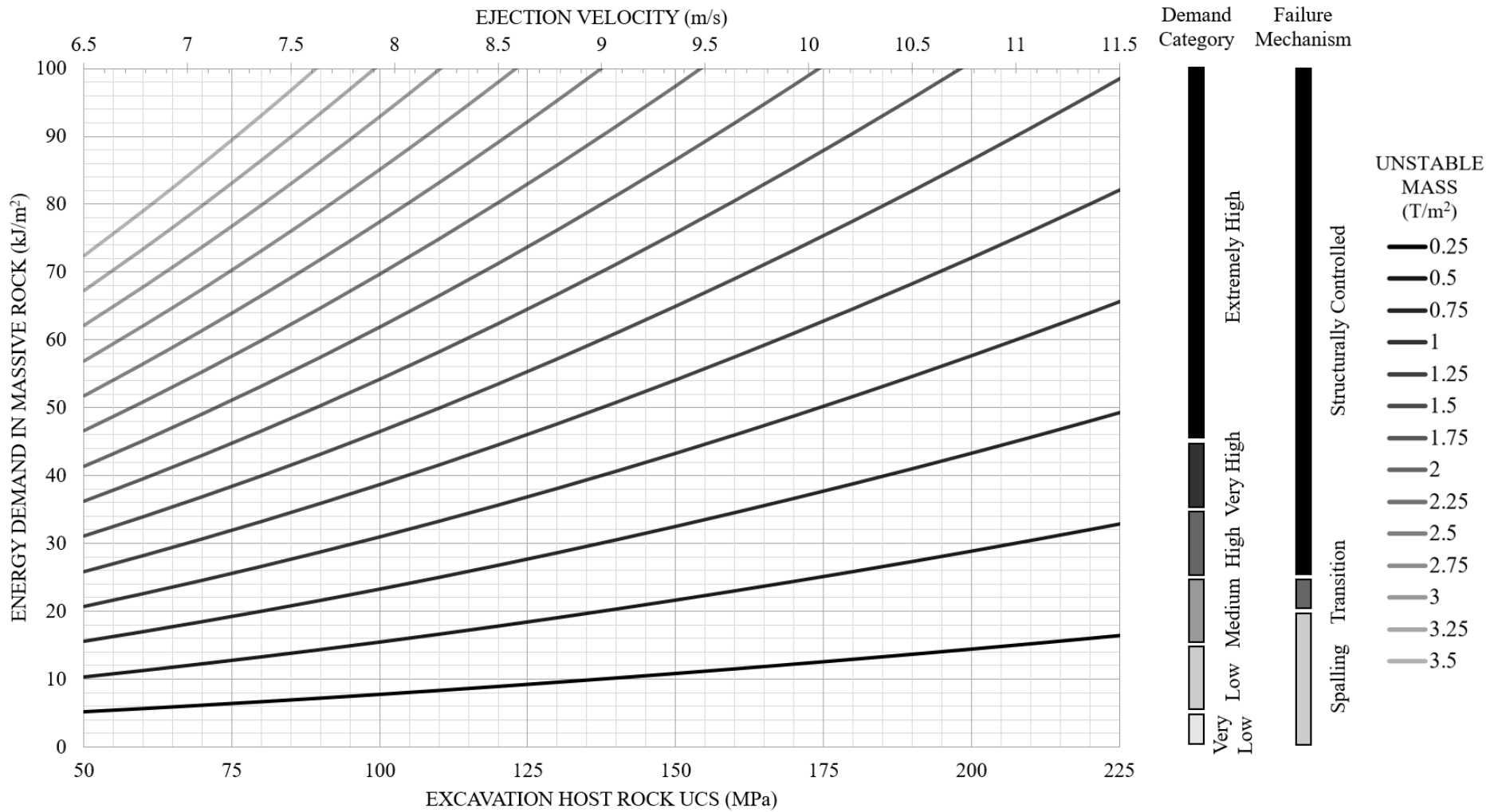


Figure 152 - Energy demand chart for ground support design in massive hard rock.

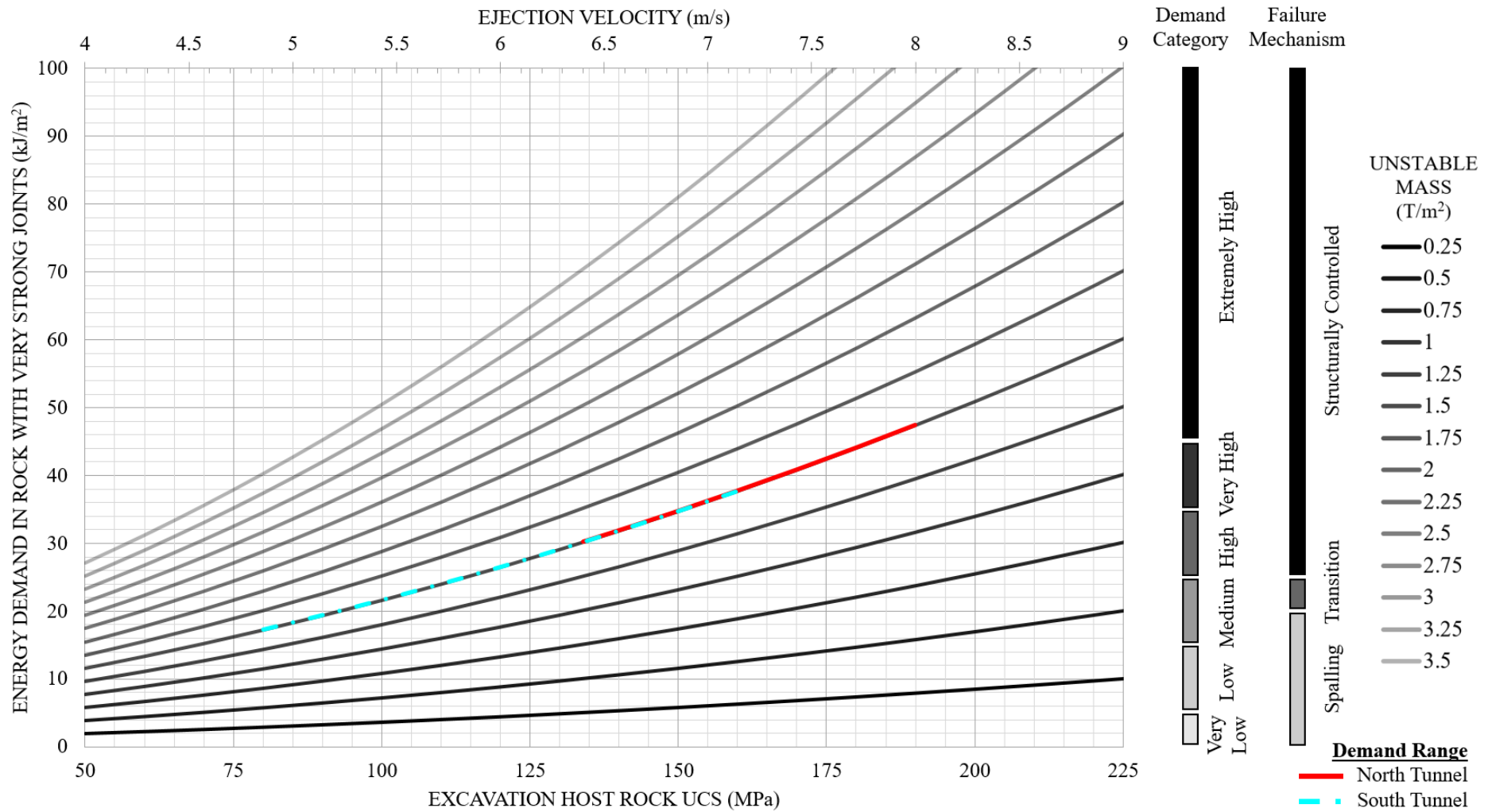


Figure 153 - Energy demand chart for ground support design in hard rock with strong joints.

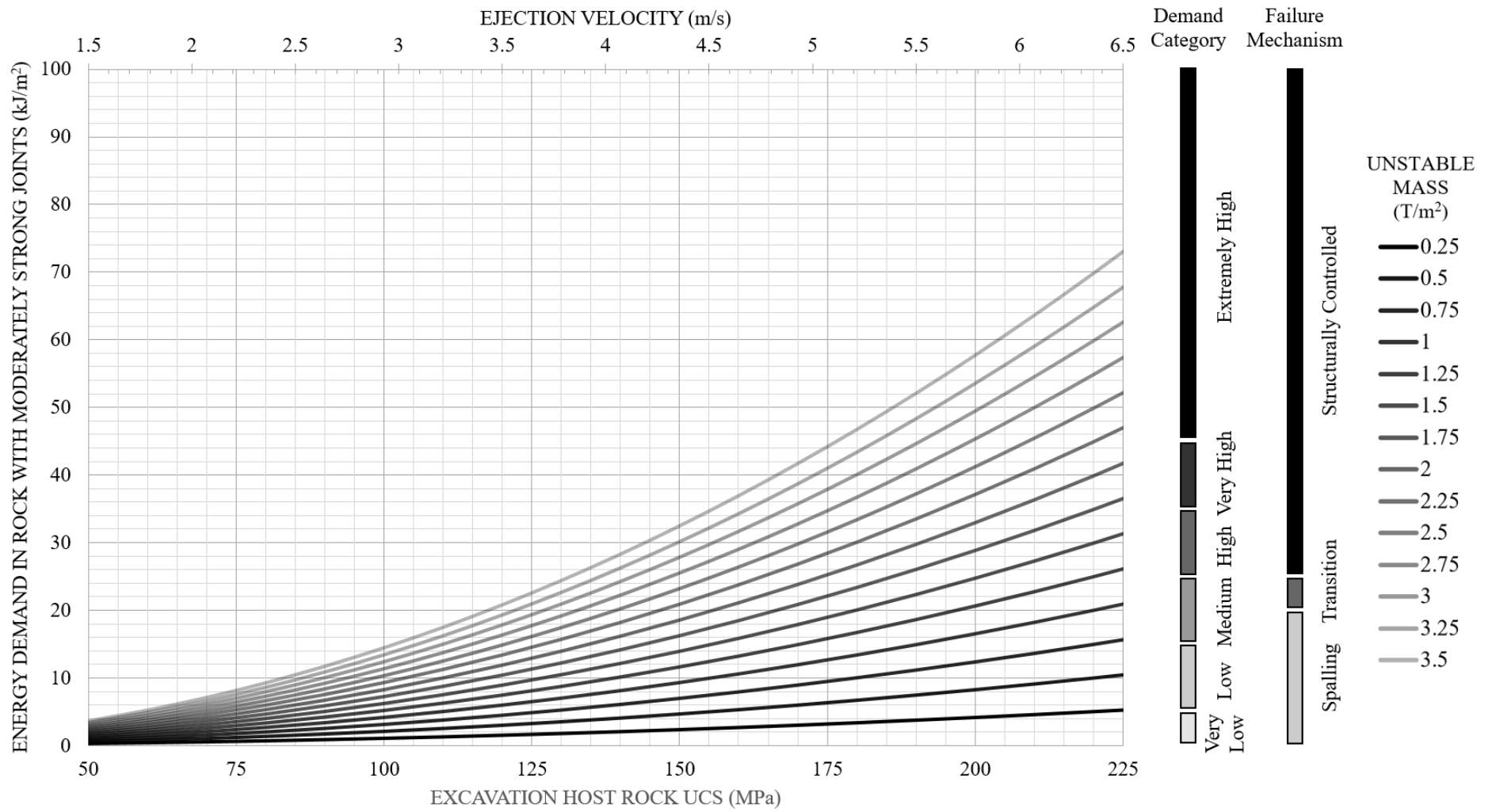


Figure 154 - Energy demand chart for ground support design in hard rock with moderately strong joints.

4.6.3.2 Reinforcement and Surface Support Selection

The WA School of Mines have produced a large database of the energy dissipation capacity of various reinforcement elements and surface support components. This data was used to select the appropriate capacity ground support components, and specify their arrangement, to meet the rock mass demand. The WASM reinforcement design chart was first introduced by Villaescusa, et al. (2014). That chart was updated for this thesis as shown in Figure 155. The chart now contains three design regions for specific energy and displacement demand requirements. These three regions are shaded green, yellow and blue. These regions were used to ascertain what type of reinforcement elements would prove suitable to meet the rock mass demand in the Dacite unit and whether the ground support scheme required one or more interconnected layers of reinforcement and surface support.

The design regions and corresponding ground support scheme arrangements have been selected on the basis of the large database of WASM dynamic tests as well as field observations. The green design region on the chart implies that single-layered ground support schemes are appropriate where maximum displacements are 200mm and the energy demand is less than 45 kJ/m². The yellow transitional zone, between 200-300mm displacement and 35-45 kJ/m² energy demand, indicates that two interconnected layers of reinforcement and surface support may be appropriate in this demand range. The chart also implies that two interconnected ground support layers are necessary wherever the rock mass demand exceeds 45 kJ/m².

According to this methodology, suitable reinforcement elements are selected on the basis of their measured energy dissipation and displacement capacity falling within the relevant design region. That is, the suitable reinforcement element should plot within the green, yellow or blue design region. For a ground support scheme with a single reinforcement layer, the suitable element should plot above the relevant demand category indicated by the black dashed polygons. The element may plot above or within the *Very Low* to *Very High* demand category polygons if two passes of reinforcement are installed to increase the capacity. Reinforcement elements plotting within the remaining white zone of the chart (i.e. below the *Very Low* to *Very High* demand polygons, and within the *Extremely High* demand polygon) are regarded as unsuitable for any given design. This is due to their displacement performance being mismatched to most surface support systems.

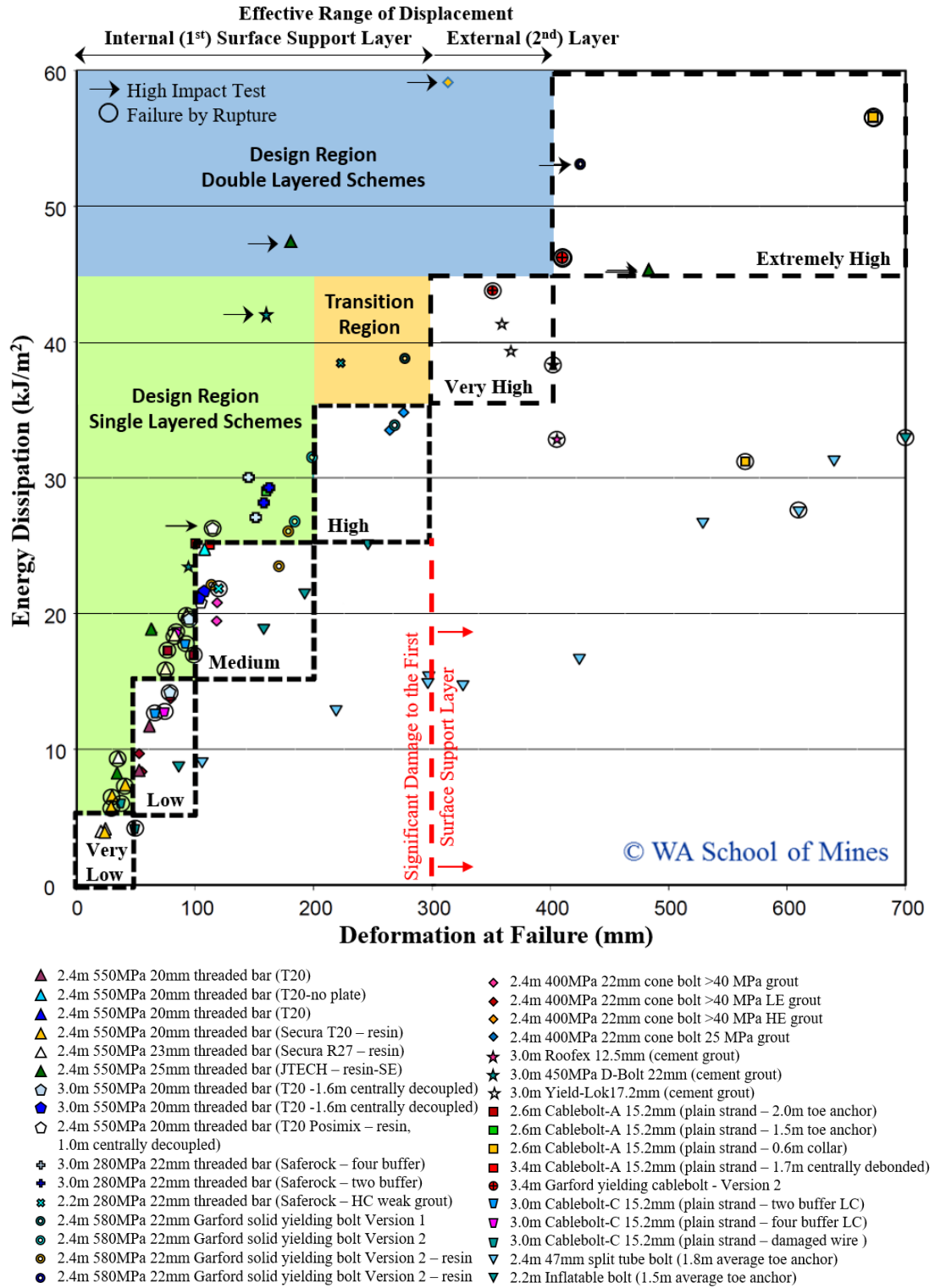


Figure 155 - Reinforcement design chart, modified after Villaescusa, et al., (2014).

Reference to surface support displacement information is useful to attach to the reinforcement design chart, as the chosen reinforcement elements must be compatible with the surface support scheme. That is, the maximum energy dissipation capacity of both the reinforcement and surface support components must be achieved over the same range of displacement. In this way, premature failure of weaker elements in the system, potentially leading to catastrophic failure, is avoided. Where the displacement capacity of all components in the ground support scheme are similar, or identical, the entire system could be expected to dissipate the maximum possible energy prior to individual component failures.

In general, a ground support scheme may include a primary and secondary scheme of reinforcement and surface support. The primary scheme may be installed first, and the secondary scheme at some later time. The effective range of displacement for the primary and secondary surface support layers are indicated by the arrows above the main chart. For a single-layered surface support system, typically consisting of welded or woven mesh encapsulated in shotcrete, the effective range of displacement is $\leq 300\text{mm}$ (Drover & Villaescusa, 2015a). Beyond this threshold, observational evidence indicates that the surface support will suffer significant damage (Villaescusa, et al., 2014). Therefore, the chart implies that two layers of reinforcement and support are necessary wherever the displacement demand exceeds this 300mm limit, for example due to structurally controlled failures with large blocks.

Demand conditions plotting in the far upper right region of the chart are extremely high, and it is assumed that significant damage will be sustained to the primary surface support layer in such conditions. For double-layered schemes, an external layer of high-tensile woven mesh may be able to tolerate 700mm or more of displacement, prior to catastrophic failure. The deformation capacity would depend on the connectivity of the mesh to reinforcement elements in adjacent stable ground (Figure 156). More than 700mm of radial deformation of the mesh may be survivable if the mesh is connected to reinforcement elements which also experience some displacement at the collar. However, as a design assumption, secondary surface support layer deformation is suggested to be limited to 400mm. Weld mesh cannot reliably tolerate such levels of deformation, due to its rigid strand connections and mild steel construction (Villaescusa, et al., 2012). Therefore, high tensile woven mesh is preferred for very high demand dynamic loading conditions.



Figure 156 - Large displacement of external woven mesh connected to adjacent stable reinforcement.

With regard to the case of the northern research tunnel, the maximum energy demand on the ground support was estimated to be 50kJ/m^2 . This falls into the *Extremely High* demand category. According to this design method, a double-layered ground support scheme was needed to contain any potential future instability. The reinforcement element selected for the first pass ground support installation is referred to as the primary reinforcement element. The primary reinforcement chosen for implementation in the north tunnel was a continuously mechanically coupled, 25mm diameter, 550 MPa mild steel threaded bar, fully cement-grouted. This element was compatible with a woven mesh-reinforced shotcrete surface support system, as its maximum energy dissipation capacity of 45kJ may be achieved after only 180mm of axial displacement. That is, less than the 300mm threshold for significant surface support damage.

In addition to the high energy dissipation capacity, these CMC elements were chosen due to reliable load transfer characteristics in structurally complex rock under high stress. Certain DMFC reinforcement elements, such as toe and collar resin or cement encapsulated bars, may also be suited to such conditions. The centrally decoupled segment of the element assists energy dissipation through yield of the bar. However, sufficient encapsulation of the element must be achieved at the desired points of load transfer to the rock mass. Other DMFC elements, such as point anchor bolts, were considered to be poorly suited to such conditions, due to unreliable load transfer at the collar and anchor assembly. CFC elements were also avoided due to poor load transfer characteristics and low energy dissipation capacity (Villaescusa, et al., 2016b).

G80/4 high tensile (1770 MPa) woven mesh was selected for use in the primary surface support layer, due to its superior energy dissipation and displacement capacity in comparison to mild steel weld mesh (Villaescusa, et al., 2012). This mesh has an aperture of 80mm and wire diameter of 4mm. The results of WASM dynamic testing on 1.3m x 1.3m mesh samples indicate approximately 8.3kJ/m² of energy dissipation at 300mm displacement, corresponding to the point of first strand rupture (Figure 157). In practice, the mesh was confined and embedded within a 50mm thick shotcrete layer, which increases its capacity. As such, the mesh was less liable to suffer unravelling of the wire after individual strand failures. Considering the superior performance of mesh-reinforced shotcrete, as well as the material improvements made by the mesh manufacturers since the original WASM testing, this arrangement was expected to provide energy dissipation capacity as high as 15kJ/m².

The secondary reinforcement elements chosen for the ground support scheme were 15.2mm diameter, 1770 MPa high tensile, twin plain strand cable bolts, in a cement-grouted CMC arrangement. Cable bolts were chosen for several reasons, including their high energy dissipation capacity, reliable load transfer characteristics, deep embedment capability and displacement compatibility with an external high tensile mesh system. Single plain-strand cables are capable of dissipating 28kJ of energy over a displacement range of 150mm (Figure 155). Continuous mechanical coupling of the cable using cement grout retains load transfer capability along the entire length of the cable, which also improves the shear capacity of the excavation. The complete encapsulation of the cable element also avoids preferential load transfer to the surface fixtures, which may weaken over time due to corrosion. The cable-bolting secondary reinforcement was designed to manage deep structurally-controlled instability.

The secondary surface support system consisted of G65/4 high tensile (1770 MPa) woven mesh. This secondary layer of surface support was installed externally, over the primary ground support layer of mesh-reinforced shotcrete and threaded bar reinforcement. The external mesh layer was intended to provide additional energy dissipation capacity to the system, as well as contain any failure of the primary ground support scheme. The secondary mesh layer was connected to the cable bolts and threaded bars via surface fixtures. Given recent WASM testing (Villaescusa, et al., 2012) and manufacturer improvements to the mesh, this secondary layer of woven mesh was assumed to contribute 15 kJ/m² of energy dissipation capacity to the system.

Shotcrete was not included in the secondary ground support layer for several reasons (Villaescusa, et al., 2016b). Firstly, the secondary surface support layer was intended to have a larger displacement capacity than the primary layer, such that it could contain it in the event of it failing. Secondly, external shotcrete layers have potential to spall, releasing large shotcrete fragments. This may occur at cold joints between the layers or through intact shotcrete (Figure 158). To control this, the secondary mesh layer was installed within a short timeframe.

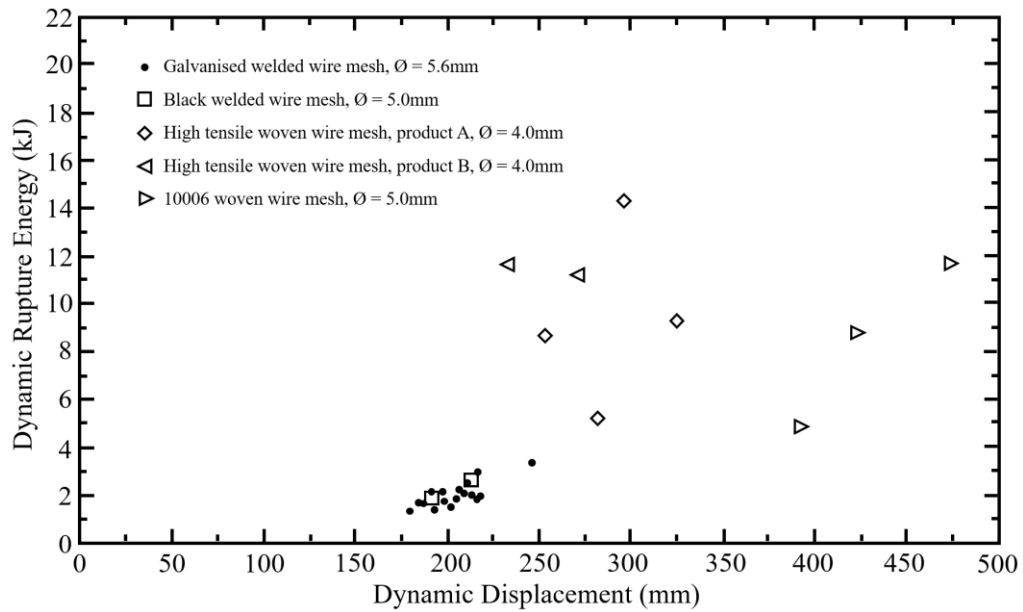


Figure 157 – Dynamic energy dissipation and displacement capacity of mesh (Villaescusa, et al., 2012).



Figure 158 - Failure of an exposed mesh-reinforced shotcrete layer due to violent spalling.

4.6.3.2.1 Tensile/Radial Capacity

For failure mechanisms involving radially inward deformation of the rock mass, each reinforcement element may experience a combination of tensile, shear, torsional and bending loads. Similarly, the surface support may experience compression, tension, shear or flexural loads. For simplicity and consistency in reporting, the capacities of the reinforcement and surface support components are generally quantified in terms of their tensile and radial capacities, respectively. This relates to excavation failure mechanisms in which the failure motion is predominantly radially inward towards the excavation.

The following data in Table 41 summarises the design assumptions in terms of energy, force and displacement dynamic capacity of the reinforcement and surface support components selected for the extremely high energy dissipation ground support scheme.

Table 41 - Summary of ground support component force, displacement and energy dynamic capacity.

Component	Force	Energy	Disp.
Shotcrete	80 kN	2.5 kJ/m ²	50mm
G80/4 (Internal)	200 kN	12.5 kJ/m ²	300mm
25mm Bar	295 kN	45 kJ	180mm
G65/4 (External)	300 kN	15 kJ/m ²	300mm
Twin 15.2mm Cable	530 kN	56 kJ	150mm

4.6.3.2.2 Shear Capacity

In addition to providing tensile capacity to manage radial instability, the installed reinforcement also resists shear failure of the excavation. Shear may occur along natural structures or any other failure plane adjacent the excavation. The shear capacity of the cable bolts for the range of potential shear conditions was assumed to follow the behaviour observed by Bawden, et al. (1995). In this case, the shear capacity of the cable was assumed to remain relatively consistent with the ultimate tensile strength for shear angles between 0 (pure tensile) and 40 degrees (oblique shear), beyond which point the shear strength decreased. This behaviour was also assumed for the threaded bar reinforcement. Both reinforcement elements were assumed to have an ultimate shear force capacity of 70% of the UTS for shear angles of 90 degrees (pure shear), as defined in Table 42.

Table 42 - Summary of reinforcement ultimate shear force capacity.

Reinforcement Element	Ultimate Capacity (Pure Shear)
25mm Thread Bar (Primary)	205 kN
15.2mm Twin Strand Cable (Secondary)	370 kN

Where reinforcement elements were installed crossing a shear failure plane perpendicularly, their shear capacity was assumed to be 70% of the ultimate tensile capacity of the element. A chart illustrating the assumed shear force capacity of the reinforcement elements as a function of the shear angle, measured from the pure tension condition, is depicted in Figure 159. Note that the assumed relationship between the shear angle and shear capacity as a percentage of the ultimate tensile strength is plotted as the black dashed line on the primary (left) axis. The reinforcement element force capacities used for design purposes are plotted on the secondary (right) axis. The shear capacity of the ground support scheme was quantified as the sum of the shear capacity of the individual reinforcement elements that were activated by a particular shear mechanism.

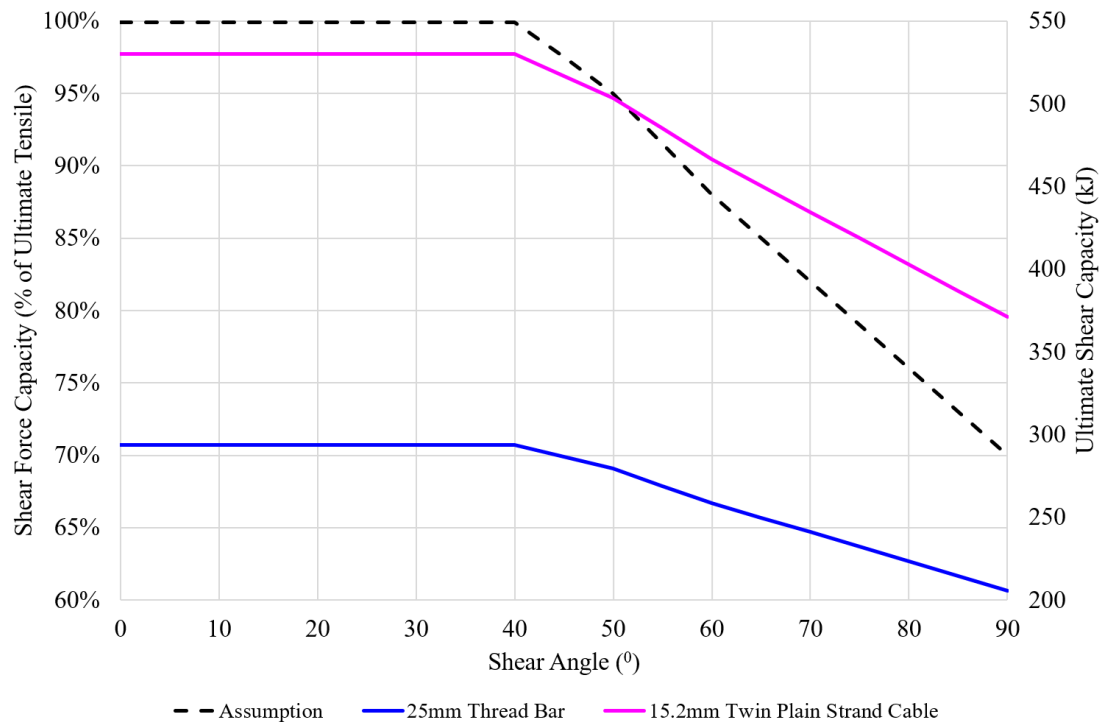


Figure 159 - Reinforcement shear force capacity assumptions used for ground support scheme design.

4.6.3.3 Ground Support Scheme Specification

The ground support scheme installed for extremely high energy dissipation (HED) capacity in the northern research tunnel consisted of two systems. The primary system of reinforcement and surface support was installed to control spalling and medium demand ($< 25\text{kJ/m}^2$) stress-driven instability. The secondary ground support system provided additional capacity with deep reinforcement embedment. This was designed to manage structurally controlled excavation failure and extremely high energy demand in the event of failure or significant damage to the primary system. The reinforcement and surface support components of both systems were interconnected to ensure load transfer to all components of the scheme during all failure mechanisms.

The longitudinal and transverse cross section drawings of the primary ground support system are shown in Figure 160. The primary surface support system consisted of an 80mm thick layer of mesh-reinforced shotcrete. This was installed from floor-to-floor to completely cover the excavation sidewalls, shoulders and roof. The shotcrete strength specification was 30 MPa UCS after 28 days. Fibres were not included in the shotcrete mix, as they provide minimal strength benefit when the shotcrete is internally reinforced with mesh (Drover & Villaescusa, 2015a). The shotcrete was applied in two layers and was internally reinforced with G80/4 articulating mesh. Mesh was installed in the form of 2.4m wide sheets which were continuous from floor to floor.

The primary reinforcement elements consisted of 3.5m-long, 25mm diameter, CMC cement-grouted threaded bars, installed in a 1m x 1m staggered pattern. This pattern resulted in an effective in-row spacing of 2.0m between the threaded bar elements. This in-row spacing provided sufficient short-term energy dissipation capacity of 37.5kJ/m^2 in the primary ground support scheme to safely exceed the predicted areal demand for spalling mechanisms of failure. This pattern was eventually infilled by the secondary reinforcement pattern. The depth of embedment of the primary reinforcement elements was 3.25m, leaving a 250mm long tail exposed for double-plating. Mild steel domed plates, 200mm x 200mm x 8mm with spherical seated nuts provided load transfer between the reinforcement element and surface support layers. The 80mm thick mesh-reinforced shotcrete layer and 1m x 1m staggered pattern of threaded bar reinforcement formed the primary ground support system.

Chapter 4: Design

The secondary ground support system was installed over the primary layer of surface support. The longitudinal and transverse cross section drawings of the secondary ground support system are shown in Figure 161. G65/4 woven mesh was installed in 2.4m wide sheets over the primary surface support layer. These secondary mesh sheets were continuous from floor to floor and offset laterally by 1.0m with respect to the mesh sheets in the primary support layer, such that the mesh overlaps of both layers did not coincide with the same row of reinforcement. This arrangement is illustrated in Figure 162 and Figure 163, which also illustrates the complete ground support scheme arrangement. G80/4 and G65/4 mesh sheets were overlapped at Cross-section A and Cross-section B, respectively, as illustrated. Offsetting the mesh sheets in this manner reduced the risk of ejected rock breaching the surface support layers due to separation of the mesh sheets at the overlap.

Secondary reinforcement elements were high tensile, twin strand plain cables, CMC fully cement grouted and installed equidistantly within the spacing of the primary reinforcement pattern. As such, the pattern of cable bolts mirrored the 1m x 1m staggered pattern of the primary reinforcement, with cables installed between the existing threaded bars. Cables were 5.5m in overall length, with a 5.0m depth of embedment and a 0.5m exposed tail. The primary and secondary reinforcement were designed to be positioned in parallel rows coinciding with each mesh overlap. Mesh overlaps were a minimum of 300mm wide to ensure load transfer (Figure 164). Securing each overlap of the mesh layers was critical to ensure that load transfer was able to occur between all the surface support and reinforcement elements.

A detailed view of the arrangement of the complete ground support scheme is shown in Figure 165. Load transfer mechanics between each layer are illustrated in a force diagram in Figure 166, and the list of relevant symbols is shown in Table 43. Load transfer between both surface support layers and both the primary and secondary reinforcement elements was achieved using a double plate arrangement on the threaded bars, as well as a plate assembly on each twin strand cable. Two plates were installed on each threaded bar, one prior to the second shotcrete application and the other subsequent to it. Furthermore, both cable strands were tensioned using barrel and wedges so as to ensure load transfer to both strands through the plate. The external cable bolt strands were also unwound, so as to increase the axial force capacity needed to cause displacement of the cable strand through the barrel and wedge.

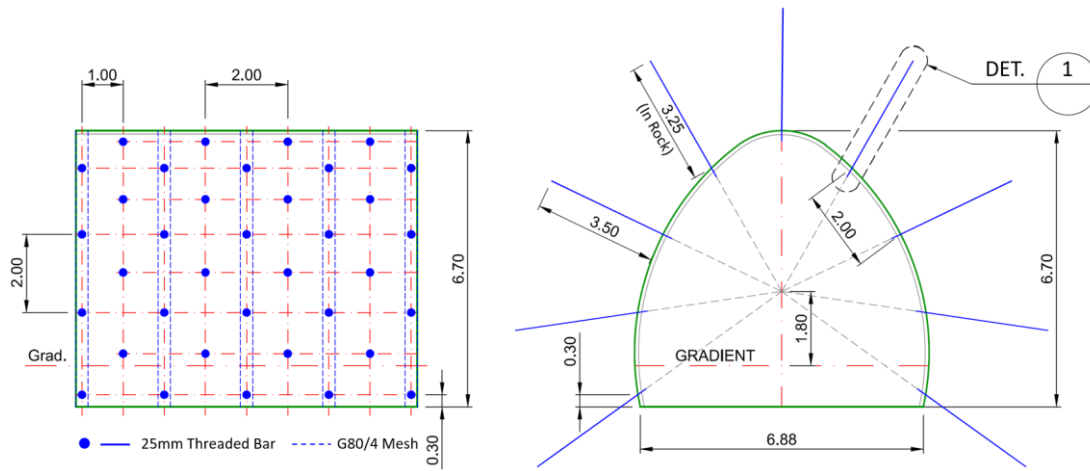


Figure 160 - Primary ground support layer, reinforcement pattern and surface support .

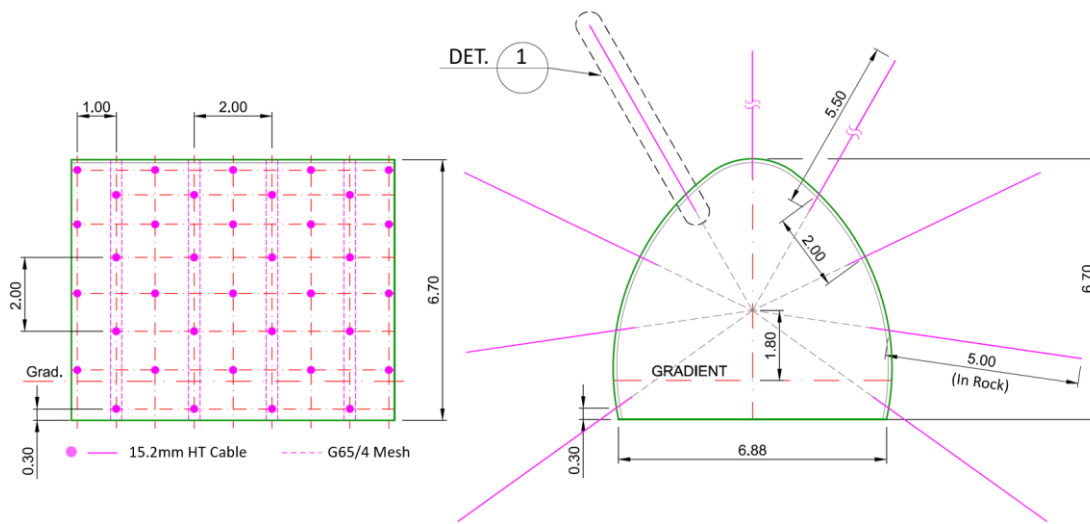


Figure 161 - Secondary ground support layer, reinforcement pattern and surface support.

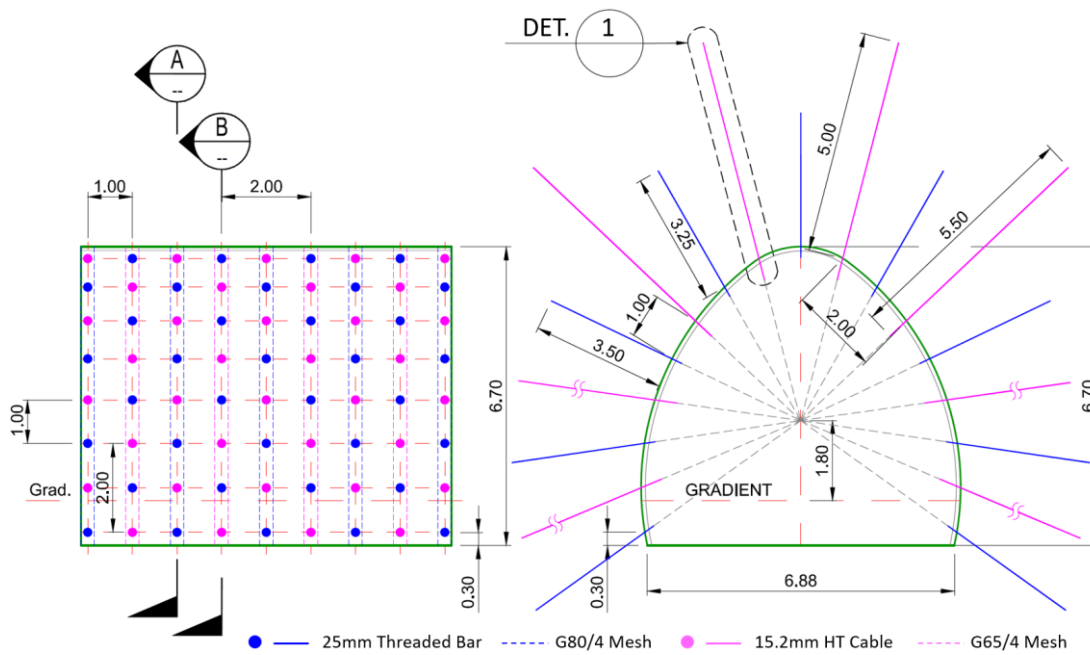


Figure 162 - Complete ground support scheme arrangement and Cross-Section A.

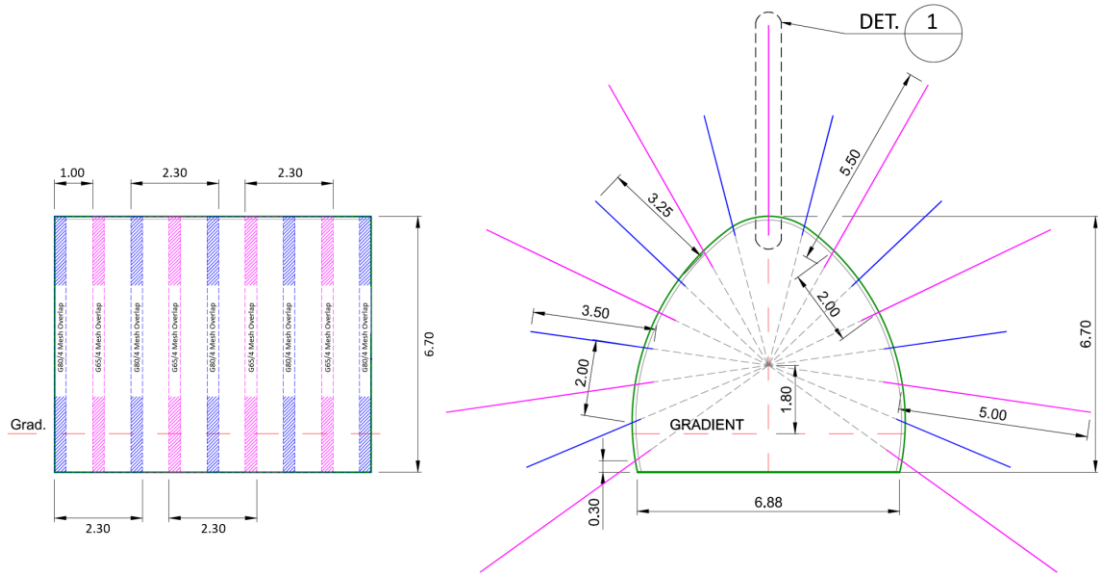


Figure 163 – Mesh overlap pattern and complete ground support scheme arrangement at Cross-Section B.

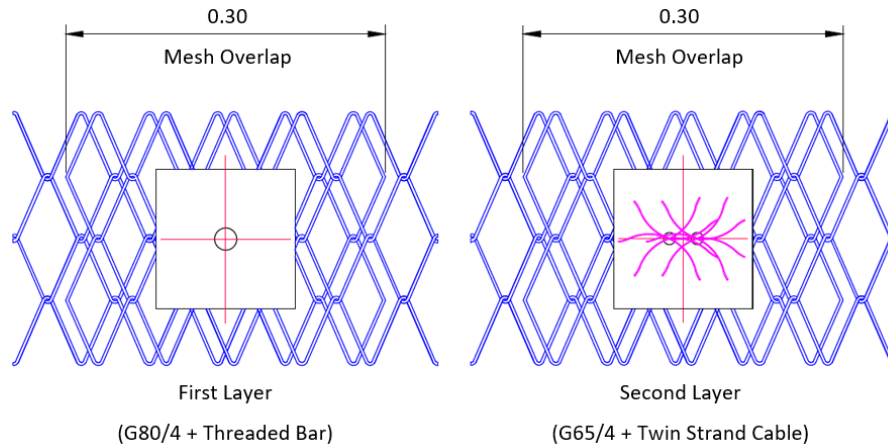


Figure 164 – Detailed view of mesh overlap arrangement for the first and second ground support layers.

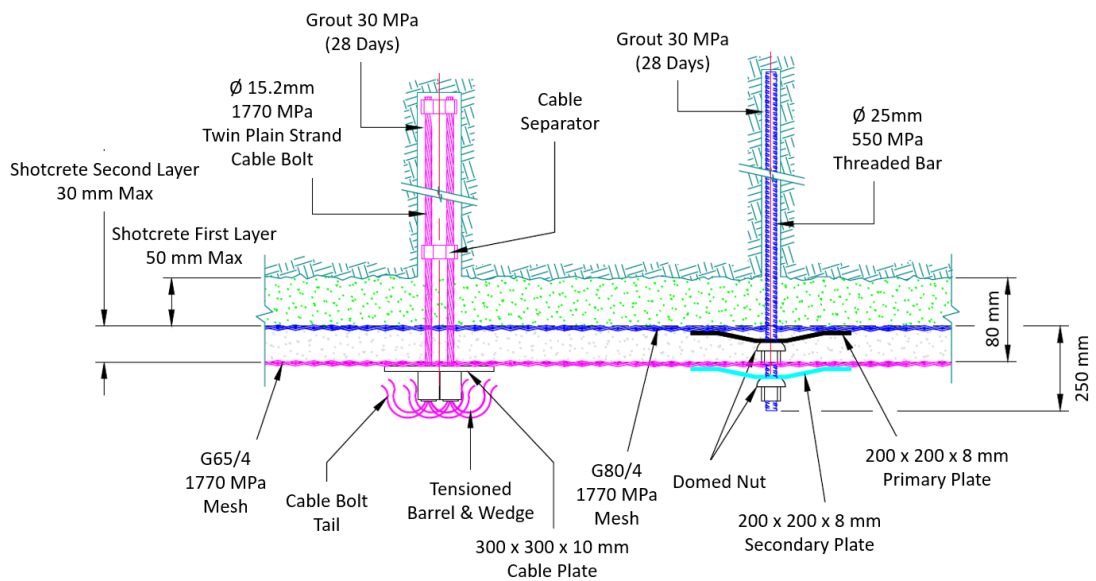


Figure 165 - Detailed view (*Det. 1*) of ground support scheme for extremely high energy dissipation.

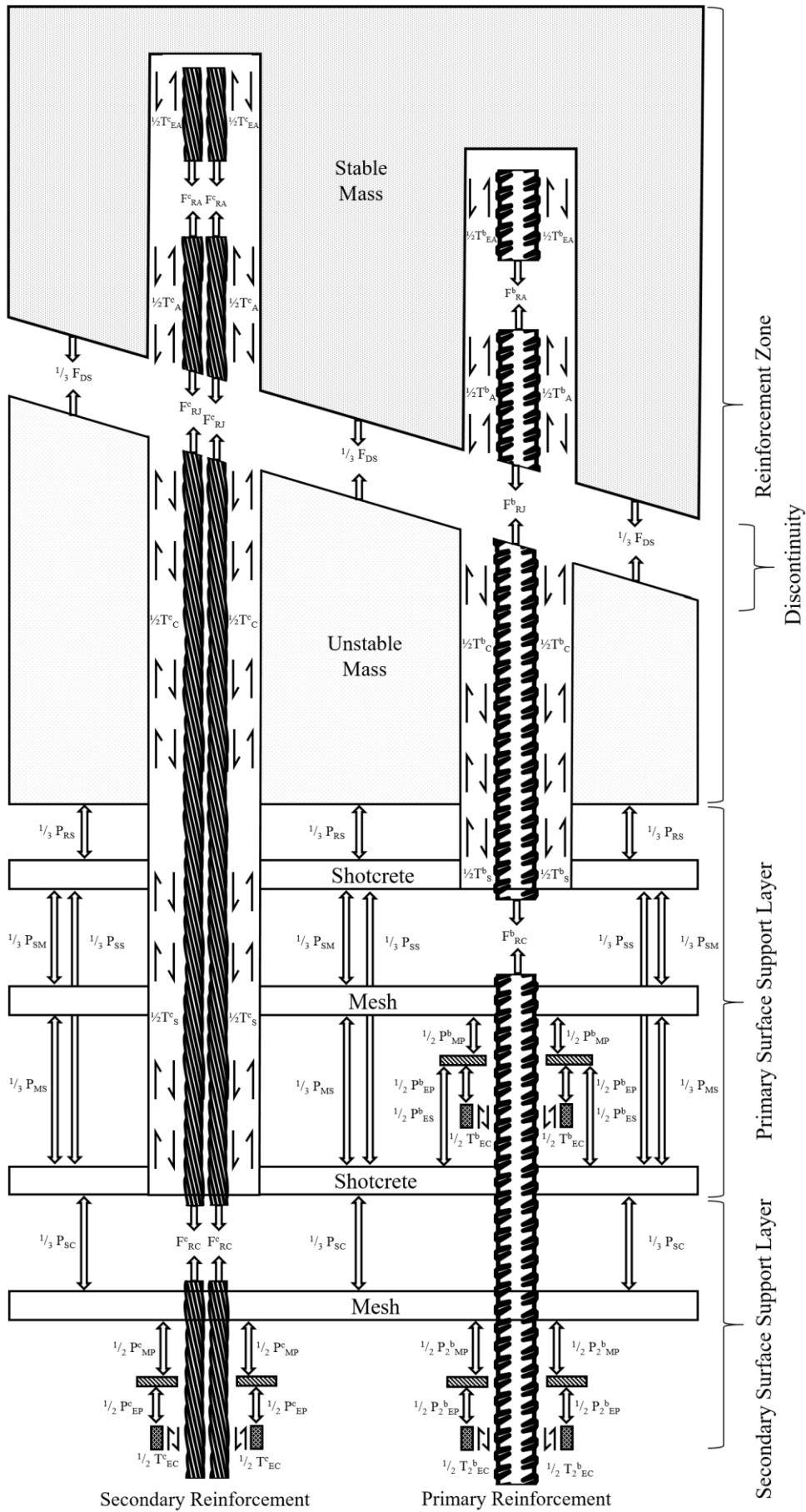


Figure 166 - Schematic of ground support scheme load transfer mechanisms.

Table 43 - Ground support scheme load transfer symbols (following Villaescusa, et al., 2005 notation).

T_{EA}^b	Load transfer between the bar element and borehole wall at a discrete anchor point.	T_A^b	Load transfer between the bar element and borehole wall in the anchor zone.
T_C^b	Load transfer between the bar element and borehole wall in the unstable zone near the collar.	T_S^b	Load transfer between the bar element and primary shotcrete layer at the collar.
T_{EA}^c	Load transfer between the cable element and borehole wall at a discrete anchor point.	T_A^c	Load transfer between the cable element and borehole wall in the anchor zone.
T_C^c	Load transfer between the cable element and borehole wall in the unstable zone near the collar.	T_S^c	Load transfer between the cable element and shotcrete layers at the collar.
T_{EC}^b	Load transfer between bar element and nut of first external fixture.	T_{2EC}^b	Load transfer between bar element and nut of second external fixture.
T_{EC}^c	Load transfer between cable element and barrel/wedge assembly.	F_{RA}^b	Force within the bar element at a discrete internal fixture within the stable zone.
F_{RJ}^b	Bar element force at the interface between the stable anchor and unstable collar zones.	F_{RC}^b	Bar element force at the collar fixture.
F_{RA}^c	Force within the cable element at a discrete internal fixture within the stable zone.	F_{RJ}^c	Cable element force at the interface between the stable anchor and unstable collar zones.
F_{RC}^c	Cable element force at the collar fixture.	F_{DS}	Force at the discontinuity surface separating stable and unstable rock.
P_{EP}^b	Force transfer between bar's first external fixture and plate at the collar.	P_{2EP}^b	Force transfer between bar's second external fixture and plate at the collar.
P_{EP}^c	Force transfer between cable barrel and wedge and plate at the collar.	P_{RS}	Force transfer between ejected rock and first shotcrete layer.
P_{SM}	Force transfer between first shotcrete layer and first mesh (encapsulated) layer.	P_{MS}	Force transfer between first mesh layer and second shotcrete layer.
P_{SC}	Force transfer between second shotcrete layer and second (external) mesh layer.	P_{SS}	Force transfer between the first and second shotcrete layers at the cold joint.
P_{MP}^b	Force transfer between the encapsulated mesh layer and plate of the bar element.	P_{MP}^c	Force transfer between the external mesh layer and cable bolt plate.
P_{2MP}^b	Force transfer between the external mesh layer and second plate of the bar element.	P_{ES}^b	Force transfer between the encapsulated plate of the bar element and the second shotcrete layer.

4.6.3.3.1 Axial/Radial Capacity of the Scheme

The design energy dissipation capacity of the northern tunnel’s ground support scheme is reported below in terms of tensile capacity for the reinforcement, and radial capacity for the surface support. This relates to failure mechanisms where the deformation is primarily radially inward. The energy dissipation and displacement capacity for the entire ground support scheme is summarised below in Table 44. The values in this table reflect both the ideal and likely in-situ capacities. Considering field practicalities, it was assumed that the actual *installed capacity* was 80% efficient. That is, the capacity of the ground support scheme in-situ was only 80% of the idealised design value. In this case the installed capacity of 64 kJ/m² exceeded forecast demand by 28%.

Table 44 - Energy dissipation and displacement capacity of ground support scheme for radial failures.

Ground Support Component	Design Capacity	Combined Capacity	Displacement Capacity	Installed Capacity
Primary Surface Support	15 kJ/m ²	37.5 kJ/m ²	300mm	~ 64 kJ/m²
Primary Reinforcement	22.5 kJ/m ²			
Secondary Surface Support	15 kJ/m ²	43.0 kJ/m ²	400mm	<i>Surplus</i> 28 %
Secondary Reinforcement	28 kJ/m ²			

4.6.3.3.2 Shear Capacity

The shear capacity of the ground support scheme was also quantified. It was assumed to be the sum of the shear force capacity of all reinforcement elements that were activated in shear near the tunnel boundary. In order to estimate the shear capacity of the ground support scheme, an assumption was made regarding the number of reinforcement elements that were engaged in shear for each of the three failure mechanisms described in Section 4.4.1. Sketches of each scenario are presented below in Figure 167 to Figure 169. The angular divergence from pure shear and expected shear capacity supplied by each reinforcement element are annotated in the figures.

The force capacity of each element was calculated based upon its angle of installation with respect to the assumed shear planes, and considering the assumptions stated in Section 4.6.3.2.2. The stated shear capacity of the ground support scheme varied depending on which of the three mechanisms of shear failure were considered, and therefore how many reinforcement elements were expected to be loaded. A summary of the combined shear capacity of the two reinforcement ring sections (*A & B*) is presented in Table 45. Capacity is reported separately for each failure mechanism.

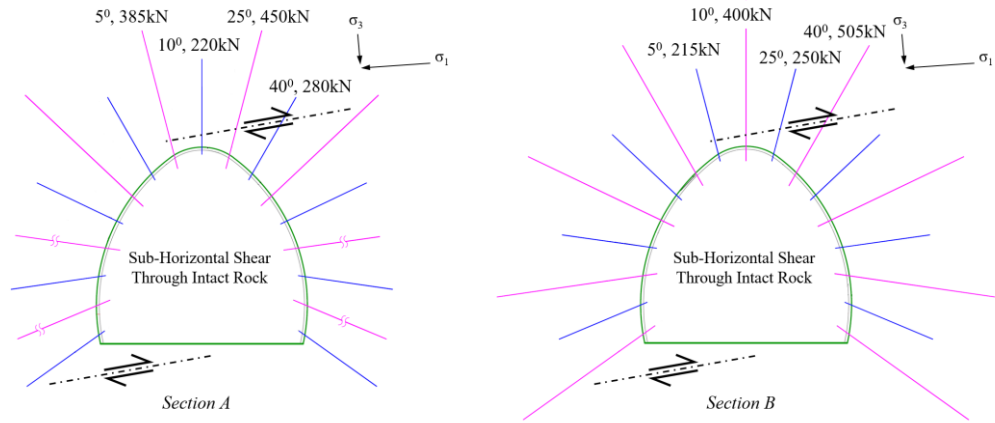


Figure 167 - Ground support scheme shear capacity for shear failure mechanism #1.

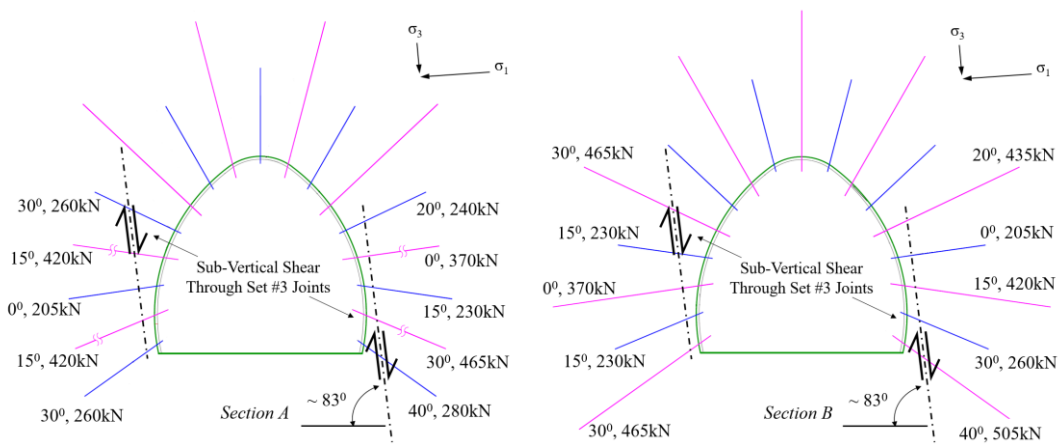


Figure 168 - Ground support scheme shear capacity for shear failure mechanism #2.

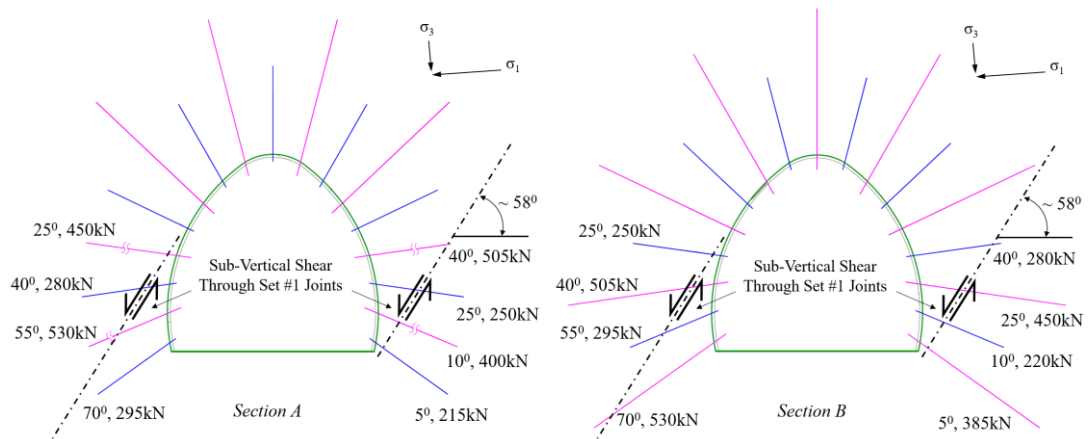


Figure 169 - Ground support scheme shear capacity for shear failure mechanism #3.

Table 45 - Shear force capacity of HED ground support scheme for three shear failure mechanisms.

Failure Mechanism	Bars Per Ring		Cables Per Ring		GS Scheme Shear Capacity (kN) Design / Installed
	Section A	Section B	Section A	Section B	
#1	2	2	2	2	2,705 / 2,164
#2	6	4	4	6	6,735 / 5,388
#3	4	4	4	4	5,840 / 4,672

Chapter 4: Design

It must be noted that the design assumptions for the shear force capacity of the reinforcement carry some limitations. Firstly, the capacity of both threaded bar and cable elements is assumed based on laboratory testing of cable bolt performance conducted by Bawden, et al. (1995). The laboratory testing apparatus is an imperfect representation of true in-situ rock conditions. As such, the strength performance of the elements measured in the laboratory may vary from the performance in a real tunnelling environment.

Secondly, the capacity of the threaded bar may not reflect the same performance as the cable bolts as the reinforcement shear angle changes. The capacity depends on numerous factors, such as the reinforcement material strength, borehole diameter, as well as the strength and stiffness of both the rock mass and internal fixture (i.e. grout). Cable bolts also tolerate larger bending loads than threaded bar prior to yield. As such, the stated assumptions on threaded bar shear force capacity should be taken to be an estimation only.

The design analysis indicated that the ground support scheme was most resistant to shear failure mechanism #2, which involved sub-vertical shear along Joint Set #3 discontinuities. The ability of the ground support scheme to resist shear failure along Joint Set #1 was also relatively high. Conversely, due to the lack of reinforcement installed in the floor of the northern tunnel, the excavation had a relatively low capacity to sub-horizontal shear failure through the floor and roof (i.e. mechanism #1). This was potentially the most likely mechanism of failure, given the sub-horizontal major principal stress. However, based on the results of the stability assessment, this shear failure mechanism was not considered likely to occur until later in the mine life, and only then if the major principal stress increased significantly. The sub-vertical minor principal stress was such that shear failure mechanisms #2 and #3 were considered to be highly unlikely at any time.

Chapter 5

Construction

Chapter 5: Construction

From a safety perspective, hard rock tunnel development at great depth must achieve two basic objectives. First, the excavations must be constructed safely. Second, the excavation must remain safe and in serviceable condition for its intended lifespan. This second objective does not exclude the possibility of the excavation suffering damage, which may be inevitable in some environments. However, it must not be damaged to the point where safety or ongoing serviceability is compromised. The solution proposed here for achieving safe construction of the excavation incorporates three elements. These include:

1. Face destress blasting to reduce stress-driven face instability (Figure 170),
2. Mechanised ground support installation to remove personnel from the hazard,
3. High energy dissipation ground support to control any instability that occurs.

While these principles have been implemented in mines and tunnels for many years, the construction process defined here seeks to innovates in these areas. This chapter describes the complete construction method for the safe and economical implementation of the blasting and ground support designs that were described in the preceding chapter. The method was implemented in the northern research tunnel with the southern tunnel serving as the experimental control.



Figure 170 - Violent stress-driven failure causing ejection of rock from the development face.

5.1 Development Strategy

The north and south research tunnels were constructed simultaneously by alternating the development blasts in both tunnels. It was desired to advance the face in both excavations at the same rate, so as to minimise potential for one excavation to alter the stress conditions at the face of the other. By implementing this strategy, it was expected that the stress conditions at the face of both tunnels were consistent during development. The first blast in the project was taken in the southern tunnel, the second in the north tunnel, the third blast in the south and so on, in a continuous alternating sequence. The complete sequence of development blasts in both tunnels is illustrated in Figure 171 and Figure 172. The construction sequence ensured that the southern face was always slightly ahead of that in the north, within 5 metres. Ten development rounds were blasted in the southern tunnel, for a total length of development of 34.4m. Nine blasts were taken in the north, for 32.4m of development.

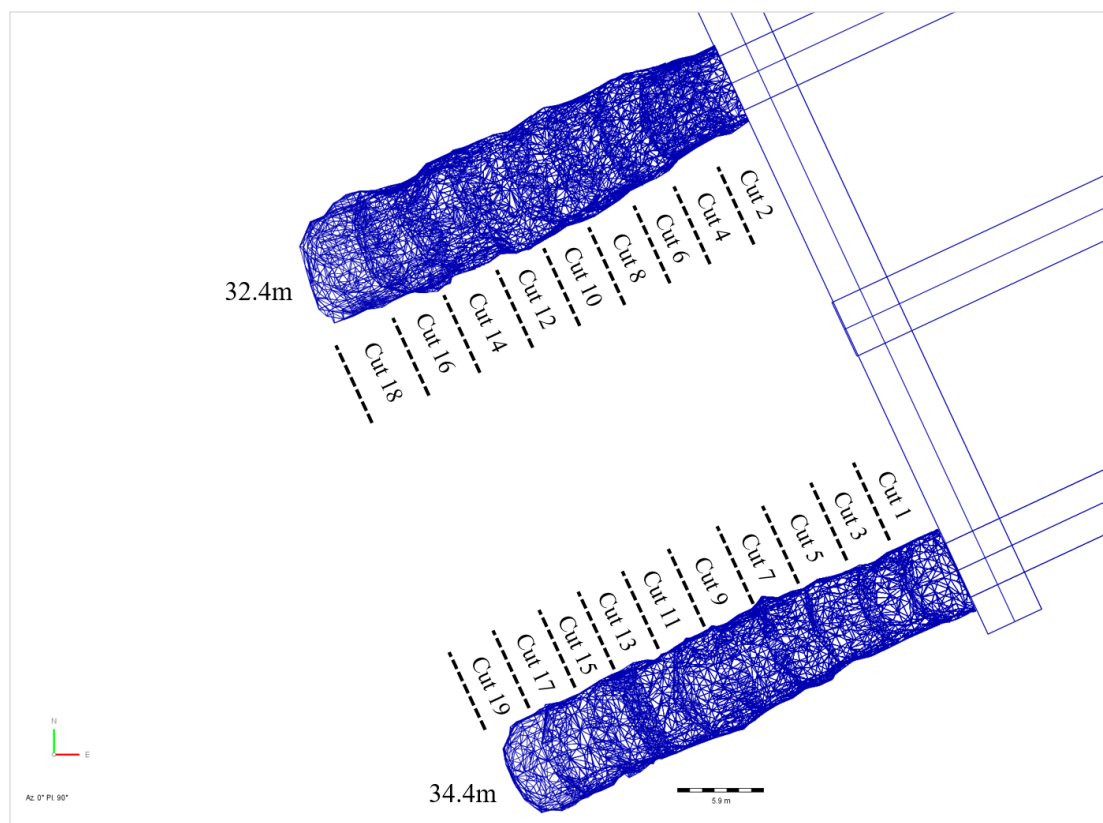


Figure 171 - Alternating sequence of development advances across the two research tunnels.

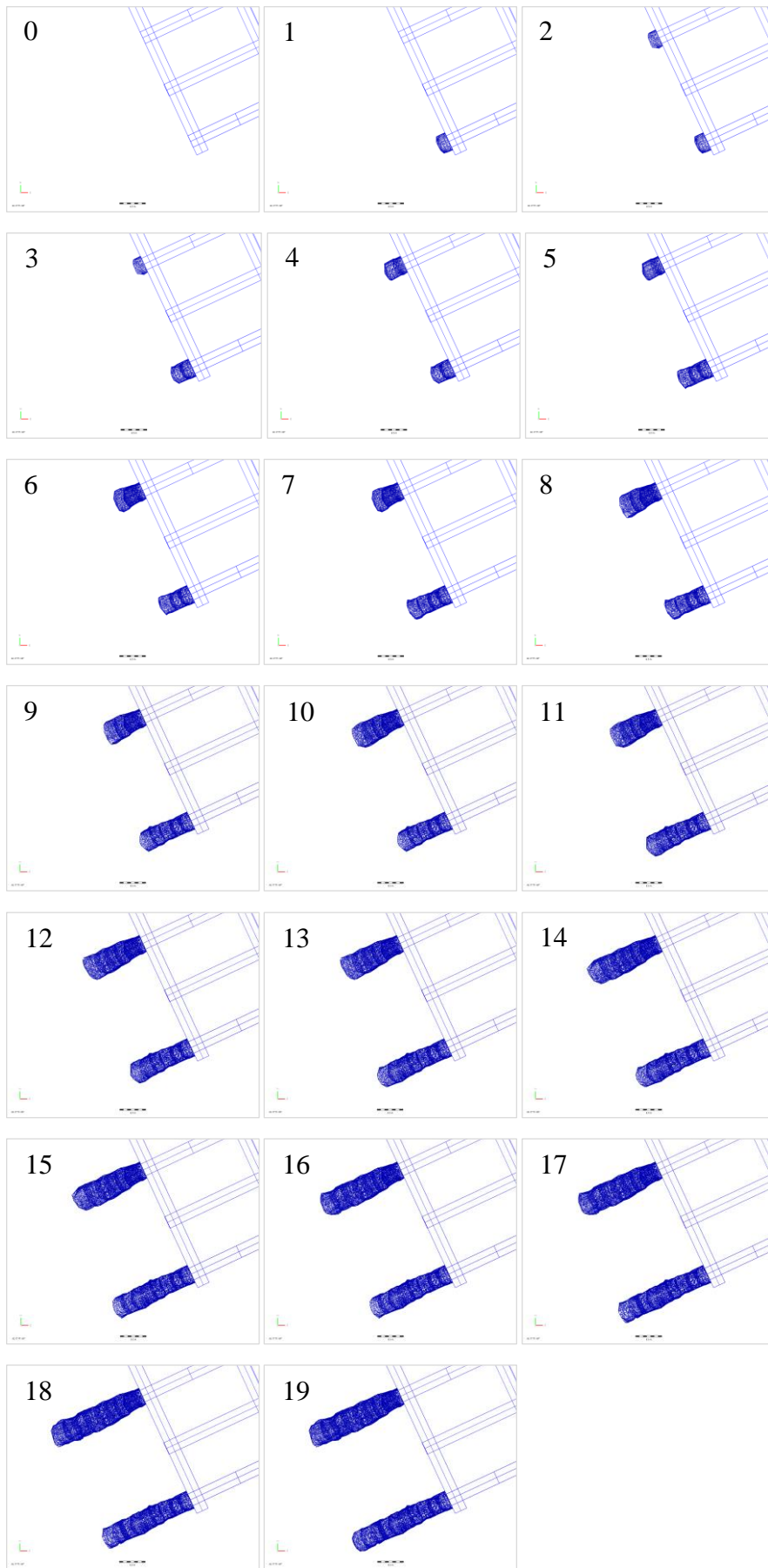


Figure 172 - Development construction sequence of alternating blasts in each tunnel.

Chapter 5: Construction

The various drill, blast and ground support designs described in the preceding chapter were implemented selectively in the tunnel constructions. These designs were monitored during construction using instrumentation and visual observations for subsequent analysis. The rock mass response and excavation performance were assessed for each of the various construction designs with the view to quantify the performance of each. A diagram of the various construction strategies that were implemented during the construction trials is shown in Figure 173. The entire southern tunnel was developed according to the conventional designs described in Section 4.5.

The northern tunnel was developed according to the various designs described in Section 4.6. The first two blasts in this heading were conventional, without destressing, in order to form the turnout and basic excavation shape. The subsequent three blasts were conducted according to *Destressing Design 1*. The final four blasts in the northern tunnel followed *Destressing Design 2*. This design was implemented so as to incorporate several learnings from the initial destressing blasts. The entire tunnel was constructed using mechanised ground support. Due to instructions from the mine site engineers, only the final sixteen metres (four cuts) in the northern tunnel were constructed as per the ground support design described in Section 4.6.3.

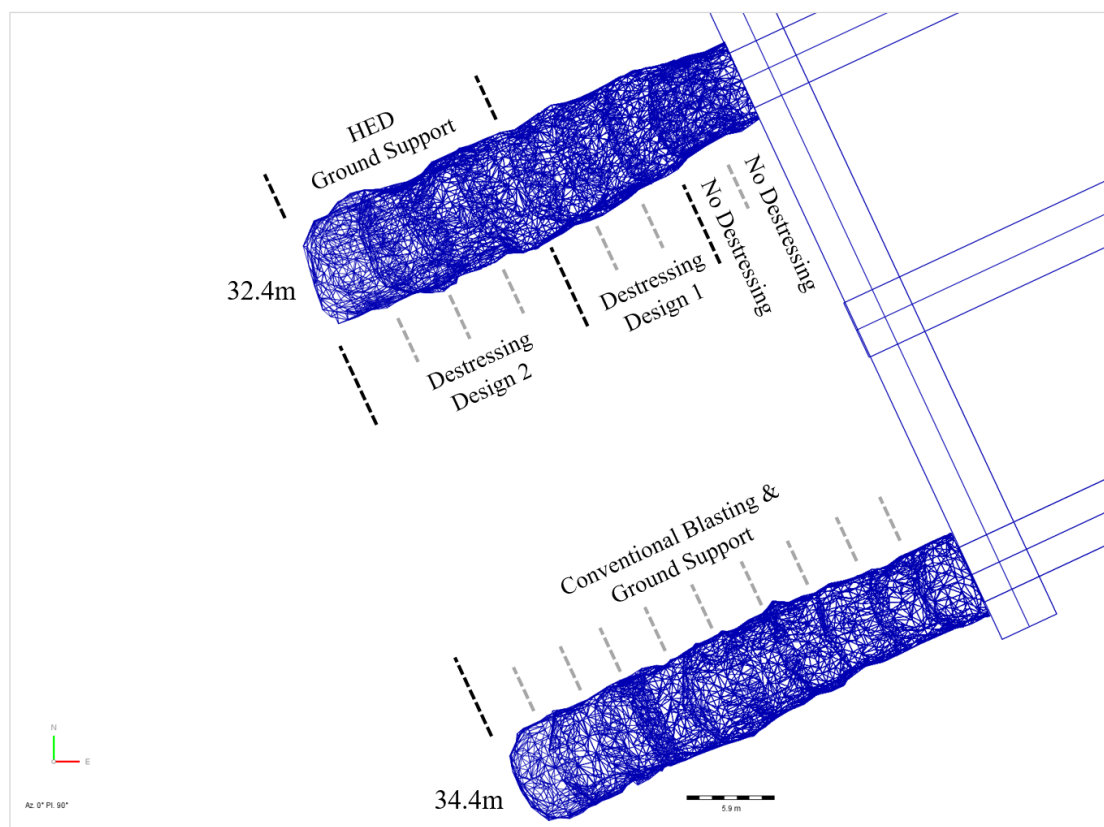


Figure 173 - Construction strategy used to test various development methods.

5.2 Development Rate

Construction of the two research tunnels took place from 1st November 2016 to 30th June, 2017. Initially, the construction progressed rapidly, with the first seven development blasts in the project being completed within two weeks. This included the first four cuts in the south tunnel and initial three cuts in the northern excavation. This rate of advance benefited from a constant availability of the mechanised construction equipment. The rate of development dropped significantly from the third week of construction onwards. This was a direct result of the mechanised jumbos focusing on priority development elsewhere in the mine.

The research development was third on the list of mining priorities for the majority of the construction period. As such, the availability of the ground support jumbos dictated the rate of development advance, with a significant amount of inactivity occurring during construction due to the activity elsewhere. A plot of cumulative development metres as a function of the number of construction days is presented in Figure 174. Blasts are shown as dots on the data series. Overall, the average rate of face advance was 4.65m/month and 4.5m/month in the south and north tunnels, respectively.

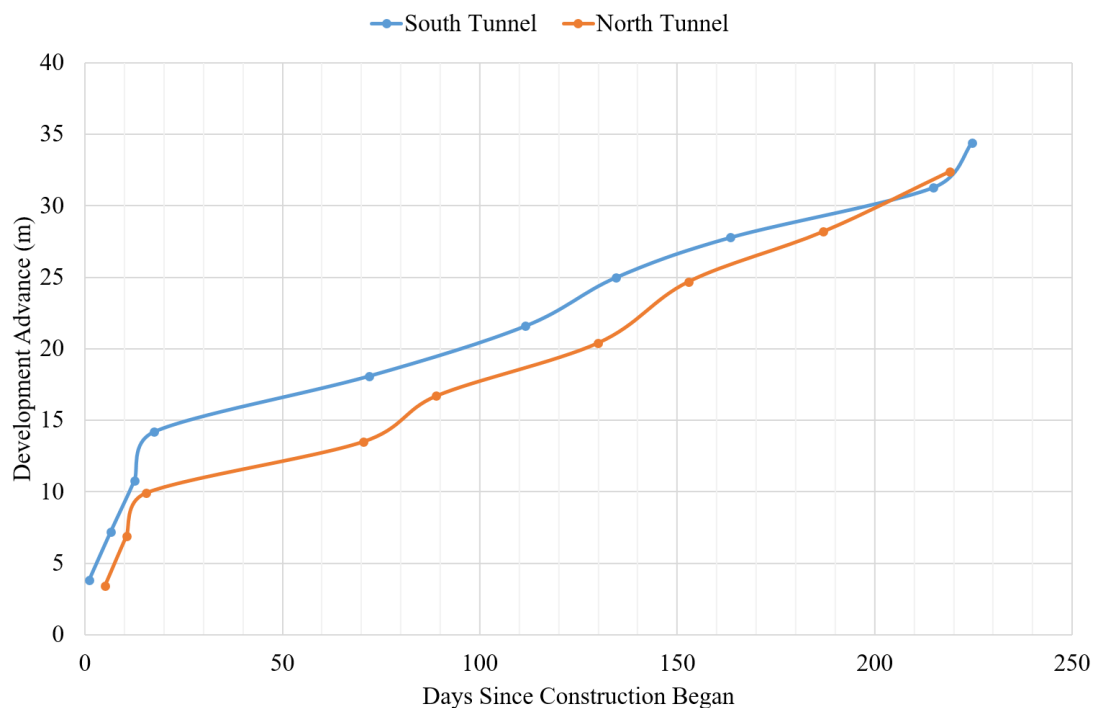


Figure 174 – Cumulative development metres for the south and north tunnels.

5.3 Development Blasting with Face Destressing

5.3.1 Profile Survey Control

Survey control was implemented throughout the construction in order to ensure compliance between as-built excavation geometry and the design. This included surveying and marking the excavation centreline, gradeline and profile boundary on the face before drilling each development blast (Figure 175). Surveys of the 3-dimensional profile of the development face were also collected and analysed prior to drilling the blast holes. Marking of the profile boundary on the face assisted the boring jumbo operator to position the perimeter blastholes correctly. This was desired to maintain the required excavation shape. The exact position of the destressing blast hole collars was also surveyed and marked on the face. It was critical to accurately locate the collar of the destressing holes, since their spacing was expected to have a large influence on the likelihood of fracture interaction between the charges and therefore also the effectiveness of the destressing technique.



Figure 175 - Excavation perimeter, centreline and gradeline markings for profile control.

5.3.2 Drilling for Destressing

The rock mass conditions of each face were reviewed prior to commencing drilling of the destressing boreholes. It was common to observe concavity in the face due to fall-off of loose rock. Two main causes of this concave face profile were considered. The first was relatively high stress concentration in the centre of the face, potentially causing fracturing and a zone of loosening. The second cause was induced rock mass damage from the destressing charges of the previous development round. This loose material was mechanically scaled to provide a hard surface for drilling and charging. The destressing process was expected to cause damage to the face, and this appeared to result in additional fracturing of the face causing fall-off within the destressing pattern.

Typically, overbreak of the face was most significant in the centre of the face, with the left and right hand sides of the face tapering into the adjacent walls. Occasionally the irregular face profile had a concavity exceeding one metre, and required the corrective measure of modifying the destressing drill length. Significant face concavity presented the risk of deviation from the standard blast design, as the charge column positions of adjacent blast holes might not be aligned in that case. On some occasions the length of the destressing holes and position of the explosive charge was modified, in order to adjust for the face irregularity and maintain correct relative positioning of the column of explosives of adjacent blast holes. Surveys of the 3D face profile were reviewed and used to guide any required modifications to individual blast hole length.

The destressing blast holes were drilled using the standard boring jumbo (Figure 176). This jumbo was equipped with a rotating carousel capable of holding ten boring rods of 1.0m length (Figure 177). This was more than sufficient to drill the 7.0m long destressing holes that were called for by the design. Parallelism between the destressing blast holes was desired to be maintained as accurately as possible, in order to ensure a consistent spacing between the explosive in adjacent holes. On most occasions an inclinometer was used to ensure holes were drilled as close to horizontal as possible, although field measurements indicated that some holes were drilled with an inclination of up to 6.5°. Azimuth control was performed manually by aligning the jumbo boom parallel to the painted face centreline and a back-sight station.

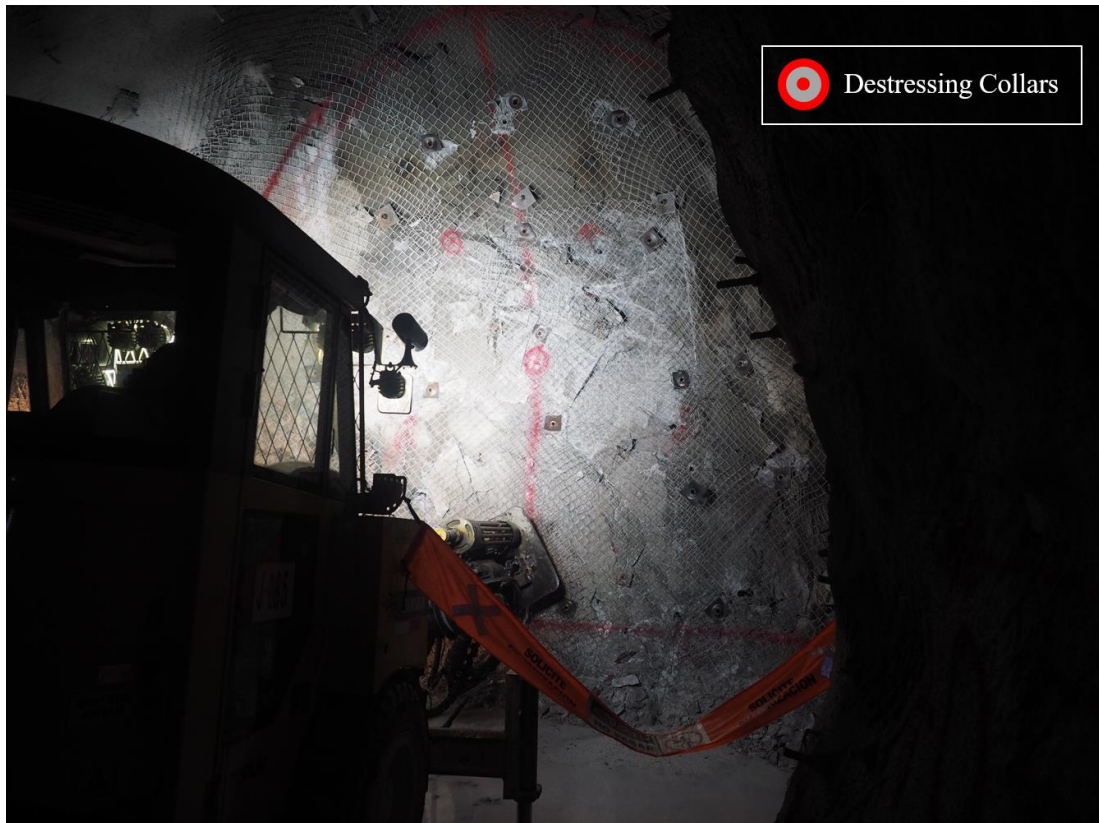


Figure 176 - Destressing blasthole collars surveyed and marked on the face prior to commencing boring.

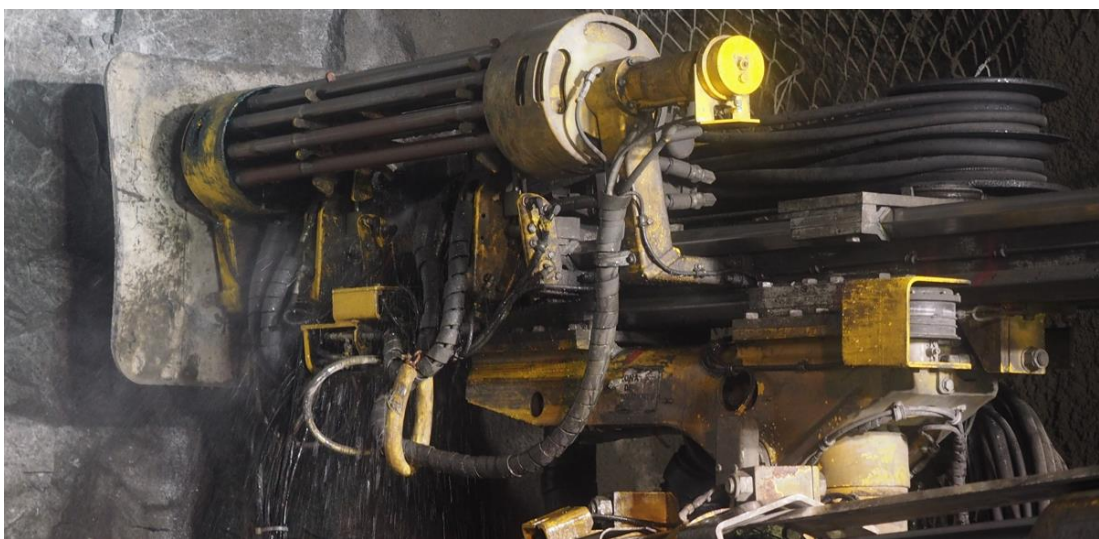


Figure 177 - Boring jumbo with eight 1.0m-long connecting rods on a rotating carousel.

5.3.3 Development Blast Hole Drilling

The standard development round blast holes were drilled to suit the design specification using a mechanised drilling jumbo. This conventional practice was typical of that already used in most mechanised mines in Australia, South America and elsewhere for drill and blast development. This practical phase of the blasting process was not modified in any way to suit this trial.

5.3.4 Securing the Face

Boring the face generated additional loose rock scats which could get hung up behind the mesh. The face mesh was therefore installed loosely initially, with a 150mm-wide gap between the mesh and rock face. After boring was completed, and before charging explosives, all loose rock fragments behind the mesh were manually scaled down to floor level using crowbars from a raised work platform. This removed the hazard of rock scats posed to the charge crew. It also made the task of locating and charging the blast holes easier. The mesh was then push hard against the face by driving the split sets to full depth with the jumbo. The floor was cleared by the loader prior to commencing charging operations. Figure 178 shows an example of typical face conditions following boring, which required minor remedial scaling prior to charging.



Figure 178 - Typical face conditions requiring minor remedial scaling behind mesh prior to charging.

5.3.5 Destressing Blast Hole Surveys

An important aspect of the implementation of the destressing method was the geometric arrangement of adjacent explosive charges and their compliance to the design. Ideally, the explosive charges were required to retain consistent spacing between one another along their entire length. Also, the longitudinal position of each charge column was designed to be aligned with that of its adjacent neighbour. That is,

Chapter 5: Construction

the toes and collars of all destressing charges were designed to be at the same tunnel chainage. This was desired for several reasons. Firstly, to ensure that the entire length of each explosive charge column had an adjacent charge to interact with, thus maximising the chance of creating adjoining fractures. Secondly, to ensure that the blasted zone ahead of the face was of consistent shape and length for destressing purposes. This aspect of the destressing implementation was challenging to manage where the development face was concaved due to stress-related overbreak, and often it was required to make some adjustments to the borehole lengths.

The length and deviation of destressing blast holes was measured using a small gyroscope instrument that was purpose built for this project. This instrument consisted of a gyroscope mounted within a hollow brass rod. The gyroscope assembly was connected to a series of narrow yellow push rods, which were fed through a tripod-mounted distance logger (Figure 179). As the gyroscope instrument was inserted into the borehole, time-stamped readings of orientation and downhole distance were recorded and subsequently used to construct a fully oriented 3D trace of the hole. The prototype deviation survey tool was tested during the final three blasts in the north tunnel. Due to operational issues with the instrument, a deviation trace of the complete destressing pattern of 12 holes was only successfully achieved for North Cut 14.

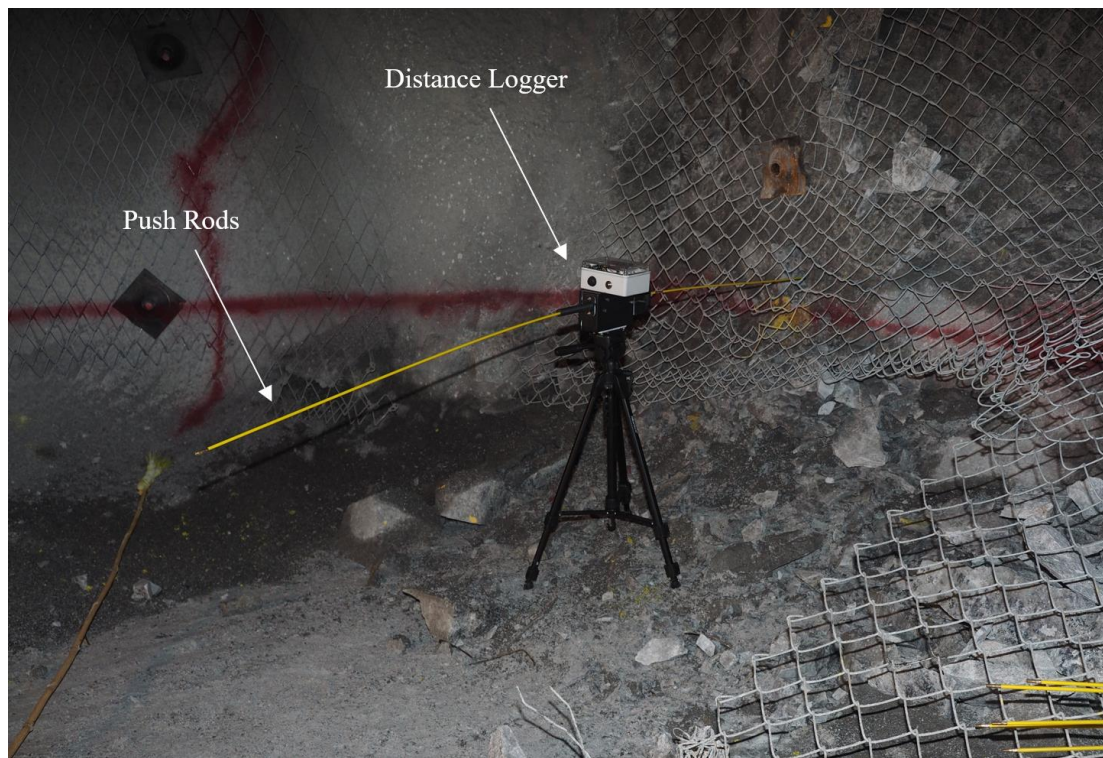


Figure 179 - Instrumentation for measuring the deviation of destressing boreholes.

The deviation survey of the Cut 14 destressing holes is presented in Figure 180. Exact collar positions were not available in this case. It must be noted that magnetic disturbance from steel ground support in the face caused the orientation of the boreholes to be inaccurate for the first 1.5 to 2.5m from the collar. This was a recognised and unavoidable risk to the data quality, due to the safety requirement to install face mesh and 2.5m split sets prior to working at the face. The inaccurate initial portion of the borehole trace made it impossible to precisely quantify the spacing characteristics between the destressing charges.

In qualitative terms, the toe regions of all holes exhibited minimal drilling deviation. However, some spacing non-conformance to design was observed at the toe. This appeared to be caused by variability in the collaring point of the hole as well as variable initial drill azimuth set-up. In this case, azimuth mis-match particularly affected the two central face holes on the #11 delay. Charge spacing was also affected by inconsistencies in borehole inclinations, which varied from 0° to $+6.5^{\circ}$ throughout the pattern. In practice, the greater-than-design spacing between some destressing charges would have reduced the likelihood of fracture interaction between those charges.

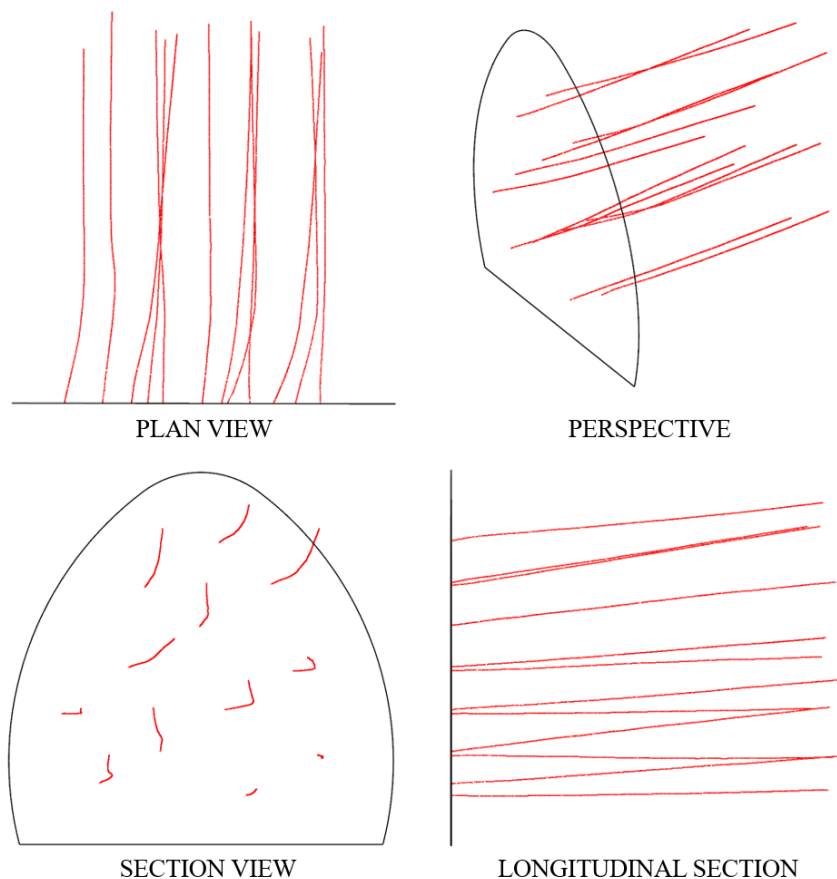


Figure 180 - Measured orientation and deviations of destressing boreholes (north tunnel, Cut 14).

5.3.6 Charging, Priming and Stemming Destressing Blast Holes

Immediately prior to charging with regular blown ANFO, the length of each destressing blast hole was measured again, in case of debris in the hole. In the event of over-drilling, clay stems were inserted to the toe of the hole at this point and tamped until the required hole length was achieved. The destressing blast design called for a 2.9m long charge, with the primer at the collar of the explosive. ANFO was installed from a kettle using a poly hose. The ANFO hose was marked with tape, typically at distances of 7.0m and 4.1m from the in-hole tip of the hose (Figure 181). These markings on the pipe served as a visual guide to assist the charge crew to strictly install no more than a 2.9m-long explosive charge, then to shut off the ANFO supply once the charge column was installed to within 4.1m of the blast hole collar. This method of installation left an uncharged burden of approximately 0.3m between the toes of the development loads and collars of the destressing charges. This reduced the potential for the destressing charges to interact with the standard development loads and cause sympathetic detonations.

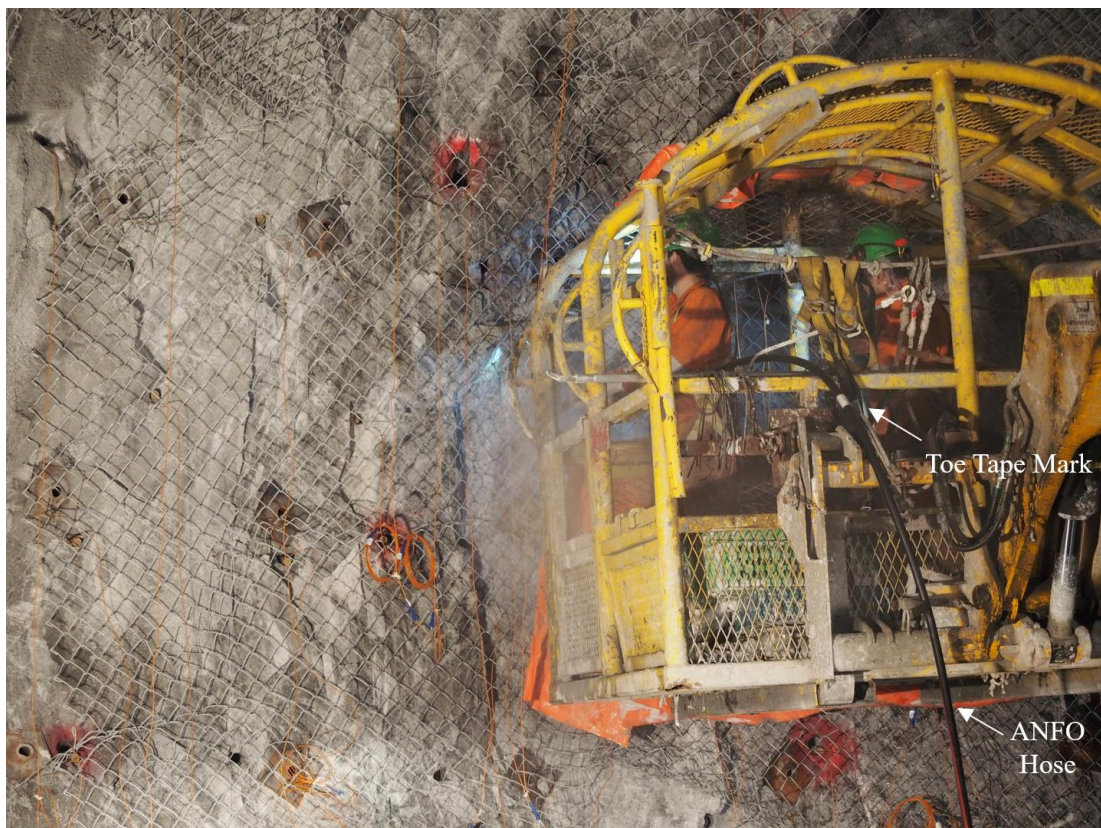


Figure 181 - Working from an elevated platform to charge a destressing hole with blown ANFO.

Chapter 5: Construction

Following charging of a destressing blast hole with ANFO, the Tronex primer was installed. The primer was inserted using a long rod, ensuring solid contact was achieved between the primer and ANFO (Figure 182). The blast hole was subsequently stemmed with damp clay packs (Figure 183). Clay packs were typically installed individually, or at most two at any one time, so as to avoid the stems prematurely blocking the hole. A length of approximately 1.5m metres was stemmed in this way, beginning at the destressing primer and progressing towards the blast hole collar. It was imperative that the stemming was tamped hard up against the explosive, thus minimising the available void for gas expansion during detonation and maximising the detonation pressure in the destressing zone.



Figure 182 – Insertion of the Tronex collar primer for a destressing charge.



Figure 183 - Damp clay stem packs inserted into the destressing borehole prior to tamping.

5.3.7 Charging and Priming Development Blast Holes

The standard development loads in a destressing blast were charged normally, following the routine practice for the mine site. Face holes were charged with regular blown ANFO, perimeter holes with Softron and the lifters using Tronex. All charges were toe primed and left un-stemmed. Destressing blastholes were previously marked with paint so as to avoid confusion with the standard development holes (Figure 184).

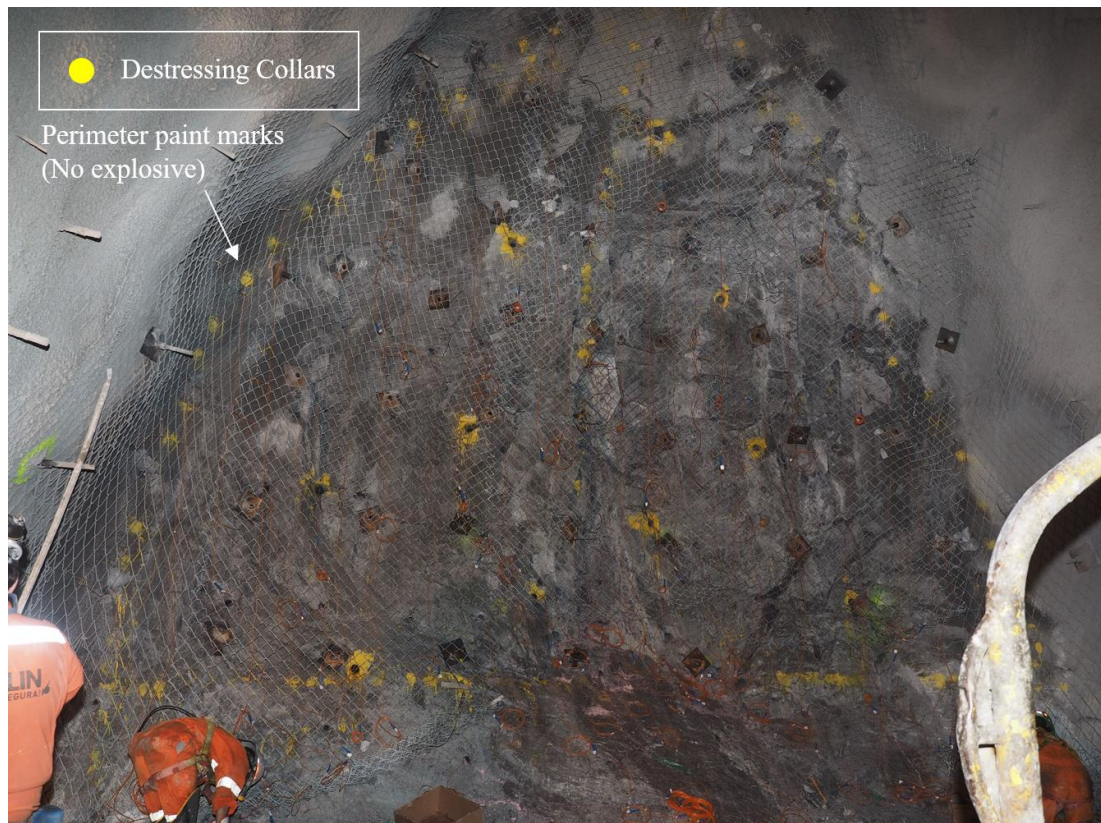


Figure 184 - Charging standard development blastholes following destressing loads (marked yellow).

5.3.8 Detonator Tie-In and Shot-Firing

The intent of the destressing charges was to create elongated fracturing between the blast holes with minimal associated rock mass deformation. All destressing charges were therefore initiated prior to the main development blast. This method ensured that the destressing charges were heavily confined and did not cause undue rock mass damage to what would be exposed as the new face. Initially, all destressing charges were initiated simultaneously (*Design 1*). Due to the large concussion air blast that was generated, the subsequent blast design initiated the destressing charges on three separate delays, spread over approximately one second. This reduced the concussion impacts and focused on generating fracturing confined within each sub-horizontal row of charges. The detonator tie-in and initiation followed a conventional process.

5.3.9 Seismic Exclusions

A seismic exclusion zone of approximately 50 metres radius was implemented surrounding the tunnelling precinct following each development blast. The rate of ongoing seismic activity was monitored and re-entry performed after either the activity had returned to normal background levels, or 24 hours, whichever occurred later.

5.3.10 Waste Rock Removal

Removal of blasted rock (Figure 185) was performed according to the standard operating procedures of the mine site. Occasionally the removal of blasted rock coincided with an increase in the seismic activity. In that case the mine procedure called for cessation of load and haul activities and exclusion of the area until such time as the seismic activity decayed to safe levels.



Figure 185 – Development blast rock and damaged temporary face ground support to be removed.

5.4 Ground Support Scheme Implementation

The ground support scheme in the northern tunnel was a novel design and construction arrangement unique to this thesis. It was installed using a more highly mechanised method of installation when compared to the typical conventions used in Australia and elsewhere. The construction of this ground support scheme was performed according to the following sequence of activities.

5.4.1 Clearing Temporary Support

The requirement for face mesh during charging operations resulted in a significant amount of damaged temporary ground support hanging from the backs and adjacent sidewalls following blasting (Figure 186). This ground support was deliberately sacrificial to provide temporary protection from face ejections for the blast crew during their activities. This damaged ground support was required to be removed following completion of load and haulage of the blasted muck pile, in order to provide a clear work area for mechanical scaling.

The damaged support was manually removed using an oxy torch. The operator was positioned in a closed elevated work basket, with side mesh panels for protection. The operator used cutting equipment that permitted them to maintain a safe standoff distance of at least 1.5m from the last row of permanent reinforcement, such that at no time was the operator exposed to unsupported ground. Mesh sheets and protruding rock bolt tails were cut flush to the rock surface to minimise interference with the later installation of permanent ground support.



Figure 186 - Damaged temporary face support required to be removed following blasting.

5.4.2 Mechanical Scaling

Mechanical scaling of the roof and sidewalls of the excavation was performed in order to remove loose and broken rock disturbed by blasting. Scaling served several important purposes. Firstly, scaling provided a more uniform and stable surface for application of the shotcrete. Unstable rock remaining on the surface might fail under the additional weight of the sprayed shotcrete, causing fall-off and unnecessary additional spray volumes. Secondly, removing broken rock on the excavation perimeter removed what would otherwise be unnecessary static load on the ground support. Thirdly, scaling broken ground ensured the ground support scheme was as close as possible to firm solid contact with intact rock. This limited the amount of radial deformation that could occur prior to loading the ground support scheme. The removal of the broken layer allowed the ground support to provide an immediate containment effect on the rock.

Mechanical scaling was performed using a purpose-designed piece of mobile equipment (Figure 187). Observations during construction indicated that scaling typically generated a significant seismic response, often with spalling occurring from the excavation. This inherently hazardous phase of the construction was made safe by the use of equipment which removed the operator from the danger zone. In this case, the operator was stationed within the machine, 4 to 5 metres behind the last row of permanent reinforcement within a rockfall protection cabin (Figure 188).



Figure 187 - Dedicated machinery for mechanical scaling of the unsupported sidewalls and roof.



Figure 188 - Mechanical scaling of loose rock from the tunnel walls prior to shotcreting.

5.4.3 Structural Geological Mapping with Photogrammetry

A small number of the freshly exposed faces were mapped using digital photogrammetry. It was desired to ascertain whether sufficient structural information could be obtained for a SAFEX analysis. The photogrammetry process initially involved hosing down the face with water to remove dust and expose a clear view of the rock mass. A high resolution digital camera was then stationed to one side of the tunnel. This camera was set well back from the face to limit the exposure to face instability. Additional lighting was installed to highlight the joint planes (Figure 189). A series of photographs were taken from one side of the excavation, then the camera was moved to the opposite side and the process repeated.

An analysis by WASM (Windsor, 2016) concluded that the full suite of SAFEX input data could not yet be collected accurately using photogrammetry techniques. However, photogrammetry was deemed to be sufficient to collect the level of data necessary to perform a block analysis of the same nature as that previously documented in Section 4.4.2. Ultimately, the collection of structural data for design purposes was performed via manual window mapping after ground support had been installed. It will be recommended to further investigate the compatibility of photogrammetry techniques with the data collection requirements of the SAFEX software.



Figure 189 - Typical digital photogrammetry station for face structural mapping.

5.4.4 Shotcrete Application

The application of the 50mm-thick primary layer of sprayed shotcrete was performed using a diesel-hydraulic powered mobile spraying machine with air-jet spray nozzle. This method of shotcrete installation is conventional in the mining industry and no deviation from the common shotcreting practice was implemented or investigated as a part of this research. The shotcreting process followed standard operating procedures for the mine.

The conventional shotcreting process in underground development may expose the operator to the hazard of face instability. In this case, the operator was located close to the edge of unsupported ground when controlling the spray jet nozzle with the handheld control unit (Figure 190). Potentially the operator is exposed to flyrock from the face, sidewall and especially the roof. Although the period of exposure was relatively brief, perhaps no more than 45 minutes, this activity usually occurred within 60 minutes of mechanical scaling. As such, caution was adopted when deciding to commence this activity following a field assessment of the seismic activity in the heading. Shotcreting was delayed whenever instability such as rock noise or spalling was detected at the face.

Chapter 5: Construction

Following shotcrete application, a pause was implemented to allow for curing of the shotcrete. This aspect of the development cycle affected the construction efficiency. The ground support installation could not commence while the shotcrete was yet to obtain sufficient strength. Historically, in many mines an early age shotcrete compressive strength of 1 MPa has been used as the threshold for re-entry. However, this criterion does not realistically consider the fact that shotcrete early age failure is typically due to shear failure. Saw, et al. (2017) recommend that an alternative strength threshold be applied. Specifically, the shear strength of shotcrete should be sufficient to stabilise a kinematically free-falling tetrahedral block of rock with 1m edge lengths. For a 50mm thick layer of typical shotcrete composition, this equates to a shear strength of approximately 20kPa, which can be achieved within an hour. As such, following the shotcrete application a conservative stand-off period of two hour was deemed appropriate, prior to re-entry for installation of the remaining ground support.



Figure 190 - Application of the primary shotcrete layer.

5.4.5 Primary Reinforcement Mark-Up

The load transfer characteristics of the two integrated passes of ground support relied heavily on the spacing regularity and symmetry in the reinforcement pattern and mesh sheet overlaps. As such, practical implementation of the reinforcement and mesh placement was an important area of focus during the construction.

Initially, the reinforcement pattern compliance was controlled in one of two ways. The first method involved marking the pattern on the shotcrete using paint poles from an elevated work platform. This was done with extended poles so that the operators were several metres from the edge of unsupported ground. Figure 191 illustrates the typical paint markings of a 1m x 1m staggered reinforcement pattern used to guide the operators of the bolting jumbo. This figure shows the primary ground support layer from a previous development round to the right in the figure, and fresh shotcrete and reinforcement pattern paint mark-ups of the most recent round to the left. For a 3.5m development round, approximately 20 minutes was needed to mark the complete reinforcement pattern in this way.

The second method of controlling the position of the reinforcement involved unfurling each of the mesh rolls on a flat surface, measuring the desired reinforcement pattern spacings on the mesh and marking the apertures in the mesh which were intended to receive the bolts. The mesh apertures were marked with paint. Alternatively, high visibility survey ribbon could also have been used. The mesh was then rolled back up and installed on the jumbo mesh handler arm for installation. This process took approximately 15 to 20 minutes. The visual markers on the mesh were used as guides for the jumbo operator when collaring the reinforcement elements.

These aforementioned methods of guiding the reinforcement pattern were relatively simplistic, but necessary to ensure compliance with the ground support scheme design. Jumbo technology is available which assists to guide the jumbo boom into the correct collaring position for reinforcement installation. An example of this technology is the Sandvik Bolting Instrumentation (SBI) system (Sandvik, 2018) which is installed on the various DS model bolting jumbos. This system utilises a fan laser or theodolite to visually locate the correct collaring position for the reinforcement. A jumbo with this technology was commissioned onto the research development towards the very end of the construction. However, the tunnels were completed before the operators were able to be trained in the laser system. Ideally, similarly sophisticated methods of reinforcement pattern guidance should be used routinely in the future.

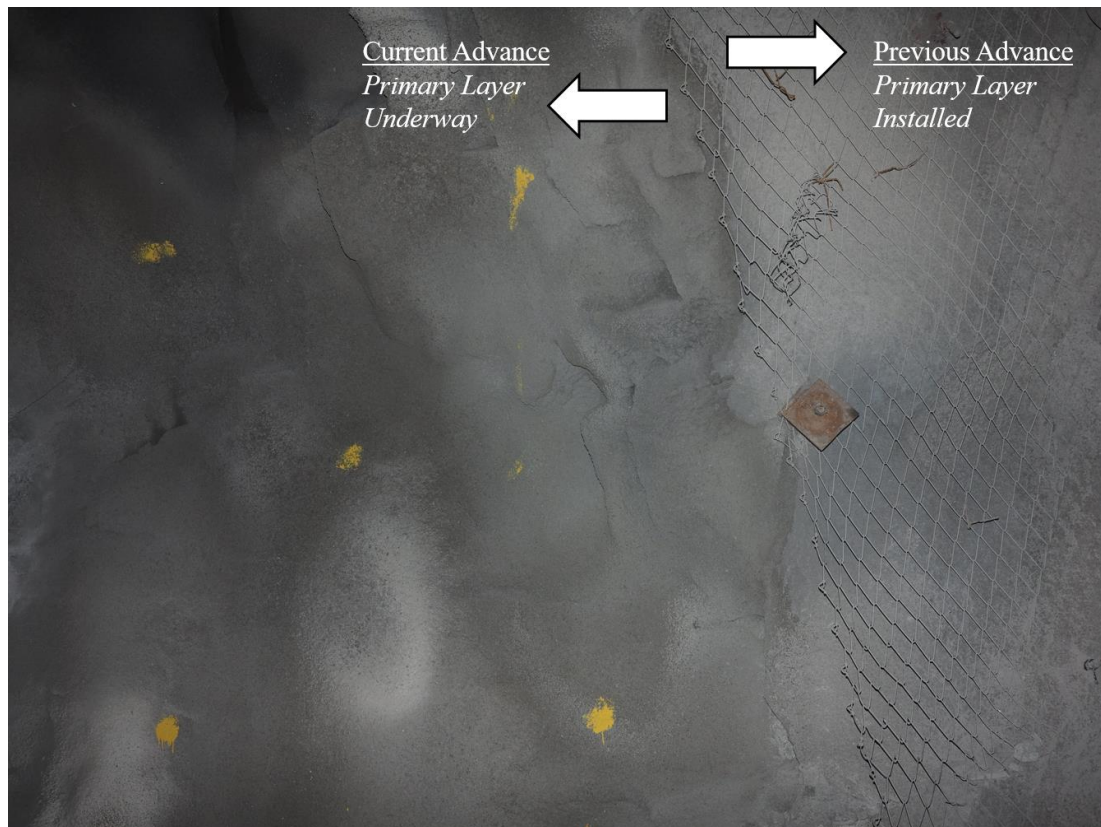


Figure 191 – Position control of primary reinforcement elements.

5.4.6 Installation of Primary Reinforcement and Mesh

The installation of the primary system of reinforcement and mesh was completed using fully mechanised ground support jumbos. Two jumbos were used during the construction process. These included an Atlas Copco BOLTEC (Figure 192), and later a Sandvik model DS411-C jumbo (Figure 193). The two jumbos have a similar design. The jumbos are diesel engine-powered and connect to the mine electricity supply. They both consist of a hydraulically-operated twin-boom arrangement. One of the booms on each jumbo is dedicated to the task of installing the reinforcement. The other is dedicated to mesh handling (Figure 194).

The bolting boom (Figure 195) consists of a hydraulic rock drill, a rotating carousel for storing and installing the reinforcement elements and a grout insertion tube connected to a jumbo-mounted grout mixing bowl (Figure 196). The grout insertion tube functions in the same fashion as that of a regular cable bolter. A grout mixing bowl is in-built on the jumbo (Figure 197). Grout is prepared on-site and pumped into the borehole via the insertion tube. The bolt carousel is capable of storing between 8 and 16 reinforcement elements, depending on the plate size. Bolts are loaded onto the carousel prior to the jumbo approaching the face and commencing installations.

The mesh handling arm is typically an optional attachment. In this case, the fitted arm was designed to manoeuvre 16.0m long x 2.4m wide woven mesh sheets in the G80/4 specification. The arm has independently controllable rotation, such that the mesh sheet can be controllably unfurled to cover the excavation surface as the reinforcement pattern is progressively installed. The arm is fully manoeuvrable from floor-to-floor level to permit full coverage of the excavation perimeter with the mesh product. A close up view of the mesh handler arm of the Sandvik machine is shown in Figure 198. Figure 199 presents the Atlas jumbo in operation installing reinforcement and mesh.



Figure 192 – Mechanised Boltec jumbo used for ground support installations (AtlasCopco, 2017).

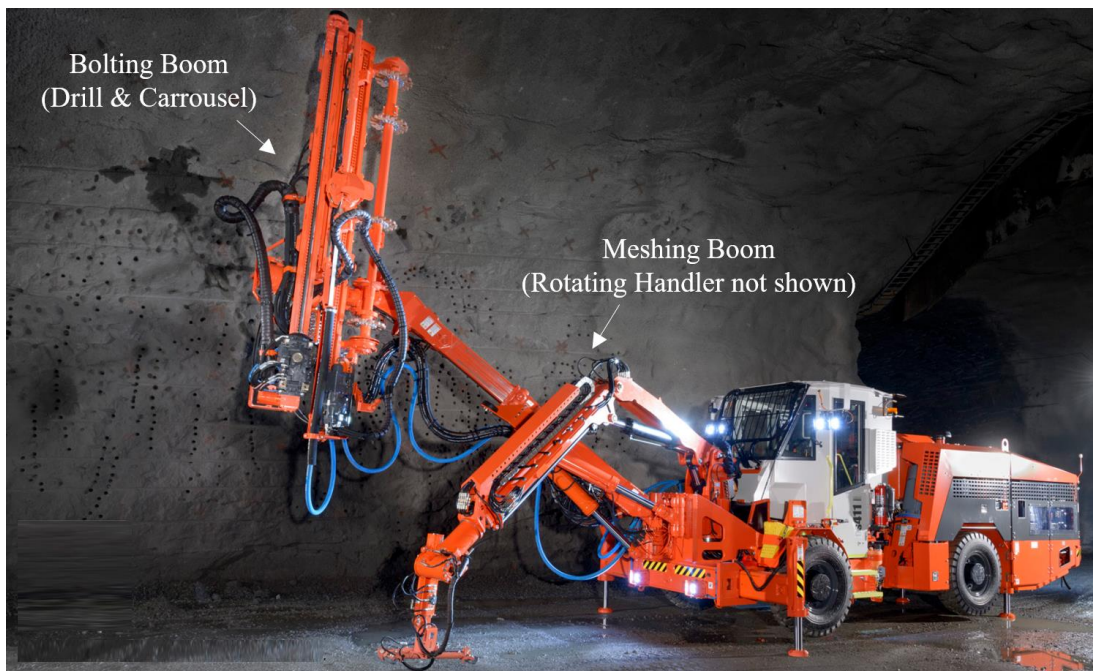


Figure 193 - Mechanised DS411 bolting jumbo used for ground support installation (Sandvik, 2018).

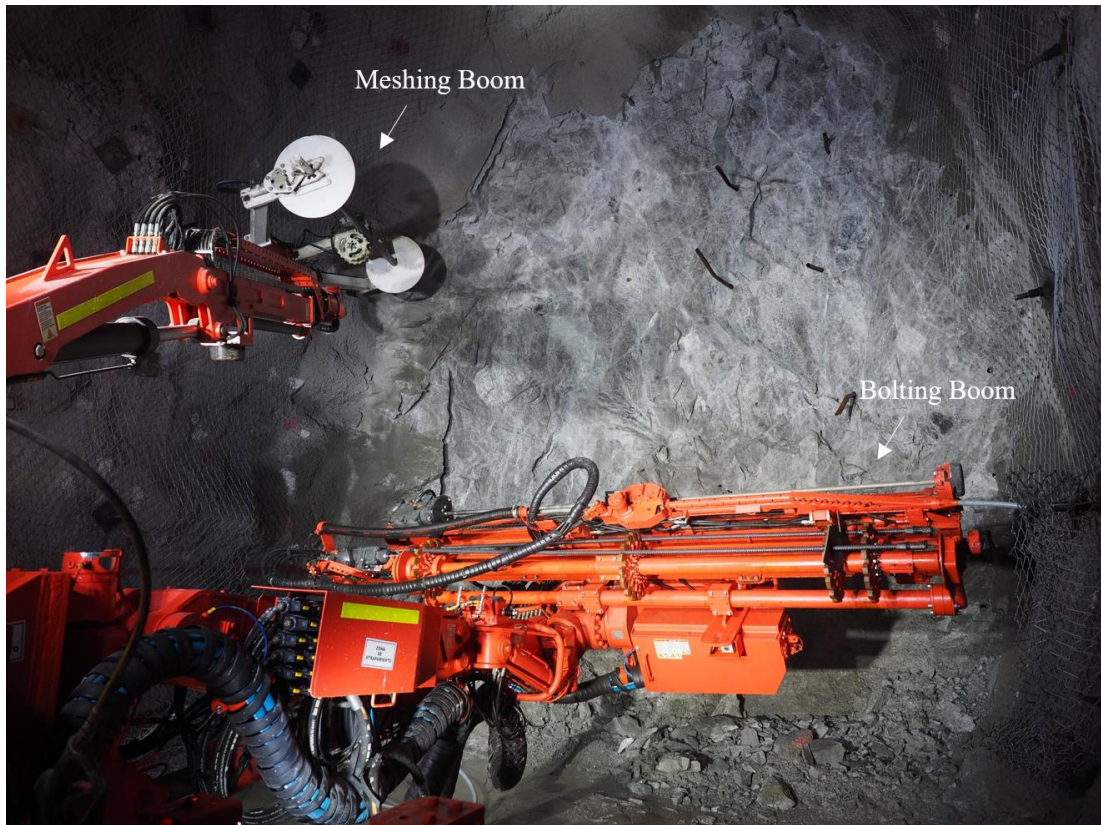


Figure 194 - Reinforcement and mesh installation booms.



Figure 195 – Mechanised jumbo boom for drilling, grouting and installing reinforcement.



Figure 196 - Drilling, grouting and bolting attachments on the mechanised jumbo.



Figure 197 - Integrated grout mixing bowl on the mechanised ground support jumbo.



Figure 198 - Mesh handler arm for mechanised ground support installation (mesh roll not shown).



Figure 199 - Mechanised ground support jumbo (Sandvik DS411-C) in operation.

The jumbo carousel was loaded with up to 10 reinforcement elements prior to approaching the face. Once loaded, the jumbo tracked to the face and parked, with jack stands raised. Access barriers were placed between the jumbo's forward jack stands and the adjacent sidewall of the tunnel, preventing operators or bystanders accessing forward of the jumbo. At this time the reinforcement and mesh installation commenced. The philosophy of the primary ground support system was to control spalling failure as quickly as possible. As such, the installation of the mesh and reinforcement was initially targeted towards any visible areas of stress driven instability in the tunnel profile. Evidence of notching in the profile due to spalling (Figure 200) guided the focused initial installation of reinforcement and mesh.



Figure 200 - Prioritisation of ground support installation to zones of stress-driven overbreak.

The process of installing the reinforcement elements followed a series of distinct steps. After initially drilling the borehole, the grout tube was inserted into the borehole and grout pumped into the hole, commencing at the toe and gradually progressing towards the collar by slowly retracting the grout tube. Once the borehole was fully grouted, the threaded bars were slowly inserted into the borehole. Closed circuit video cameras on the jumbo boom assisted the operator to align each reinforcement element with the borehole for insertion. The operator was not required to leave the cab for these tasks.

Chapter 5: Construction

The camera technology removed the need for a jumbo off-sider to perform the function of spotter, again eliminating human exposure to potentially hazardous conditions at the face. An expansion shell temporary point anchor (Figure 201) was used to secure the threaded bar in place during curing of the grout. A surface fixture was installed using a torqued nut at the collar. It should be noted that the threaded tails of all the reinforcement elements were lightly greased prior to installation, in order to prevent the secondary shotcrete layer from adhering to the tails. Once the areas identified to be at risk of spalling instability were reinforced and meshed, the jumbo was backed away from the face and reloaded with a full carousel of new bolts. The jumbo then returned to the face and continued to install ground support in the adjacent walls and roof to complete the floor-to-floor pattern.



Figure 201 - Expansion shell temporary point anchor for primary reinforcement.

Figure 202 presents a typical view of the primary reinforcement and surface support system, in this case installed in the lower wall. Continuity of load transfer between the ground support installed in consecutive development rounds was ensured by securing the mesh sheet overlaps with reinforcement. Due to mine site safety policy, it was necessary to install permanent reinforcement up to and including the last row of bolts in each development round. It was not permitted to install a row of temporary reinforcement, such as split sets in this last row at the face. Therefore, in practice, every fourth row of reinforcement required double the regular number of bolts, in order to secure the mesh overlap between consecutive cuts. Figure 202 illustrates this requirement, as well as the advance of the primary ground support layer for consecutive development cycles. A close-up view of the primary reinforcement, shotcrete and mesh layer prior to application of the shotcrete overspray is shown in Figure 203. Figure 204 depicts the primary ground support scheme in the same stage of completion (i.e. prior to shotcrete overspray) in a view looking towards the face.

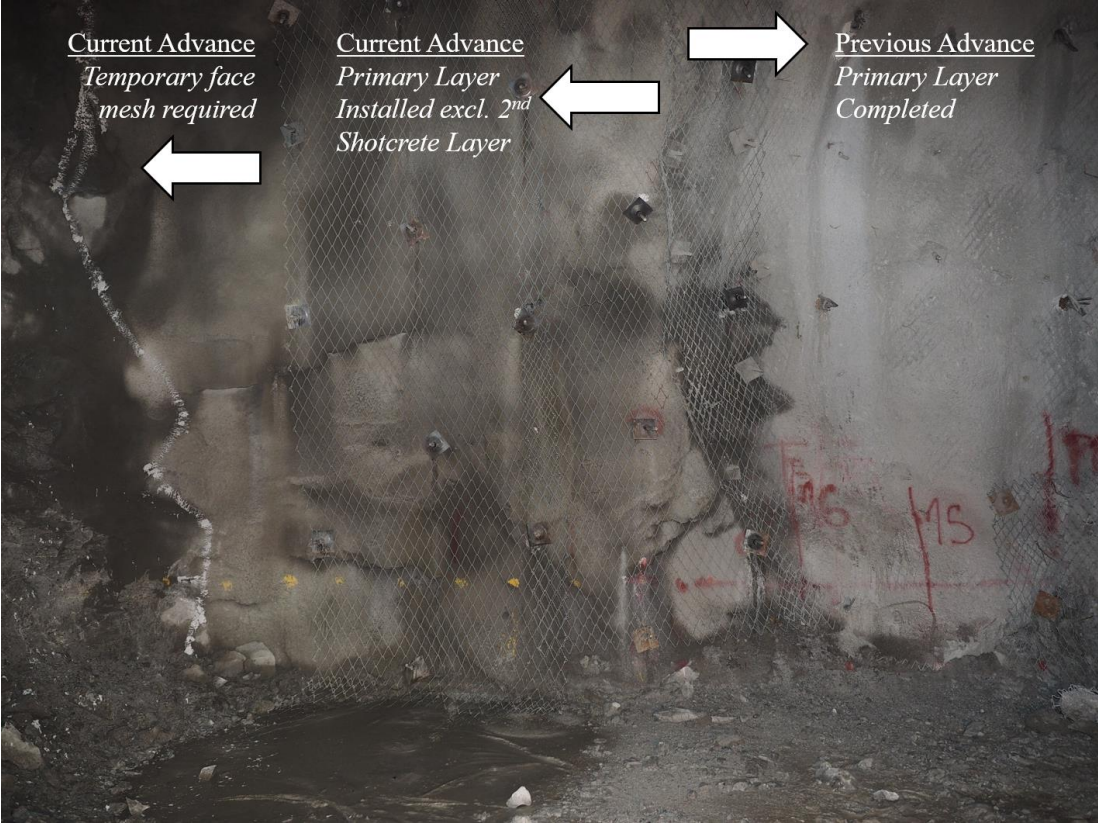


Figure 202 - Installation of primary reinforcement in a consistent pattern with high capacity mesh.



Figure 203 - Close up view of primary reinforcement, shotcrete and mesh arrangement.



Figure 204 - Completed installation of primary reinforcement and mesh awaiting shotcrete overspray.

5.4.7 Secondary Shotcrete Layer Application

The primary ground support scheme was completed by applying a 25mm second spray of shotcrete over the existing reinforcement, 50mm shotcrete layer and G80/4 mesh. The shotcrete overspray was designed to fully encapsulate the mesh. As discussed earlier, mesh-reinforced shotcrete has significantly greater energy dissipation capacity than shotcrete with an exposed (external) mesh layer. Mesh-reinforced shotcrete also has superior load transfer characteristics. Since both surface support components are rigidly connected, they deform at the same time and rate. This allows the ultimate capacity of both components to be achieved over a compatible range of displacement.

The primary shotcrete layer and exposed mesh was hosed down prior to application of the secondary shotcrete spray (Figure 205). This served to remove all dust from the primary shotcrete layer, improving adhesion between the two layers. The addition of water to the surface between the two shotcrete layers also aided hydration of the second shotcrete layer during curing. This was important to prevent preferential absorption of moisture into the primary shotcrete layer during curing of the overspray. This would have had a detrimental strength affect to the second layer, making the formation of a weakened cold joint more likely.

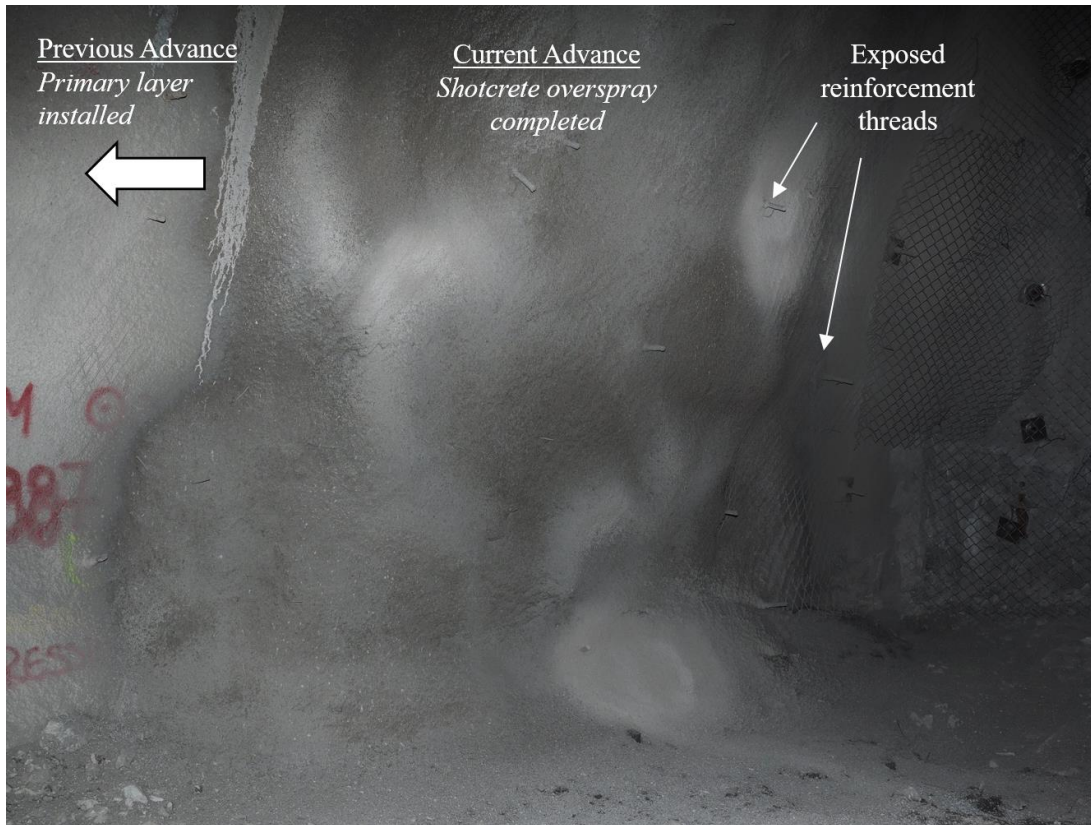


Figure 205 - Application of a second shotcrete layer with exposed reinforcement threads for second plating.

5.4.8 Installation of Temporary Face Support

It was not assumed that development face destress blasting would completely eliminate the potential for stress-driven spalling of the face. Therefore, temporary ground support was installed to control potential instability and provide a barrier between the face and the charge crew. Face support included mild steel chain-link mesh from roof-to-floor level, secured with 2.4m-long SS46 friction bolts on a 1m x 1m spacing. The development face destressing was observed to cause some remnant damage to the face, typically with dislodgement of a limited number of small loose blocks. This posed a risk, particularly to charge crew operators hands and arms, due to rock scats falling down the face. When securing the mesh to the face using split sets, the mesh was not initially installed flush with the face. A gap of 100-150mm between the rock and mesh was maintained during blast hole drilling. This allowed loose scats generated by drilling to fall to floor level behind the mesh, preventing later interference with loading the explosives (Figure 206). Prior to charging the face, the loose rock was scaled down and then the jumbo returned to install the split sets to full embedment, thus securing the mesh flush against the rock face.



Figure 206 - Temporary face support to contain face instability during drill and blast activities.

5.4.9 Primary to Secondary Support Installation Sequence

The philosophy of the ground support construction was to install the primary ground support layer as soon as possible after blasting, in order to control spalling of the excavation. The secondary ground support layer was installed in campaigns, after a set number of development advances were completed with the primary ground support layer only (Figure 207). The secondary ground support layer was installed prior to the possible onset of structurally controlled instability of the excavation. The potential timing of structural instability was considered with regard to the results of the probabilistic block analysis, as well as general observations of structural failures at other mines.

Field observations indicate that the instantaneous ejection of large structurally controlled blocks does not occur immediately after the excavation surface has been exposed (Figure 208). Typically, structural failures occur after the development face has advanced by some distance beyond the zone of instability. The reasons for this are not yet well understood. However, it is speculated that stress redistributions on the tunnel boundary have a time-dependent action on the block-forming joint surfaces, and the associated damage develops progressively, as the excavation is advanced.

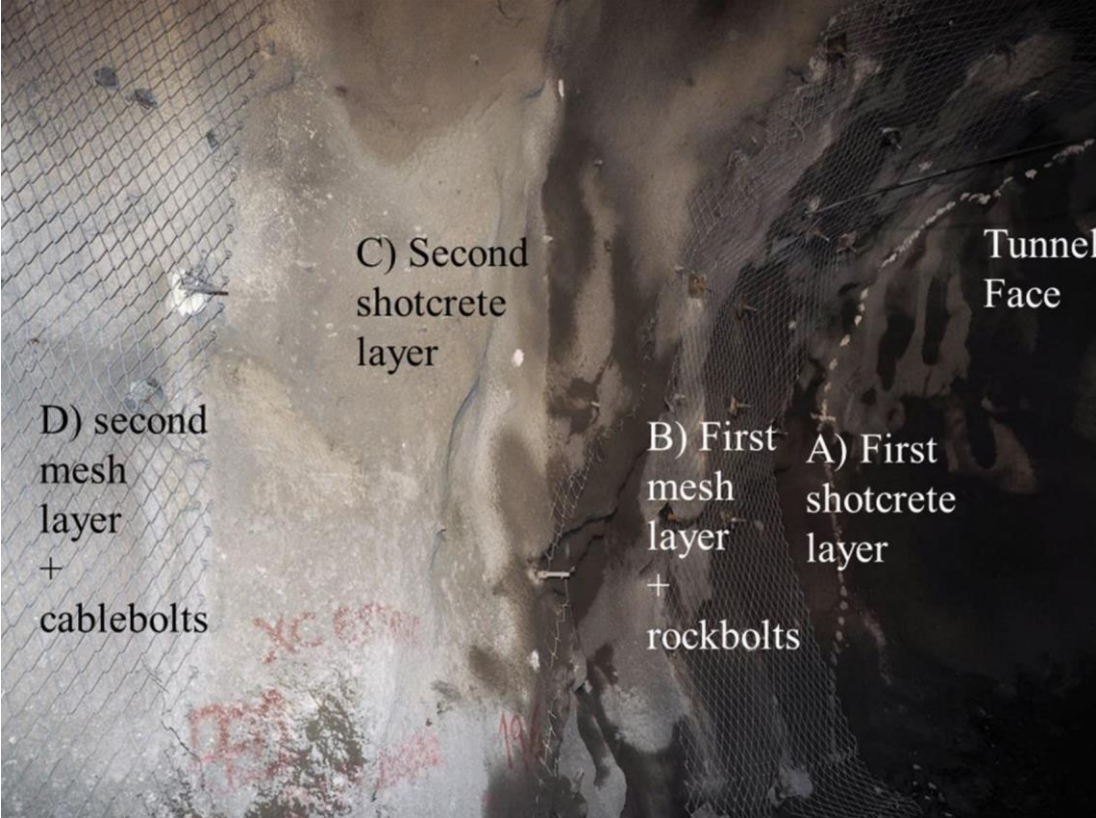


Figure 207 – Installation sequence of two integrated layers of high energy dissipation ground support.



Figure 208 - Structurally controlled excavation failure more than 20m from the development face.

Chapter 5: Construction

Field observations of structural failure from other mines typically reveal that deep instability occurs at a distance of four or more development cut lengths behind the face. In addition, with regard to the northern tunnel's specific design, the geometry of structural blocks identified by the SAFEX analysis was considered. In particular, the long, slender geometry of span-limited Blocks 1 and 3 indicated some potential for the local apex height to compromise the critical reinforcement embedment length after 10-15 metres of lateral development advance. As such, the need to install cable bolts for deep reinforcement capacity was deemed necessary within these distance limits.

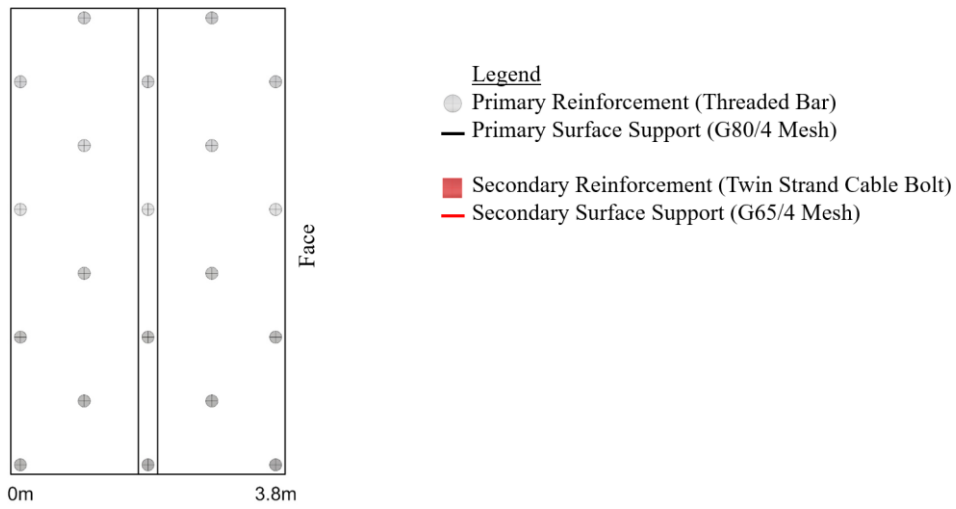
The installation of the secondary ground support layer was scheduled to be completed in short, repetitive campaigns. Initially, three blast advances were developed in the northern tunnel with the primary ground support layer. This exposed an 11.4m length of development reinforced with the primary ground support scheme only. Then, the secondary layer of cable bolts and external mesh was installed for the first two of these three cut distances. A minimum offset distance of one cut, or approximately 3.8m, was always maintained between the end of the secondary ground support pattern and the current face. The purpose of maintaining this offset was to reduce the potential for blasted flyrock to damage the exposed second mesh layer. A series of sketches illustrating the sequence of the ground support installation for the four final ground support rounds in the northern tunnel are presented in Figure 209 and Figure 210.

The ground support installation sequence implemented during the construction trials was largely dictated by how many cuts were able to be taken during the experiment. Under different circumstances, it would be recommended to install the high energy dissipation ground support scheme following a sequence as described below:

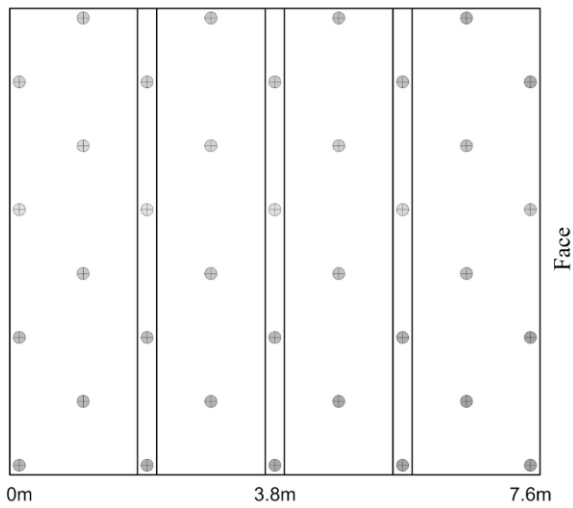
1. Develop three cuts (#1, 2 & 3) with primary ground support layer (in-cycle),
2. Install the first two cuts (#1 & 2) with the secondary layer (campaign),
3. Develop two more cuts (#4 & 5) with the primary layer (in-cycle),
4. Install the next two cuts (#3 & 4) with the secondary layer (campaign),
5. Continue the 2 cuts primary, 2 cuts secondary support sequence, as needed.

This sequence sees the secondary ground support lag the face by at most three development cuts, at any one time. Based on engineering experience and structural analysis of the block geometries, this sequence ensures deep reinforcement is installed prior to any structural instability occurring in the excavation.

Step 1 – Primary Ground Support (First Advance)



Step 2 – Primary Ground Support (Second Advance)



Step 3 – Primary Ground Support (Third Advance)

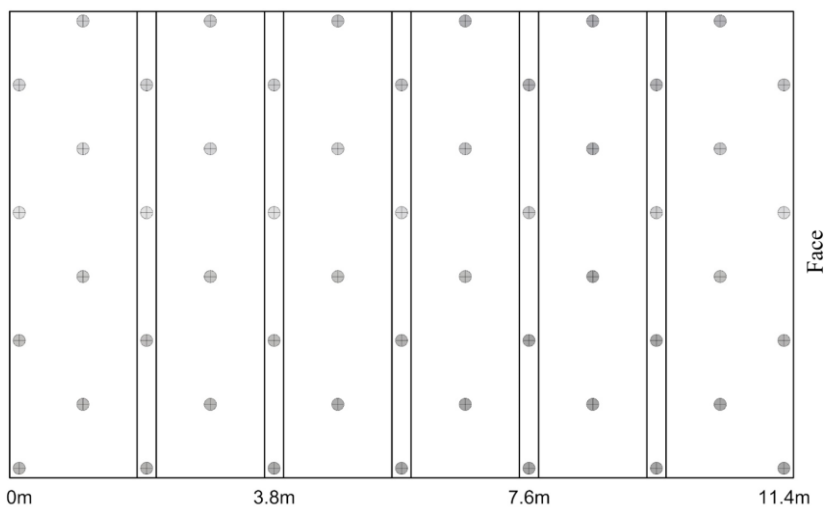
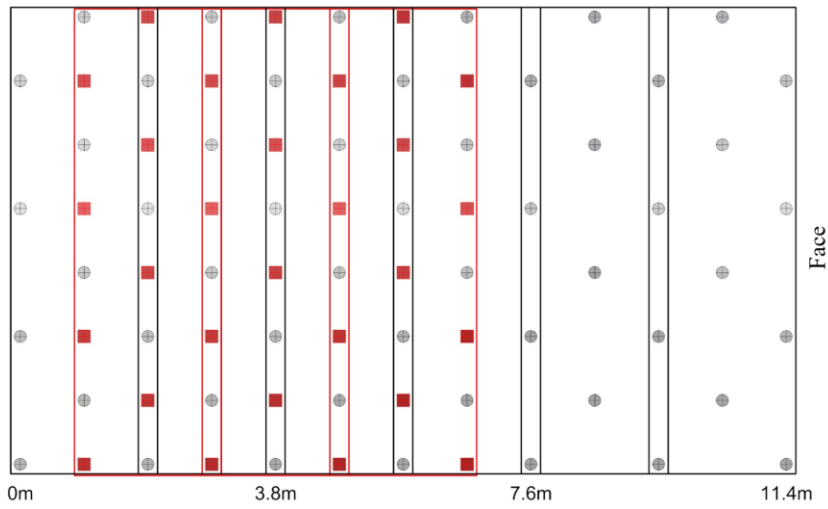
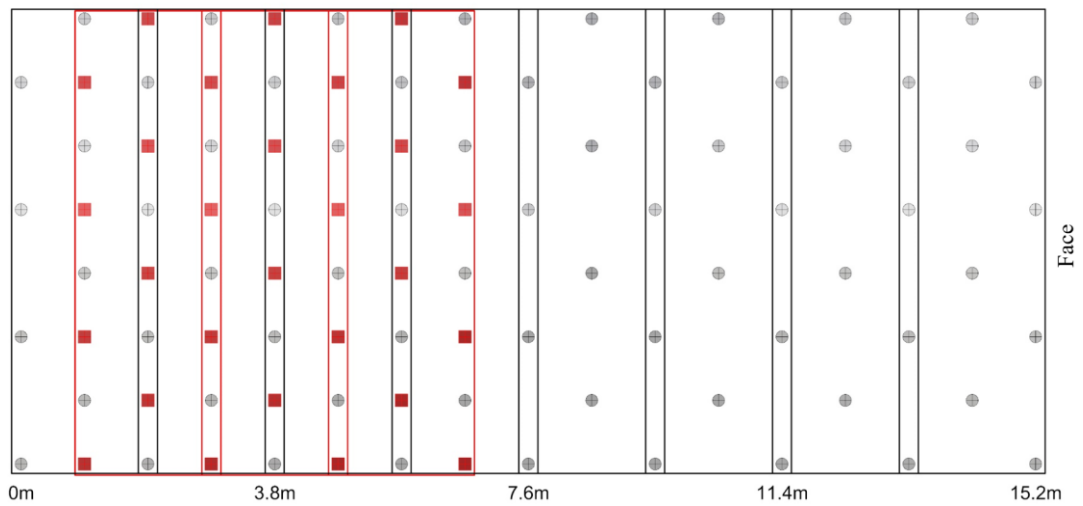


Figure 209 – Long section view of the primary ground support installation sequence.

Step 4 – Secondary Ground Support (First and Second Advance)



Step 5 – Primary Ground Support (Fourth Advance)



Step 6 – Secondary Ground Support (Third and Fourth Advance)

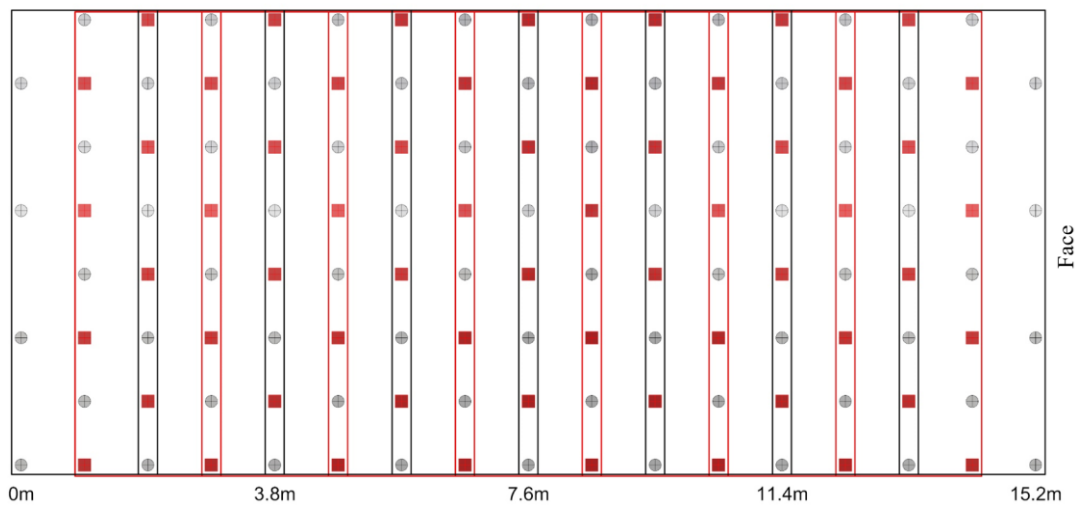


Figure 210 – Long section view of the secondary ground support installation sequence.

5.4.10 Secondary Reinforcement Collar Mark-Up and Drilling

As was performed for the primary reinforcement elements, the collar positions of the secondary reinforcement elements were marked on the shotcrete surface prior to drilling. This was done in order to ensure that the correct spacing and positioning of the cable bolts was maintained with respect to the primary reinforcement and mesh overlaps. This process was performed manually from an elevated work platform.

5.4.11 Installation of Secondary Reinforcement

Installation of cable bolts is generally safer and more efficient when using a fully mechanised cable bolting jumbo. As a cable jumbo was not available to the project, the cable bolts were installed and grouted manually. This task was undertaken from an elevated work platform after the cable boreholes were created by the drilling jumbo. The cables were installed prior to the secondary layer of mesh, as it was desired to avoid potentially damaging the mesh during the drilling process. The cables were installed on a 1m x 1m staggered pattern infilling between the existing primary reinforcement elements (Figure 211). The cables were fully cement grouted and then left for the grout to cure for at least 12 hours prior to mesh installation, plating and tensioning (Figure 212).

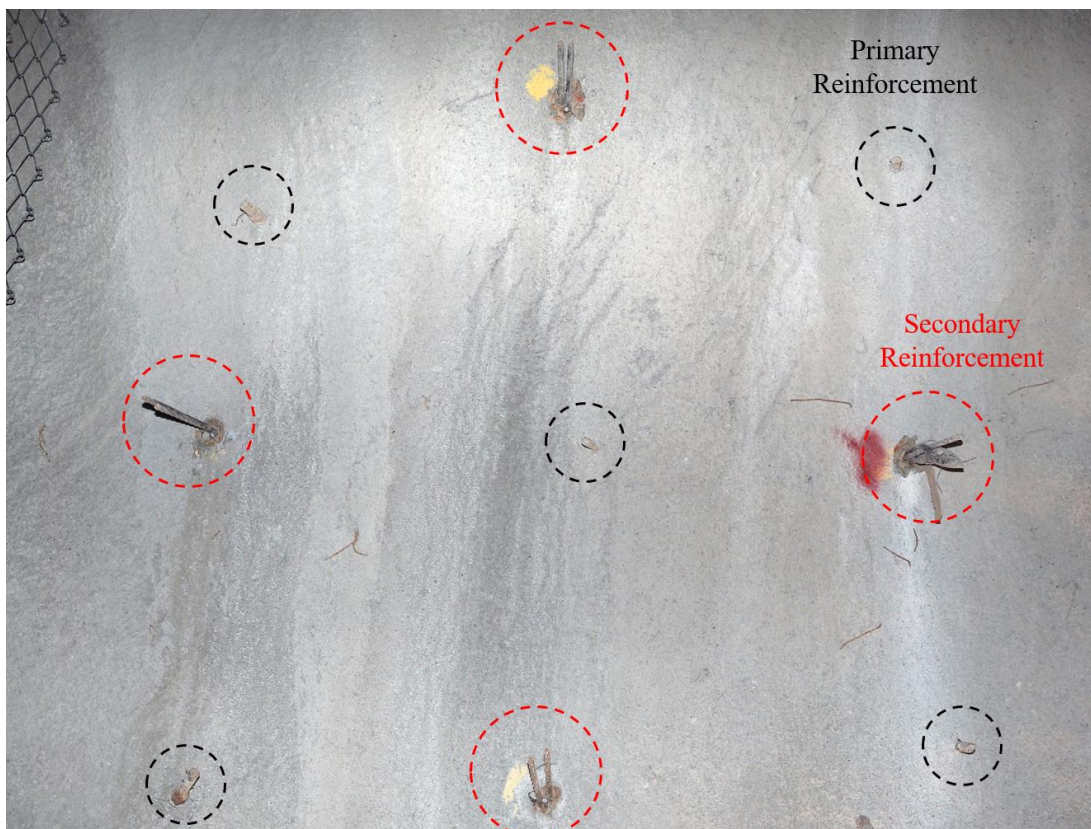


Figure 211 – Installation of secondary reinforcement within the primary reinforcement pattern spacing.



Figure 212 - Secondary reinforcement installed awaiting the second layer of high capacity woven mesh.

5.4.12 Installation of Secondary Mesh and External Fixtures

The second layer of mesh was installed external to the primary surface support layer. As the mechanised ground support jumbos were not designed to install mesh on a pre-existing reinforcement pattern, the second layer of mesh was installed manually and secured using surface fixtures on the existing elements. The mesh was draped over a purpose built elevated work cage (Figure 213) and manually moved into position on the excavation surface, before being fixed to the reinforcement elements (Figure 214).

The mesh was secured to the excavation surface using plates on the reinforcement. As the tails of the threaded bars were all covered in shotcrete (Figure 215), it was necessary to clean the tails prior to installation of the plate. All threaded bar tails were lightly greased during their installation, and were thus able to be easily cleaned of shotcrete in under 20 seconds each. Cleaning the tails was performed by striking the tails with a steel hammer several times to shock most of the shotcrete from the tail. A steel wire brush was then used to remove any stubborn excess. Cleaning the reinforcement tails in this way left a clear thread to install the plate and nut (Figure 216). Installation of the mesh and second plate on the primary reinforcement (Figure 217) was completed by torqueing a nut using a pneumatic wrench (Figure 218).



Figure 213 - Installation of the second mesh layer from an elevated work platform.



Figure 214 – Fixation of secondary mesh layer to the primary reinforcement elements.



Figure 215 - Primary reinforcement element threaded tail after second shotcrete application.



Figure 216 -Primary reinforcement element threaded tail after removing shotcrete.



Figure 217 - Primary reinforcement element connected to secondary mesh via an external fixture.

In some cases, the second mesh layer could not be positioned flush to the rock surface using manual force, due to concavity in the tunnel surface and resulting tension in the mesh. This situation required the use of a hydraulically operated ram rod to position the mesh flush to the tunnel surface. Figure 218 depicts this process, which allowed installation of the second plates on the threaded bars.



Figure 218 - Use of a hydraulic ram to install mesh and second plates on the primary reinforcement.

Both the primary and secondary surface support layers were connected to both the primary and secondary reinforcement elements. In order to provide the means of load transfer between the surface support layers and cable bolts, plates were installed on all the cables. The plates were installed on both strands according to the conventional process. A two-hole plate was placed over the cables and tensioned to both strands using barrel and wedge assemblies and a hydraulic ram. Each strand was tensioned to a load of 5 tonnes. As the exposed tails of the cables were generally 500mm in length, there was usually no difficulty in positioning the mesh over the cable tails in areas where the excavation surface was concave and the mesh under tension.

Once the plates were installed on the cables and tensioned hard against the tunnel surface, the tails were cut down to a length of 250mm using an angle grinder. The individual strands on each cable tail were then unfurled and bent at an approximately 90 degree angle around the barrel and wedge (Figure 219). This thought to have slightly increased the axial force needed to cause displacement of the strand through the barrel and wedge assembly, which in turn increased the energy dissipation capacity of the cables.



Figure 219 – Unfurled cable strands at the external fixture.

5.4.13 Securing of Secondary Mesh Overlaps

Observations of stress-driven violent failures at many mines indicate that separation of mesh at the overlap is a frequent cause of uncontained rock ejection through the ground support scheme. An optional tactic which can significantly reduce this vulnerability in the ground support scheme is to install steel wire lacing through the mesh overlaps (Figure 220). The stitching of a flexible, 6mm-diameter wire rope through the mesh overlaps requires manual work from an elevated platform. The overlaps in all mesh sheets may be stitched together from floor-to-floor level and the wire crimped at both ends (Figure 221).

In the event of separation of the mesh, including fracture of the shotcrete layers at the overlaps of the primary mesh layer, these wire ropes provide additional capacity to hold the mesh overlaps closed. This reduces the chance of large blocks being ejected between the mesh sheets. At a minimum, this stitching is beneficial to install in the secondary mesh layer, which is the external surface support component. However, stitching the overlap in the primary mesh layer prior to installing the second shotcrete spray is also advantageous. This provides redundancy in connectivity between the components, which is in addition to the encapsulation function of the shotcrete.

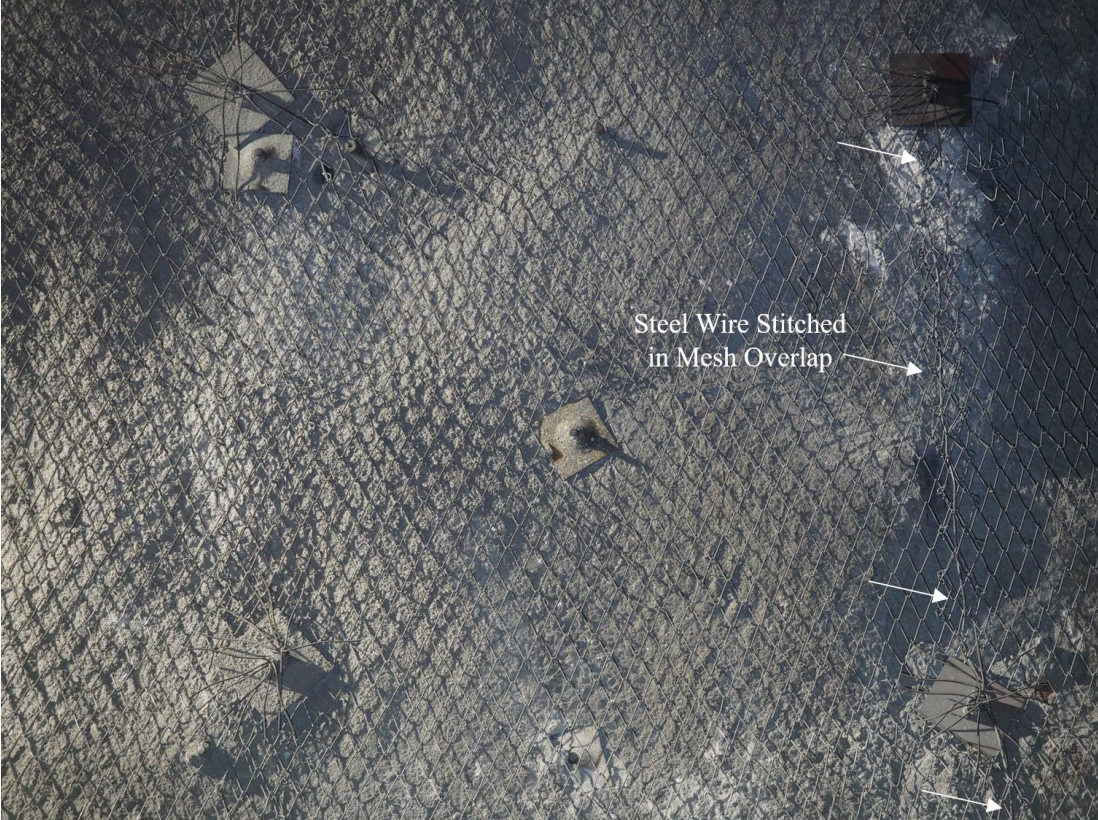


Figure 220 - High strength and flexible steel wire stitching through the mesh sheet overlap.



Figure 221 - Wire stitching through mesh sheet overlaps terminated with three crimps at floor level.

5.4.14 Final Ground Support Scheme Arrangement

In summary, the completed installation of the mechanised ground support scheme for high energy dissipation included the following components:

Primary Surface Support

- 75mm-thick shotcrete layer (50mm initially + 25mm overspray), internally reinforced with high tensile G80/4 articulating mesh (floor to floor).

Primary Reinforcement

- Mild steel threaded bar, 25mm diameter, 3.25m-long (3.0m embedment) on a 1m x 1m staggered pattern spacing, continuously mechanically coupled, fully cement encapsulated, double plated using 200 x 200 x 8mm dome plates.

Secondary Surface Support

- G65/4 high tensile woven mesh (floor to floor).

Secondary Reinforcement

- High tensile, twin strand, plain cable bolts, 15.2mm diameter, 5.5m-long (5.0m embedment) on a 1m x 1m staggered pattern spacing, continuously mechanically coupled, fully cement encapsulated, 300 x 300 x 10mm face plates, both strands tensioned to 5 tonnes.

Figure 222 presents a close up view of this ground support scheme arrangement installed in the wall of the northern tunnel. This photograph focuses on an area of approximately 4m² in which the arrangement of the surface support layers and multiple passes of reinforcement can be visualised. A view of the entire tunnel profile following installation of the complete dual-layer ground support scheme is depicted in Figure 223. Laboratory testing of the individual components of this scheme at WASM provides the best available quantification of the energy dissipation capacity of this scheme. As described earlier, the total energy dissipation capacity of the scheme was approximately 65 kJ/m², with an associated range of displacement of 300mm for the primary ground support scheme and 400mm for the secondary layer. Installation of the primary layer was highly mechanised, as this work occurred adjacent unsupported ground. Once the rock was permanently supported, manual methods were required, given the available mining equipment. Further mechanisation of the secondary ground support layer would significantly improve construction efficiency.

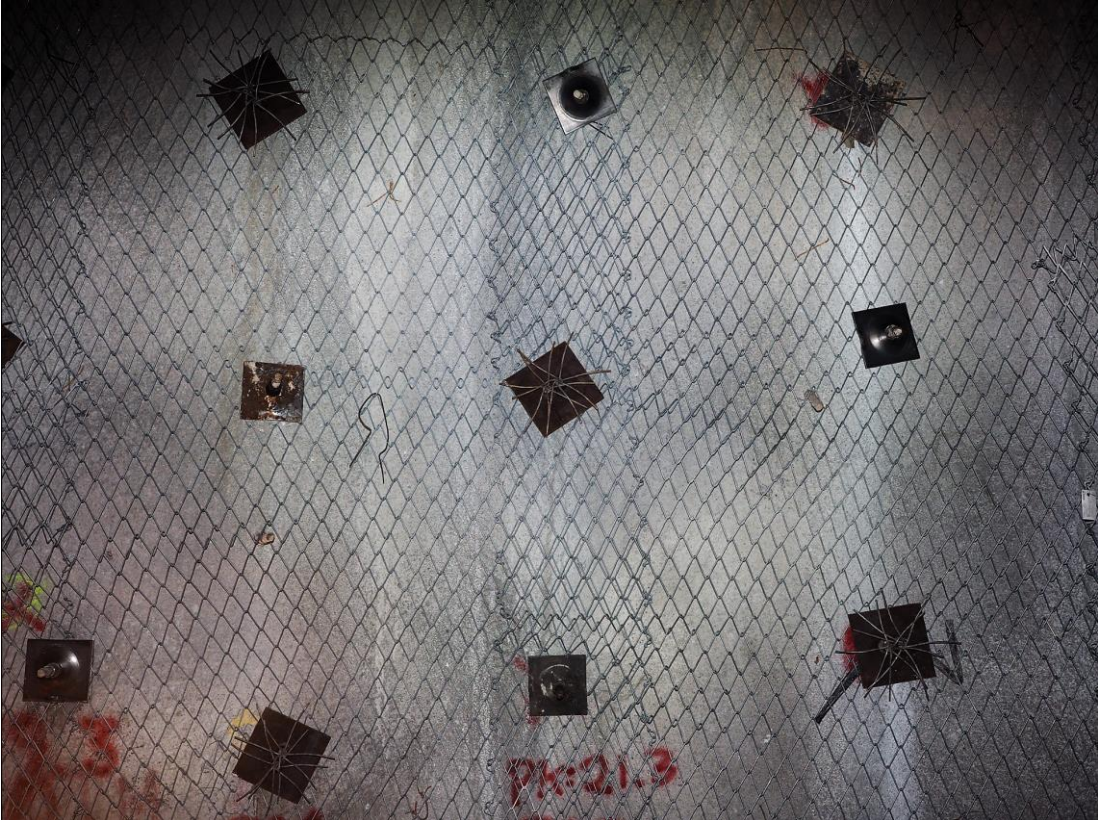


Figure 222 - Close-up view of final reinforcement pattern and surface support arrangement.



Figure 223 – Multi-layered, high energy dissipation ground support scheme installed in the north tunnel.

Chapter 6

Monitoring & Analysis

This chapter presents the detailed methods of data collection for this research, as well as interpretation of the results.

The three phenomena that were monitored and analysed throughout this research project were:

1. rock mass seismicity,
2. blast-induced rock mass fracturing, and
3. excavation profile overbreak.

Seismic activity related to the construction of the research tunnels was monitored using a high resolution local seismic monitoring system. A number of sensors were installed in a three-dimensional array entirely surrounding the two tunnels. These sensors were designed to detect and accurately locate the range of seismic events generated by the creation of the excavations. These included very small magnitude events close to the tunnel boundary. The system was optimised for the magnitude range of expected seismicity. It had the capability to measure and record the seismic event hypocentres, source parameters such as magnitude, moment, radiated energy, potency, as well as the source mechanisms for some events.

The physical characteristics of the destress blasting-induced fracture networks were primarily measured manually during tunnel construction. Data collection techniques included photography and manual scale measurement of the radial fractures generated around the destressing charges. The orientation of fractures was also measured and assessed with respect to the known stress conditions. A ground penetrating radar experiment was also conducted prior to the tunnel constructions. The preliminary tests were designed to develop an initial appreciation of the GPR frequencies needed for fracture zone mapping in weakly conductive rock. The results guided recommendations for the manufacture of a purpose-designed borehole radar instrument which could be used to monitor the fracturing caused by destress blasting.

Overbreak of the excavation shape caused by stress and/or structural influences was measured using a GeoSlam Zeb laser survey instrument. This measurement technique provided spatial information on the final excavation geometry, which permitted analysis of the depth of progressive spalling instability.

6.1 Local Seismic Monitoring System Design

6.1.1 Sensor Type

The sensors chosen for the seismic system were 25kHz tri-axial accelerometers. Tri-axial sensors were chosen as they allowed accurate determination of event hypocentre coordinates, seismic source parameters and mechanisms, given the three orthogonal recording channels. Uniaxial sensors were not used as they are primarily suited to determining event locations and are unsuitable for more detailed scientific investigation of the seismic sources. In comparison to standard geophones, accelerometers are generally capable of measuring much smaller ground motions. This was of critical importance to this research, considering the small source radii of rock mass instabilities associated with the tunnel construction. As such, accelerometers were used exclusively in the seismic sensor array.

In order to initially select an appropriate accelerometer frequency, it was necessary to consider the minimum magnitude of the seismic events desired to be recorded. In this case, small macro-scale fracturing events associated with development and destressing ahead of the tunnel face were expected to have a local magnitude (M_L) as low as $-4.0M_L$. The necessary sensor frequency needed to reliably record these small events was determined via the following equations. The assumptions were: $M_L = -4.0$, $V_p = 4770\text{m/s}$, $V_s = 2490\text{ m/s}$, $\Delta\sigma = 1\text{ MPa}$.

The seismic moment M_O of the smallest recordable event was calculated via Hanks & Kanamori (1978) and Mendecki (1997), as follows:

$$M_O = 10^{1.5(M_L+6.06)} = 10^{1.5(-4.0+6.06)} = 1230\text{ N.m} \quad (\text{Eq. 6.1})$$

Then, the source radius (Keilis-Borok, 1959) for a $-4.0M_L$ event was quantified where $M_O = 1230\text{ N.m}$:

$$r = \left(\frac{7M_O}{16\Delta\sigma}\right)^{1/3} = \left(\frac{7(1230)}{16(1 \times 10^6)}\right)^{1/3} = 0.081\text{m} \quad (\text{Eq. 6.2})$$

The corner frequency of both the P wave (f_{op}) and S wave (f_{os}) radiated from the events of minimum recordable magnitude ($-4.0M_L$) were then calculated by assuming the Brune model (Brune, 1970) for the source and using the following relationships from Mendecki (1997):

$$f_{0P} = \frac{V_P}{V_S} f_{oS} = \frac{4770}{2490} (11,448) = 21,930 \text{ Hz} \quad (\text{Eq. 6.3})$$

$$f_{oS} = \frac{KV_S}{2\pi r} = \frac{2.34(2490)}{2\pi(0.081)} = 11,448 \text{ Hz} \quad (\text{Eq. 6.4})$$

Considering that source parameters are frequently derived from the P-waveforms, it was necessary for the sensors to reliably record in the range of $f_{0P} = 21,930 \text{ Hz}$.

The closest available accelerometer frequency of 25kHz was selected, theoretically permitting detection of seismic events with a source radius as low as eight centimetres. This was a relatively high frequency sensor in comparison to most seismic monitoring applications in mining. However, this frequency was deemed to be optimal for detecting the dominant corner frequencies of very small seismic events, given the rock mass response to the prevailing conditions.

These sensors provided the necessary detail to investigate the source mechanisms at their true scale. Generally, the larger the seismic event desired to be recorded, the lower the necessary sensor frequency. In this case, a high frequency was chosen to focus on the small seismic sources. Nonetheless, the 25kHz frequency accelerometers did not exclude reliable recording of larger events around the excavations. Events within the range of -4.0 to +1.5 M_L were expected to be reliably captured by the monitoring system.

6.1.2 Array Size and Sensor Locations

The zone of interest surrounding the two research excavations was approximately 80m wide x 70m long x 40m high, or 224,000m³ in total volume. Very high resolution seismic data was desired to be captured throughout this zone. Considering that the seismogenic zone ahead of the tunnel face shifted position with the development, an important requirement of the sensor array was that it maintain consistently high sensitivity across the entire tunnel length. It was critical that system sensitivity be as consistent as possible across the experimental site, so that seismic data was not biased by significant sensitivity differences in location error or seismic source parameters. Such variability in the accuracy of recorded data was avoided to ensure valid interpretations of the seismic response along the entire tunnel length.

The local seismic system consisted of eight fully-grouted borehole accelerometers positioned in a symmetrical, three-dimensional array. The sensor array completely surrounded both tunnels. Design and actual installed sensor coordinates are presented in Table 46. The array design and final installed sensor locations are also illustrated in Figure 224. Sensors were permanently grouted into boreholes drilled from various locations on the access development. Gyroscope trace surveys of every borehole were conducted to ensure that the final position of the installed accelerometers was accurately known with less than 0.2m location uncertainty. Due to drilling deviation and a decision to co-locate the sensors with the gyroscope survey point nearest the designed sensor location, the actual installed position of the sensors varied slightly from the design that was planned. The 3D vector distance between the design and actual position of each sensor is quantified by the ΔD value in the table below.

Table 46 - Design versus Installed sensor locations (mine coordinate system).

Sensor Number	Design Location			Installed Location			ΔD (m)
	X	Y	Z	X	Y	Z	
1	559.57	746.89	1883.80	559.14	746.44	1880.95	2.92
2	523.31	729.98	1883.80	526.67	732.05	1883.65	3.95
3	551.67	669.01	1883.80	556.84	670.17	1881.68	5.71
4	587.93	685.92	1883.80	586.64	688.95	1880.97	4.34
5	555.59	707.81	1903.80	558.96	709.79	1902.37	4.16
6	519.34	690.90	1903.80	525.12	696.38	1903.94	7.97
7	555.59	707.81	1863.80	559.29	709.75	1865.88	4.67
8	519.34	690.90	1863.80	520.98	692.59	1864.23	2.39

Sensors 1, 2, 3 and 4 were positioned at the same elevation as the tunnel. The distance between the excavations and these sensors was decided as a compromise between minimising the distance of separation, for improved source parameter sensitivity, and risking blast induced sensor damage. The minimum distance between any sensor and a planned tunnel was 10m (sensor #4). An analysis was completed to ensure that the distance between the excavation and nearest accelerometer was sufficient to prevent blast damage to this or any other sensor. The 25kHz accelerometers were rated to survive 5000g shock loads. Conservatively assuming that blast-induced peak ground motions (V , PGV) at a distance of 10m were in the order of 0.2m/s and peak blasting frequencies (f_0) were in the 10kHz range, an estimate of the instantaneous shock loading (i.e. peak ground acceleration, PGA) on the sensors was performed as follows:

$$\begin{aligned}PGA &= 2\pi f_o V = 2\pi(10000)(0.2) && \text{(Eq. 6.5)} \\ &= 12,566m/s^2 = 1280g\end{aligned}$$

This value of 1280g was safely within the 5000g performance envelope of the accelerometers. Therefore, 10m was deemed a safe distance of separation between the experimental tunnels and nearest seismic sensors.

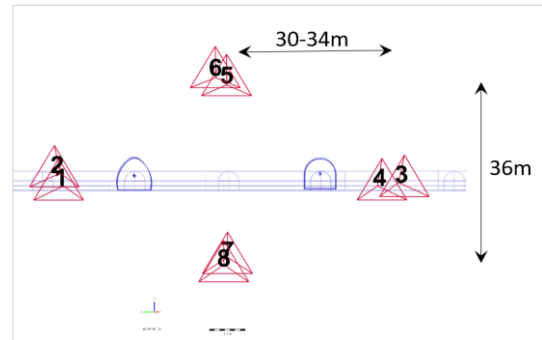
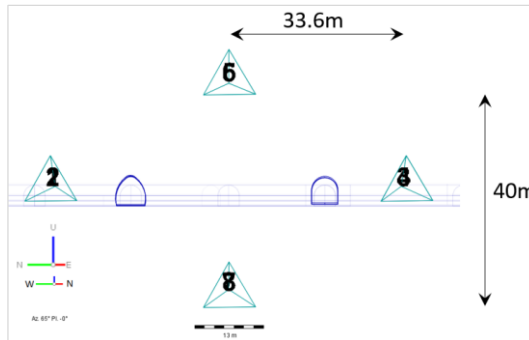
Sensors 5, 6, 7 and 8 were positioned within the central pillar between the two tunnels. Sensors 5 and 6 were positioned approximately 18-20 metres above the elevation of the tunnels. Sensors 7 and 8 were positioned the same distance below. The centroid of the vertical plane formed between sensors 5, 6, 7 and 8 was offset by approximately 20m to the southwest of the centroid of the horizontal plane formed between sensors 1, 2, 3 and 4. Sensitivity analysis indicated that this offset increased the system sensitivity ahead of the final face of the excavations, such that the seismogenic zone could be more accurately recorded ahead of the final faces. The 40m vertical separation between the highest sensors (5 & 6) and lowest sensors (7 & 8) in the array was also chosen over a 20m vertical separation based on sensitivity modelling analysis of both arrangements. Sensitivity analysis indicated that a larger vertical separation of around 40m significantly improved event location accuracy, while slightly raising the minimum detectable magnitude sensitivity. This was an accepted compromise in the system design. Further detail on the sensitivity analysis is presented in a subsequent section.

The overall objective of the array design was to place sensors such that location accuracy of the events was as high as possible. This required sensors to completely surround the excavations, and to have as many sensors as possible ahead of the face for uninterrupted ray paths. The final array design was deemed to be the best arrangement for these objective, with some compromises made. For example, some sensors were necessarily positioned behind the advancing face in order to ensure that the face was not outside the array boundary and thus at risk of greater event location errors.

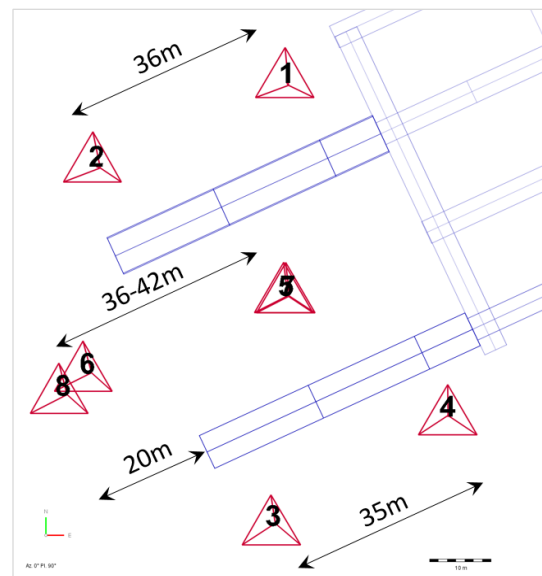
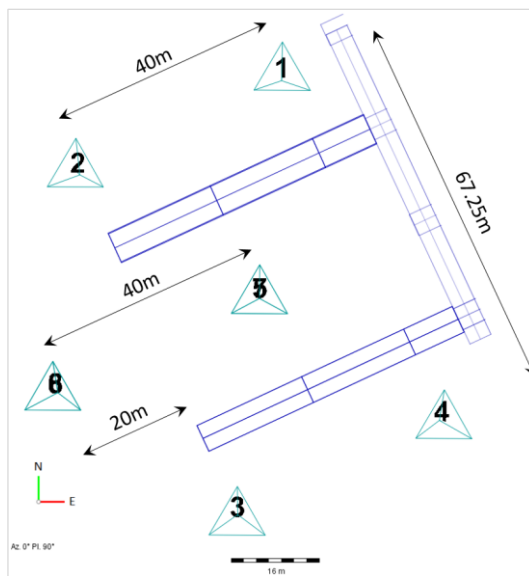
Design Sensor Positions

Actual Installed Sensor Positions

Cross Section (view ENE)



Plan View



Perspective View (View NNE)

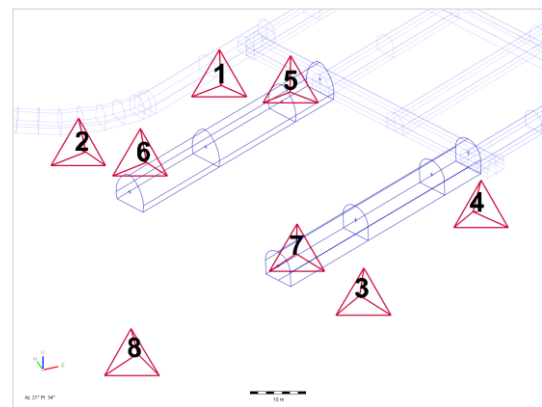
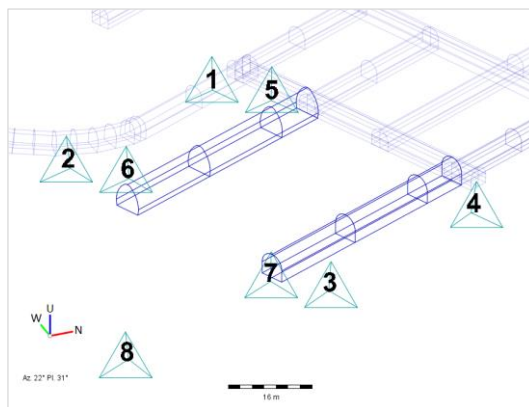


Figure 224 – Design and actual installed locations of the seismic sensors.

6.1.3 3D Location Error

Location error is the 3D vector distance between the true seismic event hypocentre coordinates and those calculated and reported by the seismic monitoring system. The 3D location error was theoretically analysed for a number of seismic array options using the *Sensitivity Analysis* plugin from the IMS Vantage software. This software was used during design of the accelerometer array in order to conduct and compare sensitivity performance for a number of array options, prior to finalising the system design for installation. Of all the possible sensor arrangements that were considered, the aforementioned final design displayed the optimum characteristics of minimal location error, maximum seismic source parameter sensitivity and spatial consistency in this sensitivity surrounding the two excavations. The input parameter assumptions for the sensitivity analyses are shown in Table 47. Table 48 presents the rock mass velocity model parameters used for the analyses. Input values for P and S-wave propagation velocity were assumed based on values for similar rock types.

Table 47 - IMS Vantage sensitivity analysis input parameters.

Sensor Properties		Sensitivity Analysis Properties	
P-wave pick error	1 x 10 ⁻⁴ s	Minimum number of sites	5
S-wave pick error	1 x 10 ⁻⁴ s	Maximum number of sites	8
Site position error	0.1 m	PPV Magnitude Coefficient	0.98
Sensor Type	Tri-Axial	PPV Distance Coefficient	1.8
		PPV Constant	3.8

Table 48 - Velocity model parameters for the Dacite rock type, used in seismic sensitivity analysis.

Parameter	Input Value	Parameter	Input Value
P-wave Velocity	4770 m/s	S-wave Velocity	2490 m/s
Velocity P-error	0 %	Velocity S-error	0 %

The location error sensitivity analysis results for the final sensor array design are shown in Figure 225, Figure 226 and Figure 227. Each of these figures presents the horizontal section of the location error results at the 1882mRL elevation. This is the excavation mid-height. The three images also show a vertical section of the results taken at a distance of 10m, 30m and 60m from the turnout location of the experimental drifts, respectively. These results indicated that within 3 diameters of each tunnel the recorded seismic event location error could be expected to be less than or equal to 0.5m. Between 3 and 6 diameters of each tunnel the hypocentre location error should not exceed 1.1m.

Considering the dimensions of the seismogenic volume to be monitored and the available number of sensors, this was considered to be the optimal result. Hypocentre location error of this scale was sufficiently small to permit very detailed analysis of the spatial characteristics of the local seismogenic zones surrounding each excavation, down to sub-metre scale. It is important to note that the predicted 3D location error varied by less than 0.1m along the entire axis of each tunnel. Consistency in the location accuracy of the seismic array ensured that spatial data on seismic events was equally accurate at the start of the drift as it was at the final face. Hence, observations and conclusions on the shape, size and spatial characteristics of the seismogenic zones could be reliably compared along the entire length of the excavations. Data bias due to spatial variability in 3D location accuracy was minimised with this array design.

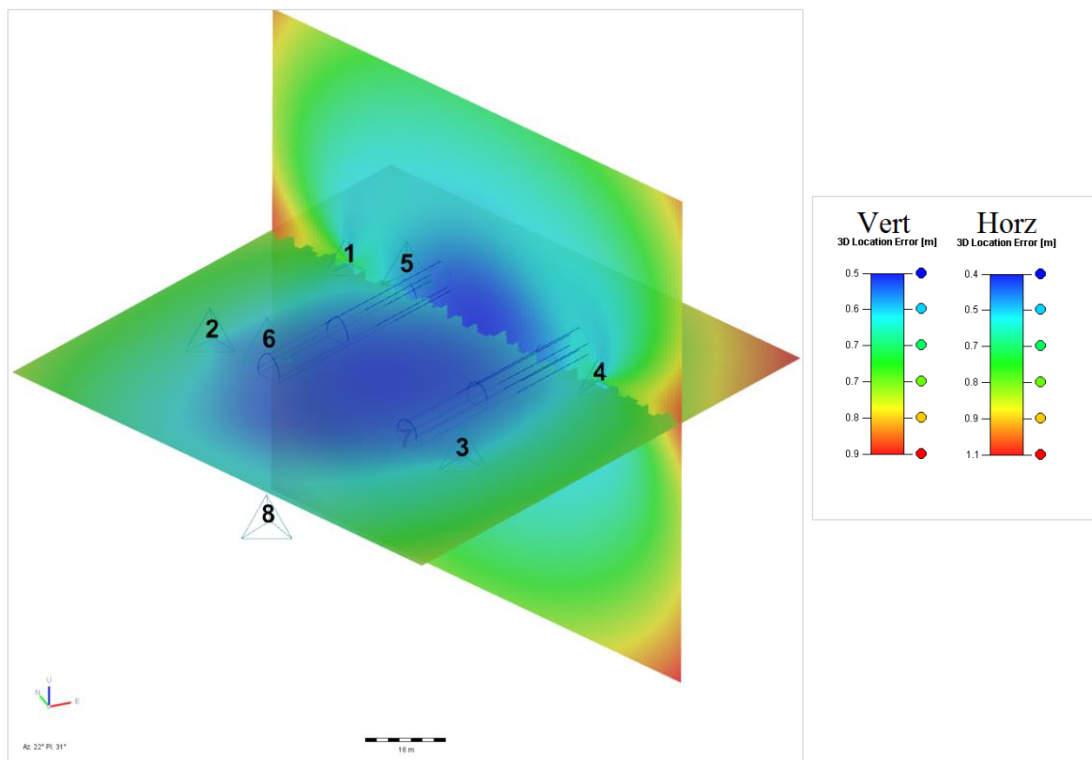


Figure 225 - 3D location error: horizontal section at 1882mRL and vertical section 10m from turnout.

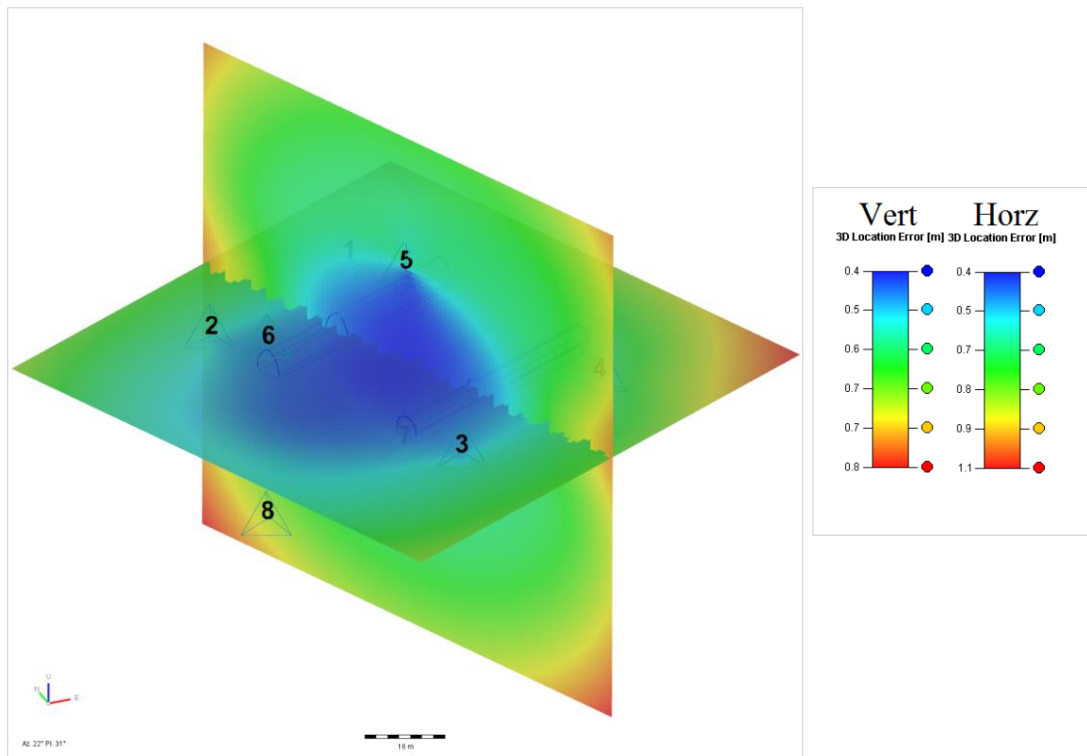


Figure 226 - 3D location error: horizontal section at 1882mRL and vertical section 30m from turnout.

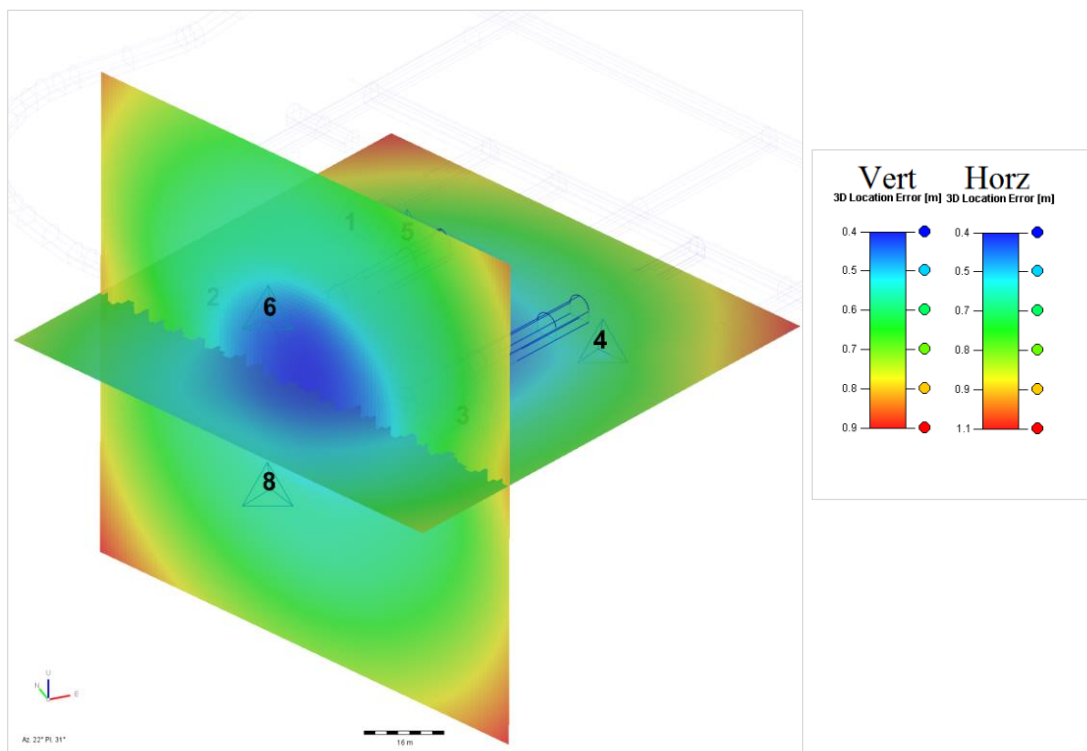


Figure 227 - 3D location error: horizontal section at 1882mRL and vertical section 60m from turnout.

6.1.4 Source Parameter Sensitivity

In addition to 3D location error, sensitivity of the seismic system to source parameters also varied spatially, depending on the position of installed sensors. As part of the array design, *Minimum Magnitude* sensitivity modelling was conducted using the IMS Vantage software. The minimum magnitude results for the final array design shown below represent the magnitude threshold above which all mining induced seismic events were expected to be reliably recorded. Events smaller than the stated minimum magnitude may also have been recorded. However, the population of events smaller than the magnitude threshold may have been incomplete, as the system was not expected to be sensitive enough to detect all such events which occur.

The sensitivity to which seismic source parameters other than magnitude were measured was also subject to variability, although the Vantage sensitivity analysis plugin had no specific tools to model this. On advice from the Institute of Mine Seismology (Lynch, R, 2015, pers.comm.) the 25kHz accelerometers used in this array configuration were expected to quantify seismic potency and source mechanisms for events with magnitude as low as $-4.0M_L$ and radiated seismic energy down to $-3.3M_L$. These thresholds applied to the volume where array sensitivity was at its maximum. Sensitivity may have varied in other zones.

Figure 228, Figure 229 and Figure 230 present horizontal sections of the minimum magnitude sensitivity modelling results at elevations of 1862mRL (20m below tunnels), 1882mRL (same elevation as tunnels) and 1902mRL (20m above tunnels), respectively. These modelling results indicated that the accelerometer array was slightly more sensitive towards the western half of each tunnel. However, the difference was expected to be minimal at around $0.2M_L$. The modelling suggested that for the first 30m of development in each tunnel, all seismic events above $-2.4M_L$ should have been recorded. Whereas for the last 20m of development, all events above $-2.6M_L$ should have been recorded. This slight variability in source parameter sensitivity along the axis of each tunnel was a known compromise, in order to improve location error accuracy. An alternative accelerometer array configuration with a 20m vertical distance separating sensors 5 and 7, and 6 and 8, was considered. However, although this arrangement achieved superior source parameter sensitivity, the modelled hypocentre location error around the position of the tunnel faces was significantly poorer. Sensor 5 and 7, and 6 and 8 were therefore separated by 40m vertically.

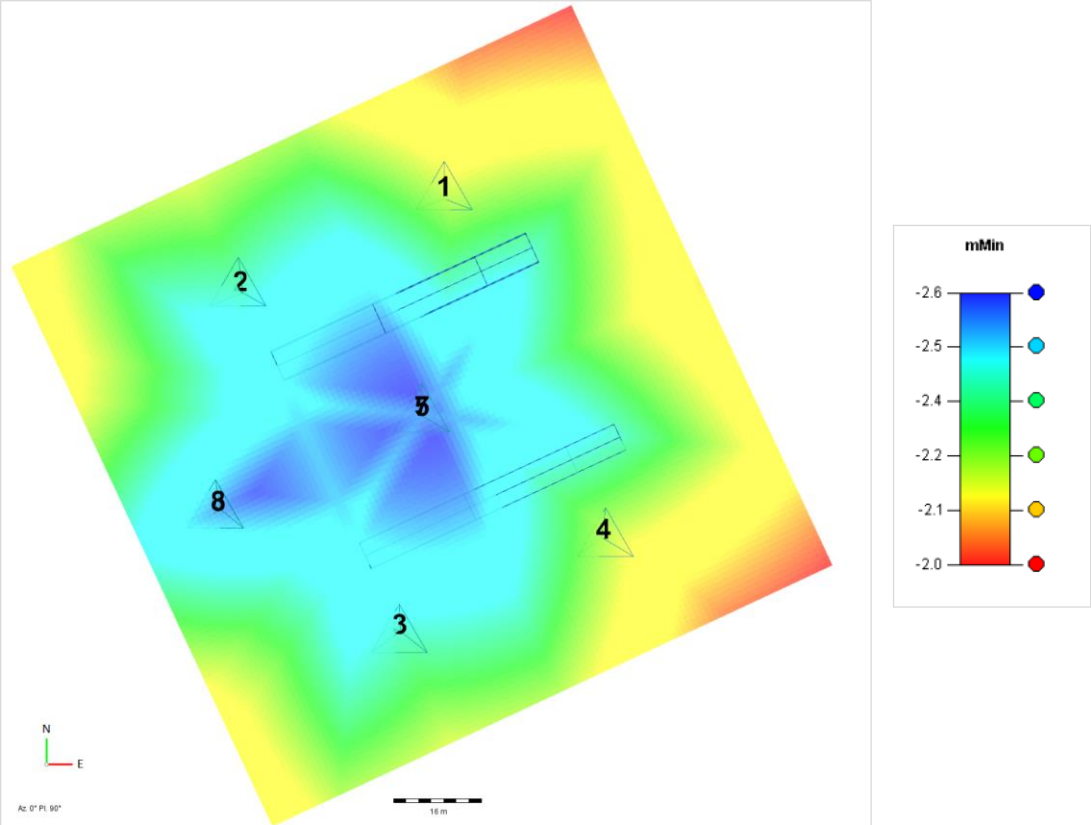


Figure 228 - Horizontal section of minimum magnitude sensitivity at 1862mRL (20m below tunnels).

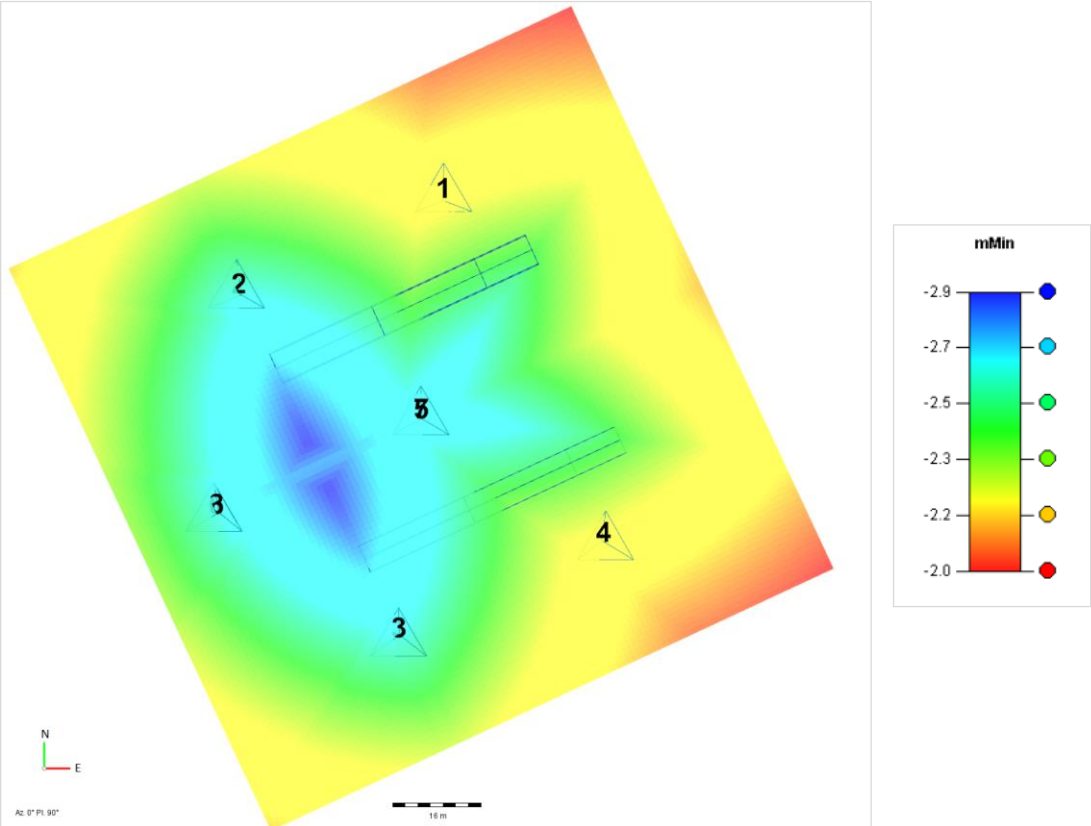


Figure 229 - Horizontal section of minimum magnitude sensitivity at 1882mRL (same level as tunnels).

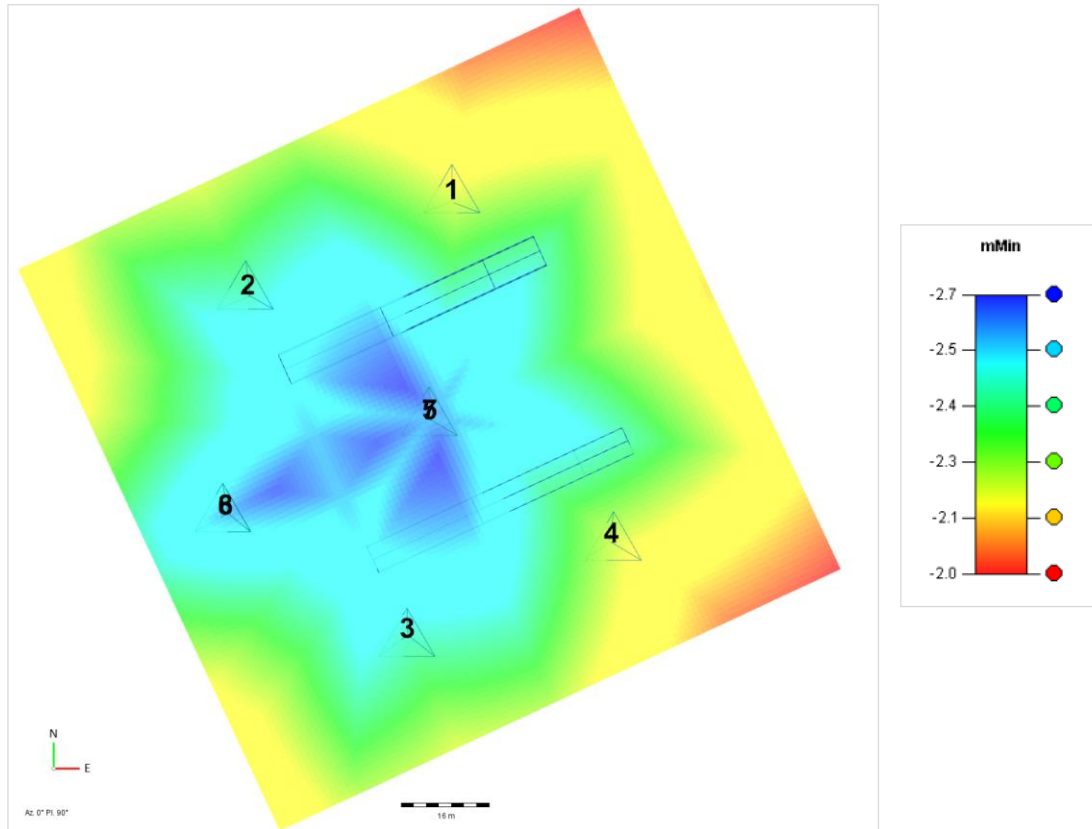


Figure 230 - Horizontal section of minimum magnitude sensitivity at 1902mRL (20m above tunnels).

Figure 231, Figure 232 and Figure 233 below present vertical cross sections of the minimum magnitude sensitivity modelling at distances of 10m, 30m and 60m from the turnout position of the drifts, respectively. The view in each image is towards the azimuth of 65° , relative to mine north. Note that the coloured sensitivity contour values vary slightly for each image. When interpreting these results, it was important to consider that the accelerometers were necessarily positioned to surround both excavations in three dimensions. As such, the array often provided the greatest sensitivity to source parameters within the pillar separating the two excavations.

In the vicinity of the faces of the excavations the minimum magnitude sensitivity was predicted to be approximately $-2.4M_L$ to $-2.6M_L$. At the final face, sensitivity was greatest, estimated to be as low as $-2.8M_W$. This level of source parameter sensitivity along the axis of the excavations was quite consistent and well suited to capturing the small scale rock mass response to mining. Particular emphasis was placed on identifying the rock mass response within the zone immediately ahead of the drift face, which was expected to be affected by conventional and development face destress blasting procedures.

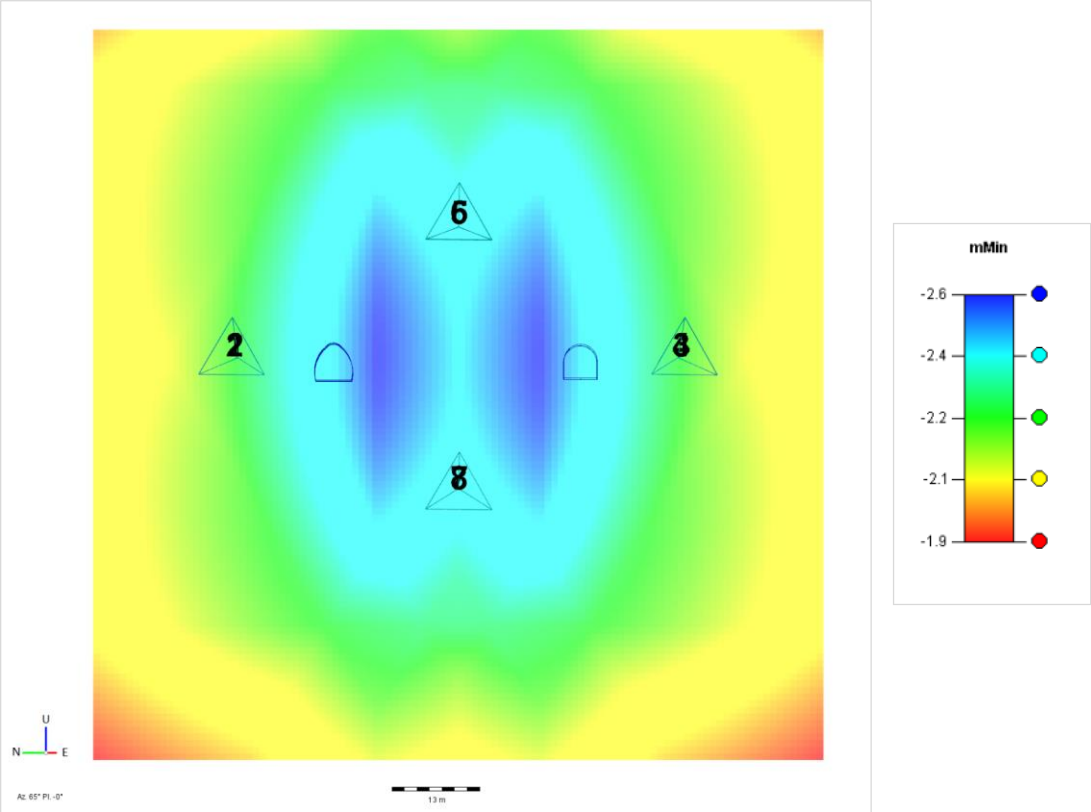


Figure 231 - Vertical section of minimum magnitude sensitivity at 10m from tunnel turnout.

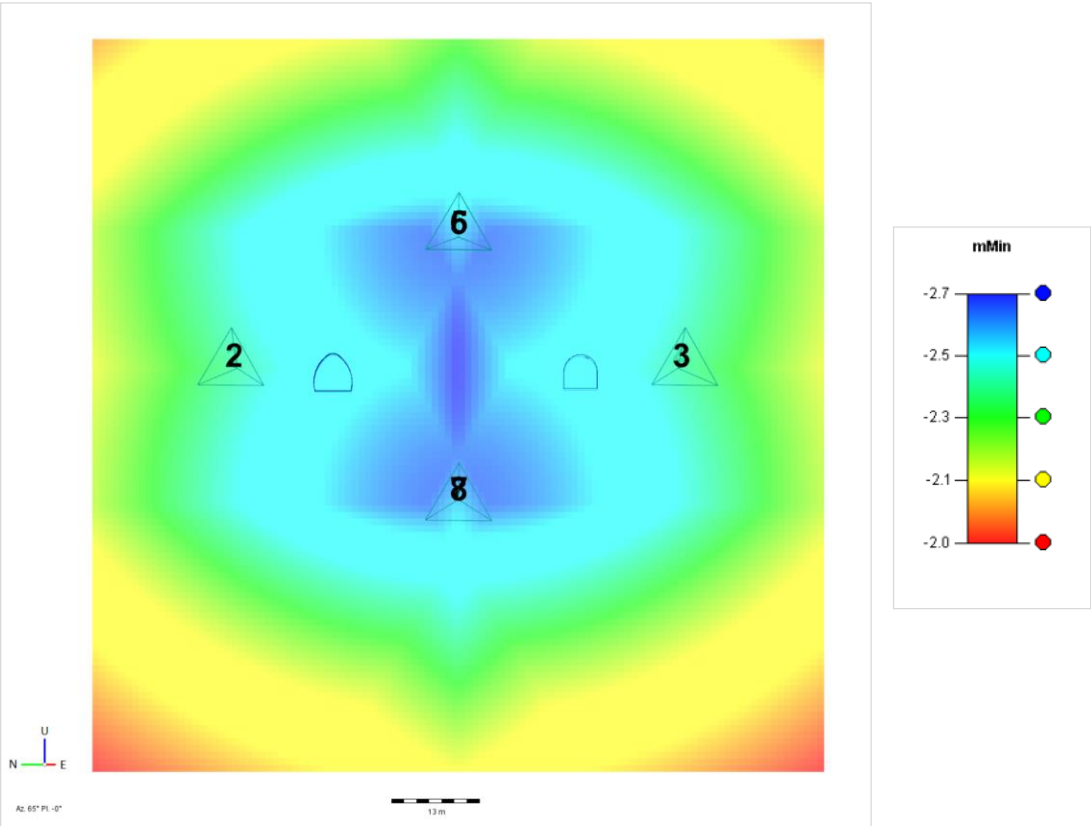


Figure 232 - Vertical section of minimum magnitude sensitivity at 30m from tunnel turnout.

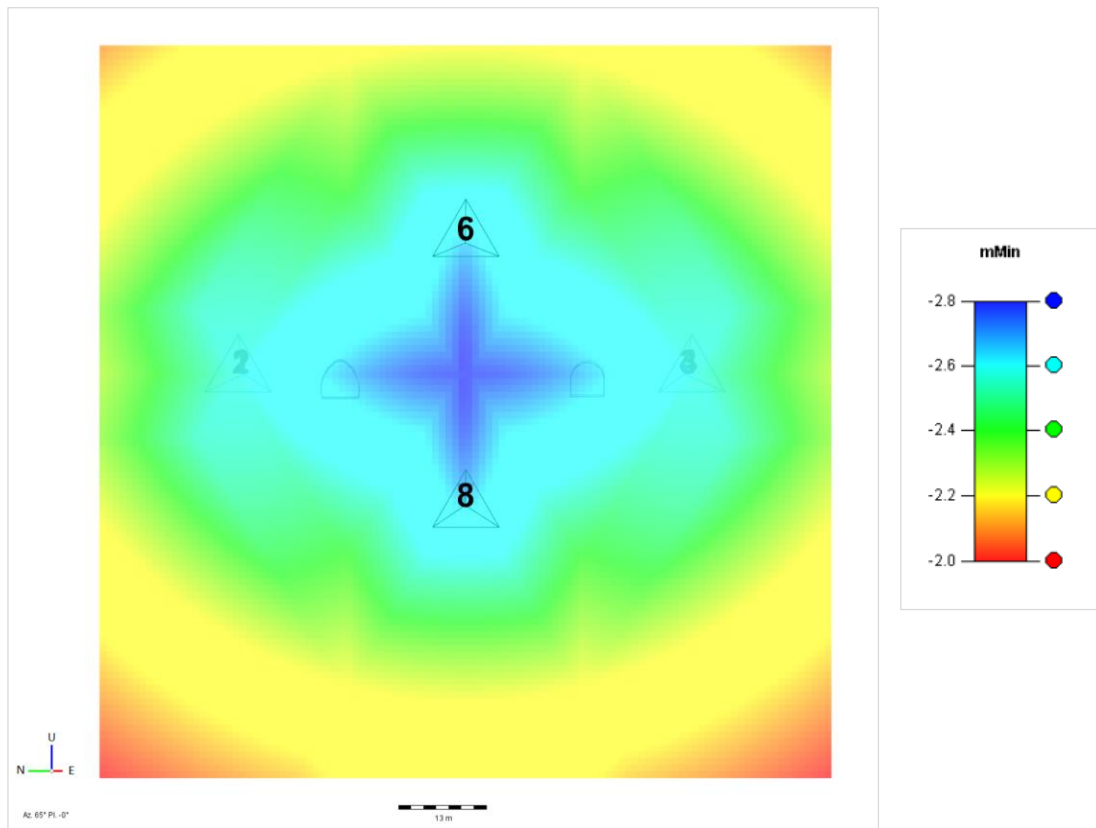


Figure 233 - Vertical section of minimum magnitude sensitivity at 60m from tunnel turnout.

6.1.5 Velocity Model Calibration

Accurate event hypocentre calculations were critical for spatial tracking of the seismogenic zone surrounding the development face. The desired performance of the seismic system was 3D location error of one metre or less. In order to achieve this level of location accuracy, it was necessary to measure the seismic P and S-wave velocities of the rock mass. The P and S-wave velocities were critical input settings for the local seismic system configuration. In order to quantify the seismic velocities, a velocity calibration was performed. This required the use of artificial seismic sources at precisely known locations within the volume enclosed by the seismic array. The energy radiated from these sources was recorded by the sensors at their known positions.

Eight electronic iKon detonators were used as artificial seismic sources (Figure 234). Single-mode fibre optic cables were wrapped around each detonator. Prior to excavating the tunnels, the detonators were installed within the geotechnical pilot boreholes previously use for the rock mass characterisation sampling. The detonators and fibre optic cables were manually installed into the boreholes by securely attaching them to accurately measured lengths of 25mm-diameter rigid electrical conduit.



Figure 234 - Electronic iKon detonator used as an artificial seismic source for velocity calibration.

Four detonators, each bound to a fibre optic cable, were installed at regular distances within each pilot hole, as shown in Figure 235 and Figure 236. The relative position of all artificial sources are shown as red shapes with black outline in the figures. The seismic sensor positions, as they were installed, are shown as grey shaded spheres. Detonators were placed precisely at 10m, 18m, 25m and 32m distance from the borehole collar. The exact location of each detonator was known in mine coordinates, as the pilot boreholes were gyroscopically surveyed in advance. The maximum distance of 32m of the furthest detonator from the collar was controlled by the limited length of the detonator lead. All detonators were installed in a position aligned with the tunnel's longitudinal axis, at approximately gradeline height.

The position of multiple artificial sources in this manner provided a significant velocity dataset and many different seismic ray paths throughout the rock mass. This ensured that the velocity calibration was representative of a multitude of seismic ray paths within the seismic array, rather than just a single ray path. Positioning of the artificial sources along the planned tunnel axes optimised the velocity model for events in close proximity to the face of the research excavations, as the ray paths between the artificial and mining induced seismic sources were very similar. Therefore, the calibrated velocity model was considered the most accurate possible for travel time and location calculations of events located close to the excavations.

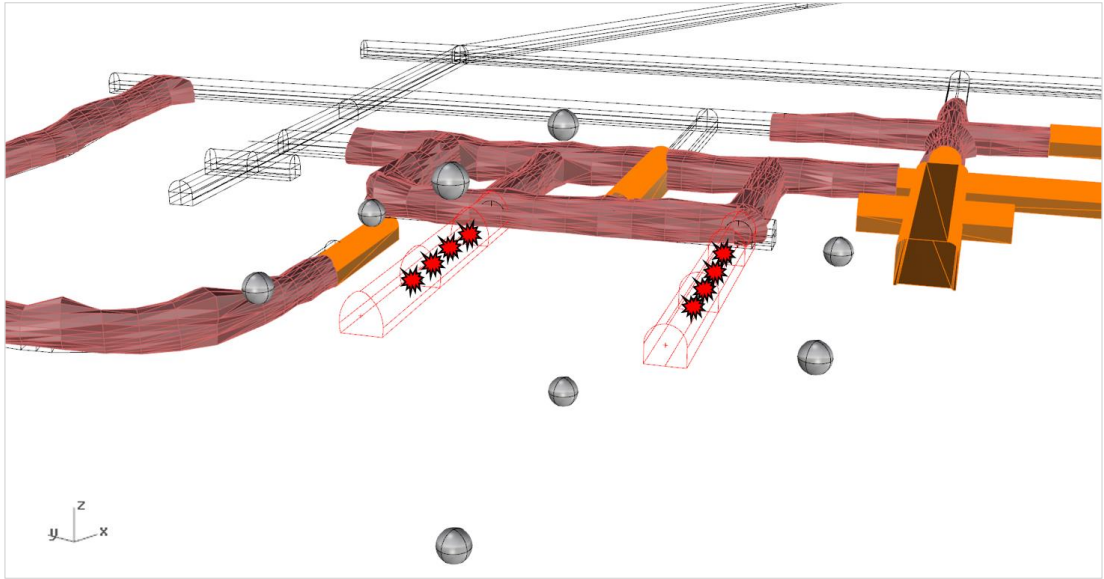


Figure 235 – Perspective view of artificial seismic sources used for seismic velocity model calibration

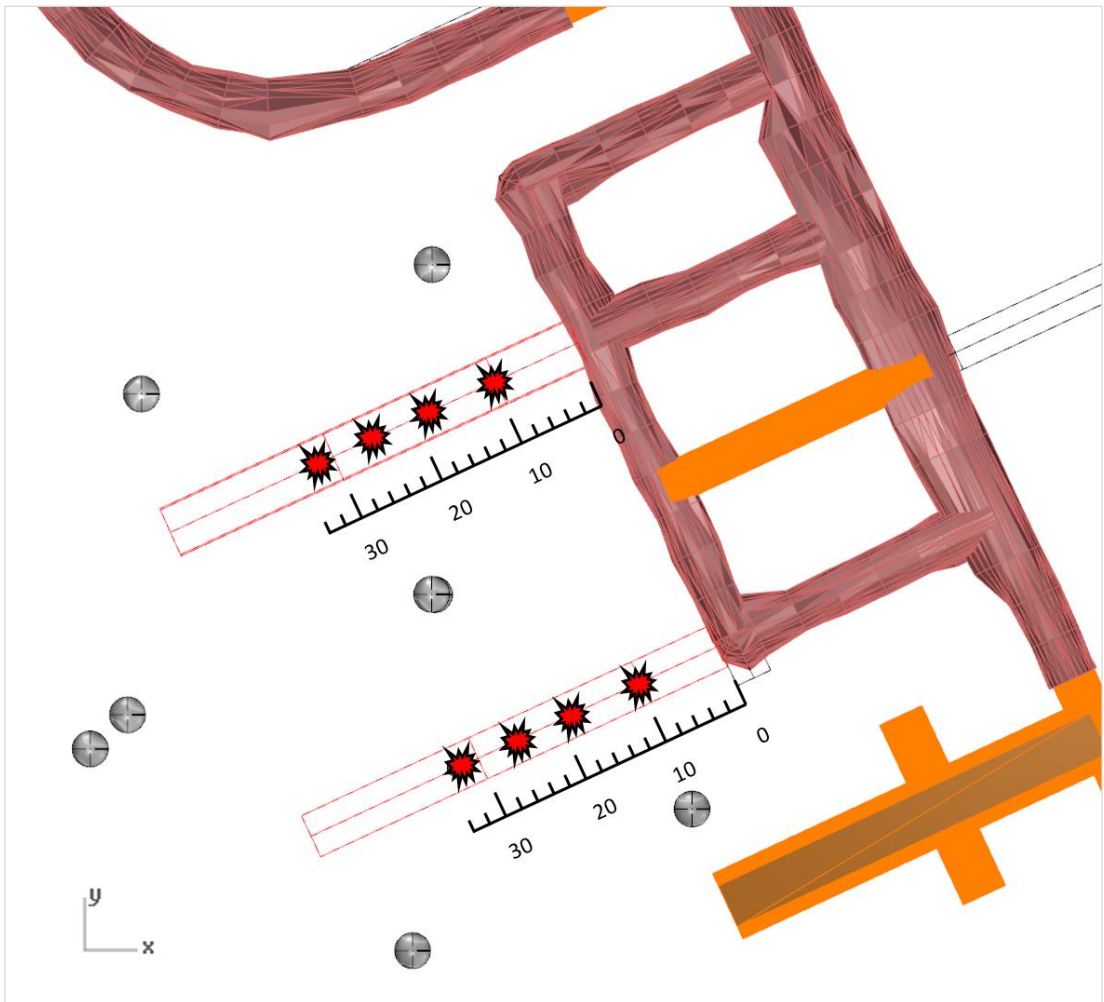


Figure 236 - Plan view of artificial seismic sources used for seismic velocity model calibration.

The arrangement of detonators and instrumentation installed in the borehole is shown below in Figure 237. Once all the detonators were installed to the correct depth, the borehole collar was sealed using expanding polyurethane foam. At this point the fibre optic cables were routed from the borehole collar to a fibre-optic break reader (Figure 238). The fibre reader was then connected to the seismic monitoring system via Ethernet cable. Water was then pumped into the borehole, filling it completely. Continuous overflow of water from the borehole via a breather tube was observed and then the detonators were initiated in sequence. The detonator furthest from the borehole collar was initiated first, with the adjacent detonators initiated in sequential retreat towards the collar of the borehole at 2000ms delay intervals.

Each detonator was fully immersed in water at the time of its detonation, providing a complete hydraulic coupling between the detonators and borehole wall at all times. The hydraulic coupling increased energy transfer between the detonator and rock mass, causing maximum radiation of seismic energy towards the accelerometers. Therefore, clearer waveforms were recorded. Each fibre optic cable was severed in sequence by the attached detonator. Signal loss along the fibre optic cable was detected by the fibre break reader and a voltage offset immediately recorded by the seismic system. The timing of this signal was correlated to the seismic system time and used as the source zero time for seismic velocity calculations.



Figure 237 - Installation and arrangement of components in the borehole, prior to immersion in water.



Figure 238 - Fibre optic break reader used to correlate detonator initiation to seismic system timing.

A system diagram of the seismic velocity model calibration is shown below in Figure 239. This diagram illustrates the arrangement of explosive detonators and fibre-optic instrumentation used for a velocity calibration sequence of four detonators. Only four detonators were monitored in a single recording cycle. Therefore, the group of four detonators in each of the two boreholes were initiated and recorded separately, approximately 30 minutes apart, using an identical instrumentation set-up.

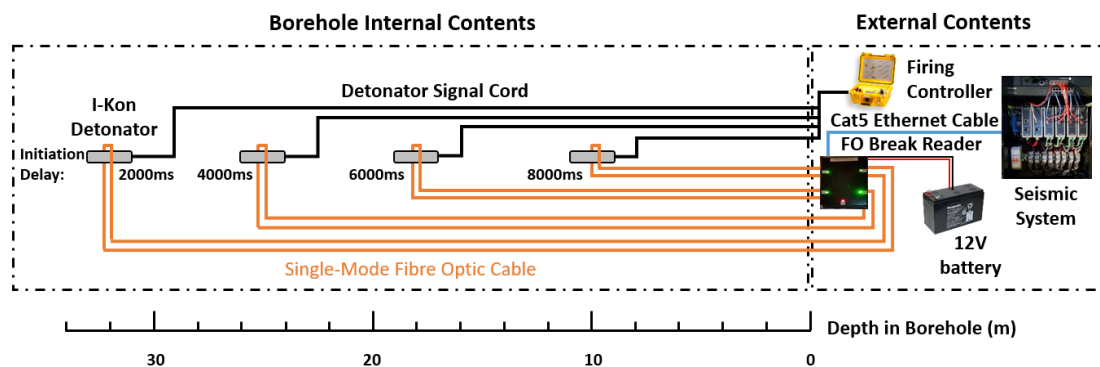


Figure 239 – Schematic of detonators and instrumentation used for seismic velocity data collection.

The result of the calibration blasts was a series of seismograms recorded by the seismic system. Example waveforms used for the velocity model calibration are shown below. Figure 240 presents the waveform of a typical fibre break recorded by the seismic system. This was a voltage offset generated by the fibre-break reader, which occurred at the precise instant that the fibre optical cable was severed by the detonator. This waveform defined the initiation time for each artificial source with millisecond precision.

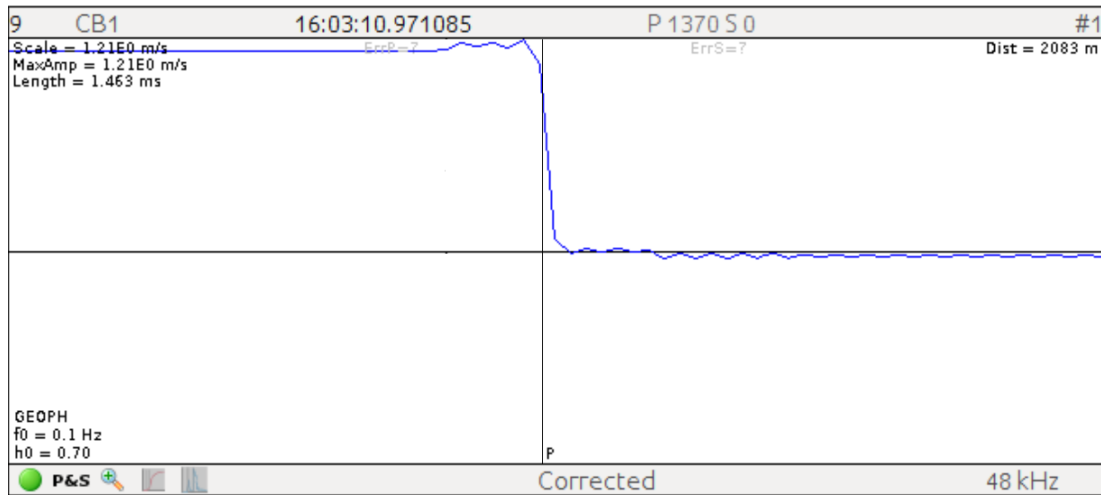


Figure 240 - Waveform data showing the voltage offset timing from the fibre-optic break reader.

Figure 241 shows a typical seismogram generated by the initiation of a detonator. These waveforms were of good quality for velocity calibration purposes, considering the very clear P and S-wave arrivals and the low signal-to-noise ratio.

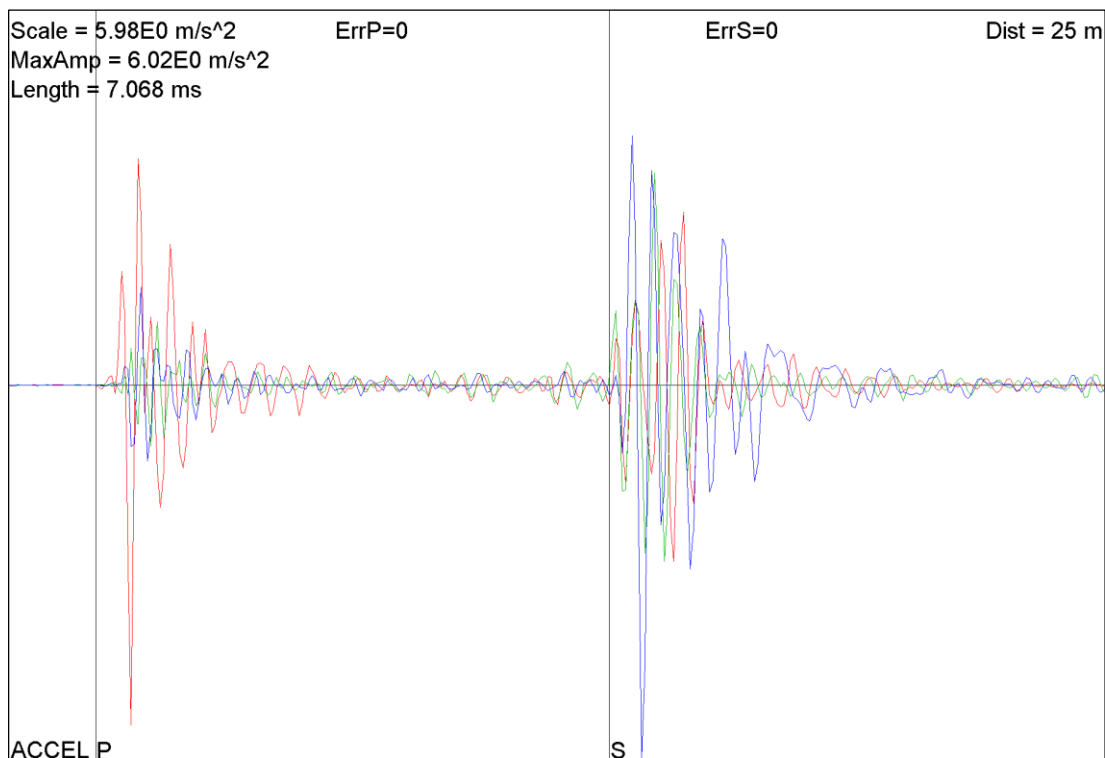


Figure 241 - Typical seismogram generated using an explosive detonator as an artificial seismic source.

Following waveform collection, all recorded seismograms were processed for P and S-wave arrivals. The velocity profile of the rock mass for both P and S waves was generated from the resulting dataset (Figure 242). This distance-arrival data shows P and S-wave arrival time for all sensors relative to the distance from each artificial source. From this dataset, the following values of P-wave (V_P) and S-Wave (V_S) seismic velocity were calculated for the Dacite rock mass.

$$V_P = 5,694 \text{ m/s} \pm 159.8\text{m/s} \quad V_S = 3,262\text{m/s} \pm 68.0\text{m/s} \quad (\text{Eq. 6.6})$$

These values of V_P and V_S represent the ‘best-fit’ velocities derived from the raw calibration data. These values form a 3D *homogeneous* velocity model of the Dacite rock mass. That is, a model where the entire Dacite rock mass was assigned the same values of V_P and V_S . In this case, seismic energy was assumed to radiate uniformly and omni-directionally from all event sources. However, the natural rock mass seldom behaves in such a uniform manner and therefore the homogeneous velocity model was deemed to be inherently inaccurate. A *heterogeneous* velocity model was also assessed during this calibration process. The heterogeneous model specifies spatial variation in the seismic velocities throughout the Dacite rock. Such variation may occur, for example, due to variable rock mass properties or the presence of structures.

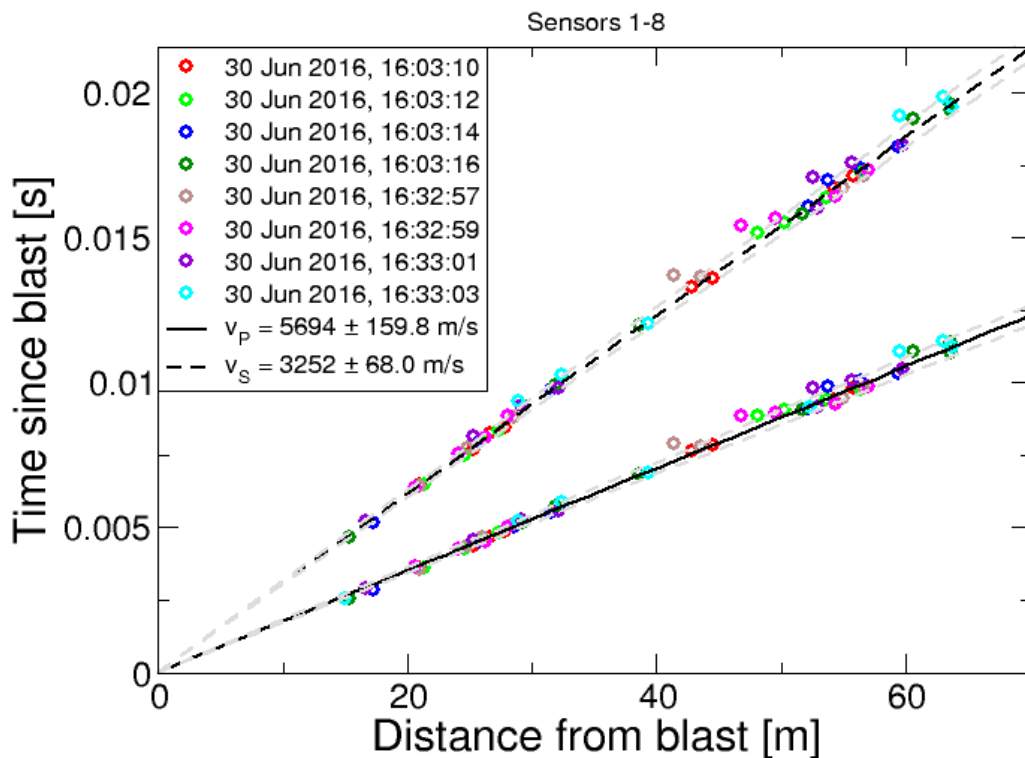


Figure 242 - Distance-Arrival data for artificial seismic sources within the triaxial accelerometer array.

When defining the heterogeneous 3D velocity model, V_P and V_S were assessed for each individual sensor site, rather than collectively. Seismic velocities between each accelerometer site and all eight artificial sources were calculated in the IMS software. Each sensor site was then assigned a unique V_P and V_S value in the system settings, based on best-fit results. The resulting seismic velocities assigned to each of the eight sensors are shown in Table 49. In a small number of cases the S-wave was not clear in the waveform from the artificial source, and was therefore not used for calculations.

Table 49 – Heterogeneous seismic velocity model data.

SiteID	v_p	error		v_s	error		P-Picks	S-Picks
	(m/s)	(m/s)	%	(m/s)	(m/s)	%	(Blast #)	(Blast #)
1	5740	79	1.3	3260	25	0.7	1,2,3,4,5,6,7,8	1,2,3,4,6,7
2	5810	61	1.0	3280	13	0.3	1,2,3,4,5,6,7,8	1,2,3,4,5,6,7,8
3	5760	53	0.9	3270	22	0.6	1,2,3,4,5,6,7,8	1,2,3,4,5,6,7,8
4	5890	136	2.3	3310	31	0.9	1,2,3,4,5,6,7,8	1,2,3,4,5,6,7
5	5650	73	1.3	3230	49	1.5	1,2,3,4,5,6,7,8	1,2,3,4,5,6,7,8
6	5420	102	1.8	3130	66	2.1	1,2,3,4,5,6,7,8	1,2,3,4,5,6,7,8
7	5700	86	1.5	3210	67	2.1	1,2,3,4,5,6,7,8	1,2,3,4,5,6,7,8
8	5590	53	0.9	3220	40	1.2	1,2,3,4,5,6,7,8	1,2,3,4,5,6,7,8

These P and S-wave velocities were used for absolute location calculations. Absolute location is a method of calculating the seismic event hypocentre which assumes straight line ray paths between the seismic source and recording sensors. The absolute location method is less accurate when mining voids are introduced between the seismic sources and sensors. This is due to the fact that the seismic ray paths travel the fastest path around the excavations, which is not a straight line. Absolute location calculations invariably underestimate the ray path distance. In this situation, ray tracing calculations may provide a more accurate hypocentre calculation.

6.1.6 Ray Tracing Location Calculations

Given the geometry of the seismic sensor array, the two research tunnels represented a significant barrier to direct seismic ray paths between the events and some sensors. Without ray path correction, the presence of the tunnels was expected to increase 3D location errors in the recorded seismic data. Therefore, three ray-tracing velocity

models were prepared and the location error of each was quantified and compared to that of the absolute location methods. The accuracy of the models in locating seismic sources prior to construction of the tunnels was tested using verification blasts. The location verification blasts were similar to the artificial sources used for the initial velocity calibration. The tests took place prior to tunnel construction. The most accurate location method was then assigned to the seismic system settings.

The three ray-tracing models that were tested were created in the IMS software by defining a three-dimensional lattice of coordinate nodes. The nodes were uniformly distributed within the geometry of the model, with an equal spacing in each direction. The ray tracing models formed a lattice of nodes completely surrounding the tunnels, the spatial extent of which is shown in Figure 243 and Figure 244. Simulated voids in the model were assigned P and S-wave velocities of air, i.e. 300m/s and 200m/s respectively. A simple algorithm was used to define whether a node in the model was within a mining void or not, based on digital survey files of the development geometry (Malovichko, 2016, pers.comm).

The remaining nodes of the ray tracing models, which represented solid rock, were then assigned P and S-wave velocities. The heterogeneous P and S-wave velocities of individual sensor sites defined earlier in Table 49 were first assigned to their relevant position in the 3D lattice. This yielded n values of both P and S-wave velocity (V_p , V_s) for n points in space, where $n=8$, i.e. the number of sensors, as indicated below:

$$V1(x1, y1, z1), V2(x2, y2, z2) \dots Vn(xn, yn, zn) \quad (Eq. 6.7)$$

A Gaussian Kernel method was then used to extrapolate each of the n points of known velocity to the remaining nodes in the model (Malovichko, 2016, pers.comm). The kernel functions were applied using various smoothing factors (σ), as follows.

$$\begin{aligned} K1 &= \exp\left(-\frac{(x-x1)^2 + (y-y1)^2 + (z-z1)^2}{2\sigma^2}\right) \\ K2 &= \exp\left(-\frac{(x-x2)^2 + (y-y2)^2 + (z-z2)^2}{2\sigma^2}\right) \dots \\ Kn &= \exp\left(-\frac{(x-xn)^2 + (y-yn)^2 + (z-zn)^2}{2\sigma^2}\right) \end{aligned} \quad (Eq. 6.8)$$

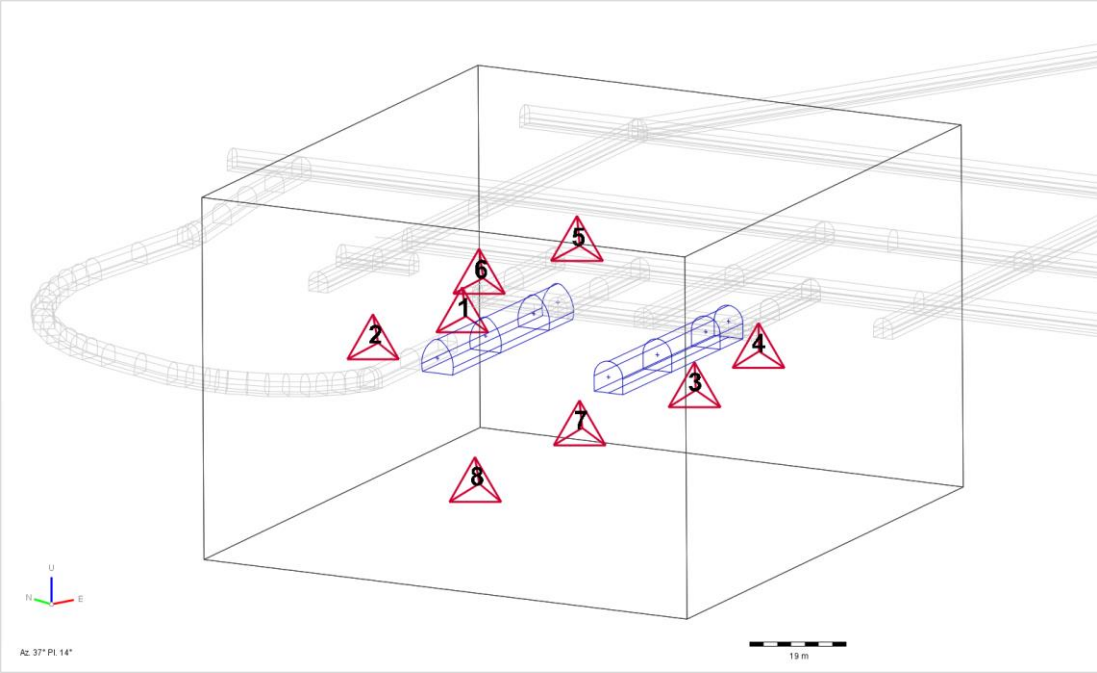


Figure 243 – Perspective view of ray-tracing velocity model spatial limits.

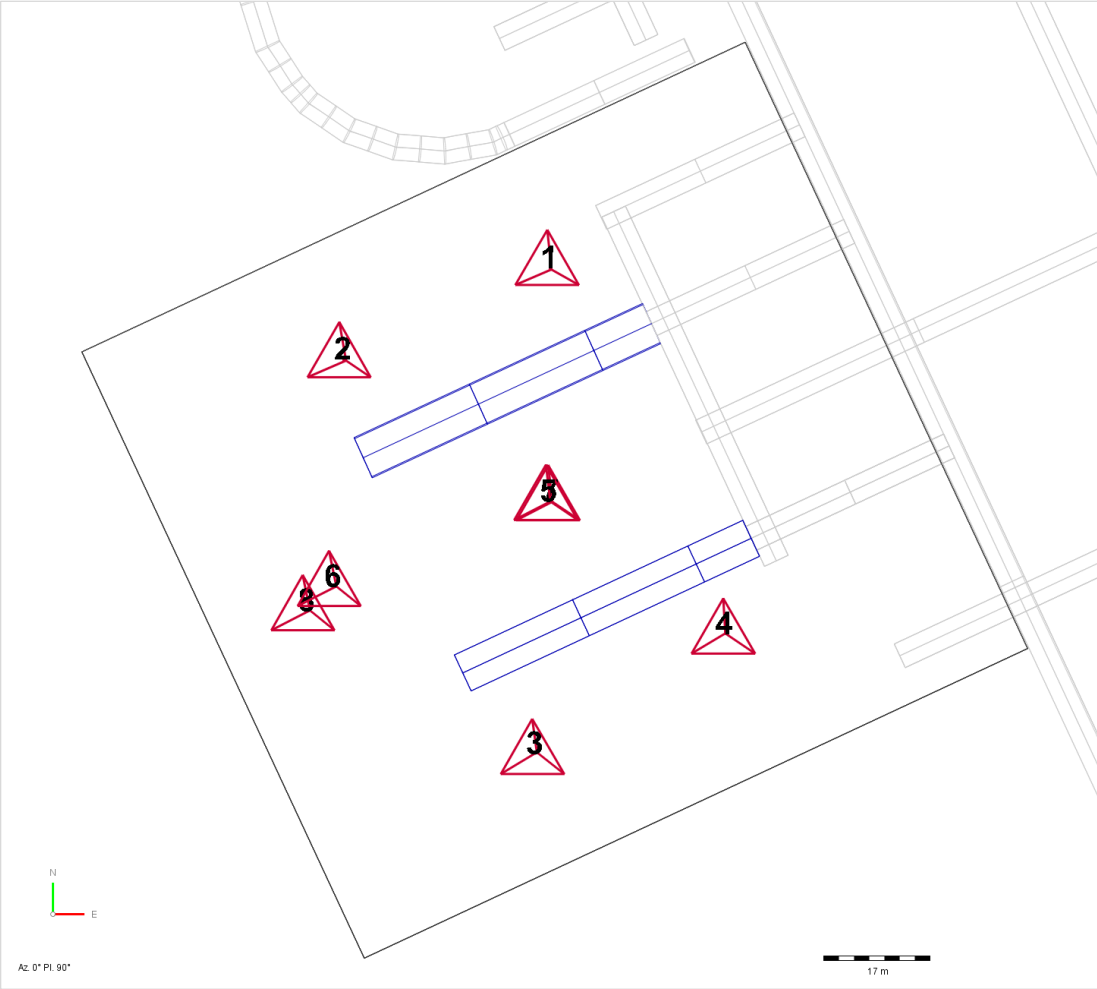


Figure 244 – Plan view of ray-tracing velocity model spatial limits.

V_P and V_S at the relevant lattice node (x,y,z) in the velocity model were defined by:

$$V(x, y, z) = \frac{(K1V1 + K2V2 + \dots + KnVn)}{(K1 + K2 + \dots + Kn)} \quad (Eq. 6.9)$$

This process was repeated automatically until all points in the 3D velocity lattice were assigned a V_P and V_S . This process generated the 3D lattice of coordinates populated with both V_P and V_S values. Visualisation of the P and S-wave velocity results generated using this Kernel smoothing method are shown below in Figure 245 and Figure 246, respectively. These images show the coloured isosurfaces of V_P and V_S thresholds throughout one example of a 3D model lattice. The two images represent the heterogeneous ray-tracing velocity model results prior to the research tunnel development, i.e. including the void geometry for pre-existing access development.

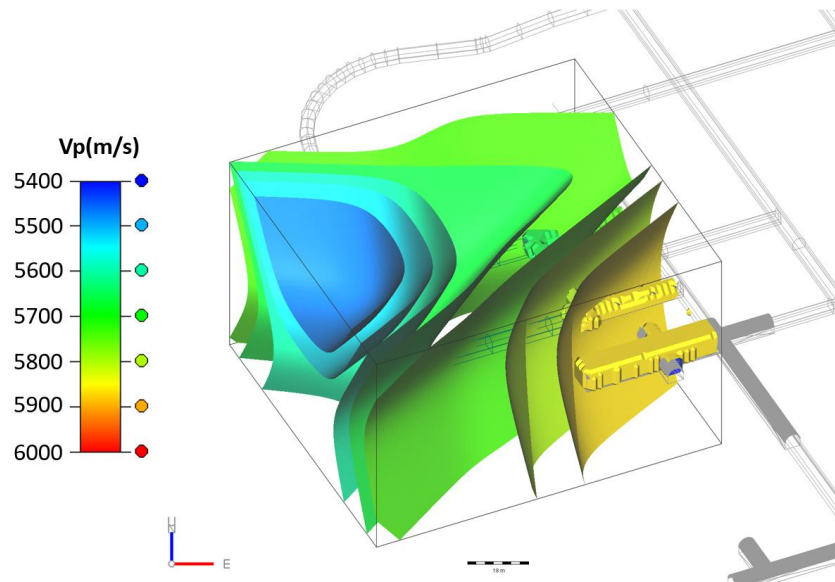


Figure 245 – One of three heterogeneous P-wave velocity models tested for location error.

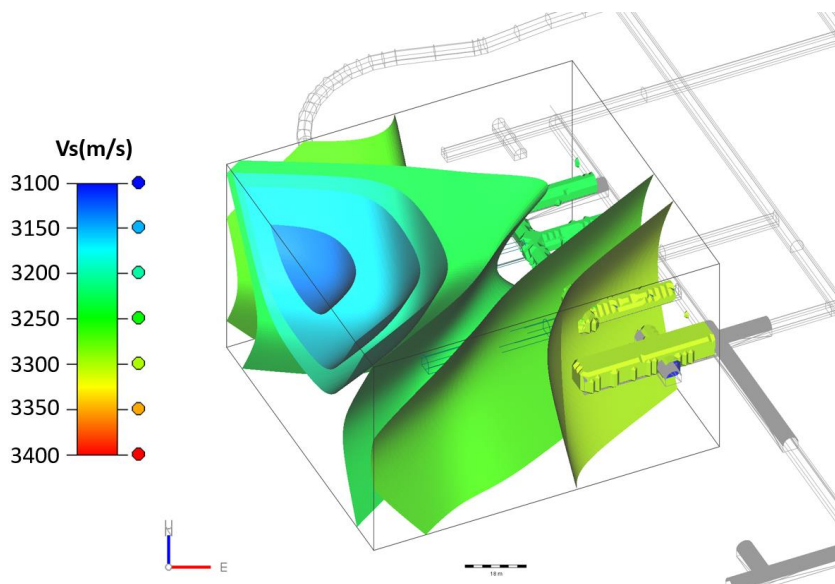


Figure 246 – One of three heterogeneous S-wave velocity models tested for location error.

6.1.7 Location Method and Velocity Model Testing

In order to assess which combination of location method and velocity model produced the most accurate seismic event hypocentres, a number of verification blasts were conducted. Verification blasts were small seismic sources positioned at known coordinates. The blast locations were calculated using five velocity model system settings and the 3D location errors of each method were compared. The verification blasts mimicked the velocity calibration method, only without any fibre optics.

Four detonators were again inserted into each of the two pilot borehole at specific depths using rigid plastic conduit (Figure 247). In this case, the precise location of the detonators was varied from that of the prior calibration blasts. Detonators were initially intended to be installed at distances of 10m, 20m, 30m and 40m from the collar. However, due to implementation practicalities, the detonators were offset by 0.5m from their original planned positions and were actually installed at 9.5m, 19.5m, 29.5m and 39.5m from the collar of each hole (Figure 248). The mine coordinates of the detonators were calculated based on the gyroscope traces of the pilot boreholes.

Following installation of the detonators, the borehole collar was sealed again with foam and the hole completely filled with water to ensure good seismic energy transfer between the detonator and borehole wall. Detonators 1 to 4 were initiated sequentially, with a 2000ms delay interval between charges, starting with detonator #1 which was furthest from the collar. Detonators 5 to 8 were detonated in the other borehole 30 minutes later following the same methodology.



Figure 247 - Detonators were inserted into the boreholes at specific lengths using rigid conduit.

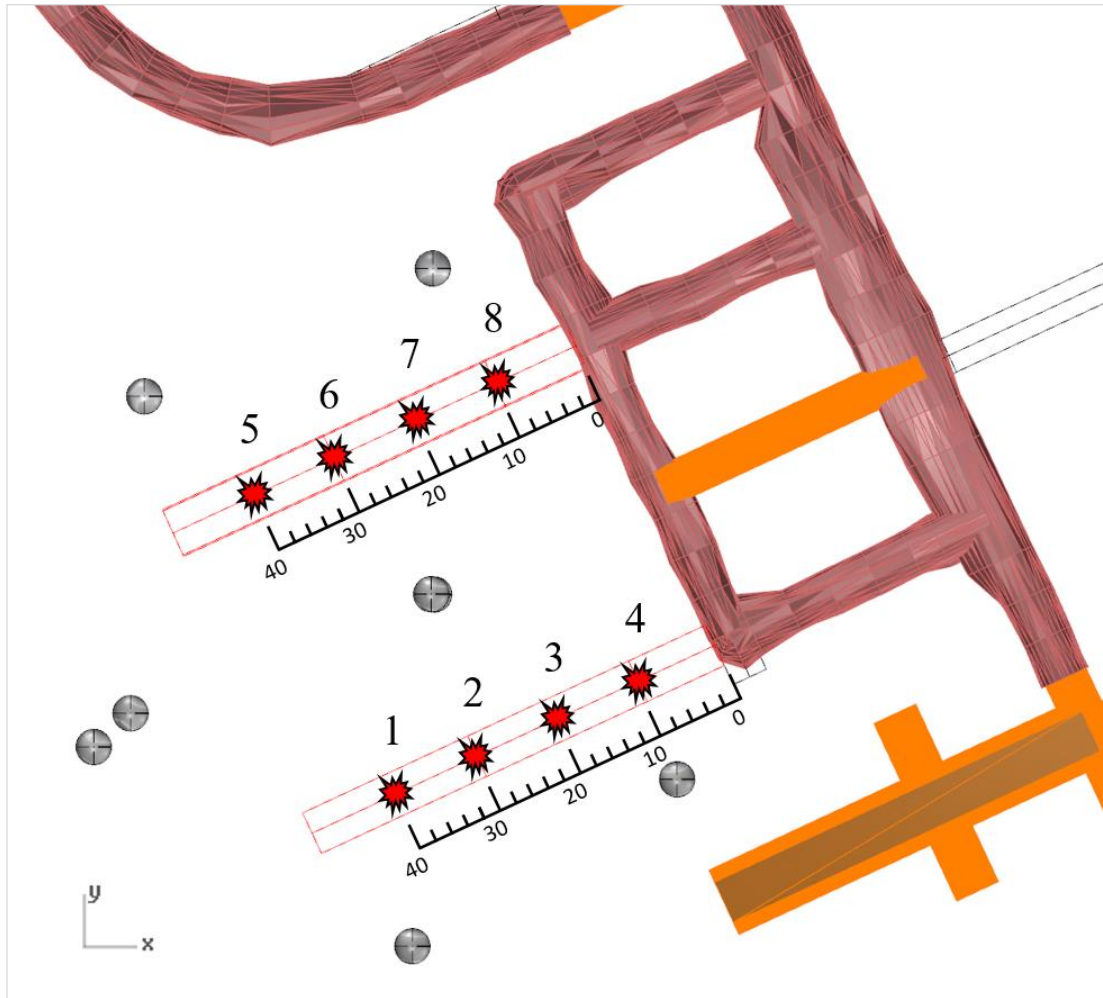


Figure 248 - Plan view of verification blasts for location error tests.

A typical waveform generated by these verification blasts is shown in Figure 249. Waveforms from the eight verification blasts were recorded by all eight accelerometers and processed for P and S-wave arrivals. The verification blasts registered in the magnitude range of -2.0 to $-2.5M_L$. Five separate seismic system configuration settings were applied sequentially, in order to process the seismic waveforms and give a hypocentre location for each of the eight verification blasts. The source hypocentres calculated by the system for each velocity model setting were recorded and compared to the known coordinates of each blast in order to quantify the 3D location errors. The five location method and velocity model settings used to process the blast locations were as follows:

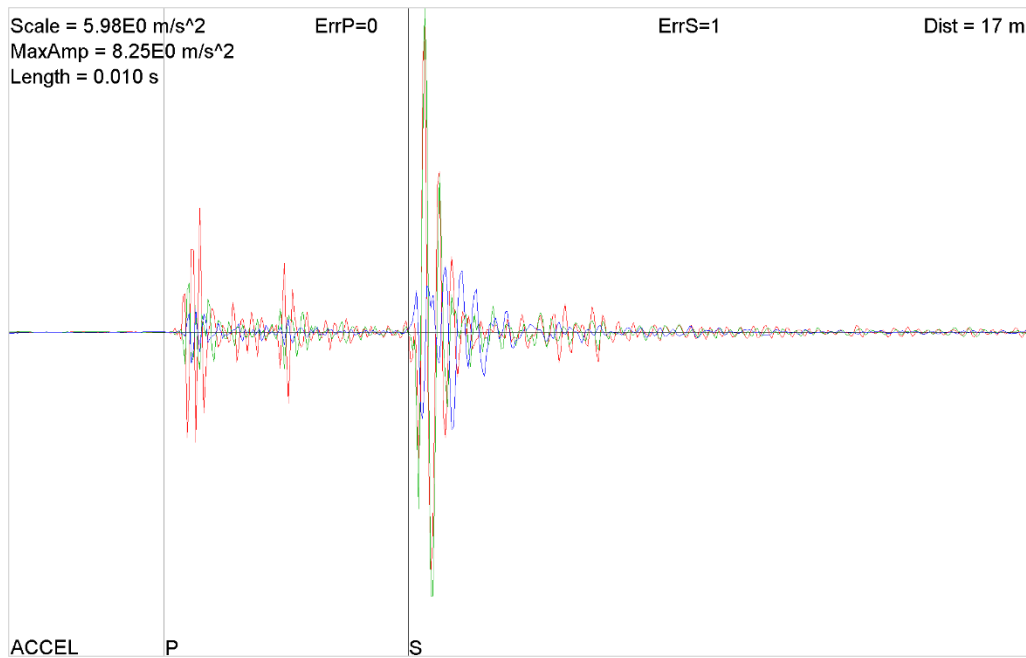


Figure 249 - Example waveform of artificial seismic sources used for 3D location error analysis.

Model 1. Homogeneous – Absolute Location

Standard Absolute location algorithms of the IMS software were used with a fully homogeneous velocity model. The entire Dacite rock mass was assumed to have P and S-wave velocities consistent with the values shown in Eq.6.6 and all seismic sensor sites were assigned these velocity values.

Model 2. Heterogeneous – Absolute Location

This model utilised standard absolute location calculation algorithms of the IMS software. Site-specific values of the P and S-wave velocities were assigned to each sensor site based on the heterogeneous velocity calibration data shown in Table 49.

Model 3. Heterogeneous – Ray Tracing 1x1x1m Spacing, 30m Kernel Smoothing

The ray-tracing location algorithms of the IMS software were used with an input velocity model consisting of a 3D ray tracing lattice with 1x1x1m node spacing. The model consisted of a total of 897,608 individual nodes. Heterogeneous P and S-wave velocity values presented in Table 49 were extrapolated throughout the model lattice from the known sensor locations using a Kernel function with smoothing parameter $\sigma=30\text{m}$.

Model 4. Heterogeneous – Ray Tracing 1x1x1m Spacing, 15m Kernel Smoothing

As per model 3, with Kernel smoothing parameter of $\sigma=15\text{m}$, resulting in a slightly different distribution of P and S-wave velocity values throughout the 3D model lattice.

Model 5. Heterogeneous – Ray Tracing 0.8x0.8x0.8m Spacing, 15m Kernel Smoothing

As per Model 4, but with 3D lattice node spacing reduced to 0.8x0.8x0.8m for a total of 1,754,935 individual lattice nodes within the velocity model boundaries.

The location of each of the eight verification blasts was calculated using these five combinations of location method and velocity model. The 3D straight-line distance between the known position of each blast and the system-calculated hypocentre was plotted as a histogram shown in Figure 250. This figure illustrates the relative accuracy of each location method and associated velocity model in correctly calculating the location of each verification blast. The results indicated that of the two absolute location methods, the heterogeneous model was marginally more accurate. Of the three heterogeneous ray tracing models, the one with 1x1x1m node spacing, and 30m kernel smoothing (i.e. model 3) consistently produced the lowest 3D location error.

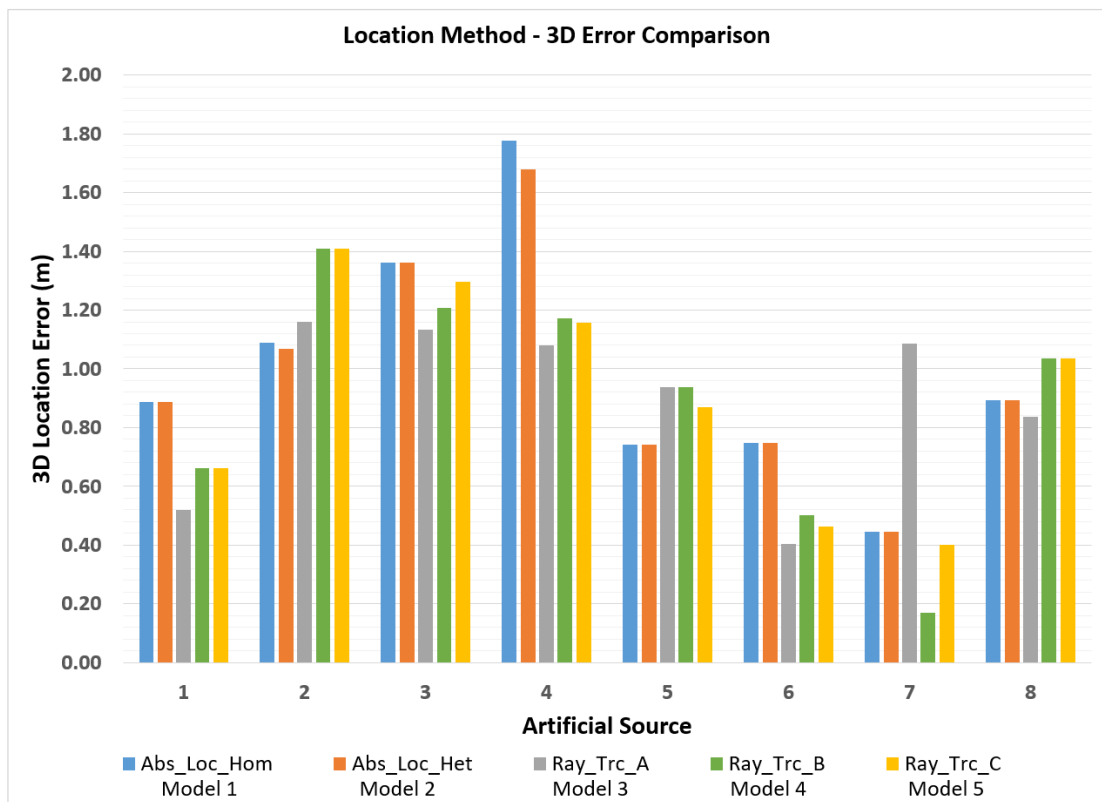


Figure 250 - Quantitative comparison of 3D source location error for all five velocity models.

Velocity model 3 with ray-tracing was selected as the *preliminary* choice for implementation in the seismic system settings. It was chosen for two principle reasons. Firstly, this model demonstrated the equal-lowest average 3D location error across all eight verification blasts, at 0.89m. Secondly, the standard deviation of the location errors was also significantly lower than that of the four other methods. This indicated that the location error performance of this velocity model was most consistent between the north and south tunnel. This fact was an important validation that the seismogenic zone tracking was equally accurate in both tunnels.

However, later in the project, when processing natural seismic data, it was discovered that the ray-tracing location algorithms of the seismic analysis software produced artefacts in the data. This resulted in a significant number of seismic events being preferentially located on the nodes of the velocity model, rather than in a natural position. The effect was visually identifiable as unrealistic linearity in the event location data for some seismic events. This effect is illustrated in a real example of ray-traced seismic data from the research tunnel shown in Figure 251.

An attempt was made to re-process the data and in doing so remove reciprocal distance weighting from the ray-tracing calculations. This removed the effect of increasing the importance of sensors nearest the event hypocentres in the per-trigger terms of the cost function of the location calculations (Birch, 2018, pers.comm). However, this did not remove the artefacts from the re-processed data. Therefore, in order to avoid this artificiality in the seismic data, a decision was made to discontinue ray-tracing. Instead, the absolute location method and heterogeneous velocity mode (i.e. model 2) was implemented in the final seismic system settings for all location processing.

The linear artefacts of the location calculations visible in the ray tracing data were eliminated when re-processing the data using the heterogeneous absolute location algorithm, as illustrated by comparing Figure 251 and Figure 252. For reference, the location error statistics for the verification blasts, calculated using the heterogeneous absolute location method, are shown in Table 50. The average 3D location error for all blasts was 0.98m. In the south and north pilot hole blast groups, the average error was 1.25m and 0.71m respectively. The plan views of the system-calculated locations of all verification blasts and the associated seismic ray paths using the final system location settings are shown in Figure 253.

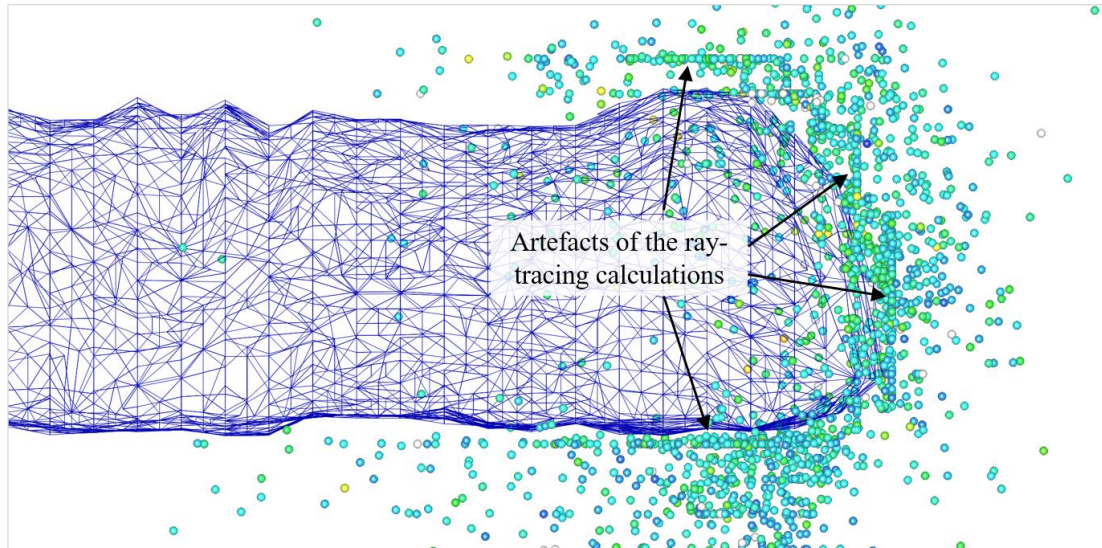


Figure 251 - Examples of linear artefacts in the ray-tracing location calculations of real seismic data.

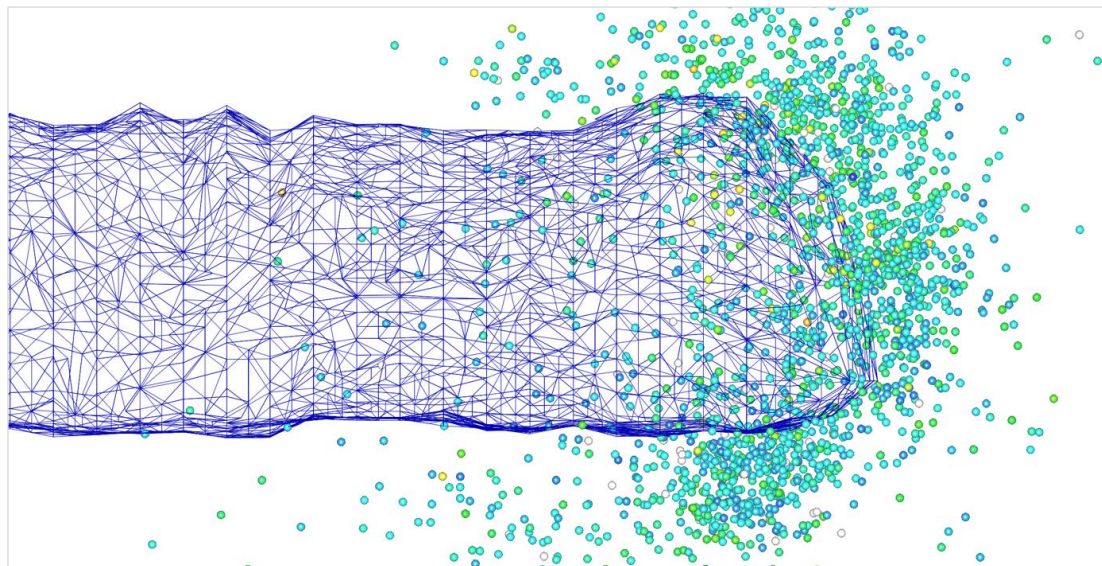


Figure 252 – Re-processed seismic data using a heterogeneous absolute velocity model.

Table 50 – Verification blast location error statistics using absolute method and heterogeneous velocities.

Source (Blast)	Location Error (m)			3D Error	System Statistics			
	X	Y	Z					
1	0.76	0.43	0.15	0.89	Avg. Error per Axis (m)			
2	1.02	0.25	0.19	1.07	X	Y	Z	
3	1.29	0.28	0.33	1.36	0.78	0.25	0.24	
4	1.65	0.32	0.07	1.68	Average 3D Error (m)			
5	0.01	0.69	0.27	0.74	South Group 1-4		1.25	
6	0.16	0.00	0.73	0.75	North Group 5-8		0.71	
7	0.43	0.01	0.11	0.44	System 3D Error (m)			
8	0.89	0.03	0.05	0.89	Maximum		1.68	
					Minimum		0.44	
System Average 3D Location Error (m)							0.98	

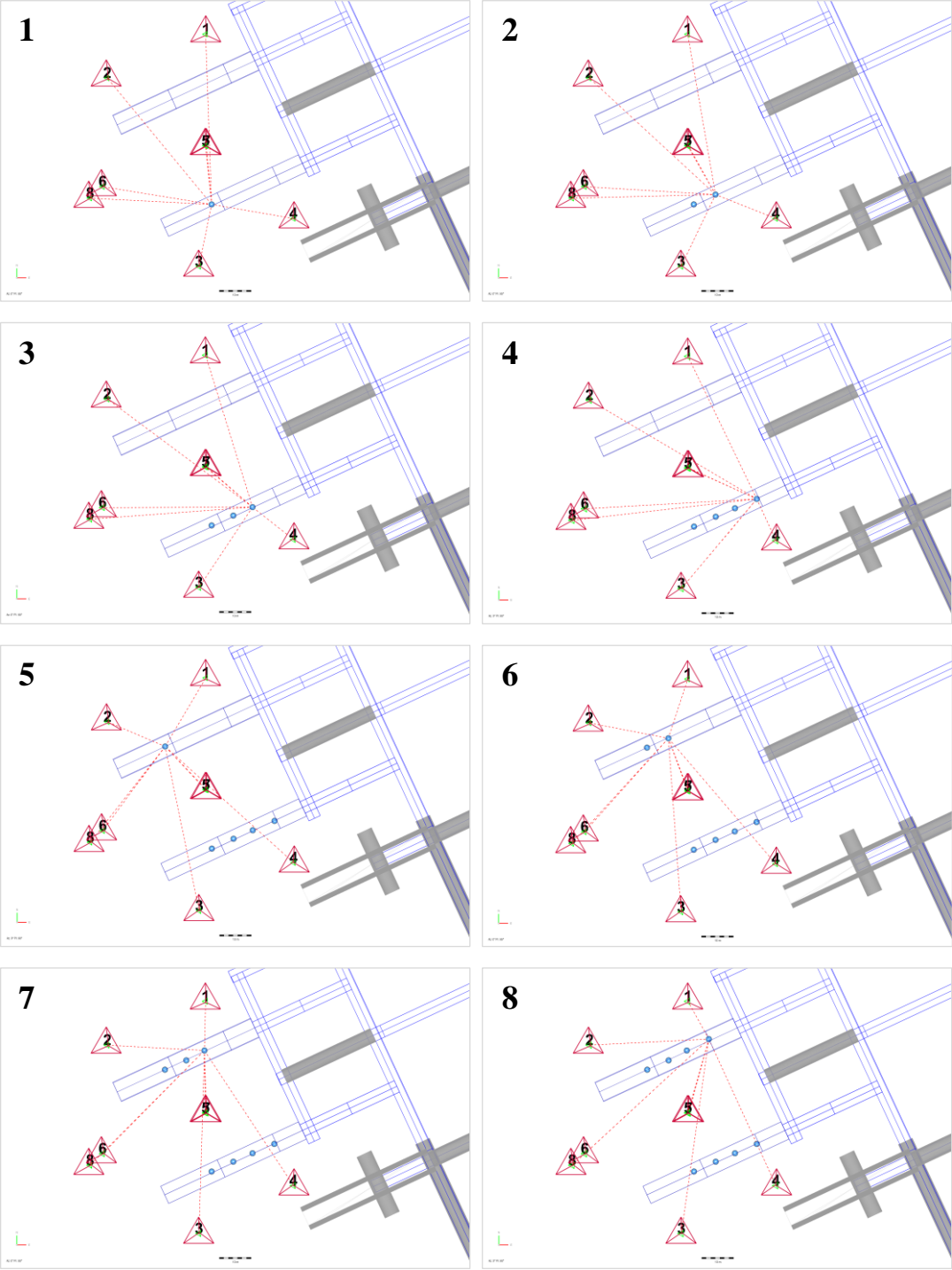


Figure 253 – Verification blast locations using heterogeneous velocity absolute location method.

6.2 Seismic Response to Development

6.2.1 Seismic System Performance Assessment

Prior to detailed analysis of the seismic data, it was worthwhile to quantify the seismic system's true performance using real seismic data collected during the construction of the two tunnels. The performance review of the seismic system examined data for event location calculations, as well as the measurement of source parameters and mechanisms. The real performance was compared to the predictions of the aforementioned sensitivity analysis.

The performance analysis examined location accuracy around each of the two excavations independently, and the results were compared as a means of evaluating the relative accuracy of the data adjacent both tunnels. The data was spatially filtered for this purpose. The boundary geometry of the spatial filters for the seismic system performance review are illustrated in Figure 254. The dimensions of each spatial filter were 70 x 30 x 30m, as illustrated below. The filters were centred on the excavation survey wireframe, in order to capture the surrounding seismicity.

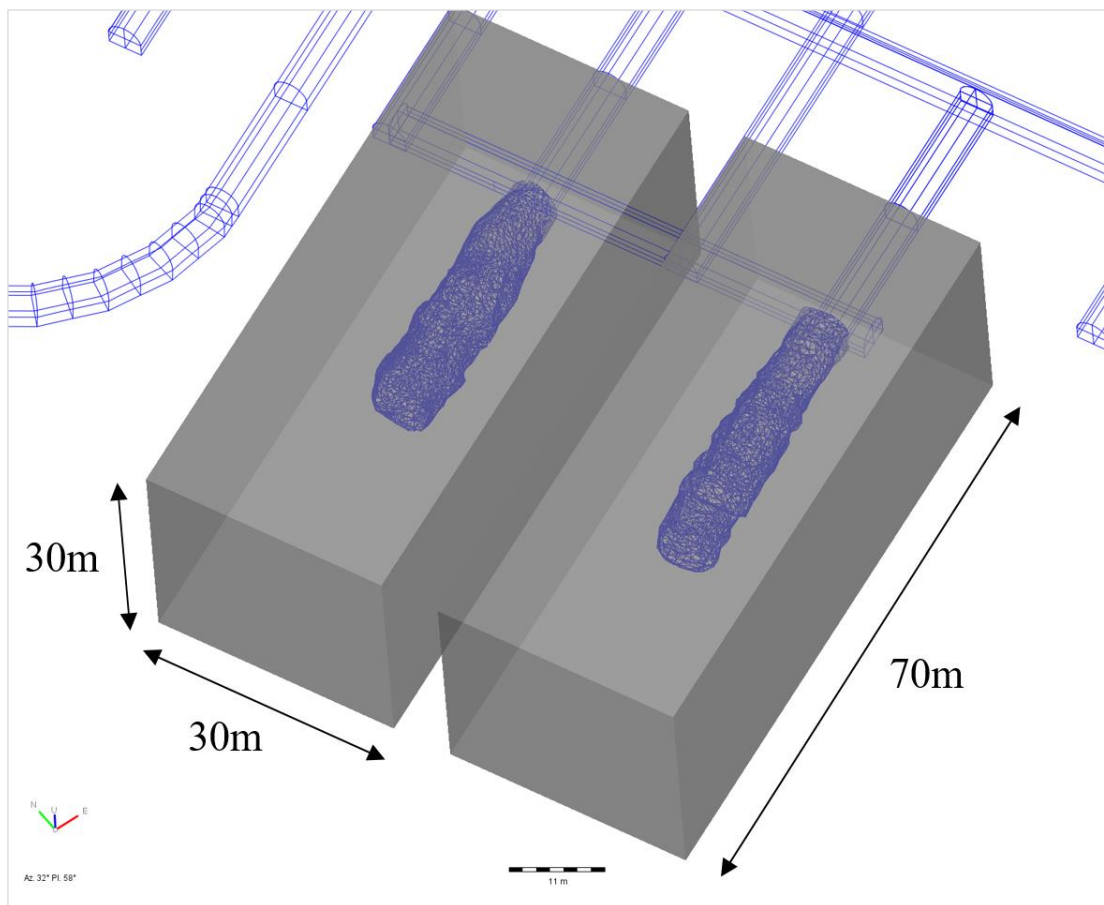


Figure 254 – North and south tunnel spatial filters for location accuracy analysis.

6.2.1.1 Event Hypocentre Location

The theoretical location error of every seismic event was automatically reported by the local seismic monitoring system. A frequency distribution of location error for the complete population of seismic events within the north and south tunnel spatial filters is presented in Figure 255. The results indicated that the majority of the seismic events in the north tunnel exhibited location errors within the range of 0.2 to 0.5m and the modal location error was 0.3m. In the south tunnel, the majority of events exhibited errors within the range of 0.2 to 0.4m, with the modal error value also being 0.3m.

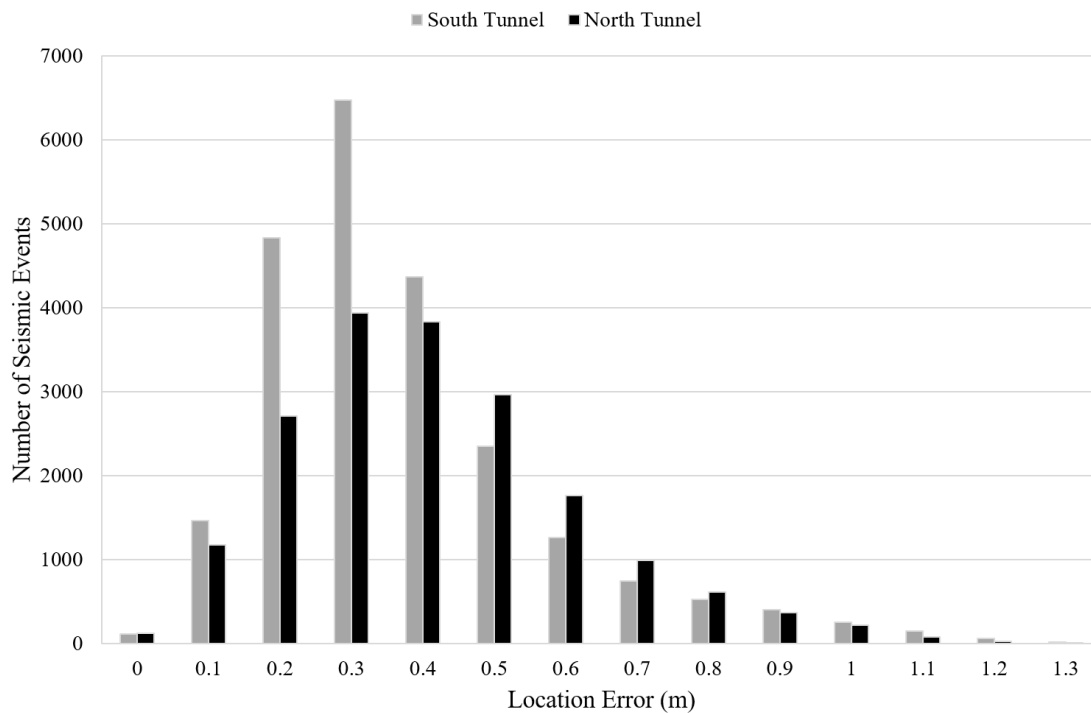


Figure 255- Hypocentre location error statistics reported by the seismic system.

The frequency distribution of location error expressed as a percentage of the average hypocentral distance (%AHD), that is, the distance between the event hypocentre and seismic sensors, is presented in Figure 256. This metric provides additional insight into the seismic system’s location accuracy, as the distance between the source and sensors is directly considered in the measure of the error. The results indicate that almost the entire population of seismic events exhibited location error of less than 3.5% AHD across both tunnels, with the vast majority less than 1.5% AHD. In the north tunnel the modal error value was 0.8% AHD. In the south tunnel, the modal error was slightly lower at 0.7% AHD. For comparison, typical seismic monitoring systems on mine sites would aim to achieve location errors of less than 20m, equating to perhaps 10% of the AHD. This would be regarded as reasonable performance (Mikula, et al., 2008).

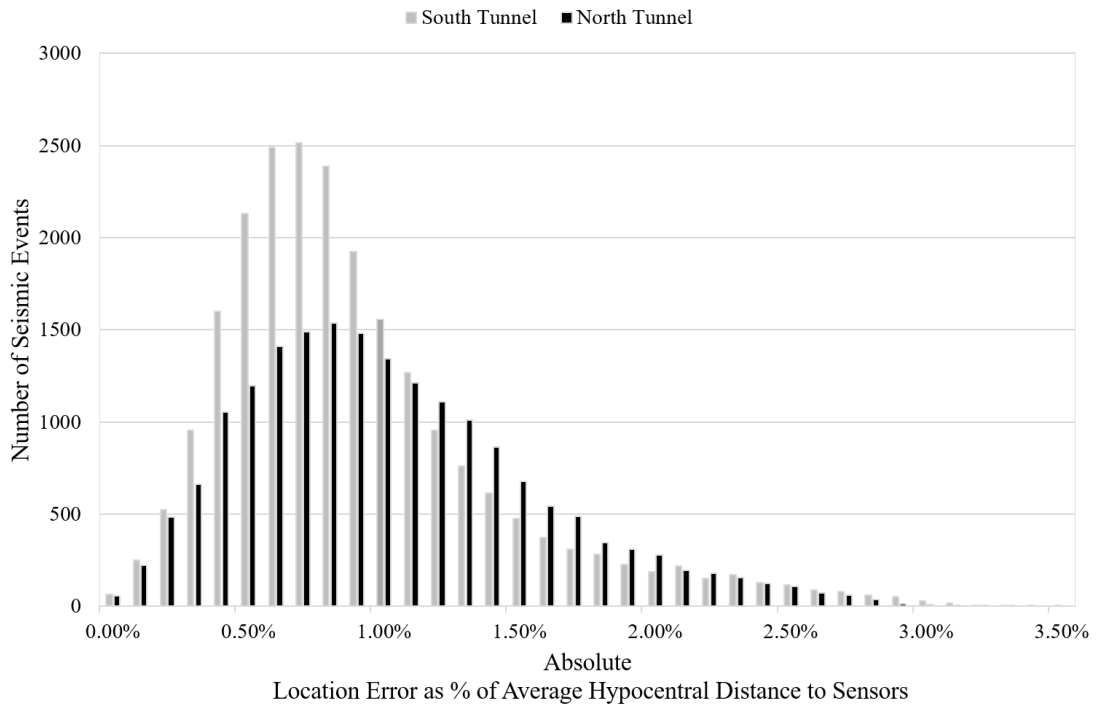


Figure 256 - Location error plotted as a percentage of absolute hypocentral distance to sensors.

The accuracy of the seismic event locations as a function of the distance (chainage) along each tunnel was also quantified. A number of local spatial filters of the seismic data were created for this purpose. These filters coincided with each incremental excavation step in the tunnel construction sequence. The spatial filters also extended laterally into the adjacent perimeter rock. The cross section and plan views of the spatial filters are shown in Figure 257 and Figure 258, respectively. The average location error for the complete population of seismic events within each filter was calculated. The results presented in Figure 259 indicate that location calculations were consistently accurate within the range of 0.3m to 0.45m along the entire length of the tunnels. The error was approximately 0.2m lower through the mid portion of each tunnel when compared to the final few cuts. These observations in the real data closely reflect the location error modelling presented earlier in Section 6.1.3.

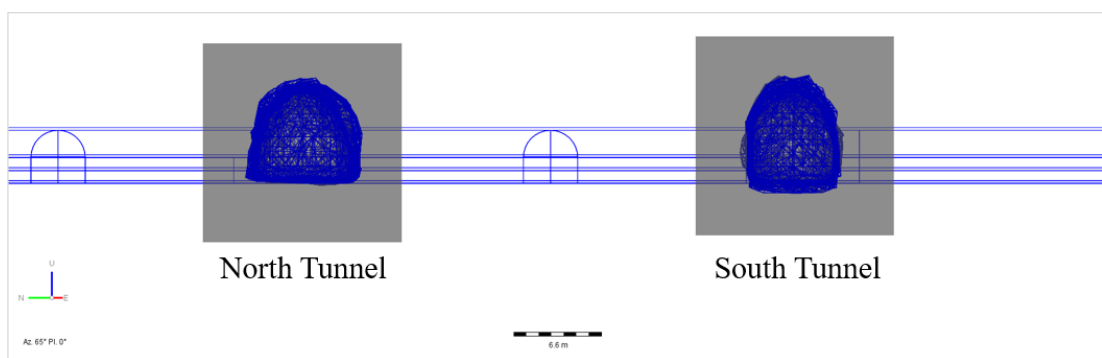


Figure 257 – Cross section view of spatial filters for location accuracy analysis (view direction is NE).

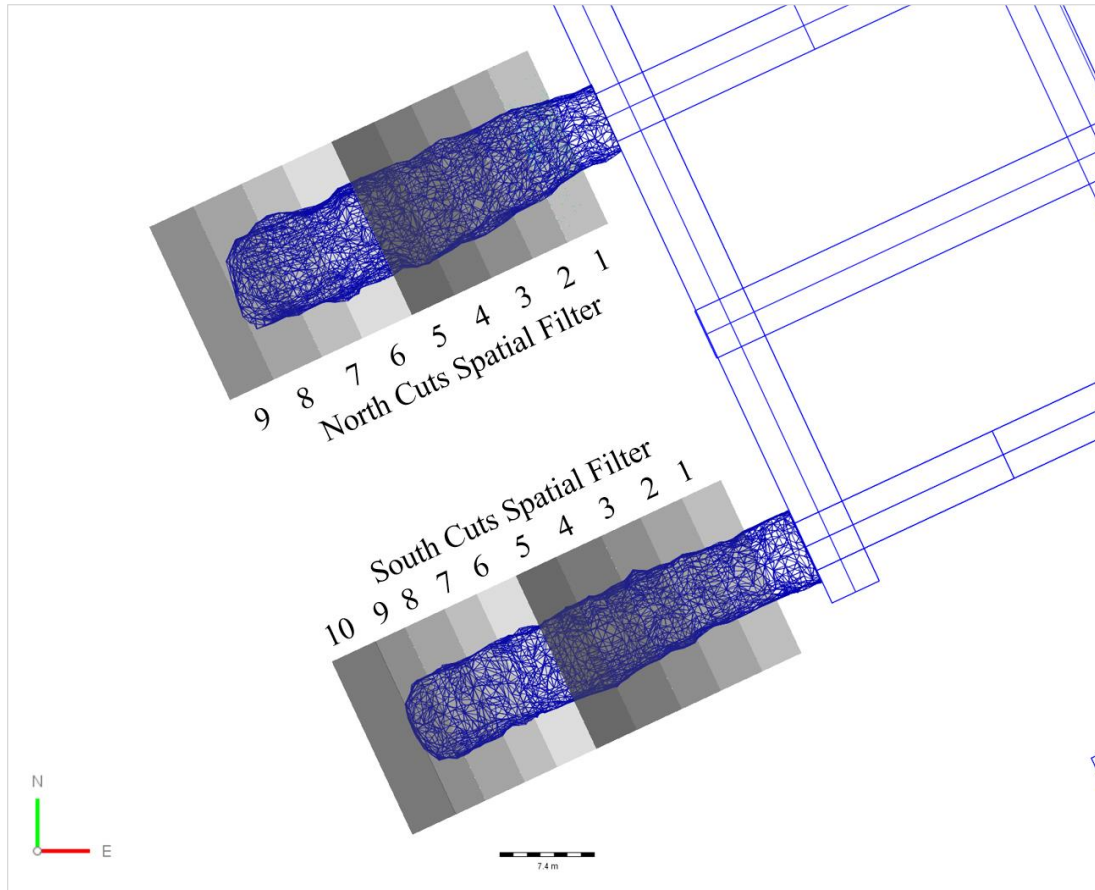


Figure 258 - Plan view of spatial event filters coinciding with each incremental development advance.

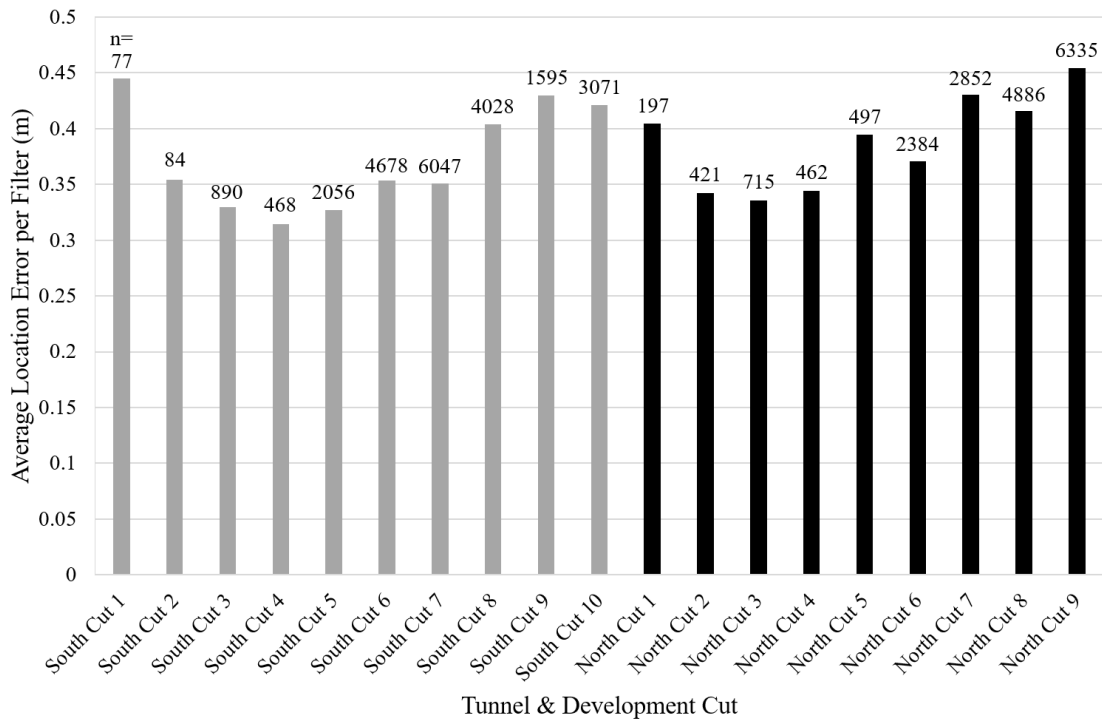


Figure 259 - Average seismic event location error for the population of events within each spatial filter.

It was useful to visualise the location error in the north and south tunnel using location error spheres. Conceptually, location error spheres are centred on a true failure hypocentre, such as an unstable discontinuity. Their dimensions enclose the possible locations of the event hypocentre as calculated by the seismic system, assuming the modal error value. In this case, the radii of the error spheres for the north and south tunnel were defined by the modal error values indicated in Figure 255. The error spheres simply provided a visualisation of the location accuracy of the seismic system in comparison to the scale of the excavations.

The modal location error values in the northern tunnel (0.3m) and southern tunnel (0.3m) are approximately the same as the source radii (Keilis-Borok, 1959) of a -2.8 M_L seismic event. Many events of larger magnitude recorded by the seismic system were likely to have had a source radius larger than the location error recorded by the system. In that case, the calculated hypocentre location would very likely have been somewhere within the real source radii of the event, although perhaps not the exact centre. Models of the location error spheres for the north and south tunnel are presented in Figure 260 and Figure 261. The size of each sphere is to scale, as are the wireframes of the tunnel survey data. The data indicate that the modal 3D location errors of the seismic system are approximately 1/23rd of the maximum span of the northern tunnel and 1/20th of the span in the south. On this basis the local seismic monitoring system had sufficient capability to accurately measure the spatial characteristics of the seismogenic zones surrounding the two tunnels.

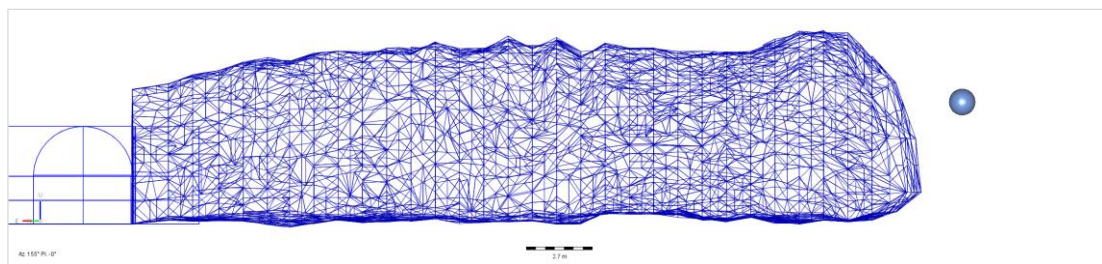


Figure 260 – Error sphere (0.3m radius) representing modal location error adjacent the north tunnel.

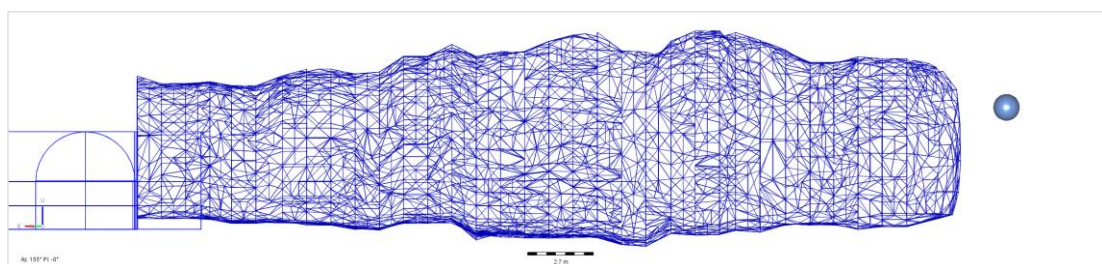


Figure 261 - Error sphere (0.3m radius) representing modal location error adjacent the south tunnel.

6.2.1.2 Seismic Source Parameters

The performance of the seismic system’s source parameter sensitivity was also assessed. This included the minimum magnitude sensitivity, as well as the accuracy of other source parameters, such as seismic potency. Due to the high frequency accelerometers and very small events required to be detected, it was necessary for the Institute of Mine Seismology to make some minor adjustments to the system’s recording settings, in order to calculate the source parameters as accurately as possible.

As described by Birch (2018), appropriate frequency cut-offs were applied to the raw seismic data so as to remove low frequency noise and amplification effects observed around 200Hz and 3kHz. New Q-values, used to estimate energy loss from the seismic wave between the source and sensor, were calculated for each sensor site using the Brune ω^2 model and assuming the same Q value for both the P and S-wave. The Q-values applied to the system for each sensor site are tabulated below. Event source parameters were calculated by applying these Q-values and a 300Hz low-frequency and 10kHz high-frequency cut-off to the entire seismic dataset. The signal-to-noise ratio on the P and S-wave spectra was also reduced from 2.0 to 1.5, in order to increase the number of legitimate events with calculated source parameters (Birch, 2018).

Table 51 - Q-values applied to sensors sites for source parameter calculations.

Site	Q _P = Q _S	Site	Q _P = Q _S
1	400	5	290
2	500	6	350
3	420	7	860
4	400	8	860

The event magnitude frequency distribution for the entire population of seismic events recorded during the tunnel construction is shown in Figure 262. The data was subdivided by proximity to each tunnel, as per the spatial filters in Figure 254, so that the magnitude distributions of events adjacent each tunnel are charted separately. The data indicated that the distribution of recorded event magnitudes was highly consistent between both tunnels. Firstly, this indicated that the magnitude sensitivity of the system was spatially consistent. The data also indicated that the magnitude sensitivity decayed rapidly below $-3.3M_L$ surrounding both tunnels. Furthermore, the b-value for both excavations was largely identical, as indicated by the slope of the line plot of N/N_{Total} , indicating no significant difference in the ratio of small to large events.

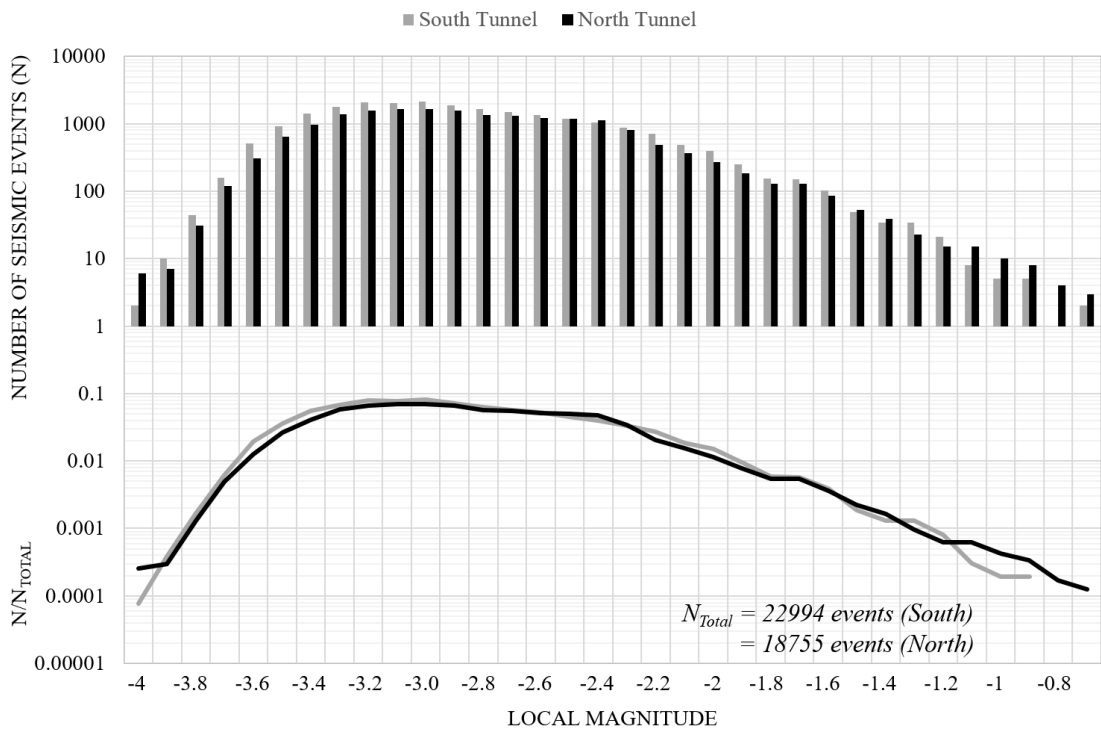


Figure 262 – Magnitude frequency distribution of all recorded seismic events.

The magnitude-time chart presents the range of recorded event magnitudes for any given day (Figure 263). This chart confirms that no events less than $-4.0M_L$ or greater than $-0.5M_L$ were recorded. Fewer events within the range -1.5 to -0.5 were recorded during the first 95 days of the construction, potentially due to mining within the zone of influence of existing development. Note that there was a 14-day loss of data around the 100-day mark, due to a contract-related work stoppage at the mine. Numerous sparsely populated periods on the chart correspond to construction downtime.

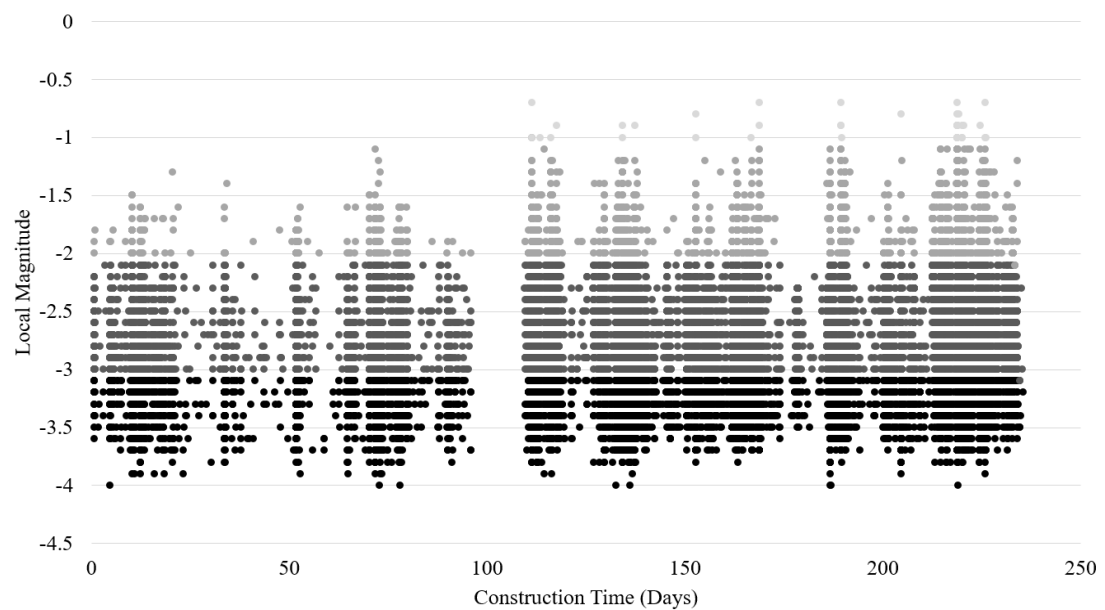


Figure 263 - Magnitude-Time chart for entire seismic event dataset.

The Log (Energy) vs. Log (Potency) plot provided further information on the source parameter performance of the seismic system (Figure 264). Typically, this plot would be expected to show all events clustering consistently around the trend given by the linear equation $\text{Log}(E) = d \text{Log}(P) + c$. However, in this case the dataset demonstrated a noticeable positive (upwards) splay for events in the range $\text{Log}(P) \leq -5.0$. This indicated that seismic potency had been overestimated for events within this range. The cause of this was interpreted as overestimation of the displacement spectral plateau, due to contamination by low frequency noise, which is a known issue for accelerometers (Birch, 2018). This minor overestimation in the seismic potency was an accepted compromise given the selection of accelerometers in the sensor network, which are far superior to geophones when detecting small magnitude seismicity. It was noted that the splay in the Log(E) vs Log(P) plot was significantly reduced when plotting events which triggered all eight of the seismic sensors.

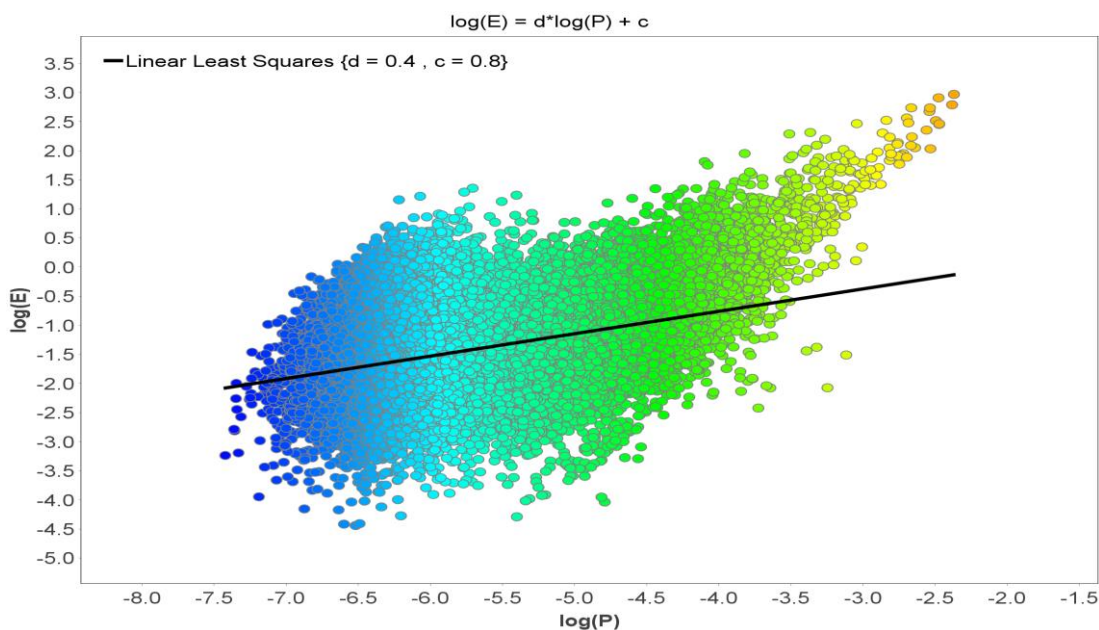


Figure 264 - Log(E) vs Log(P) plot for the entire seismic event population.

6.2.1.3 Seismic Source Mechanisms

Source mechanisms of the seismic events were calculated manually using the full-waveform moment tensor inversion method. It was not possible to calculate accurate mechanisms for a large portion of the total event dataset. Of the 48,005 events recorded around the research tunnels, only 350 were deemed acceptable for mechanism processing. Of these 350 events, only 170 were able to be successfully processed to produce a reliable mechanism solution.

In order to select suitable events for mechanism processing, a filter was applied to select only those events where at least 3 recording sensors experienced Peak Ground Acceleration (PGA) of $> 10\text{m/s}^2$. This yielded 350 suitable events being selected for further processing. The optimal frequency band for processing was then found to be 300 - 800Hz. The 350 selected events were processed manually using the full waveform moment tensor method. An example of a moment tensor mechanism solution is illustrated below in Figure 265. This is a typical mechanism solution for the seismic dataset, which exhibited a close agreement between the observed and synthetic displacement waveforms. Solutions with fewer triggered sites also displayed closely matched waveforms.

Overall, the number of events with source mechanism solutions was very small as a percentage of the total seismic record. This was largely due to the complexity of extracting mechanism solutions from extremely small events, and also the fact that low-confidence mechanism solutions were excluded by the data quality control process. This was necessary in order to ensure high confidence in the data interpretations. Nonetheless, there were a significant number of mechanisms calculated, with 170 total solutions. The total number of mechanism solutions was fairly evenly divided between both tunnels, ensuring that the mechanism characteristics of both tunnels were able to be substantially compared.

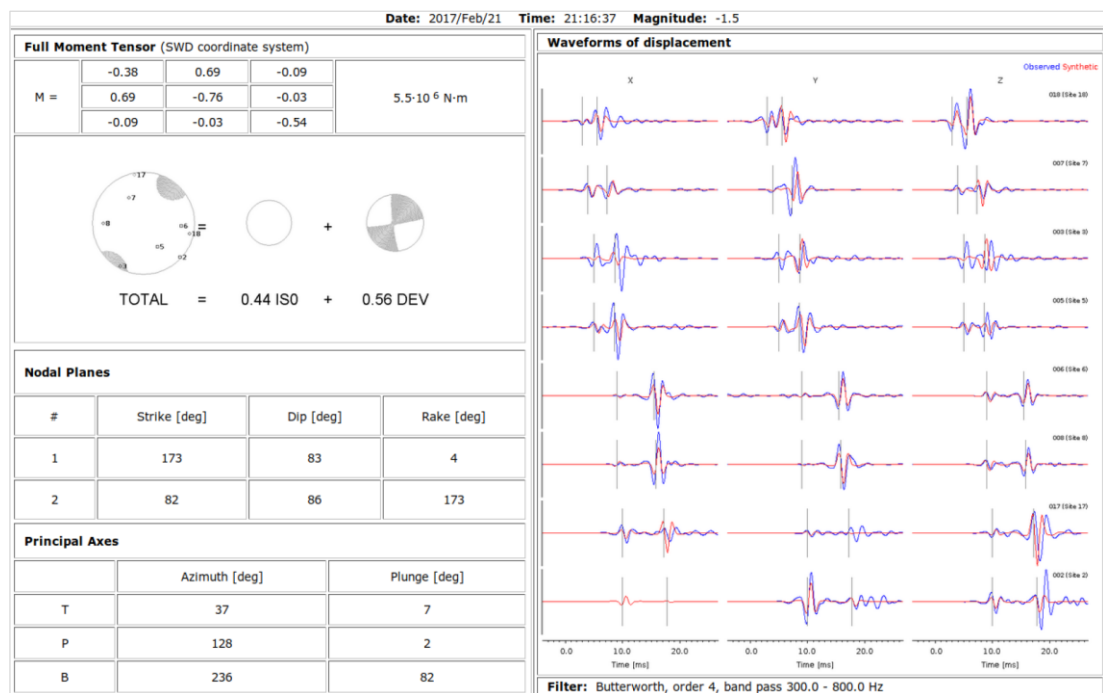


Figure 265- Example source mechanism calculations in IMS software (Birch, 2018).

6.2.1.4 Seismic Data Loss and Data Selection for Analysis

It must be noted that some seismic data was lost during four of the first five development cycles of the tunnel construction. This was due to unplanned power interruptions to the seismic system during blasting. During these outages, the seismic system was not operating to record data. The data loss was limited to the immediate seismic reaction to blasting. The duration of the system outages ranged from between 45 minutes to 12 hours, post-firing. The activities affected by the loss of seismic data were Cuts 3, 6, 7 and 10. That is, two blasts in both the north and south tunnels. This occurred relatively early during the construction project. As such, the seismic record was incomplete for development cycles 2, 3, 4 and 5. The development sequence showing the cuts affected by data loss is illustrated in Figure 266.

The loss of some seismic data after blasting affected the number of conventional and destressing development cycles which were able to be assessed and compared in terms of their seismic response. Cycles with lost data were deemed invalid for analysis due to the incomplete seismic history of events and related source parameter data. Considering the specific blasts which were affected with data loss, a direct comparison of the rock mass response to the destressing and conventional tunnel construction strategies could only be made for development cycles 6, 7, 8 and 9. Blast #8 (destressing, north tunnel) and blasts #9 and #19 (conventional, south tunnel) were also included in the analysis. In short, the complex seismic response from five destressing blasts in the north tunnel was assessed and compared to that of six conventional development blasts in the south tunnel. In total, these blasts reflected 19.3m of destressed development and 19.6m of conventional construction.

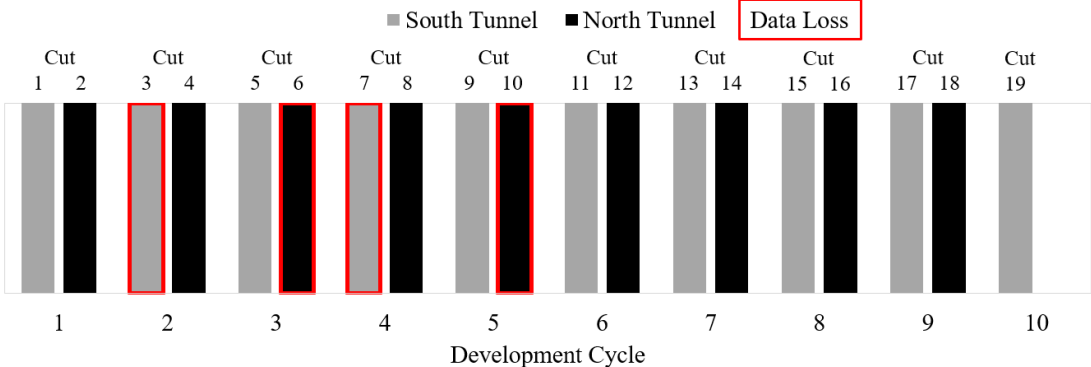


Figure 266 - Selection of development cycles for comparison seismic analysis.

6.2.2 Seismogenic Zone Spatial Characteristics

The vast majority of the recorded seismicity occurred within two primary clusters, one closely enveloping each tunnel. There was relatively little seismicity recorded beyond the immediate tunnel boundaries. There was also no notable interaction of the two main seismogenic zones through the horizontal pillar separating the tunnels. This suggested that the stability of each excavation was largely independent to that of the other. Consistent with the prior stability assessment (Section 4.4), rock mass instability during development was restricted to relatively small-scale failure mechanisms, including spalling on the tunnel boundary caused by local overstressing. This generated seismic events within the magnitude range of -0.7 to $-4.0M_L$. Often, this led to progressive spalling overbreak of the tunnel profile. Large scale instabilities involving geological structures were not observed in the field or in the seismic record.

Figure 267 presents a plan view of the entire seismic dataset. The data spans the entire construction period and focuses on the tunnel geometry. The final tunnel survey wireframe and access development design strings are also shown for location reference. It is evident in this broad view of the seismic response that the activity increased in intensity in both tunnels after the face had advanced by approximately five cuts from the access turnout. For the first five blasts there were comparatively few seismic events recorded around the excavations. However, as the excavations advanced further into virgin rock, the dimensions of the development-induced seismogenic zone increased.

A perspective view looking northeast and cross-section view looking southwest through the seismic data are presented in Figure 268 and Figure 269, respectively. These images further highlight the concentrated seismogenic zones encircling the excavations. From these viewpoints, in particular the cross-section, it is evident that the seismogenic zones around both tunnels were concentrated within approximately one diameter of the tunnel boundary. The depth of stress-driven instability in both tunnels was greatest in the face, roof and beneath the floor of the excavation and relatively shallow in the adjacent sidewalls. However, in the northern excavation with rounded profile and face distress blasting, there was a notably greater distribution of seismicity within the sidewalls. These spatial characteristics of the seismogenic zones reflect classic behaviour for excavations developed sub-perpendicular to a high sub-horizontal stress field.

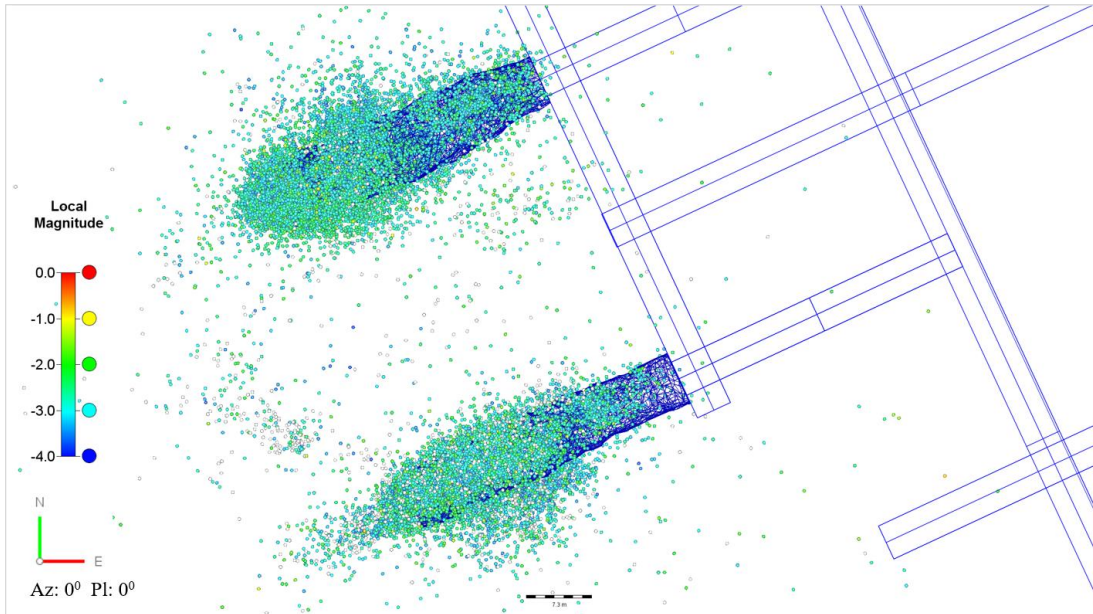


Figure 267 - Plan view of the seismic response showing two dominant seismic clusters.

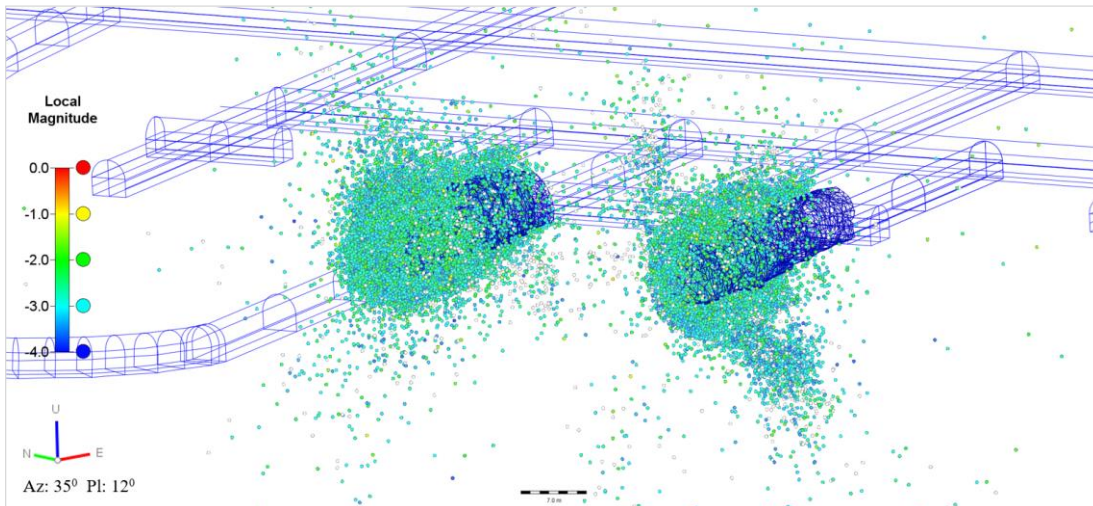


Figure 268 - Perspective view (looking northeast) of the seismic response to development.

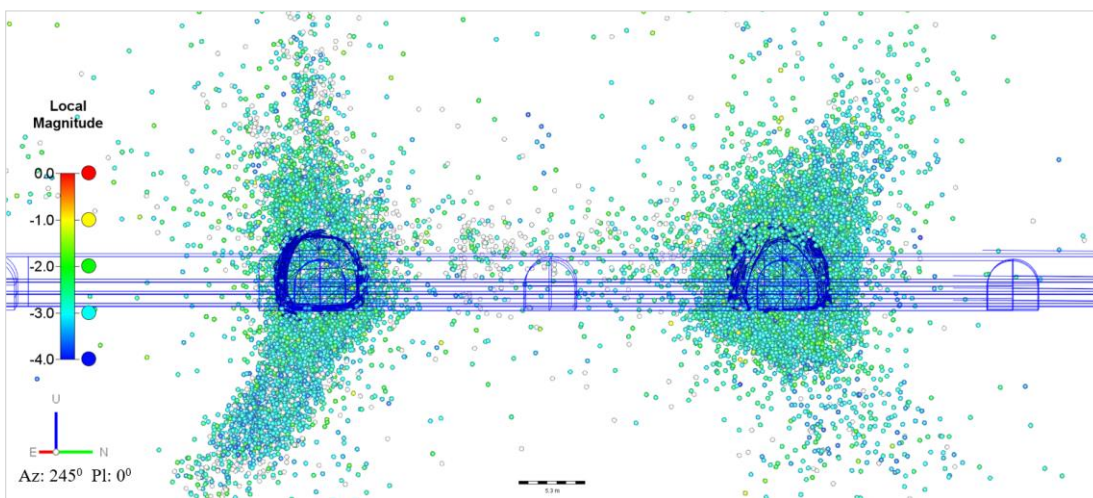


Figure 269 - Cross-sectional view (looking southwest) of the seismic response to development.

The spatial characteristics of the seismogenic zones associated with each development cycle during the last ~19m of construction in each tunnel (i.e. beyond the influence of the access development) are shown below. Figure 270 presents the longitudinal sections (looking towards the southeast) for five development cuts in the southern tunnel using conventional drill and blast techniques. Figure 271 shows the longitudinal sections of the seismic response to face distress blasting in the northern tunnel from the same viewpoint. The data reflect all seismic events recorded during the complete development cycle (i.e. blast-to-blast).

The seismic data from the southern excavation reveal that the seismogenic zone was highly consistent in its basic shape. It always formed a crescent shape enveloping the zone of high stress concentration ahead of the face. There was some distribution of seismicity into the roof of the excavation, although this did not extend beyond the unsupported ground of the recently fired blast. During the latter blasts, the seismogenic zone below the floor of the tunnel was observed to extend several cuts back from the face. This was consistent with concentration of the sub-horizontal stress. The absence of any such seismic response in the roof at that time may be indicative of the effective stabilising action of the ground support scheme.

The characteristics of the seismogenic zones associated with face destressing development were significantly more diverse. Generally, the seismogenic zone was larger and of a less uniform shape when compared to that of the south tunnel at the same distance from the access turnout. The seismicity also extended considerably further into the roof and floor of the tunnel where destressing was applied, with instability often induced behind the supported surfaces of the excavation. Destressing also generated some clustering of events further ahead of the face than was observed ahead of the conventional drill and blast tunnel.

When viewed in cross-section, the data from the southern tunnel (Figure 272) reveal a general lack of any instability in the sidewalls, and sometimes the absence of seismicity in the left hand side of the face. Furthermore, the seismicity in the roof and floor are very locally confined to the centre of these surfaces where the maximum stress concentration occurred. In contrast, the seismicity following face destressing (Figure 273) extended deeper into the sidewalls, indicating that stress redistribution occurred over a much greater percentage of the excavation circumference.

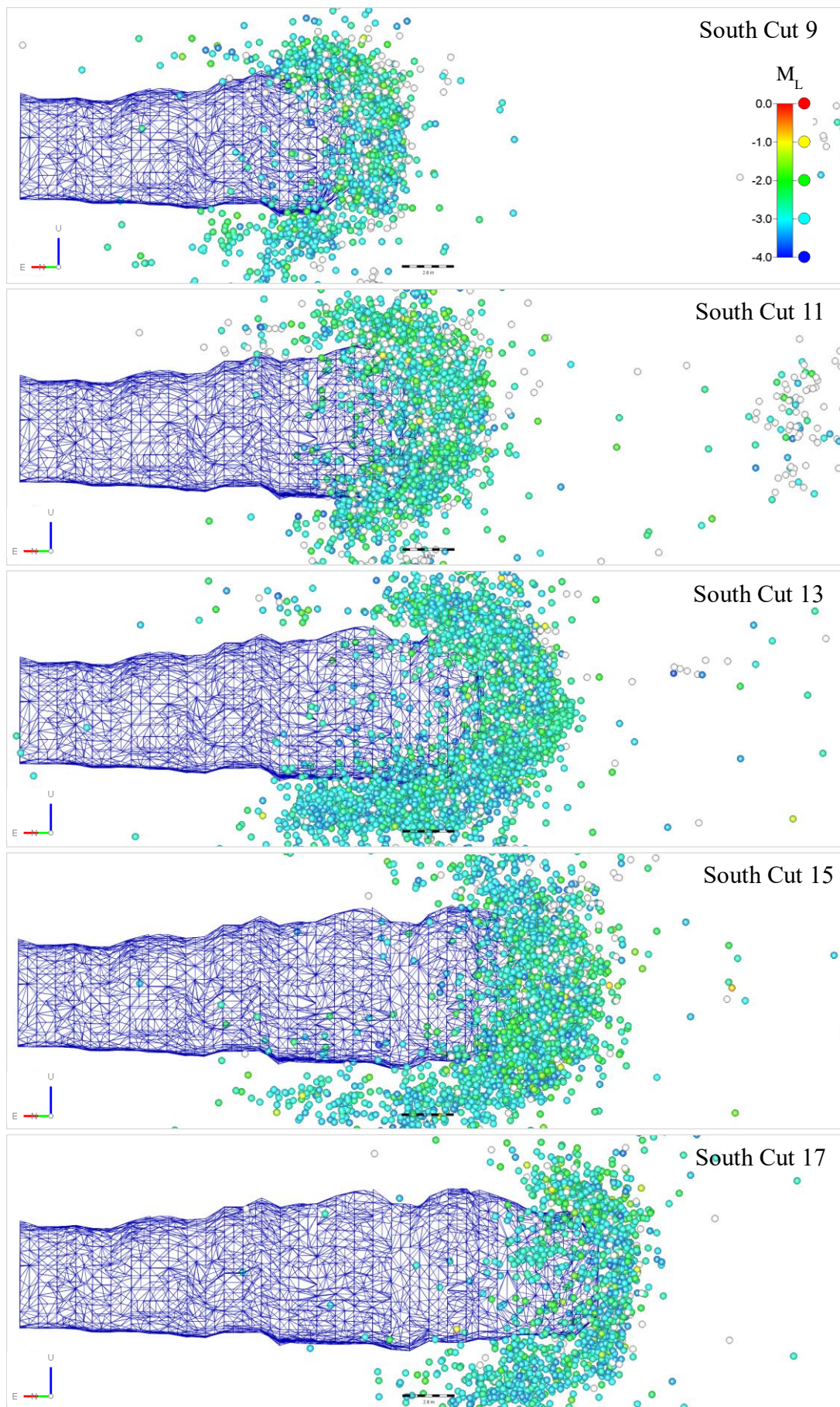


Figure 270 - Longitudinal sections of the seismic response to conventional drill and blast development.

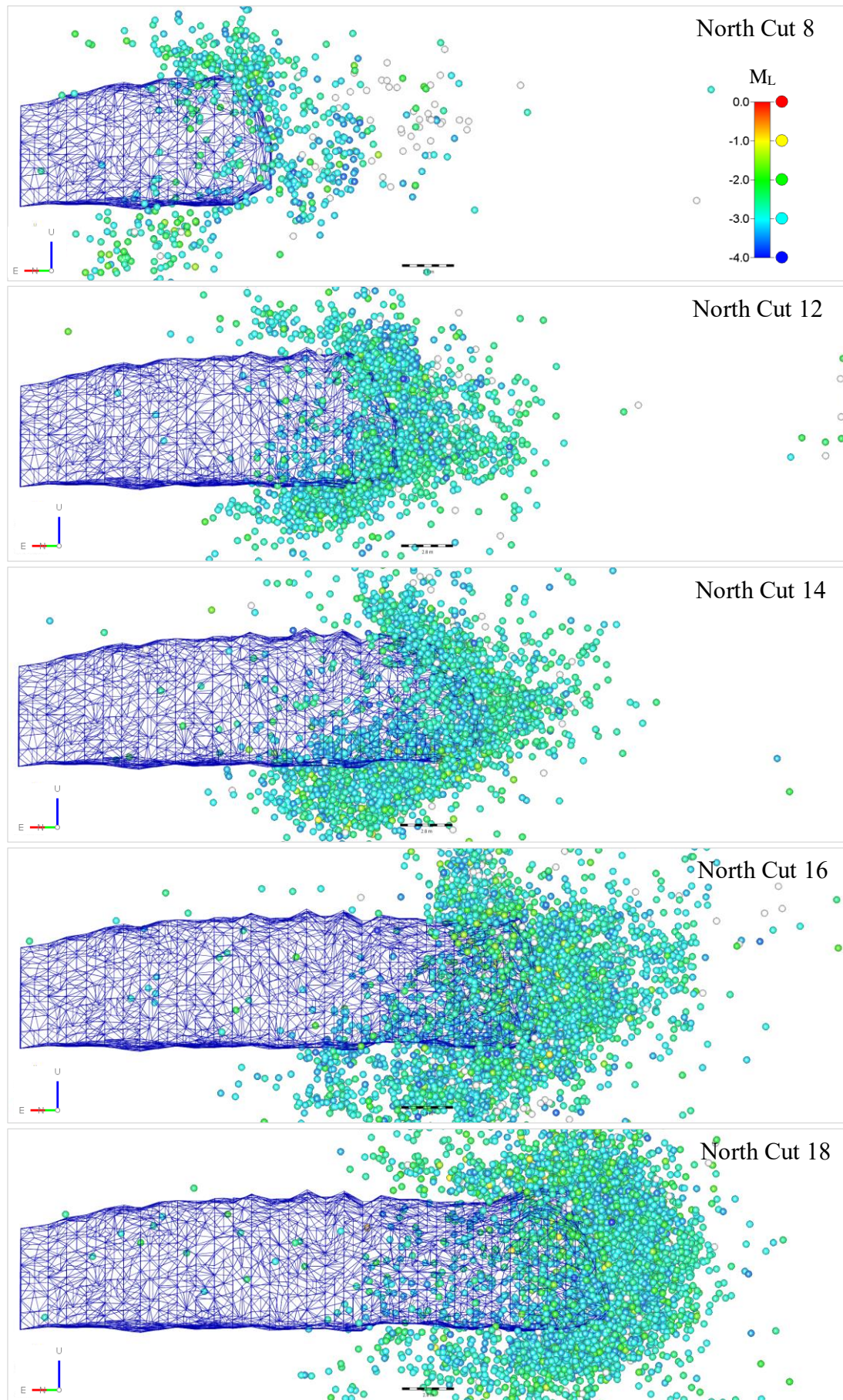


Figure 271 - Longitudinal sections of the seismic response to face destressing drill and blast development.

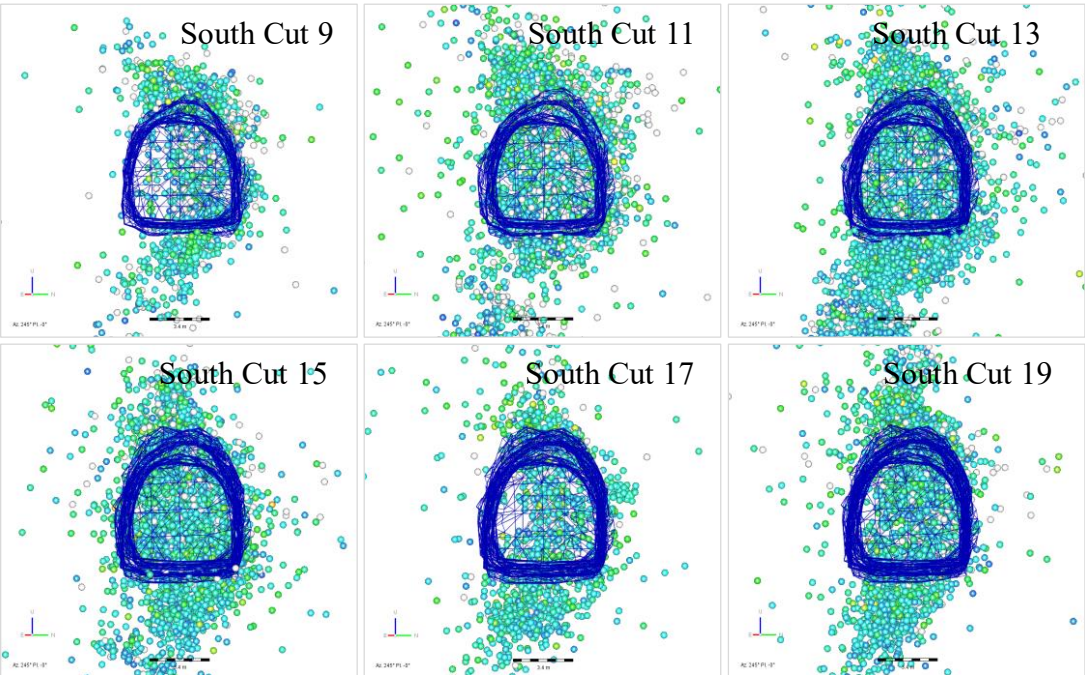


Figure 272 – Transverse sections of the seismic response to conventional drill and blast development.

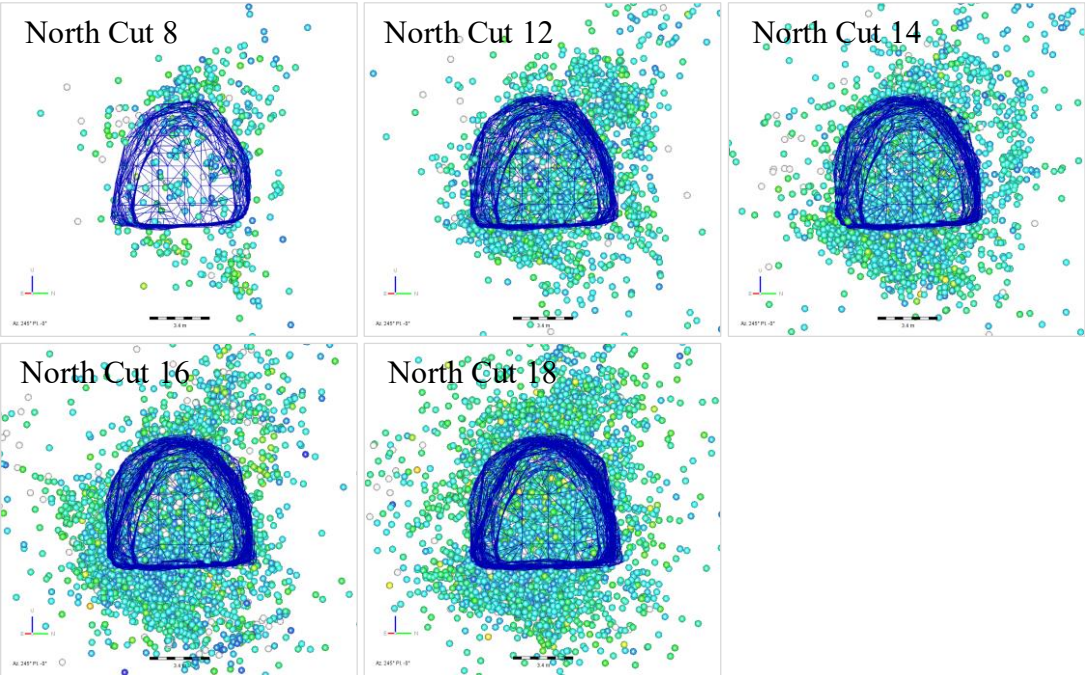


Figure 273 - Transverse sections of the seismic response to development with face distress blasting.

6.2.3 Time History of Seismic Parameters

A time-history chart showing the cumulative number of events, radiated seismic energy and seismic potency for the entire dataset of recorded seismicity is presented in Figure 274. Seismic energy is the measure of the energy radiated from the seismic source as a transient stress wave. Seismic potency is the volume of rock, of whatever shape, associated with co-seismic inelastic deformation at the source (Mendecki, et al., 2010). The time-history data for these parameters was selected within a spatially filtered volume that excluded seismicity from unrelated nearby mining activity. The dimensions of this spatial filter are identical to those of the ray-tracing velocity models illustrated previously in Figure 243 and Figure 244.

The time-history chart shows both long and short-term (i.e. day-to-day) temporal trends in each of these three seismic parameters for the entire construction period. The timing of development blasts in each tunnel are illustrated by coloured black and grey markers. The data indicate that there were 48,005 seismic events in total during the construction of the two tunnels. The cumulative radiated seismic energy and potency during this period was 21kJ and 0.53m³, respectively.

The relatively flat portion of the time history from November 2016 to mid-February 2017 indicates that the two tunnels did not generate a substantial seismic response during the initial 18m of development. This distance was equal to approximately 3½ times the diameter of the pre-existing access development. The relatively low seismic response within this zone was interpreted to be a result of pre-existing rock mass damage within the zone of influence of the access development. Specifically, induced stresses surrounding the access excavations likely caused some structural deformation prior to construction, limiting the seismic response during the early development.

The seismic response did increase once the tunnels had advanced more than three diameters from the access development. A cursory analysis of the plotted time-history data indicated that the number of events, energy and potency response to conventional tunnelling was generally more violent than that associated with the face destressing tunnel, but not always. The same data used to construct the time-history plot was also examined in a series of histograms (Figure 275 to Figure 277). The data was time-filtered for each cycle and spatially filtered to select data adjacent each tunnel individually. The main observations of the seismic time-history are as follows:

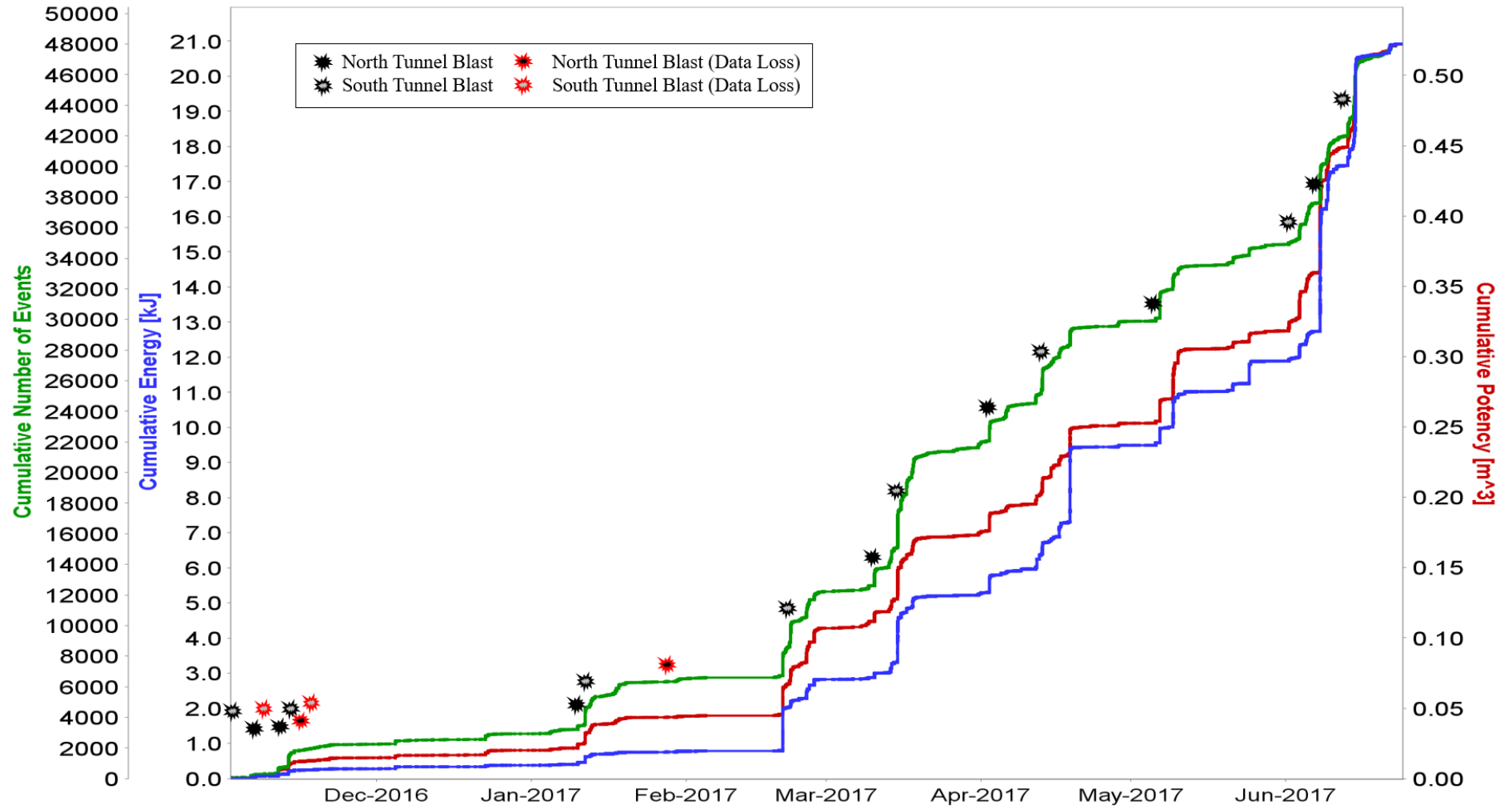


Figure 274 - Cumulative event count, seismic energy and potency for the entire seismic dataset.

Development Cycles 1-5 (South Cuts 1,3,5,7,9 & North Cuts 2,4,6,8,10)

Notwithstanding the loss of some seismic data during the early phase of construction, the time-history data indicated that the first five development cycles of the tunnelling process were completed with a relatively low number of seismic events. The combined energy release of < 1kJ and seismic potency of 0.05m³ during these first five cycles was also very low in comparison to the total values of 21kJ and 0.53m³ for the entire construction. This indicated that the seismic response of the first five development cycles was significantly less-intense than subsequent development in the two tunnels.

Development Cycle 6 (South Cut 11, North Cut 12)

The first activity to demonstrate a significant seismic event count and energy release was face drilling for the 6th development cycle, i.e. boring the face of Cut 11, in the south tunnel. It was noted that the seismic intensity increased due to disturbance at the face caused by drilling, not blasting. At that point both tunnels had been developed to approximately 18m in length and were assumed to be beyond the zone of influence of the pre-existing access development. The number of seismic events (6202), total radiated energy (2.3kJ) and seismic potency (0.065m³) in the south tunnel were all significantly greater than in the north during this cycle. In the northern destressing tunnel these metrics were 2524, 0.3kJ and 0.013m³, respectively. The energy release per unit volume of damage of 35kJ/m³ in the south versus 23kJ/m³ in the north indicated less violent instability where destressing was applied.

Development Cycle 7 (South Cut 13, North Cut 14)

During this development cycle there was again a more substantial seismic response in the conventional southern tunnel than there was in the destressed north. In terms of the event count, 6914 events were recorded around the south tunnel and 2972 around the north. The radiated energy recorded around the south tunnel was 1.9kJ, compared to 0.7kJ around the northern tunnel. The volume of inelastic rock mass deformation during this cycle was 0.049m³ in the south and 0.026m³ in the north. These raw statistics indicated that there was approximately twice the volume of co-seismic inelastic rock mass damage associated with the conventional blasting when compared to destressing, but nearly three times the radiated energy. The energy release per unit volume of damage of 39kJ/m³ in the south versus 27kJ/m³ in the north again indicated that the stress-driven instability was less violent where destressing was applied.

Development Cycle 8 (South Cut 15, North Cut 16)

The distribution of seismic events between the north and south tunnels during the 8th development cycle was relatively even, with 4533 events in the south compared to 5205 events in the north. This was the first recorded instance during the experiment where the number of seismic events located around the destressed excavation exceeded those surrounding the conventional tunnel through one complete development cycle. Despite this, there was 2.9kJ of energy radiated around the southern tunnel compared to 2.4kJ where the destress blasting was applied. The seismic potency surrounding the southern excavation (0.047m³) was also lower than that recorded around the northern destressing tunnel (0.066m³) for the first time. This indicated a larger volume of rock mass damage associated with the destressing. However, the energy release per unit volume of damage of 61kJ/m³ in the south versus 36kJ/m³ in the north indicated that the destress blasting significantly reduced the violence of the rock mass response.

Development Cycles 9 &10 (South Cuts 17 & 19, North Cut 18)

The seismic response to the 9th development cycle was characterised by a significant minority of the events, radiated energy and seismic potency being recorded around the southern tunnel. A total of 1768 events were recorded around the conventional tunnel, with 0.55kJ of associated radiated energy and 0.026m³ potency. In comparison, there were 6565 events around the northern tunnel with destressing at the equivalent distance from the access turnout. There was also 6.9kJ of radiated energy and 0.122m³ potency. In this case the energy release per unit volume of 21kJ/m³ was abnormally low in the conventional tunnel, and unusually high in the destressed excavation at 57kJ/m³. This indicated that the rock mass instability in the last destressing round was much more violent and energetic than the final conventional development rounds. This observation was the opposite to that observed previously in the tunnels, which was a more violent response in the conventionally constructed tunnel. As discussed later, approximately half of the number of seismic source mechanisms recorded around the northern tunnel occurred during Cut #18. This indicated that the rock mass response involved a more violent response on structure, which could explain the elevated seismic parameters in this case.

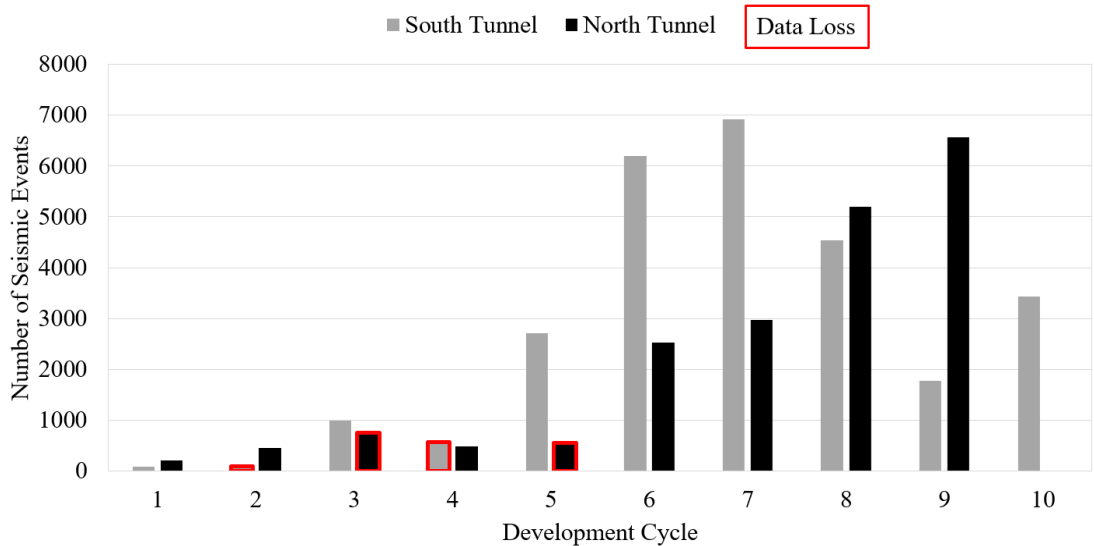


Figure 275 - Total seismic events per tunnel per development cycle.

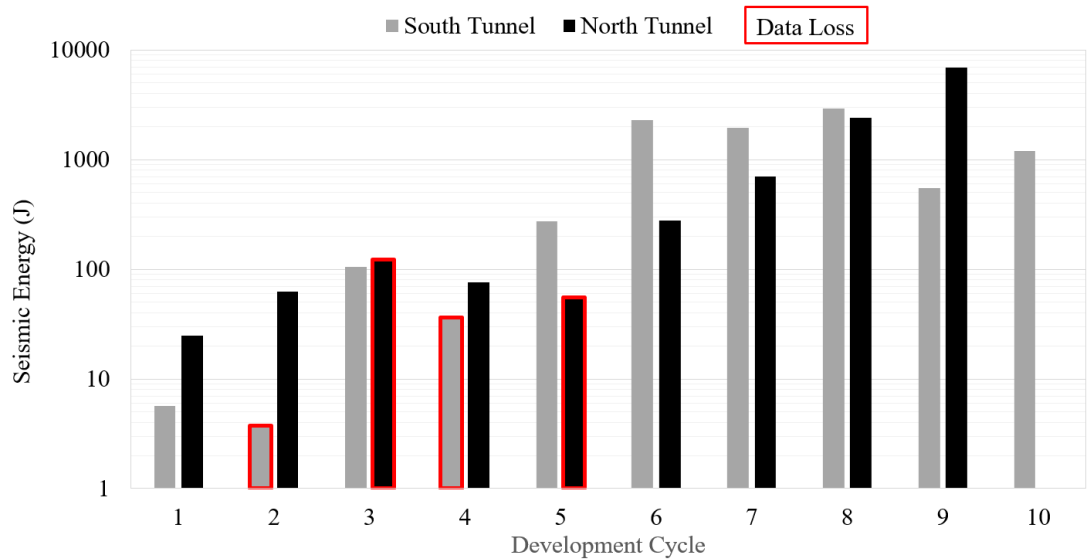


Figure 276 - Total radiated seismic energy per tunnel per development cycle.

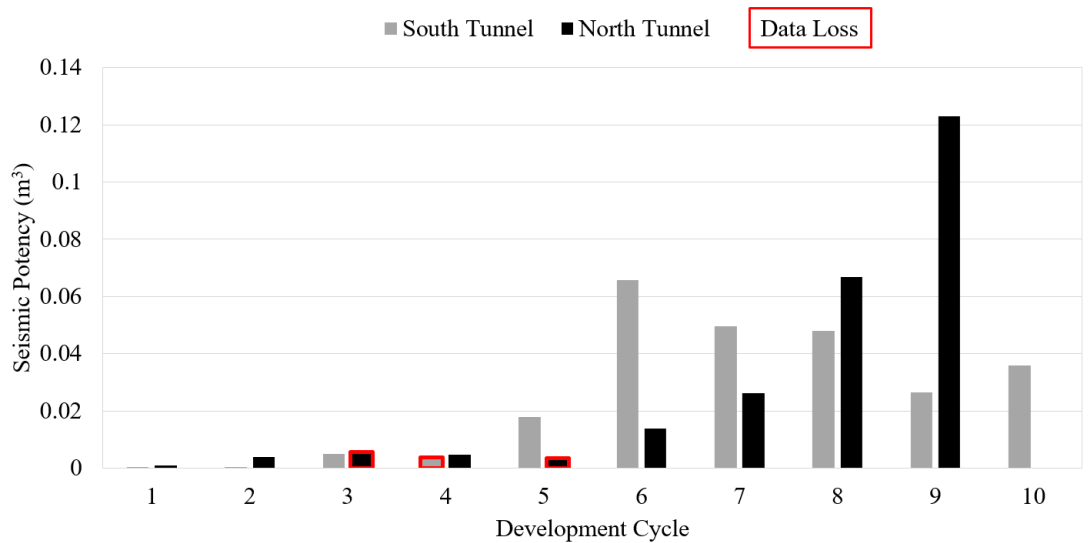


Figure 277 - Total seismic potency per tunnel per development cycle.

The broad trends in the three main seismic parameters can be summarised as follows. In terms of the number of seismic events, the data indicated that the event count was generally increasing with each destressing development cycle in the northern tunnel as the face advanced further from the influence of the access development. The number of events in the south tunnel was fairly consistent for cycles 6, 7 and 8, until the last two cuts, where the event count decreased significantly. The cause of this drop in the number of events was unclear.

Low energy release for the first five development cycles in each tunnel indicated that the rock mass was previously damaged due to induced stress concentrations around the existing development. As a result, the rock did not generate significant further seismicity within three tunnel diameters of the access. Energy release around the destressed tunnel was lower than that surrounding the south tunnel on three out of the last four cycles that were directly compared at the same chainage. The exception was the 8th cycle, which was elevated in the three main seismic parameters, likely due to a structural response. Energy release adjacent the destressing tunnel consistently increased with increasing distance from the access. The trend in energy increase during cycles 6, 7, 8 and 9 was highly uniform. This may indicate that the seismic energy release increased as the degree of rock mass damage induced by the pre-existing access development decreased. This trend was similar in the south tunnel, although there was a reduction in energy recorded for the last two cuts.

The seismic potency increased steadily with each cut in the destressing tunnel from development cycle #6 onwards, while steadily decreasing in the conventional excavation. These opposing trends were interpreted to be related to very similar trends in the core diskings observations. Specifically, the pilot drill holes indicated minimal stress-related core damage in the south tunnel beyond the 25m chainage, whereas in the north tunnel the core diskings were increasingly more intense towards the end of the hole (Figure 73). As core diskings and seismic potency are both related to inelastic rock mass deformation, the consistent trends across both tunnels appear logical. However, it must be noted that due to the very low potency values that were recorded, the actual difference in co-seismic damage between both tunnels was minute.

Figure 278 presents a bar chart of the average joules of radiated energy per seismic event, calculated as the total radiated energy divided by the total number of events in each cycle. Figure 279 presents the chart of radiated seismic energy per unit volume of potency. This chart estimates how many joules of energy would likely be radiated for each cubic metre of inelastic rock mass deformation. The values in this chart are inferred from the ratio of the seismic energy to potency for each development cycle. Both charts indicate that the instability was usually much more aggressive in the southern tunnel. The energy/potency ratios suggest that higher strain energy densities were present around the conventional tunnel, which would possibly increase the demand on ground support there, in the event of a failure. Given the uniformity of the stress conditions, the data also suggest that destressing weakened the rock mass.

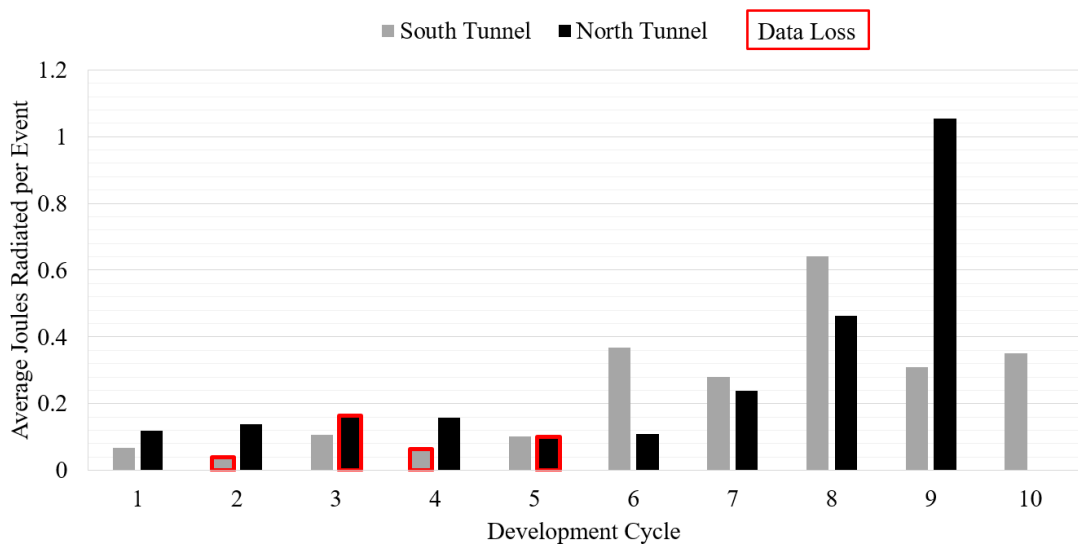


Figure 278 - Average joules of radiated seismic energy per event for each development cycle.

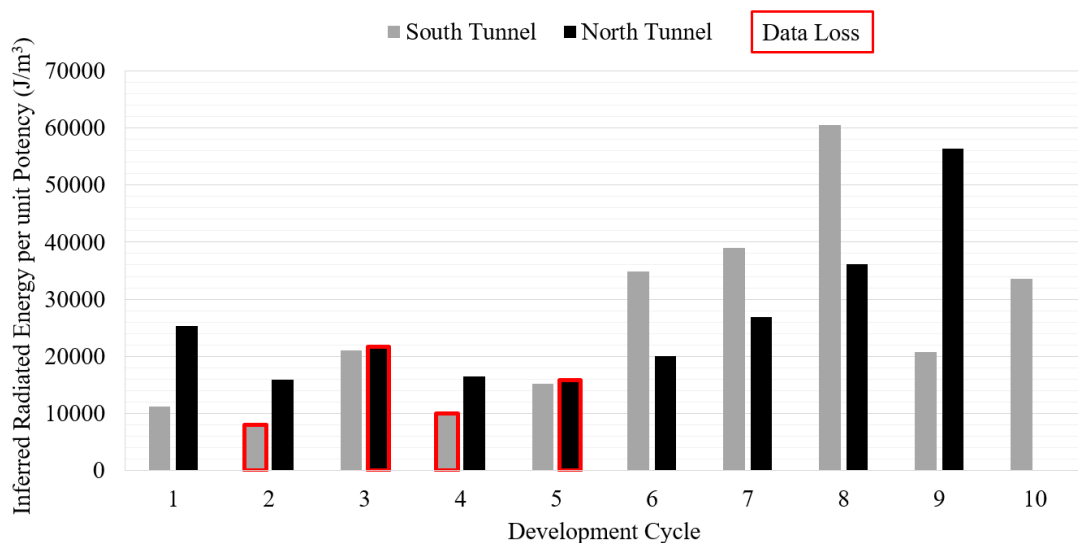


Figure 279 - Inferred radiated energy per unit of seismic potency for each development cycle.

6.2.4 Distribution of Seismicity Across the Excavation Surfaces

A number of spatial filters were created in order to quantify the distribution of seismicity across the various excavation surfaces. The total number of events, cumulative radiated energy and cumulative seismic potency adjacent the faces, floor, roof and sidewalls of each excavation was quantified. The boundaries of the spatial filters applied to select the relevant seismic data in the north tunnel are shown in Figure 280 and Figure 281. Filters with the same shape and relative position were also applied to the seismic data from the southern tunnel. The data was spatially filtered so as to only select data corresponding to the five aforementioned destressing cycles and six conventional development cycles which were chosen for the principle seismic analysis. Bar charts of the total cumulative count of seismic events, radiated energy and seismic potency recorded within each filter are presented Figure 282, Figure 283 and Figure 284, respectively.

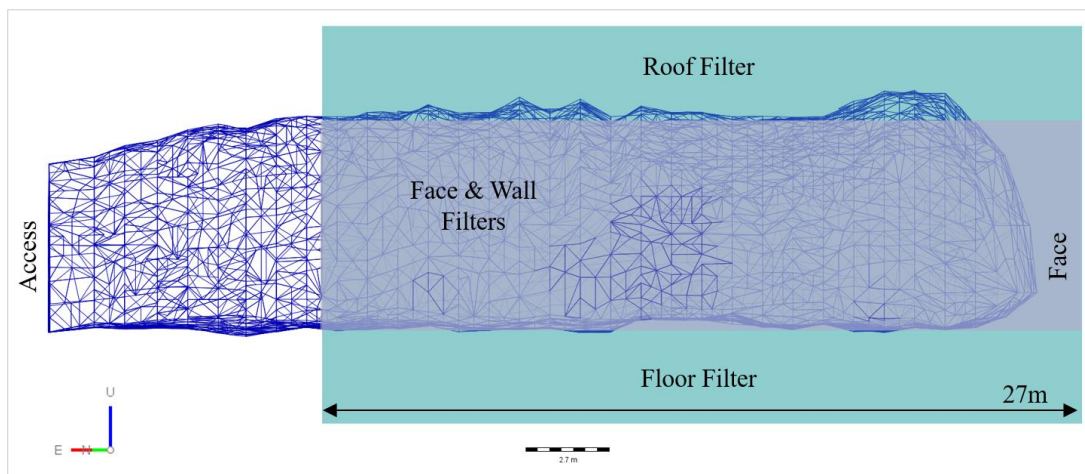


Figure 280 - Longitudinal section view of spatial filters for assessing the distribution of seismicity.

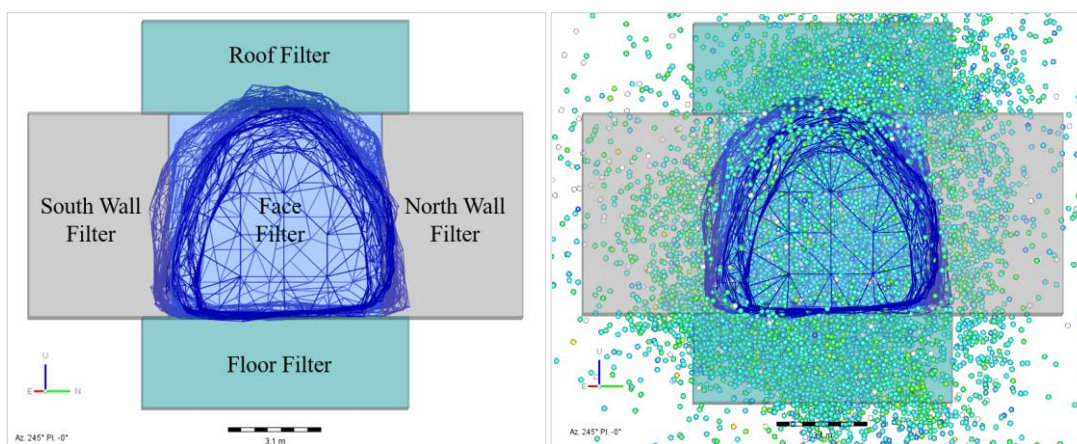


Figure 281 - Cross section view of spatial filters and their coverage of the seismogenic zone (looking SW).

The data in Figure 282 indicated that most events occurred ahead of the face in both tunnels. There were 4184 fewer events ahead of the face in the destressing tunnel over the entire duration of construction. The number of events recorded in the floor varied by around 200 across both tunnels, whereas 2345 fewer events were recorded in the roof of the destressing tunnel. The sidewalls recorded the least number of events. These observations are consistent with the face being the excavation surface with the widest unsupported span and potentially highest or equal highest stress concentration, as it was sub-parallel to the major principle stress. Similarly, the roof and floor of each tunnel were also highly stressed by the σ_1 concentration. However, their smaller unsupported span did not generate the same instability. The data indicated that the walls were considerably more stable than the roof and floor of the tunnel. This was consistent with the minor principal stress being the sub-vertical component.

Radiated energy data for each surface is presented in Figure 283. This confirmed that the most violently unstable excavation surface was the face in both tunnels. The total cumulative radiated energy released at the face was 33% higher where destress blasting was applied. This statistic was heavily influenced by the response to Cut #18 in the north tunnel, which had an unusually high-energy structural response. Excluding this instance, the energy release at the destressing face was much lower than the conventional tunnel. The timing of energy release in relation to the specific construction activities was also important, and this is investigated in the *Activity Analysis* later. The second most violent excavation surface was the roof of each tunnel. The energy release adjacent the roof was 31% greater in the south tunnel when compared to the north tunnel with destressing. The sidewalls were the most stable of the excavation surfaces by a significant margin.

The seismic potency data shown in Figure 284 reveal that co-seismic inelastic rock mass damage was most intense ahead of the face, and very consistent between both the conventional and face-destressed excavations. In both excavations the cumulative potency at the face was approximately 0.11m^3 . With the exception of the southern sidewall, there was generally similar or lesser damage in all other surfaces of the destressing tunnel compared to the conventional development. The most significant difference in the observed potency was the reduction in the damage recorded in the roof, and increased damage in the southern sidewall when destressing was applied.

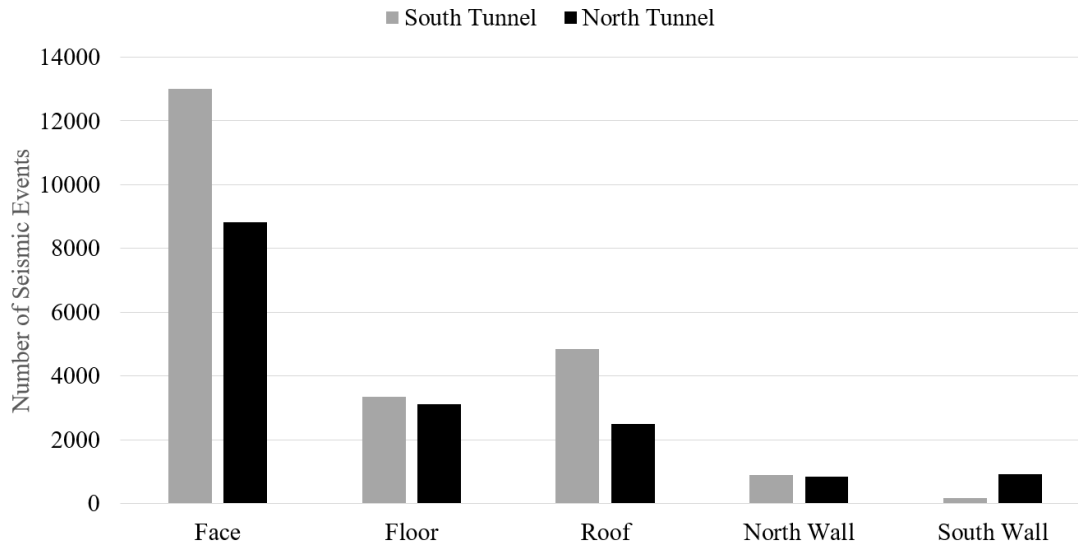


Figure 282 - The total number of recorded seismic events for each excavation surface.

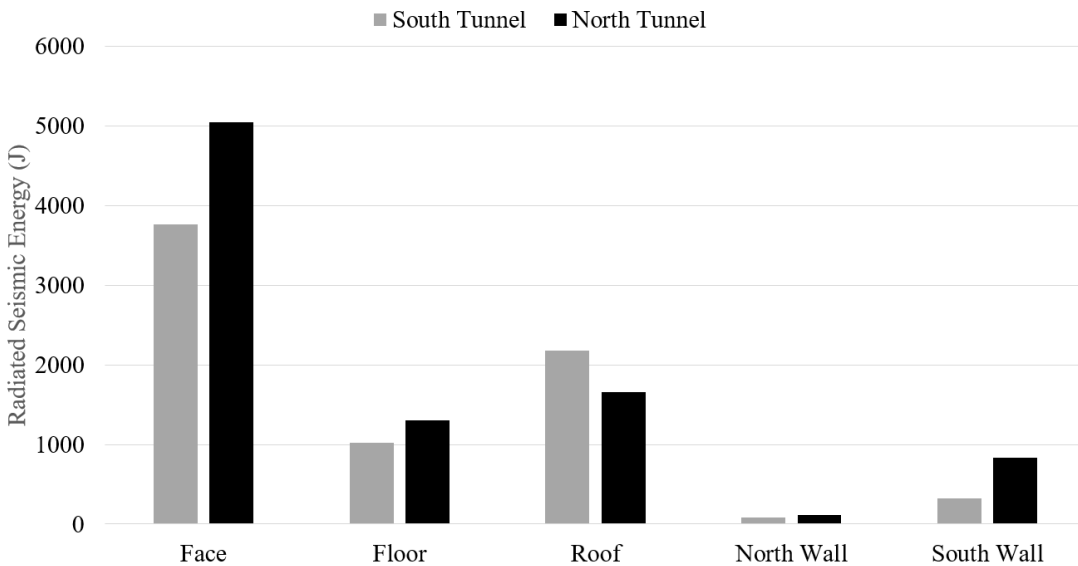


Figure 283 - The total radiated seismic energy for each excavation surface.

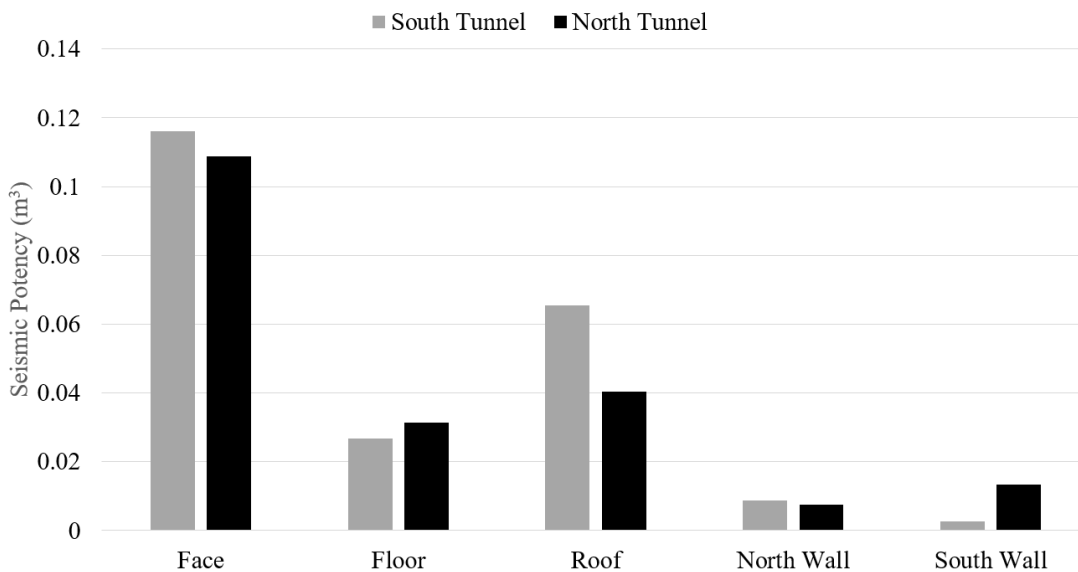


Figure 284 - The total seismic potency (inelastic damage) for each excavation surface.

6.2.5 High Resolution Spatial Analysis

A high resolution spatial analysis of the seismic data was conducted for both the conventional and destressed development. The intent of this analysis was to characterise the seismic response at the face in high detail, establishing what effect destress blasting had on the seismogenic zone and whether energy release and damage at the face were reduced. A spatial analysis of event count and source parameters was performed for the aforementioned eleven development cycles in each tunnel, including six conventional blasts in the south tunnel and five with destressing in the north.

The seismic database was initially time-filtered, such that each analysis included seismicity for one complete development cycle, commencing with the development firing and terminating at the time of the subsequent blast firing. Therefore, the seismic data included in the analysis of each cycle reflected the immediate seismic response to blasting, mechanical scaling, ground support installation and blast hole drilling for the subsequent round. Only legitimate seismic events were included in the analysis. Seismic noise from mechanical sources such as drilling and scaling was filtered and rejected from the seismic database prior to any analysis of the data.

Once the seismic database was time-filtered to select events within a single development cycle, the data was then spatially filtered by creating a large number of *slice* filters in a transverse orientation across each tunnel. The filters were centred on each tunnel and sampled all seismic events within approximately one radius of the tunnel boundary. Each slice filter was 15m wide by 15m high by 0.3m long and took a slice of the seismogenic zone at 0.3m distance increments along the tunnel length.

A longitudinal section, plan view and transverse section view showing the limits of the spatial filters relative to a typical seismic response are shown in Figure 285 to Figure 287. The limits of the spatial filtering for each development cycle analysis began 11.4m behind the surveyed face position. This captured seismic data spanning the last three development cuts in the tunnel (i.e. one unsupported and two supported, ~3.8m each). The analysis also examined 8.1m ahead of the face through un-mined rock. This filtering strategy allowed analysis of seismicity ahead of the face, as well as activity occurring within the recently developed sections of the tunnel which had only primary ground support installed. Sixty-five slice filters defined the total filtered volume, which fully enclosed the main seismogenic cluster around the tunnel (Figure 288).

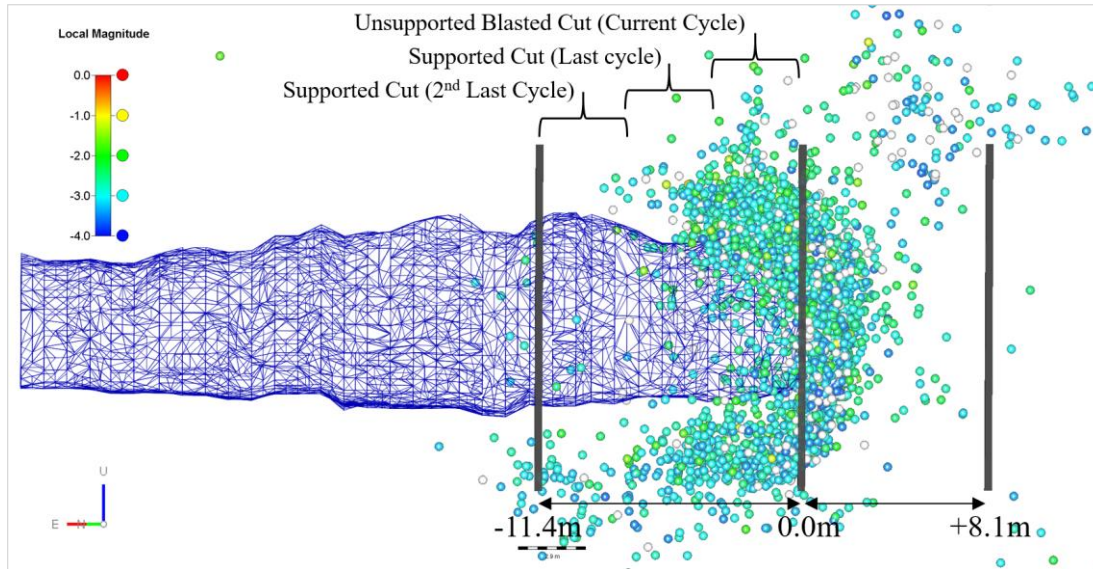


Figure 285 - Long section view of spatial filter limits for high resolution analysis of seismic data.

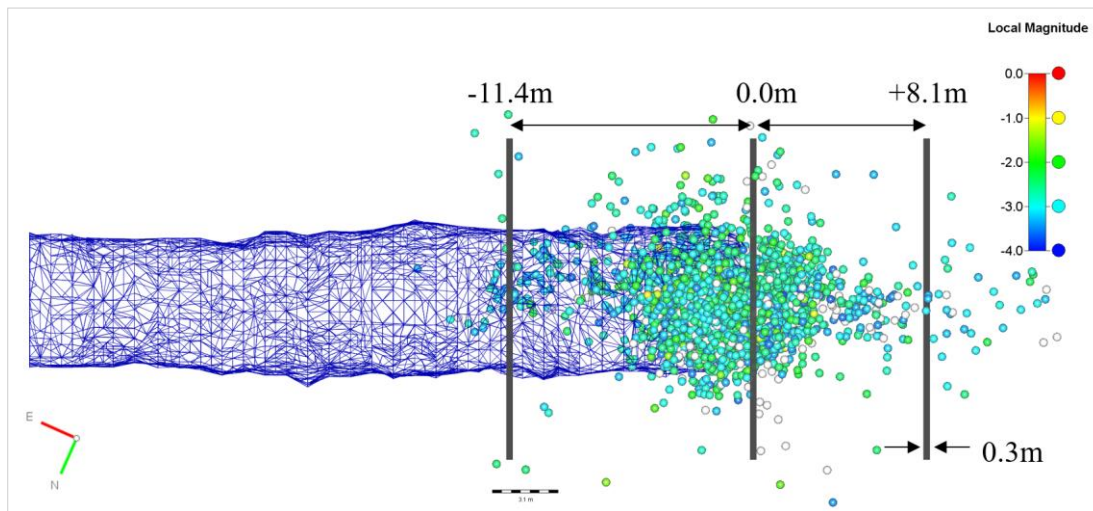


Figure 286 - Plan view of spatial filter limits for high resolution analysis of seismic data.

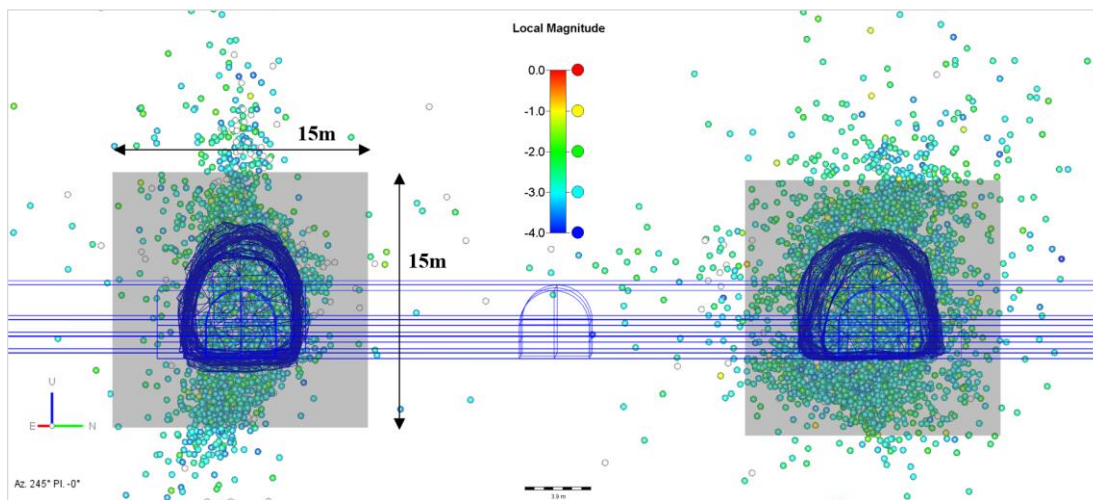


Figure 287 - Cross section view of filter geometry for high resolution spatial analysis of seismic data.

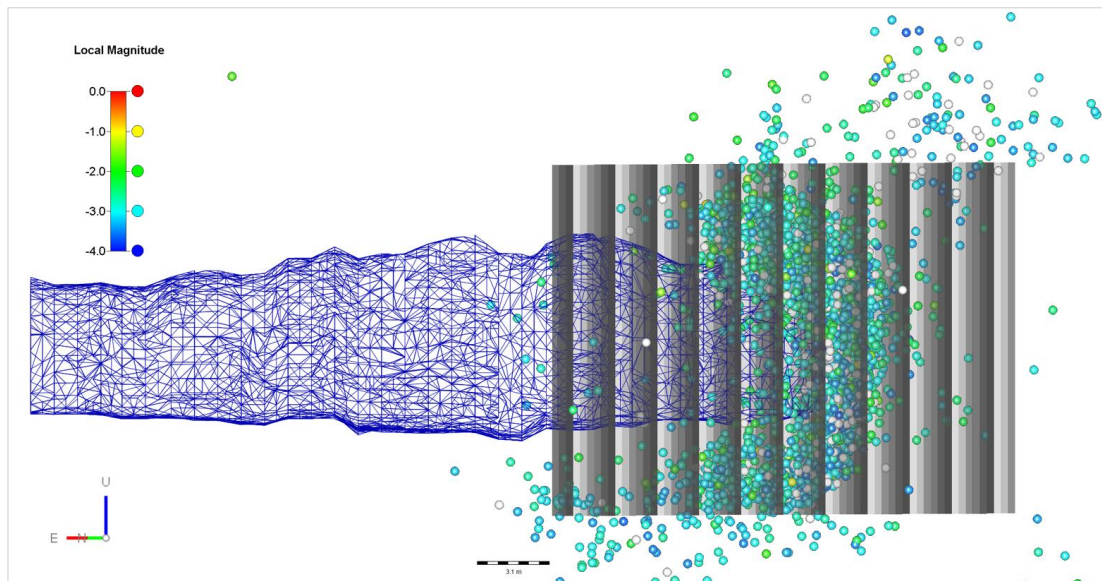


Figure 288 - Long section view of the entire sequence of sixty-five 0.3m-long spatial filters.

6.2.5.1 Event Locations

The first seismic data to be examined were the event counts within each slice filter. The total number of seismic events contained within each 0.3m-wide slice filter, plotted as a function of each filter's longitudinal distance from the face, are presented in the following two figures. Figure 289 presents the results for the six conventional development cycles in the southern tunnel. Figure 290 contains the results for the face destressing development cycles in the northern excavation.

The characteristic seismic response to conventional development can be described as a relatively small number of seismic events adjacent the supported surfaces of the excavation. The number of seismic events then increased exponentially adjacent the unsupported ground and continued to a peak a short distance ahead of the face. The event count within the seismogenic zone was greatest between +0.9m and +1.8m ahead of the face. The number of events in the seismogenic zone then decayed rapidly over the distance range of +1.5m to +3.0m ahead of the face. Very little seismicity was recorded more than 3.6m ahead of the face, as the rock mass was heavily confined. Therefore, the seismic data from the conventional tunnel development indicated that the optimal destressing zone was required to extend between 3.0m to 3.6m ahead of the face. This was consistent with the destressing blast pattern design that was implemented in the northern tunnel, which placed the destressing charges up to a distance of approximately 3.2m ahead of the face.

The data indicated some variability in terms of the total number of events recorded during each development cycle. This may be attributable to local strength or structural variations in the rock mass, which influenced the stability response. However, the characteristic response of the seismogenic zone was a rapidly increasing frequency of events approaching the face with the concentrated peak ahead of the face. This was highly consistent across all six development cycles with conventional blasting.

The characteristic response to face destress blasting was a broader spatial distribution of seismic events about the face position, when compared to the conventional development. A sharp increase in the event count leading to a high peak in the seismogenic zone ahead of the face was not observed in the destressing development, as it was in the conventional tunnel. Instead, where destressing was applied there was a relatively even spatial distribution of the number of events throughout both the unsupported ground of the recent cut and the first 1.8m of the destressed zone immediately ahead of the face. This was indicated by the relatively flat profile of the event count curves over the distance range of -3.8m to +1.8m. The peak of the seismogenic zone was generally ahead of the face, but not always. The event count peaks for the various cuts were observed between -0.9m and +1.2m about the face position. However, the increase and decay in the number of events either side of these peaks was more gradual in the destressing tunnel, as indicated by the lower slope in the event count curves. This suggests a lower likelihood of violent face instability.

The steep increase and decay gradients in the event count curves for the conventional development suggested that relatively high strain gradients existed within the rock mass adjacent and immediately ahead of the face position. By contrast, the much flatter event count curves and gradual decays around the destressed face strongly suggest that the strain gradients there were significantly lower. The much more broadly spatially distributed seismogenic zone was interpreted to be a result of a reduced rock mass stiffness adjacent the destressing development. The shape of the seismogenic zone was also more erratic around the destressed face. Overall, this response to destressing indicated that the strain conditions adjacent the excavation were less conducive to violent face ejection, when compared to conventional blasting. This contrasting rock mass response across the two tunnels is also visible in the images of the seismogenic zones about the face, shown earlier in Figure 270 and Figure 271.

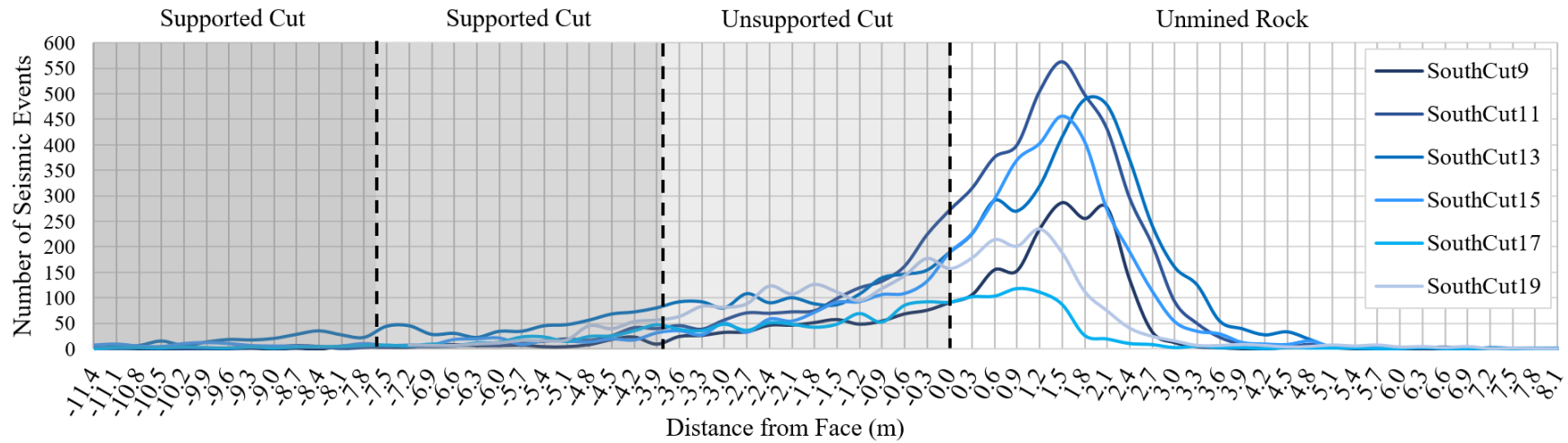


Figure 289 - Number of seismic events as a function of distance from the face for conventional blasting.

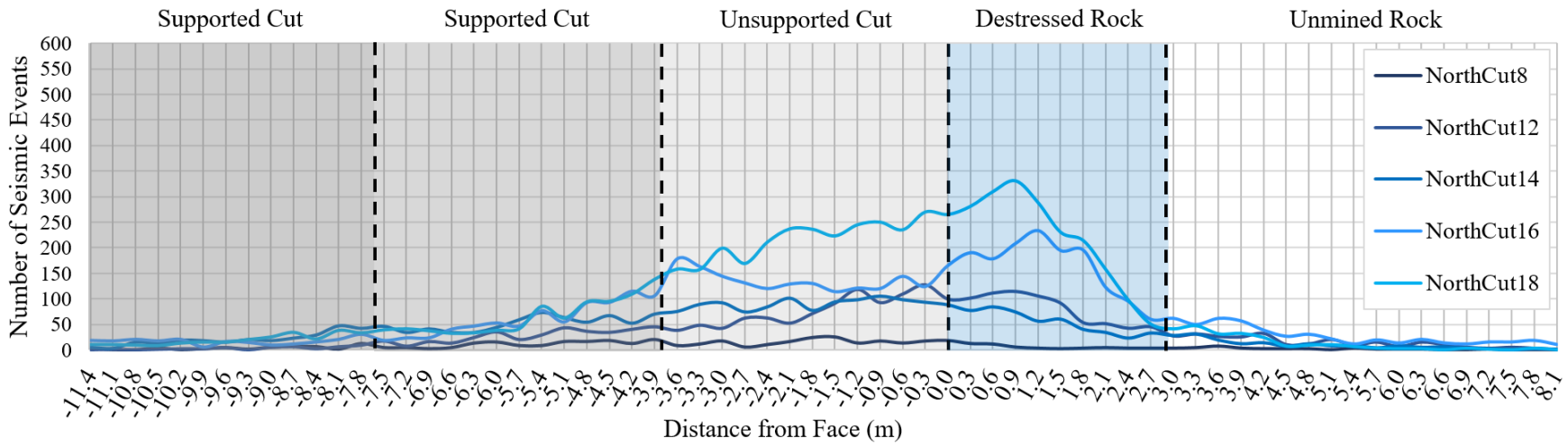


Figure 290 - Number of seismic events as a function of distance from the face for destress blasting.

6.2.5.2 Seismic Energy

The second seismic source parameter to be examined using this spatial filtering approach was the *radiated energy*. It is the portion of the total strain energy released by unstable, loaded rock which was not previously consumed by plastic work (i.e. fracture creation), frictional sliding on fractures or production of heat at the fracture plane. The faster the rupture and slip velocity of the rock mass failure, the more seismic energy radiated from the source (Mendecki, 2013). The plot of the sum of the radiated energy of all events within each 0.3m-wide spatial filter is presented in the following figures as a function of the longitudinal distance of the filter from the face. Figure 291 presents data for the conventional development cycles and Figure 292 the data for the destressing development.

The data relating to the conventional development indicate that there was only a very small release of seismic energy adjacent the supported walls of the excavations. There was relatively trivial energy release adjacent the 2nd last development round. The energy slightly increased adjacent the most recently supported cut, although it remained at fairly low levels (<200J per filter). For most of the conventional development there was minimal energy release adjacent the unsupported ground, with one exception being an energy peak of approximately 734J located 1.5m before the face following Cut #11. The majority of the energy release in the conventional tunnel was typically ahead of the face, with frequent energy spikes of between 200 and 600J located up to 4.2m ahead of the face. The rock mass beyond the face was typically the main zone of stress-driven instability adjacent the conventional development.

In comparison, three of the five monitored development cycles with destressing registered much less energy release than the conventional tunnel, and these largely plotted as a flat-line trace in Figure 292. The two destressing cycles that plotted notable energy values both indicated that destressing had the effect of reducing the energy of instability ahead of the face, while increasing energy adjacent the other excavation surfaces, including unsupported and supported ground. This spatial broadening of the distribution of instability associated with destressing was consistent with a reduced rock mass stiffness adjacent the face. However, there was one instance whereby 1600J of energy was released at the face during Cut #18. This occurred 7 days after blasting following bolting and meshing of the face, and was likely a response of structure.

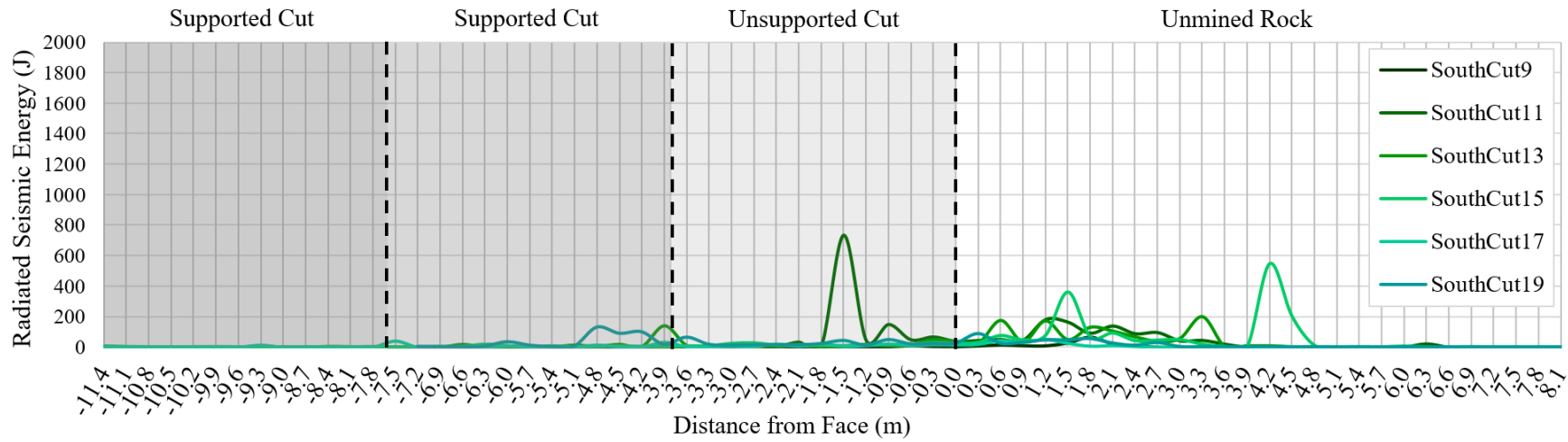


Figure 291 - Radiated seismic energy as a function of distance from the face for conventional blasts.

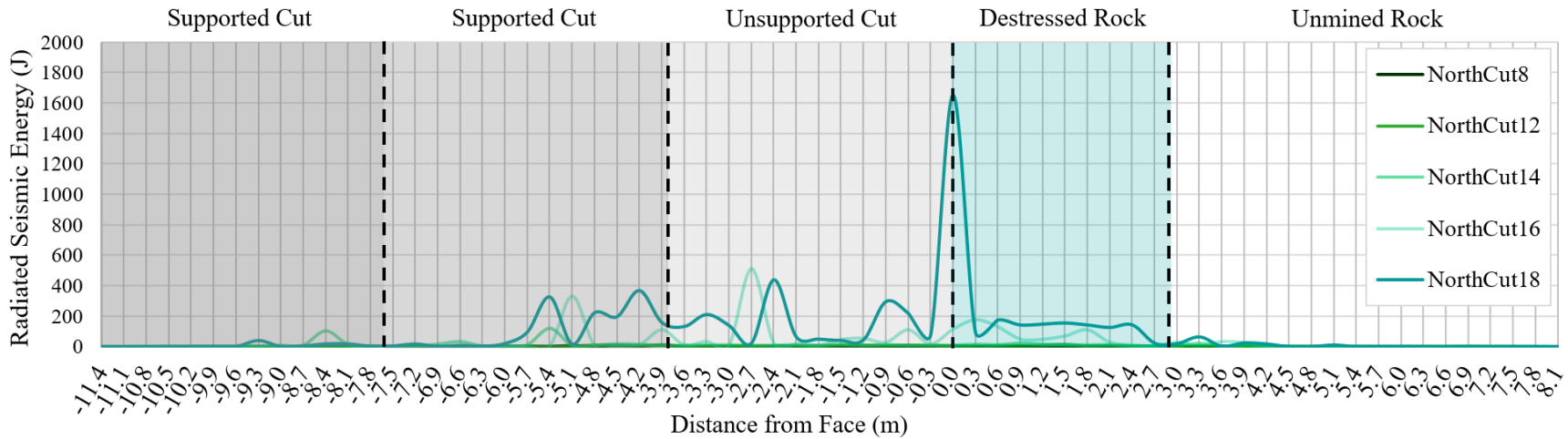


Figure 292 - Radiated seismic energy as a function of distance from the face for destressing blasts.

6.2.5.3 Inelastic Deformation

The third parameter examined in the spatial analysis was the *seismic potency*. Charts of the total potency recorded within each spatial filter, during each development cycle, are presented in the following figures. The plots for conventional and destressing development are shown in Figure 293 and Figure 294, respectively.

The potency data relating to the conventional development indicated that co-seismic rock mass damage was low around the supported ground, increasing and occasionally high adjacent the unsupported cut and consistently elevated ahead of the face. The damage was most intense for the first +3.0m ahead of the tunnel. There were also several peaks in the recorded damage as far as +4.5m ahead of the face, for example during Cut 15. The most intense level of inelastic deformation recorded in any 0.3m spatial filter increment of the conventional tunnel was 0.0064m³. This figure does not reflect the volume of unstable rock loading the ground support.

The potency results for the destressing excavation were variable. In three of the five development cycles (Cuts 8, 12 & 14), the recorded potency was close to zero over the entire spatial analysis, and especially low in comparison to conventional blasting ahead of the face. This further supported the conclusion that destressing reduced the damage potential in this zone. However, in the other two destressing development cycles (Cut 16 & 18), the recorded potency was generally higher adjacent the supported ground than that which was observed for the conventional development. This included a relatively high potency value within the 0.0m filter, indicating damage at the face. The wide variation in the potency trends between the first three and final two destressing cuts was most likely indicative of variable rock mass conditions. The exact cause was not clear. An elevated structural response during the final two destressing cycles cuts may have contributed.

Overall, less co-seismic damage was recorded adjacent the destressing tunnels. The data indicated that destressing frequently reduced the rock mass damage, especially ahead of the face, which was mostly unsupported and had the highest instability risk. However, when examined on a cycle-by-cycle basis, destressing often resulted in elevated co-seismic inelastic damage adjacent the other excavation surfaces. Increased damage in those cases may have been associated with the general reduction in rock mass stiffness caused by destressing and consequently greater rock mass deformations.

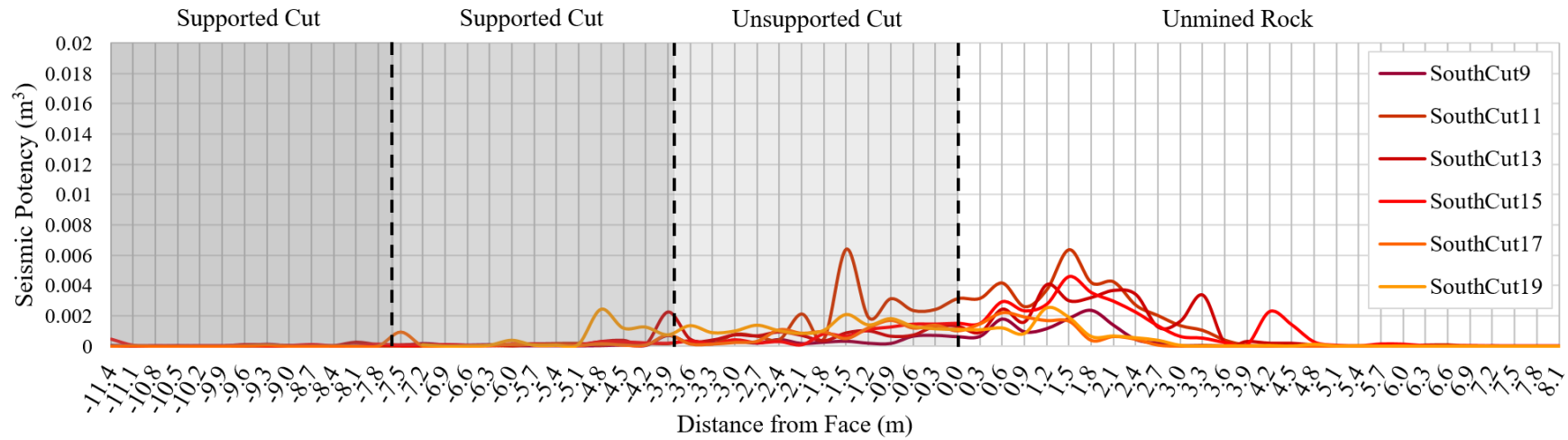


Figure 293 - Inelastic deformation (seismic potency) as a function of distance from the face for conventional blasts.

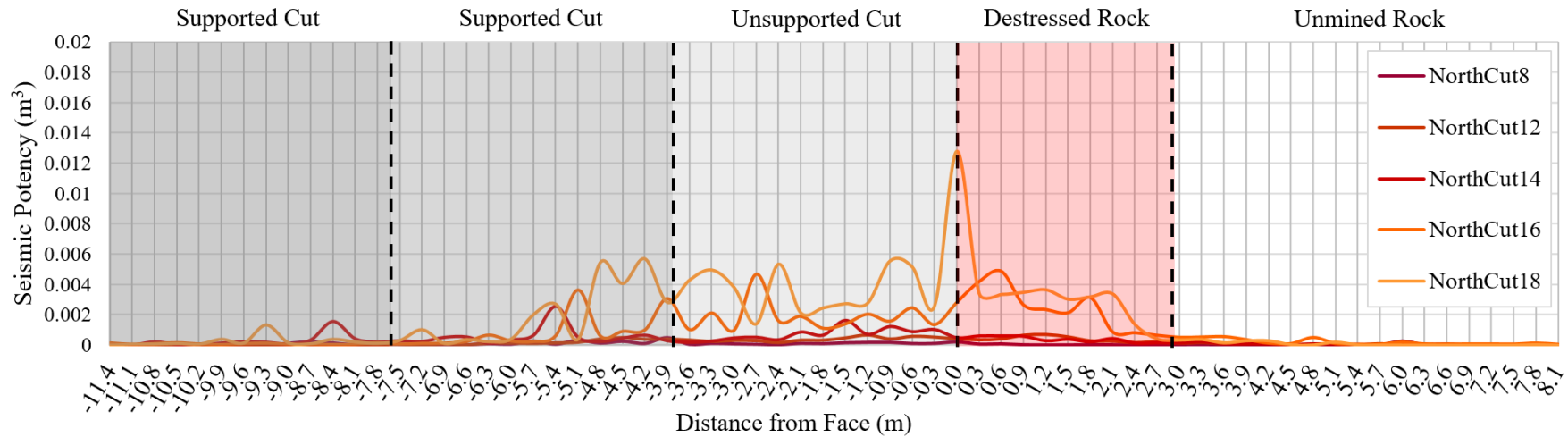


Figure 294 - Inelastic deformation (seismic potency) as a function of distance from the face for destressing blasts

6.2.6 Source Mechanism Solutions

Analysis of the seismic source mechanisms was intended to investigate five main questions, including:

1. Was the majority of the instability associated with natural or blast induced fractures?
2. Which of the natural joint sets were activated by induced stress during development, if any?
3. Which of the principal stresses were controlling structural instability?
4. Were there any significant differences in the failure mechanisms between the conventional and destressing development?
5. Did any of the recorded fault plane solutions indicate the successful creation of blast-induced sub-horizontal fracture planes co-aligned with the rows of destressing charges?

Source mechanism solutions were obtained for 170 seismic events within the database. The location of all events with solutions are shown as beachballs in Figure 295. Most events with solutions were located within the final 15m of development. The number of solutions was relatively evenly split between both tunnels, with 92 in the south and 78 in the northern tunnel. The even distribution of solutions between each tunnel provided a sufficient population of data for comparison of the mechanism response to both conventional and destress blasting. The mechanism solutions provided useful information concerning the mechanical characteristics of the associated seismic events. Information derived from the solutions included the mechanism of rupture, the two nodal plane orientations which represent the two possible orientations of the fault plane that was activated during the event, as well as the principal strain axes of the moment tensor.

The *P-axis*, *T-axis* and *B-axis* of the moment tensor may be regarded as proxies for the major, minor and intermediate principal stress orientations acting at the source. This assumes that the rock mass was originally isotropic and unfaulted prior to stress-driven failure (Frohlich & Apperson, 1992). This was not the case in this experiment. However, this assumption is regularly made in seismological investigations, as the P, T and B axes provide the best available information regarding the stress field orientation (Scholz, 1990).

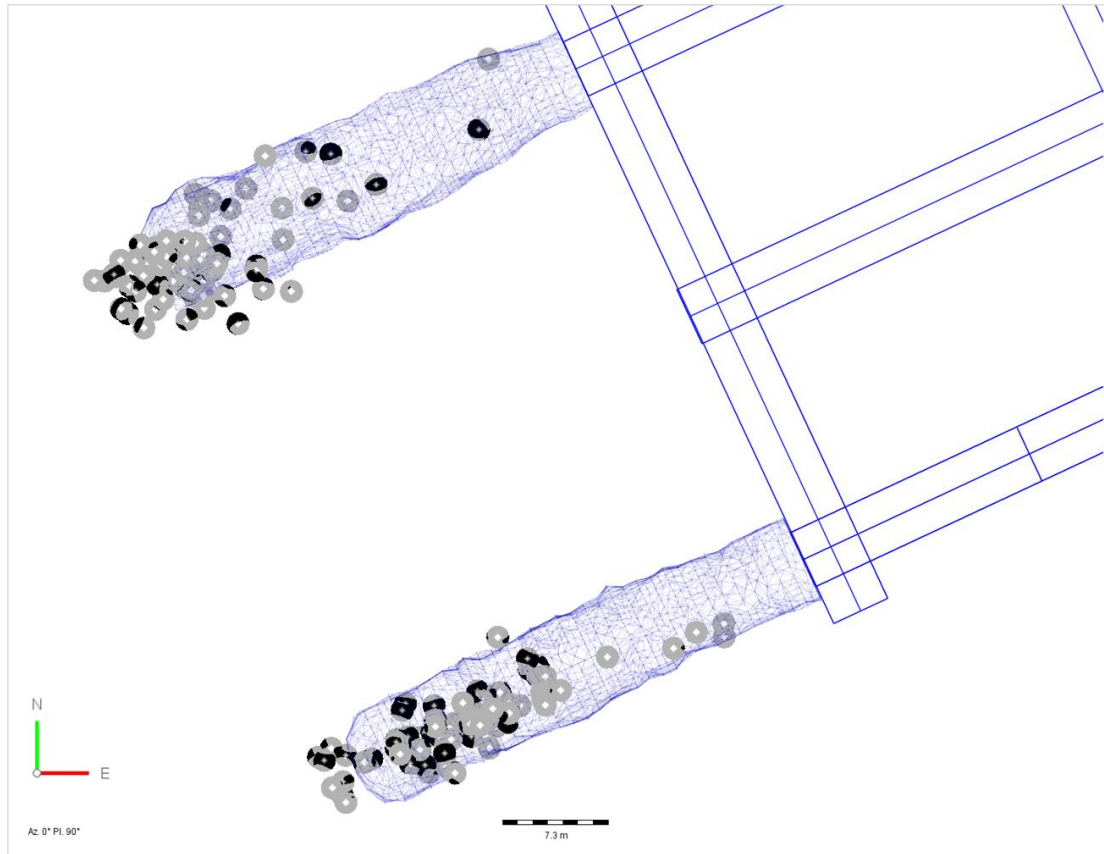


Figure 295 - Locations of seismic events with mechanism solutions marked by beachball spheres.

The measured principal stress orientations (Figure 296a) showed good agreement with the principal strain axes derived from the source mechanism solutions around the southern tunnel (Figure 296b), although the T and B axes were reversed with respect to σ_3 and σ_2 . The measured stress orientations also showed good agreement with the P-axis of mechanism solutions from the north tunnel. However, the T and B axes showed greater dispersion (Figure 296c). This was attributed to the wider variety of failure mechanisms that occurred in the rock mass surrounding the destressing tunnel.

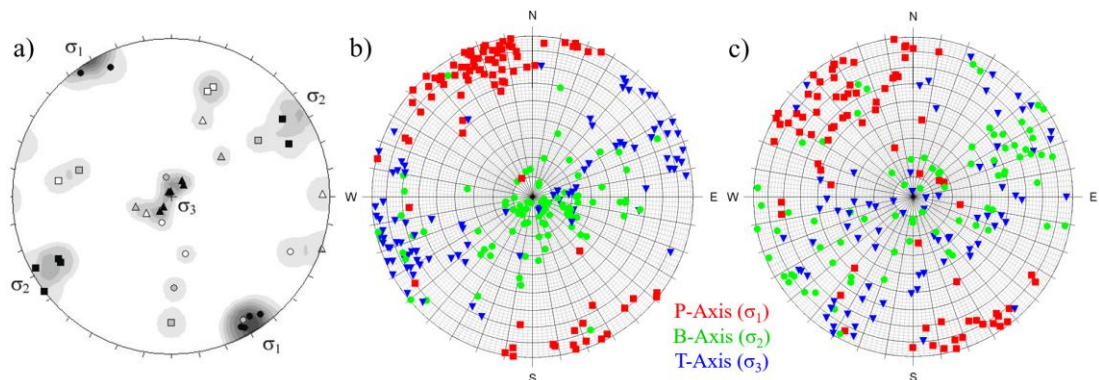


Figure 296 - a) measured stresses (Windsor, et al., 2006), b) strain axes in the south tunnel and c) north.

In order to investigate whether the natural structural features of the rock mass became unstable during development, the dip and dip direction of the nodal planes of the source mechanism solutions were examined in SAFEX. The data for each of the two sets of nodal planes were analysed separately. The nodal plane poles and fisher contours are shown in Figure 297. It was assumed that no statistically significant set of new structures were created during the construction of the tunnel. It was appreciated that some blast-induced fractures would likely have been created. However, given the complex pre-existing natural jointing, it was assumed that the blasting fractures did not form a significant population in the nodal plane data. According to this assumption, the majority of valid nodal planes represented natural joints mobilised by induced stress changes.

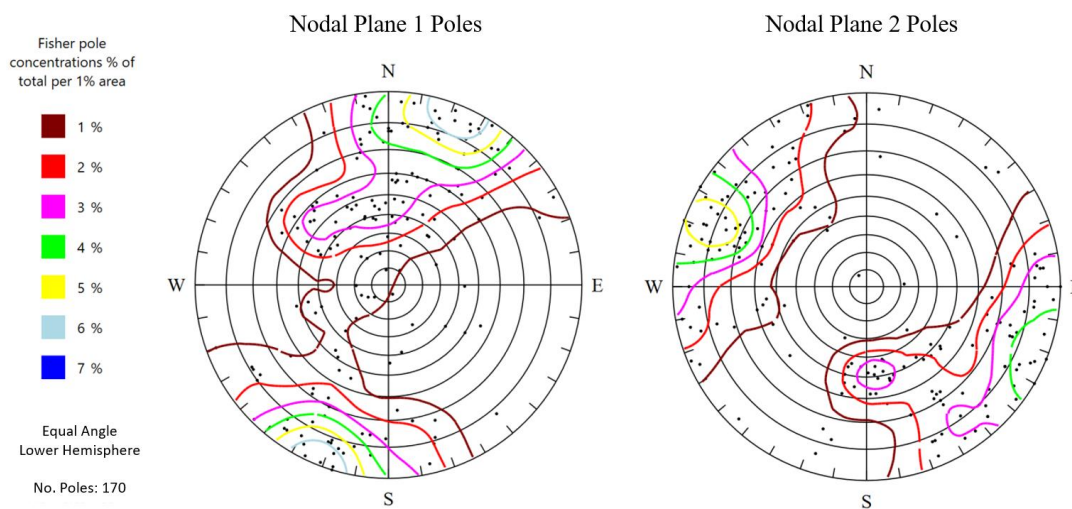


Figure 297 - Nodal plane sets 1 and 2 poles, with fisher pole contours, plotted in SAFEX.

As the nodal planes were assumed to represent natural joints, the joint set boundaries defined during the original structural analysis (Figure 105b) were applied to the two nodal plane sets, as shown in Figure 298. The possible joint set characteristics were then inferred from the two nodal plane sets and compared to the joint sets calculated from the face mapping (Table 52). The basic joint set properties inferred from the nodal plane set 1 and set 2 data are presented in Table 53 and Table 54, respectively. Nodal plane data was deemed valid if it closely matched the mapped joint sets. The set data deemed to be valid is underlined in the tables. The nodal plane data indicated that there were strong groupings of valid fault plane solutions in all four joint sets. The most common failure plane was identified as joint set #2, with 75 observations in the *Nodal Plane 2* data. Set #2 was the sub-vertical face-forming set.

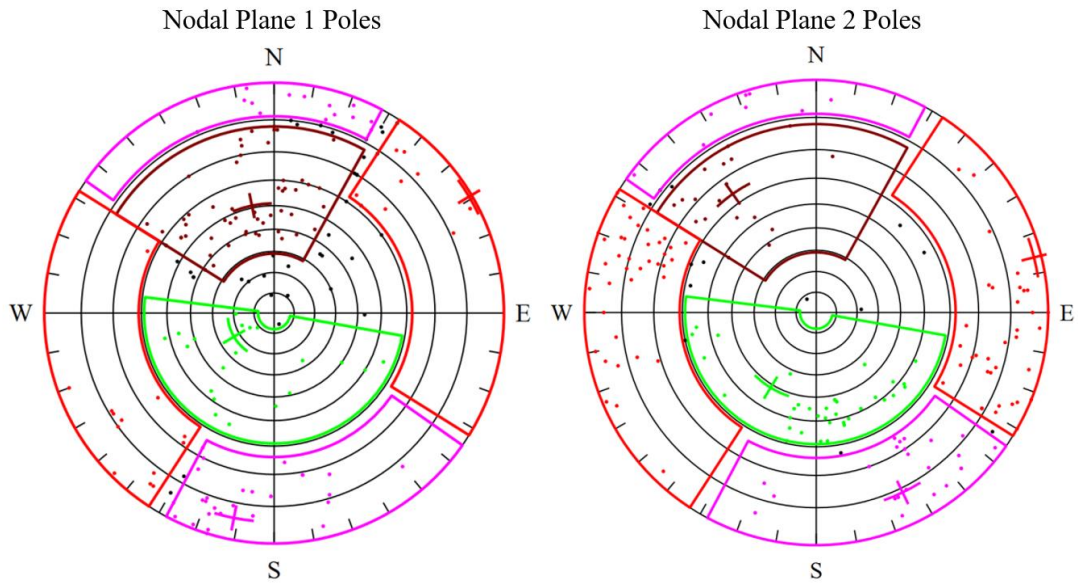


Figure 298 - Joint set boundary assumptions applied to the nodal plane data.

Table 52 - Joint set basic parameters measured from structural face mapping.

Joint Set		Weighted			
Number	Total Joints	Plane Orientation	Normal Orientation	Fisher Constant	Vector Magnitude
1	50	54/161	36/341	32.4	48.5
2	110	78/072	12/252	22.1	105.1
3	63	83/349	07/169	16.3	59.2
4	42	33/053	58/233	17.7	39.7
Residuals					15

Table 53 – Parameters of potential joints inferred from nodal plane set 1.

Joint Set		Weighted			
Number	Total Joints	Plane Orientation	Normal Orientation	Fisher Constant	Vector Magnitude
<u>1</u>	<u>51</u>	<u>51/168</u>	<u>39/348</u>	<u>13.2</u>	<u>47.2</u>
2	21	89/239	01/059	24.8	20.2
3	40	84/011	06/191	20.4	38.1
<u>4</u>	<u>21</u>	<u>23/060</u>	<u>67/240</u>	<u>18.2</u>	<u>19.9</u>
Residuals					39

Table 54 - Parameters of potential joints inferred from nodal plane set 2.

Joint Set		Weighted			
Number	Total Joints	Plane Orientation	Normal Orientation	Fisher Constant	Vector Magnitude
1	17	64/145	26/325	18.6	16.1
<u>2</u>	<u>75</u>	<u>88/256</u>	<u>02/076</u>	<u>15.9</u>	<u>70.3</u>
<u>3</u>	<u>31</u>	<u>81/334</u>	<u>09/154</u>	<u>13.9</u>	<u>28.8</u>
4	35	41/031	49/211	5.9	29.3
Residuals					14

There were some differences between the average set orientation of the mapped joints and those inferred from the nodal planes. However, the difference was less than the typical orientation dispersion in the mapped sets. The largest difference in average dip direction was observed in Set #3. The difference of 15⁰ between the mapping data and average nodal plane is typical of natural orientation dispersion within a joint set.

It was also noted that a large portion of the seismic source mechanism solutions had no clear auxiliary nodal plane. That is, a large percentage of the seismic event mechanisms had nodal planes which both matched the orientation of a known joint set. When comparing the nodal plane data adjacent each tunnel to the joint set boundaries defined in Figure 298, it was determined that both nodal planes matched known joint sets in 63% of the mechanism solutions in the south tunnel and 65% in the north. In those instances, it was not possible to conclusively determine which nodal plane was the valid joint and which was the auxiliary plane. Therefore, there was some uncertainty regarding which joint set was in fact activated during the seismic event.

For the majority of the remaining mechanism solutions, only one of the nodal planes aligned with a known joint set, and hence a conclusive determination of the failure mode could be made. For a very small minority, neither of the nodal planes matched a known joint set orientation. In those instances, the event was assumed to be caused by shear failure of intact rock or an unclassified discontinuity. The number of events with a conclusive failure mode was quantified for each tunnel. A bar chart indicating the number of unique nodal plane solutions for each joint set is shown in Figure 299.

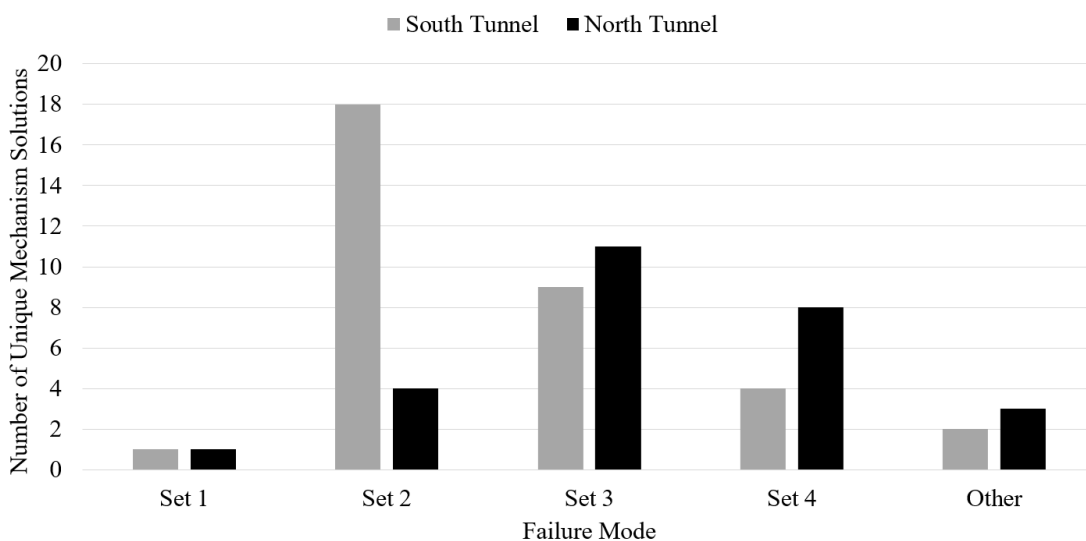


Figure 299 - Number of unique fault plane solutions in each tunnel.

These results confirmed that all of the four known joint sets were mobilised in each tunnel due to induced stress changes on the tunnel boundary (Figure 300). In the south tunnel the largest number of unique mechanism solutions involved rupture of the face-forming joints in Set #2. This was consistent with strike-slip on this set, the orientation of which was almost perfectly parallel to the major principal stress. Joint sets #3 and #4 were the second and third most frequent rupture orientation, respectively. The unclassified failure planes assumed to be shear of intact rock or shear along unique joints were the next most frequent rupture orientation. The least number of events involved rupture of Set #1. In the northern tunnel with face destressing the dominant response of Set #2 was not repeated. The most reactive joint set was instead Set #3, followed closely by Set #4, then Set #2. Set #1 appeared to be mobilised infrequently in comparison.

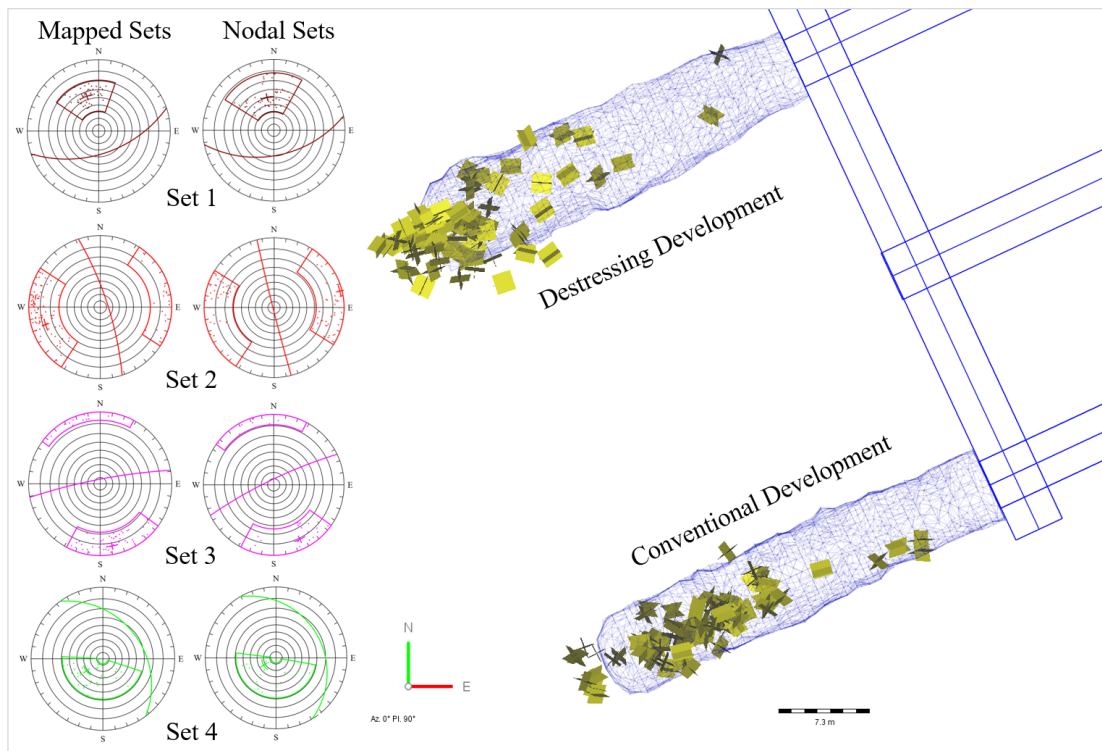


Figure 300 - Plan view of mapped and inferred joint sets compared to nodal planes.

The plan view of the P-axis of all recorded event mechanisms is presented in Figure 301. This figure reveals that the vast majority of the P-axis solutions in the southern tunnel were aligned in an approximately north-south orientation, with a slight rotation towards the northwest. By contrast, in the destressing tunnel the P-axes indicated a significant alignment of the P-axis north-south, but also in several other orientations, including east-west, northwest-southeast and northeast-southwest.

Furthermore, when viewed in cross section, the overwhelming majority of P-axis solutions in the southern tunnel were sub-horizontal (Figure 302). A small number of events below the excavation and at the vertices between the sidewall and floor demonstrated some rotation in the major principal strain axis. This was likely due to highly localised rotations of the induced stress field due to the excavation geometry. There was one solution with a vertical P-axis visible in the south tunnel. In contrast, the P-axes in the northern tunnel varied substantially in orientation, frequently ranging from sub-horizontal, through moderately steeply dipping to almost vertical across multiple orientations (Figure 303).

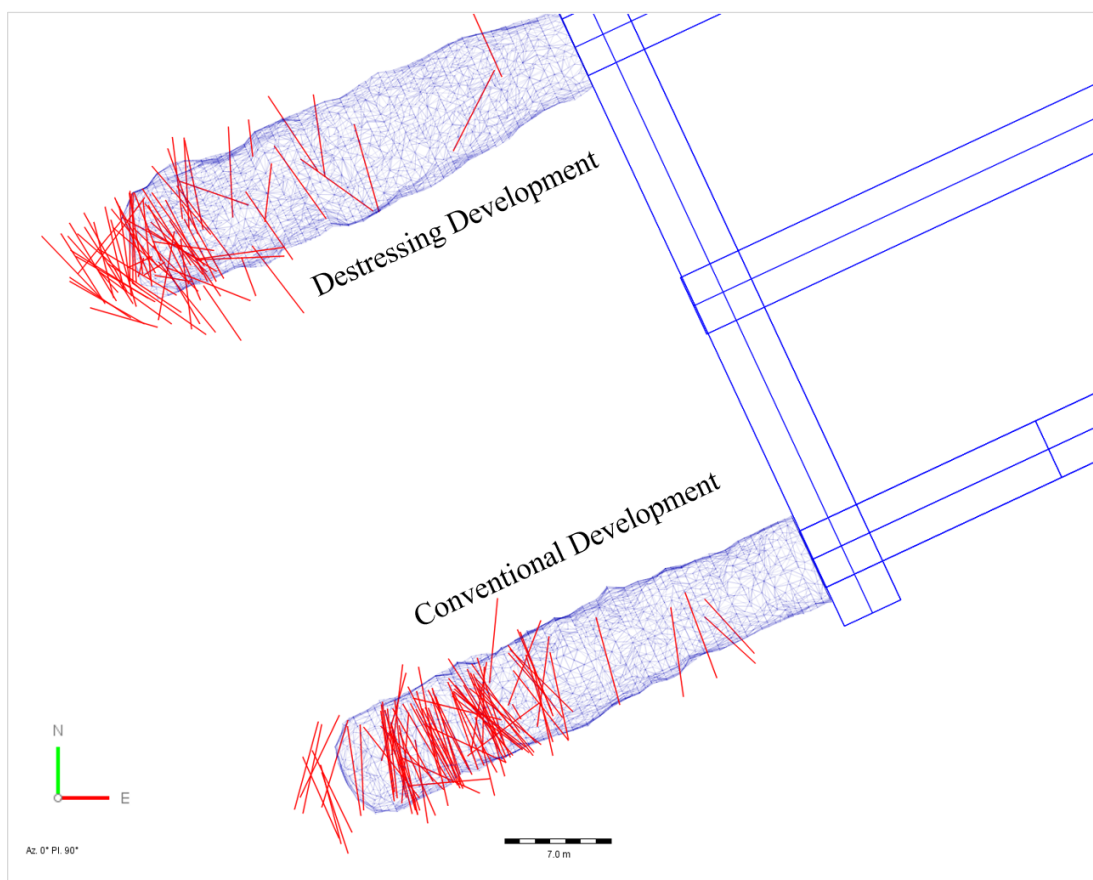


Figure 301 - Plan view of P-axis orientation for all source mechanisms solutions.

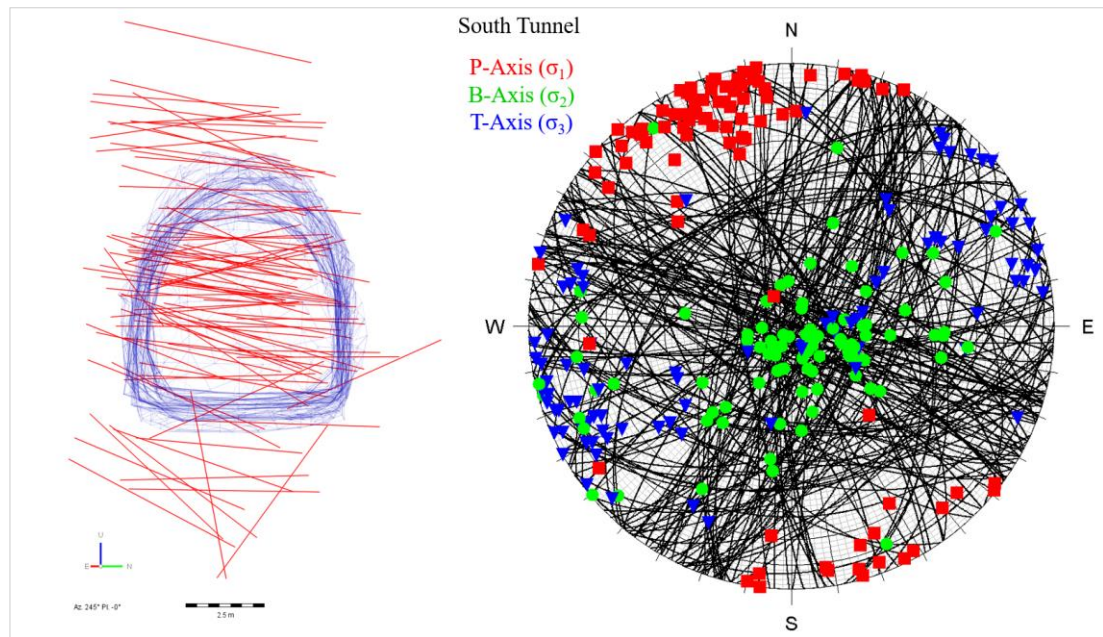


Figure 302 – South tunnel P-Axis orientations and the stereonet of nodal planes and principal strain axes.

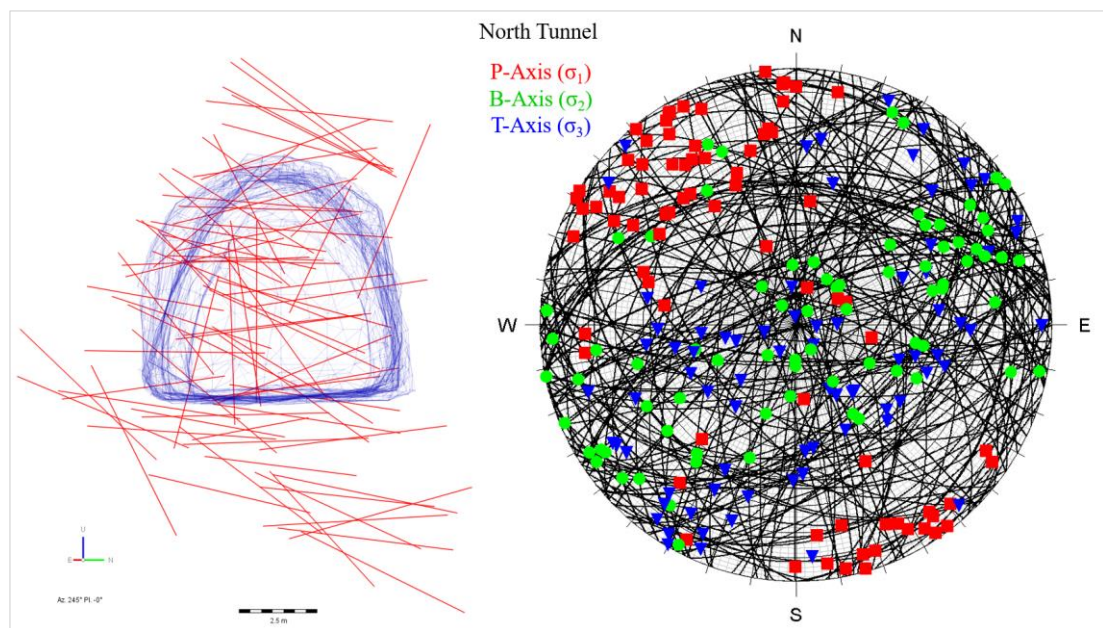


Figure 303 - North tunnel P-Axis orientations and the stereonet of nodal planes and principal strain axes.

The data from the southern tunnel indicated that the majority of failure mechanisms were controlled by the sub-horizontal major principal stress and joint set #2. Whereas in the northern tunnel the discontinuities were mobilised in a far wider variety of orientations. This implied that failure was influenced by both sub-horizontal (tectonic) and sub-vertical (lithostatic) components of stress. This observation was a significant point of difference between the destressing and conventionally blasted tunnel. In this case the destress blasting appeared to weaken all the joint sets ahead of the face, such that the minor principal stress was sufficient to induced instability in some cases.

The source mechanisms in the southern tunnel were significantly less diverse than those in the northern tunnel where destressing was implemented. The dispersion of the different modes of failure in each tunnel is illustrated in the ternary mechanism diagrams below. Figure 304 presents the diagram for the southern tunnel. Figure 305 presents the failure mechanisms in the north. The most frequent failure mechanism in the southern tunnel was determined to be strike-slip rupture of the face forming joints. That is, strike-slip of joint set #2, which was approximately north-south striking with very steep dip. This failure mechanism was indicated by the dense grouping of mechanisms in the upper vertex of the ternary diagram. This was consistent with the sub-horizontal stress controlling failure.

The strike of Set #2 was sub-parallel to the face and consistent with a large number of the nodal plane solutions. The majority of the P-axes calculated for the southern tunnel were consistent with the orientation of the major principal stress measured nearby using WASM AE and CSIRO HI Cell, which were also ideally oriented to cause strike slip behaviour on this joint set. The ternary diagram for the southern tunnel also indicated that there was some distribution of failure mechanisms consisting of oblique reverse and reverse joint rupture. These mechanisms were likely to have been associated with rupture of discontinuities in sets other than set #2. There was also one observation of vertical dip slip and another of normal rupture, but these mechanisms were a small percentage of the total population.

In contrast to conventional development, the face destressing excavation experienced a much broader dispersion of failure mechanisms. As indicated by the ternary mechanism diagram (Figure 305), the destressed tunnel generated a much larger population of reverse, oblique reverse and vertical dip-slip style rupture events, in addition to strike slip sources. There were also a number of events with normal and oblique normal source characteristics. The much larger population of events with sub-vertical and moderately inclined deformation mechanics around the northern tunnel indicated that destress blasting damaged the joint sets to the point whereby the minor principal stress also became an important control on stability. This consequence of destressing is suggested to be favourable one. Joint weakening to facilitate a greater diversity of failure modes effectively reduces the rock mass strength. This in turn reduces the likelihood of high strain energy accumulation, which might culminate in a single large instability causing ground support damage.

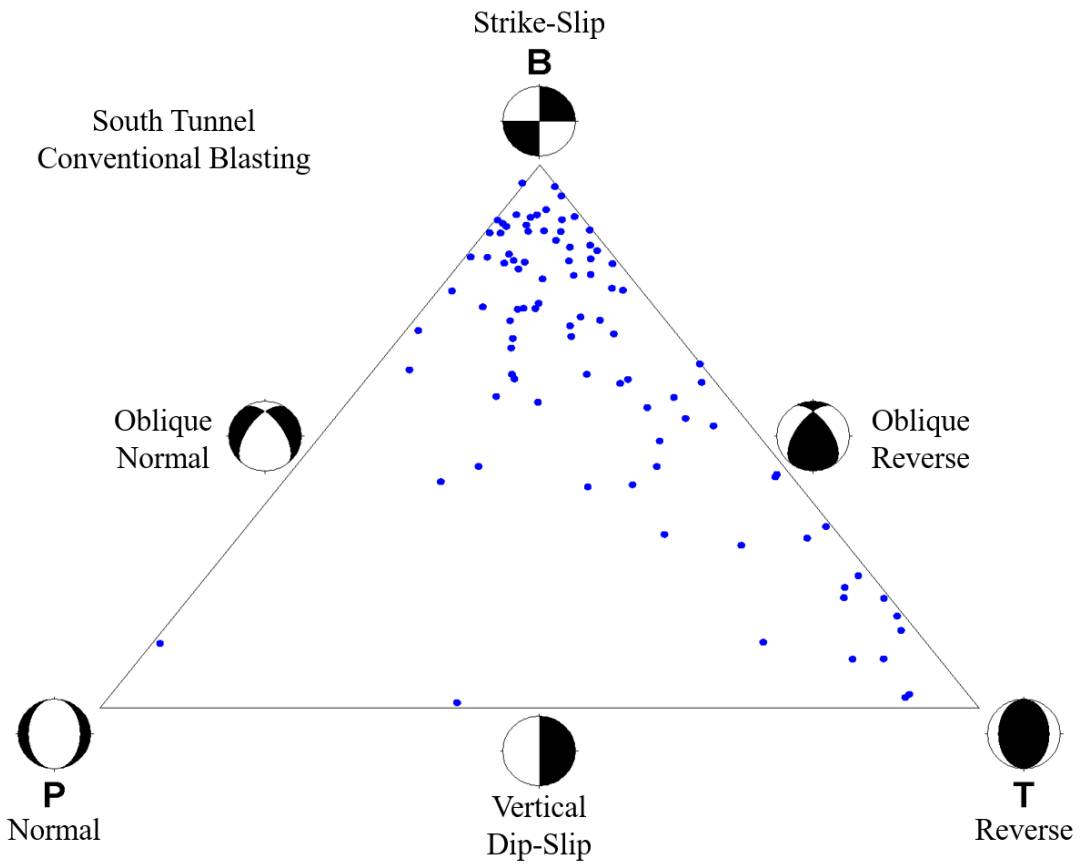


Figure 304 - Ternary diagram of seismic source mechanisms adjacent conventional tunnel development.

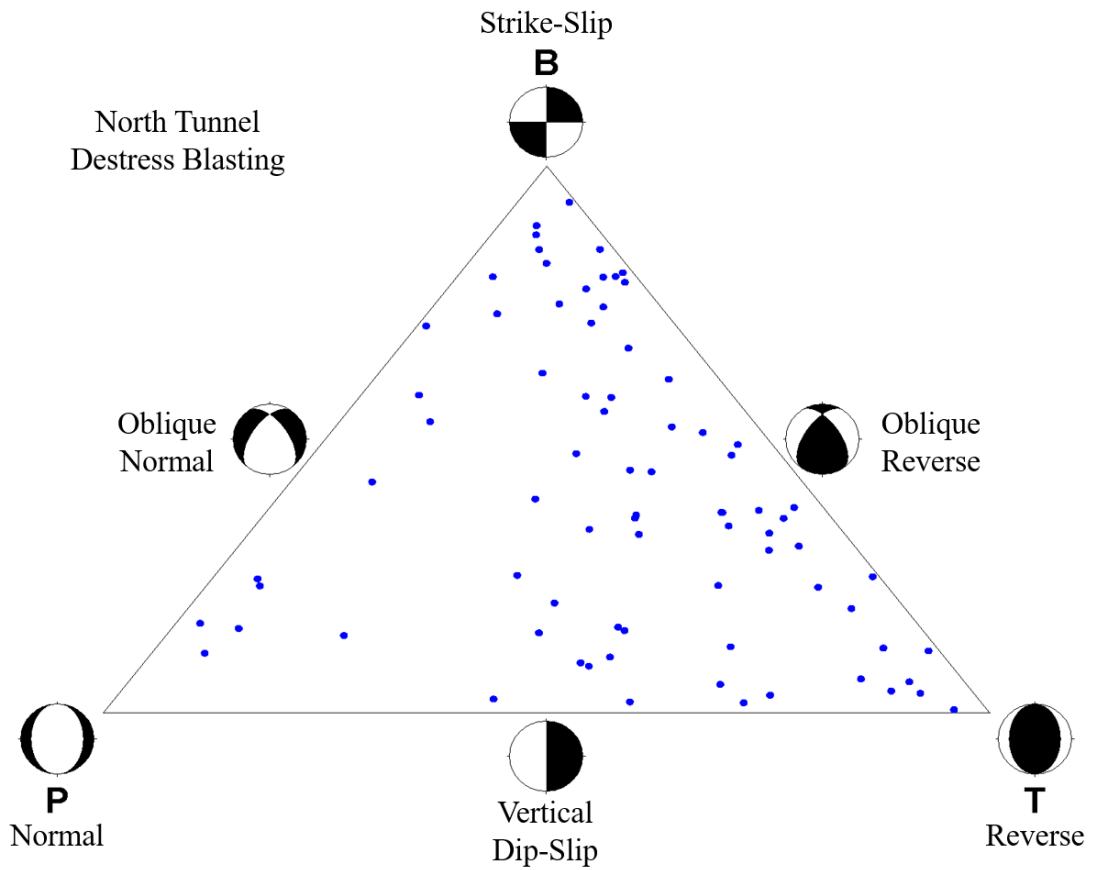


Figure 305 - Ternary diagram of seismic source mechanisms adjacent destressed tunnel development.

In order to further investigate the mechanism of the events, the data from both the south and northern tunnel were plotted separately on Hudson source-type diagrams. The Hudson diagram is a graphical representation of the seismic source based on two plotted parameters, T and k , which represent the relative proportion of constant-volume (i.e. shear) and volume-change (i.e. dilation/contraction) of the source (Hudson, et al., 1989). The diagram takes the form of a rhombic-shaped two-dimensional grid, with T and k plotting on the horizontal and vertical axes, respectively. Purely explosive sources plot where $k=1$ and $T=0$. Purely implosive sources plot where $k=-1$ and $T=0$. Constant volume shear source mechanisms plot along the line $k=0$. For example, a simple double-couple source (i.e. unidirectional displacement along a single joint plane with no dilation) plots in the centre of the diagram where $T=k=0$.

The Hudson diagrams for the southern and northern tunnel mechanisms are presented in Figure 306 and Figure 307, respectively. The diagrams have been broadly divided into three sectors, separated by the dashed blue lines on the diagram. Events plotting within the upper region predominantly demonstrated explosive characteristics. Events in the central region had a high deviatoric nature, indicative of shear failure. Whereas events plotting in the lowest of the three regions had implosive source characteristics typical of compressive overstepping failure such as spalling.

The minority of event mechanisms plotted within the explosive region of the Hudson diagram, and all therein were located very close to the deviatoric boundary. There were a significant number of mechanisms in the south tunnel which plotted within the deviatoric region, confirming that there were many shear failure style ruptures adjacent the southern tunnel. This was consistent with strike slip behaviour of the face forming joints. In comparison, there were approximately three times fewer mechanisms with primarily deviatoric characteristics recorded adjacent the face-destressing tunnel. The majority of the mechanisms in both tunnels plotted within the implosive region of the Hudson diagram. This indicated that compressive overstepping and/or crack closure was the dominant failure mode in both tunnels. The primary difference in the data from each tunnel was that the destressing tunnel mechanisms grouped much nearer to crack closure than that of the south tunnel, and with considerably less dispersion on the Hudson plot. This indicated that the seismic source mechanisms were more clearly indicative of stress-driven fracture closure where destressing was applied. This was consistent with more intense destress blasting-induced damage to the joint sets.

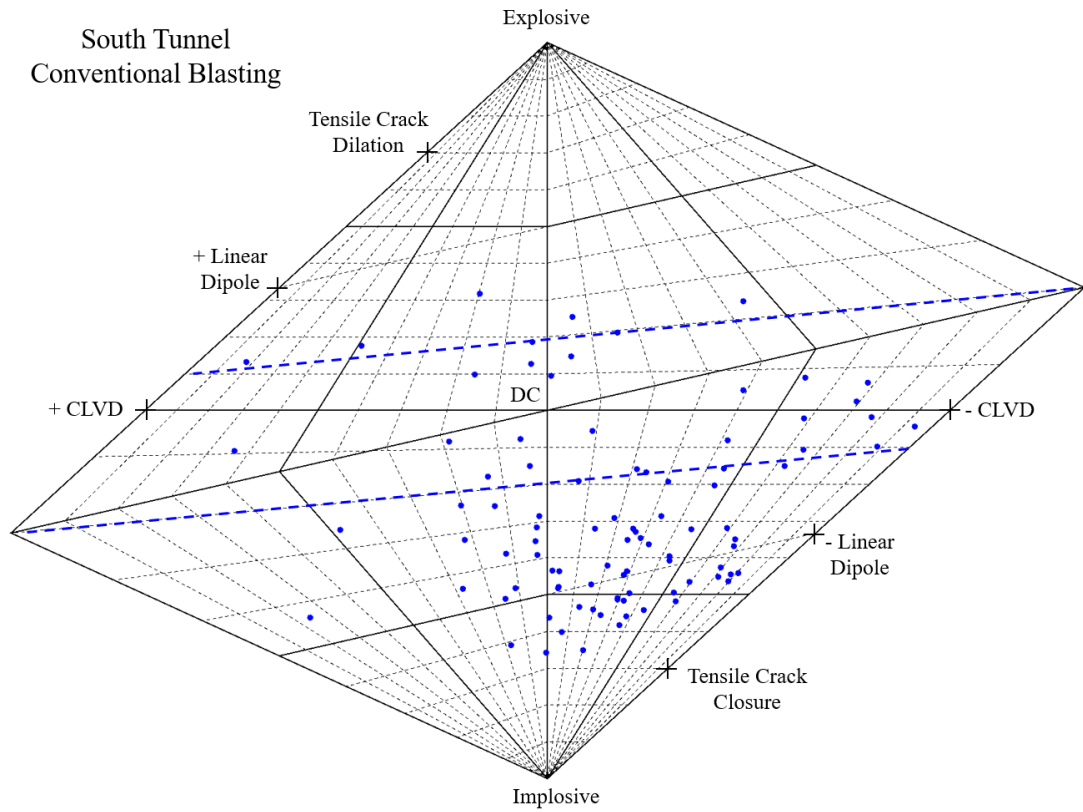


Figure 306 - Hudson diagram of seismic source mechanisms adjacent conventional development.

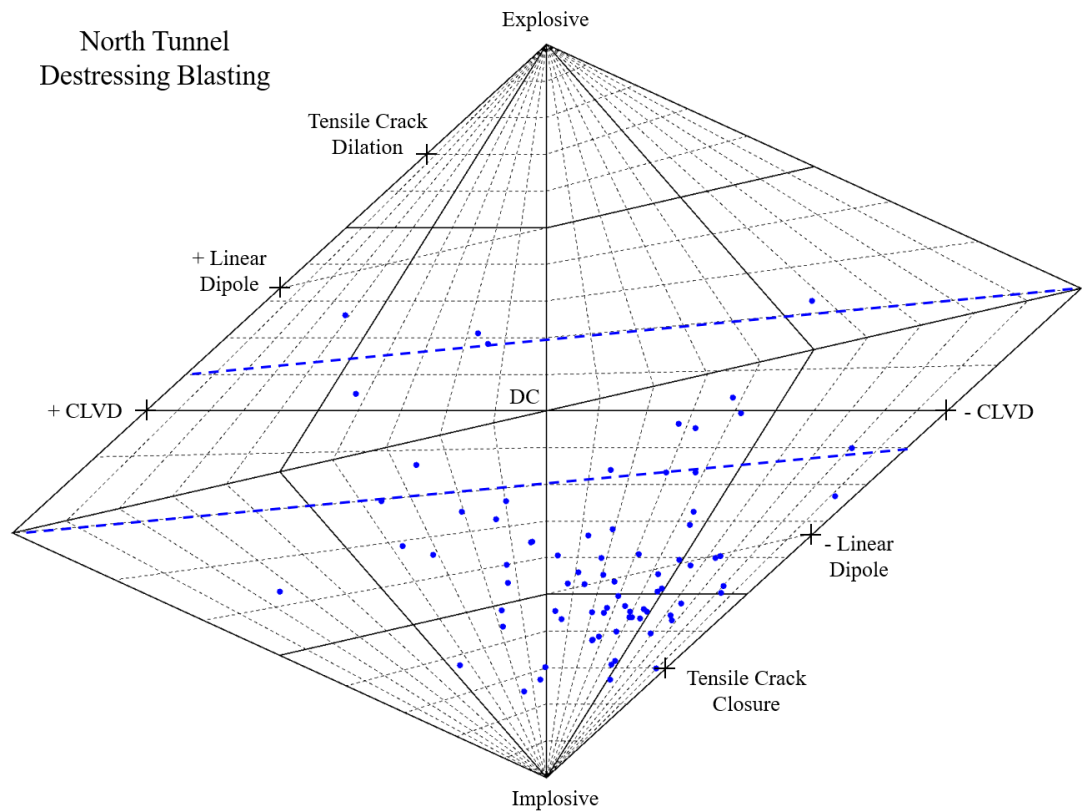


Figure 307 - Hudson diagram of seismic source mechanisms adjacent face destressing development.

One of the physical objectives of destress blasting, specifically *Destressing Design 2*, was to dilate natural fractures in joint set #1. A simultaneous and equally desirable goal was to create a series of blast-induced fracture planes on a similar orientation to this joint set. These fracture planes were intended to be created with an inclination of 30° to the horizontal, aligned with the inclination of the rows of destressing charges on each detonation delay (see Figure 146). As the destressing holes were drilled horizontally on the 245° tunnel azimuth, the destressing blast was intended to create up to four blast-induced fractures with an approximately 30/155 orientation (Figure 308). That is, blast-induced radial destressing fractures were desired to dip at 30° to the southeast, sub-parallel to joint set #1 and almost oblique to the major-principal stress. Assuming these fracture planes were successfully created, they were anticipated to assist energy dissipation from the rock mass via shear, with limited deformation. This was an intended destressing mechanism of the experimental blast design.

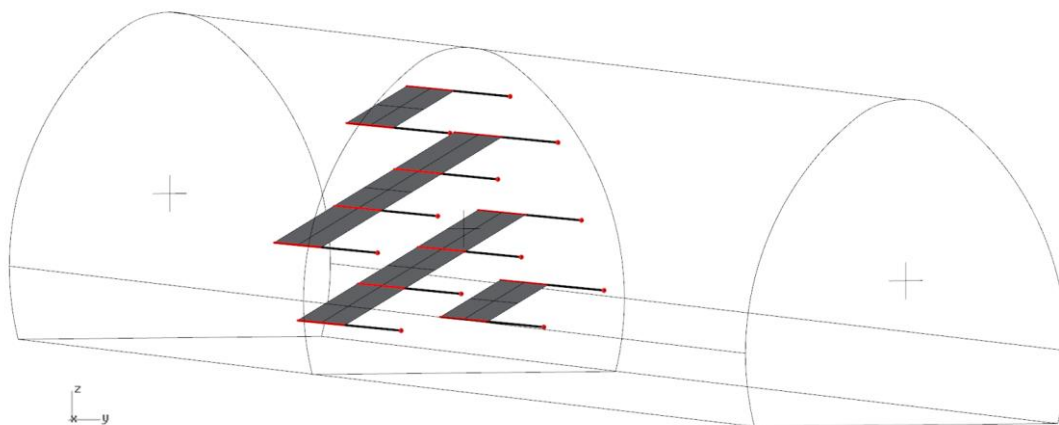


Figure 308 - Intended blast-induced fracture planes created by face destressing explosives.

In order to assess whether this destressing mechanism occurred in practice, the seismicity was analysed following each implementation cycle of the *Destressing Design 2* blast pattern in the northern tunnel (i.e. Cuts #12, 14, 16 & 18). *Destressing Design 1* was not investigated, as its charge pattern design was not optimised for such a shear failure mode of face destressing. For the relevant blasts, the collar position of the destressing boreholes were surveyed before and after drilling, providing a close approximation of the most likely trace of the blast-induced fractures. Seismic source mechanisms located within the destressing zone ahead of the face were then investigated in order to determine whether their nodal planes aligned with the expected radial fractures. The mechanisms compatible with the expected mode of destressing were noted during each development cycle and the nodal planes interpreted as follows.

A seismic event was assumed to have occurred on a natural fracture if the nodal planes aligned exclusively with any of the four pre-defined natural joint sets. A seismic event was assumed to have occurred either on a natural fracture dilated by destressing, or a blast-induced radial crack, if a nodal plane aligned closely to both Set #1 and the plane orientation formed by the destressing charges. A seismic event was assumed to have occurred on a blast-induced radial destressing fracture if neither of the nodal planes aligned with a predefined joint set and one nodal plane aligned closely to the plane of destressing charges. An event was assumed to have occurred due to stress-induced fracture of intact rock or slip of an unclassified joint if neither nodal planes aligned with the predefined joint sets or the plane formed by the rows of destressing charges.

The first cut to be examined was Cut #12. During this entire development cycle only three seismic events yielded accurate source mechanism solutions. A transverse and longitudinal section view of the tunnel geometry, destressing boreholes, the assumed destressing fracture plane and hypocentre locations of the three seismic events are presented in Figure 309. The event locations are illustrated by the two nodal plane solutions. In this case, a seismic event occurring 29 seconds after the blast had a nodal plane solution of 20/141. This nodal plane was consistent with the 30/155 assumed orientation of the destressing fractures, within a reasonable orientation error. This event is circled by the red dashed line in Figure 309. The location error of this event was approximately 0.6m, which may place it on either of the two rows of four destressing charges in the lower left side of the face.

The moment tensor decomposition of this event is presented in Figure 310. The event time after blasting and valid nodal plane orientation is also stated. It indicated that the event was characterised by a negative volume change (isotropic component 70.3%) consistent with closure of a previously dilated fracture. The negative compensated linear vector dipole (CLVD) component (27.4%) indicated a compressive clamping force acting on the failure plane at the time of the event. The nodal plane solutions and deviatoric component (2.3%) were consistent with reverse faulting across the failure plane. The Hudson diagram (Figure 311) indicated the source-type as being crack closure, where $T=0.92$ and $k=-0.70$ for the event. In summary, this event was consistent with the rapid stress-driven closure of a blast-dilated fracture, occurring 29 seconds after blasting, with high clamping force at the time of closure and downwards displacement of the fracture footwall with respect to the hangingwall.

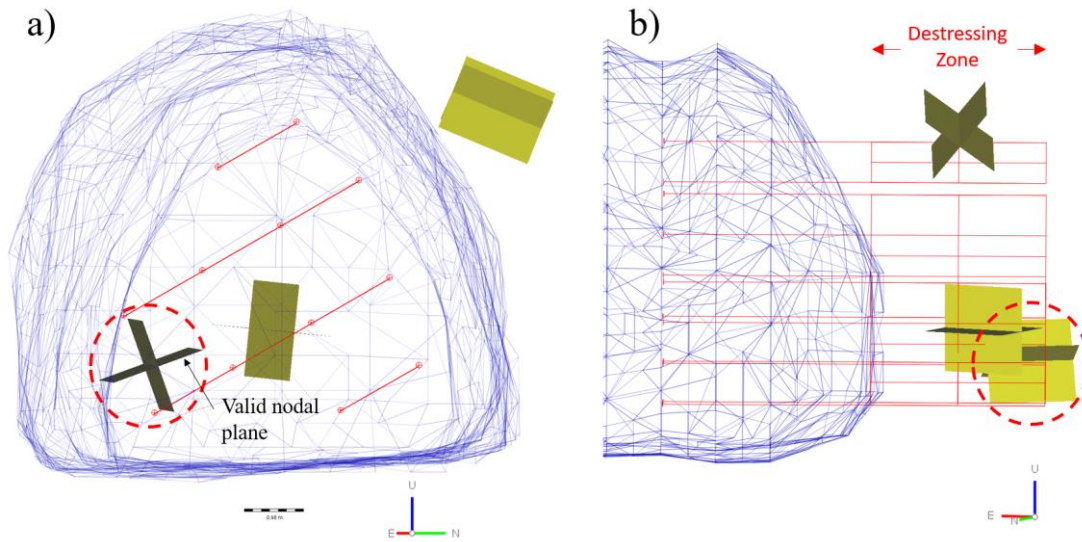


Figure 309 - a) Transverse and b) longitudinal section views of mechanism nodal planes during Cut #12.

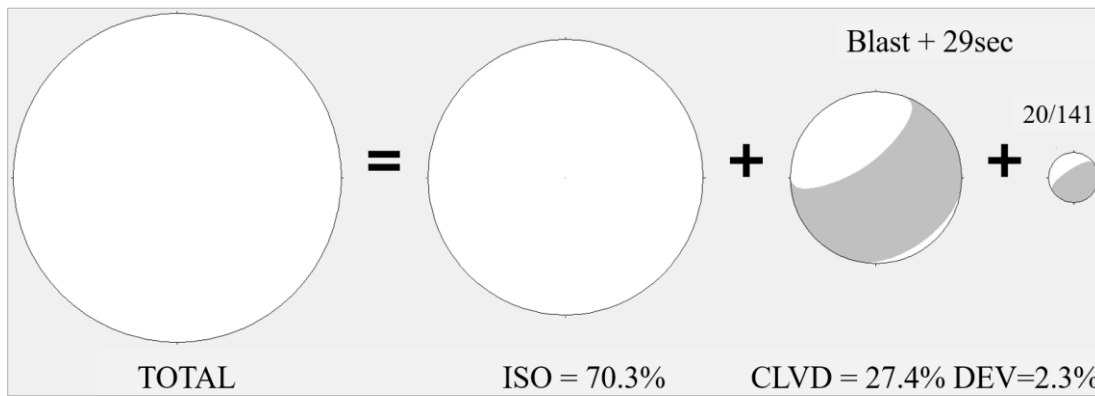


Figure 310 - Moment tensor decomposition from Cut #12 consistent with the destressing mechanism.

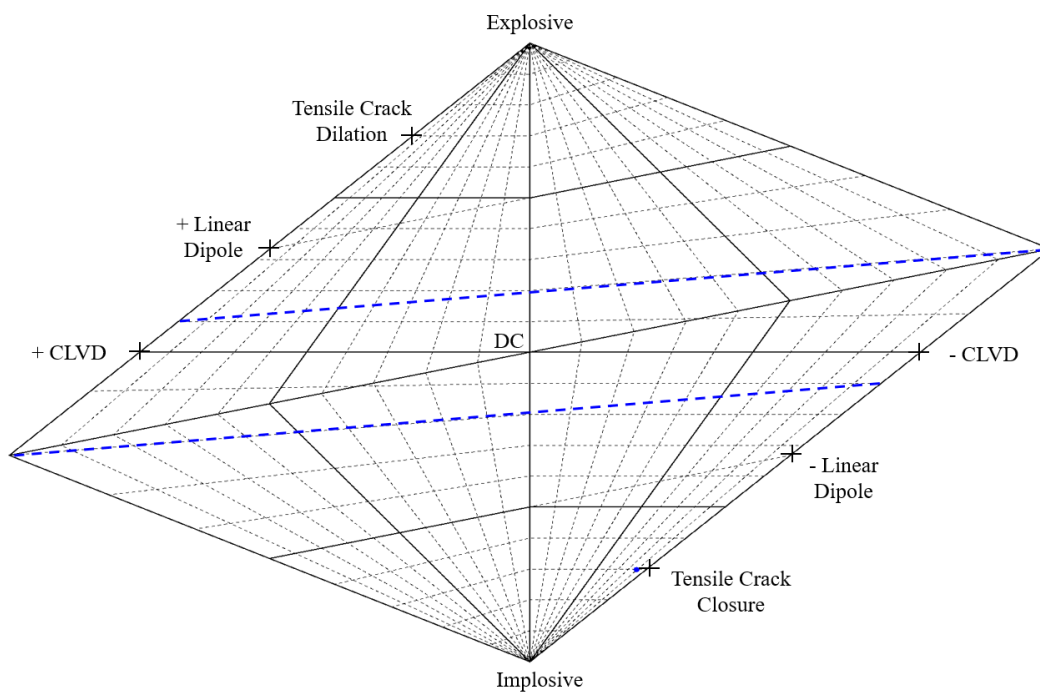


Figure 311 - Hudson source-type diagram for a destressing mechanism during Cut #12.

The second implementation of *Destressing Design 2* was during Cut #14. Of the 2972 seismic events recorded during this development cycle, only five were able to be processed with a reliable source mechanism solution. Of these five events, only one was located ahead of the face within the destressing zone. The other four were located below the excavation, as indicated in the transverse and longitudinal section views shown in Figure 312. The event within the zone of destressing did not have a source mechanism consistent with the anticipated failure mode, although this does not indicate that no such events occurred. It must be noted that the only known misfire of a destressing charge occurred during this blast, whereby one of the holes on delay #18 in the lower centre of the face was observed to have failed to initiate (Figure 313). This certainly reduced the likelihood of suitable rock fracturing during this blast.

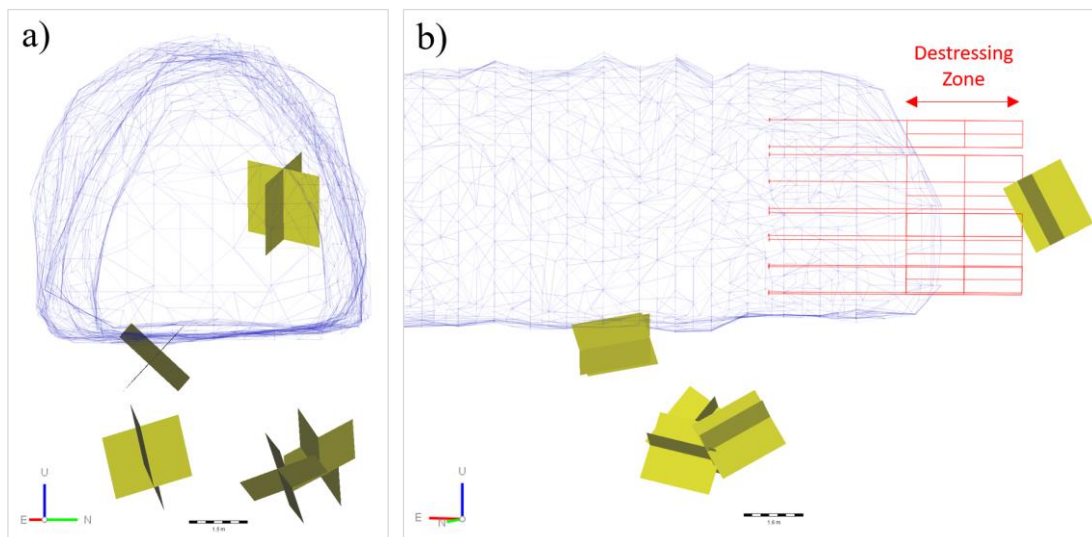


Figure 312 - a) Transverse and b) longitudinal section views of mechanism nodal planes during Cut #14.

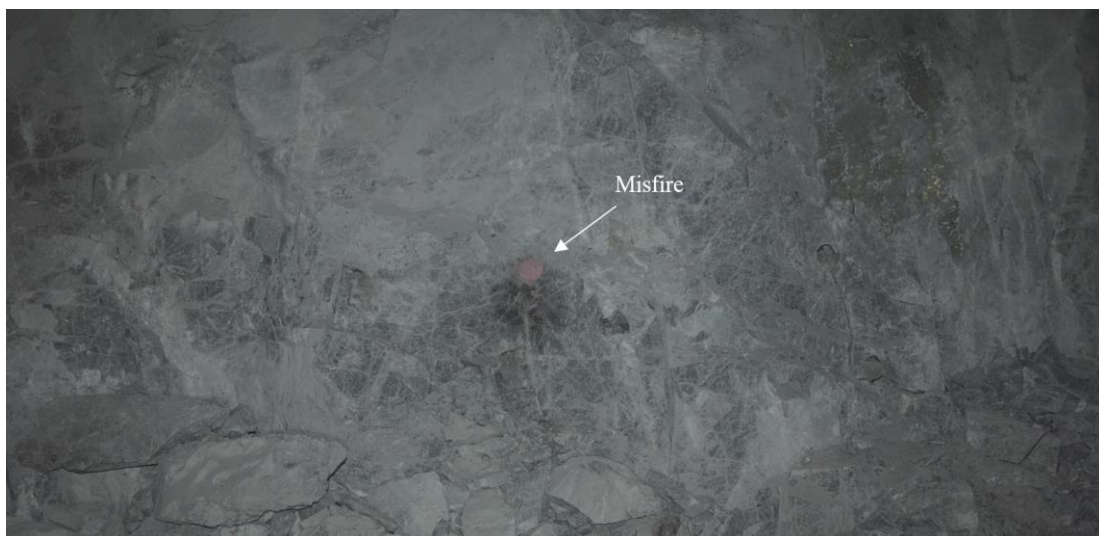


Figure 313 - Misfired destressing charge identified in Cut 14.

The next destressing development cycle in the north tunnel, Cut #16, yielded twenty-five events with source mechanism solutions, two of which were consistent with shear failure on a blast-induced crack. These two events occurred within 200ms of one another some 30 days after the previous blast during boring of the subsequent development round. In this instance the two events were located in the centre-left of the face, in between the two rows of four destressing charges. However, considering the location error of the seismic system, the actual hypocentres may have been coincident with either of the two planes formed along the adjacent rows of destressing charges. The lowest of the two events was the first to occur. The transverse and longitudinal section views of the events and tunnel geometry are shown in Figure 314.

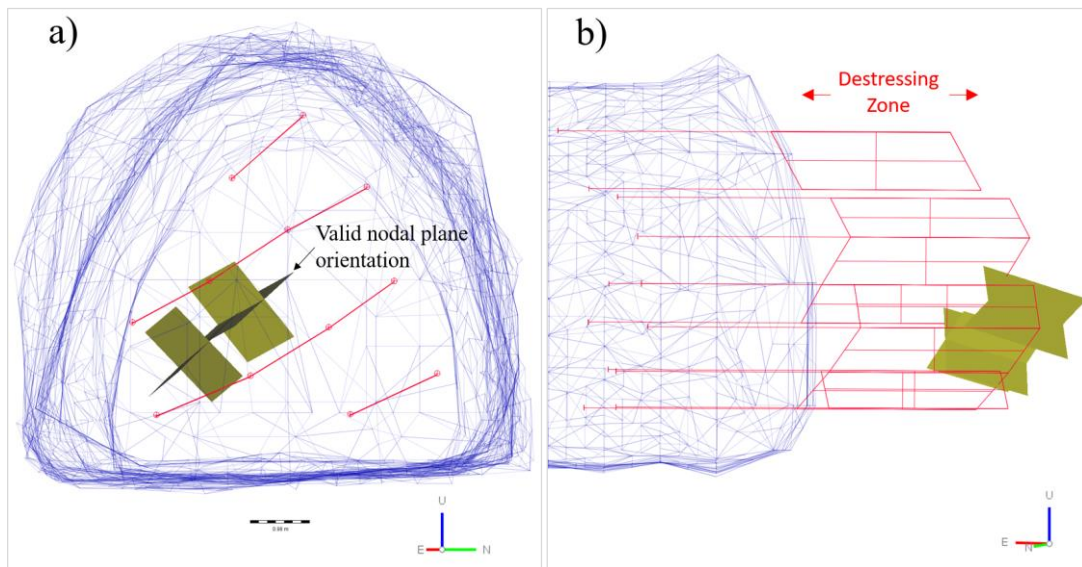


Figure 314 - a) Transverse and b) longitudinal section views of mechanism nodal planes after Cut #16.

The moment tensor decompositions for both events are presented in Figure 315. Both of these events yielded mechanism solutions with a strong implosive isotropic component, indicative of crack closure, and deviatoric component typical of normal faulting. This indicated that the hangingwall of the destressing fracture plane was deformed downwards relative to the footwall side. This mechanism was in contrast to the reverse faulting instability on the same orientation observed in the source mechanism of the Cut #12 event described earlier. The similarity in the isotropic characteristics of these two events were confirmed by the Hudson source-type plot (Figure 316). When contrasted to the reverse faulting destressing mechanism identified from Cut #12, these two events in Cut #16 illustrated that a variety of rupture mechanics could take place.

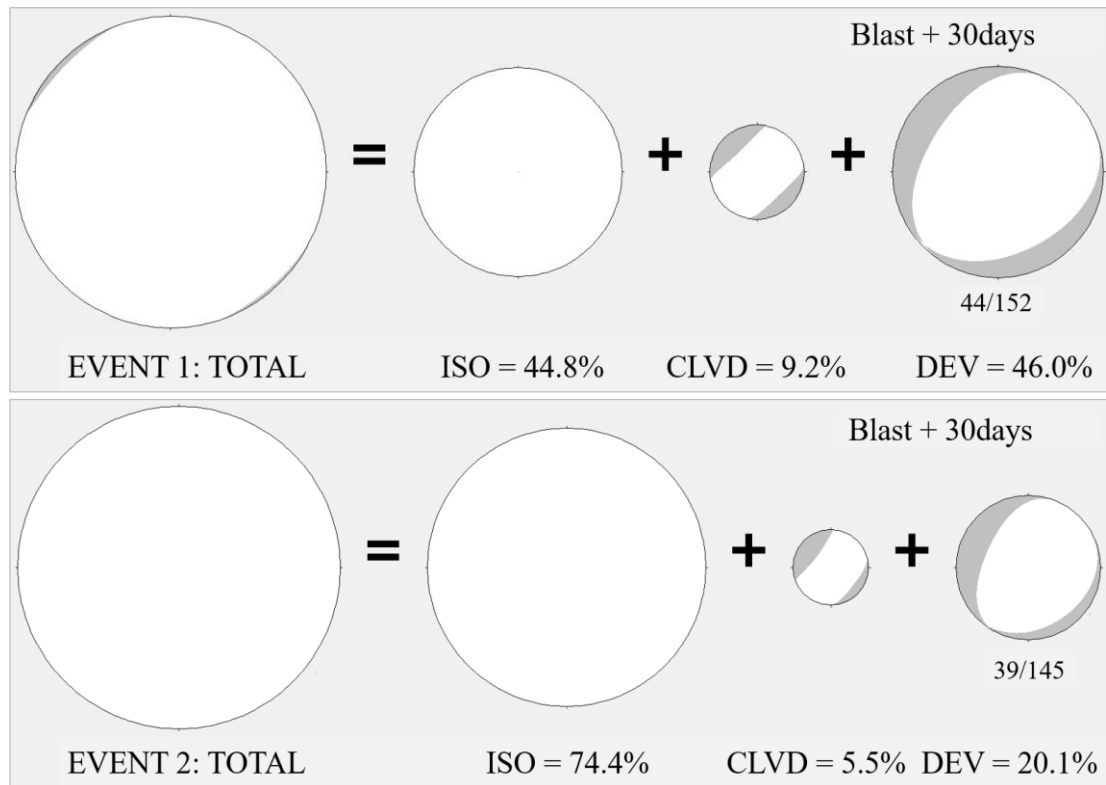


Figure 315 - Moment tensor decompositions from Cut #16 consistent with the destressing mechanism.

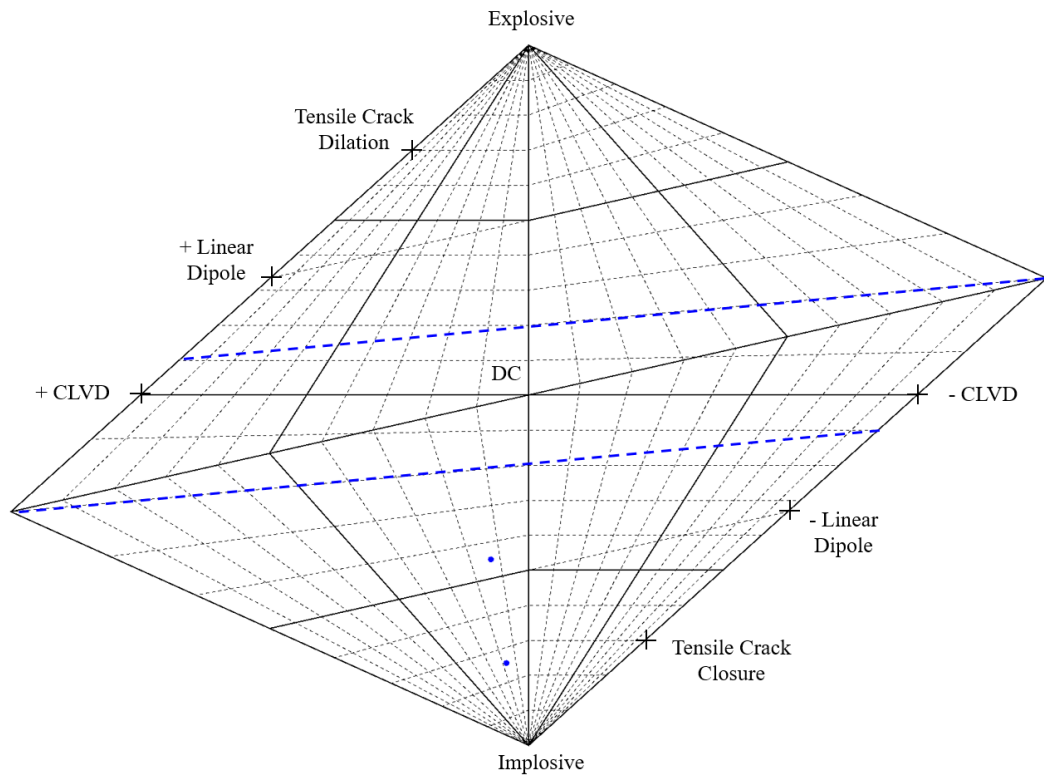


Figure 316 - Hudson source-type diagram for destressing mechanisms during Cut #16.

The final destressing development cycle (Cut #18) registered forty-two seismic events with valid source mechanism solutions, which was the largest number of any destressing cycle in the northern tunnel. This cycle also included the most solutions consistent with shear failure on blast-induced radial destressing cracks. In total, there were five events consistent with the conceptual mechanism of destressing on a fresh blast-induced crack or Set #1 joint. These events occurred at various times, ranging from two minutes to 14 days after blasting. The events were all located centrally ahead of the face and coincident with the row of destressing charges on delay #18. The events were located at various distances ahead of the face, ranging from less than 0.5m up to 3.0m. The relevant events are circled within the red dashed line in Figure 317.

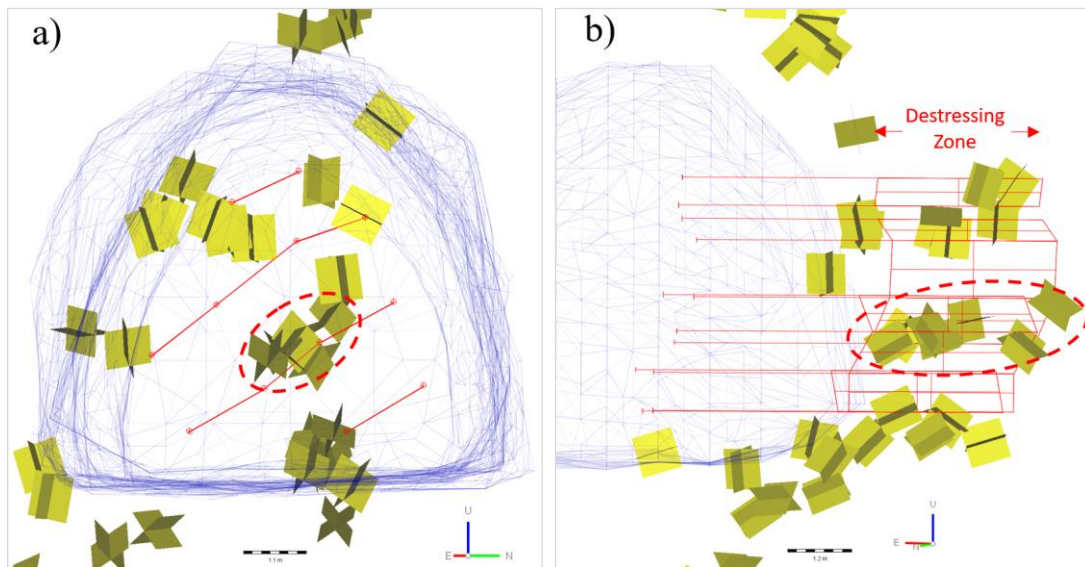


Figure 317 -- a) Transverse and b) longitudinal section views of mechanism nodal planes after Cut #18.

The moment tensor decompositions for all five events are presented in Figure 318. All five events shared very similar mechanisms, consistent with reverse faulting along a plane dipping shallowly towards the southeast, as anticipated by the destressing design concept. This indicated a direction of slip on the destressing fracture that was consistent with time. Each mechanism solution was also characterised by a high isotropic component with negative volume change, reflecting stress-driven closure of a previously dilated crack. The dip of the valid nodal planes ranged from 19° to 59° and dip direction 89° to 195° . The shallow dipping nodal planes were likely radial fractures generated by destressing blast gases, whereas the steeper planes were more likely dilated pre-existing joints within Set #1. Both the creation of new fractures and dilation of pre-existing joints were visually observed in the face throughout the duration of the experiment, as discussed in the later section on fracture analysis.

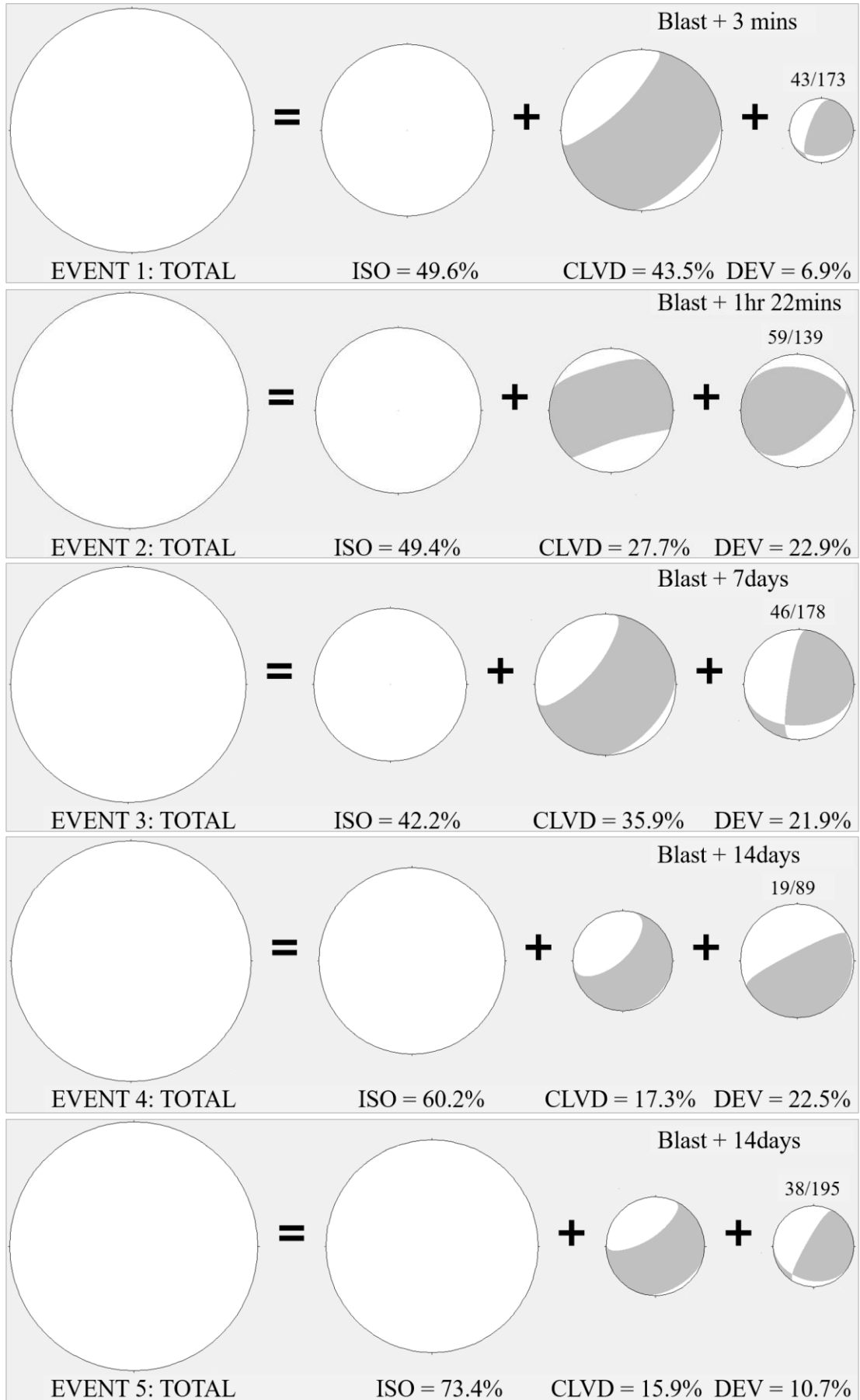


Figure 318 - Moment tensor decomposition from Cut #18 consistent with the destressing mechanism.

All five event mechanisms from this cycle were plotted on the Hudson source-type diagram shown in Figure 319. Each event plotted well within the negative volume change region of the source-type diagram and in close proximity to the T and k values representing tensile crack closure. The position of the five events to the right of the k axis reflects the reverse faulting style mechanism associated with each event, similar to the event from Cut #12 and in direct contrast to the two normal rupture destressing events from Cut #16. The five event locations and mechanisms strongly suggest that they were all associated with the same fracture, which deformed in a consistent orientation several times throughout the complete development cycle.

In this case, the only event of the five to have a clear nodal plane and auxiliary plane solution was *Event 5*. Therefore, for the reasons outlined earlier, there remained some uncertainty as to whether the nodal planes assessed above were the valid ones. In the alternate case, the mechanism solutions indicate destressing on a valid joint set, but not necessarily a blast-induced radial crack created by the destressing charges. Nonetheless, the interpretations above are supported by observations of radial fractures that were visually observed in the face, as discussed later.

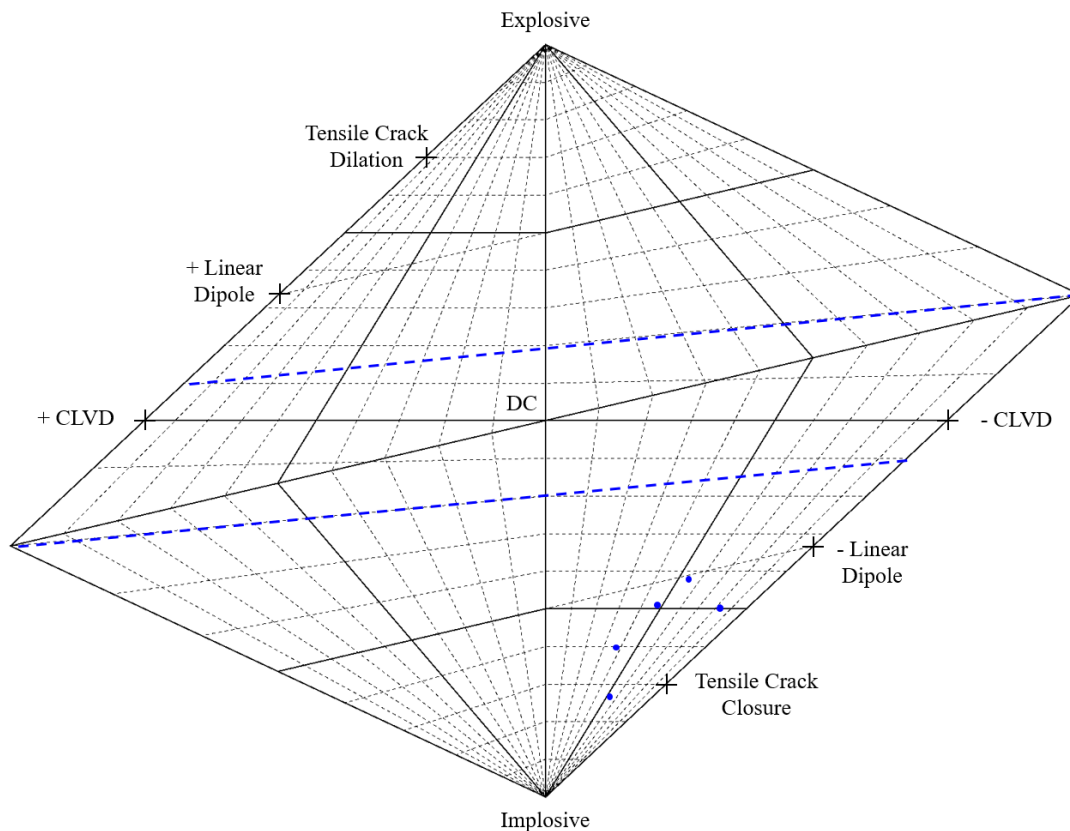


Figure 319 - Hudson source-type diagram for five destressing mechanisms during Cut #18.

In summary, seventy-eight source mechanism solutions were recorded around the northern tunnel, generating a total of 2.04kJ of radiated energy. The eight aforementioned events consistent with shear failure of blast-induced radial fractures collectively radiated 0.18kJ of energy, representing 9% of the total. The orientation and energy released by these events was significant as a percentage of the total. However, these statistics indicate that most energy was dissipated from the rock mass via failure of the natural discontinuities, not via rupture of blast-induced radial fractures. Nonetheless, the much greater diversity of failure mechanisms in the destressing development indicated that destress blasting weakened the pre-existing joint sets. This was interpreted to have reduced the rock mass stiffness and potential for strain energy accumulation in the rock ahead of the face.

In the absence of destress blasting, the majority of failure mechanisms were controlled by the sub-horizontal major principal stress. This was evident from the principal strain axis of the moment tensors solutions, which aligned well with the measured major principal stress. Also, the majority of failure mechanisms in the conventional tunnel involved strike-slip behaviour on the face-forming joints. Where destressing was applied, the sub-vertical orientation of the principal strain axes of some moment tensor solutions indicated that numerous joints were sufficiently weakened by blasting to also allow the sub-vertical stress component to induce instability.

Simultaneous shear and fracture closure was the most common characteristic of the seismic source mechanisms associated with destressing in the north tunnel. This was also a common mode of failure in the southern tunnel, although the mechanisms there were not as dominant in the negative isotropic component. That is, fracture closure was not as dominant in the conventional tunnel. This indicated that the fracture planes in the northern tunnel had been dilated to a greater extent due to the destressing charges. Due to the comparatively low shock energy of ANFO, this outcome was most likely due to the gas penetration. The data also indicated that destress blasting had the effect of dilating pre-existing natural fractures in all known joint sets.

6.2.7 Activity Analysis

One of the uncertainties concerning distress blasting is whether the method actually reduces the severity of violent face instability when personnel are completing construction activities at the face. Another related question is whether or not distressing triggers a proportionally larger release of energy from the rock mass immediately after blasting. In order to examine these questions, the seismic data was filtered temporally, so as to selectively sample the seismicity which occurred during specific construction activities. The development construction cycles were divided into four main tasks, including 1) drilling and charging of the face, 2) the 24-hour period of seismic exclusion immediately after blasting, 3) mechanical scaling of the unsupported tunnel perimeter and 4) ground support installation. The cumulative seismic event count, radiated energy and seismic potency were quantified for each of these activities. The results were totalled over the final six development cycles in the southern tunnel (for 19.6m advance) and for five cuts in the northern tunnel (for 19.3m advance).

The activity-time-filtered seismic parameters from the distressing tunnel were also quantified excluding data recorded during Cut #18. This development cycle generated an abnormally high seismic response that heavily skewed the results of the analysis. For example, the total seismic energy and potency recorded during blasting and scaling of Cut #18 were up to ten times greater than all other distressing cuts combined. Furthermore, a much higher percentage of the seismic events during Cut #18 yielded valid source mechanisms. This suggested that a much more unstable response of the joint structures occurred during this development cycle. Overall, the seismic parameter statistics during Cut #18 was significantly elevated when compared to the other distressing cycles. Therefore, in order to gain a clearer insight into the activity analysis of the seismic data, it was deemed necessary to compare the conventional excavation seismic response to the distressing response both including, and excluding the Cut #18 seismicity.

The total number of seismic events recorded during each construction activity, in each tunnel, is presented by the bar chart in Figure 320. The total radiated seismic energy recorded during each activity is presented in Figure 321. Seismic potency for each construction task, totalled over all the development cycles, is presented in Figure 322.

The data in Figure 320 indicate that destress blasting reduced the total number of events during each construction activity most of the time, but not always. One exception was the abnormally large seismic response during the ground support work in Cut #18 in the northern tunnel. This reaction was deemed to be structurally controlled and it occurred despite destress blasting being implemented there. The seismic response during that specific activity was atypical when compared to that observed during ground support work in the previous development cycles. It indicated that destressing may not always be effective in favourably altering the stress redistributions around an excavation, in particular when complex structurally-controlled failure mechanisms occur. For certain stress and structural conditions, violent unstable failure may be unavoidable, even when implementing destressing.

The radiated energy data in Figure 321 reveal the impact that the structural response to development during Cut #18 had on the seismic data. The complete datasets (i.e. with all cuts included) from the south and north tunnels indicate that destressing actually increased seismic energy release during both the 24-hour post-blast exclusion and the ground support installation. However, when the anomalous structural response to Cut #18 is removed from the analysis, the data indicate that destressing typically had the effect of significantly reducing violent energy release from the rock mass during all the construction activities. Again, the data indicate that destressing mostly had a positive effect in reducing instability. However, certain structural mechanisms could not be prevented by the destressing method. The data relating to the seismic potency during each activity reflects the same overall trend as the seismic energy. That is, excluding the anomalous structural response during Cut #18, destress blasting effectively reduced this parameter.

In the southern tunnel with conventional blasting, the most seismic events, radiated energy and potency were recorded during the 24-hour period of exclusion following blasting. The activity with the second most intense period of stress-driven instability was mechanical scaling, followed by boring/charging of the face and then ground support installation. In the northern tunnel with destressing, the post-blast seismic exclusion was also the period of most intense seismic activity. For most destressing cycles, mechanical scaling induced more instability than face boring/charging and ground support installation, with the exception of Cut #18. In that instance ground support work coincided with a relatively large, structurally-controlled energy release.

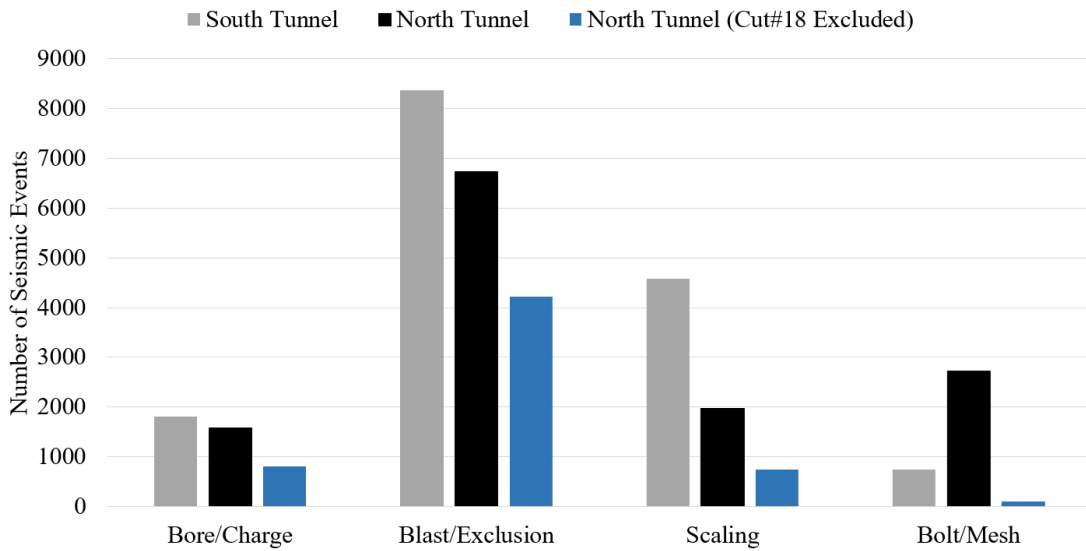


Figure 320 - Cumulative seismic event count for each construction activity.

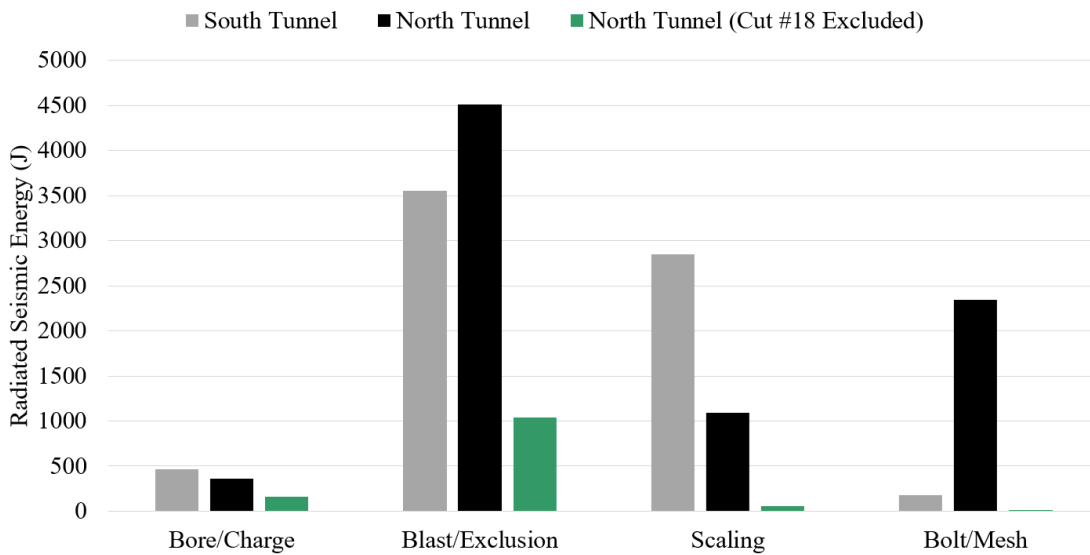


Figure 321 - Cumulative radiated seismic energy for each construction activity.

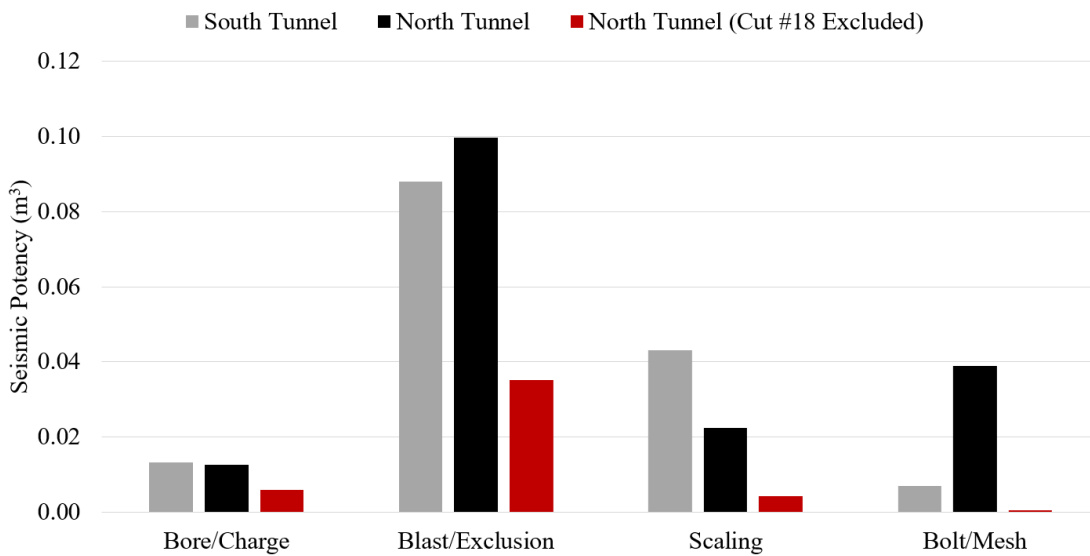


Figure 322 - Cumulative seismic potency for each construction activity.

The radiated seismic energy is perhaps the most useful of the statistics to examine in the activity analysis, as it is closely related to the violence of the rock mass failure. It is not a direct measure of demand on the ground support, but it qualitatively reflects the energy of the failure mechanisms and therefore may provide a metric for qualitative comparison of the instability during the various construction activities. The bar chart in Figure 323 presents the cumulative seismic energy recorded during each construction activity, expressed as a percentage of the total energy recorded around each tunnel throughout the entire experiment.

Considering the typical blasting response (i.e. excluding Cut #18), the results indicate that face distress blasting triggered more than 80% of the total seismic energy release during the first 24 hours after blasting. By comparison, around 50% of the total energy was released around the conventional tunnel during the same exclusion period. This is a positive outcome, as one objective of destressing was to trigger stress-driven instability in a controlled manner. Specifically, instability was desired to be triggered during the exclusion when personnel were not working at the face and exposed to the risk of rock ejections. In this sense, the distress blasting had a positive effect.

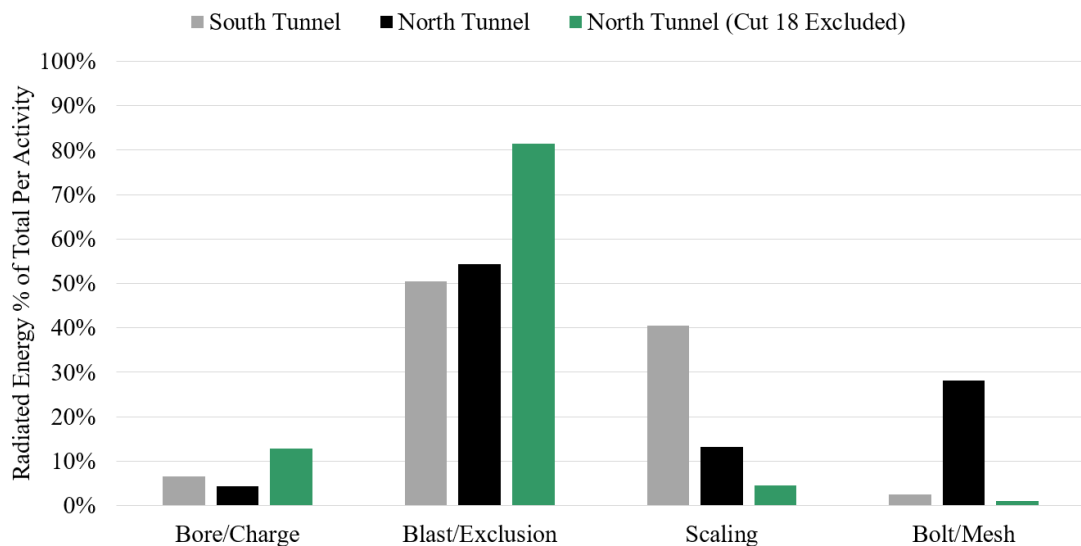


Figure 323 - Distribution of total recorded radiated energy across all development construction tasks.

6.3 Blast-Induced Fracture Network Characteristics

The mechanism of face destressing was proposed to achieve one or both of the following two objectives. First, to create connecting radial fractures extending between adjacent destressing charges in orientations sub-parallel and yet almost oblique to the major principal stress. Second, to dilate pre-existing natural rock fractures, primarily those in joint set #1 which were favourably oriented, but also those of other joint sets. In order to assess whether these objectives were achieved, visual observations were made of the fracture networks which were exposed in the development face after blasting. The visible fracture networks associated with face destress blasting were photographed and analysed in-situ, in order to answer the following basic questions:

- Were the intended modes of fracture creation successful?
- Were borehole spacings defined by the HSBM model and blast design process effective for creating fracture interaction between adjacent charges?
- Did the fracture patterns induced by the destressing charges demonstrate a dependence on the major principal stress orientation?

In order to differentiate between conventional blast damage, stress-driven damage and damage induced specifically by the destressing charges, it was necessary to set criteria for the interpretation of the visual observations. For instance, the observations of face damage were regarded as valid destressing fractures if the cracks connected to the precise location of a visible destressing charge, either directly or via another dilated fracture, and the fractures were observed in solid rock which had not debonded as a block from the face. Fractures associated with loose blocks of rock were assumed to be normal blast damage or stress-driven sloughing.

Rock mass damage positively correlated to destressing charges was not observed in every one of the destressed development faces. The primary reason for this was the fact that the destressing charges were intentionally located at a distance ahead of the face position and therefore separated from the conventional blast pattern. A minimum 0.3m-wide buffer zone of unblasted rock existed between the collar of the destressing charges and toe of the conventional charges. As a result, the destressing fractures were not typically expected to be exposed in the tunnel face. Only in the event of face overbreak or extensive fracturing were the destressing fractures able to be seen.

6.3.1 Modes of Fracturing

Areas of valid destressing fractures exposed in the face were immediately identifiable by the crush zone surrounding the original location of the explosive charge (Figure 324). All visible crush zones exposed at the face were located at the collar region of the original charge. This zone was characterised by complete collapse of the original borehole, which was filled with pulverised rock fragments. A zone of tensile damage with circumferential fractures extended approximately 50-100mm beyond the zone of crushing. It was noted that tensile damage to the borehole wall was sometimes limited only to those sections of the original borehole circumference which were sub-parallel to the major principal stress (i.e. the upper left and lower right quadrants of the borehole circumference, as shown in Figure 324). Beyond the immediate damage zone, radial fractures were frequently present. The fractures were typically observed in orientations sub-parallel to the major principal stress. These damage observations confirm that the use of the clay stem packs was sufficient to generate very high borehole pressures during detonation of the destressing loads.

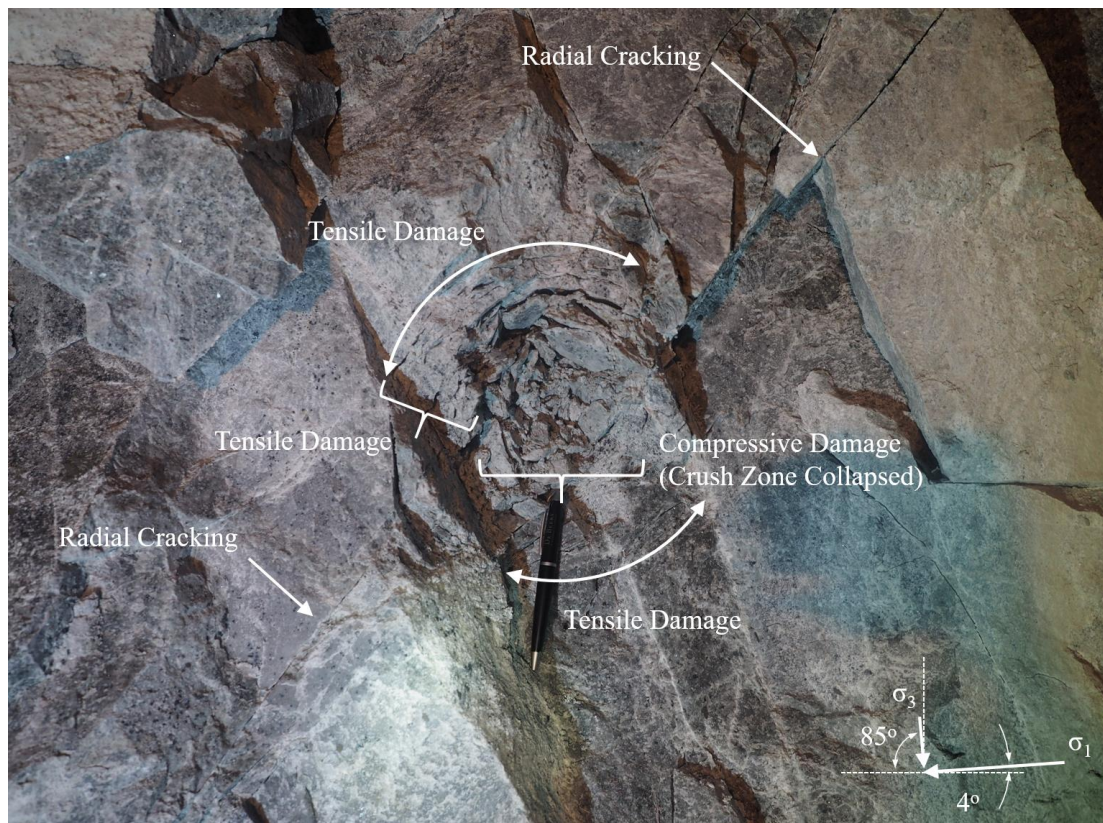


Figure 324 – Zones of blast-induced compressive, tensile and radial damage around a destressing charge.

Most of the visible fractures connected to the destressing loads were dilated pre-existing natural discontinuities. As expected, the dilated joints were primarily those within Set #1, which were oriented sub-parallel to the major principal stress and therefore under the least normal stress. Figure 325 presents a photograph of a series of closely spaced joints within Set #1 which had been visibly disturbed and dilated. These joints intersected a destressing charge, which is visible in the upper right of the photograph. These dilated joints were planar and were assumed to be extremely well healed prior to blasting, based on nearby observations of undisturbed joints in the same set. Disturbance to the joints was observed more than 750mm from the destressing charge. This was some evidence to indicate that the HSBM modelling of fracture interactions across a 1.5m borehole spacing were realistic in practice.

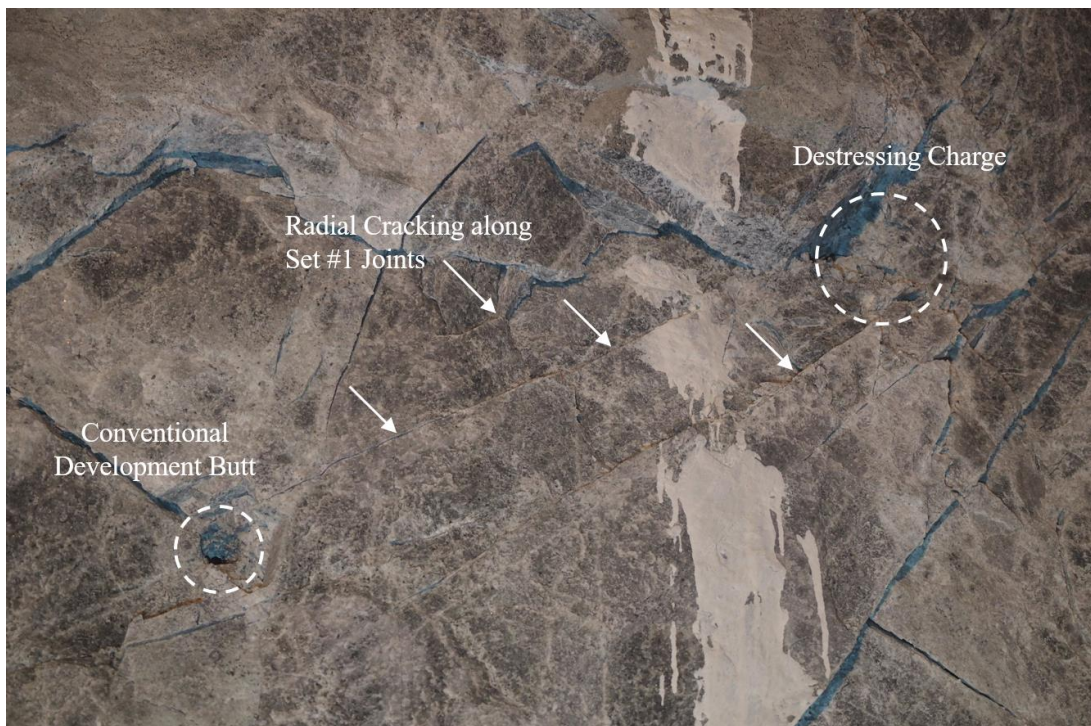


Figure 325 - Blast-induced fracture through pre-existing structure.

Blast induced fracture through intact rock was also observed, although it appeared to be less common than joint dilation. In most cases, radial fracturing through intact rock was observed within 500mm of the destressing charge. There was no clear evidence that the destressing charges generated radial fracturing through intact rock in orientations sub-perpendicular to the major principal stress. However, as illustrated in Figure 326 and Figure 327, intact rock fracturing did occur sub-parallel to the major principal stress. This occurred despite the high confinement conditions present throughout the destressing zone at the time of initiating the explosives.

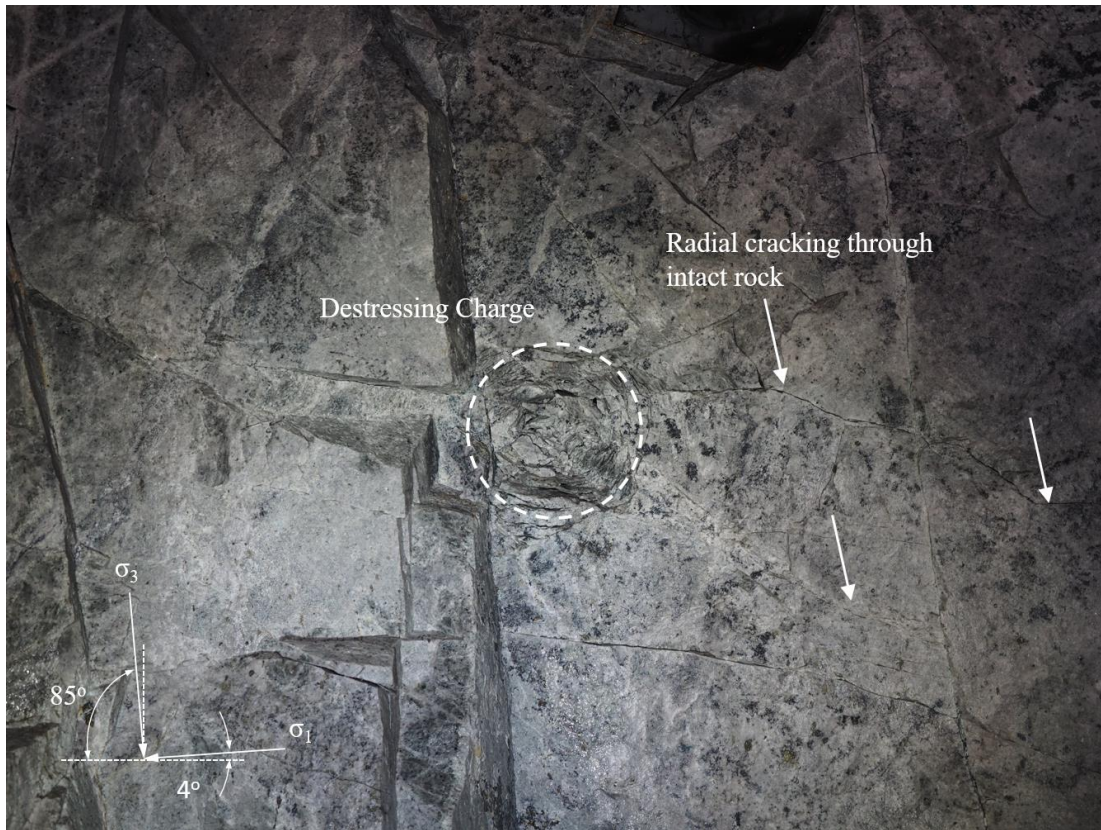


Figure 326 - Destressing blast-induced radial fractures through intact rock.



Figure 327 - Close-up view of destressing blast-induced radial fractures through intact rock.

Radial fracturing through intact rock was observed to occur sub-parallel to the major principal stress in two opposite directions. The photograph in Figure 328 shows evidence of such fracturing. This is a view of the exposed collar region of a destressing borehole. This section of the borehole was exposed at the face with no evidence of crushing of the borehole wall. Figure 329 is a photograph of the same borehole from a slightly different orientation looking towards the opposite wall of the hole. Horizontal radial cracks were visible in the borehole walls, but none in the upper or lower surfaces. This was physical evidence to indicate that destressing fractures were generated in opposing directions. Therefore, the destressing charges had the potential to interact with multiple neighbouring charges.



Figure 328 - Borehole internal view of radial fracturing through intact rock.



Figure 329 - Borehole internal view of radial fracturing through intact rock (opposite direction).

Chapter 6: Monitoring & Analysis

An observation was made whereby gas was deemed to have migrated from the destressing load, through a discontinuity in Set #4, causing dilation of a joint in Set #1. This was an example of gas from the destressing charge migrating through multiple discontinuity orientations causing fracture dilation. In this specific case, illustrated in Figure 330 and Figure 331, a joint in Set #4 intersected both a destressing charge and a joint in Set #1. Both joints were visibly damaged with some separation of the fracture surfaces. As the Set #1 joint was 200mm offset from the destressing charge, the most likely route for the blast gases to penetrate this discontinuity was via the intersecting joint from Set #4. In this case the Set #1 joint was dilated over a distance of approximately one metre from the point where the two joints intersected. This observation indicated that blast gases could migrate significant distances along multiple orientations and still create the desired reduction in joint strength to assist face destressing.

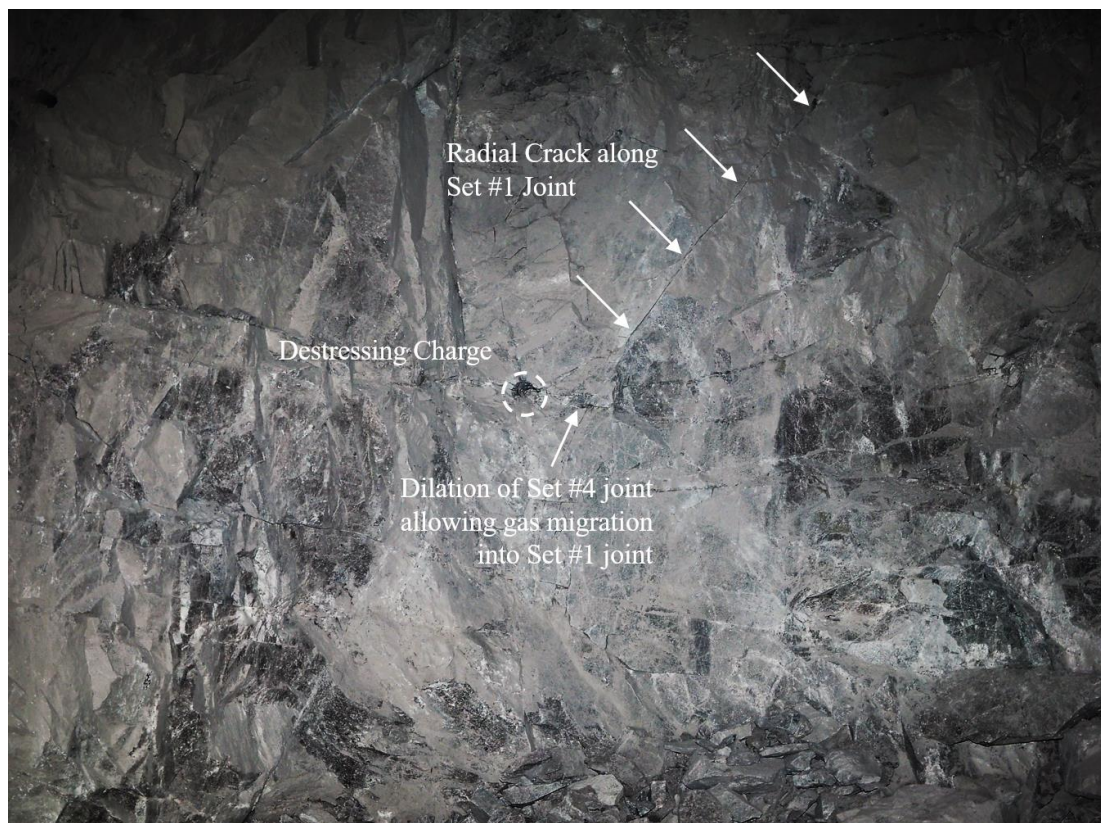


Figure 330 – Gas migration via multiple joint orientations originating from the destressing charge.

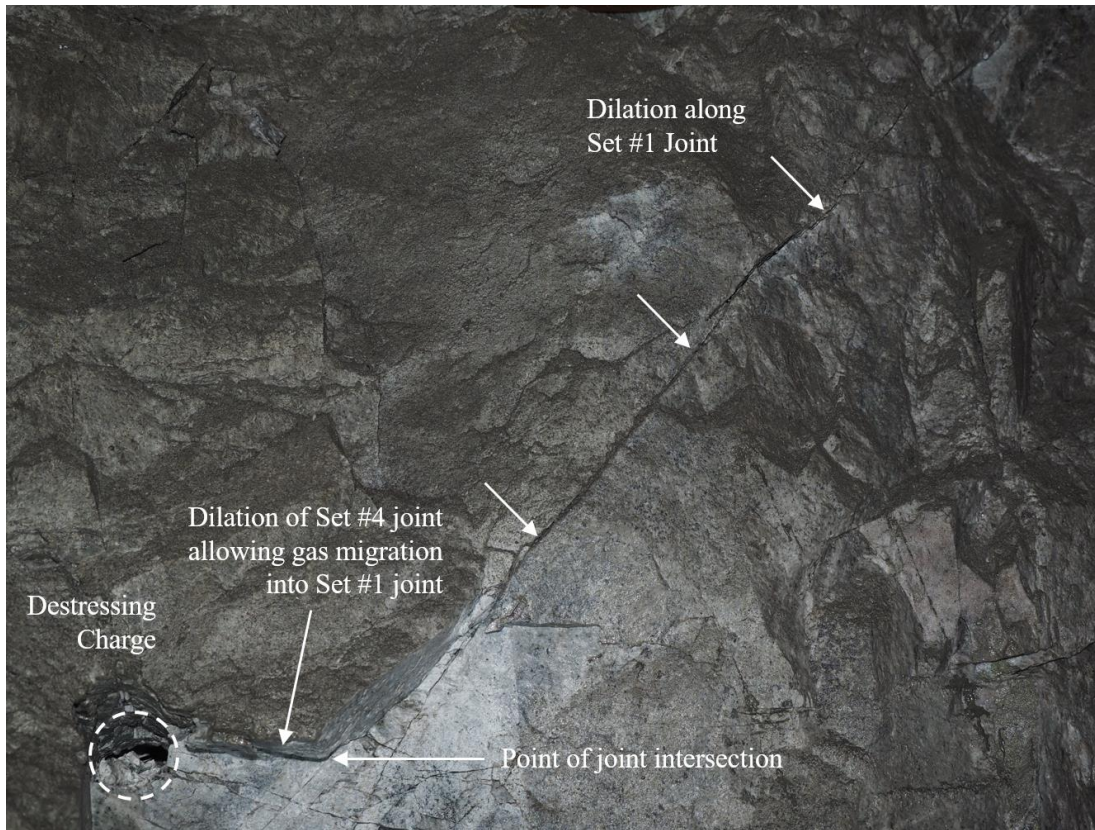


Figure 331 - Dilation of Set #1 joint following gas migration through nearby Set #4 structure.

Radial fracturing was not commonly observed in orientations sub-perpendicular to the major principal stress, either through intact rock or pre-existing joints. In one specific case where two joints directly intersected the destressing charge, there was no evidence of dilation of the joint surface due to gas penetration. This example is illustrated in Figure 332. Here two discontinuities belonging to joint set #3 directly intersected a destressing charge but were not dilated or damaged. The major principal stress was normal to these joints and hence a high confining stress was present to inhibit their expansion. Radial cracking was observed in that case, but only in orientations sub-parallel to the major principal stress. This was an example of preferential fracture formation along this orientation. However, the lack of visual observations of fracturing sub-perpendicular to the major principal stress does not confirm that no such fracturing was occurring. As discussed, most fracturing was expected to be concealed ahead of the face.

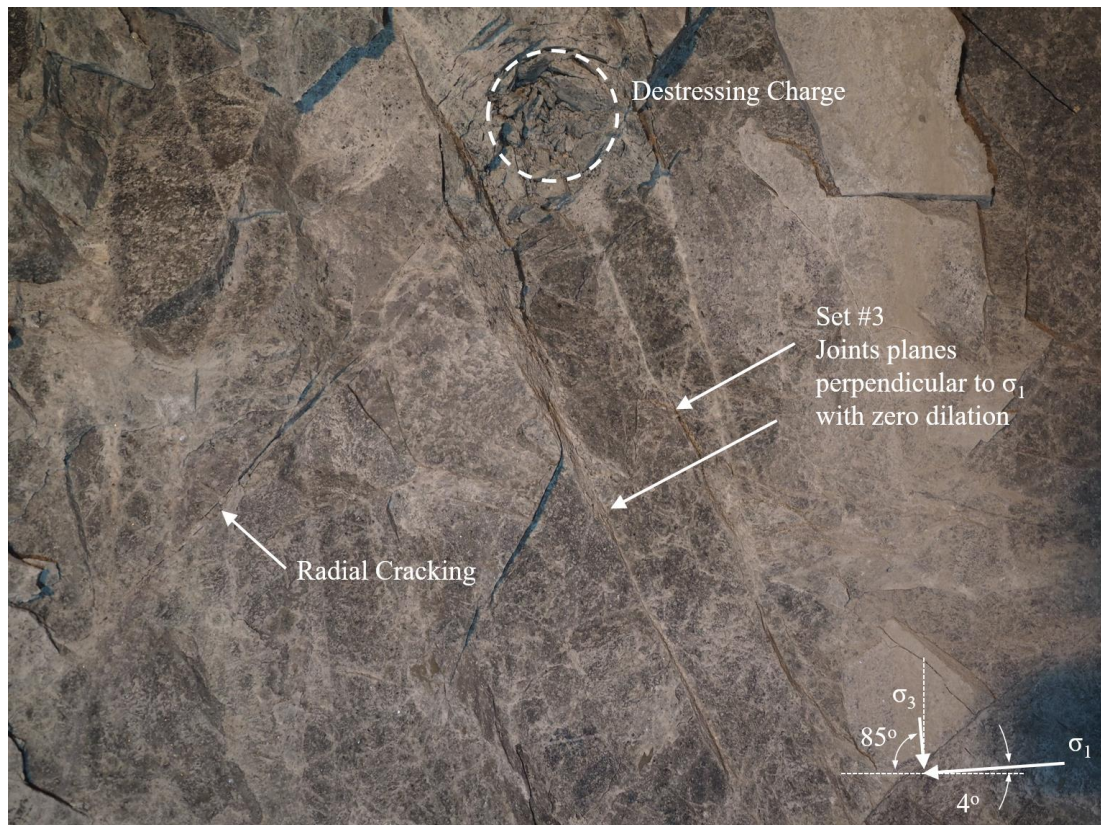


Figure 332 - Evidence of preferential fracture formation sub-parallel to the major principal stress.

6.3.2 Cross-Borehole Fracture Interactions

Evidence of radial fracture interaction across the spacing of the destressing charges is shown in Figure 333. In this case one continuous dilated fracture was generated between two adjacent destressing charges separated by a distance of 1.8 metres. Evidence of gas penetration was visible in the form of ANFO residue on the entire fracture surface. The residue was a combination of oil, moisture and rock dust which is visible as the darker coloured zones in the figure. Explosive residue within the entire crack was the only clear evidence of fracture interaction between destressing charges, and it was only observed to align sub-parallel to the major principal stress field.

It was not obvious if this particular fracture was continuous across more than two boreholes in this case. Potentially, the fracture was continuous behind the surface of the face. Nonetheless, this was a physical example of the desired mechanism of fracturing, which was intended to facilitate shear deformation of the face. In this case the fracture connecting the two destressing charges appeared to be formed through a combination of joint dilation and intact rock rupture. Numerous natural discontinuities in close proximity to each borehole were also dilated and hence may have also played a role in assisting the path of the blast gases.

Further evidence of gas penetration within favourably oriented geological structure is indicated by the red arrow in the image. In this case, the fractures appeared to be dilated along natural joint planes with a dip and dip direction of 55/172. This was consistent with joint Set #1.

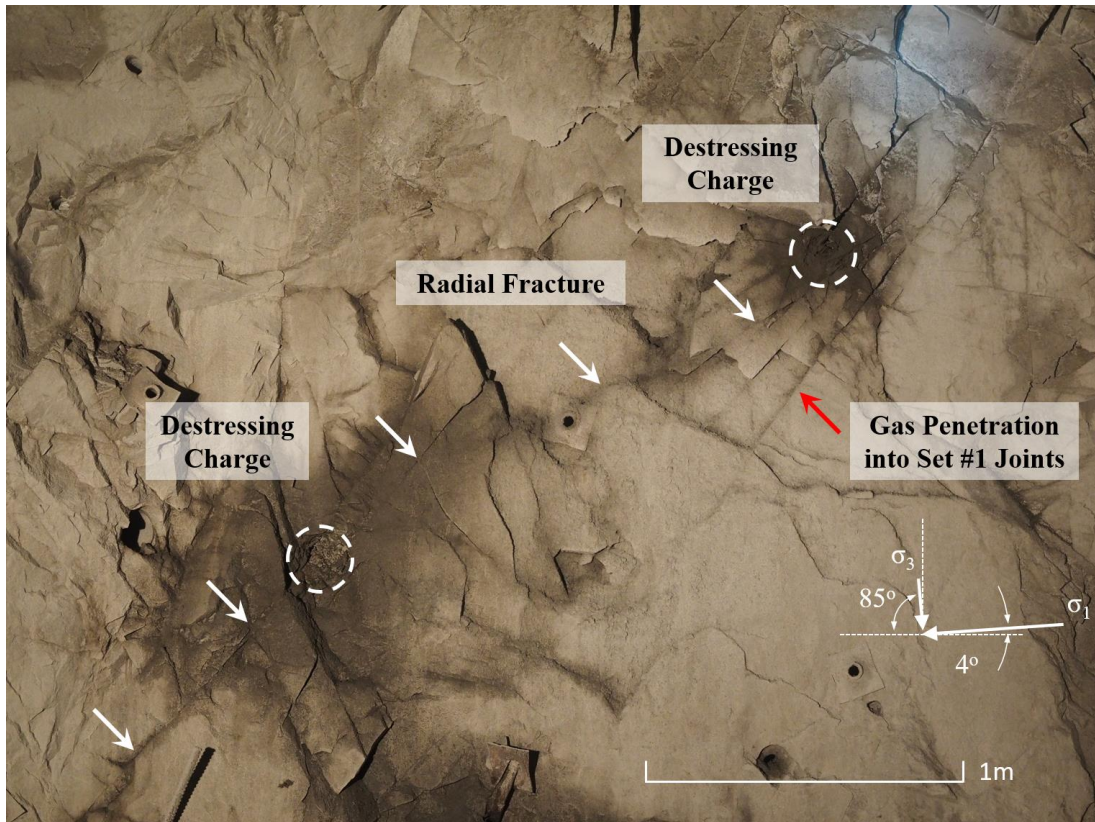


Figure 333 – Visible ANFO residue within a radial crack confirming gas interaction between charges.

Observations of the angular range of fracturing generated by the distressing charge in the lower left of Figure 333 are presented in Figure 334. The inclination of the shallowest and steepest observable radial fractures, identified by the red arrows in Figure 334, was measured to be 17° to 57° , respectively. For visual reference, the angular range was sketched (not to scale) onto the photographs to identify the zones where radial fracturing was and was not observed. These limits are depicted as the white dashed lines. Fracturing was not observed in orientations perpendicular to the major principal stress. The range of 17° to 57° dip of the radial fractures was similar to the range of dip for Set #1 joints, which was approximately 30° to 80° . As it was confirmed that some Set #1 joints were dilated by blast gases, this difference in the dip range suggested that the shallower radial fractures were created through intact rock, and the steeper fractures were formed by dilation of Set #1 joints. These angular fracturing limits indicated the zone of cross-borehole crack interaction (Figure 335).

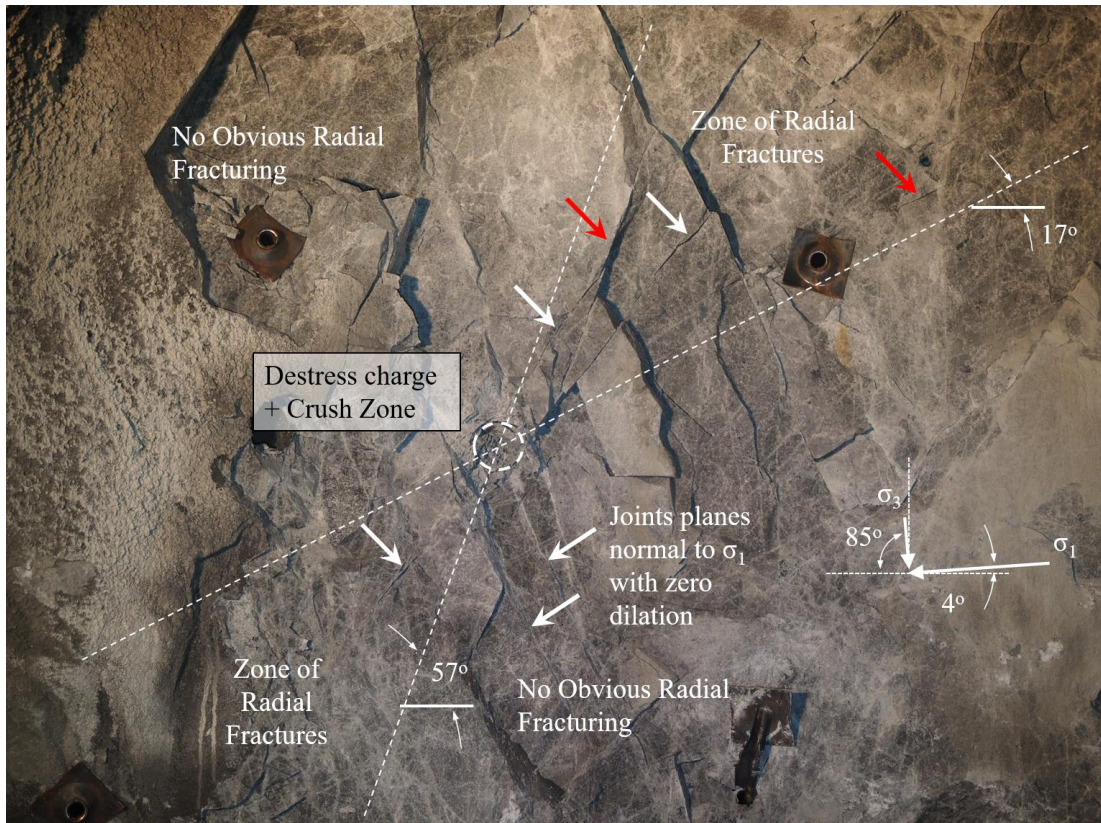


Figure 334 - Directional characteristics of observed radial fracturing due to destressing charges.

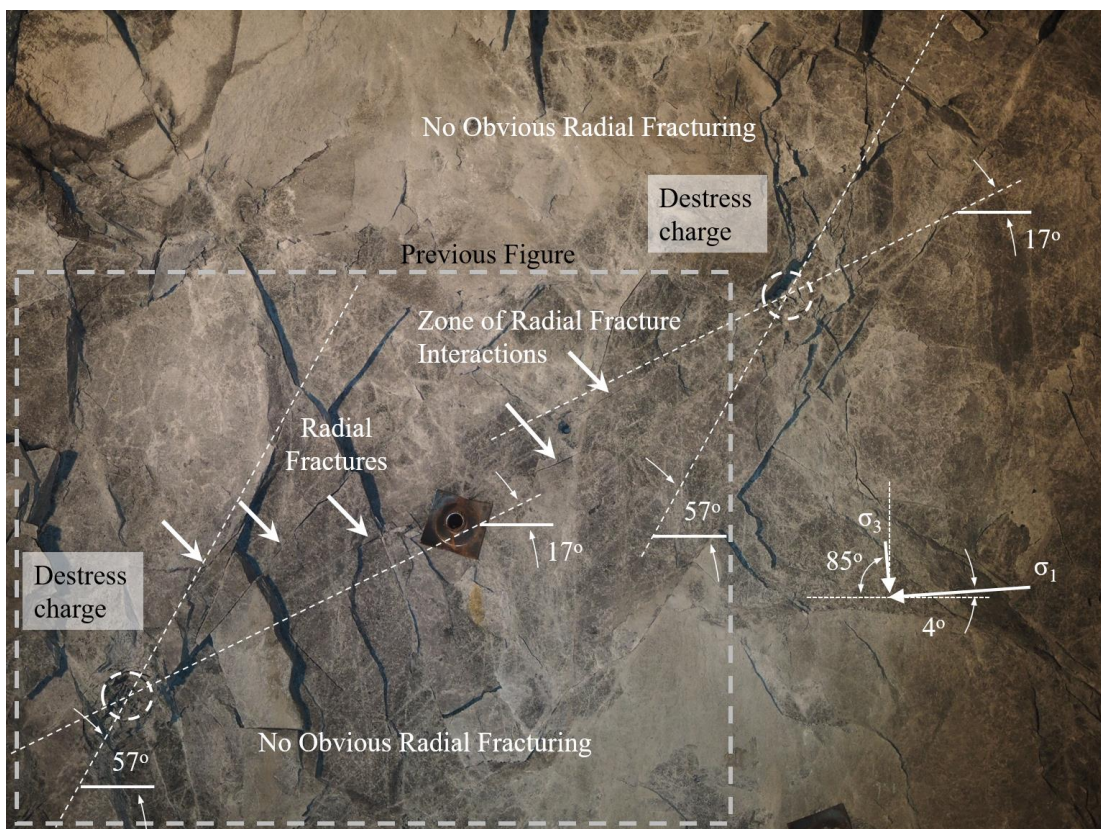


Figure 335 - Wide view of directional fracturing characteristics showing cross-borehole interaction.

The dip of visible destressing fractures throughout the charge interaction zone was measured. These details are presented in Figure 336, which is a close-up photograph looking directly at the face. Figure 337 is a diagram of the angular characteristics of this fracture pattern with respect to the major and minor principal stresses. The diagram presents the upper and lower limits of the measured dip of the visible radial fractures, the median dip of all radial fractures and the average dip of Joint Set #1. The diagram also illustrates the inclination of the major and minor principal stresses, which were both approximately orthogonal to the longitudinal axis of the tunnel. The observations indicate that destress blasting gasses penetrated natural joints in Set #1 at angles of up to 56° oblique to the major principal stress. Furthermore, the average dip of the visible destressing fractures was much more closely aligned to the average dip of Joint Set #1 than to the orientation of the major principal stress. This indicated that the natural discontinuities provided less resistance to gas penetration when compared to intact rock fracture perfectly parallel to the major principal stress.

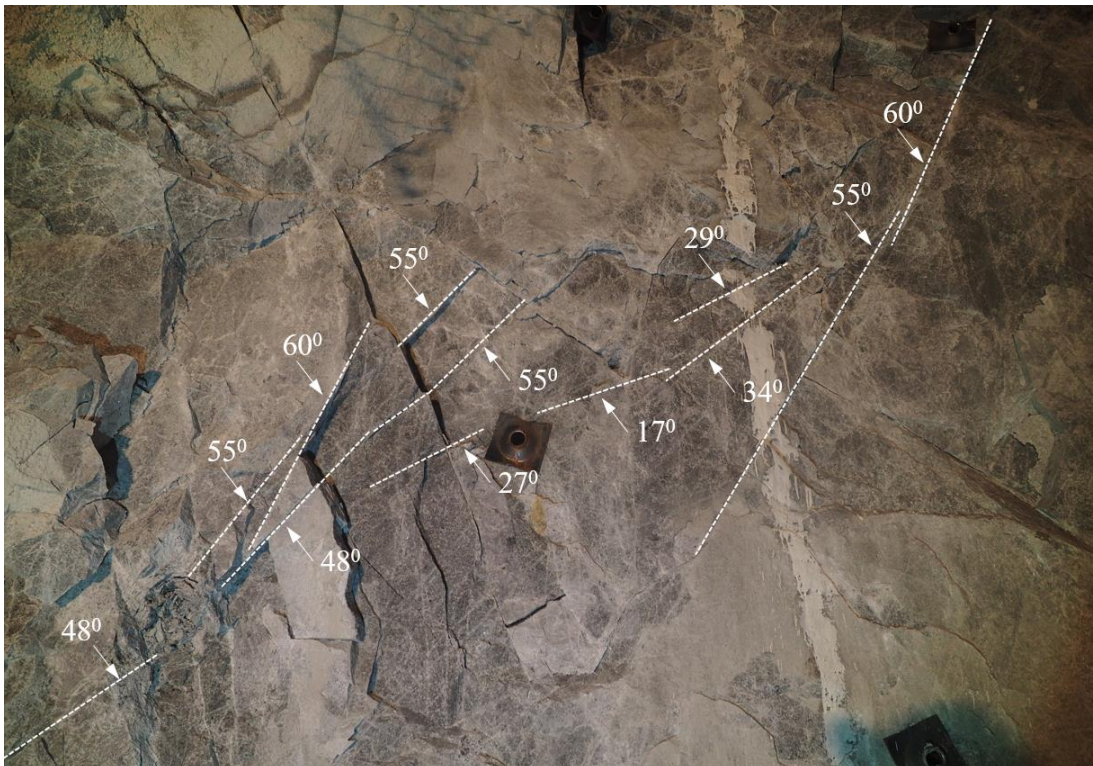


Figure 336 - Dip angle of observed radial destressing fractures in the charge interaction zone.

This conclusion is beneficial for destressing blast design, in terms of the alignment of the rows of destressing holes. It is suggested to align the destressing charges in rows which are parallel to the average orientation of any joint set which is sub-parallel to the major principal stress. This should maximise the likelihood of fracture interaction between adjacent destressing charges. Bearing in mind, in order to facilitate shear in the rock, it is also considered necessary to form destressing fractures in orientations almost oblique to the major principal stress.

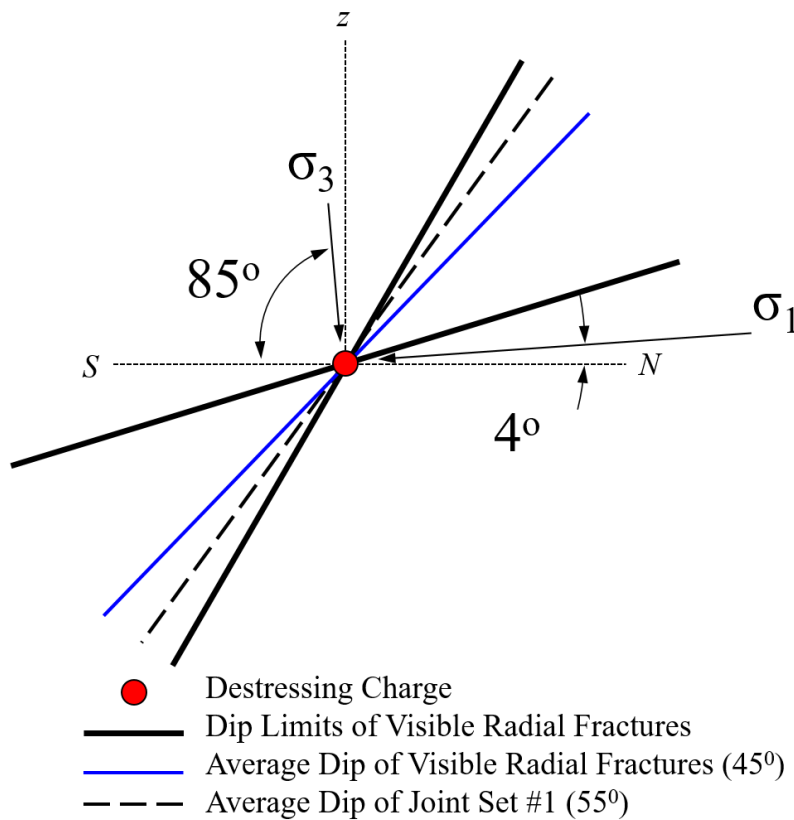


Figure 337 - Angular characteristics of blast induced fractures relative to the principal stresses.

6.4 Excavation Profile Performance

The geometry of the final supported profile shape of both tunnels was examined in order to answer the following questions:

1. Was the drill and blast design for the semi-elliptical profile successful in forming the excavation shape and minimising damage to the permanent tunnel boundary?
2. Did the implementation of face destressing have any detrimental effect on the excavation profile?
3. Did either tunnel experience instability or loss of the profile shape consistent with the structural blocks defined by the SAFEX analysis?

In order to answer these questions, the final tunnel shapes were surveyed using a GeoSlam Zeb1 laser scanning device (Figure 338). The ZEB1 is a 2D time-of-flight laser range scanning instrument which is rigidly coupled to an inertial measurement unit (IMU) mounted on an oscillating spring. The system consists of a datalogger, battery and laser scanner which is hand-operated while walking through the area desired to be surveyed. The scanner head oscillates on the spring when in motion, providing the third dimension required to generate 3D information. A simultaneous localization and mapping (SLAM) algorithm is used to combine the 2D laser scan data with the IMU data to generate accurate 3D point clouds (GeoSlam, 2013).



Figure 338 - GeoSlam Zeb1 laser scanner (GeoSlam, 2013).

An image of the entire point cloud dataset of the surveyed development is presented in Figure 339. The dataset consisted of 111,731,552 individual XYZ coordinates defining the point cloud of the south tunnel, north tunnel and nearby access development. In the below image, the data is coloured using a height ramp algorithm, which colour codes individual points based on their position (elevation) on the Z-axis. In this case the highest points in the dataset appear in warmer colours. When viewed in longitudinal section, the zones of roof overbreak appear in red. Cross section views of the complete data for the southern and northern tunnel are presented in Figure 340. These images reveal the very high resolution spatial data able to be captured by the Zeb1 system. The survey error range of the instrument is estimated to be less than 20mm.

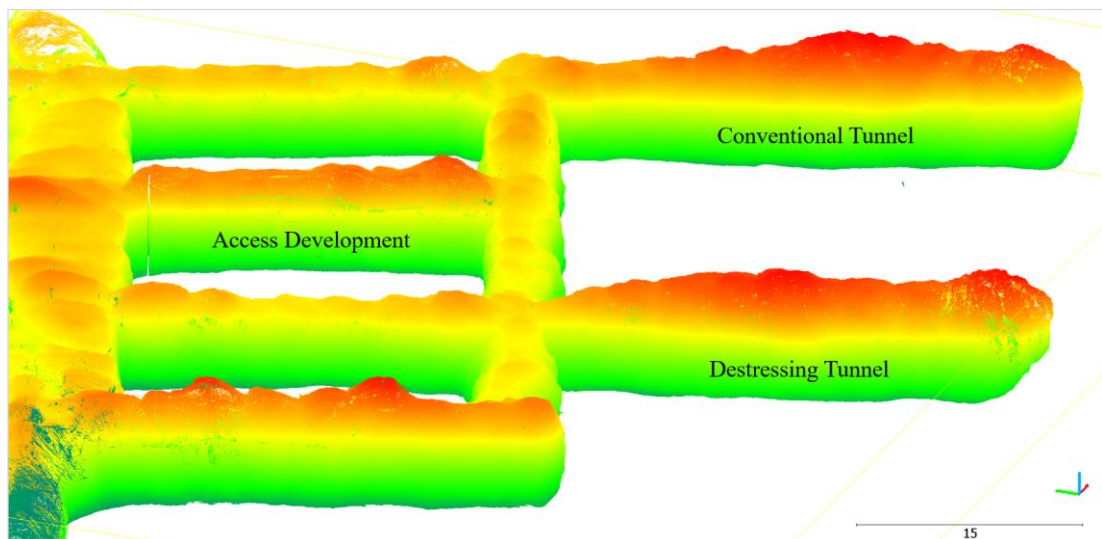


Figure 339 - 3D point cloud data of tunnel geometry collected using the GeoSlam Zeb scanner.

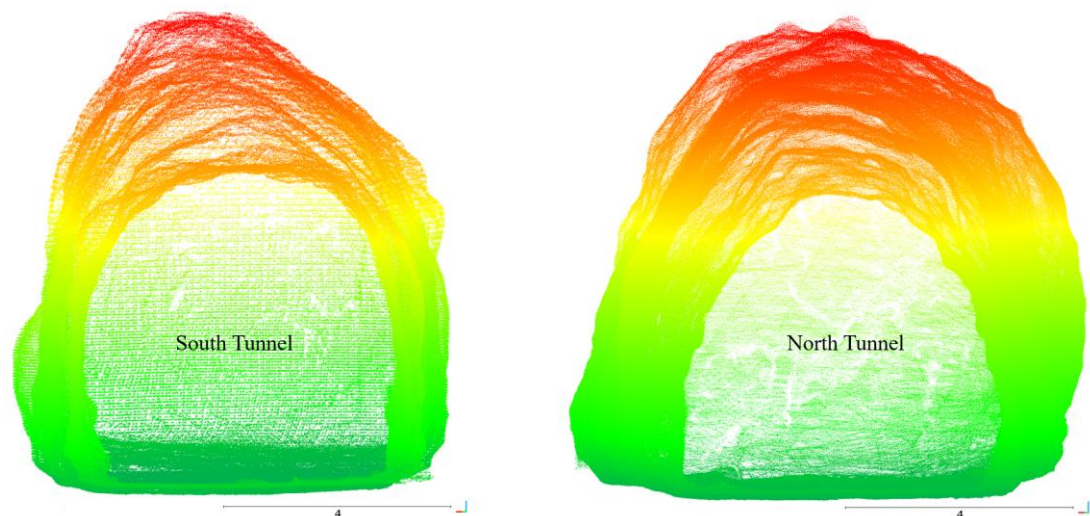


Figure 340 - Cross section views of the complete 3D scan of each tunnel.

The profile shape was examined at regular intervals along the length of each tunnel. This included zones of uniform profile compliance, as well as those zones with substantial overbreak. Transverse cross section samples through the point cloud data were taken at the following chainage distances within each tunnel: 3.5m, 8.5m, 14.0m, 19.5m, 24.5m and 29.0m, as measured from the turnout location. These distances were taken at approximately 5.0m increments, with minor adjustment to focus on points of interest such as where overbreak was noted due to structural features. The locations of each profile cross section in each tunnel are illustrated in Figure 341. The relevant cross sections of the final tunnel geometry are presented in Figure 342 to Figure 347.

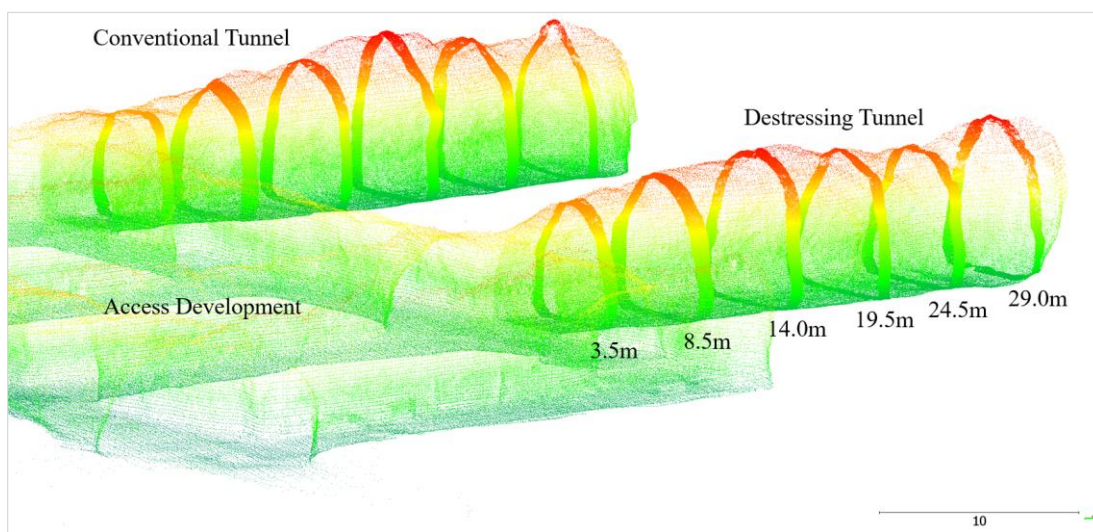


Figure 341 - Cross sections of the scanned tunnel profile.

The initial profile of each tunnel at 3.5m chainage (Figure 342) indicated that the shape was smaller than the final design. This was due to the tunnels ramping up to full width and height from the much smaller dimensions of the access development. Nonetheless, the profile shape in the northern tunnel was relatively uniform and in good compliance to the semi-elliptical geometry. At the 8.5m chainage (Figure 343) both tunnels had been formed to their full size. Survey data from both tunnels indicated compliance to the excavation profile design. In the case of the northern tunnel, the overbreak was typically no more than 0.5m, which showed that the contour blasting parameters were appropriate. There was some evidence of overstressing of the roof of the southern tunnel. The characteristic notch formation typical of spalling was evident in the centre of the roof, to a depth of around 0.75m. Such damage was not observed in the semi-elliptical tunnel shape, although there was evidence that the left shoulder profile was formed by a Set #1 discontinuity.

At the 14.0m chainage (Figure 344) both the northern and southern tunnels experienced overbreak in the shoulder and/or roof. Overbreak in the left hand shoulder of the south tunnel and left hand upper wall of the northern tunnel appeared to be controlled by break-back to Set #1 joints. The maximum depth of overbreak at this chainage was approximately 2.0m in both tunnels. In the case of the northern tunnel with destressing, this was the point of maximum overbreak. Throughout the remainder of this tunnel the overbreak was significantly less. However, the overbreak in the conventional southern tunnel continued to increase.

At the 19.5m chainage (Figure 345) the destressing tunnel profile improved, but again some overbreak was controlled by joint structures. The left and right hand side walls were defined by Set #1 and Set #3 joints, respectively. The roof overbreak terminated on a joint in Set #4. This form of structurally-controlled excavation shape was not associated with significant energy release or instantaneous ejection of large volumes. The overbreak mechanism was gradual and progressive spalling of small blocks.

Overbreak in the southern tunnel reached a maximum at the 19.5m chainage. The horizontal limit of the overbreak was defined by a Set #3 joint in the left wall and a Set #1 joint in the right wall. A Set #4 structure with trace length exceeding the tunnel width formed the overbreak surface in the roof. The depth of overbreak in the roof was approximately 3.0m. The overbreak geometry was controlled by the same joints sets as those forming Block 4, from the SAFEX analysis. However, the overbreak was again a result of progressive spalling terminating at these structures, not an instantaneous ejection. It is important to make the distinction between sudden ejection of large blocks and progressive spalling mechanisms, which may have similar final geometry, but very different mechanics.

The overbreak geometry at the 24.5m (Figure 346) and 29.0m (Figure 347) chainage in the southern tunnel was again heavily controlled by both Set #1 and Set #4 joint structures. At these locations the overbreak was approximately 1.75m to 2.0m. The laser mapping data confirmed that the shallow dipping Set #1 and #4 joints were again dominant in controlling the depth of failure. In particular, at the 29.0m chainage the overbreak profile formed a classic notch shape characteristic of progressive spalling.

In comparison, overbreak performance was improved in the northern tunnel over these same chainage increments. At 24.5m the semi-elliptical profile shape was controlled to within 1.0m. There was up to 1.5m of overbreak at the 29.0m chainage, although the semi-elliptical profile shape was maintained.

The process of progressive spalling and incrementally increasing depth of failure was visually observed during the construction process, often taking place over the course of several hours after blasting. It is important to differentiate between progressive spalling during construction, which mobilises and/or terminates on structures with a large depth of overbreak, and the *structurally controlled failure* discussed previously. Structurally controlled failure describes the case whereby large structurally defined blocks are ejected in their entirety in a singular violent event. Typically, this occurs following completion of tunnel construction.

The recorded seismic response during the initial development cycles in both tunnels was substantially lower than that recorded during the latter stages. The low levels of stress-driven instability and controlled profile shape through the preliminary development indicated that the blast design specifications were appropriate for the rock mass strength conditions. In the latter half of the tunnel development the increasing seismic response was accompanied by a loss of profile. The correlation between increased seismicity and profile overbreak indicated that stress-driven instability after blasting was the main factor affecting compliance with the excavation design shape.

A photograph of the joint structures forming the overbreak limits in the south tunnel at the 19.5m chainage is presented in Figure 348. The precise geometry of the overbreak at this location was not purely tetrahedral. It formed a slightly more complex polyhedron, given the overbreak to the Set #1 joint beyond the right hand wall. This overbreak geometry was much larger than that of a span-limited, structurally controlled Block 4 defined in SAFEX. Also considering its progressive nature, the overbreak geometry measured here should not be confused with the structurally controlled mass of instability used for ground support design.

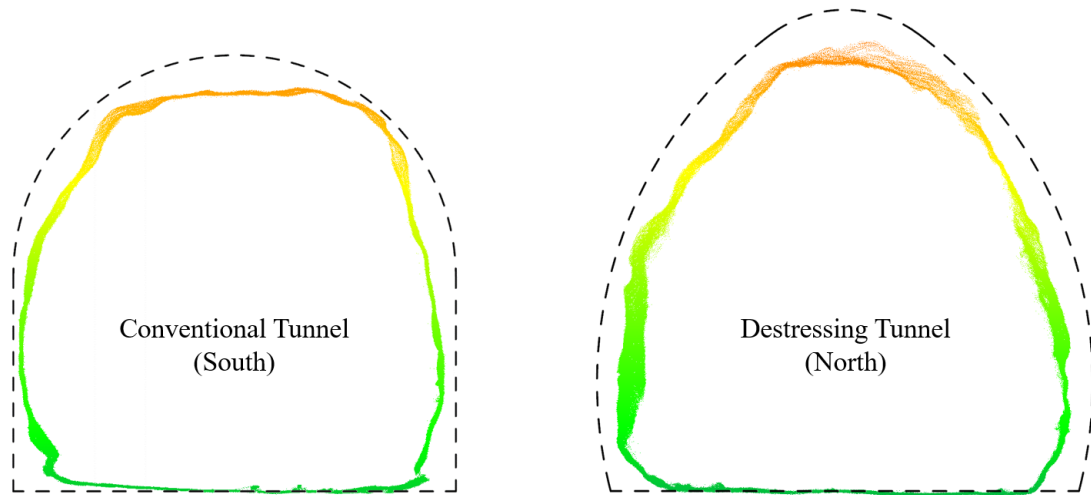


Figure 342 - South and north tunnel cross sections of scan data at 3.5m chainage.

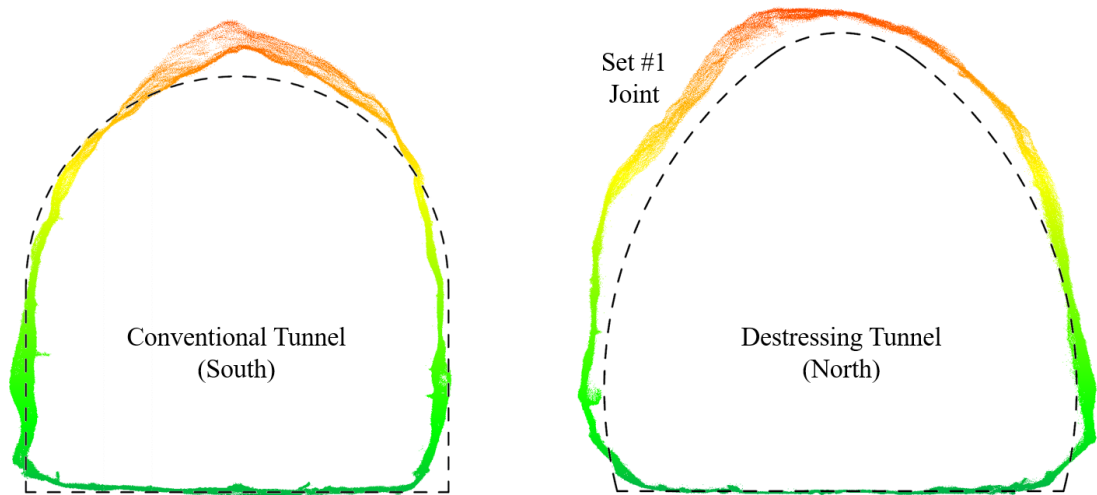


Figure 343 - South and north tunnel cross sections of scan data at 8.5m chainage.

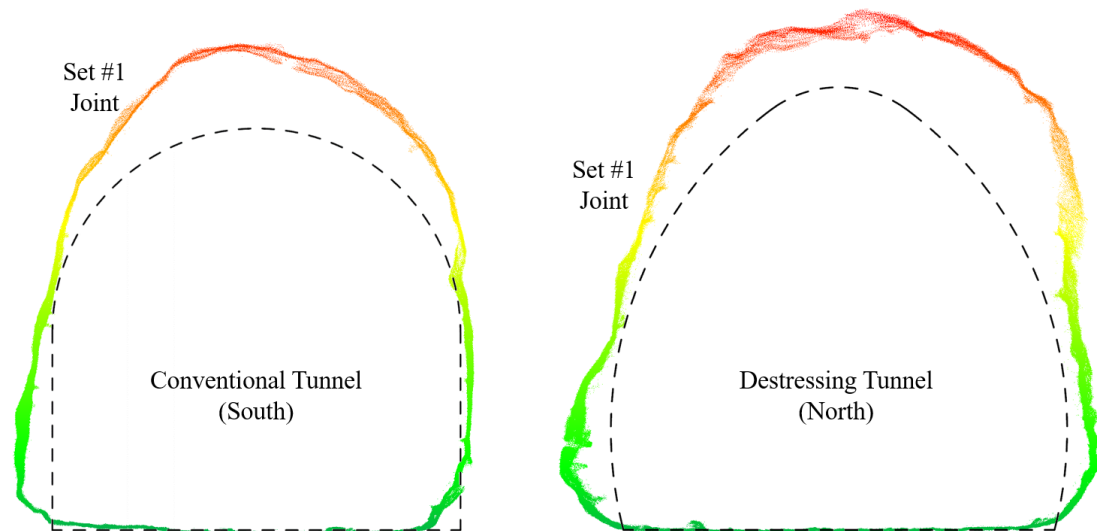


Figure 344 - South and north tunnel cross sections of scan data at 14.0m chainage.

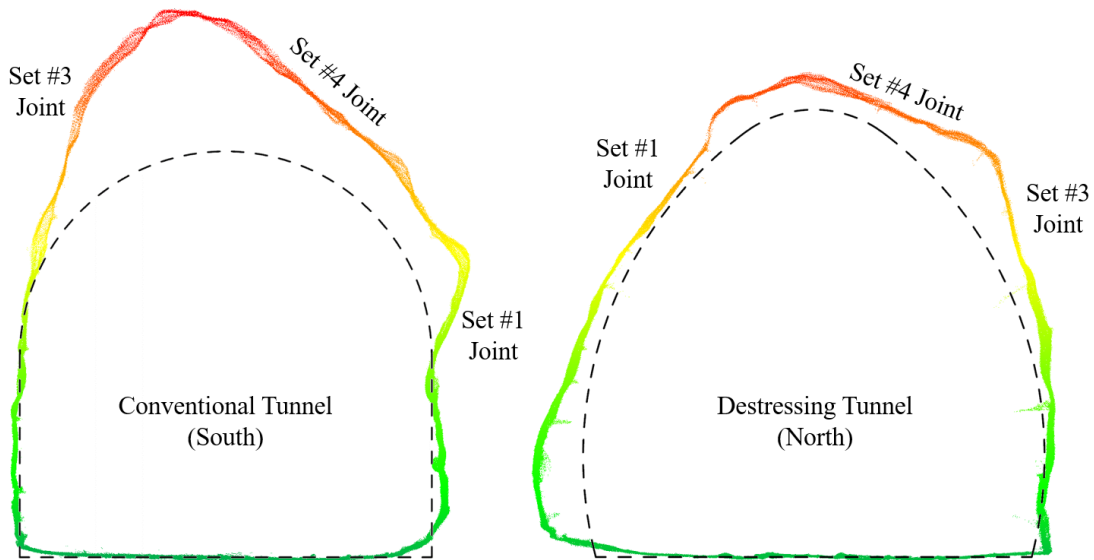


Figure 345 – Scan cross sections at 19.5m chainage showing SAFEX priority block formed in south tunnel.

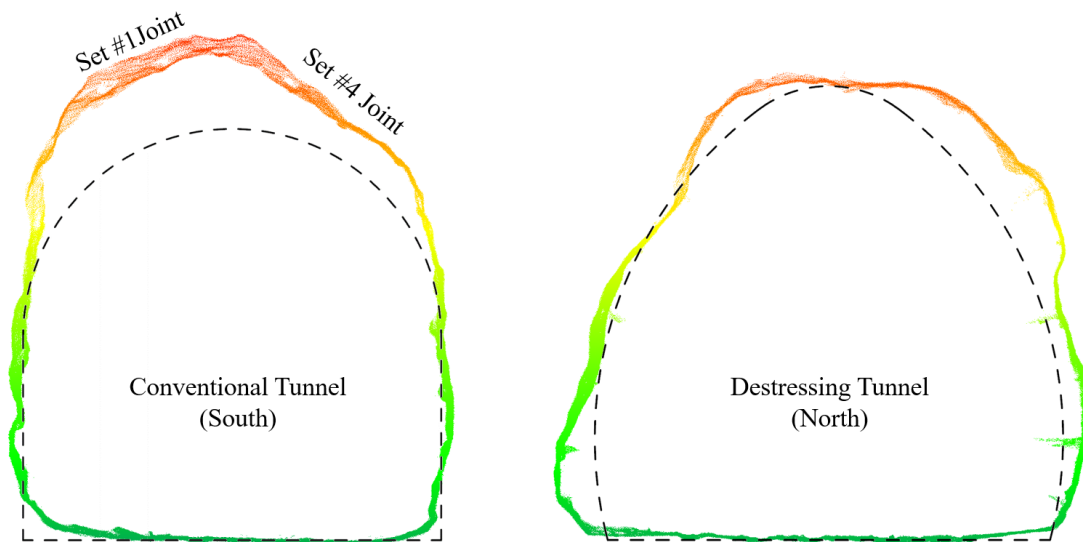


Figure 346 - South and north tunnel cross sections of scan data at 24.5m chainage.

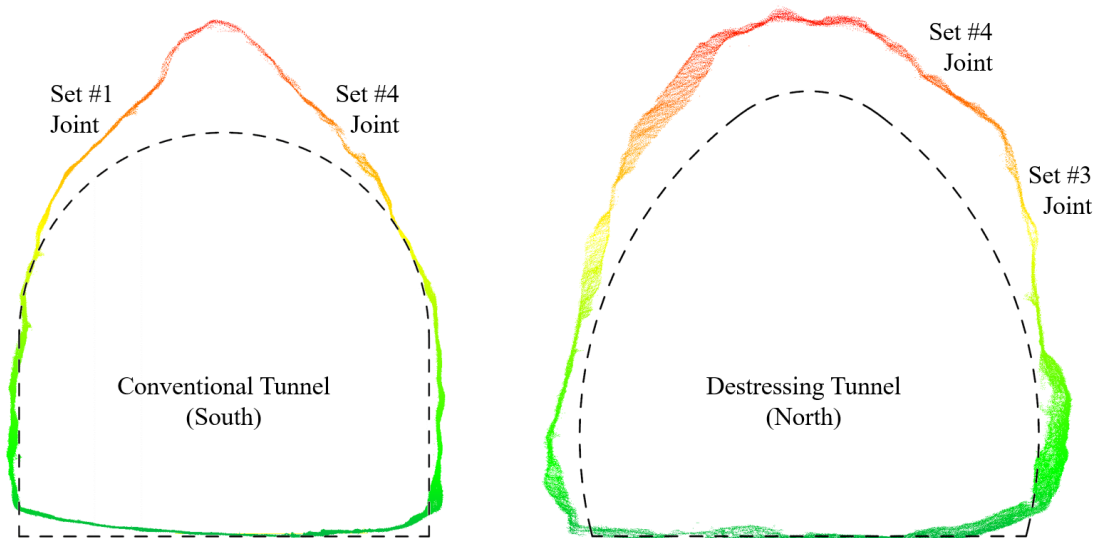


Figure 347 - South and north tunnel cross sections of scan data at 29.0m chainage.

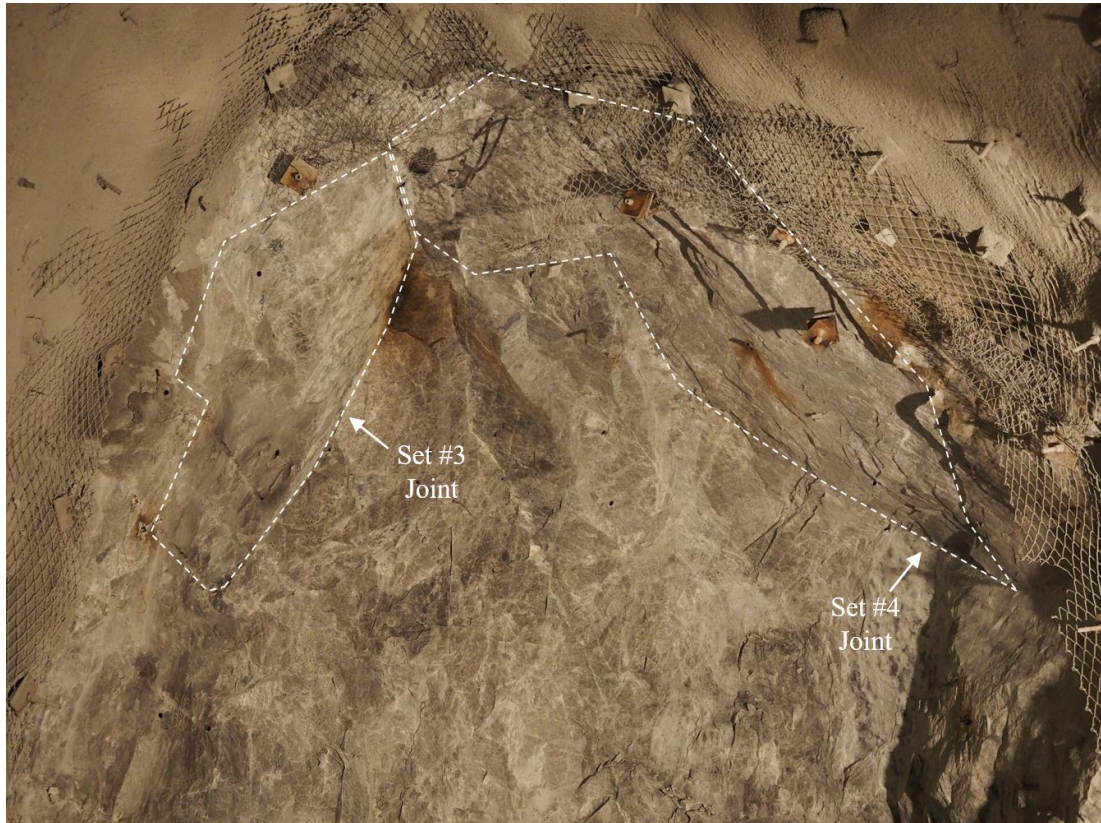


Figure 348 -Structural controls on overbreak in the southern tunnel.

In summary, the absence of any significant overbreak during the initial development indicated that the blast design parameters for the semi-elliptical profile were appropriate for the rock strength. The frequent overbreak of the roof of both tunnels during later development was located at the zones of maximum stress concentration induced by the sub-horizontal major principal stress. An increased rate of seismic activity coincided with increased overbreak. The higher overall seismic energy release and seismic potency recorded in the roof of the southern tunnel was consistent with the deeper overbreak recorded there, when compared to that in the north.

Rock that was damaged due to overstressing on the tunnel boundary was either ejected naturally via spalling, or brought down during mechanically scaling, in order to reduce the static ground support load. The limit of this overbreak was frequently defined by joint set geometries identified by SAFEX, in particular Set #1 and #3 joints in the walls and Set #4 joints in the roof. There was greater control maintained on the excavation profile in the northern tunnel where destressing was applied. It was considered most likely that the rounded profile minimised stress concentrations and instability. Furthermore, the superior profile performance in this tunnel indicated that the destressing charges in the face did not adversely affect the final profile shape.

6.5 Ground Penetrating Radar Geophysics

Prior to construction of the experimental tunnels, it was anticipated that direct visual observation of face destressing fractures would be limited. The 0.3m-long buffer zone of unblasted rock designed to be left between the toe of the conventional development charges and the collar of the destressing loads was expected to prevent most destressing fractures from being visible. As a result, geophysical methods of quantifying the destressing fracture networks were initially considered in lieu of visual observations. Specifically, ground penetrating radar (GPR) was regarded as a potentially viable method of mapping fracture intensity, given the previous success of this technique for destressing applications in South African gold mines (Mahne, 2004 and Topper, 2007).

Use of GPR for the specific application of development face destressing in un-mineralised hard rock tunnelling is a significantly different application to that of destressing the production faces of deep gold reefs, where GPR has been used successfully in the past. The main difference being that in hard rock tunnelling, the blast-induced fractures do not typically provide a highly radar-reflective surface. This is largely due to the rock mass composition, which does not provide high conductivity variations across the fracture surface. As such, there was no known methodology or suitable hardware for GPR investigation for the specific application of development face destressing.

A potential GPR data collection strategy involving two separate borehole radar (BHR) instruments was conceptualised in this research. The concept involved drilling two or more boreholes in the face following destressing, then installing one transmitter BHR and a second receiver some distance away, beyond the zone of anticipated fractures. The concept was intended to implement a modified version of the GeoMole BHR instrument. However, the GeoMole instrument was originally designed for mineral exploration use. Consequently, it has a low frequency range designed to detect significant geological features, such as orebody boundaries and faults, at distances of up to 80m from an exploration borehole. This radar was unsuitable for the destressing application where the features required to be detected were fractures several millimetres in width, within a distance range of at most 7.5 metres. Therefore, it was necessary to investigate an alternative radar frequency for the borehole instrument which was optimised for this destressing application.

In order to select an appropriate frequency for a prototype BHR, a series of GPR surveys were conducted within the Dacite rock type domain prior to construction of the research tunnels. The surveys were conducted in unblasted rock and then repeated in the same rock following initiation of small explosive charges designed to simulate destressing blast damage. The objectives of the surveys were to:

1. test radar general suitability for the rock mass conditions at the mine site, given the rock mass conductivity, groundwater and fracture properties etc.,
2. measure the radar response (fracture intensity) of unblasted and blasted rock,
3. trial several high frequency radars and assess which frequency, if any, had sufficient range and resolution to measure blast-induced fractures.

6.5.1 GPR Instrumentation

GPR instruments consist of a radar transmitter antenna and receiver antenna. The specific instruments utilised during this survey were all monostatic radars. That is, the transmitter and receiver antennas were housed together within the same instrument. In order to perform a GPR survey, the transmitting antenna transmits an electromagnetic pulse into the rock mass. A portion of the energy of this pulse may be reflected by some electrical interface within the rock mass, such as an open joint plane. This reflected energy is detected by the receiver antenna and its distance from the antenna determined based on the velocity of signal propagation as well as the signal travel time.

Three GPR instruments were utilised for the test survey. The first was the GeoMole mono-static BHR unit. This unit was designed by Mining3 (then CRC Mining) and commercialised by GeoMole. The unit was designed primarily for underground mining. It is a slim-fit instrument designed to be deployed in exploration drill holes with diameters as low as 48mm. The instrument has a broadband frequency range of 10-120MHz, and a centre frequency of 50MHz. This gives the instrument a depth range of between 30m and 80m, depending on rock mass dielectric properties. The BHR instrument has a 'blanking distance' due to the inability of the receiver to detect pulses until after the transmitter has completed sending them. In practice this means the BHR cannot resolve reflectors within a certain distance of the instrument (Mouton, 2015). In this case, the blanking zone was within approximately 2m of the borehole. As a result, the BHR was not used to detect simulated destressing fractures during the pre-tunnelling trial surveys, but to gauge baseline rock mass data, if possible.

The two GPR instruments used to compare unblasted to blasted rock mass characteristics during the pre-tunnelling surveys were 500MHz and 800MHz surface radars (Figure 349). These two radar frequencies were chosen based on the dimensions of the simulated destressing pattern and scale of the fractures desired to be mapped. The higher the antenna frequency, the smaller the electrical interfaces that may be identified. This comes at the expense of the depth that may be effectively scanned. The assumed penetration depth of each radar is summarised in Table 55.



Figure 349 - Surface monostatic ground penetrating radars in 500MHz and 800MHz frequency.

Table 55 – Assumed depth of penetration properties for each radar instrument.

Antenna	Nominal Depth (m)	Maximum Depth (m)
500MHz	3.0	7.5
800MHz	1.8	4.0

The surface radars used for these surveys produced a pulse at regular intervals based on a preset time trigger. In order to ensure each radar trace was assigned to the correct location along a survey traverse, a distance calibration was performed on each radar instrument prior to use. Figure 350 presents a photograph of the distance calibration of the 500MHz radar. The process required each radar to be calibrated over a known distance of 10 metres using a measuring wheel (Mouton, 2015).

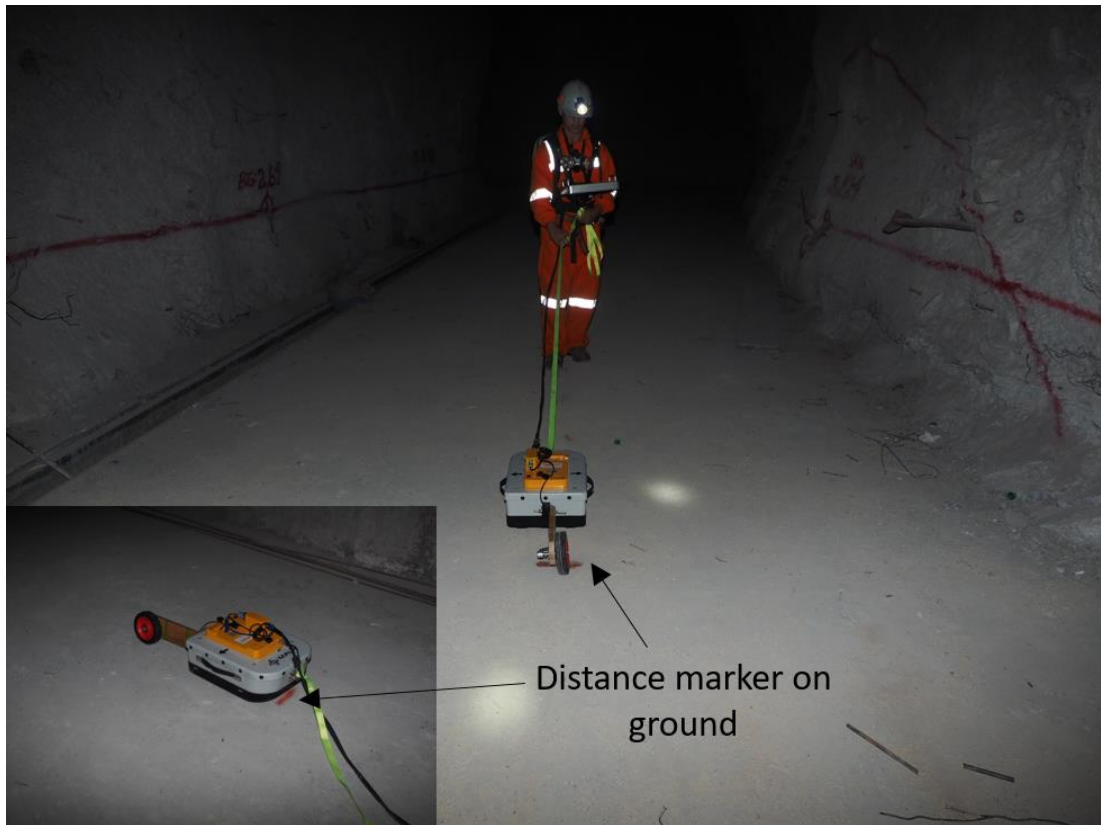


Figure 350 - Radar distance calibration prior to surveying.

6.5.2 GPR Survey Methodology

The radar surveys were conducted in close proximity to the planned site of the experimental tunnels (Figure 351) so as to match the rock type. The borehole radar survey was conducted in one of the pre-existing HI Cell holes. The surveys with the two surface radars were conducted nearby and also in the Dacite rock type.



Figure 351 - Locations of radar geophysics surveys.

The process of conducting the borehole survey involved feeding the radar instrument into the hole in specific distance increments. Its position was controlled using a number of push rods (Figure 352). Data was logged at specific downhole distances using a hand-held PDA device with Bluetooth link to the downhole instrument. The survey was conducted over a length of seven metres from the borehole collar.



Figure 352 - Borehole radar survey.

The GPR surveys using the two surface radars were conducted in the wall of the nearby access development. Initially, two 45mm diameter, 2.0m-long boreholes were drilled in the wall at 1.5m centres and at a height of 1.0m above floor level. Four surveys of the unblasted rock mass were then performed using both the 500MHz and 800MHz radars. The surveys followed four horizontal traverse lines, as depicted in Figure 353. Due to floor-to-floor ground support in all areas, only one of the four initial traverses was able to be surveyed with a bare rock face. This was not ideal, due to the radar signal interference caused by the steel ground support, which included a small number of reinforcement elements and an approximately 75-100mm thick layer of mesh-reinforced shotcrete. The surveys were conducted by manually manoeuvring the radar instruments along the traverse line from right to left, at all times keeping the radar as close to and as perpendicular to the excavation surface as possible.

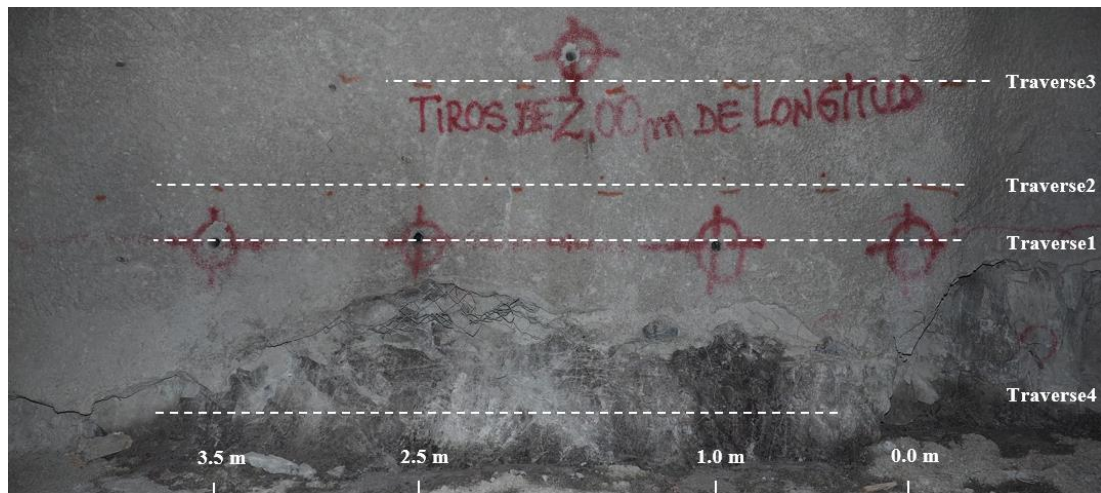


Figure 353 - Preliminary GPR survey traverses prior to simulated destressing blasts.

Following completion of the 500MHz and 800MHz surveys of the unblasted rock mass, the two central boreholes were charged and fired to simulate destressing damage. The simulated destressing charges consisted of a 0.5m long ANFO load at the borehole toe, with 0.3m of stemming. The 1.5m horizontal distance of separation of the two charges was the same distance indicated by the HSBM analysis as being optimal for cross-borehole fracture interactions in the Dacite rock type. The borehole spacing was also the same as that which was implemented in the final destressing design of the northern tunnel, albeit with a slightly different row orientation with respect to the major principal stress. Figure 354 presents a sketch of the geometry of the simulated destressing charges used for the radar trials. Following initiation of the explosives, the surface radar surveys were repeated following the same traverse lines as those of the original survey. Some cratering at the borehole collars caused ejection of the ground support layer. This meant that the second radar surveys were conducted over a bare rock surface and thus had less interference from the steel ground support elements (Figure 355).

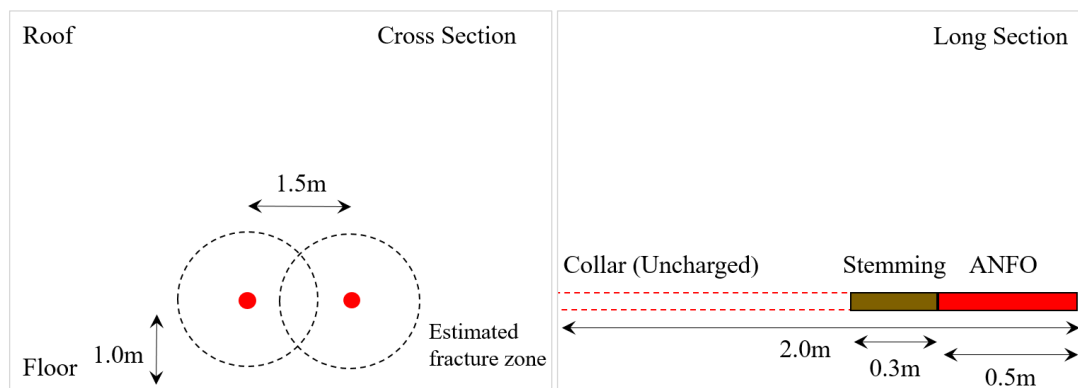


Figure 354 - Geometry of simulated destressing charges for GPR survey.



Figure 355 - GPR survey of the rock mass following simulated destressing blast damage.

6.5.3 Survey Results

A radargram of the Dacite rock type generated by the GeoMole borehole instrument is presented in Figure 356. It was appreciated from the outset that this borehole radar was unlikely to record any valid structural features, given the radar's low frequency characteristics and the relative uniformity of the local geology at the resolution scale of the instrument. The main intent of the BHR survey was to demonstrate the process, gain exposure to the instrument hardware in preparation for potential future prototype trials and to see what reflections, if any, were visible. Consistent with expectations, there were no radar reflections of structural features recorded within the scan.

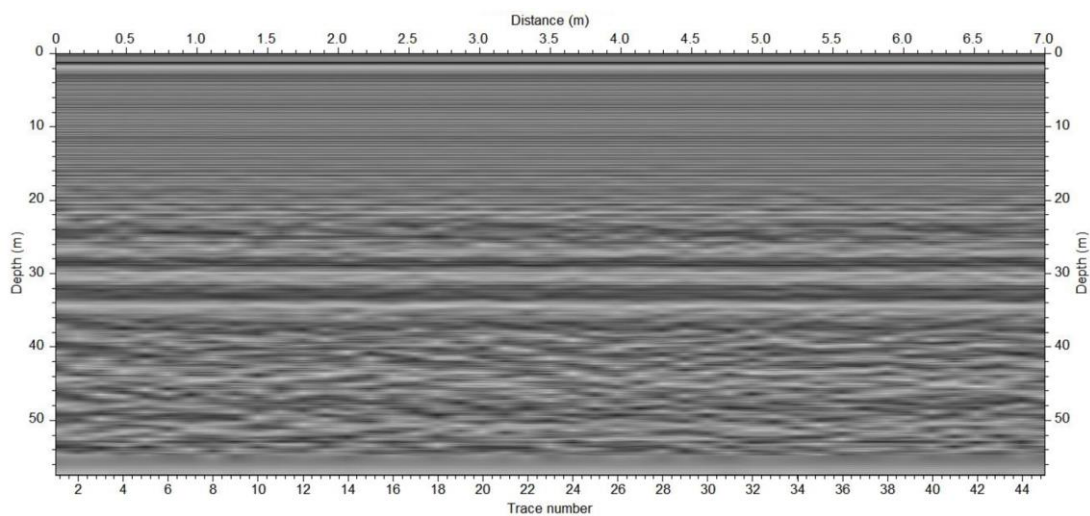


Figure 356 - Radargram of GeoMole borehole radar.

In terms of the surface radar instruments, each of the four aforementioned survey traverses were scanned with both the 500MHz and 800MHz radars both before and after blasting, giving a total of sixteen radar surveys. The radargrams were visually compared in an effort to evaluate the ground conditions before and after the simulated destressing blasts. The radargrams of all sixteen surveys are presented in Appendix C. Some specific examples of observations are discussed here. Overall, the GPR data quality varied from good to poor. The data quality was primarily influenced by the uneven surface profile of the traverse, which despite best efforts resulted in the radar being positioned at various angles and distances from the rock surface. Steel ground support also interfered with the radar scans, causing some artefacts in the recorded data.

The data collected prior to blasting was often affected by high amplitude reverberations (Figure 357). These were interpreted to have masked the reflections of natural rock features in some, but not all surveys (Mouton, 2015). Some radar-reflective features were only visible in the post-blasting radargrams (Figure 358). Two possible reasons for the visibility of features solely in the post-blasting surveys were:

1. The absence of the ground support layer during the post-blasting surveys meant that high amplitude reverberations caused by the support layer were no longer present in the data,
2. The amplified reflections were due to legitimate rock mass structural features that were damaged by the simulated destressing blast.

The specific cause of the visible reflections in the post-blasting scan data could not be conclusively established.

The ground support layer present for the initial surveys did not always inhibit the detection of sub-surface radar reflective features, as indicated in Figure 359 and Figure 360. In this case involving Traverse 4 with the 500MHz radar, visible reflections were present in both pre and post-blasting GPR data, indicating that the radar survey was unaffected by the support layer. There was also evidence of new reflections in the post-blasting data, which may have been natural structural features or new fractures (Mouton, 2015).

Overall, there was no clearly identifiable zone of blast-induced damage associated with the location of the two simulated destressing loads. Cratering of both blasthole collars suggested that the charge confinement may have been insufficient to generate significant fracturing. Alternatively, given the anisotropic stress conditions, the blast-induced fractures may have been preferentially created sub-parallel to the scan axis of the radar. A low angle of incidence between the scan axis and an open fracture plane would be unlikely to return strong radar reflections (Mouton, 2015). It may also have been the case that the chosen radar frequencies did not provide sufficient resolution to detect what would be millimetre or even sub-millimetre-wide fractures.

The orientation of some reflection features appeared to be consistent with oblique jointing/veining and therefore inconsistent with radial fracturing. One example is the 500MHz Traverse 4 data (Figure 359). It is therefore more likely that the reflection features were in fact quartz-filled veins, rather than blast-induced radial fractures.

In the absence of any other distinct reflection features in the radargrams, it was concluded that the minute radial fractures of the explosive charges were of insufficient size to be detected by either of the radars. However, the fact that reflective features were identified at depths of up to 3.0m indicated that these radar frequencies were effective in penetrating the Dacite rock mass. The visual analysis of the radargrams indicated that the 500MHz radar provided an effective signal penetration depth of approximately 4.0m, which was a superior to that of the 800MHz instrument.

It appeared likely that the small size and limited radar-reflectivity of the blasting induced radial fractures prohibited their detection in this specific test. Only in the event of a sufficient dielectric contrast existing between the intact rock and fracture surface would the GPR method be likely to identify blast damage associated with destressing (Mouton, 2015). The results of these initial radar surveys indicated that significantly more research was required in order to establish the optimal hardware characteristics for routine GPR survey of destressing fractures in similar hard rock tunnelling applications. Also, considering the manufacturing lead-time for a prototype borehole instrument with the necessary specifications, a decision was made to remove GPR from the scope of the experimental tunnelling instrumentation plan and focus on seismic data and visual observations of the fracture networks. Further focused research in the development of GPR for this application will be recommended.

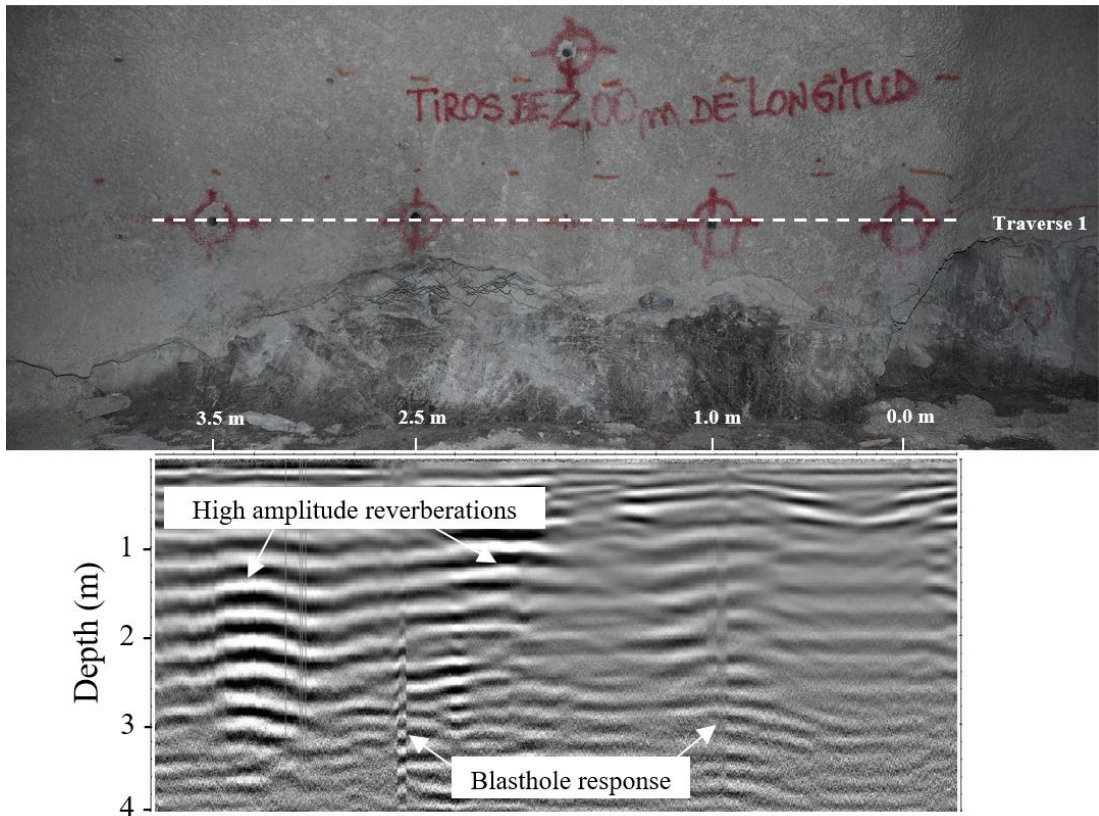


Figure 357 - GPR radargram, 500MHz, Traverse 1, prior to blasting.

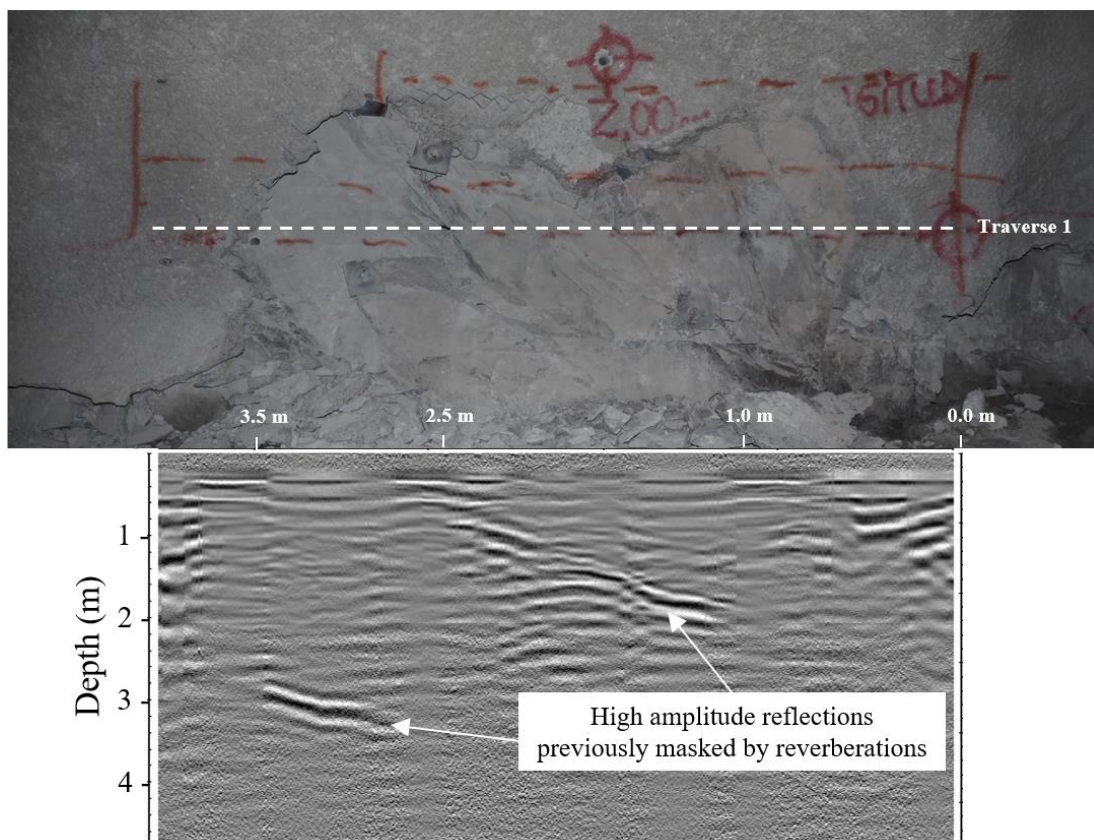


Figure 358 - GPR radargram, 500MHz, Traverse 1, post-blasting.

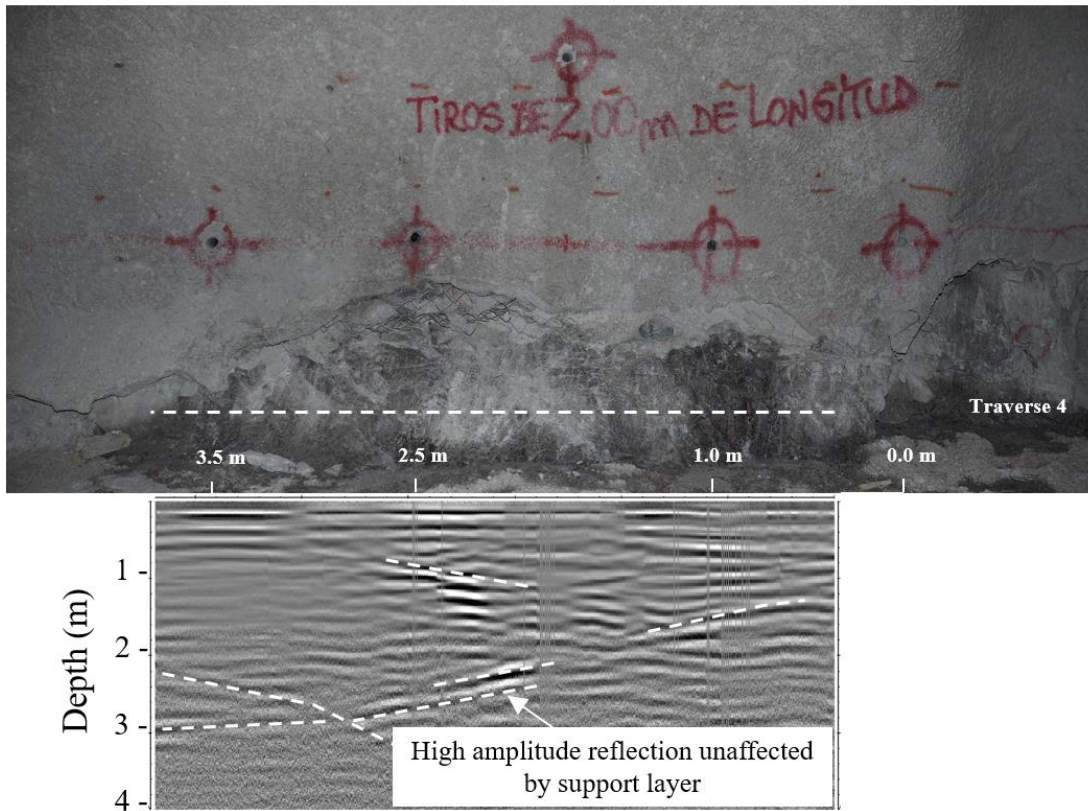


Figure 359 - GPR radargram, 500MHz, Traverse 4, prior to blasting.

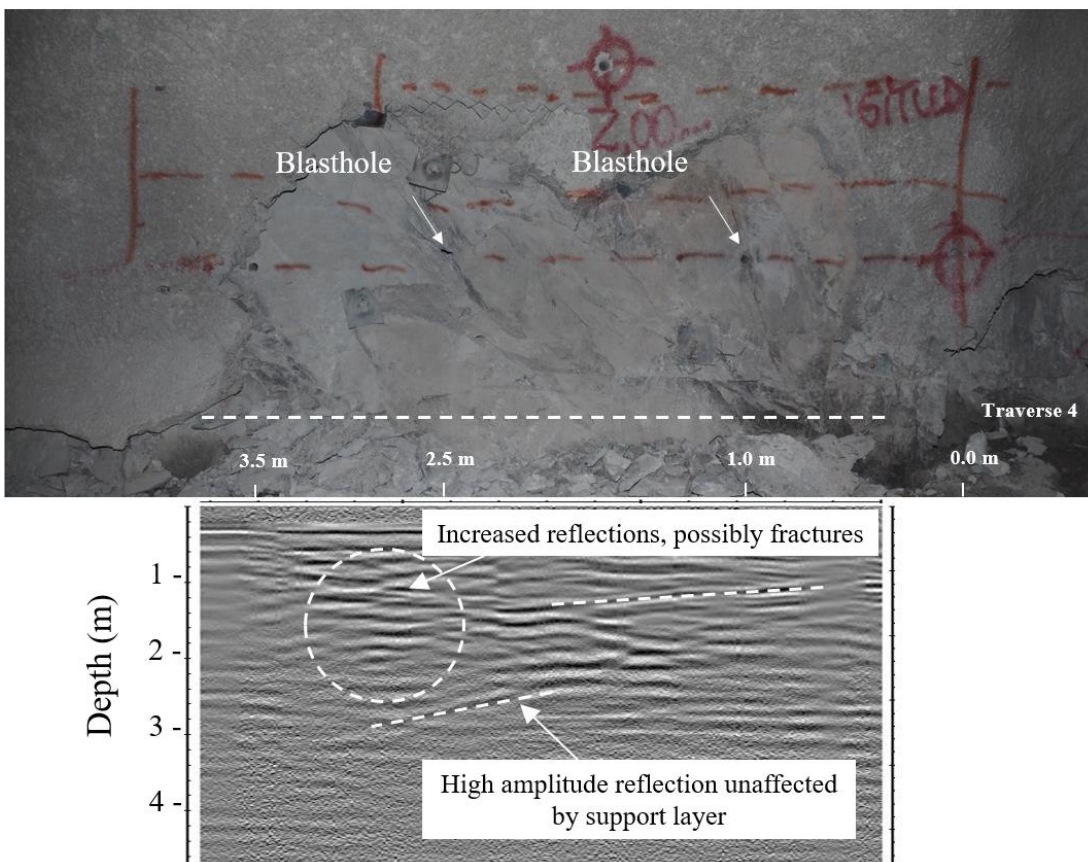


Figure 360 - GPR radargram, 500MHz, Traverse 4, post-blasting.

Chapter 7

Conclusions & Recommendations

7.1 Conclusions

This thesis has proposed an innovative method for the design and construction of deep hard rock tunnels where violent stress-driven instability of the rock mass can occur very soon after construction. This method has been implemented in a practical, full scale tunnelling trial at a deep mine site, and the rock mass response has been monitored and compared to that of conventional development. The methodology proposed here provides an alternative to the prevailing design and construction strategies, which in recent years have proven to be unsustainable at numerous underground mining projects.

The design process proposed in this thesis follows six key stages. The first stage is to characterise the rock mass strength, structure, stress and strain. This requires investment in data collection, including stress measurement and rock strength testing from exploration core drilling, as well as numerical mine modelling. The second stage is a stability assessment. Violent stress-driven spalling and pillar crushing of hard rock excavations are known to initiate at specific ratios of strength to induced stress, which vary predictably depending on rock type. The stability assessment therefore forecasts the onset of tunnel instability based on the prevailing geotechnical conditions identified by the rock mass characterisation. Spatial maps of potential instability may be readily prepared at either the tunnel or global mine scale using 3D data modelling software.

The third stage of the design process is the definition of an excavation geometry which is harmonic to the high stress conditions and as naturally stable as possible. The fourth stage is to prepare a development blast design to suit this excavation shape, which also includes face destressing charges. The intent of destress blasting is to fracture the rock mass in such a way that the rock stiffness, strain gradients and associated potential for violent instability are all reduced. The optimal destressing design is suggested to be one in which the explosive charges are aligned in rows sub-parallel, yet almost oblique to the major principal stress. When detonated, these charges dilate natural rock joints and create new radial fractures, thus facilitating shear within the rock mass, with minimal deformation. The HSBM modelling software has been demonstrated as a suitable tool with which to model the explosive process, thus optimising the blast design parameters to achieve this objective in each specific rock mass environment.

Chapter 7: Conclusions & Recommendations

The fifth design task is to accurately quantify the expected loading conditions on ground support. The method of doing so utilises a combination of analytical, probabilistic and empirical techniques. The demand assessment is based on the predictable physical characteristics of the instability. These include its mass and ejection velocity, both of which are readily quantifiable from a comprehensive characterisation of rock mass strength, structure and induced stress. The demand assessment first quantifies the mass of instability for the predicted modes of failure, which at a minimum include spalling and structurally-controlled block ejection. For structurally controlled failures, the SAFEX software package was used to identify the rock blocks that were expected to generate the largest load demand. The geometry and mass of these blocks are then defined probabilistically. The demand assessment estimates the ejection velocity of the failure based on the UCS strength. Finally, the kinetic energy demand is quantified analytically and the displacement and force demands defined empirically.

The sixth and final stage of the design process is to specify a ground support scheme arrangement with sufficient energy dissipation and displacement capacity to exceed the rock mass demand. The selection of suitable reinforcement and surface support components for the ground support scheme is conducted with reference to the large database of static and dynamic strength testing results compiled by the WA School of Mines. An updated reinforcement design chart has been prepared, which guides the selection of reinforcement elements in either single and dual layered ground support schemes, depending on the energy dissipation and displacement demand of the rock mass. Surface support components are chosen based on WASM testing results. It has been proposed that the optimum ground support scheme design for conditions of extremely high energy demand is as follows:

Primary Ground Support Layer

- 75-100mm shotcrete from floor to floor, internally reinforced with high tensile woven mesh, such as G80/4,
- 1m x 1m staggered pattern of high capacity CMC or DMFC reinforcement, such as 25mm mild steel threaded bar, fully cement encapsulated, up to 3.5m embedment length,

Secondary Ground Support Layer

- External layer of high tensile woven mesh from floor to floor (with wire lacing in overlaps and secondary plates on primary reinforcement elements for load transfer)
- 1m x 1m staggered infill pattern of twin plain strand, CMC, fully cement encapsulated and tensioned deep cable bolt reinforcement, >5m embedment length.

The constructability of this ground support scheme was tested using fully mechanised equipment. Development jumbos with a mechanised meshing arm, 10-bolt capacity rotating reinforcement carousel and grouting capability were used to install the primary layer of reinforcement and surface support. This equipment eliminated exposure of the operators to the unsupported and potentially unstable rock at the face while the primary ground support layer was installed. The multiple layers of ground support were installed in a staged sequence. The primary layer was installed immediately for each development cut. The secondary layer was installed in short repetitive campaigns after several advances, but with no more than a 12m lag from the face. This staged sequence ensured that the secondary layer was installed as efficiently as possible, and prior to the onset of deep structurally controlled instability.

Development face destress blasting was also trialled during the constructions. The final optimised design that was implemented included several rows of destressing charges oriented sub-parallel, yet almost oblique to the major principal stress. The charges were spaced consistently at 1.5m within each row, in order to foster fracture interaction between the charges and a shear response from the rock mass, with minimal deformation. The destressing charges consisted of 63mm diameter, collar primed, fully coupled and confined ANFO loads. The loads were stemmed in order to maximise borehole pressures and increase gas volumes penetrating into the natural discontinuities surrounding the charges. The destressing loads were 2.9m long, spanning from 0.3 to 3.2m ahead of the development face. These charges were desired to dilate existing joints in the rock, as well as create new fractures parallel to the charge rows. This facilitated multiple shear mechanisms of failure and strain reduction surrounding the face. It was proposed that such destress blasting designs should be optimised for the specific rock mass conditions of each application.

Chapter 7: Conclusions & Recommendations

High resolution seismic monitoring was utilised to record the rock mass response to both conventional and destressing development. The data indicated that the seismogenic zone surrounding the conventional development was highly consistent in its shape and size from blast-to-blast. It formed a crescent shape around the face, centred on the zones of high stress concentration. By contrast, the seismogenic zone associated with destress blasting was less consistent in its spatial characteristics. It was generally larger, with more erratic boundaries. Destress blasting did not cause the seismogenic zone to be uniformly translated further ahead of the face. Instead, spatial analysis of the data indicated a broader distribution of stress-driven instability in the opposite direction. That is, surrounding the unsupported walls of the excavation.

The face was the most unstable surface in both the conventional and destressing development in terms of the number of events, radiated energy and seismic potency. However, these parameters were usually reduced ahead of the face when destressing was applied. The consequence was a redistribution and modest increase in these parameters around the unsupported walls. Spatial analysis indicated that the density of events around the conventional development face increased rapidly over short distances. This was deemed to be characteristic of high rock mass stiffness and strain gradients. In the destressing tunnel, the spatial density of seismicity changed much more gradually. Energy release and damage were also generally lower and/or more broadly spatially distributed, indicating that destressing reduced rock mass stiffness.

Analysis of seismic source mechanism data indicated that a much wider variety of failure mechanisms surrounded the face where destress blasting was implemented. When compared to the conventional tunnel excavated in rock with the same pre-existing physical and structural characteristics, the greater variety of mechanisms associated with destressing provided significantly increase pathways for rock mass deformation, however small the deformations may have been. The greater variety of failure mechanisms further supported the conclusion that destress blasting reduced the rock mass stiffness. This in turn was interpreted to have reduced the strain gradients and strain energy accumulation in the destressing tunnel. Following destressing, the majority of recorded seismic source mechanisms were consistent with crack closure along pre-existing natural joints. Only a minority of the mechanisms were consistent with shear sub-parallel to the major principal stress along the likely planes of fracture interaction between adjacent destressing charges.

Chapter 7: Conclusions & Recommendations

Visual observations were made of the fracture networks associated with face distress blasting. There was clear evidence of radial fracturing through intact rock, as well as gas penetration into natural joint planes causing their dilation. Most observations of fractures were made along joints oriented sub-parallel to the major principal stress. One observation was made where explosive gasses originating from a single destressing charge likely migrated through multiple joint set orientations. In another case, explosive residues were also observed along the entire length of a continuous fracture spanning two destressing charges spaced 1.8m apart. This was clear evidence of gas interaction between adjacent destressing charges causing dilation of pre-existing joint structures. These observations supported the numerical optimisation of the blast design in HSBM, which indicated fracture interaction between destressing charges 1.5m apart along planes sub-parallel to the major principal stress.

Laser scanning of the excavations revealed details of the overbreak geometry. Two main characteristics of the overbreak were noted. First, overbreak was primarily located in the zone of highest stress concentration on the tunnel boundary, typically the tunnel roof and adjacent shoulders. Secondly, the overbreak dimensions were structurally controlled, forming complex tetrahedral and polyhedral geometries limited by the known joint sets. Although the overbreak was consistent with structurally-controlled geometry, the mechanism of overbreak was visually observed to be gradual, progressive spalling of the unsupported rock prior to installation of the ground support. The final overbreak geometry was not the result of a single large ejection. A distinction must therefore be made between progressive overbreak and structurally controlled block ejection, which may place large instantaneous demand on ground support at a later stage. The overbreak geometry did confirm that the SAFEX analysis defined realistic tetrahedral block shapes on the tunnel boundary.

Ground penetrating radar scans were also performed on blasted and unblasted rock in an effort to test the effectiveness of several radar frequencies when detecting blast-induced fractures. These tests were intended to inform the manufacture of a prototype borehole radar device which could be used for routine monitoring of distress blasting performance. The surveys indicated that radial blast fractures were very difficult to identify in the Dacite host rock. Some potentially blasting-related reflections were visible in the radargrams of some scans. The 500-600MHz frequency band was suggested to be the most promising for future GPR destressing investigations.

7.2 Recommendations for Future Research

A number of suggestions arise for future research. The recommended endeavours are as follows:

1. It is recommended to repeat this experiment in an environment of similarly strong rock where the major principal stress is in the order of 75-100MPa. Firstly, this will allow collection of seismic data related to distress blasting performance in much higher stress regimes, and an evaluation of the relevance of the conclusions of this thesis for those conditions. Furthermore, repetition of this work in a higher stress regime may see the excavations loaded to late-stage, high energy demand failure mechanisms. This will permit field performance assessment of the twin-layer ground support scheme after high demand instability, which was not able to be performed in this case due to the comparatively modest stresses.
2. It would be advantageous to repeat a distress blasting trial using electronic detonators for all charges and local blast vibration monitoring. Electronic detonators will ensure simultaneous detonation of all distressing charges, maximum gas pressure and therefore the highest likelihood of generating the fracture networks and rock mass damage needed to facilitate distressing. The non-electric detonators used during this experiment are sub-optimal for this application, due to the potential for timing scatter of the initiations.
3. It has been suggested that the 2.5m/s variability in ejection velocity of the Kusui (2015) scale tunnel experiments had some dependence upon the rock mass structure and discontinuity strength within the tested samples. This assumption was applied to the ground support design method when estimating ejection velocity for the rock mass demand assessment. It is recommended to perform further scale tunnel experiments on a wider variety of rock types, with specific attention paid to the structural characteristics of the samples and the effect of those characteristics on the ejection velocity of the scale tunnels.
4. On-site visualisation (OSV) is a geotechnical tool used in some underground infrastructure such as road tunnels. This technology links a load cell on a reinforcement or surface support component to an LED light, the colour of which depends on the percentage consumption of the available axial/radial load capacity of the component. It is recommended to trial this technology in a future field test of the twin-layered ground support scheme that was proposed in this thesis.

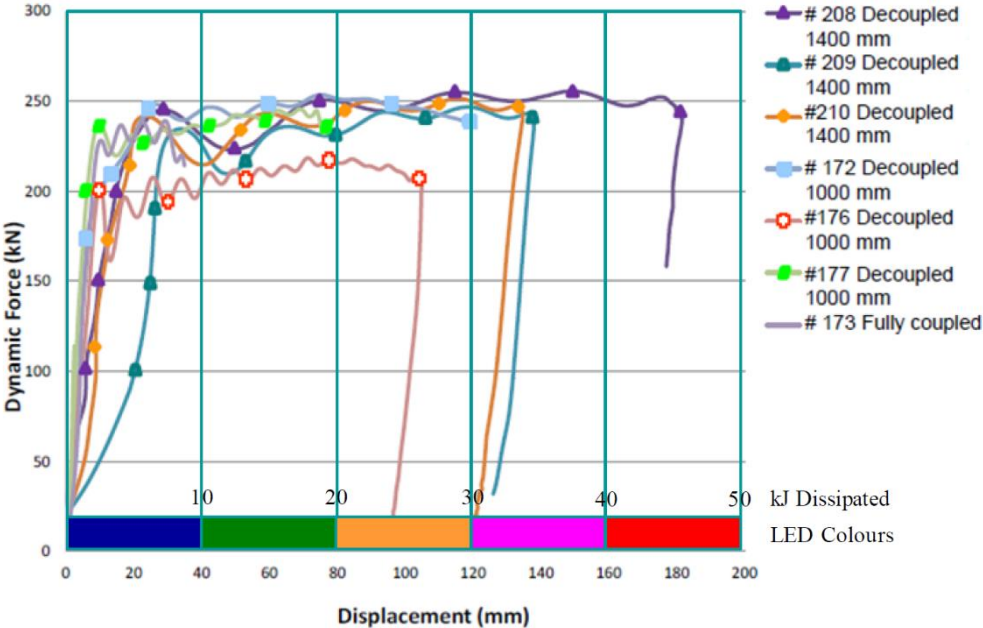


Figure 361 - Example reinforcement capacity versus OSV LED indications.

5. Structural mapping is fundamentally important as a source of input data to the aforementioned excavation design method, as the structural model is used to assess the mass of instability loading the ground support. However, the frequent underground application of shotcrete prevents manual mapping of the walls and roof of the excavation, which, for reasons of instability, cannot usually be accessed prior to the ground support installation. Digital photogrammetry may be used to collect mapping data prior to shotcreting. However, current photogrammetry methods do not provide sufficient data for a full SAFEX analysis. It is therefore recommended to investigate an optimal process of structural data collection in deep and high stress tunnelling conditions where access to the unsupported rock face may not be possible. One option may include a combination of photogrammetry for collection of joint orientation data and then core drilling after support installation to assess the joint surface conditions. It is also recommended that the SAFEX software be modified to include more complex excavation geometries, including curved profiles.
6. The load, displacement and energy dissipation capacities of reinforcement and surface support components previously quoted in this thesis are based on laboratory dynamic testing results of the individual elements at the WA School of Mines. Summing the capacities of each individual components provides an estimation of the total capacity of the ground support scheme which consists of those elements. However, the individual capacities may not reflect the total

capacity of the ground support scheme when in-situ and dynamically loaded by the rock. In order to more accurately quantify the in-situ capacity of a complex ground support scheme consisting of many individual components, it is recommended to dynamically test complete scheme arrangements in a laboratory setting. Efforts in this regard have recently begun. For example, some combined schemes have been tested at the WA School of Mines in Kalgoorlie (Villaescusa, et al., 2016a).

7. Initial tests with surface ground penetrating radar instruments indicated that radar frequencies in the order of 500-600MHz were capable of penetrating the Dacite rock mass up to a depth of 4.0m. Some radar reflective features were identified, although no positive identification of blasting induced fractures could be made. Therefore, it is recommended that further field trials be undertaken using this frequency range of GPR. Field trials should be conducted in hard rock, free of interference with ground support, where a replica destressing charge arrangement may be surveyed. The suggested intent of the trials is to further refine the GPR hardware specifications suited to blast-induced fracture mapping in un-mineralised hard rock.
8. Finally, it is recommended to perform long-term deformation monitoring of otherwise identical destressing and conventional development, in an effort to compare the wall deformations of each. This may provide further evidence to identify any reduction in rock mass stiffness caused by destress blasting.

References

- Adams, D. & Gay, N., 1993. *Preconditioning - A technique for controlling rockbursts*. Rotterdam.
- Ashby, M., 1992. *Materials Selection in Mechanical Design*. 2nd ed. Pergamon Press: Oxford.
- AtlasCopco, 2017. *Boltec E - Technical Specification*. Atlas Copco: Australia.
- Barla, G., 2014. *TBM tunnelling in deep underground excavation in hard rock with spalling behaviour*. Proceedings of the 43rd Geomechanics Colloquium, 25-39.
- Barton, N., Lien, R. & Lunde, J., 1974. *Engineering classification of rock masses for design of tunnel support*. Rock Mechanics, 6(4), pp. 189-236.
- Bawden, W., Dube, S. & Hyett, A., 1995. *A laboratory study on the capacity of fully grouted cable bolts subjected to combined axial and lateral loads*, Department of Mining Engineering, Queens University: Ontario, Canada.
- Beck, D., 2013. *SLX Induced Seismic hazard - Global Coupled Cave Flow (NCA) Rock Mass Deformation (DFE) Analysis*, Confidential report.
- Beck, D., Kassbohm, S. & Putzar, G., 2010. *Multi-scale simulation of ground support designs for extreme tunnel closure*. Proceedings of Caving 2010, Perth, Australia.
- Birch, D., 2018. *WASM Project: Calculation of source parameters and mechanisms of events*, Institute of Mine Seismology: Hobart, Australia.
- Blake, W., 2011. *De-Stressing Development Headings at El Teniente Mine*, Confidential report.
- Borg, T., 1988. *Ortdrivning med avlastningssprängning; Bergmekanisk uppföljning på 815 m nivån i Malmberget*, Report BeFo 331:1/88, SveDeFo 1989:1: (In Swedish).
- Brady, B. & Brown, E., 2004. *Rock Mechanics for Underground Mining*. 3rd ed. Dordrecht, the Netherlands: Kluwer.

- Braithwaite, M., Sharpe, G. & Chitombo, G., 2009. *Simulation of real detonations as an energy source term for the Hybrid Stress Blasting Model*. In: Sanchidrián, J., ed. 9th International Symposium on Rock Fragmentation by Blasting, Granada, Spain, pp.327-333.
- Broch, E. & Sørheim, S., 1984. *Experiences from the planning, construction and supporting of a road tunnel subjected to heavy rockbursting*. Rock Mechanics and Rock Engineering, 17(1), pp. 15-35.
- Brune, J., 1970. *Tectonic stress and the spectra of seismic shear waves*. J. Geophys. Res, Volume 75, pp. 4997-5009 (Correction, J.Geophys. Res., Volume 76, 5002, 1972).
- Brune, J., 1971. *Correction*. J. Geophys. Res, Volume 76, p. 5002.
- Cai, M. & Kaiser, P., 2012. *Rock support design in burst-prone ground utilizing an interactive design tool*. Proceedings of the 46th US Rock Mechanics Symposium, Chicago, USA.
- Carlton, R., Darlington, B. & Mikula, P., 2013. *In situ dynamic drop testing of the MD bolt at Mt Charlotte Gold Mine*. Ground Support 2013 - Y. Potvin and B. Brady (eds), Australian Centre for Geomechanics, Perth, Australia, pp. 207-220.
- Carr, C., Rankin, D. & Fuykschot, J., 1999. *Development of advanced blasting practices at Forrestania Nickel Mines*. Proceedings of EXPLO '99, AusIMM, pp. 239-246.
- Christiansson, R., Hakala, M., Kemppainen, K., Siren, T. & Martin, C., 2012. *Findings from large scale in-situ experiments to establish the initiation of spalling*. ISRM International Symposium - EUROCK 2012, Stockholm, Sweden.
- Cullen, M., 1998. *Studies of distress blasting at Campbell Red Lake Mine*, MEng Thesis, Department of Mining and Metallurgical Engineering, McGill University: Montreal, 209pp.
- Cundall, P., 2011. *Lattice method for modelling brittle, jointed rock*. In: Sainsbury, Detournay & Nelson, eds. Continuum and Distinct Element Numerical Modelling

- in Geomechanics, FLACDEM, 2011, Melbourne, Australia, Itasca International Inc. Minneapolis, pp.1-9.
- Cunningham, C., Braithwaite, M. & Parker, I., 2006. *Vixen detonation codes: Energy input for the HSBM*. 9th International Symposium on Rock Fragmentation by Blasting, Santiago, Chile, pp.169-174.
- Daehnke, A., 1997. *Stress wave and fracture propagation in rock*, PhD Thesis: Vienna University of Technology.
- Dempers, G., Seymour, C. & Jenkins, P., 2006. *BHP Billiton Perseverance Deeps Project, Mining Rock Mass Model - Final Report*, Dempers & Seymour Pty Ltd: Perth, Australia.
- Diederichs, M., 2007. *Mechanistic interpretation and practical application of damage and spalling prediction criteria for deep tunnelling*. Canadian Geotechnical Journal, 44(9), pp. 1082-1116.
- Donzé, F., Bouchez, J. & Magnier, S., 1997. *Modelling fractures in rock blasting*. Int. J. Rock Mech. Min. Sci, 34(8), pp. 1153-1163.
- Drover, C., 2014. *Analysis of the rock mass response to mining, reinforcement and surface support failure dynamics at the Perseverance Underground Mine, Leinster*, MEngSc Thesis: Curtin University.
- Drover, C. & Villaescusa, E., 2015a. *Performance of shotcrete surface support following dynamic loading of mining excavations*. Proceedings of Shotcrete for Underground Support XII, Singapore.
- Drover, C. & Villaescusa, E., 2015b. *Estimation of dynamic load demand on a ground support scheme due to a large structurally controlled violent failure - a case study*. Journal of Mining Technology, 125(4).
- Dywidag, 2018. *Dywidag-Systems International*. [Online, Accessed 2018].
- Enaex Servicios S.A., 2016. *Ficha Tecnica Softron*, (Softron Data Sheet).
- Enaex Servicios S.A., 2016. *Ficha Tecnica Tronex* (Tronex Data Sheet).

- Fleetwood, K., 2010. *Near-field blast vibration monitoring and analysis for prediction of blast damage in sub-level open stoping*, Phd thesis, Western Australian School of Mines, Curtin University: Perth, Australia.
- Fleetwood, K., 2011. *Review of development-concurrent distress blasting for management of strain bursting or face spitting*. Unpublished: Curtin University, Kalgoorlie, Australia.
- Fleetwood, K., Villaescusa, E. & Li, J., 2009. *Limitations of using PPV damage models to predict rock mass damage*, Conference of the International Society of Explosive Engineers.
- Frohlich, C. & Apperson, K., 1992. *Earthquake focal mechanisms, moment tensors, and the consistency of seismic activity near plate boundaries*. *Tectonics*, 11(2), pp. 279-296.
- Furtney, J., Cundall, P. & Chitombo, G., 2009. *Developments in numerical modelling of blast induced rock fragmentation: updates from the HSBM project*. International Symposium on Rock Fragmentation by Blasting, Granada, Spain, Taylor & Francis Group, pp.335-342.
- Furtney, J., Cundall, P., Onederra, I. & Sellers, E., 2011. *Numerical modelling of rock blasting: Validation tests for Blo-Up 2.5*. In: Sainsbury, Detournay & Nelson, eds. *Continuum and Distinct Element Numerical Modelling in Geomechanics*, Melbourne, Australia. Itasca International Inc. pp.2-9.
- Geodata, 2016. *Technical Note - VAI ADIT Tunnel*, Geodata: Maipo, Chile.
- GeoSlam, 2013. *Zeb1 User's Manual*.
- Guajardo, A. & Moraga, C., 2014. *Nota Técnica - Medición de esfuerzos in situ No12, Rampa Marina ADIT74*, CODELCO: El Teniente PNNM.
- Gutenberg, B., 1956. *The energy of earthquakes*. *Quart. J. Geol. Soc. London*, Volume 112, pp. 1-14.
- Hagan, T., 1980. *A case for terrestrial photogrammetry in deep-mine rock structure studies*. *International Journal of Rock Mechanics and Mining Sciences*, 17(4), pp. 191-198.

- Hanks, T. & Kanamori, H., 1978. *A moment magnitude scale*. Journal of Geophysical Research, 84(B5), pp. 2348-2350.
- Hoek, E., 1999. *Support for very weak rock associated with faults and shear zones*. In E. Villaescusa, C. Windsor & A. Thompson (eds): *Rock Support & Reinforcement Practice in Mining* (pp. 19-32). Rotterdam: Balkema.
- Hoek, E. & Brown, E., 1980. *Underground Excavations in Rock*. London, UK: IMM.
- Hoek, E. & Marinos, P., 2000. *Predicting tunnel squeezing problems in weak heterogeneous rock masses*. Tunnels and Tunnelling International.
- Hogan, P. & Sullivan, M., 2017. *Interim report on intact rock properties testing for CODELCO Nuevo Nivel Mina*, Western Australian School of Mines, Geomechanics Laboratory: Kalgoorlie, Western Australia.
- Holmberg, R. & Persson, P., 1980. *Design of tunnel perimeter blast hole patterns to prevent rock damage*. Transactions of the Institute of Mining and Metallurgy, Volume 89, pp. A37-A40.
- Hubbert, M. & Willis, D., 1957. *Mechanics of Hydraulic Fracturing*. Trans. AIME, Volume 210, pp. 153-166.
- Hudson, J., Pearce, R. & Rogers, R., 1989. *Source type plot for inversion of the moment tensor*. Journal of Geophysical Research, 94(B1), pp. 765-774.
- Hudyma, M., 2007. *Seismic energy release in the Lift 2 Block Cave, Northparkes Mines*, Technical report for the Australian Centre for Geomechanics: Itasca Consulting Canada Inc, 1 May 2007.
- Hutchinson, D. & Diederichs, M., 1996. *Cablebolting in Underground Mines*. 406pp. Richmond, British Columbia, Canada: Bitech Publishers.
- ISRM, 1978. *Suggested methods for the quantitative description of discontinuities in rock masses*. Int. J. Rock Mech. Min. Sci. & Geomech., Volume 15, pp. 319-368.
- Itasca & Associates, 1998. *Destress Blasting Practices: A Review of the Literature and Current Industrial Practice*. Report submitted to CAMIRO Mining Division, Sudbury, Canada by Itasca Consulting Group Inc & Richard Brummer Associates.

- Jarufe, J. & Vasquez, P., 2013. *Numerical modelling and rock support design in Codelco's New Mine Level panel caving project*. Ground Support 2013, Perth, Australia, pp. 513-523.
- Jung, W., Utagawa, M., Ogata, Y., Seto, M., Katsuyama, K., Miyake, A. & Ogawa, T., 2001. *Effects of rock pressure on crack generation during tunnel blasting*. Japan Explosives Soc. 62, pp. 138-146.
- Kaiser, P. & Cai, M., 2013. *Critical review of design principles for rock support in burst-prone ground - time to rethink!*. Proceedings of Ground Support 2013, Australian Centre for Geomechanics, Perth, Australia.
- Kaiser, P., Tannant, D. & McCreath, D., 1996. *Canadian Rock Burst Support Handbook*. Geomechanics Research Centre: Sudbury.
- Kanamori, H., 1978. *Quantification of Earthquakes*. Nature, Volume 271, pp. 411-414.
- Keilis-Borok, V., 1959. *On estimation of the displacement in an earthquake source and of source dimensions*. Ann. Geofis. (Rome), Volume 12, pp. 205-214.
- Kusui, A., 2015. *Scaled down tunnel testing for comparison of surface support performance*, PhD Thesis, WA School of Mines, Curtin University: Kalgoorlie, Western Australia.
- Kusui, A. & Villaescusa, E., 2016. *Seismic response prior to spalling failure in highly stressed underground tunnels*. Proceedings of the Seventh International Conference & Exhibition on Mass Mining, Sydney, Australia.
- Kusui, A., Villaescusa, E. & Funatsu, T., 2015. *Mechanical behaviour of scaled-down unsupported tunnel walls in hard rock under high stress*. Tunnelling and Underground Space Technology, 60, pp. 30-40.
- Kutter, H. & Fairhurst, C., 1971. *On the fracture process in blasting*. International Journal of Rock Mechanics, pp. 181-202.
- Lajtai, E. & Dzik, E., 1996. *Searching for the damage threshold in intact rock*. Rock Mechanics Tools and Techniques, Aubertin, Hassani & Mitri (eds), pp. 701-708.

- Levkovitch, V., Beck, D. & Reusch, F., 2013. *Numerical simulation of the released energy in strain-softening rock materials and its application in estimating seismic hazard in mines*. 8th International Symposium on Rockbursts and Seismicity in Mines, Geophysical Survey of Russian Academy of Sciences, Obninsk, Mining Institute of Ural Branch of Russian Academy of Sciences, Perm, pp. 259-266.
- Li, C., 2010. *A new energy-absorbing bolt for rock support in high stress rock masses*. International Journal of Rock Mechanics & Mining Sciences, 47(2010), pp. 396-404.
- Lightfoot, N., Kullman, A., Toper, A., Stewart, R., Grodner, M., Janse van Rensburg, A. & Longmore, P., 1996. *Preconditioning to reduce the incidence of face bursts of highly stressed faces*. Safety in Mines Research Advisory Committee.
- Li, J., 2004. *Critical strain of intact rock and rock masses*, PhD Thesis: Curtin University of Technology, 186p.
- Louchnikov, V., Sandy, M., Watson, O., Orunesu, M. & Eremenko, V., 2015. *An overview of surface rock support for deformable ground conditions*. 12th AUSIMM Underground Operators Conference, 24-26 March, 2014, Adelaide, South Australia.
- Lu, W. & Hustrulid, W., 2003. *The Lu-Hustrulid approach for calculating the peak particle velocity caused by blasting*. 2nd World Conference on Explosives and Blasting Technique, 10-12 September, 2003, Prague, Czech Republic, pp.291-300.
- Mahne, W., 2004. *Pre-Conditioning A Tool to Combat Face Bursts at Mponeng*. South African National Institute of Rock Engineering.
- Martin, C., 1993. *The strength of massive Lac du Bonnet granite around underground openings*, PhD Thesis: University of Manitoba, Manitoba, Canada.
- Martin, C., 1997. *The effect of cohesion loss and stress path on brittle rock strength*. Can. Geotech. J, 34(5), pp. 698-725.
- Matthews, K., Hoek, E., Wyllie, D. & Stewart, S., 1980. *Predictions of stable spans for mining at depths below 1000 metres in hard rock*, Golder Associates Report to

- Canada Centre for Mining and Energy Technology (CANMET), Department of Energy and Resources: Ottawa, Ontario, Canada.
- Mendecki, A., 1997. *Seismic Monitoring in Mines*. Chapman & Hall: London.
- Mendecki, A., 2013. *Mine seismology: glossary of selected terms*. St Petersburg-Moscow, Russia.
- Mendecki, A., Lynch, R. & Malovichko, D., 2010. *Routine seismic monitoring in mines*. Perth, Western Australia, s.n.
- Mikula, P., 2012. *Progress with empirical performance charting for confident selection of ground support in seismic conditions*. AusIMM Journal of Mining Technology, 121(4), pp. 192-203.
- Mikula, P., Heal, D. & Hudyma, M., 2008. *Generic seismic risk management plan for underground hardrock mines*, Technical Report: Mine Seismicity and Rockburst Risk Management Project, Australian Centre for Geomechanics.
- Milev, A. et al., 2002. *The meaningful use of peak particle velocities at excavation surfaces for the optimisation of the rockburst criteria for tunnels and stopes*, SIMRAC GAP Project 709 - Final Report: Safety in Mine Research Advisory Committee, Johannesburg.
- Moraga, C., 2015. *Technical Note - In Situ Stress Measurements Site # 18*, Internal Report: CODELCO.
- Morissette, P., Hadjigeorgiou, J. & Thibodeau, D., 2012. *Validating a support performance database based on passive seismic monitoring*. Proceedings of the Sixth International Seminar on Deep and High Stress Mining (Deep Mining 2012), Perth Australia, 28-30 March 2012. Potvin, Y. (ed.). Australian Centre for Geomechanics, pp. 41-55.
- Morton, E., Villaescusa, E. & Rojas, E., 2018. *Seismic response of large scale geological structures at the Esmerelda Mine*, CODELCO Chile. *Publication Pending*.
- Morton, E., Villaescusa, E. & Thompson, A., 2009. *Determination of Energy Absorption Capabilities of Large Scale Shotcrete Panels*. Proceedings of the 2009

- ECI Conference on Shotcrete for Underground Support, Davos, Switzerland, 7-10 June, Paper 6, 20pp.
- Mouton, R., 2015. *Confidential report to CRC Mining*, Applied Scientific Services and Technology Pty Ltd: Perth, Australia.
- Obert, L. & Duvall, W., 1967. *Rock Mechanics and the Design of Structures in Rock*. John Wiley & Sons: New York.
- O'Donnell, J., 1999. *The development and application of destressing techniques in the mines of INCO Limited, Sudbury, Ontario*. A thesis submitted to the School of Graduate Studies in partial fulfillment of the requirements for the Degree of Master of Science, Laurentian University.
- Onederra, I., Catalan, A. & Chitombo, G., 2013. *Modelling fracturing, disturbed and interaction zones around fully confined detonating charges*. Mining Technology, 122(1), pp. 20-32.
- Onederra, I., Chitombo, G., Cundall, P. & Furtney, J., 2009. *Towards a complete validation of the lattice scheme in the Hybrid Stress Blasting Model (HSBM)*. 9th International Symposium on Rock Fragmentation by Blasting, Granada, Spain, Taylor & Francis Group, pp.343-351.
- Onederra, I. & Esen, S., 2003. *An alternative approach to determine the Holmberg-Persson constants for modelling near field peak particle velocity attenuation*. Fragblast: International Journal of Blasting and Fragmentation.
- Ortlepp, 1997. *Rock fracture and rockbursts*, Monograph Series M9, South African Institute of Mining and Metallurgy: Johannesburg, South Africa.
- Ortlepp, W., 1992. *The design of support for the containment of rockburst damage in tunnels*. Rock Support in Mining and Underground Construction, pp. 593-609.
- Ortlepp, W., 1993. *High ground displacement velocities associated with rockburst damage*. Rockbursts and Seismicity in Mines, Volume 93, pp. 101-106.
- Ortlepp, W. & Stacey, T., 1994. *Rockburst mechanisms in tunnels and shafts*. Tunnelling and Underground Space Technology, 9(1), pp. 59-65.

- Peng, Y., Zhenguo, Z., Wenbo, L., Yong, F., Xiangrong, C. & Zhigang, S., 2015. *Mitigation of rock burst events by blasting techniques during deep-tunnel excavation*. *Engineering Geology*, Volume 188, pp. 126-136.
- Player, J., 2012. *Dynamic Testing of Rock Reinforcement Systems*, PhD Thesis: Western Australian School of Mines, Curtin University of Technology, Perth, Western Australia, Australia, 501pp.
- Player, J., Villaescusa, E. & Thompson, A., 2004. *Dynamic testing of rock reinforcement using the momentum transfer concept*. Proc. 5th Int. Symp. Rock Support and Reinforcement, Perth, Balkema, Rotterdam, pp. 327-329.
- Potvin, Y., Jarufe, J. & Wesseloo, J., 2010. *Interpretation of seismic data and numerical modelling of fault reactivation at El Teniente Reservas Norte sector*. *Mining Technology*, 119(3), pp. 175-181.
- Potvin, Y. & Wesseloo, J., 2013. *Towards an Understanding of Dynamic Demand on Ground Support*. *South African Institute of Mining and Metallurgy*, 113(12), pp. 913-922.
- Rees, K., 2012. *The benefits of using photogrammetry in the geological interpretation of the Cosmos Nickel Mine*. *Proceedings of Narrow Vein Mining 2012*, The Australasian Institute of Mining and Metallurgy: Melbourne, pp. 145-148.
- Rocscience, 2018. *Rocscience Dips*. [Online, Accessed 2018].
- Roux, A., Leeman, E. & Denkhaus, H., 1957. *De-Stressing: A Means of Ameliorating Rockburst Conditions. Part 1 - The Concept of De-Stressing and the Results Obtained from its Application*. *South African Institute of Mining and Metallurgy*, pp. 101-119.
- Saharan, M., 2004. *Dynamic modelling of rock fracturing by destress blasting*, PhD Thesis: McGill University.
- Saharan, M. & Mitri, H., 2011. *Destress Blasting as a Mines Safety Tool: Some Fundamental Challenges for Successful Applications*. *First International Symposium on Mine Safety Science and Engineering*, pp. 37-47.

- Sandvik, 2018. *DS411 Rock Support Bolter - Technical Specification*. Sandvik: Mining and Rock Technology.
- Saw, H., Villaescusa, E., Windsor, C. & Thompson, A., 2017. *Surface support capabilities of freshly sprayed fibre reinforced concrete and safe re-entry time for underground excavations*. *Tunnelling and Underground Space Technology*, Volume 64, pp. 34-42.
- Scholz, C., 1990. *The mechanics of earthquakes and faulting*. Cambridge University Press: New York.
- Scott, C., Penney, A. & Fuller, P., 2008. *Competing factors in support selection for the west zone of the Beaconsfield gold mine, Tasmania*. *Narrow Vein Mining Conference*, Ballarat, Victoria, pp. 173-178.
- Scott, J., 1976. *Friction rock stabilizers - a new rock reinforcement method*. Monograph on rock mechanics applications in mining, New York: Society of Mining Engineers, American Institute of Mining, Metallurgical and Petroleum Engineers, pp. 242-249.
- Scott, J., 1983. *Friction rock stabilizer impact upon anchor design and ground control practices*. *Rock bolting: theory and application in underground construction*, Rotterdam; Balkema, pp. 407-418.
- Stillborg, B., 1994. *Professional Users Handbook for Rock Bolting*. Trans Tech Publications: Clausthal-Zellerfeld, Germany.
- Tang, B., 2000. *Rockburst control using distress blasting*, PhD Thesis: McGill University, Montreal, Canada.
- Thompson, A., 2002. *Stability assessment and reinforcement of block assemblies near underground excavations*. In: Hammah, R., Bawden, W., Curran, J., Telesnicki, M., editors, *Mining and tunnelling innovation and opportunities*, Proceedings of the 5th North American rock mechanics symposium and the 17th Tunnelling Association of Canada conference, Toronto, Canada, Toronto: University of Toronto Press 2002:2:1439-46.

- Thompson, A., Villaescusa, E. & Windsor, C., 2012. *Ground Support Terminology and Classification - An Update*. Geotechnical and Geological Engineering, 30(3), pp. 553-580.
- Thompson, A. & Windsor, C., 1992. *A classification system for reinforcement and its use in design*. Proceedings of the Western Australian Conference on Mining Geomechanics, Kalgoorlie, Western Australia, Australia, Western Australian School of Mines, pp. 115-125.
- Tooper, A., 2007. *Destressing/preconditioning to control rockbursts in South African deep-level gold mines*. Proceedings of Challenges in Deep and High Stress Mining, Australian Centre for Geomechanics, pp. 503-515.
- Tooper, A., Grodner, M., Stewart, R. & Lightfoot, N., 1997. *Preconditioning: A rockburst control technique*. Proceedings of Rockbursts and Seismicity in Mines, Balkema, Rotterdam.
- Tooper, A., Kabongo, K., Stewart, R. & Daehnke, A., 1999. *The mechanism, optimisation and effects of preconditioning*. Proceedings of the Sixth International Symposium for Rock Fragmentation by Blasting.
- Varden, R. & Player, J., 2008. *Development and Implementation of the Garford Dynamic Bolt at the Kanowna Belle Mine*. Proceedings of the 10th AusIMM Underground Operators Conference, Launceston, Tasmania, Australia.
- Villaescusa, E., 1991. *A three dimensional model of rock jointing*, PhD Thesis: University of Queensland, Brisbane, Australia.
- Villaescusa, E., 2014. *Geotechnical design for sub level open stoping*. CRC Press.
- Villaescusa, E., 2015a. *CODELCO New Mining Level (NML) - Tunnel P4600 Geotechnical Review*, Report for the CODELCO El Teniente Mine: Chile.
- Villaescusa, E., 2015b. *CODELCO New Mining Level (NML) - Tunnel Adit74 Geotechnical Review*, Report for the CODELCO El Teniente Mine: Chile.
- Villaescusa, E., Azua, J., Player, J., Thompson, A. & Morton, E., 2012. *A Database of Static and Dynamic Energy Absorption of Mesh for Rock Support*. Proceedings of

- the 2012 Australian Mining Technology Conference, Perth, Western Australia, Australia 8-10 October, pp.27-34.
- Villaescusa, E., De Zoysa, A., Player, J. & Thompson, A., 2016a. *Dynamic testing of combined rock bolt and mesh schemes*. Proceedings of the Seventh International Conference & Exhibition on Mass Mining, Sydney, Australia, pp. 789-798.
- Villaescusa, E., Kusui, A. & Drover, C., 2016b. *Ground support design for sudden and violent failures in hardrock tunnels*. Proceedings of the 9th Asian Rock Mechanics Symposium (ARMS 9), Bali, Indonesia.
- Villaescusa, E., Player, J. & Thompson, A., 2014. *A reinforcement design methodology for highly stressed rock masses*. 8th Asian Rock Mechanics Symposium, Sapporo, Japan.
- Villaescusa, E., Seto, M. & Baird, G., 2002. *Stress measurements from oriented core*. Journal of Rock Mechanics and Mining Sciences, Volume 39, pp. 603-615.
- Villaescusa, E., Thompson, A. & Player, J., 2005. *Dynamic Testing of Rock Reinforcement Systems*. Australian Mining Technology Conference, Fremantle, Western Australia.
- Villaescusa, E., Thompson, A., Player, J. & Morton, E., 2010. *Dynamic Testing of Ground Control Systems*, Report on MERIWA Research Project M349A: WA School of Mines, Curtin University of Technology.
- Webber, S., 2000. *Analysis of seismic data from a hard rock Western Australian mine: implications for support design*, Snowden technical report: unpublished.
- Windsor, C., 1995. *Rock mass characterisation - A course on structural characterisation and structural analysis*, Course notes for the Masters of Engineering Science in Mining Geomechanics. Western Australian School of Mines, Curtin University of Technology: Kalgoorlie, Western Australia, Australia, 462pp.
- Windsor, C., 1997. *Rock Reinforcement Systems*. Int. J. Rock Mech. Min. Sc, 34(6), pp. 919-951.

- Windsor, C., 1999. *Systematic design of reinforcement and support schemes for excavations in jointed rock*. Rock Support and Reinforcement Practice in Mining, Villaescusa, Windsor & Thompson (eds), Kalgoorlie, Western Australia.
- Windsor, C., 2008. *Reconciliation of Strain, Structure, Strength & Stress*. Confidential Project Report, Western Australian School of Mines.
- Windsor, C., 2016. *Confidential presentation on SAFEX-Photogrammetry compatibility review*. WA School of Mines, Mining 3.
- Windsor, C., Cavieres, P., Villaescusa, E. & Pereira, J., 2006. *Reconciliation of strain, structure and stress in the El Teniente Mine Region, Chile*, CRC Mining, WA School of Mines: Kalgoorlie, Australia
- Windsor, C., Cavieres, P., Villaescusa, E. & Pereira, J., 2006. *Rock stress tensor measurements at El Teniente Mine, Chile*, CRC Mining, WA School of Mines: Kalgoorlie, Australia.
- Windsor, C. & Thompson, A., 1993. *Rock reinforcement - technology, testing, design and evaluation*. Comprehensive Rock Engineering (eds J.A. Hudson, E.T. Brown, E. Hoek, C. Fairhurst), Pergamon: Oxford, pp. 451-484.
- Windsor, C. & Thompson, A., 1998. *Reinforcement Systems Mechanics, Design, Installation, Testing, Monitoring & Modelling*. Int. J. Rock Mech. Min. Sc., 35(4), p. 453.
- Worotnicki, G. & Walton, R., 1976. *Triaxial hollow inclusion gauges for determination of rock stresses in-situ*. Proc. ISRM Symp. on Investigation of Stress in Rock, Sydney, Supplement, 1-8. Instn Engrs, Aust.: Sydney.
- Yamamoto, K., Kuwahara, Y., Kato, N. & Hirasawa, T., 1990. *Deformation rate analysis: a new method for in-situ stress estimation from inelastic deformation of rock samples under uniaxial compression*. Tohoku Geophysical Journal, Volume 33, pp. 1-13.

Every reasonable effort has been made to acknowledge the owners of copyright material. I would be pleased to hear from any copyright owner who has been omitted or incorrectly acknowledged.

List of Figures

Figure 1 - Pole plot of WASM AE stress measurement data typically used for deep excavation design.	9
Figure 2 – Stress gradient data showing the increase in stress as a function of vertical depth below surface.	9
Figure 3 - Comparison of local stress measurement data with the global database.	10
Figure 4 - Simulated damage to a rock specimen at various strain milestones (Beck, 2013).	11
Figure 5 - Rock mass strain as an indicator of damage adjacent a deep mining excavation (Beck, et al., 2010).	12
Figure 6 - Fisher pole concentrations for structural data and resulting joint sets defined in SAFEX.	14
Figure 7 - SAFEX output of deterministic block parameters.	14
Figure 8 – Chart of UCS data for rock mass characterisation (Windsor, 2008).	15
Figure 9 - Lack of ground support retention following a violent spalling failure of the excavation surface.	16
Figure 10 - Failure of reinforcement elements following violent, structurally controlled instability.	17
Figure 11 - Prediction of the extent of boundary failure around a circular opening (Brady & Brown, 2004)	18
Figure 12 –Rock mass damage in zones of highest stress concentration (Martin, 1997).	18
Figure 13 – Cross section views of stress concentrations at the excavation face (Obert & Duvall, 1967).	19
Figure 14 - Excavation behaviour as a function of the strength/stress ratio. (Barton et al., 1974)	20
Figure 15 - Example of notch formation due to stress-driven brittle failure in an underground tunnel.	21
Figure 16 - Unsupported tunnel spalling as a function of σ_c/σ_{max} (Kusui et al, 2016).	22
Figure 17 - Spalling failure of unsupported semi-circular tunnels at the roof (Villaescusa, et al., 2016b).	23
Figure 18 - Structurally controlled failure with a large depth of instability.	23
Figure 19 – Fault rupture mechanism of excavation instability causing extreme damage (Drover, 2014).	24
Figure 20 – Global scale instability with numerous large structural reactions (Drover, 2014).	25
Figure 21 – Load and acoustic emission count vs. displacement during progressive failure (Kusui, 2015)	26
Figure 22 - Higher strength materials exhibit lower radial strain at failure (Kusui, 2015).	27
Figure 23 - Chart for assessment of energy demand on ground support (Geodata, 2016).	28
Figure 24 - Stress-Strain curve for a Dacite hard rock.	31
Figure 25 - Ejection velocities at spalling for unsupported tunnels in hard rock (Kusui, 2015).	33
Figure 26 - Determination of ejection velocity using a high speed video camera (Kusui, 2015).	33
Figure 27 – Stress data (Windsor, et al., 2006) and excavation orientation (Guajardo & Moraga, 2014).	34
Figure 28 – West-facing view of a violent failure, with ejection vector (\mathbf{E}) being orthogonal to the σ_1 stress.	34
Figure 29 - Fault rupture failure mechanisms result in highly concentrated loads on ground support.	37
Figure 30 - Fault rupture causing severe excavation damage, with very high ejection velocity of instability.	38
Figure 31 - Violent fault rupture causing severe ground support damage.	38
Figure 32 - Shear failure mode of pillar crushing in vertically loaded test samples (Kusui, 2015).	39
Figure 33 - Displacement demand during spalling (left) and pillar shear failure (right) (Kusui, 2015).	40
Figure 34 - Generic reinforcement system (Thompson, et al., 2012).	41
Figure 35 - Ground support capacity performance indicators (Thompson, et al., 2012).	42
Figure 36 - Reinforcement loading due to axial rock mass deformations (Thompson, et al., 2012).	43
Figure 37 - Reinforcement loading due to block translations (Thompson, et al., 2012).	43
Figure 38 – Reinforcement loading due to block translations and rotations (Thompson, et al., 2012).	44
Figure 39 - Reinforcement classes defined by internal load transfer mechanism (Thompson, et al., 2012).	44
Figure 40 – Reinforcement load transfer from unstable to stable rock (Thompson, et al., 2012).	45
Figure 41 – Element force distributions for the three reinforcement classes (Thompson, et al., 2012).	47
Figure 42 - WASM reinforcement design chart (Villaescusa, et al., 2014).	49
Figure 43 - Examples of point, strip and areal surface support components.	52
Figure 44 - Load transfer from surface support to adjacent reinforcement systems (Thompson, et al., 2012).	52
Figure 45 - Load transfer from surface support to surrounding rock via adhesion (Thompson, et al., 2012).	53
Figure 46 – Shotcrete static load-displacement and energy dissipation results (Morton, et al., 2009).	54
Figure 47 – Regular damage patterns in mesh-reinforced shotcrete after violent loading (Drover, 2014).	55
Figure 48 - Mesh-reinforced shotcrete failure in large blocks due to high energy demand (Drover, 2014).	55
Figure 49 – Shotcrete failure prior to significant mesh loading (Drover & Villaescusa, 2015a).	56

Figure 50 - WASM dynamic database of mesh strength and deformability (Villaescusa, et al., 2012).	57
Figure 51 - Mechanised construction with frequent human-machine interaction at the unsupported face.	59
Figure 52 – Failure of temporary face support due to violent stress-driven instability.	60
Figure 53 - The theoretical effect of destress blasting on stress concentrations (Tooper, et al., 1999).	61
Figure 54 - Consecutive stages in the fracture process of a confined charge (Kutter & Fairhurst, 1971).	64
Figure 55 - Effect of stress on the direction of fracturing in rock during blasting (Jung, et al., 2001).	65
Figure 56 – Standard destress blasting pattern of the Garson mine, Canada (Blake, 2011).	67
Figure 57 – Standard destress blasting pattern of the Inco mines, Canada (O'Donnell, 1999).	67
Figure 58 – Standard destress blasting pattern of the Cosmic Boy mine, Australia (Carr, et al., 1999).	67
Figure 59 – Perimeter destress blasting for highly localised asymmetric instability (Borg, 1988).	67
Figure 60 - Modelled destress blast designs, reproduced after (Tang, 2000).	71
Figure 61 - Spatial analysis of the destressing seismogenic zone at a wide (Tooper, 2007).	74
Figure 62 - Ground penetrating radar scan of a rock mass before destress blasting (Tooper, 2007).	76
Figure 63 - Ground penetrating radar scan of a rock mass following destress blasting (Tooper, 2007).	76
Figure 64 – Location of experimental tunnels relative to adjacent mine infrastructure and host geology.	87
Figure 65 - Detailed plan view of two parallel tunnels constructed for the experiment.	88
Figure 66 - Plan view of structural interpretations surrounding the location of experimental tunnels.	90
Figure 67 – Photogrammetry data of joint structures in the Dacite rock type.	91
Figure 68 - Window mapping data of joint structures in the Dacite rock type.	92
Figure 69 - Frequency distribution for all joint set dip data.	93
Figure 70 - Frequency distribution for all joint set dip direction data.	93
Figure 71 - Plan view of research tunnels showing position of pilot boreholes for strength characterisation.	94
Figure 72 - Examples of intact and stress-damaged diskings taken from the pilot boreholes.	95
Figure 73 - Stress-related core diskings along the north and south tunnel pilot boreholes.	95
Figure 74 - Variability in Dacite UCS as a function of distance along the research tunnels.	97
Figure 75 - Frequency distribution of all UCS values for Dacite rock.	97
Figure 76 – Frequency distribution of failure mechanism of Dacite rock as a function of UCS.	98
Figure 77 - Analysis of Dacite Young's Modulus with other historic mine data.	99
Figure 78 - Analysis of Dacite Poisson's Ratio with other historic mine data.	99
Figure 79 – Comparison analysis of the elastic properties of Dacite and mafic rock types.	100
Figure 80 - Triaxial strength testing peak values for Dacite rock.	101
Figure 81 - Triaxial strength testing residual values for Dacite rock.	101
Figure 82 - Triaxial strength testing peak and residual comparison for Dacite rock.	101
Figure 83 - Frequency distribution of all UTS values for Dacite rock.	102
Figure 84 - Frequency distribution of UTS values for Dacite core suffering stress-related damage.	102
Figure 85 - Frequency distribution of all Fracture Toughness results for Dacite rock.	103
Figure 86 - Fracture Toughness of engineering materials plotted against Strength (Ashby, 1992).	104
Figure 87 - Fracture Toughness versus UTS for Dacite rock.	105
Figure 88 - Fracture Toughness sampling locations (blue/orange) relative to core diskings (black).	105
Figure 89 – Fracture Toughness versus UTS data subdivided by the presence of stress-related core diskings.	105
Figure 90 – Principal stress magnitude distribution with depth (Windsor, et al., 2006).	107
Figure 91 – Principal stress orientations at the mine site (Windsor, et al., 2006).	107
Figure 92 - Location of CSIRO HI Cell stress measurements taken prior to tunnelling (Moraga, 2015).	108
Figure 93 - Abaqus numerical model results of major principal stress (σ_1) magnitude and orientation.	109
Figure 94- Abaqus numerical model results of minor principal stress (σ_3) magnitude and orientation.	109
Figure 95 - Generic mechanisms of tunnel instability controlled by the quasi-static stress.	111
Figure 96 - The generic mechanism of tunnel instability triggered by remote seismicity.	112
Figure 97 - Stability chart for spatially isolated excavations.	113
Figure 98 – Stability chart for excavations with thin pillars.	113
Figure 99 – Mechanism 1: shear failure of the back and floor through intact rock due to σ_1 increase.	115
Figure 100 – Mechanism 2: shear failure of the walls along set #3 joints due to σ_3 increase.	115

Figure 101 – Mechanism 3:shear failure of the walls along set #1 joints due to σ_1 and/or σ_3 increase.	115
Figure 102 - Example of spalling failure with a shallow depth of instability.....	117
Figure 103 – Reinforcement and surface support failure, with ejection of large blocks.	118
Figure 104 - Typical face conditions for structural mapping.	120
Figure 105 – a) raw joint set data with fisher contours and b) associated joint set selection windows.	120
Figure 106 - Joint set great circles (weighted) and pole groupings.	121
Figure 107 - Typical joint conditions in the face of the northern tunnel.	122
Figure 108 – Deterministically calculated block geometries for the excavation roof.....	125
Figure 109 - Deterministically calculated maximum block geometry for the excavation sidewall.....	127
Figure 110 - Range of joint set orientations for all probabilistically simulated blocks.	129
Figure 111 - Equal angle lower hemisphere stereonets of joint poles for all probabilistic block analyses.	130
Figure 112 – Probabilistic results of trace length limited apex height for each block shape.	131
Figure 113 - Probabilistic results for the apex height, free face area and mass of Block 1.	131
Figure 114 - Probabilistic results for the apex height, free face area and mass of Block 2.	132
Figure 115- Probabilistic results for the apex height, free face area and mass of Block 3.	132
Figure 116 - Probabilistic results for the apex height, free face area and mass of Block 4.	133
Figure 117 - Cumulative frequency of probabilistically defined apex heights for all block geometries.	134
Figure 118 - Probabilistic results for the apex height, free face area and mass of wall Block 2.....	135
Figure 119- Kinematic failure modes for all probabilistically identified block geometries.....	136
Figure 120 - Spectral analysis results for the Dacite structural model.....	137
Figure 121 – Conventional excavation shape of the southern research tunnel.....	138
Figure 122 - Profile geometry of the southern research tunnel with conventional square-walled design.....	139
Figure 123 – Conventional development drill and blast pattern design implemented in the southern tunnel.....	140
Figure 124 - Number of explosive charges for each detonator delay.....	142
Figure 125 - Distribution of explosive weight to each delay.....	142
Figure 126 - Installed ground support scheme in the southern research tunnel.....	143
Figure 127 - Profile geometry of the northern tunnel with semi-elliptical shape for improved stability.....	144
Figure 128 - Example modelling output of 1000mm/s contours defining damaged and interaction zones.....	148
Figure 129 - P-wave velocity estimation.....	149
Figure 130 - Preliminary test model destressing geometry.....	150
Figure 131 - Modelled damage interaction for a conventional distress blast design under increasing stress.....	151
Figure 132 – Example model geometry for preliminary destressing analyses.....	152
Figure 133 – Example HSBM output for collar primed destressing configuration.....	153
Figure 134 – Example HSBM output for toe primed destressing configuration.....	153
Figure 135 – HSBM geometry for distress blasting simulations 15-18.....	156
Figure 136 - Example HSBM output of stress wave transient for model run 16.....	156
Figure 137 - HSBM geometry for distress blasting simulations 19-21.....	157
Figure 138 - Example HSBM output of stress wave transient for model run 20.....	157
Figure 139 - HSBM Model 22 geometry, explosive charge configuration and rock stress.....	159
Figure 140 - Cross sectional view of modelled particle velocity attenuation and fracture interaction.....	160
Figure 141 - Plan views of modelled particle velocity attenuation and fracture interactions.....	161
Figure 142 – Modelled fracture interaction in-row only, with no fracture formation across the burden.....	162
Figure 143- Development Destressing Design 1.....	163
Figure 144 - Number of explosive charges per delay.....	165
Figure 145 - Distribution of explosive weight per delay.....	165
Figure 146 – Development Destressing Design 2.....	167
Figure 147 - Number of explosive charges for each detonator delay.....	168
Figure 148 - Distribution of explosive weight to each delay.....	169
Figure 149 - Development face distress blasting concept and design parameters for the blasthole pattern.....	171
Figure 150 – UCS test sample failure mechanics analogous to face destressing.....	172
Figure 151 – Hypothesised ejection velocity limits considering rock joint strength (data from Kusui, 2015).....	176

Figure 152 - Energy demand chart for ground support design in massive hard rock.	179
Figure 153 - Energy demand chart for ground support design in hard rock with strong joints.	180
Figure 154 - Energy demand chart for ground support design in hard rock with moderately strong joints.	181
Figure 155 - Reinforcement design chart, modified after Villaescusa, et al., (2014).....	183
Figure 156 - Large displacement of external woven mesh connected to adjacent stable reinforcement.	185
Figure 157 – Dynamic energy dissipation and displacement capacity of mesh (Villaescusa, et al., 2012).....	187
Figure 158 - Failure of an exposed mesh-reinforced shotcrete layer due to violent spalling.	187
Figure 159 - Reinforcement shear force capacity assumptions used for ground support scheme design.	189
Figure 160 - Primary ground support layer, reinforcement pattern and surface support	192
Figure 161 - Secondary ground support layer, reinforcement pattern and surface support.	192
Figure 162 - Complete ground support scheme arrangement and Cross-Section A.....	192
Figure 163 – Mesh overlap pattern and complete ground support scheme arrangement at Cross-Section B.....	193
Figure 164 – Detailed view of mesh overlap arrangement for the first and second ground support layers.....	193
Figure 165 - Detailed view (<i>Det. 1</i>) of ground support scheme for extremely high energy dissipation.....	193
Figure 166 - Schematic of ground support scheme load transfer mechanisms.....	194
Figure 167 - Ground support scheme shear capacity for shear failure mechanism #1.....	197
Figure 168 - Ground support scheme shear capacity for shear failure mechanism #2.....	197
Figure 169 - Ground support scheme shear capacity for shear failure mechanism #3.....	197
Figure 170 - Violent stress-driven failure causing ejection of rock from the development face.	200
Figure 171 - Alternating sequence of development advances across the two research tunnels.	201
Figure 172 - Development construction sequence of alternating blasts in each tunnel.	202
Figure 173 - Construction strategy used to test various development methods.	203
Figure 174 – Cumulative development metres for the south and north tunnels.	204
Figure 175 - Excavation perimeter, centreline and gradeline markings for profile control.	205
Figure 176 - Destressing blasthole collars surveyed and marked on the face prior to commencing boring.	207
Figure 177 - Boring jumbo with eight 1.0m-long connecting rods on a rotating carousel.	207
Figure 178 - Typical face conditions requiring minor remedial scaling behind mesh prior to charging.	208
Figure 179 - Instrumentation for measuring the deviation of destressing boreholes.	209
Figure 180 - Measured orientation and deviations of destressing boreholes (north tunnel, Cut 14).....	210
Figure 181 - Working from an elevated platform to charge a destressing hole with blown ANFO.	211
Figure 182 – Insertion of the Tronex collar primer for a destressing charge.....	212
Figure 183 - Damp clay stem packs inserted into the destressing borehole prior to tamping.	212
Figure 184 - Charging standard development blastholes following destressing loads (marked yellow).....	213
Figure 185 – Development blast rock and damaged temporary face ground support to be removed.	214
Figure 186 - Damaged temporary face support required to be removed following blasting.	215
Figure 187 - Dedicated machinery for mechanical scaling of the unsupported sidewalls and roof.....	216
Figure 188 - Mechanical scaling of loose rock from the tunnel walls prior to shotcreting.	217
Figure 189 - Typical digital photogrammetry station for face structural mapping.	218
Figure 190 - Application of the primary shotcrete layer.	219
Figure 191 – Position control of primary reinforcement elements.....	221
Figure 192 – Mechanised Boltec jumbo used for ground support installations (AtlasCopco, 2017).	222
Figure 193 - Mechanised DS411 bolting jumbo used for ground support installation (Sandvik, 2018).	222
Figure 194 - Reinforcement and mesh installation booms.....	223
Figure 195 – Mechanised jumbo boom for drilling, grouting and installing reinforcement.....	223
Figure 196 - Drilling, grouting and bolting attachments on the mechanised jumbo.	224
Figure 197 - Integrated grout mixing bowl on the mechanised ground support jumbo.	224
Figure 198 - Mesh handler arm for mechanised ground support installation (mesh roll not shown).	225
Figure 199 - Mechanised ground support jumbo (Sandvik DS411-C) in operation.	225
Figure 200 - Prioritisation of ground support installation to zones of stress-driven overbreak.....	226
Figure 201 - Expansion shell temporary point anchor for primary reinforcement.....	227
Figure 202 - Installation of primary reinforcement in a consistent pattern with high capacity mesh.	228

Figure 203 - Close up view of primary reinforcement, shotcrete and mesh arrangement.	228
Figure 204 - Completed installation of primary reinforcement and mesh awaiting shotcrete overspray.	229
Figure 205 - Application of a second shotcrete layer with exposed reinforcement threads for second plating.	230
Figure 206 - Temporary face support to contain face instability during drill and blast activities.	231
Figure 207 – Installation sequence of two integrated layers of high energy dissipation ground support.	232
Figure 208 - Structurally controlled excavation failure more than 20m from the development face.	232
Figure 209 – Long section view of the primary ground support installation sequence.	234
Figure 210 – Long section view of the secondary ground support installation sequence.	235
Figure 211 – Installation of secondary reinforcement within the primary reinforcement pattern spacing.	236
Figure 212 - Secondary reinforcement installed awaiting the second layer of high capacity woven mesh.	237
Figure 213 - Installation of the second mesh layer from an elevated work platform.	238
Figure 214 – Fixation of secondary mesh layer to the primary reinforcement elements.	238
Figure 215 - Primary reinforcement element threaded tail after second shotcrete application.	239
Figure 216 -Primary reinforcement element threaded tail after removing shotcrete.	239
Figure 217 - Primary reinforcement element connected to secondary mesh via an external fixture.	239
Figure 218 - Use of a hydraulic ram to install mesh and second plates on the primary reinforcement.	240
Figure 219 – Unfurled cable strands at the external fixture.	241
Figure 220 - High strength and flexible steel wire stitching through the mesh sheet overlap.	242
Figure 221 - Wire stitching through mesh sheet overlaps terminated with three crimps at floor level.	242
Figure 222 - Close-up view of final reinforcement pattern and surface support arrangement.	244
Figure 223 – Multi-layered, high energy dissipation ground support scheme installed in the north tunnel.	244
Figure 224 – Design and actual installed locations of the seismic sensors.	251
Figure 225 - 3D location error: horizontal section at 1882mRL and vertical section 10m from turnout.	253
Figure 226 - 3D location error: horizontal section at 1882mRL and vertical section 30m from turnout.	254
Figure 227 - 3D location error: horizontal section at 1882mRL and vertical section 60m from turnout.	254
Figure 228 - Horizontal section of minimum magnitude sensitivity at 1862mRL (20m below tunnels).	256
Figure 229 - Horizontal section of minimum magnitude sensitivity at 1882mRL (same level as tunnels).	256
Figure 230 - Horizontal section of minimum magnitude sensitivity at 1902mRL (20m above tunnels).	257
Figure 231 - Vertical section of minimum magnitude sensitivity at 10m from tunnel turnout.	258
Figure 232 - Vertical section of minimum magnitude sensitivity at 30m from tunnel turnout.	258
Figure 233 - Vertical section of minimum magnitude sensitivity at 60m from tunnel turnout.	259
Figure 234 - Electronic iKon detonator used as an artificial seismic source for velocity calibration.	260
Figure 235 – Perspective view of artificial seismic sources used for seismic velocity model calibration.	261
Figure 236 - Plan view of artificial seismic sources used for seismic velocity model calibration.	261
Figure 237 - Installation and arrangement of components in the borehole, prior to immersion in water.	262
Figure 238 - Fibre optic break reader used to correlate detonator initiation to seismic system timing.	263
Figure 239 – Schematic of detonators and instrumentation used for seismic velocity data collection.	263
Figure 240 - Waveform data showing the voltage offset timing from the fibre-optic break reader.	264
Figure 241 - Typical seismogram generated using an explosive detonator as an artificial seismic source.	264
Figure 242 - Distance-Arrival data for artificial seismic sources within the triaxial accelerometer array.	265
Figure 243 – Perspective view of ray-tracing velocity model spatial limits.	268
Figure 244 – Plan view of ray-tracing velocity model spatial limits.	268
Figure 245 – One of three heterogeneous P-wave velocity models tested for location error.	269
Figure 246 – One of three heterogeneous S-wave velocity models tested for location error.	269
Figure 247 - Detonators were inserted into the boreholes at specific lengths using rigid conduit.	270
Figure 248 - Plan view of verification blasts for location error tests.	271
Figure 249 - Example waveform of artificial seismic sources used for 3D location error analysis.	272
Figure 250 - Quantitative comparison of 3D source location error for all five velocity models.	273
Figure 251 - Examples of linear artefacts in the ray-tracing location calculations of real seismic data.	275
Figure 252 – Re-processed seismic data using a heterogeneous absolute velocity model.	275
Figure 253 – Verification blast locations using heterogeneous velocity absolute location method.	276

Figure 254 – North and south tunnel spatial filters for location accuracy analysis.	277
Figure 255- Hypocentre location error statistics reported by the seismic system.	278
Figure 256 - Location error plotted as a percentage of absolute hypocentral distance to sensors.	279
Figure 257 – Cross section view of spatial filters for location accuracy analysis (view direction is NE).	279
Figure 258 - Plan view of spatial event filters coinciding with each incremental development advance.	280
Figure 259 - Average seismic event location error for the population of events within each spatial filter.	280
Figure 260 – Error sphere (0.3m radius) representing modal location error adjacent the north tunnel.	281
Figure 261 - Error sphere (0.3m radius) representing modal location error adjacent the south tunnel.	281
Figure 262 – Magnitude frequency distribution of all recorded seismic events.	283
Figure 263 - Magnitude-Time chart for entire seismic event dataset.	283
Figure 264 - Log(E) vs Log(P) plot for the entire seismic event population.	284
Figure 265- Example source mechanism calculations in IMS software (Birch, 2018).	285
Figure 266 - Selection of development cycles for comparison seismic analysis.	286
Figure 267 - Plan view of the seismic response showing two dominant seismic clusters.	288
Figure 268 - Perspective view (looking northeast) of the seismic response to development.	288
Figure 269 - Cross-sectional view (looking southwest) of the seismic response to development.	288
Figure 270 - Longitudinal sections of the seismic response to conventional drill and blast development.	290
Figure 271 - Longitudinal sections of the seismic response to face destressing drill and blast development.	291
Figure 272 – Transverse sections of the seismic response to conventional drill and blast development.	292
Figure 273 - Transverse sections of the seismic response to development with face distress blasting.	292
Figure 274 - Cumulative event count, seismic energy and potency for the entire seismic dataset.	294
Figure 275 - Total seismic events per tunnel per development cycle.	297
Figure 276 - Total radiated seismic energy per tunnel per development cycle.	297
Figure 277 - Total seismic potency per tunnel per development cycle.	297
Figure 278 - Average joules of radiated seismic energy per event for each development cycle.	299
Figure 279 - Inferred radiated energy per unit of seismic potency for each development cycle.	299
Figure 280 - Longitudinal section view of spatial filters for assessing the distribution of seismicity.	300
Figure 281 - Cross section view of spatial filters and their coverage of the seismogenic zone (looking SW).	300
Figure 282 - The total number of recorded seismic events for each excavation surface.	302
Figure 283 - The total radiated seismic energy for each excavation surface.	302
Figure 284 – The total seismic potency (inelastic damage) for each excavation surface.	302
Figure 285 - Long section view of spatial filter limits for high resolution analysis of seismic data.	304
Figure 286 - Plan view of spatial filter limits for high resolution analysis of seismic data.	304
Figure 287 - Cross section view of filter geometry for high resolution spatial analysis of seismic data.	304
Figure 288 - Long section view of the entire sequence of sixty-five 0.3m-long spatial filters.	305
Figure 289 - Number of seismic events as a function of distance from the face for conventional blasting.	307
Figure 290 - Number of seismic events as a function of distance from the face for distress blasting.	307
Figure 291 - Radiated seismic energy as a function of distance from the face for conventional blasts.	309
Figure 292 - Radiated seismic energy as a function of distance from the face for distressing blasts.	309
Figure 293 - Inelastic deformation (seismic potency) as a function of distance from the face for conventional blasts.	311
Figure 294 - Inelastic deformation (seismic potency) as a function of distance from the face for distressing blasts.	311
Figure 295 - Locations of seismic events with mechanism solutions marked by beachball spheres.	313
Figure 296 - a) measured stresses (Windsor, et al., 2006), b) strain axes in the south tunnel and c) north.	313
Figure 297 - Nodal plane sets 1 and 2 poles, with fisher pole contours, plotted in SAFEX.	314
Figure 298 - Joint set boundary assumptions applied to the nodal plane data.	315
Figure 299 - Number of unique fault plane solutions in each tunnel.	316
Figure 300 - Plan view of mapped and inferred joint sets compared to nodal planes.	317
Figure 301 - Plan view of P-axis orientation for all source mechanisms solutions.	318
Figure 302 – South tunnel P-Axis orientations and the stereonet of nodal planes and principal strain axes.	319
Figure 303 - North tunnel P-Axis orientations and the stereonet of nodal planes and principal strain axes.	319
Figure 304 - Ternary diagram of seismic source mechanisms adjacent conventional tunnel development.	321

Figure 305 - Ternary diagram of seismic source mechanisms adjacent distressed tunnel development.	321
Figure 306 - Hudson diagram of seismic source mechanisms adjacent conventional development.	323
Figure 307 - Hudson diagram of seismic source mechanisms adjacent face destressing development.	323
Figure 308 - Intended blast-induced fracture planes created by face destressing explosives.	324
Figure 309 - a) Transverse and b) longitudinal section views of mechanism nodal planes during Cut #12.	326
Figure 310 - Moment tensor decomposition from Cut #12 consistent with the destressing mechanism.	326
Figure 311 - Hudson source-type diagram for a destressing mechanism during Cut #12.	326
Figure 312 - a) Transverse and b) longitudinal section views of mechanism nodal planes during Cut #14.	327
Figure 313 - Misfired destressing charge identified in Cut 14.	327
Figure 314 - a) Transverse and b) longitudinal section views of mechanism nodal planes after Cut #16.	328
Figure 315 - Moment tensor decompositions from Cut #16 consistent with the destressing mechanism.	329
Figure 316 - Hudson source-type diagram for destressing mechanisms during Cut #16.	329
Figure 317 -- a) Transverse and b) longitudinal section views of mechanism nodal planes after Cut #18.	330
Figure 318 - Moment tensor decomposition from Cut #18 consistent with the destressing mechanism.	331
Figure 319 - Hudson source-type diagram for five destressing mechanisms during Cut #18.	332
Figure 320 - Cumulative seismic event count for each construction activity.	336
Figure 321 - Cumulative radiated seismic energy for each construction activity.	336
Figure 322 - Cumulative seismic potency for each construction activity.	336
Figure 323 - Distribution of total recorded radiated energy across all development construction tasks.	337
Figure 324 - Zones of blast-induced compressive, tensile and radial damage around a destressing charge.	339
Figure 325 - Blast-induced fracture through pre-existing structure.	340
Figure 326 - Destressing blast-induced radial fractures through intact rock.	341
Figure 327 - Close-up view of destressing blast-induced radial fractures through intact rock.	341
Figure 328 - Borehole internal view of radial fracturing through intact rock.	342
Figure 329 - Borehole internal view of radial fracturing through intact rock (opposite direction).	342
Figure 330 - Gas migration via multiple joint orientations originating from the destressing charge.	343
Figure 331 - Dilatation of Set #1 joint following gas migration through nearby Set #4 structure.	344
Figure 332 - Evidence of preferential fracture formation sub-parallel to the major principal stress.	345
Figure 333 - Visible ANFO residue within a radial crack confirming gas interaction between charges.	346
Figure 334 - Directional characteristics of observed radial fracturing due to destressing charges.	347
Figure 335 - Wide view of directional fracturing characteristics showing cross-borehole interaction.	347
Figure 336 - Dip angle of observed radial destressing fractures in the charge interaction zone.	348
Figure 337 - Angular characteristics of blast induced fractures relative to the principal stresses.	349
Figure 338 - GeoSlam Zeb1 laser scanner (GeoSlam, 2013).	350
Figure 339 - 3D point cloud data of tunnel geometry collected using the GeoSlam Zeb scanner.	351
Figure 340 - Cross section views of the complete 3D scan of each tunnel.	351
Figure 341 - Cross sections of the scanned tunnel profile.	352
Figure 342 - South and north tunnel cross sections of scan data at 3.5m chainage.	355
Figure 343 - South and north tunnel cross sections of scan data at 8.5m chainage.	355
Figure 344 - South and north tunnel cross sections of scan data at 14.0m chainage.	355
Figure 345 - Scan cross sections at 19.5m chainage showing SAFEX priority block formed in south tunnel.	356
Figure 346 - South and north tunnel cross sections of scan data at 24.5m chainage.	356
Figure 347 - South and north tunnel cross sections of scan data at 29.0m chainage.	356
Figure 348 - Structural controls on overbreak in the southern tunnel.	357
Figure 349 - Surface monostatic ground penetrating radars in 500MHz and 800MHz frequency.	360
Figure 350 - Radar distance calibration prior to surveying.	361
Figure 351 - Locations of radar geophysics surveys.	361
Figure 352 - Borehole radar survey.	362
Figure 353 - Preliminary GPR survey traverses prior to simulated destressing blasts.	363
Figure 354 - Geometry of simulated destressing charges for GPR survey.	363
Figure 355 - GPR survey of the rock mass following simulated destressing blast damage.	364

Figure 356 - Radargram of GeoMole borehole radar.	364
Figure 357 - GPR radargram, 500MHz, Traverse 1, prior to blasting.	367
Figure 358 - GPR radargram, 500MHz, Traverse 1, post-blasting.	367
Figure 359 - GPR radargram, 500MHz, Traverse 4, prior to blasting.	368
Figure 360 - GPR radargram, 500MHz, Traverse 4, post-blasting.	368
Figure 361 - Example reinforcement capacity versus OSV LED indications.	376

List of Tables

Table 1 - Example UCS data for rock mass characterisation (Dempers, et al., 2006).....	15
Table 2 - Typical rock mass demand for ground support design (Modified after (Villaescusa, et al., 2014).	48
Table 3 - Summary of the average mechanical properties of Dacite rock at the trial site.	96
Table 4 - Summary of UCS testing data for Dacite rock.	96
Table 5 - Summary of elastic properties testing data for Dacite rock.	98
Table 6 - Summary Mohr-Coulomb failure criterion data for Dacite rock.	100
Table 7 - Summary of UTS testing data for Dacite rock.	102
Table 8 - Summary of Fracture Toughness testing data for Dacite rock.	103
Table 9 – CSIRO HI Cell stress measurement data localised to the site of experimental tunnelling.	108
Table 10 - Plausible range of the σ_c / σ_{max} and σ_c / σ_{ave} stability criteria for the northern research tunnel.	113
Table 11 - Basic joint set parameters.	121
Table 12 - Trace length and spacing data for all joint sets.	123
Table 13 - Cohesion and friction angle data for all joint sets.	123
Table 14 - Excavation geometry for SAFEX deterministic and probabilistic block analyses.	124
Table 15 - Summary of SAFEX deterministic analysis statistics for roof blocks.	124
Table 16 – Summary of SAFEX deterministic analysis statistics for sidewall blocks.	127
Table 17 – Deterministic maximum span, trace and spacing-limited parameters of sidewall Block 2.	127
Table 18 - Maximum possible apex height of each basic block shape when assessed probabilistically.	128
Table 19 - Maximum trace limited apex height, free face area and mass for the 80, 90 and 100 th percentiles.	133
Table 20 – Max. trace limited apex height, free face area and mass for the 80, 90 and 100th percentiles.	135
Table 21 - Mass of instability for the variety of structural blocks.	136
Table 22 – Basic drilling parameters for the southern tunnel.	140
Table 23 – Explosive properties of ANFO, Softron and Tronex products.	141
Table 24 - Explosive charge specifications for individual loads.	141
Table 25 - Summary of total explosives used for the southern tunnel.	142
Table 26 - Blast summary statistics for the 6.1mW x 6.1mH southern tunnel.	142
Table 27- Preliminary HSBM simulations of simple destressing configurations.	151
Table 28 - Common HSBM model parameters for preliminary analyses.	152
Table 29 – HSBM input parameters for eight detailed destressing models.	154
Table 30 - Input parameters for detailed destressing design, model runs 15-21.	155
Table 31 - Input parameters for detailed destressing design, model run 22.	158
Table 32 - Basic drilling parameters for Destressing Design 1 in the northern tunnel.	163
Table 33 - Explosive charge specifications for individual loads in Destressing Design 1.	164
Table 34 - Summary of total explosives used in each blast for Destressing Design 1 in the north tunnel.	164
Table 35 - Blast summary statistics for the 6.9mW x 6.7mH semi-elliptical Destressing Design 1.	165
Table 36 - Basic drilling parameters for Destressing Design 2 in the northern tunnel.	166
Table 37 - Explosive charge specifications for individual loads in Destressing Design 2.	167
Table 38 - Summary of total explosives used for Destressing Design 2 in the north tunnel.	169
Table 39 - Blast summary statistics for the 6.9mW x 6.7mH semi-elliptical Destressing Design 2.	169
Table 40 - Updated rock mass force-displacement-energy demand categories.	177
Table 41 - Summary of ground support component force, displacement and energy dynamic capacity.	188
Table 42 - Summary of reinforcement ultimate shear force capacity.	189
Table 43 - Ground support scheme load transfer symbols (following Villaescusa, et al., 2005 notation).	195
Table 44 - Energy dissipation and displacement capacity of ground support scheme for radial failures.	196
Table 45 - Shear force capacity of HED ground support scheme for three shear failure mechanisms.	197
Table 46 - Design versus Installed sensor locations (mine coordinate system).	249
Table 47 - IMS Vantage sensitivity analysis input parameters.	252
Table 48 - Velocity model parameters for the Dacite rock type, used in seismic sensitivity analysis.	252
Table 49 – Heterogeneous seismic velocity model data.	266

Table 50 – Verification blast location error statistics using absolute method and heterogeneous velocities.	275
Table 51 - Q-values applied to sensors sites for source parameter calculations.	282
Table 52 - Joint set basic parameters measured from structural face mapping.	315
Table 53 – Parameters of potential joints inferred from nodal plane set 1.	315
Table 54 - Parameters of potential joints inferred from nodal plane set 2.	315
Table 55 – Assumed depth of penetration properties for each radar instrument.	360

Appendix A

HSBM Modelling Results

HSBM model specifications and complete set of results images.

Model Parameters (Runs 1-14)

Model Parameter	Value
<i>Blast Hole Length</i>	<i>6m</i>
<i>Charge Length</i>	<i>2.4m</i>
<i>Blast Hole Diameter</i>	<i>52mm</i>
<i>Blast Hole Dip</i>	<i>15 degrees from longitudinal axis of drive</i>
<i>Booster</i>	<i>Modelled at both collar and toe</i>
<i>Explosive</i>	<i>Emulsion - 5000m/s VOD - 1.15 density</i>
<i>Sigma 1</i>	<i>50 MPa (assumed to be horizontal)</i>
<i>Sigma 3</i>	<i>27MPa (assumed to be vertical)</i>
<i>Development Size</i>	<i>3m x 3m x 0.5m</i>
<i>Model boundary</i>	<i>15m x 15m x 15m</i>

Model Viewpoints (Runs 1-14)

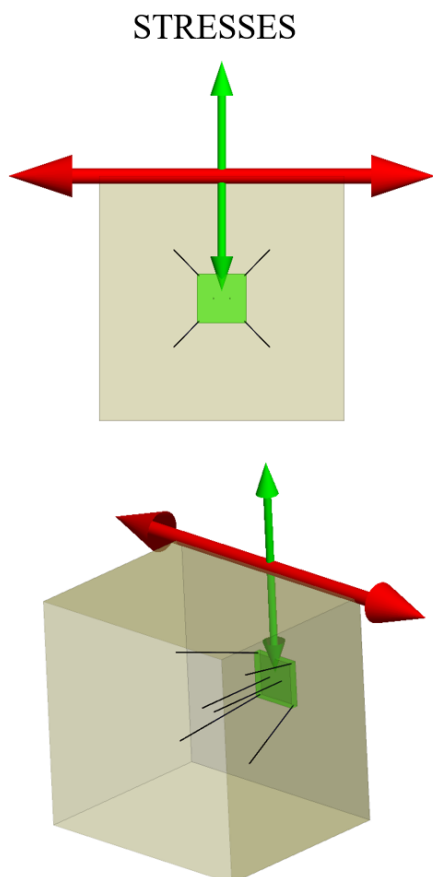
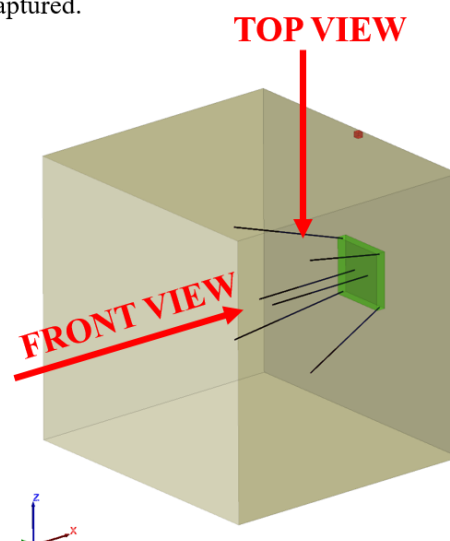


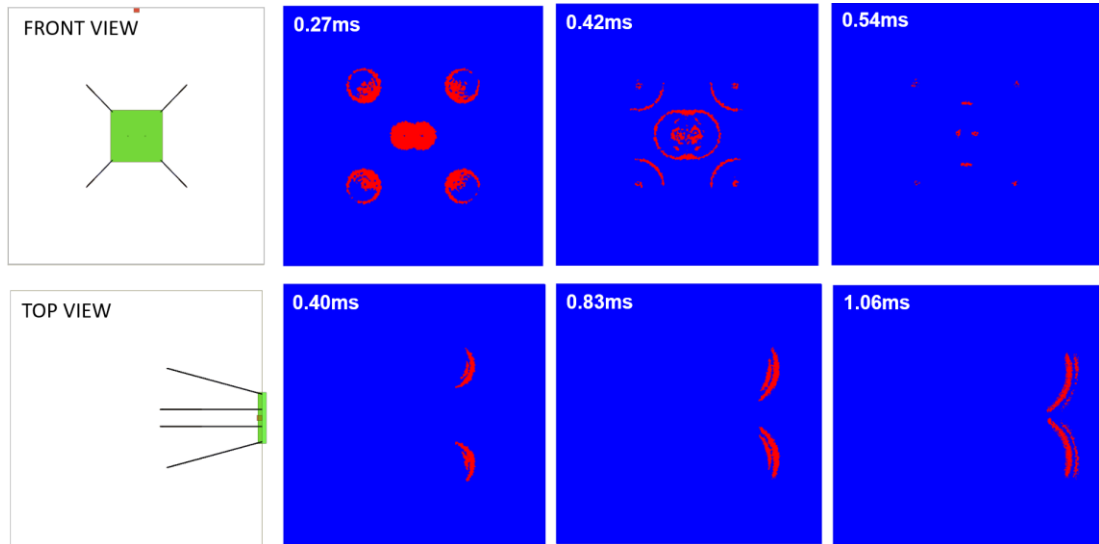
IMAGE VIEWPOINTS

2 image viewpoints were taken for each model (front / top view). The front view is looking parallel down the longitudinal axis of the drive from the toe toward the collar of the blast holes. The top view is looking perpendicular to the longitudinal axis of the drive, aligned with vertical looking from the surface downward. It should also be noted that in the top view only the stress waves from the top row of blast holes is captured.



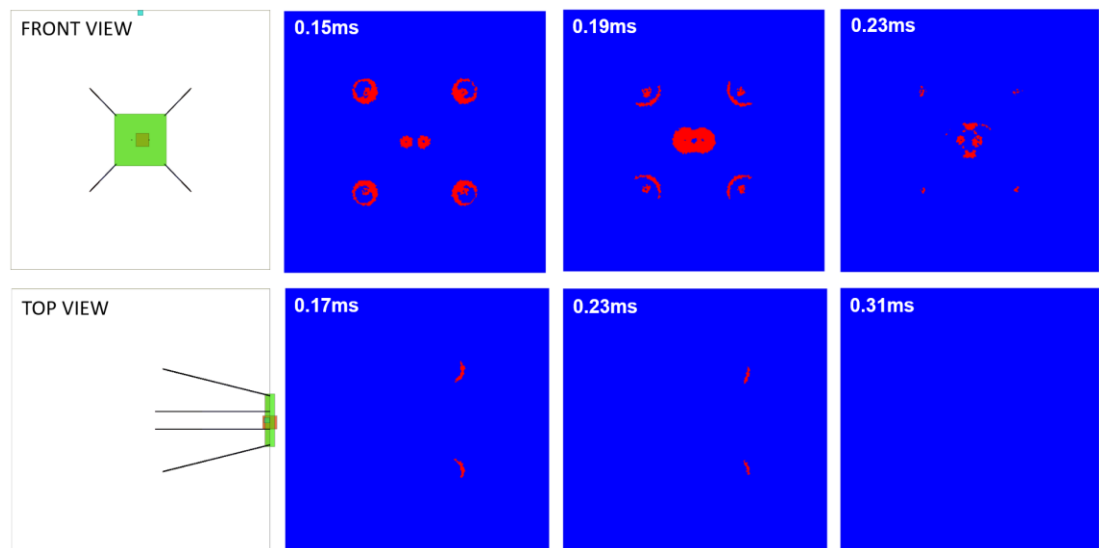
Run 1 Summary Statistics and Model Images

Model ID	Rock Type	Run Time	Stresses	No. Holes	Perimeter Holes
Run 1	Test Rock	3ms	100%	6	4
Centre Holes	Hole Length	Charge Length	Booster Location	Perimeter Holes	Delay
2	6	2.4	Toe	Corners	0ms



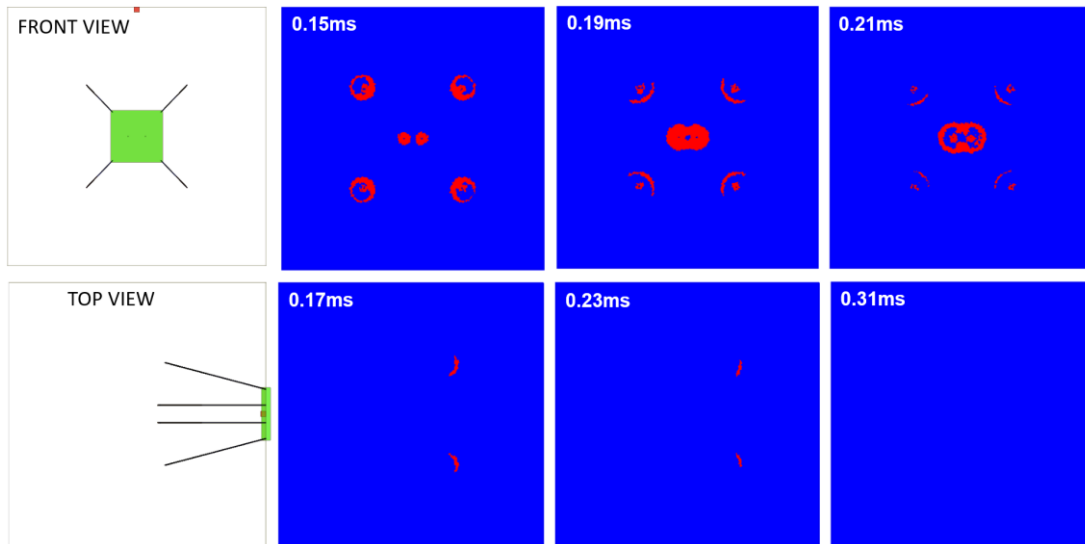
Run 2 Summary Statistics and Model Images

Model ID	Rock Type	Run Time	Stresses	No. Holes	Perimeter Holes
Run 2	Quartz/Gneiss	1 ms	100%	6	4
Centre Holes	Hole Length	Charge Length	Booster Location	Perimeter Holes	Delay
2	6	2.4	Toe	Corners	0ms



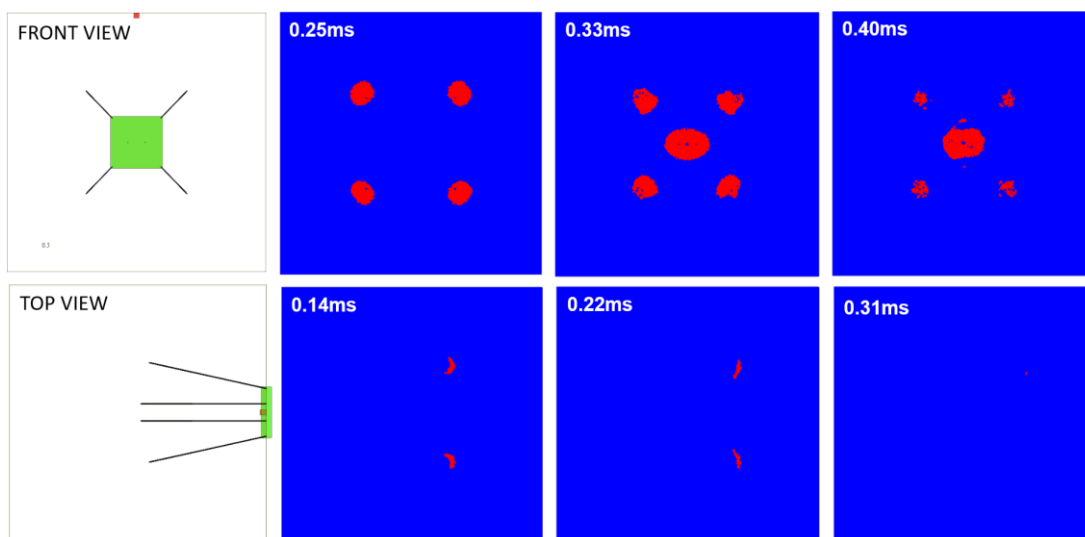
Run 3 Summary Statistics and Model Images

Model ID	Rock Type	Run Time	Stresses	No. Holes	Perimeter Holes
Run 3	Quartz/Gneiss	1ms	50%	6	4
Centre Holes	Hole Length	Charge Length	Booster Location	Perimeter Holes	Delay
2	6	2.4	Toe	Corners	0ms



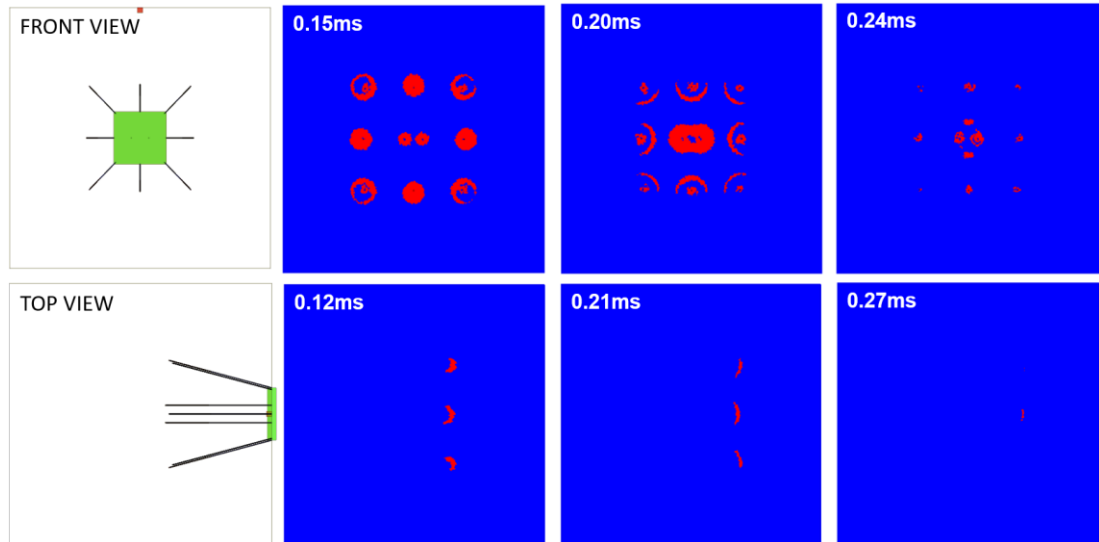
Run 4 Summary Statistics and Model Images

Model ID	Rock Type	Run Time	Stresses	No. Holes	Perimeter Holes
Run 4	Quartz/Gneiss	1ms	0%	6	4
Centre Holes	Hole Length	Charge Length	Booster Location	Perimeter Holes	Delay
2	6	2.4	Toe	Corners	0ms



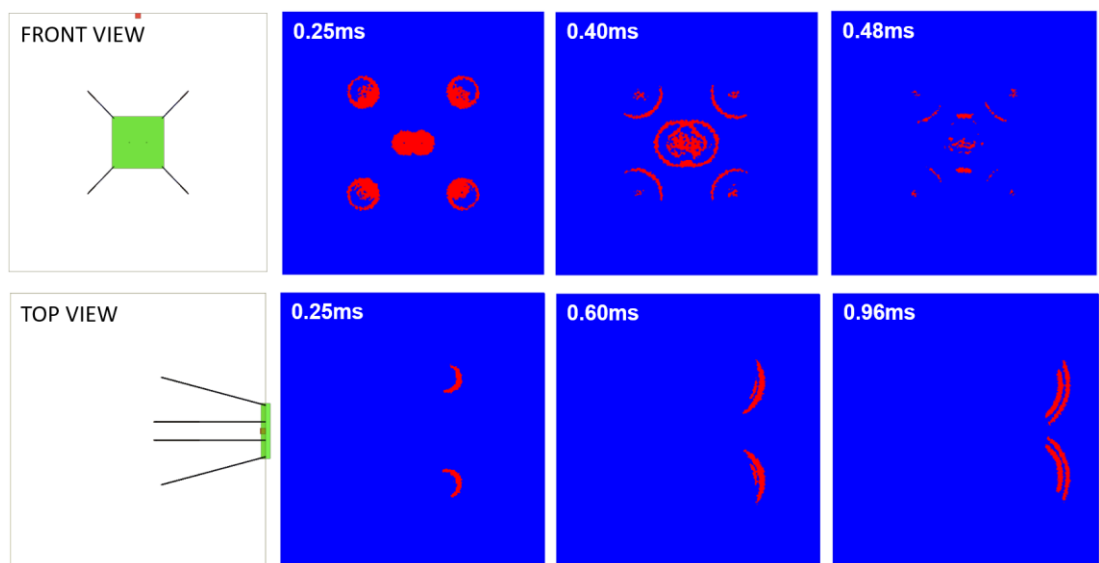
Run 5 Summary Statistics and Model Images

Model ID	Rock Type	Run Time	Stresses	No. Holes	Perimeter Holes
Run 5	Quartz/Gneiss	1ms	100%	10	8
Centre Holes	Hole Length	Charge Length	Booster Location	Perimeter Holes	Delay
2	6	2.4	Toe	Centre/Corner	0ms



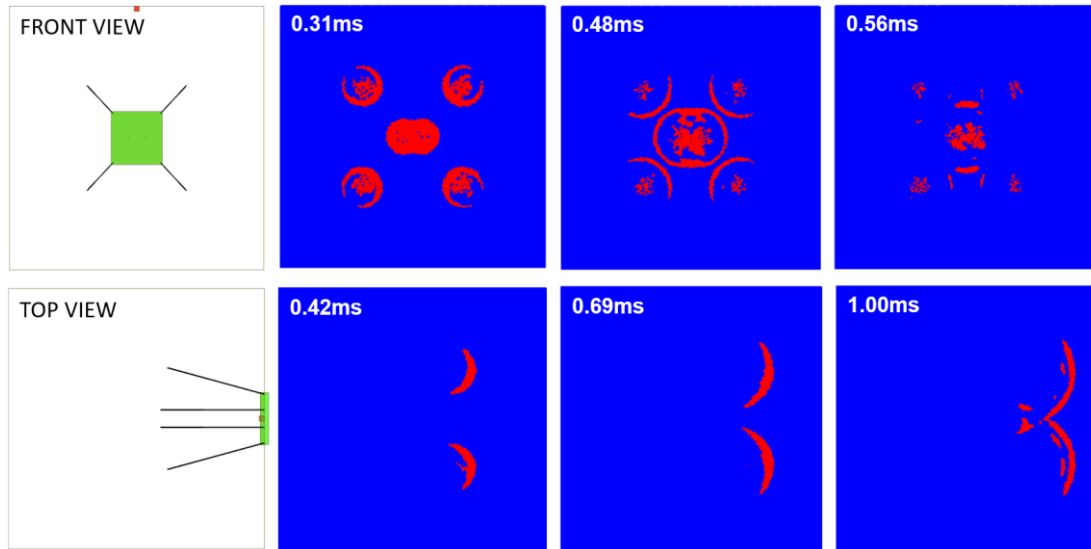
Run 6 Summary Statistics and Model Images

Model ID	Rock Type	Run Time	Stresses	No. Holes	Perimeter Holes
Run 6	Test Rock	1ms	50%	6	4
Centre Holes	Hole Length	Charge Length	Booster Location	Perimeter Holes	Delay
2	6	2.4	Toe	Corners	0ms



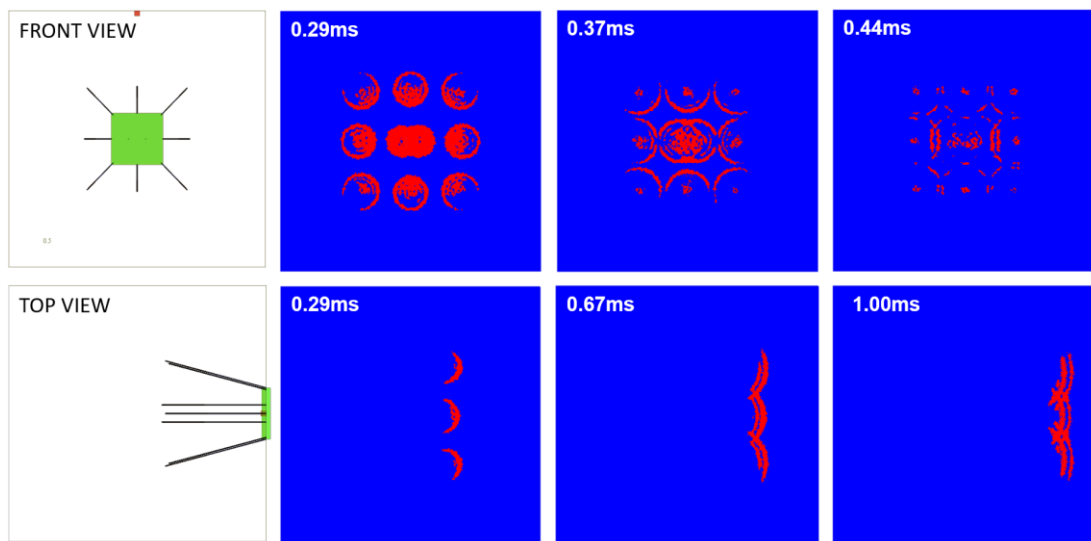
Run 7 Summary Statistics and Model Images

Model ID	Rock Type	Run Time	Stresses	No. Holes	Perimeter Holes
Run 7	Test Rock	1ms	0%	6	4
Centre Holes	Hole Length	Charge Length	Booster Location	Perimeter Holes	Delay
2	6	2.4	Toe	Corners	0ms



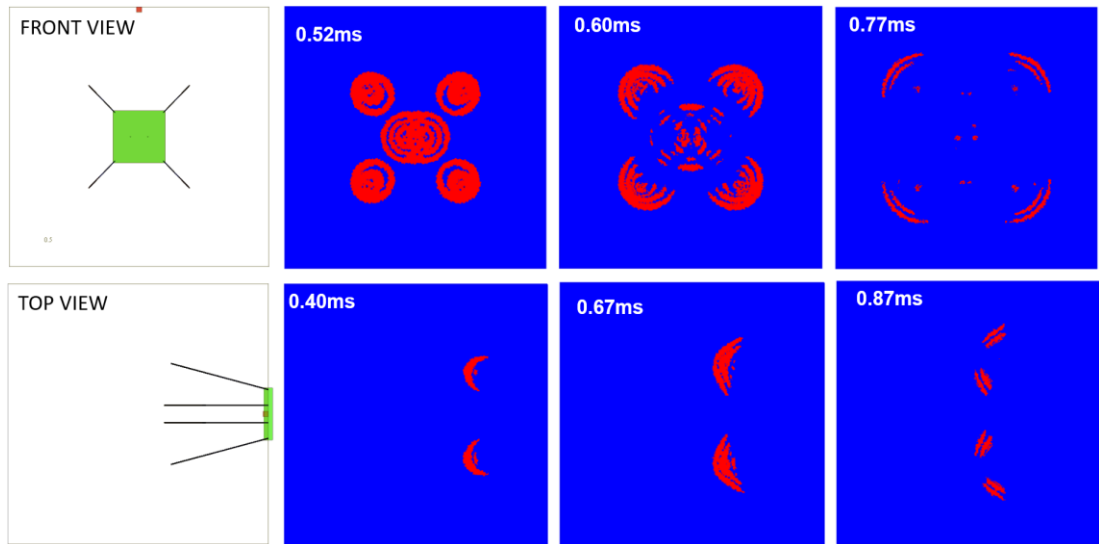
Run 8 Summary Statistics and Model Images

Model ID	Rock Type	Run Time	Stresses	No. Holes	Perimeter Holes
Run 8	Test Rock	1ms	100%	10	8
Centre Holes	Hole Length	Charge Length	Booster Location	Perimeter Holes	Delay
2	6	2.4	Toe	Corners/Centres	0ms



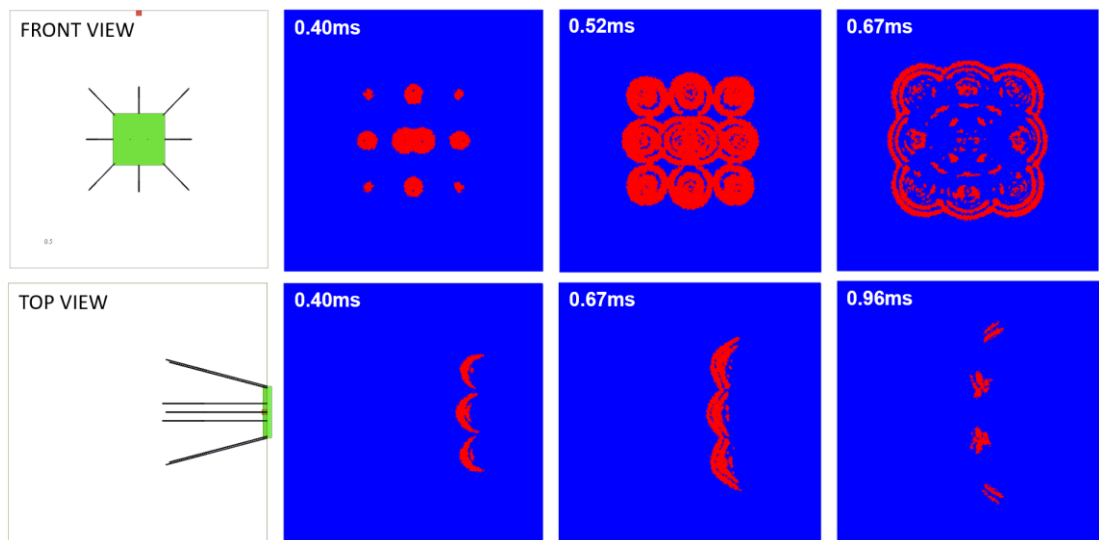
Run 9 Summary Statistics and Model Images

Model ID	Rock Type	Run Time	Stresses	No. Holes	Perimeter Holes
Run 9	Test Rock	1ms	100%	6	4
Centre Holes	Hole Length	Charge Length	Booster Location	Perimeter Holes	Delay
2	6	2.4	Collar	Corners	0ms



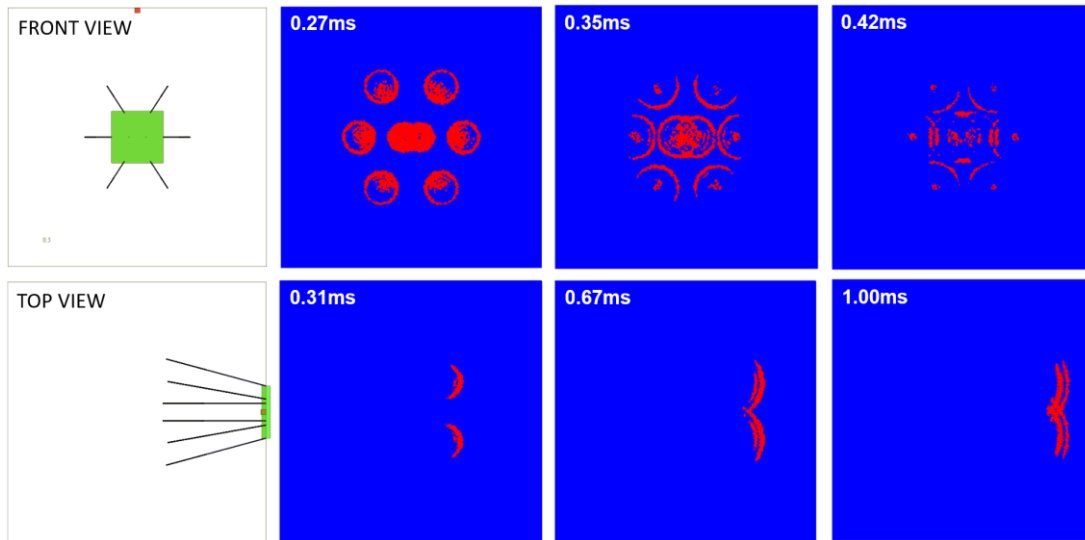
Run 10 Summary Statistics and Model Images

Model ID	Rock Type	Run Time	Stresses	No. Holes	Perimeter Holes
Run 10	Test Rock	1ms	100%	10	8
Centre Holes	Hole Length	Charge Length	Booster Location	Perimeter Holes	Delay
2	6	2.4	Collar	Corners/Centres	0ms



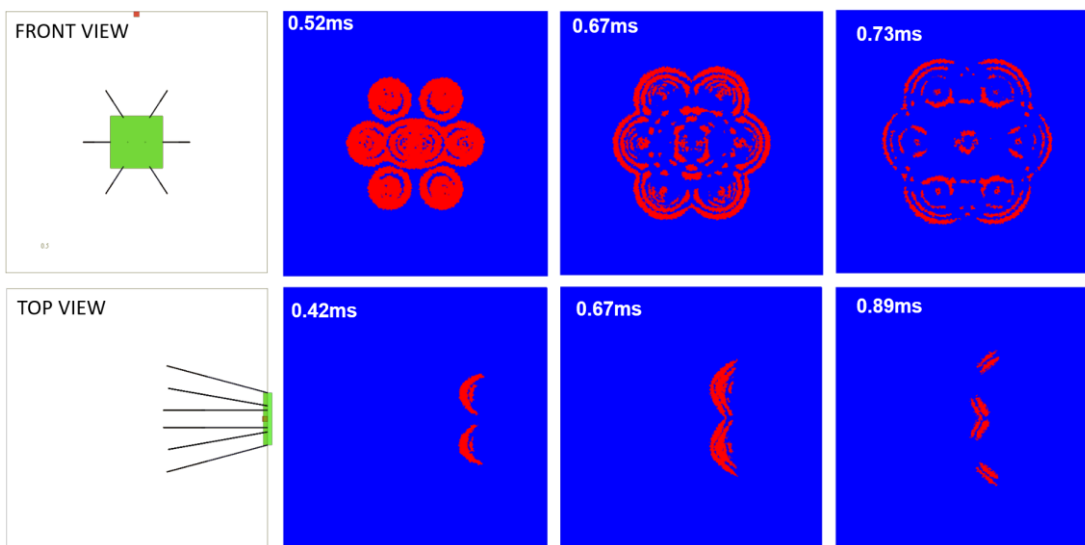
Run 11 Summary Statistics and Model Images

Model ID	Rock Type	Run Time	Stresses	No. Holes	Perimeter Holes
Run 11	Test Rock	1ms	100%	8	6
Centre Holes	Hole Length	Charge Length	Booster Location	Perimeter Holes	Delay
2	6	2.4	Toe	Centres	0ms



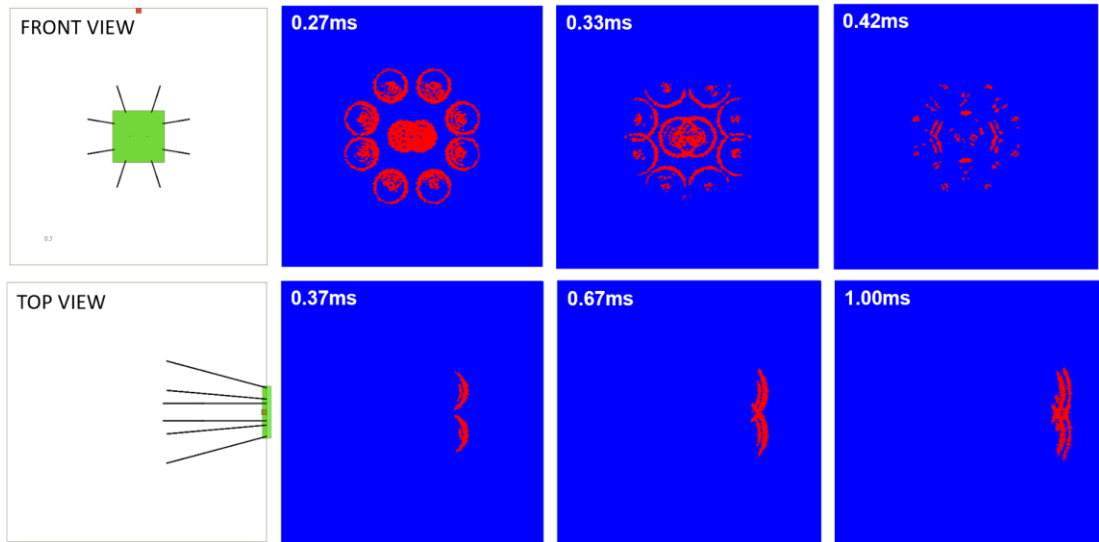
Run 12 Summary Statistics and Model Images

Model ID	Rock Type	Run Time	Stresses	No. Holes	Perimeter Holes
Run 12	Test Rock	1ms	100%	8	6
Centre Holes	Hole Length	Charge Length	Booster Location	Perimeter Holes	Delay
2	6	2.4	Collar	Centres	0ms



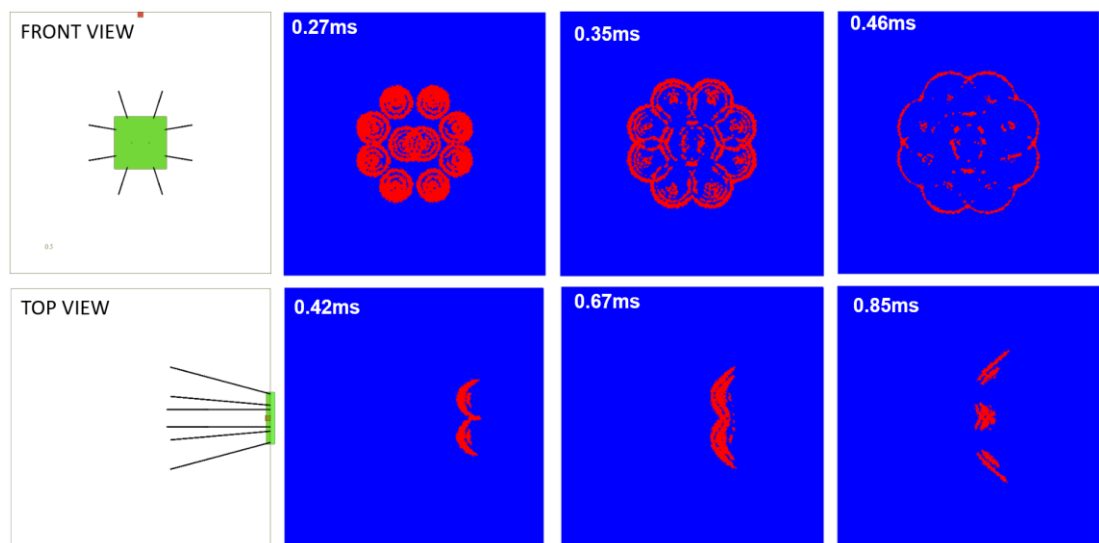
Run 13 Summary Statistics and Model Images

Model ID	Rock Type	Run Time	Stresses	No. Holes	Perimeter Holes
Run 13	Test Rock	1ms	100%	10	8
Centre Holes	Hole Length	Charge Length	Booster Location	Perimeter Holes	Delay
2	6	2.4	Toe	Centres	0ms



Run 14 Summary Statistics and Model Images

Model ID	Rock Type	Run Time	Stresses	No. Holes	Perimeter Holes
Run 14	Test Rock	1ms	100%	10	8
Centre Holes	Hole Length	Charge Length	Booster Location	Perimeter Holes	Delay
2	6	2.4	Collar	Centres	0ms



Model Parameters (Runs 15-18)

<i>Model Parameter</i>	<i>Value</i>
<i>Blast Hole Length</i>	6m
<i>Charge Length</i>	2.4m
<i>Blast Hole Diameter</i>	52mm
<i>Blast Hole Dip</i>	2 degrees
<i>Blast Hole Lookout Angle</i>	5 degrees
<i>Booster</i>	Modelled at both collar and toe
<i>Explosive</i>	Emulsion - 5000m/s VOD - 1.15 density
<i>Sigma 1</i>	50 MPa (assumed to be horizontal)
<i>Sigma 3</i>	27MPa (assumed to be vertical)
<i>Development Size</i>	ILLUSTRATED IN NEXT SLIDE
<i>Model boundary</i>	15m x 15m x 20m

Model Viewpoints (Runs 15-18)

STRESSES

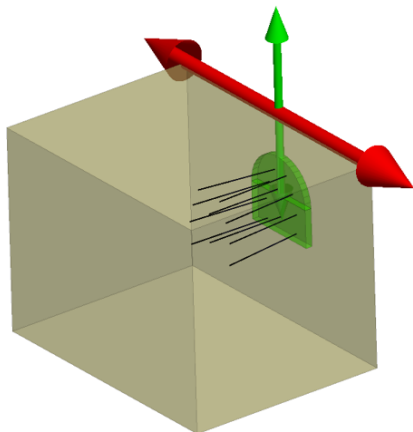
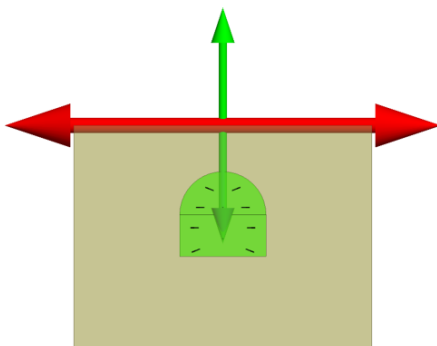
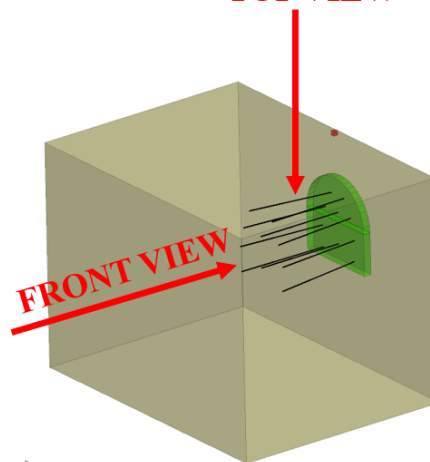
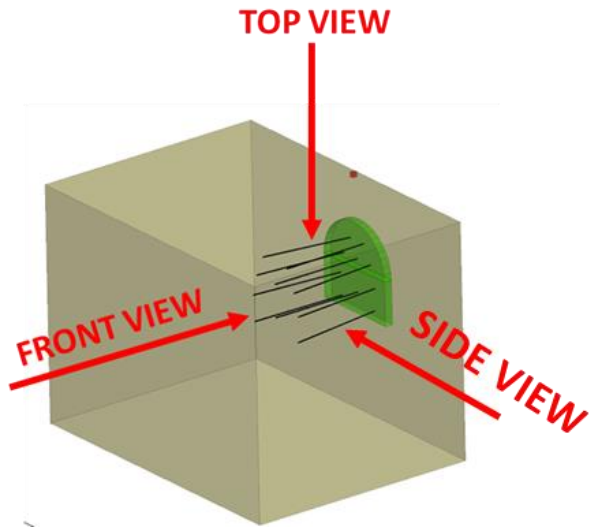


IMAGE VIEWPOINTS

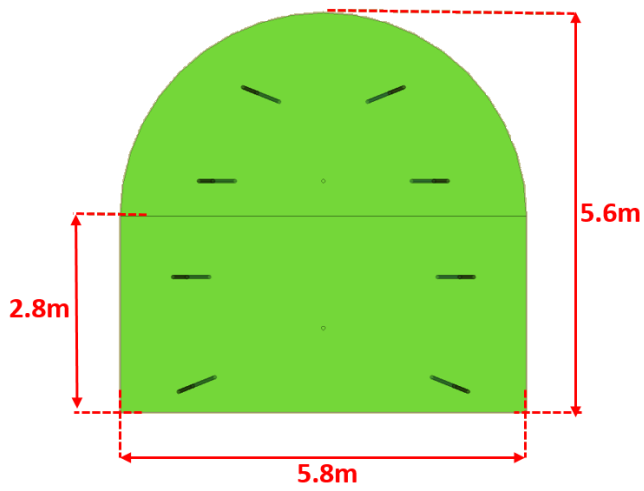
2 image viewpoints were taken for each model (front / top view). The front view is looking parallel down the longitudinal axis of the drive from the toe toward the collar of the blast holes. The top view is looking perpendicular to the longitudinal axis of the drive, aligned with vertical looking from the surface downward. It should also be noted that in the top view only the stress waves from the top row of blast holes is captured.

TOP VIEW

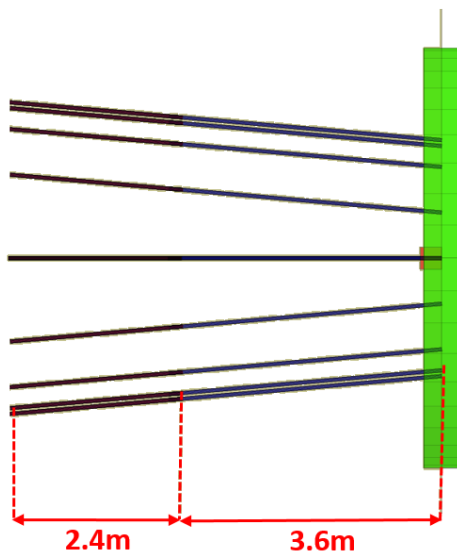




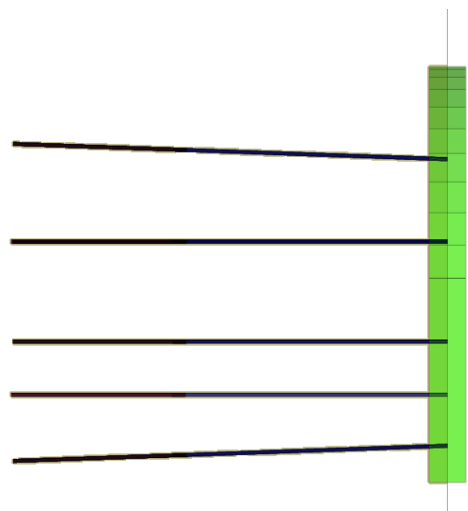
FRONT VIEW



TOP VIEW

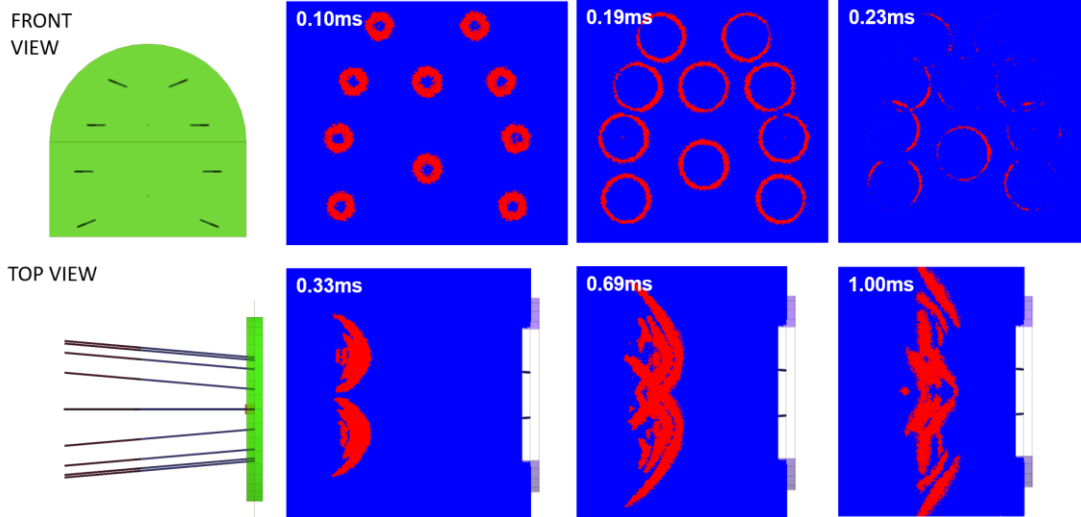


SIDE VIEW



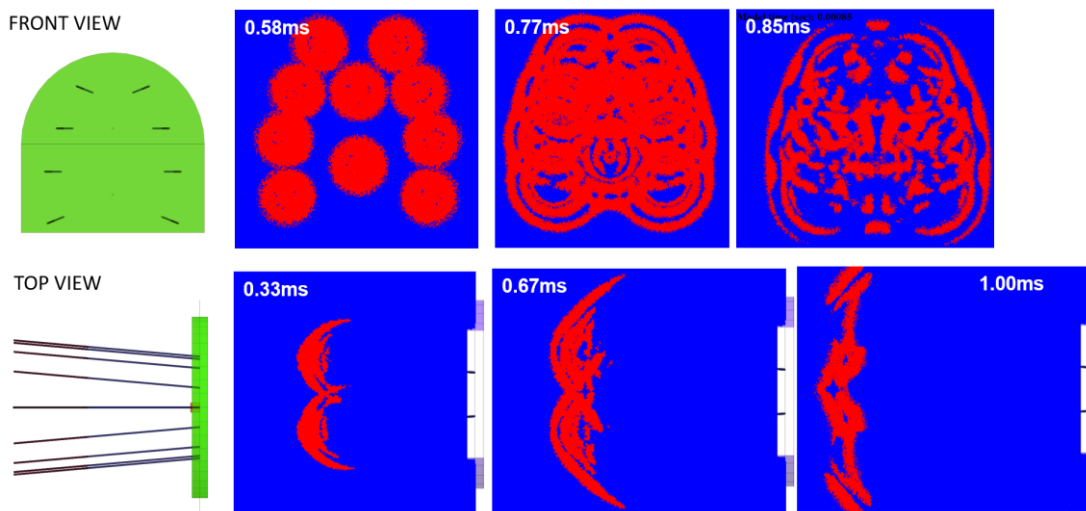
Run 15 Summary Statistics and Model Images

Model ID	Rock Type	Run Time	Stresses	No. Holes	Perimeter Holes
Run 15	Test Rock	1ms	100%	10	8
Centre Holes	Hole Length	Charge Length	Booster Location	Perimeter Holes	Delay
2	6	2.4	Toe	-	0ms



Run 16 Summary Statistics and Model Images

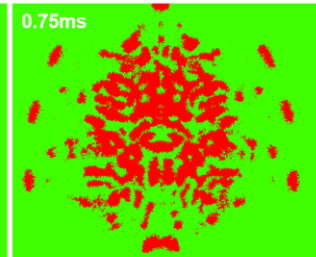
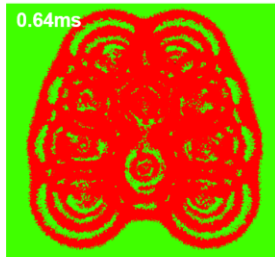
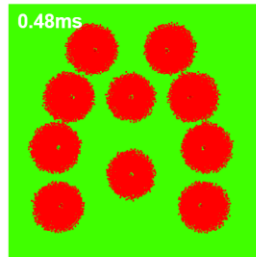
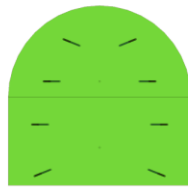
Model ID	Rock Type	Run Time	Stresses	No. Holes	Perimeter Holes
Run 16	Test Rock	1ms	100%	10	8
Centre Holes	Hole Length	Charge Length	Booster Location	Perimeter Holes	Delay
2	6	2.4	Collar	-	0ms



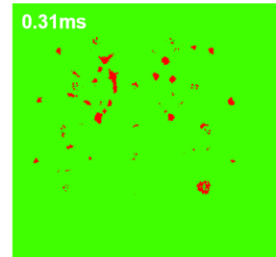
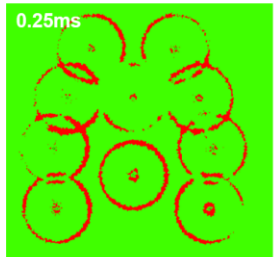
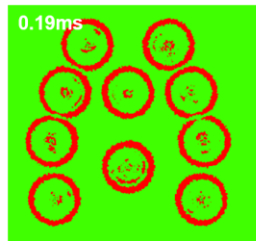
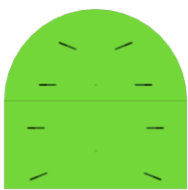
Run 17 Summary Statistics and Model Images

Model ID	Rock Type	Run Time	Stresses	No. Holes	Perimeter Holes
Run 17	Test Rock	1ms	100%	10	8
Centre Holes	Hole Length	Charge Length	Booster Location	Perimeter Holes	Delay
2	6	2.4	Toe	-	0ms

FRONT VIEW (COLLAR)



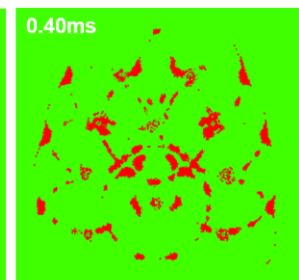
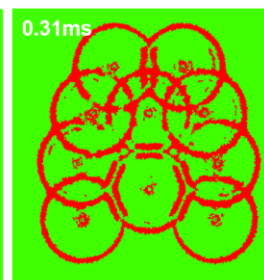
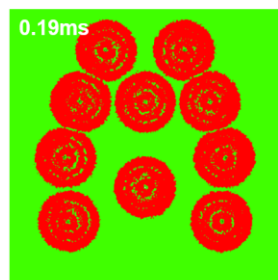
FRONT VIEW (TOE)



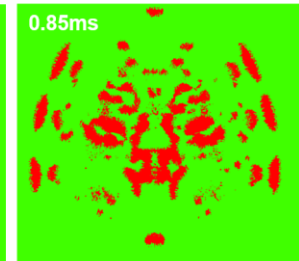
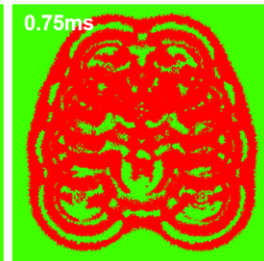
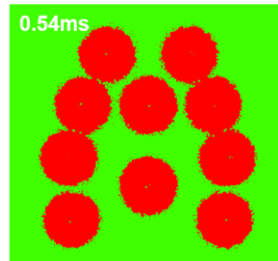
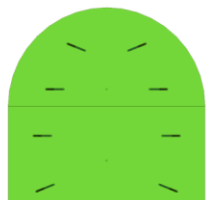
Run 18 Summary Statistics and Model Images

Model ID	Rock Type	Run Time	Stresses	No. Holes	Perimeter Holes
Run 18	Test Rock	1ms	100%	10	8
Centre Holes	Hole Length	Charge Length	Booster Location	Perimeter Holes	Delay
2	6	2.4	Collar	-	0ms

FRONT VIEW (COLLAR)



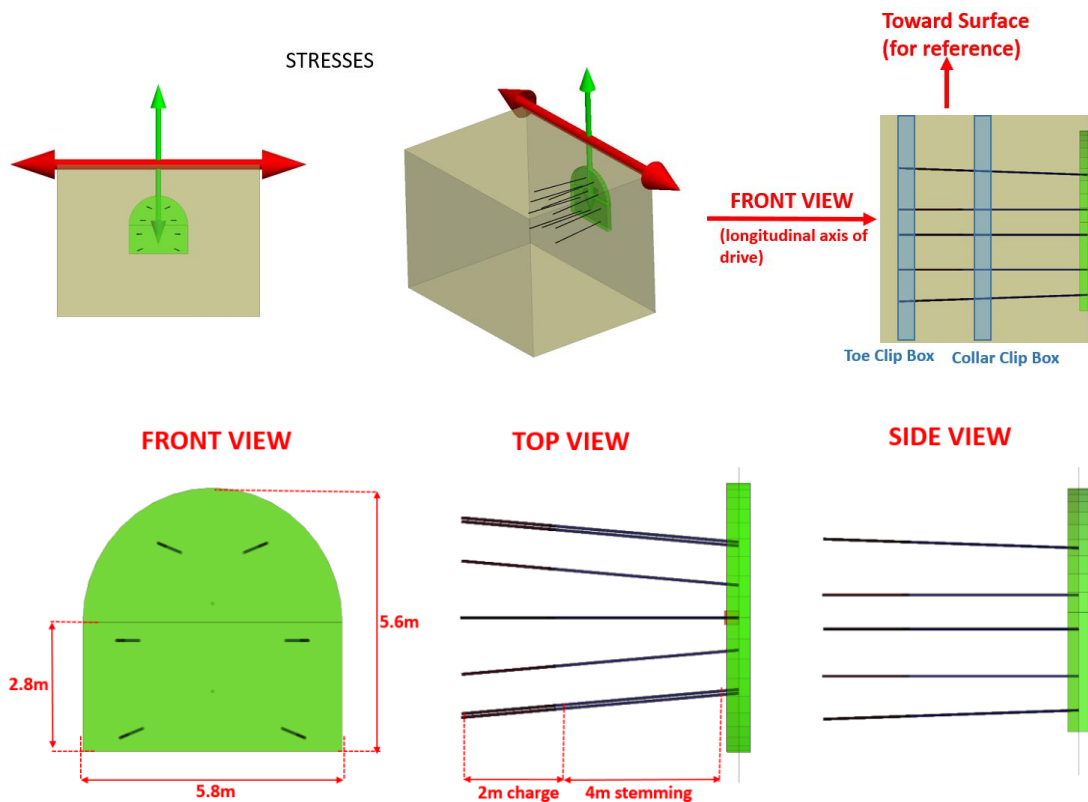
FRONT VIEW (TOE)



Model Parameters (Runs 19 & 20)

<i>Model Parameter</i>	<i>Value</i>
<i>Blast Hole Length</i>	6m
<i>Charge Length</i>	2m
<i>Blast Hole Diameter</i>	52mm
<i>Blast Hole Dip</i>	2 degrees
<i>Blast Hole Lookout Angle</i>	5 degrees
<i>Booster</i>	Modelled at both collar and toe
<i>Explosive</i>	Emulsion-5000m/s VOD – 1.15 density
<i>Sigma 1</i>	50 MPa (assumed to be horizontal)
<i>Sigma 3</i>	27 MPa (assumed to be vertical)
<i>Development Size</i>	ILLUSTRATED IN NEXT SLIDE
<i>Model boundary</i>	15m x 15m x 20m

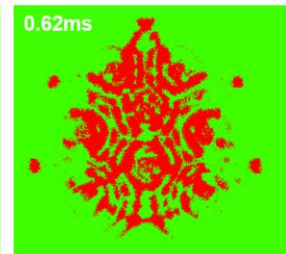
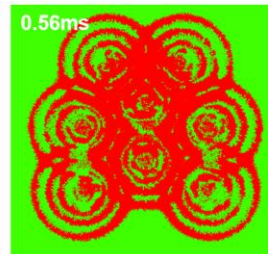
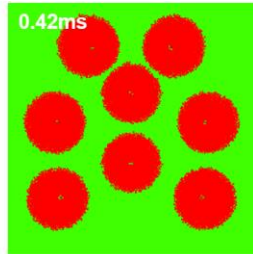
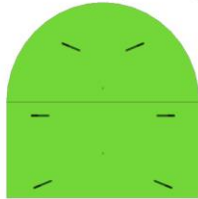
Model Viewpoints (Runs 19 - 21)



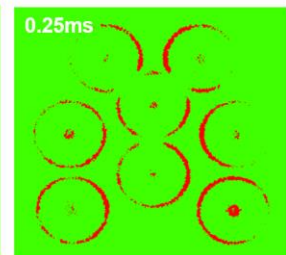
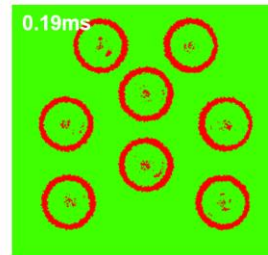
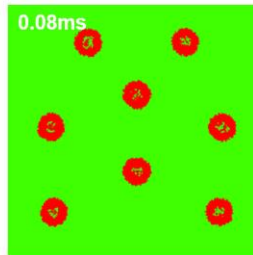
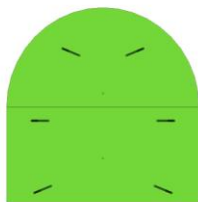
Run 19 Summary Statistics and Model Images

Model ID	Rock Type	Run Time	Stresses	No. Holes	Perimeter Holes
Run 19	Test Rock	1ms	100%	8	6
Centre Holes	Hole Length	Charge Length	Booster Location	Perimeter Holes	Delay
2	6	2.4	Toe	-	0ms

FRONT VIEW (COLLAR)



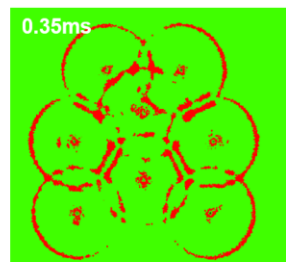
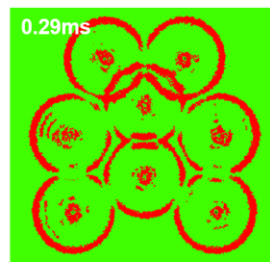
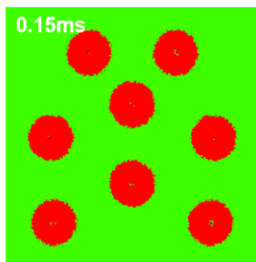
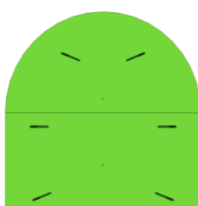
FRONT VIEW (TOE)



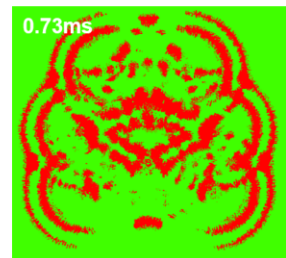
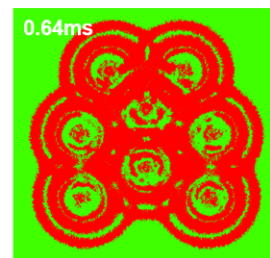
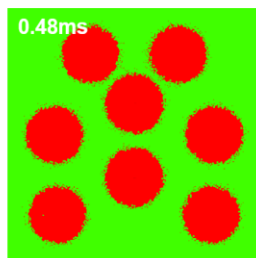
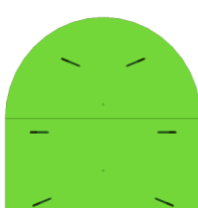
Run 20 Summary Statistics and Model Images

Model ID	Rock Type	Run Time	Stresses	No. Holes	Perimeter Holes
Run 20	Test Rock	1ms	100%	8	6
Centre Holes	Hole Length	Charge Length	Booster Location	Perimeter Holes	Delay
2	6	2.4	Collar	-	0ms

FRONT VIEW (COLLAR)



FRONT VIEW (TOE)

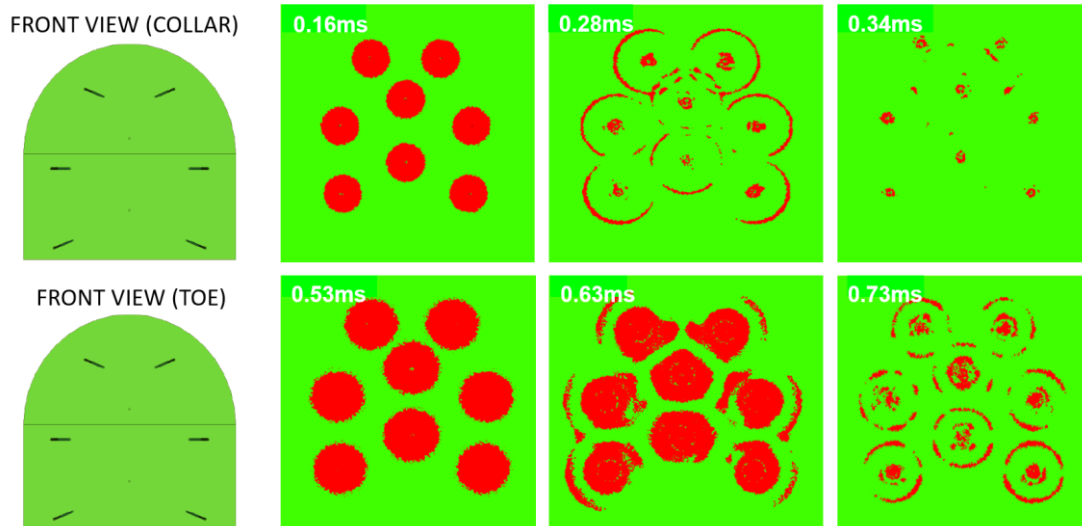


Model Parameters (Run 21)

<i>Model Parameter</i>	<i>Value</i>
<i>Blast Hole Length</i>	6m
<i>Charge Length</i>	2m
<i>Blast Hole Diameter</i>	45mm
<i>Blast Hole Dip</i>	2 degrees
<i>Blast Hole Lookout Angle</i>	5 degrees
<i>Booster</i>	Modelled at both collar and toe
<i>Explosive</i>	4000m/s VOD – 1.15 density
<i>Sigma 1</i>	50 MPa (assumed to be horizontal)
<i>Sigma 3</i>	27 MPa (assumed to be vertical)
<i>Development Size</i>	ILLUSTRATED IN NEXT SLIDE
<i>Model boundary</i>	15m x 15m x 20m

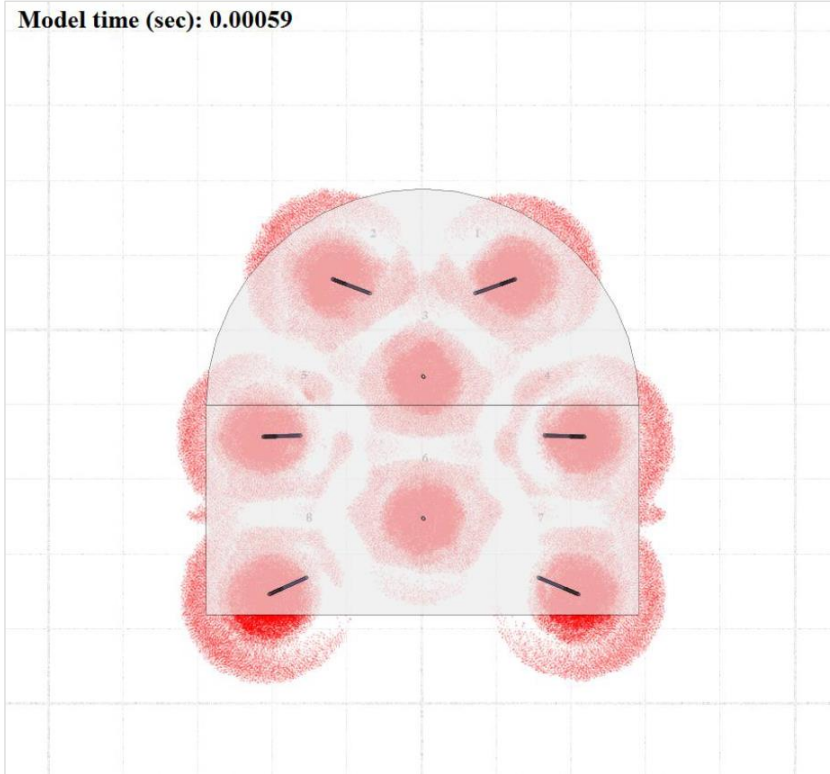
Run 21 Summary Statistics and Model Images

Model ID	Rock Type	Run Time	Stresses	No. Holes	Perimeter Holes
Run 20	Test Rock	1ms	100%	8	6
Centre Holes	Hole Length	Charge Length	Booster Location	Perimeter Holes	Delay
2	6	2.0	Collar	-	0ms



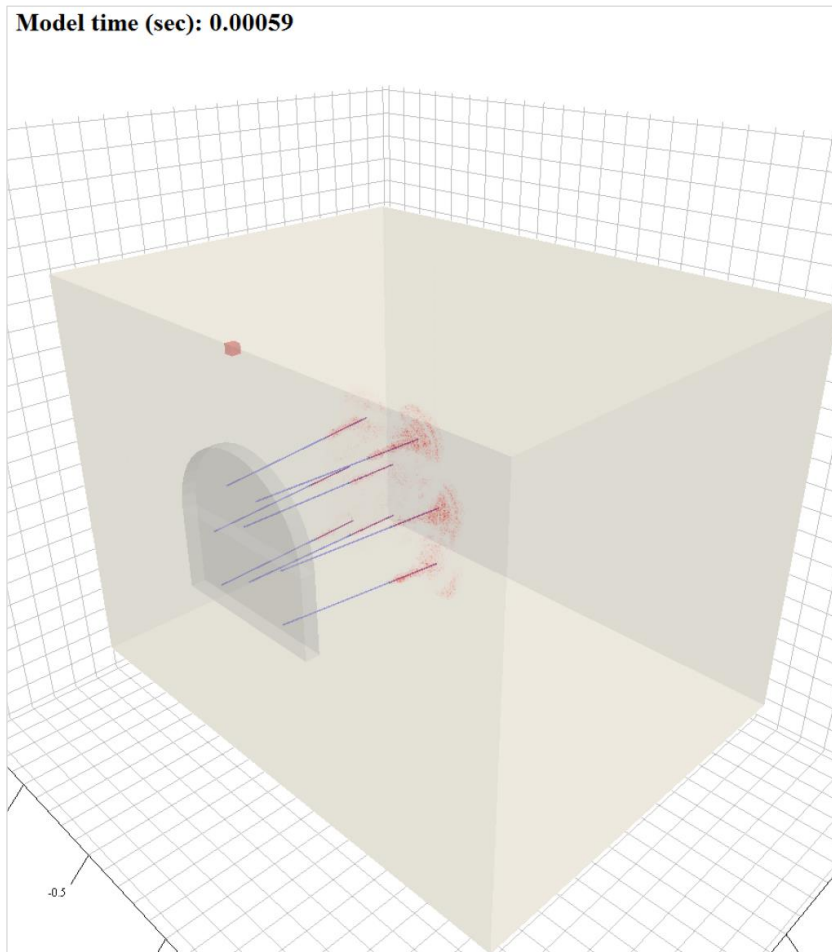
Run 21 – Cross Section View

Model time (sec): 0.00059



Run 21 Perspective View

Model time (sec): 0.00059

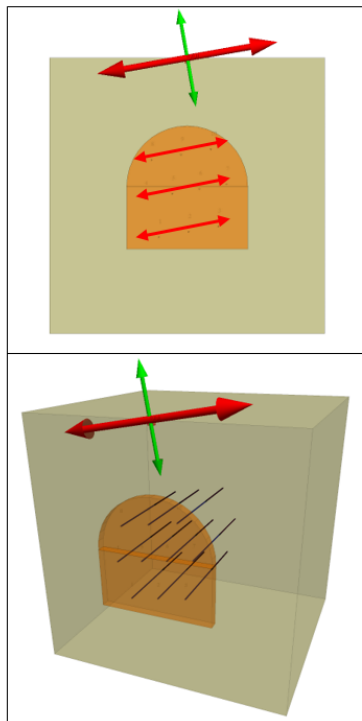


Model Parameters (Run 22)

<i>Model Parameter</i>	<i>Value</i>		
<i>Blast Hole Length</i>	7m		
	From:	To:	Length:
<i>Charge Length</i>	0m	3m*	3m*
<i>Stemming</i>	3m*	4.1m	1.1m*
<i>Air Gap</i>	4.1m	7m	2.9m
<i>Blast Hole Diameter</i>	63mm		
<i>Blast Hole Dip</i>	0°, i.e. Parallel to drive		
<i>Booster</i>	2.9m from toe		
<i>Explosive</i>	4000m/s VOD, 0.75 Reaction extent		
<i>Sigma 1</i>	50 MPa		
<i>Sigma 3</i>	27MPa		
<i>Stress Orientation</i>	-10°		
<i>Development Size</i>	ILLUSTRATED IN NEXT SLIDE		
<i>Block Model Boundary</i>	14m x 15m x 15m		

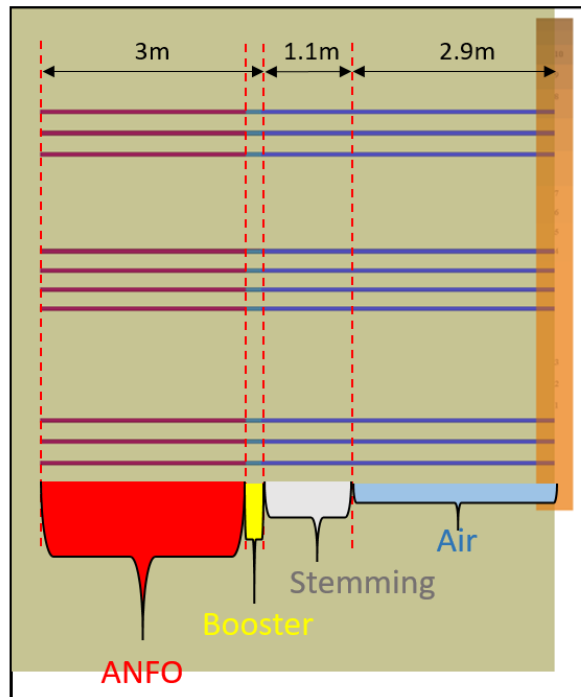
Model Geometry

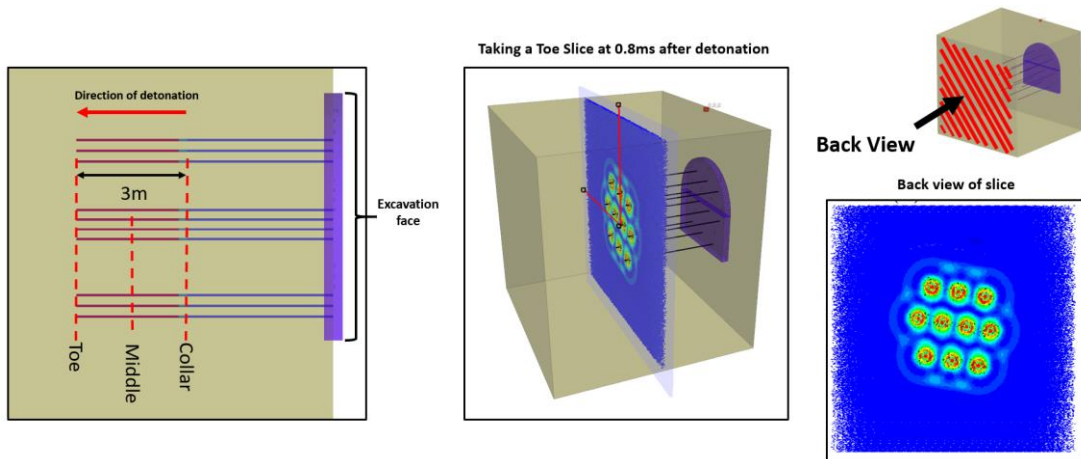
STRESSES



Note: Holes are orientated in rows running parallel to the Sigma 1 stress direction. The aim is "to maximise the number of holes which have fracture interaction".

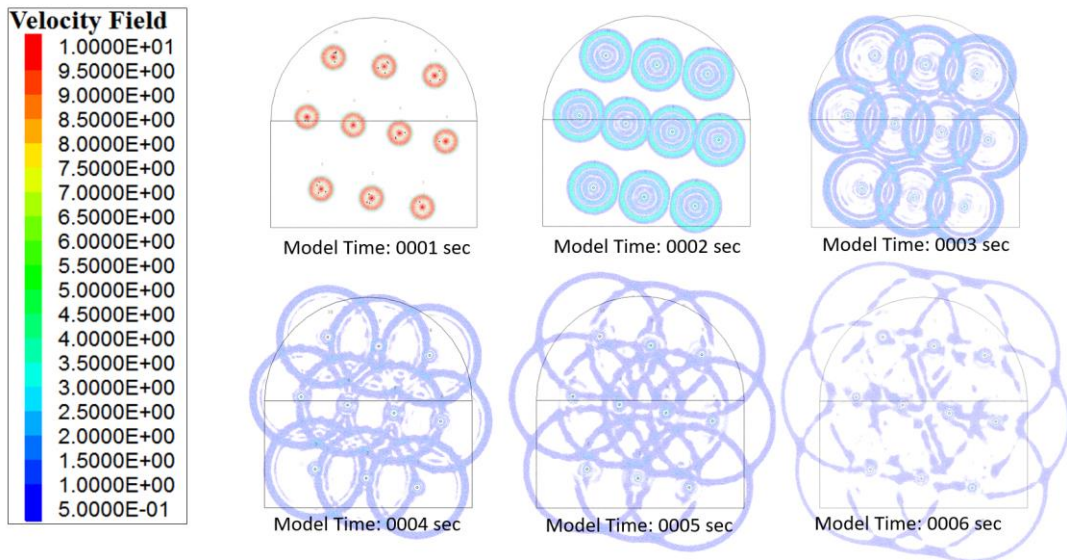
Blasthole Design Parameters



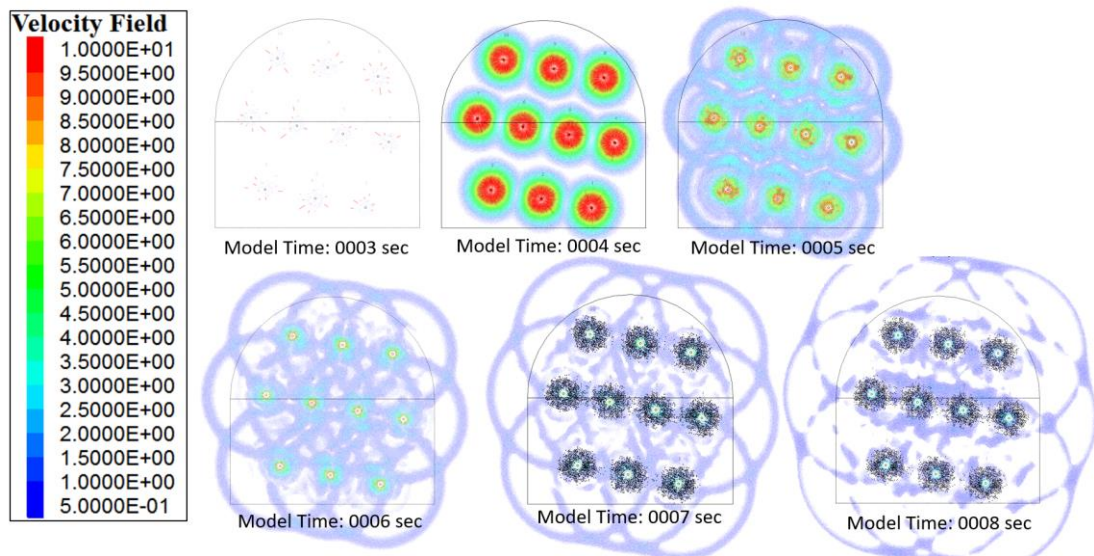


Run 22 Model Images

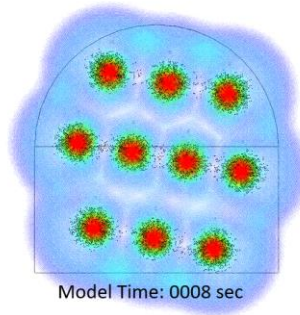
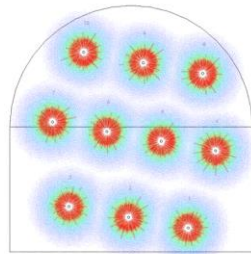
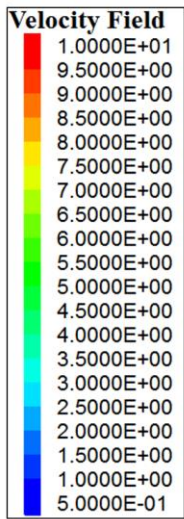
Particle Velocity Attenuation – Collar (Back view)



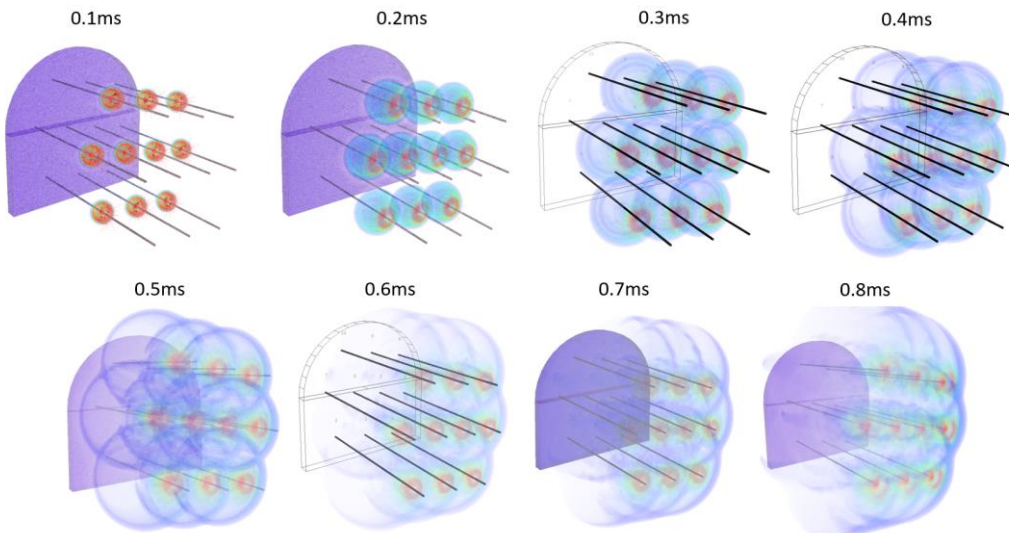
Particle Velocity Attenuation – Middle (Back view)



Particle Velocity Attenuation – Toe (Back view)



Isometric View of Blast Propagation

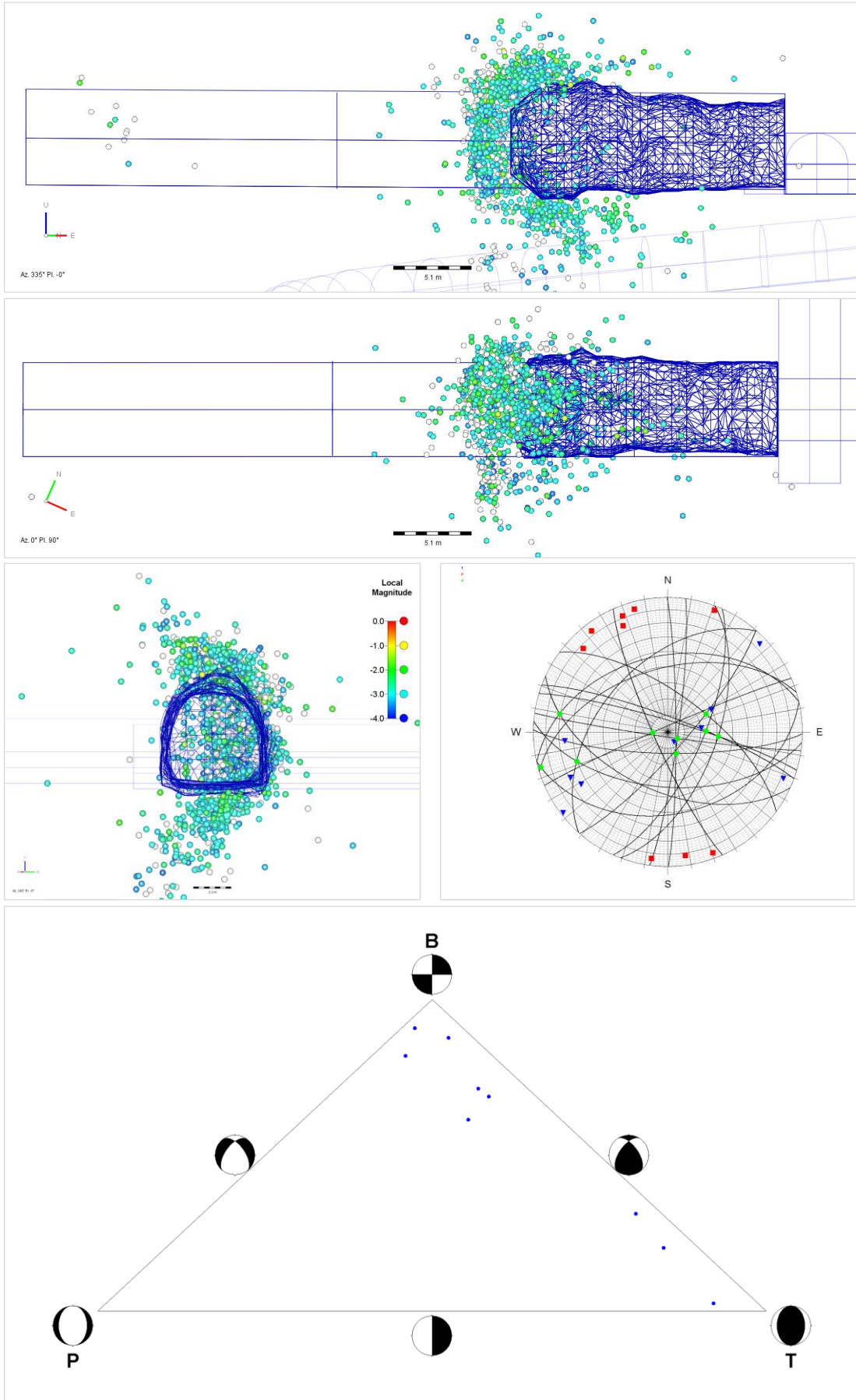


Appendix B

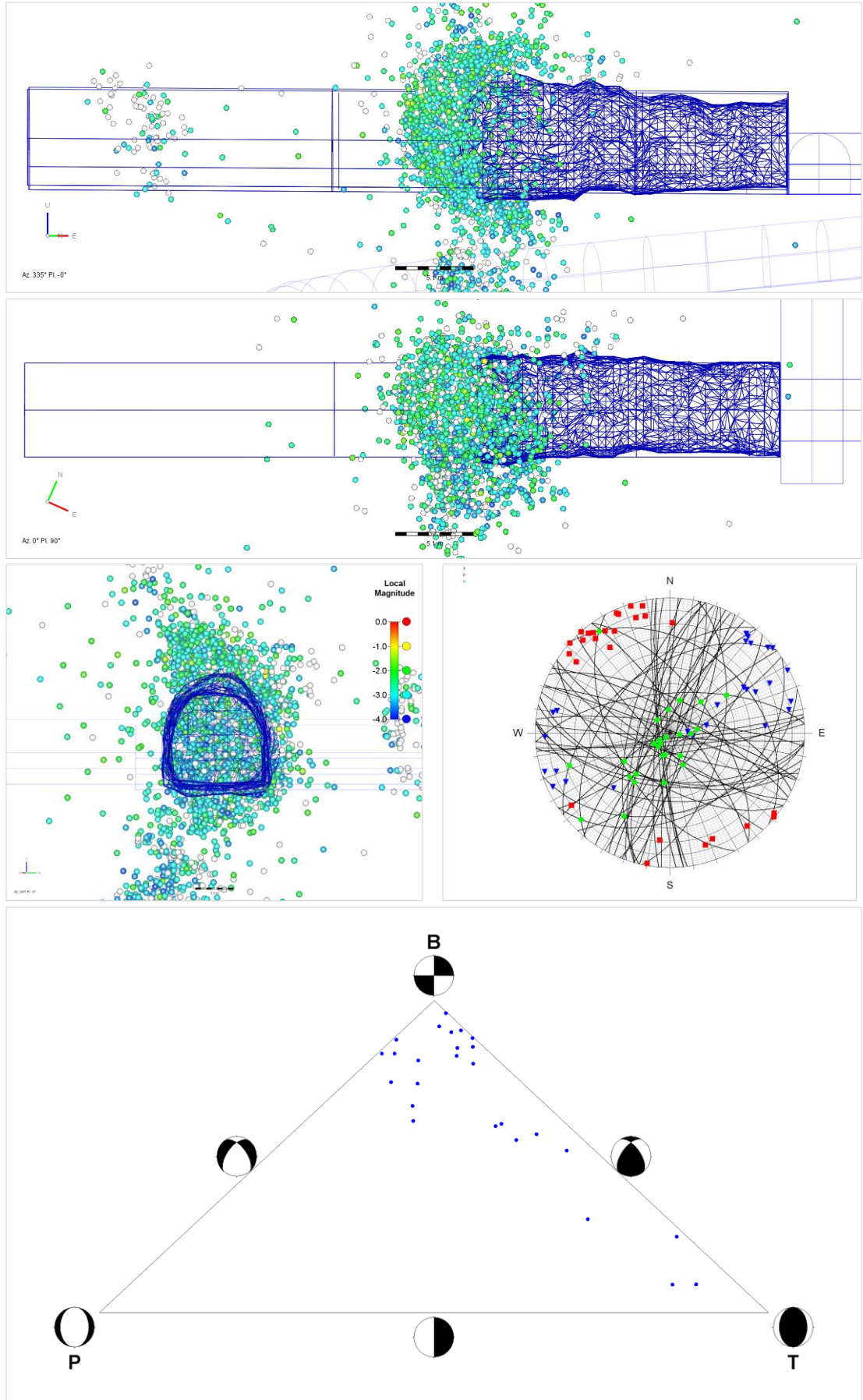
Seismic Data

Seismogenic zone images, mechanism stereonets, ternary plots and time history of events, energy and potency for each development cycle in the main seismic analysis.

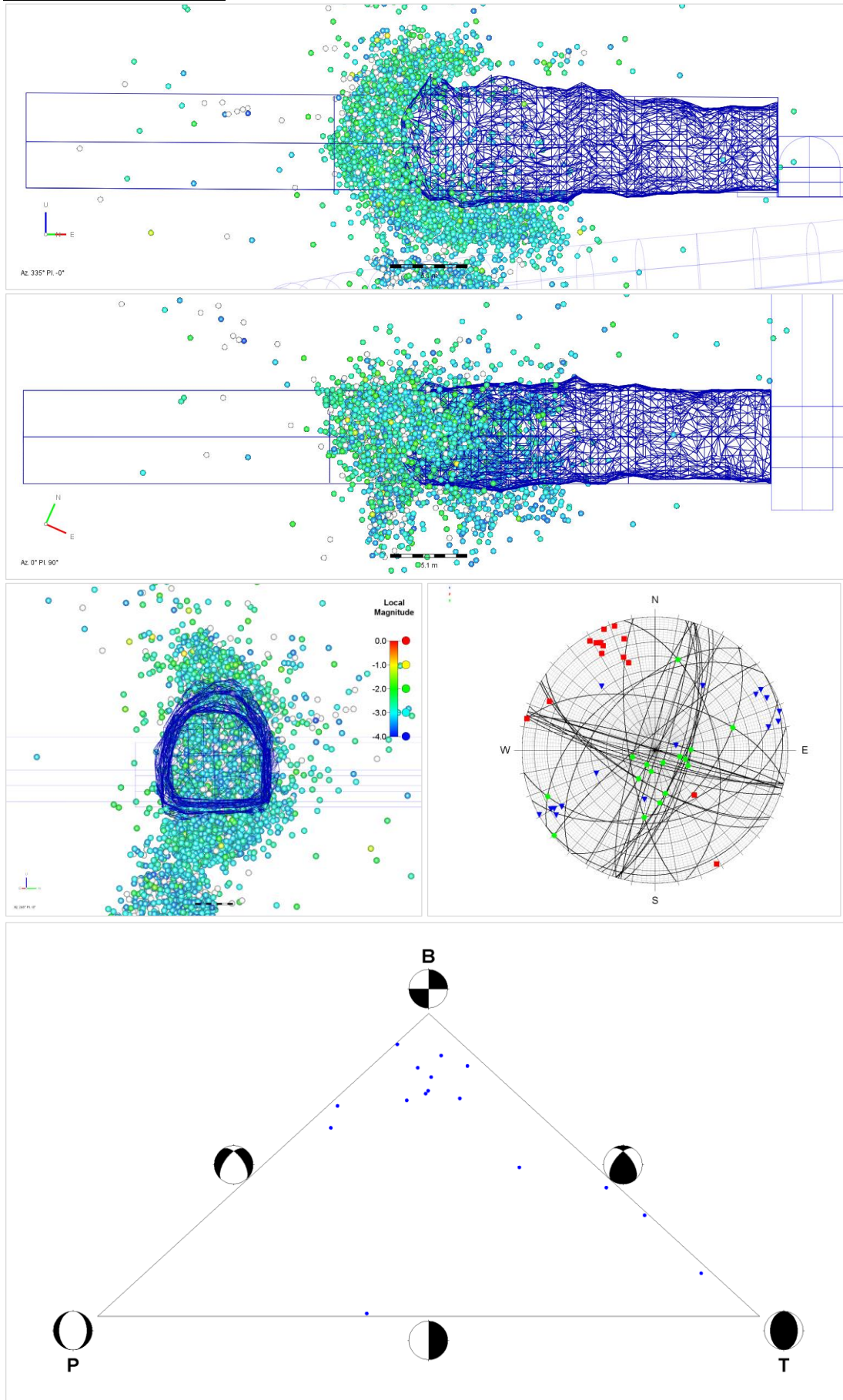
South Tunnel: Cut 9 (Longitudinal, Plan & Cross Section, Stereonet & Ternary Plot)



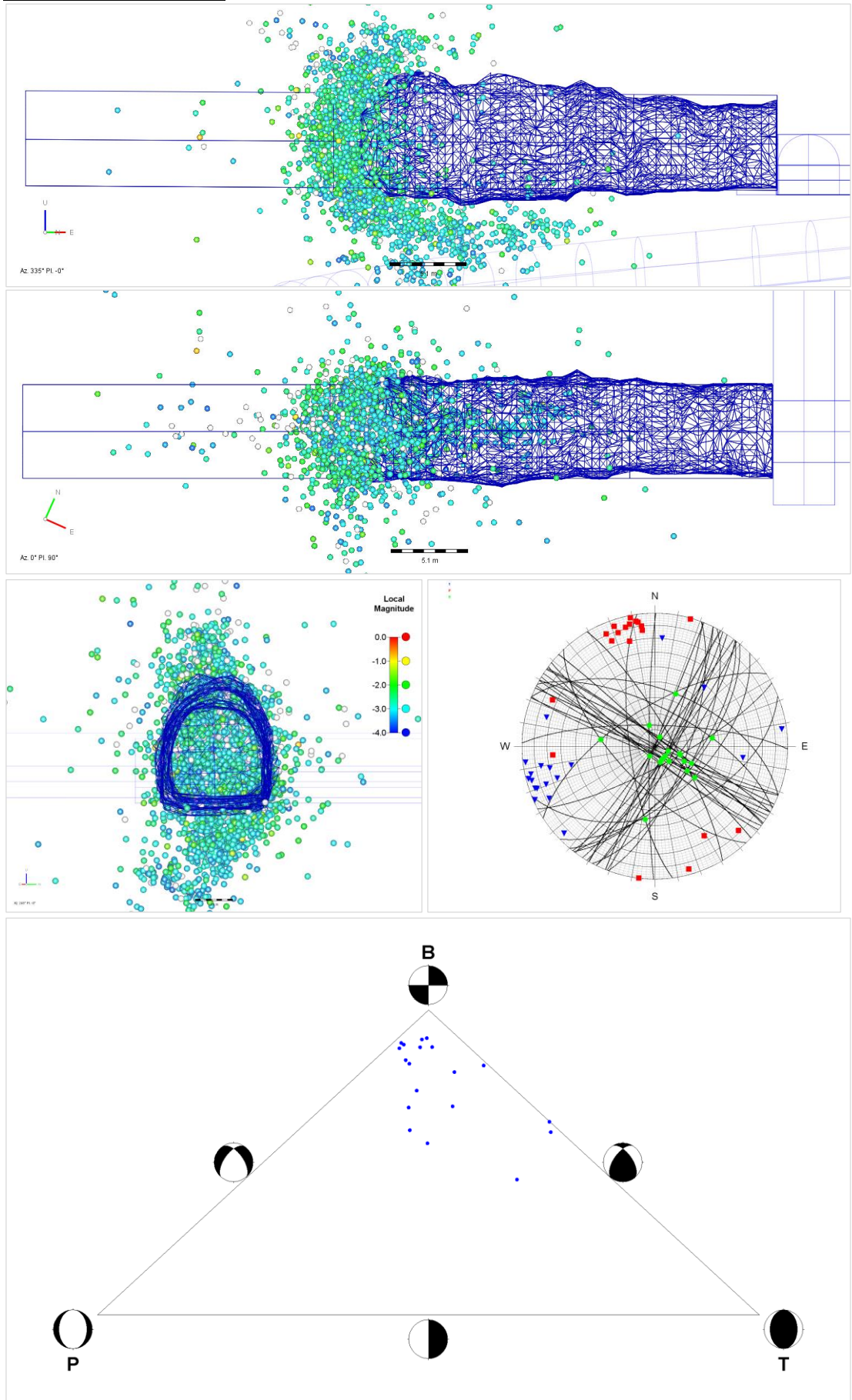
South Tunnel: Cut 11 (Longitudinal, Plan & Cross Section, Stereonet & Ternary Plot)



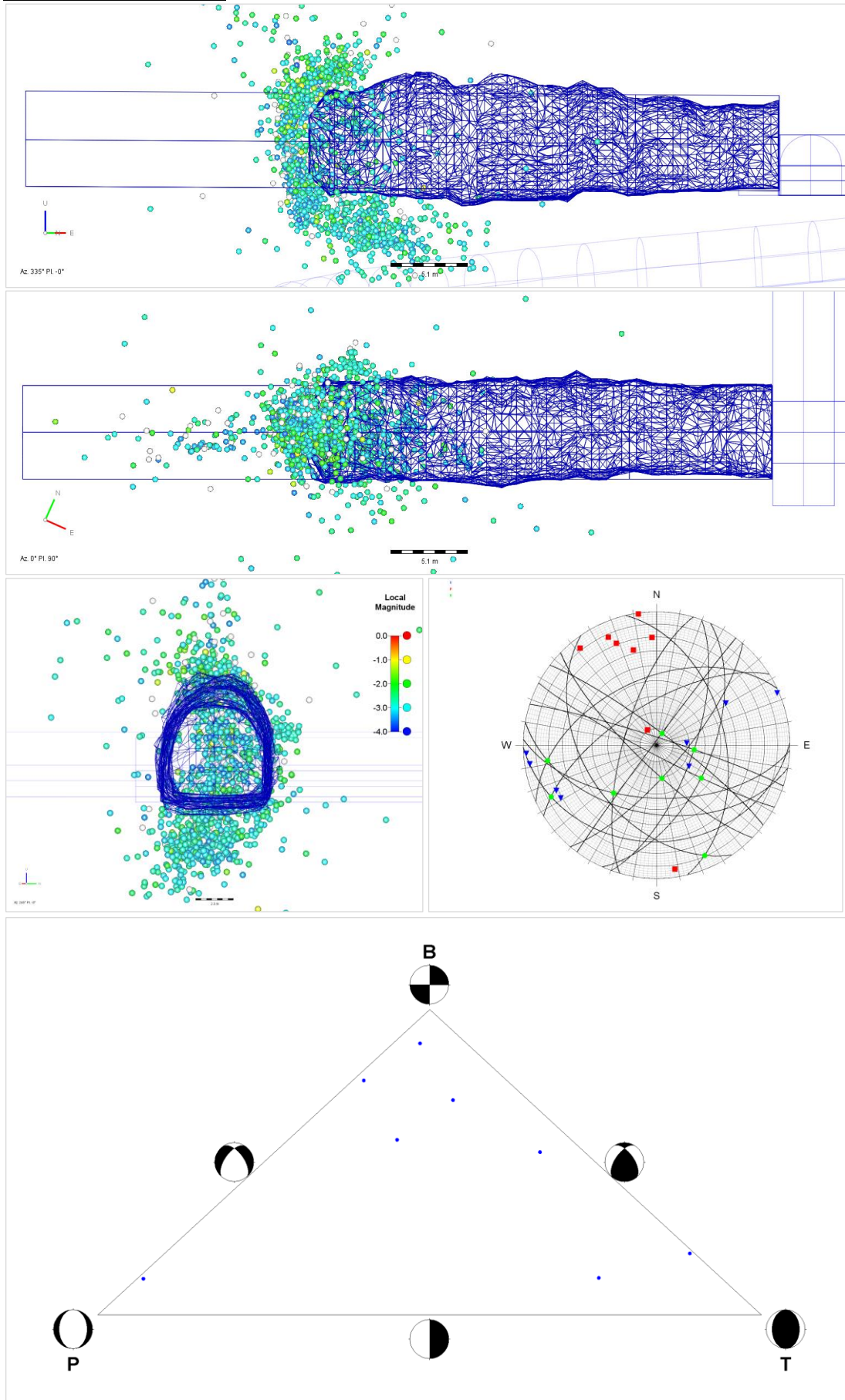
South Tunnel: Cut 13



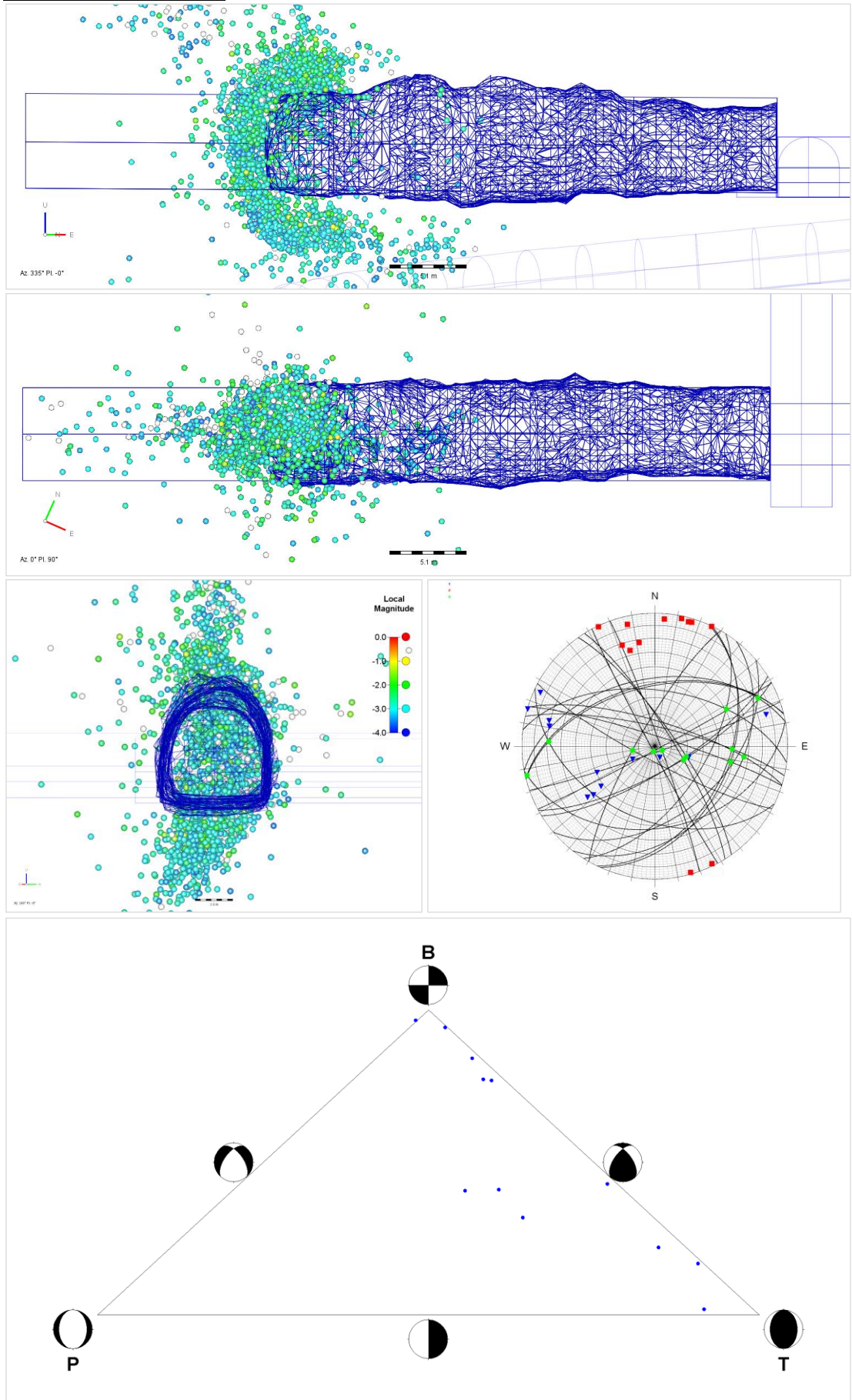
South Tunnel: Cut 15



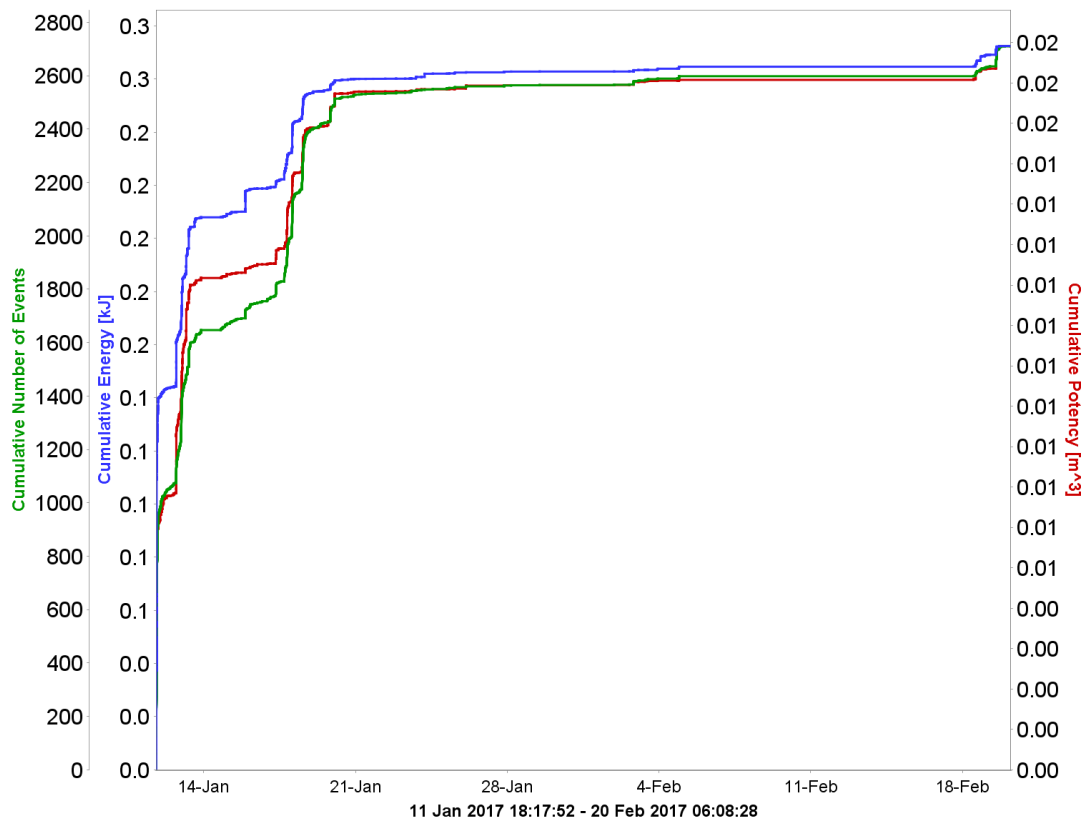
South Tunnel: Cut 17



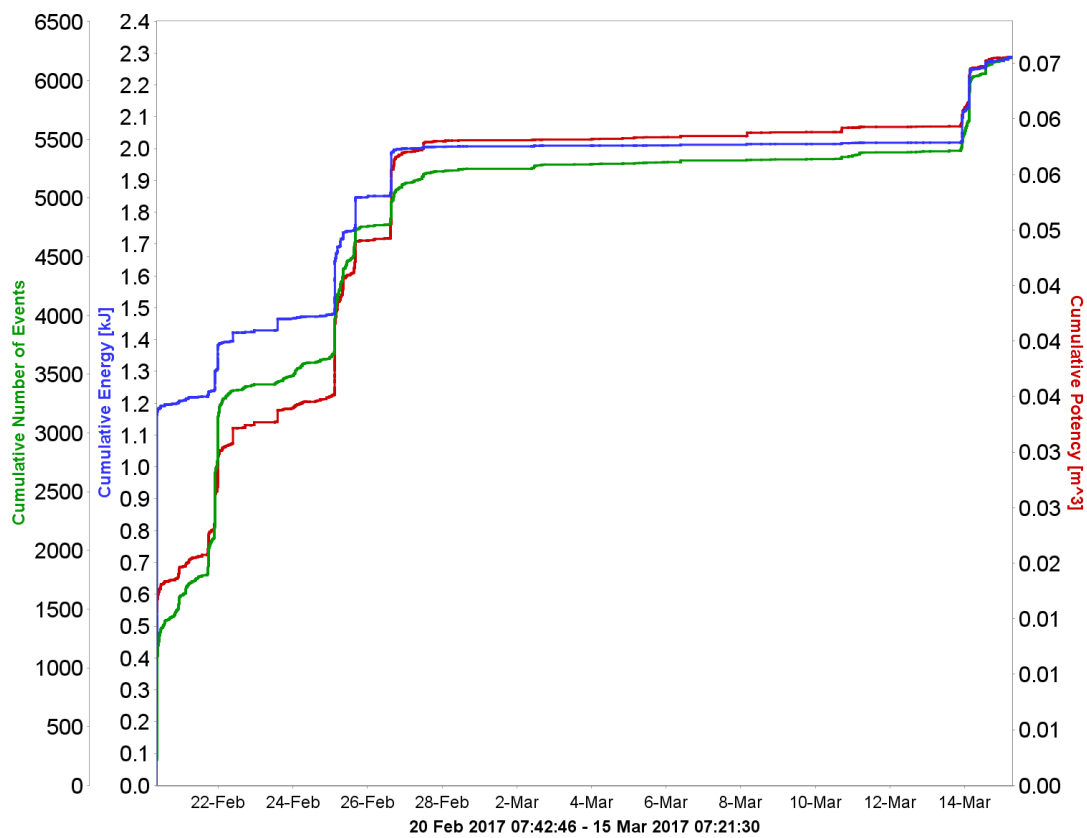
South Tunnel: Cut 19



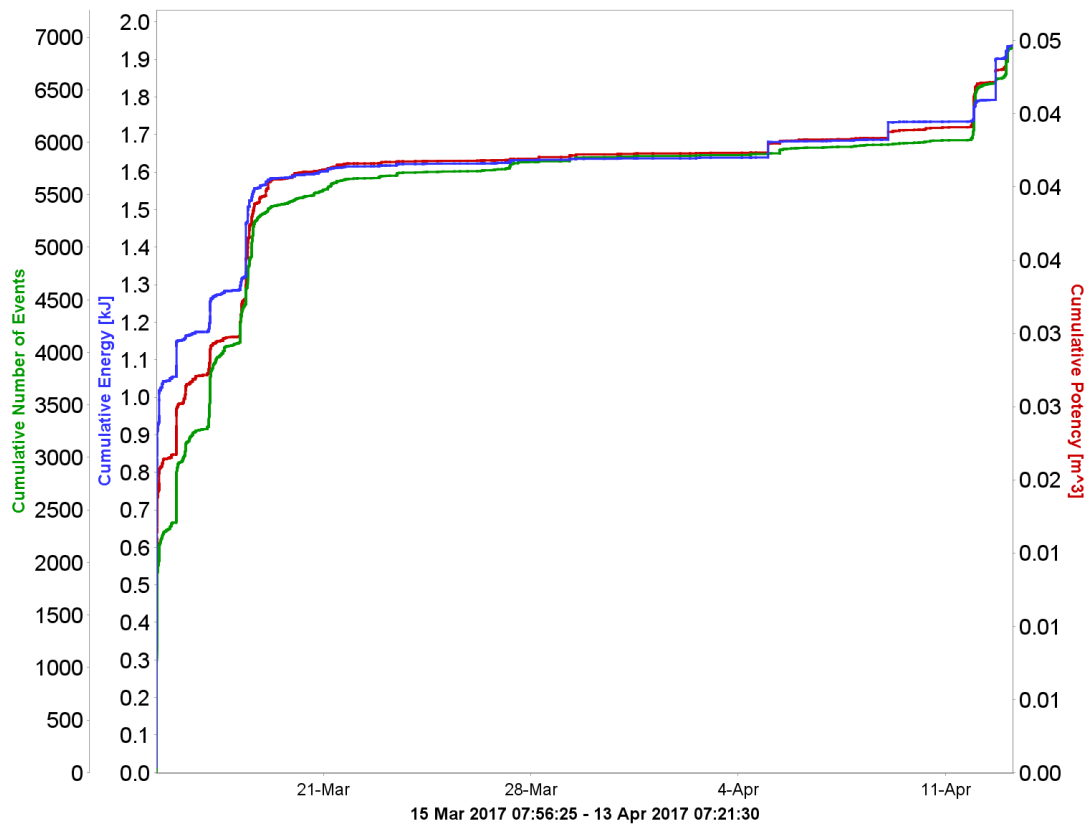
South Tunnel: Cut 9 (Time History)



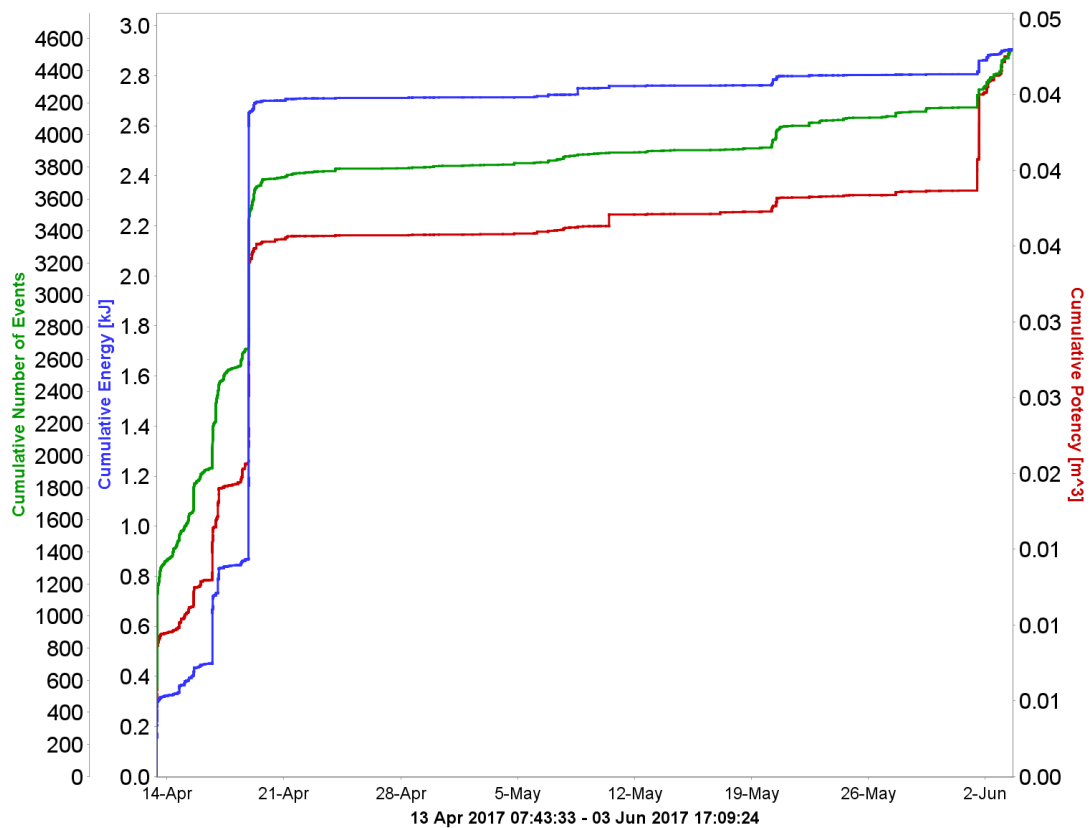
South Tunnel: Cut 11



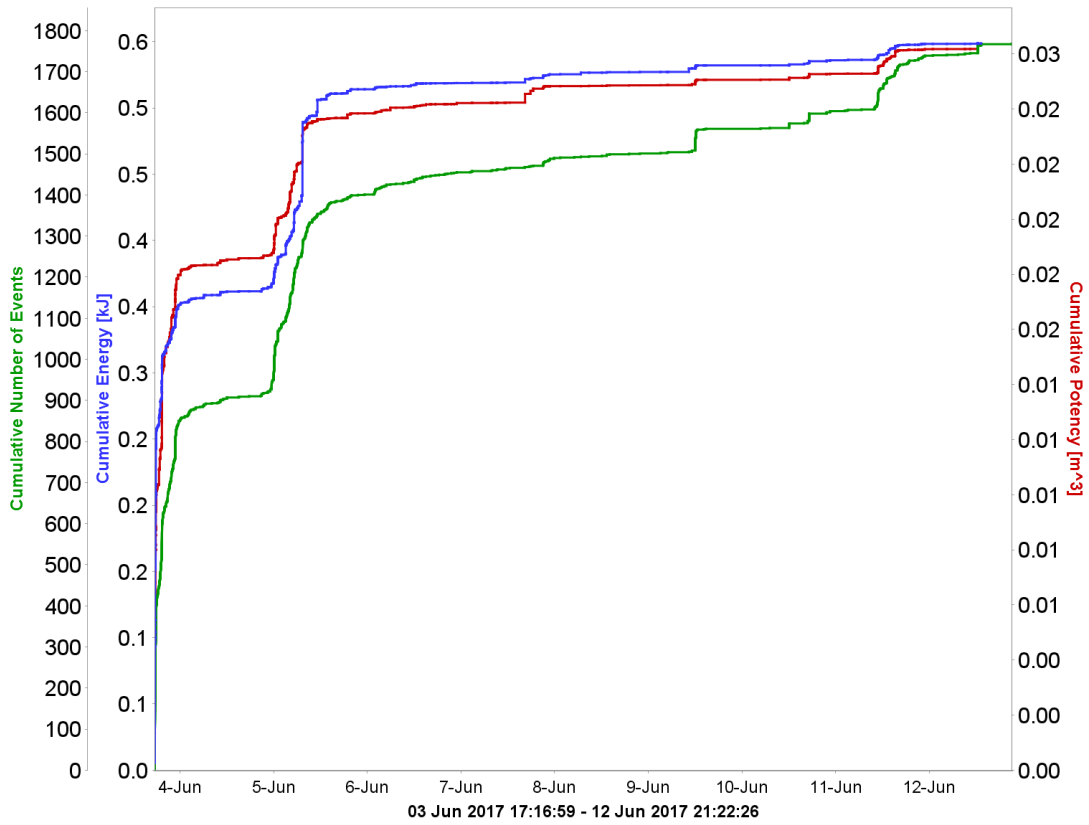
South Tunnel: Cut 13



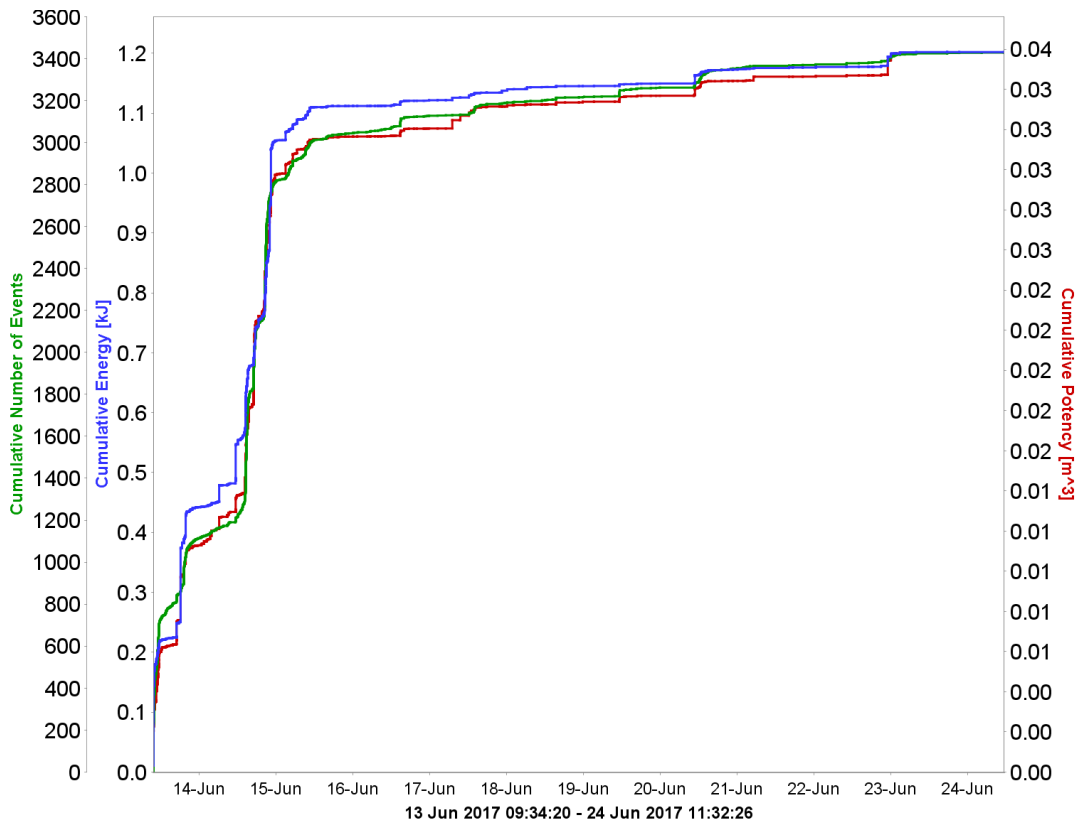
South Tunnel: Cut 15



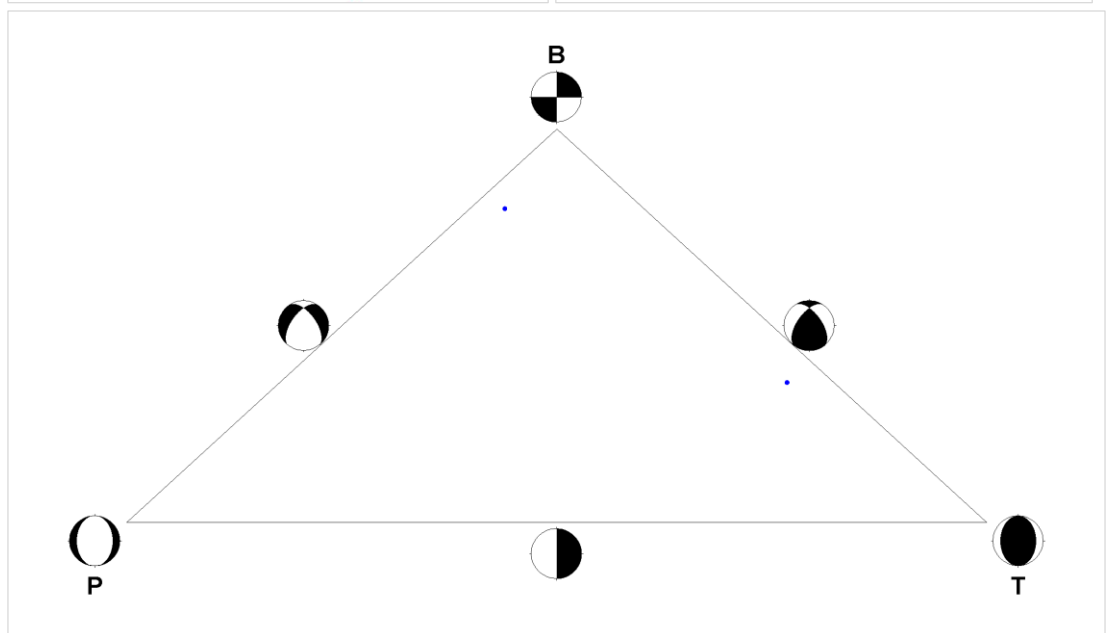
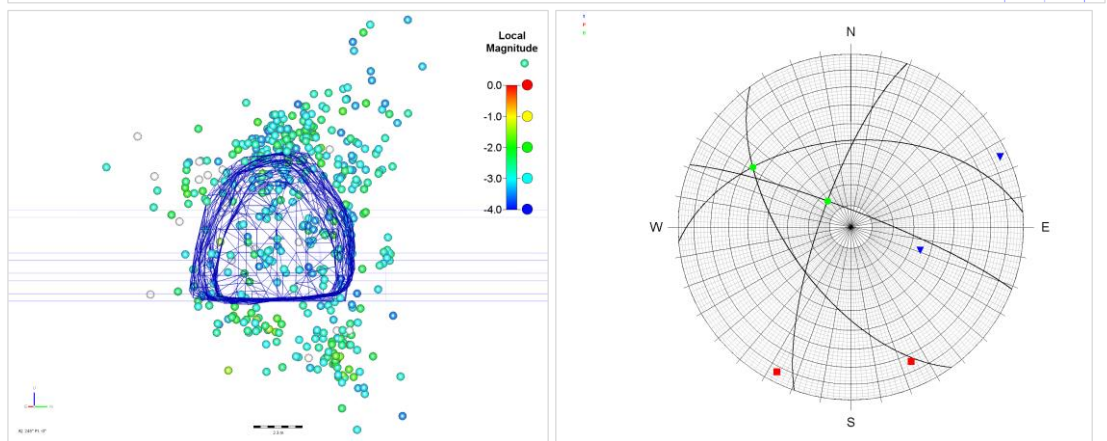
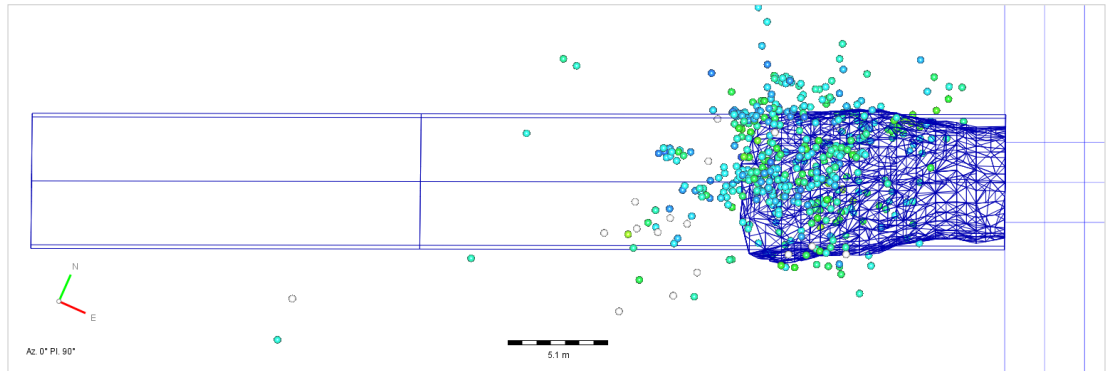
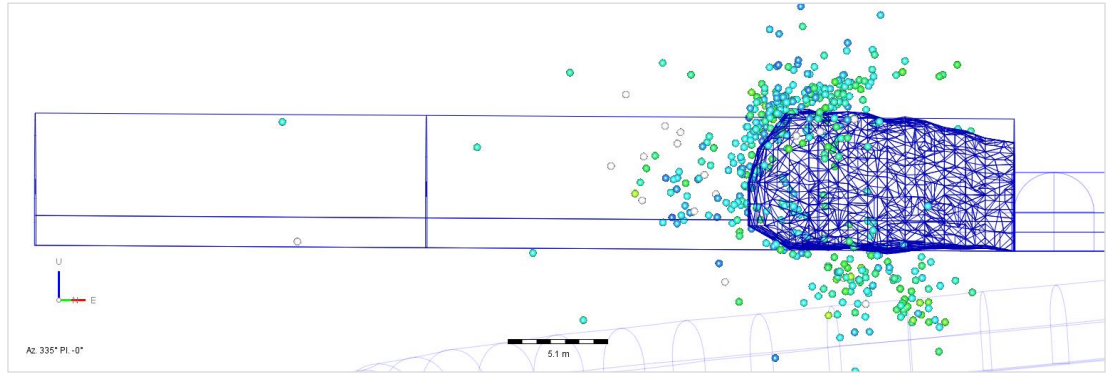
South Tunnel: Cut 17



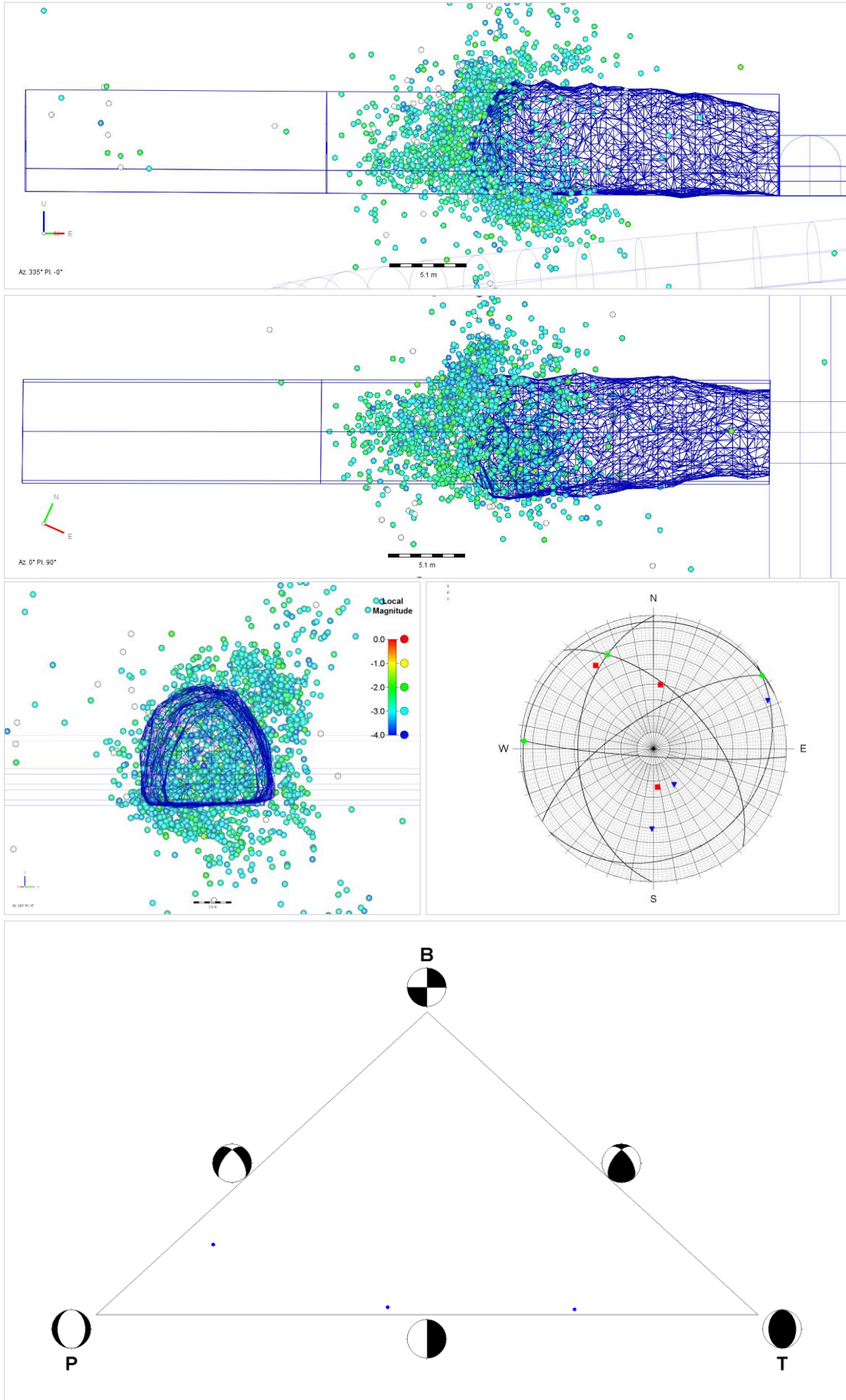
South Tunnel: Cut 19



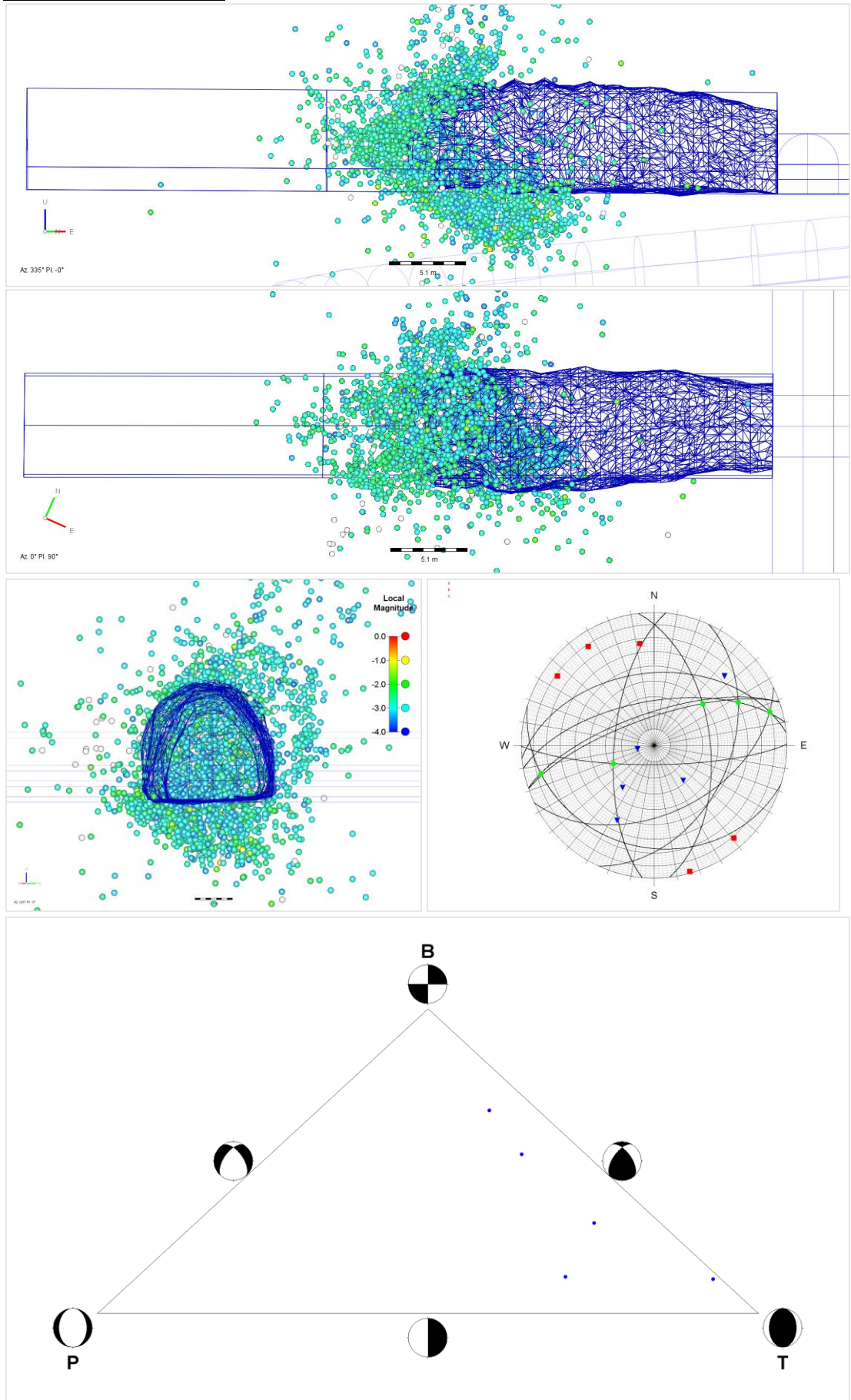
North Tunnel: Cut 8



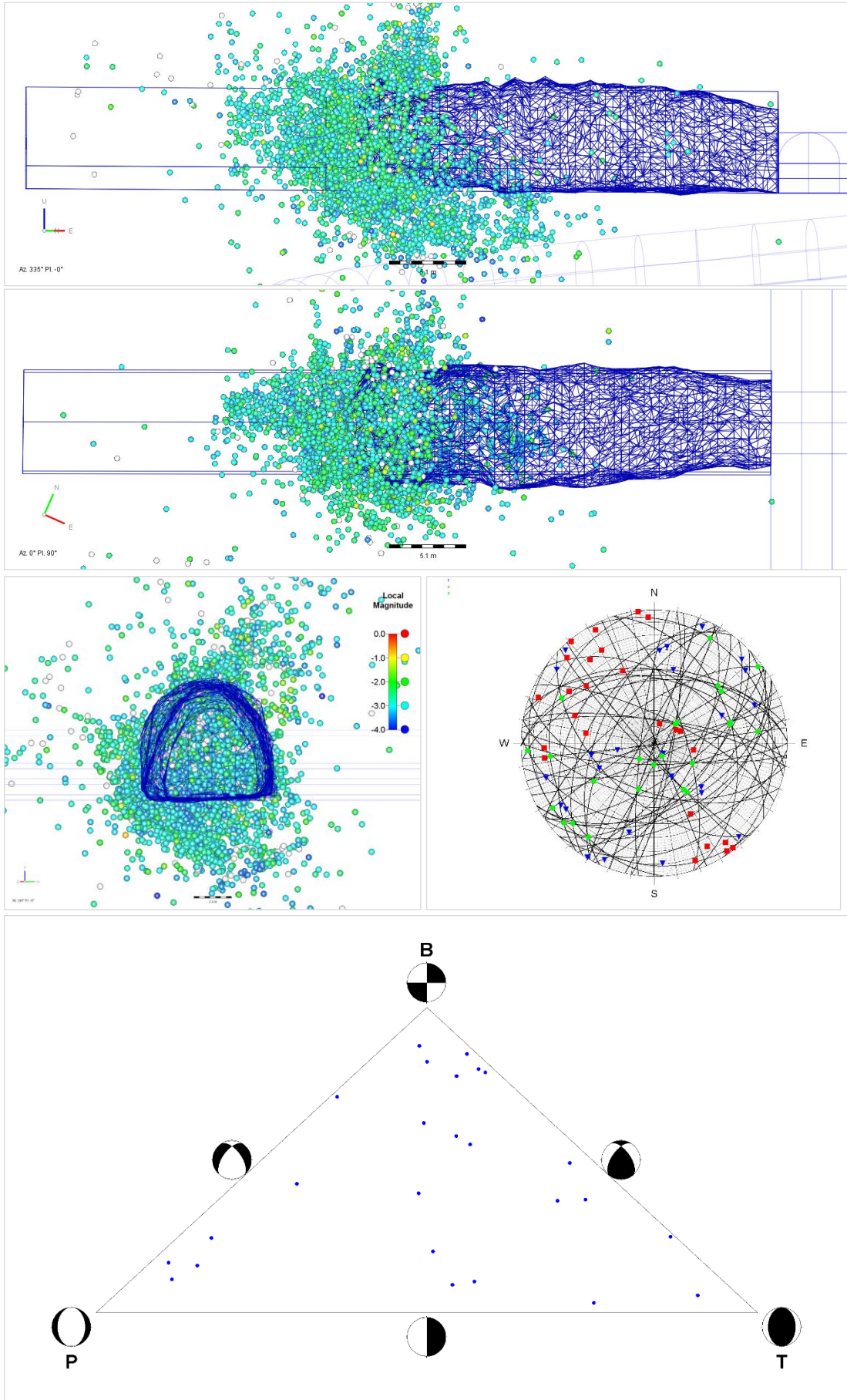
North Tunnel: Cut 12



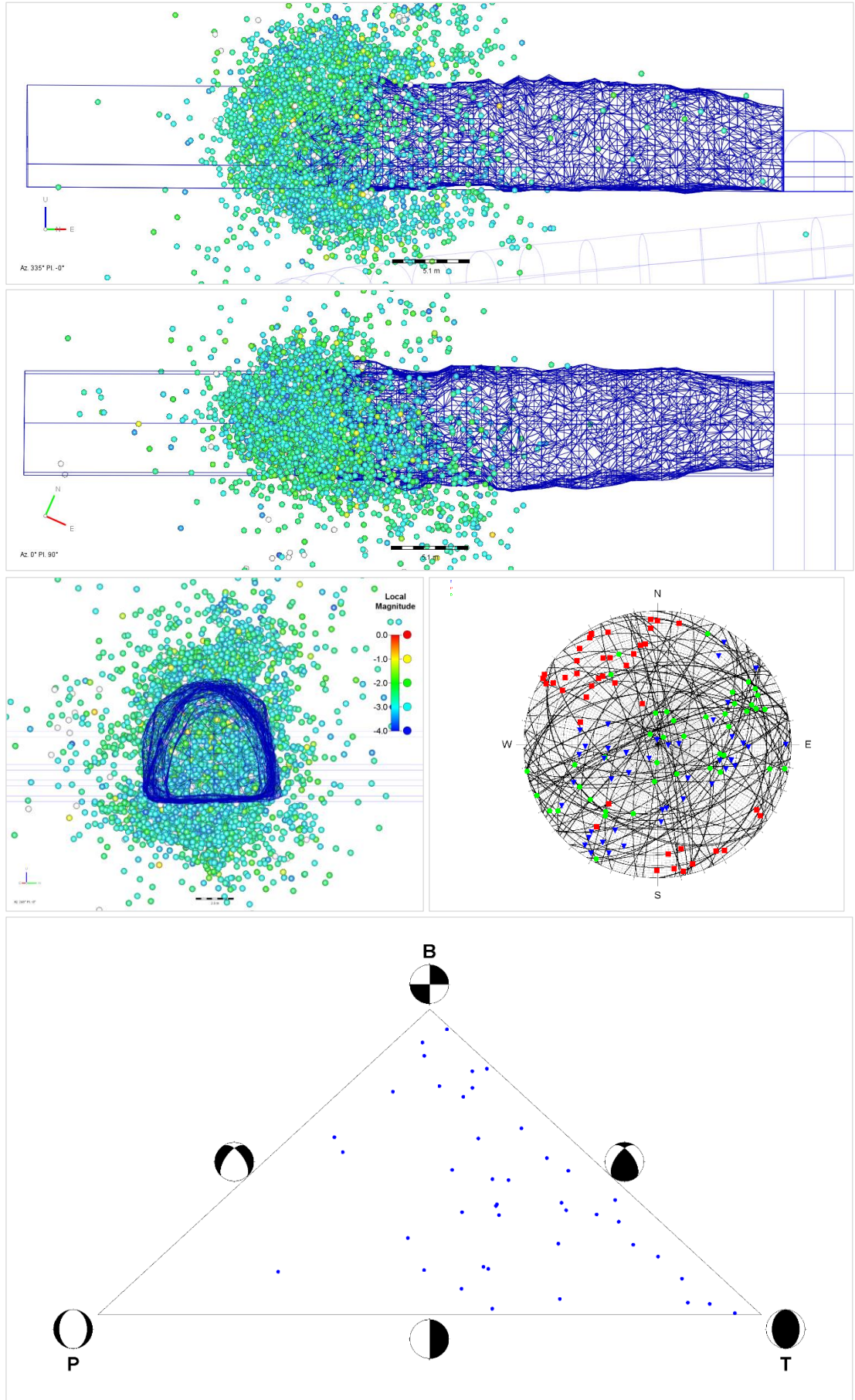
North Tunnel: Cut 14



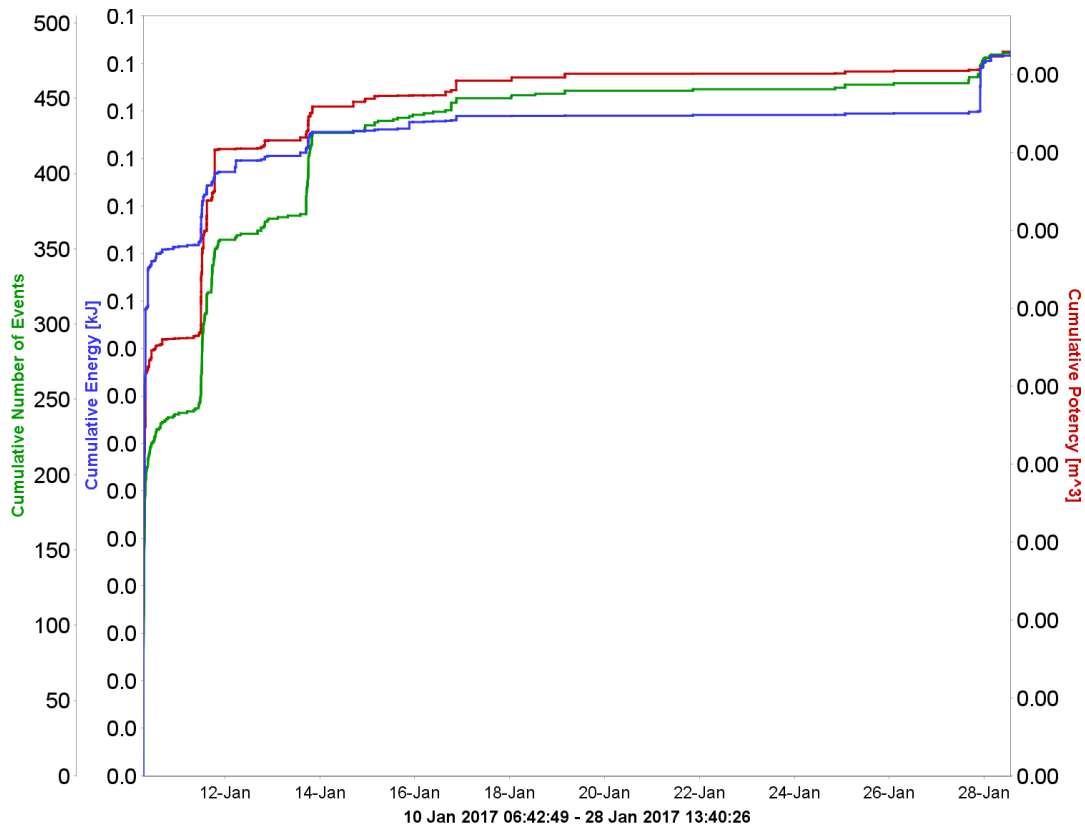
North Tunnel: Cut 16



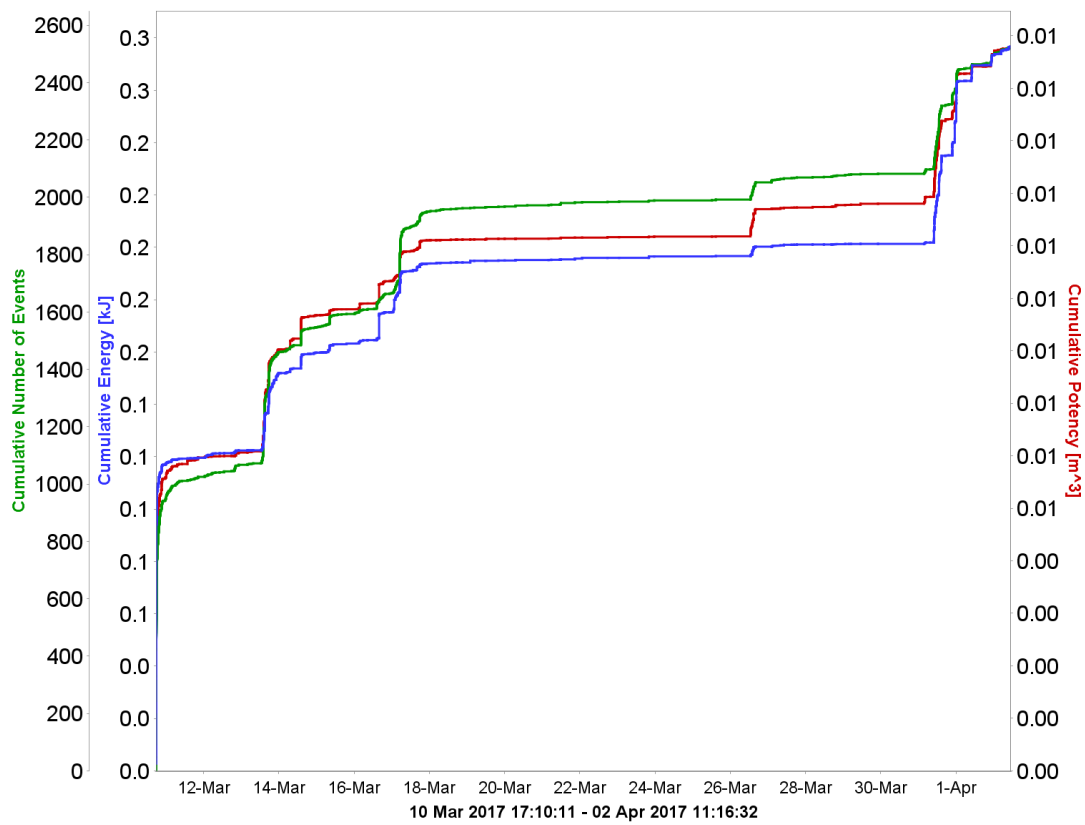
North Tunnel: Cut 18



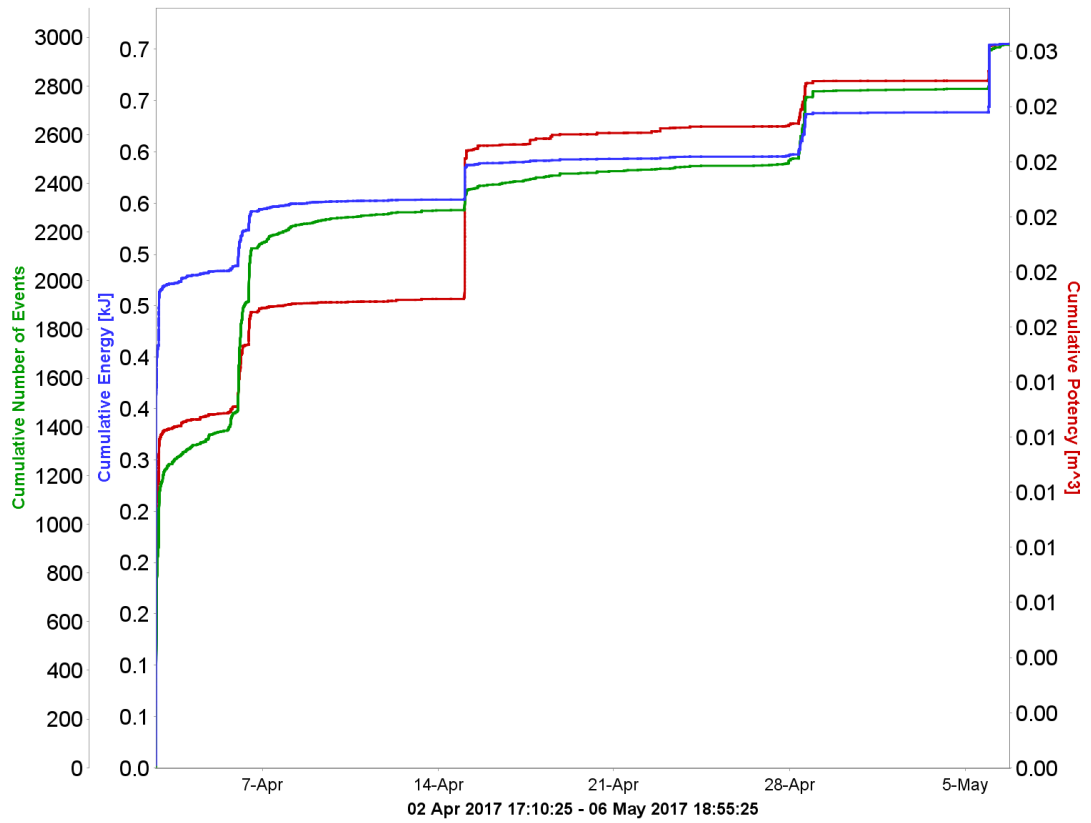
North Tunnel: Cut 8



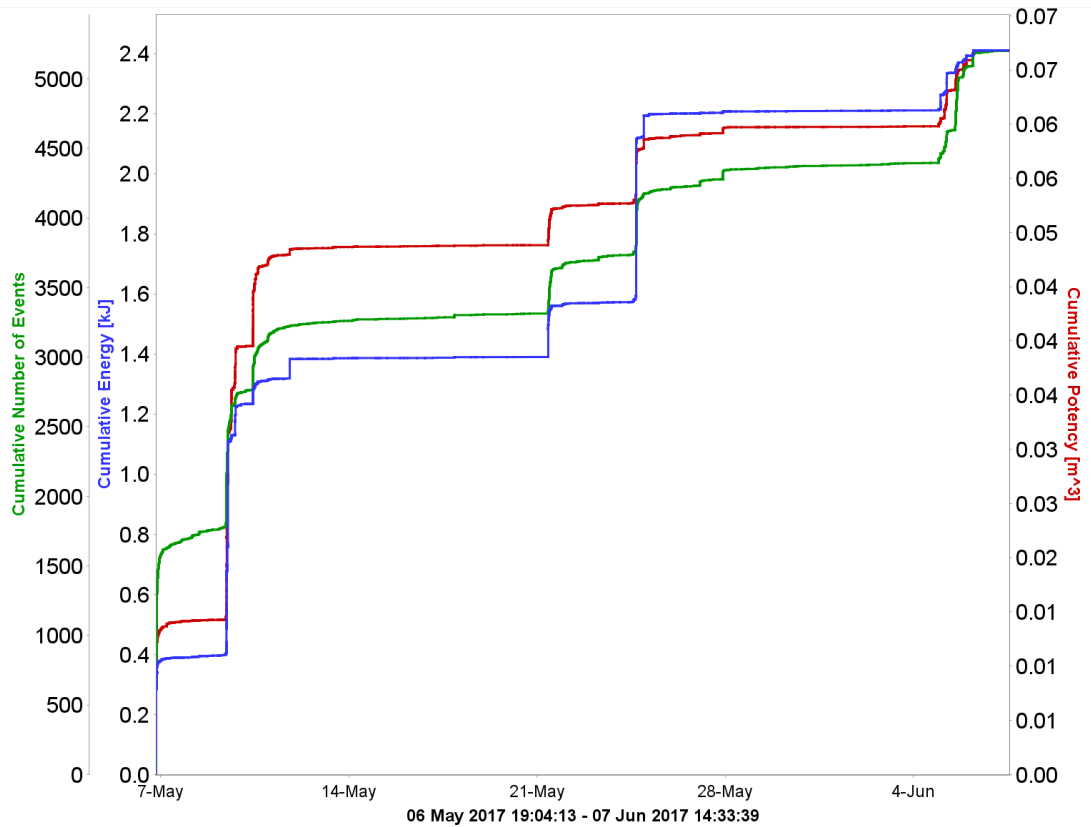
North Tunnel: Cut 12



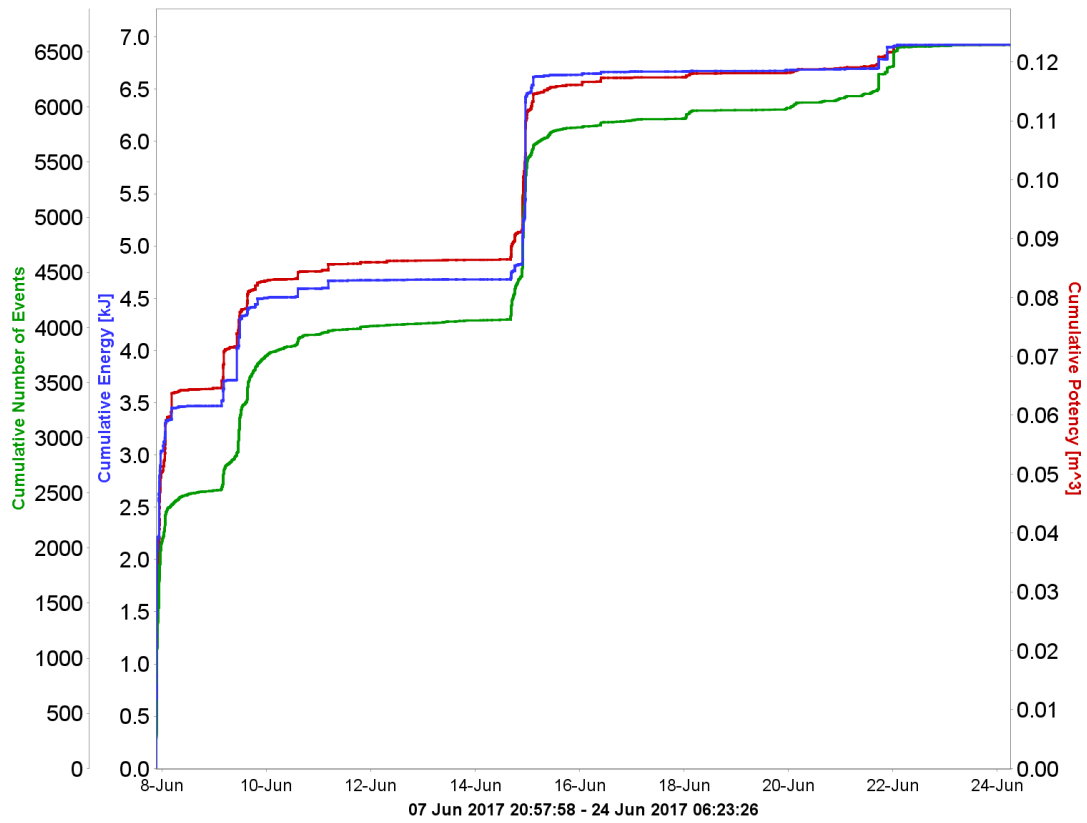
North Tunnel: Cut 14



North Tunnel: Cut 16



North Tunnel: Cut 18

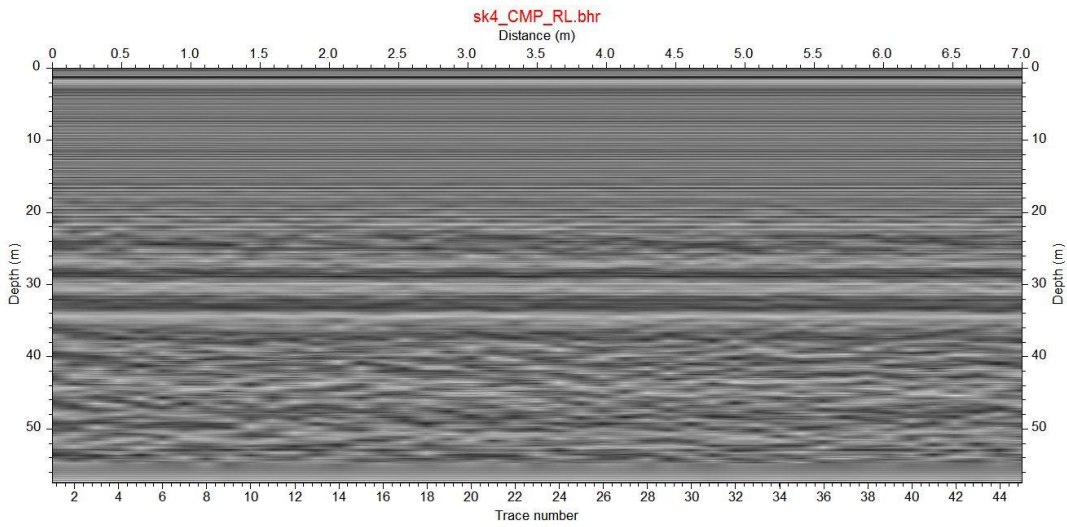
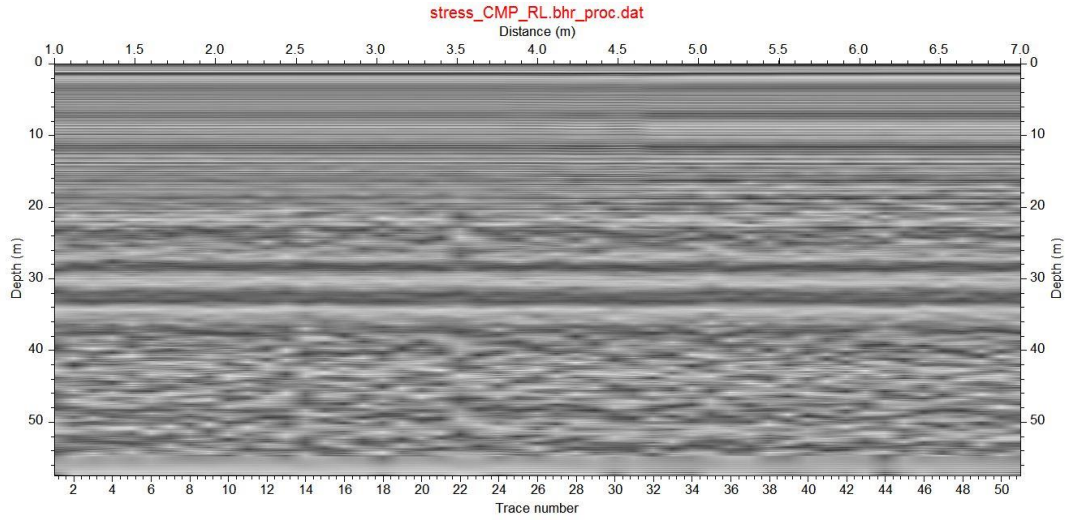


Appendix C

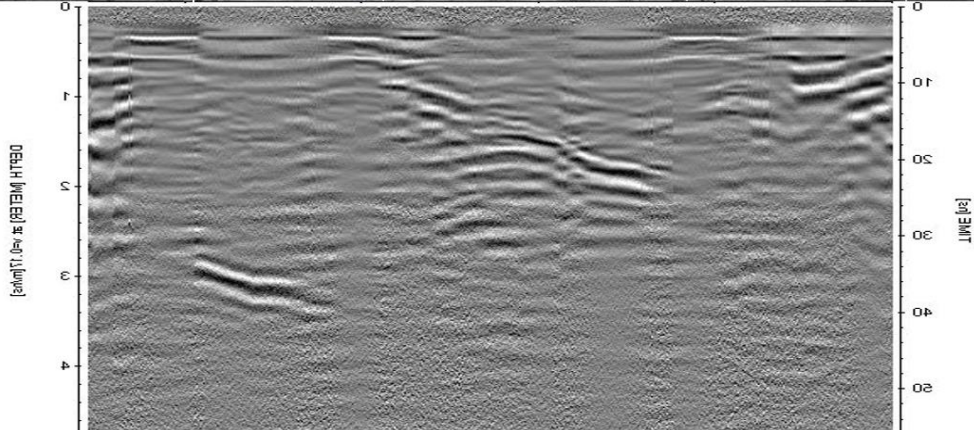
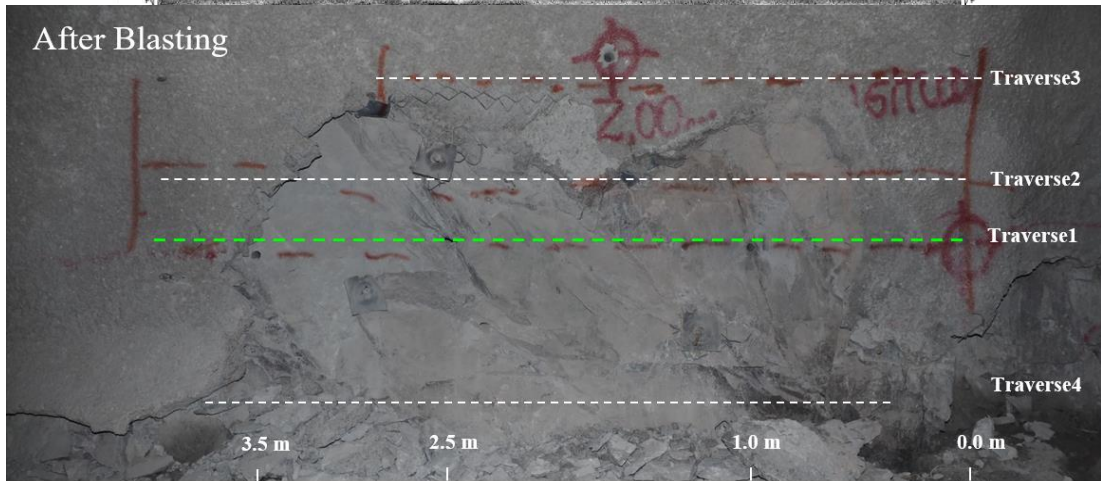
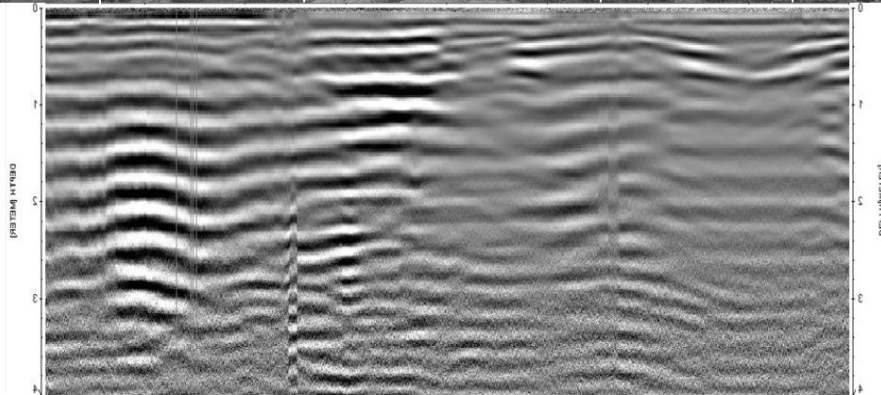
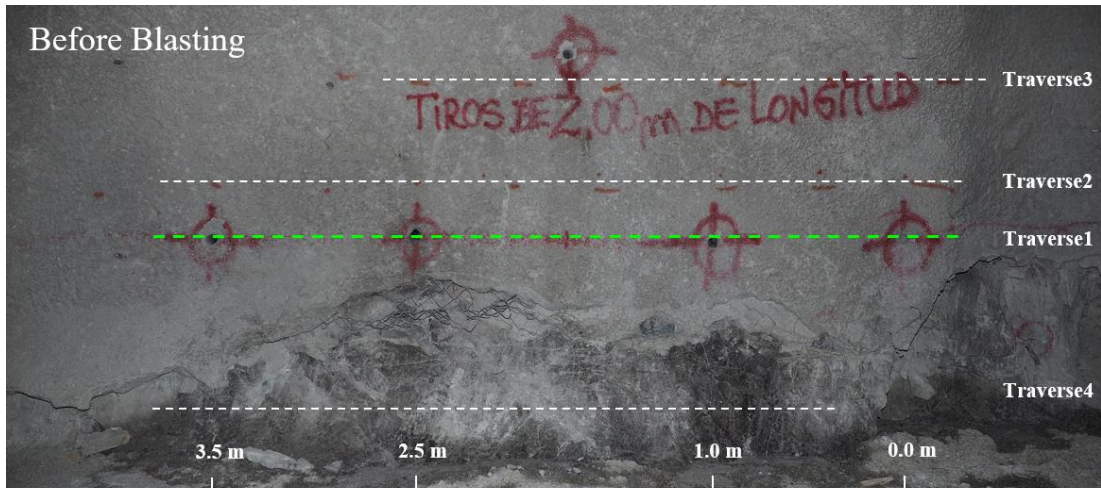
GPR Radargrams

Complete set of radargrams for all GPR surveys.

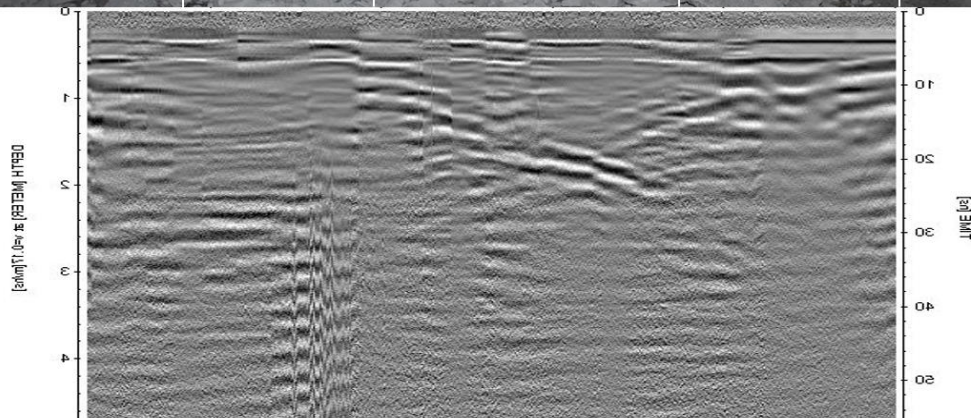
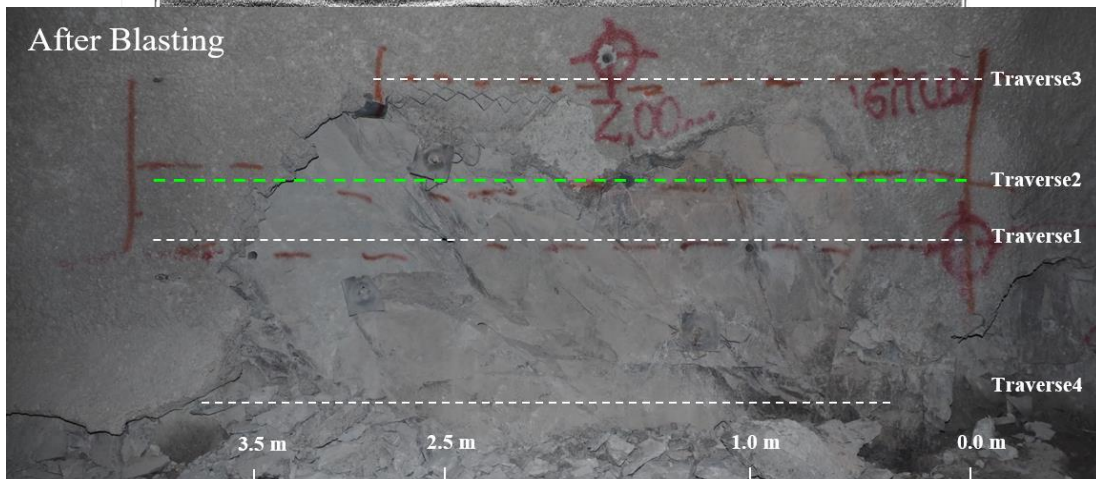
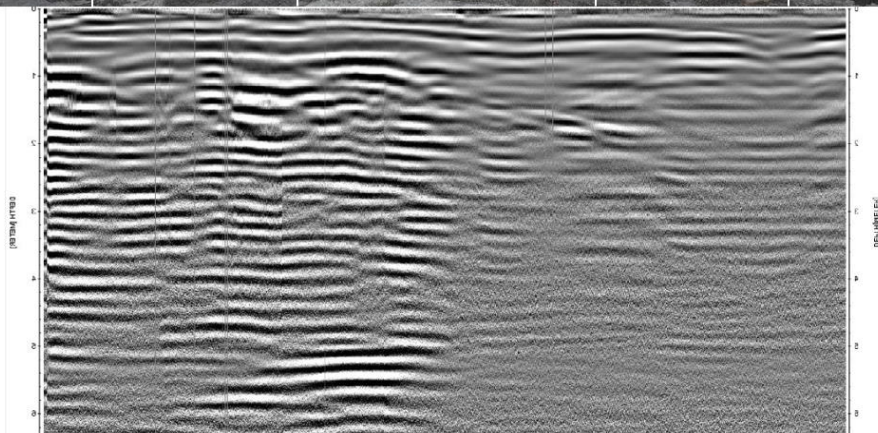
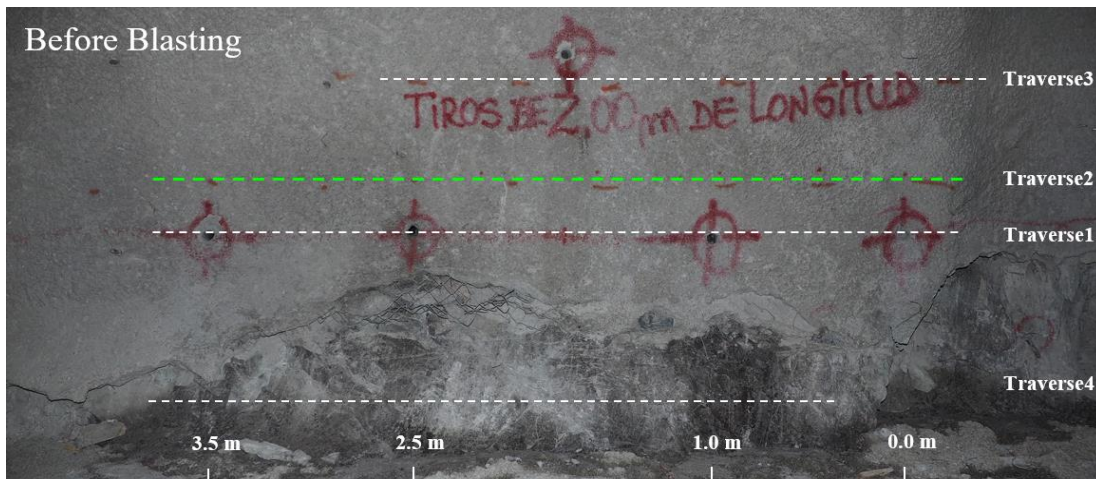
Borehole Radar – 10-120MHz



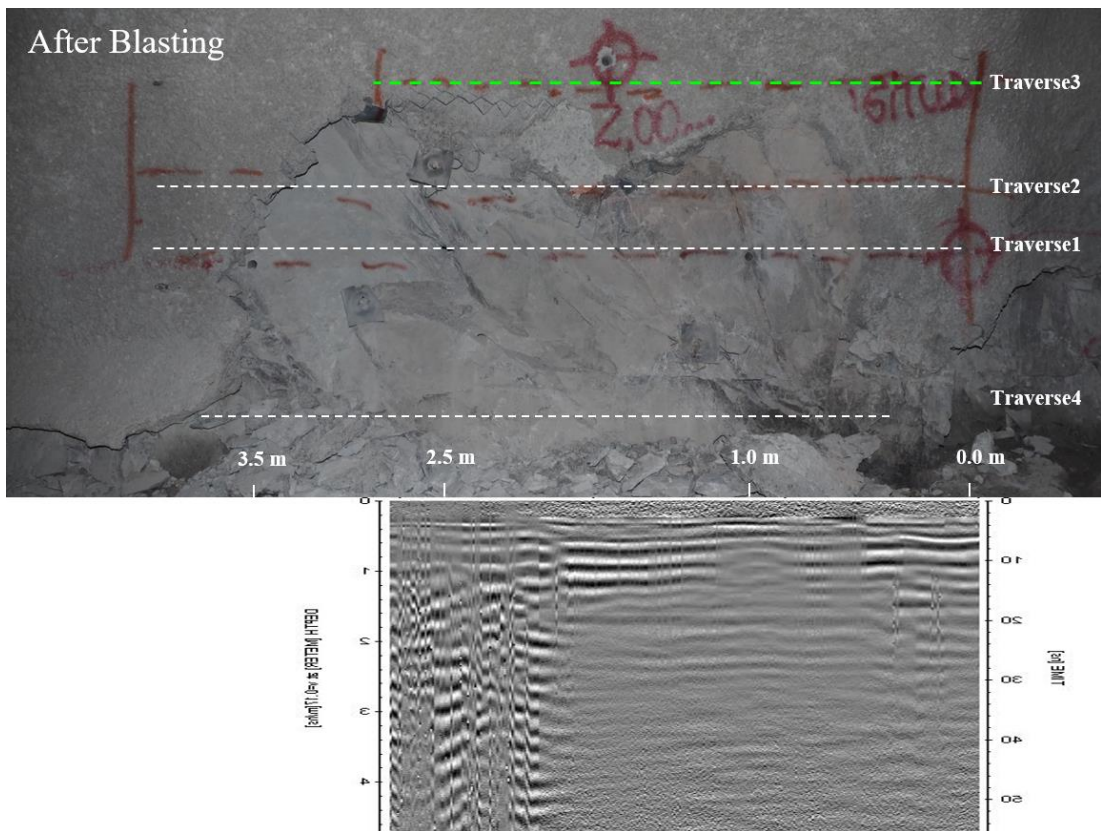
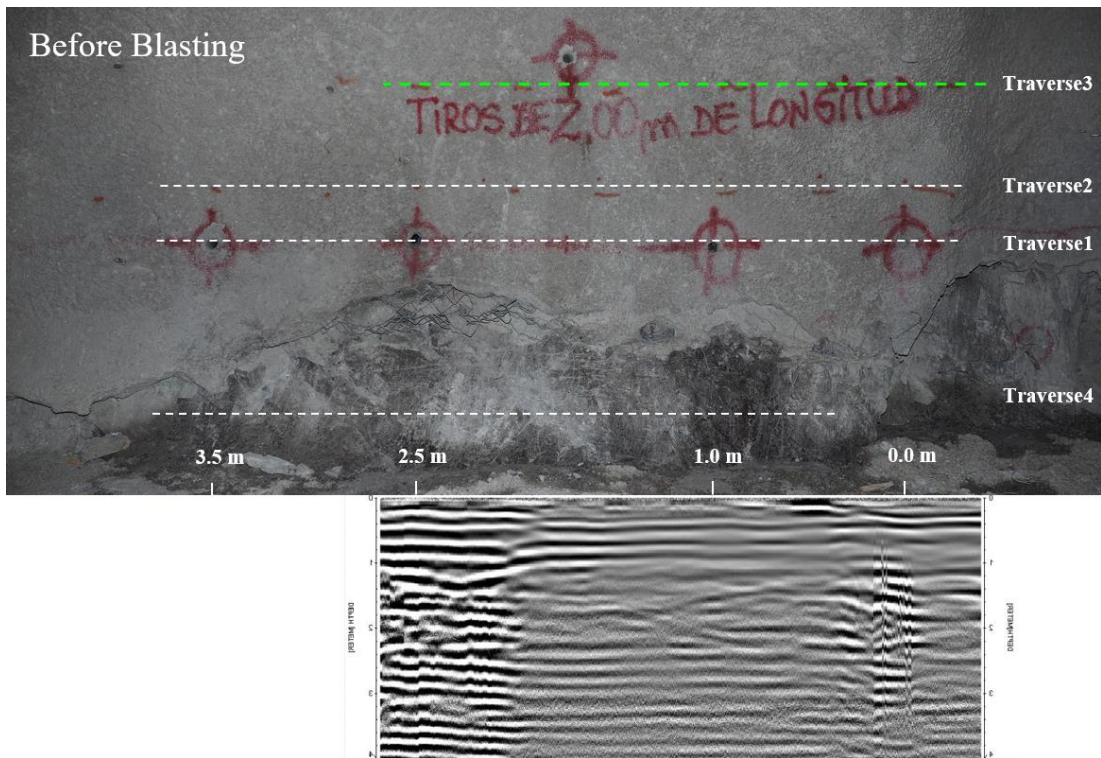
Surface Radar, Traverse 1 – 500MHz



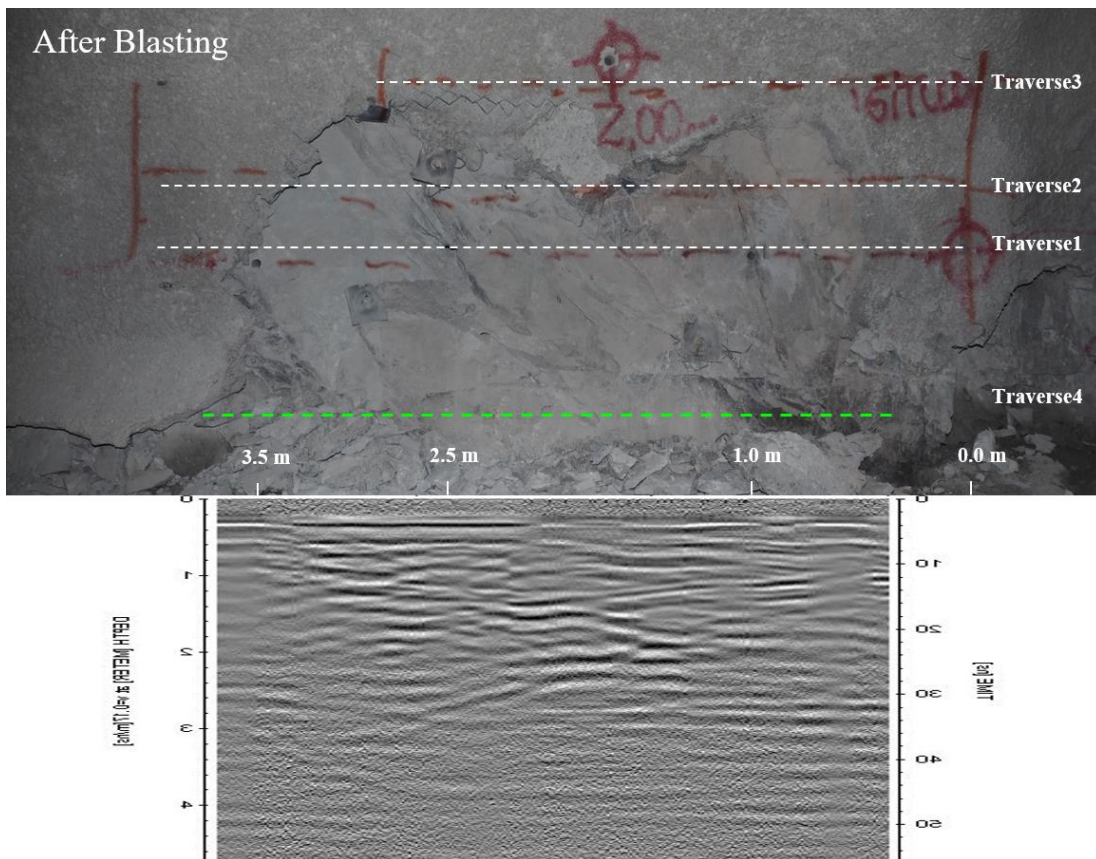
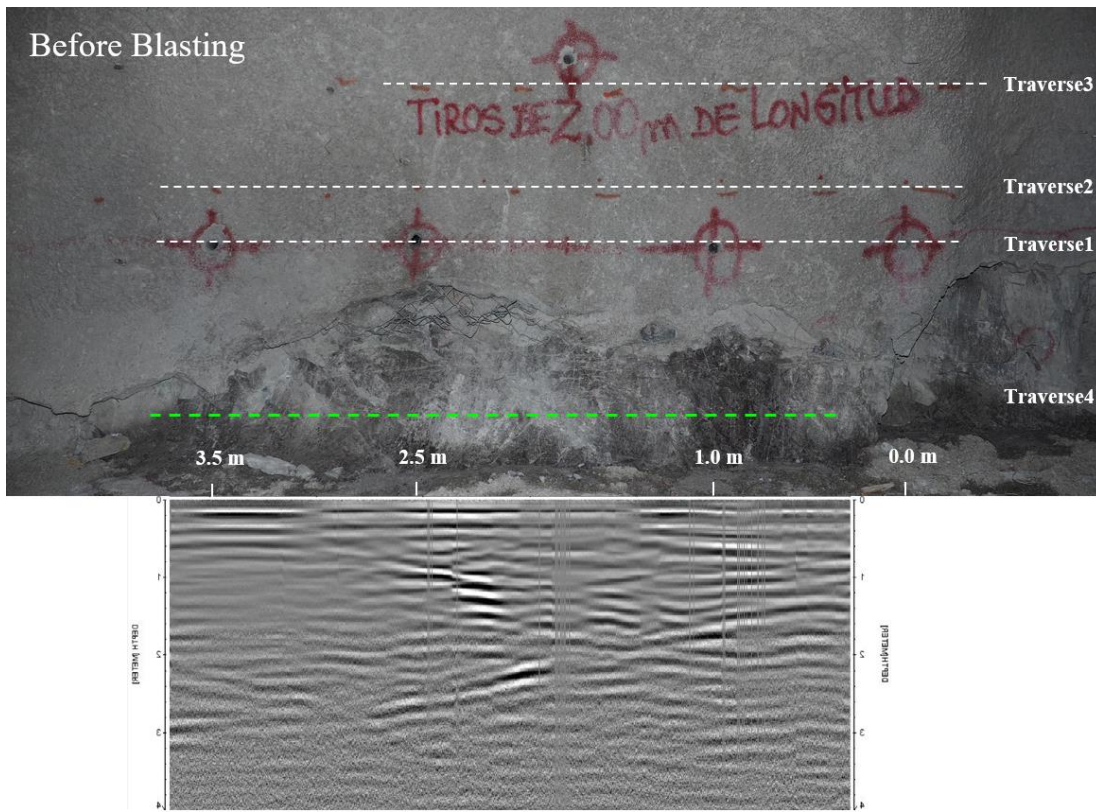
Surface Radar, Traverse 2 – 500MHz



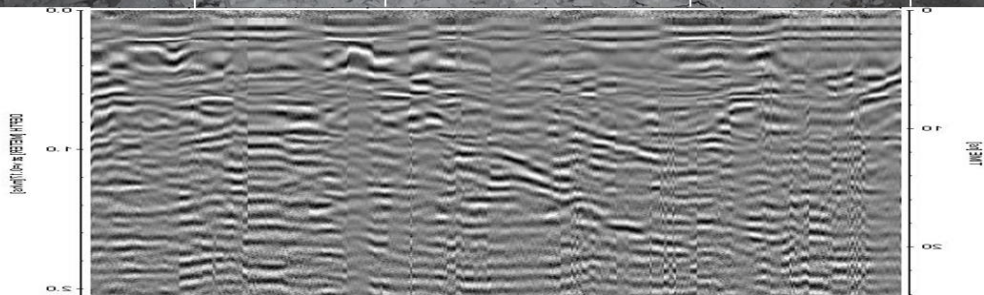
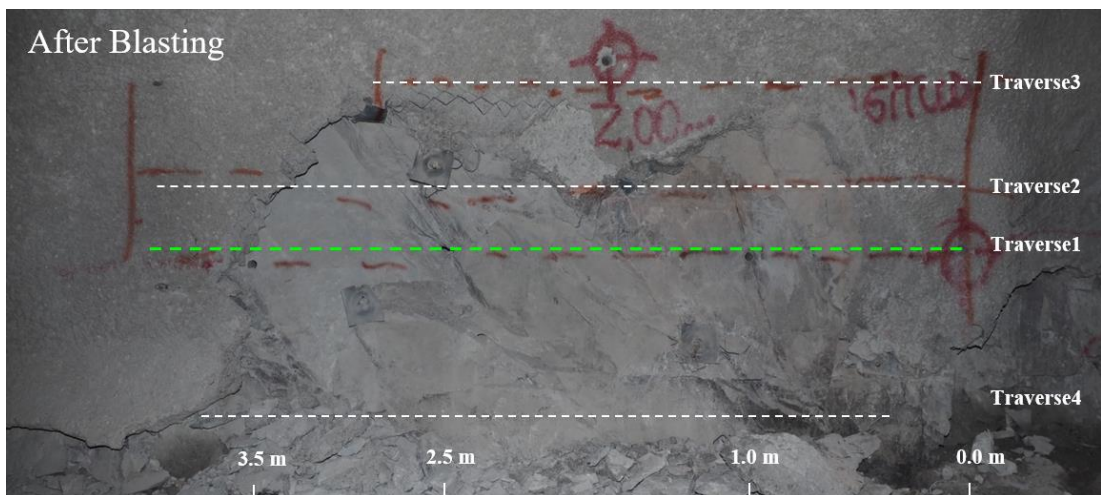
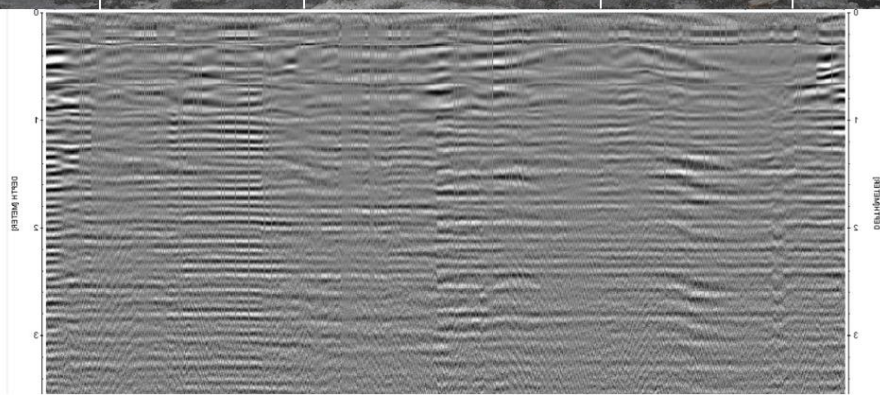
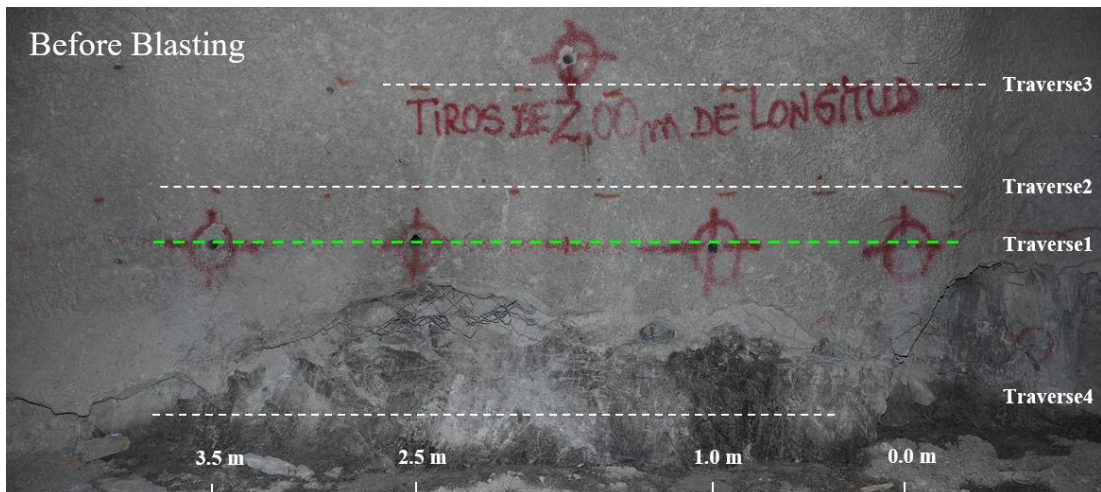
Surface Radar, Traverse 3 – 500MHz



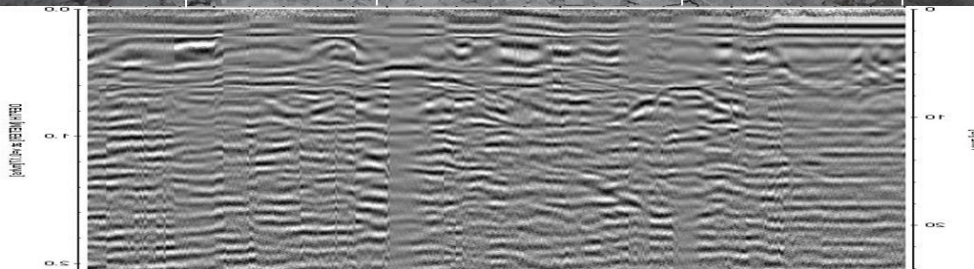
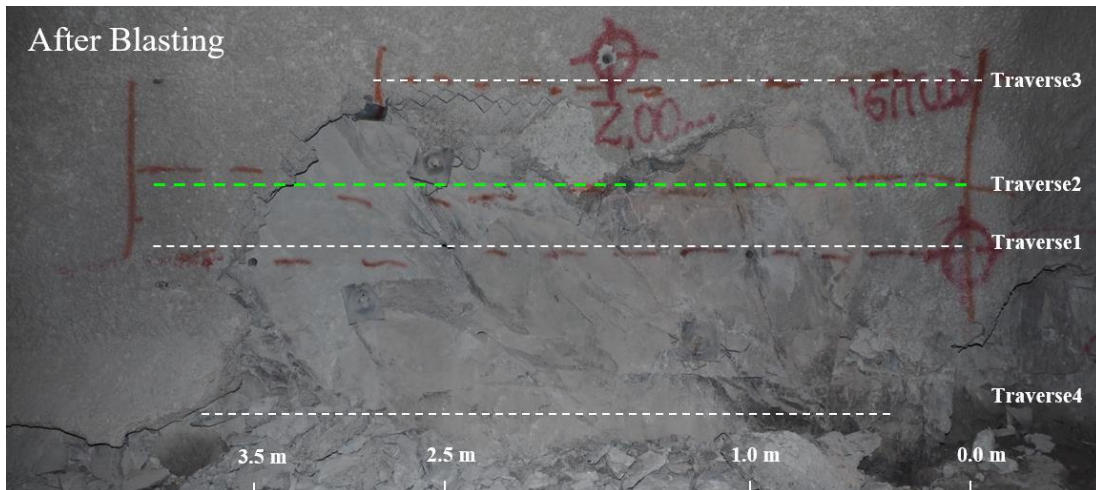
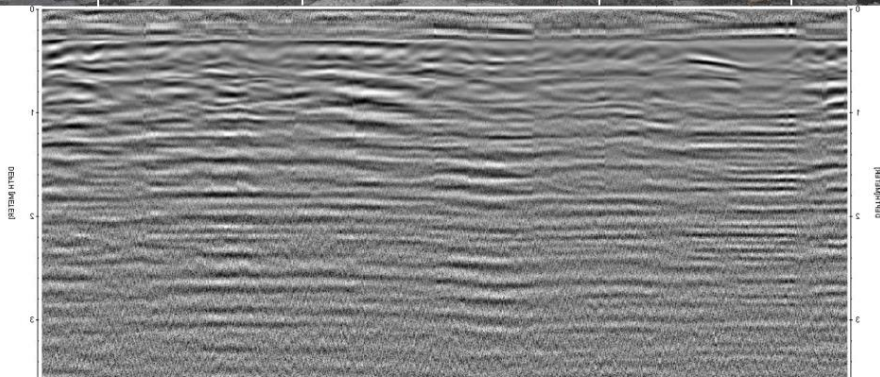
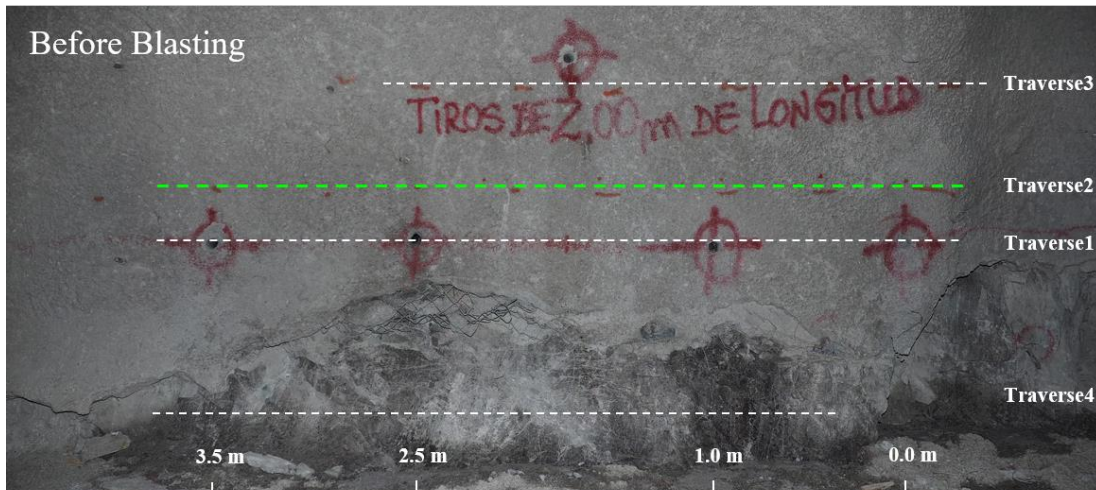
Surface Radar, Traverse 4 – 500MHz



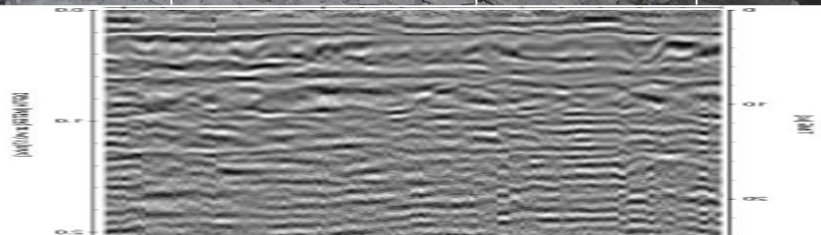
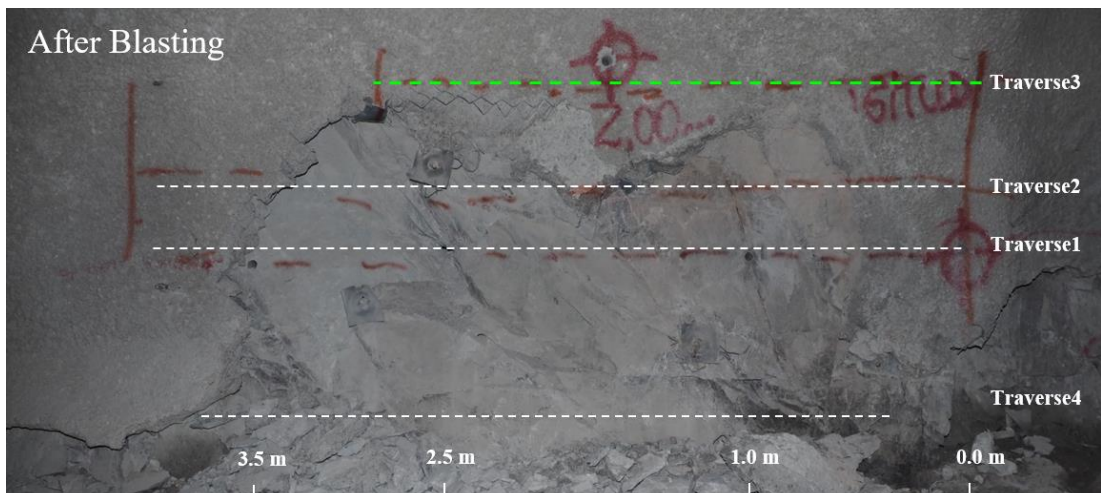
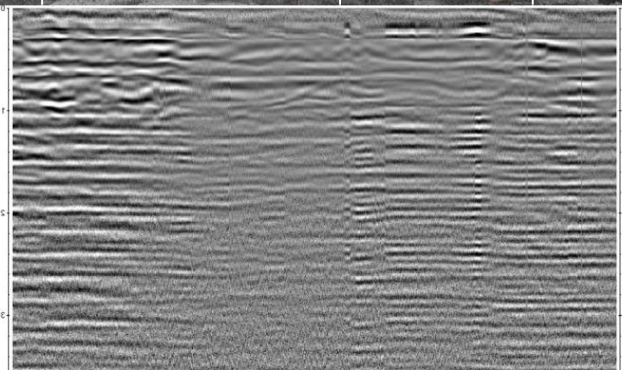
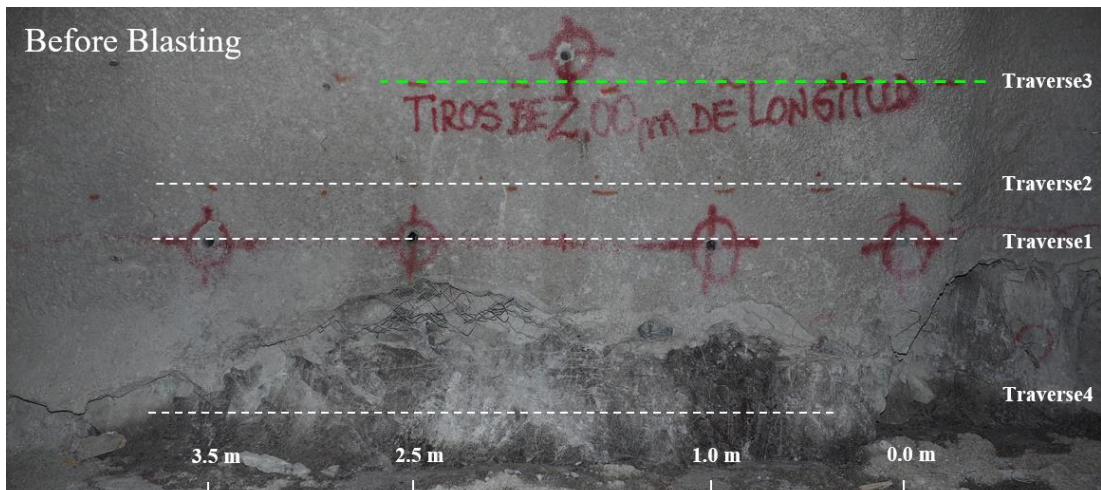
Surface Radar, Traverse 1 – 800MHz



Surface Radar, Traverse 2 – 800MHz



Surface Radar, Traverse 3 – 800MHz



Surface Radar, Traverse 4 – 800MHz

